AERODYNAMIC DESIGN OF AXIAL-FLOW COMPRESSORS

National Aeronautics and Space Administration
Washington, DC

1965

NASA SP-36

AERODYNAMIC DESIGN OF AXIAL-FLOW COMPRESSORS

REVISED

Prepared by members of the staff of Lewis Research Center, Cleveland, Ohio. Edited by Irving A. Johnsen and Robert O. Bullock. *This publication supersedes declassified NACA Memorandums E56B03, E56B03a, and E56B03b, 1956*

Scientific and Technical Information Division 1965
NATIONAL AERONAUTICS AND SPACE ADMINISTRATION
Washington, D.C.

N O T I C E

THIS DOCUMENT HAS BEEN REPRODUCED FROM THE BEST COPY FURNISHED US BY THE SPONSORING AGENCY. ALTHOUGH IT IS RECOGNIZED THAT CERTAIN PORTIONS ARE ILLEGIBLE, IT IS BEING RELEASED IN THE INTEREST OF MAKING AVAILABLE AS MUCH INFORMATION AS POSSIBLE.

FOREWORD

This work is based substantially on a three-volume Confidential Research Memorandum first issued by the National Advisory Committee for Aeronautics in 1956 and declassified in 1958 for release to the general public. The material, which was of a fundamental character, has been updated for the present edition in the light of subsequent developments in the field and has been carefully reexamined for current validity by members of the staff of the NASA Lewis Research Center, Cleveland, Ohio. It is now published for the first time in a single volume to meet continuing demand for the information and to make it readily available in convenient form to the engineering community both within and outside the National Aeronautics and Space Administration.

CONTENTS

DETAILED CONTENTS

CHAPTER I

OBJECTIVES AND SCOPE

By Irving A. Johnsen and Robert O. Bullock

This first chapter of a report on the aerodynamic design of axial-flow compressors presents the general objectives and scope of the over-all report. The basic problem of compressor design is outlined, and the approach generally taken to accomplish its solution is pointed out. The sixteen succeeding chapters in the report are summarized.

INTRODUCTION

Currently, the principal type of compressor being used in aircraft gas-turbine powerplants is the axial-flow compressor. Although some of the early turbojet engines incorporated the centrifugal compressor, the recent trend, particularly for high-speed and long-range applications, has been to the axial-flow type. This dominance is a result of the ability of the axial-flow compressor to satisfy the basic requirements of the aircraft gas turbine.

These basic requirements of compressors for aircraft gas-turbine application are well-known. In general, they include high efficiency, high air-flow capacity per unit frontal area, and high pressure ratio per stage. Because of the demand for rapid engine acceleration and for operation over a wide range of flight conditions, this high level of aerodynamic performance must be maintained over a wide range of speeds and flows. Physically, the compressor should have a minimum length and weight. The mechanical design should be simple, so as to reduce manufacturing time and cost. The resulting structure should be mechanically rugged and reliable.

It is the function of the compressor design system to provide compressors that will meet these requirements (in any given aircraft engine application). This design system should be accurate in order to minimize costly and time-consuming development. However, it should also be as straightforward and simple as possible, consistent with completeness and accuracy.

In an effort to provide the basic data for such a design system, and stimulated by the urgent need for improving gas-turbine engines, research on axial-flow compressors has been accelerated both in this country and abroad. The results of this research have been presented in numerous publications. In the majority of instances, each of these reports presents only a fragmentary bit of information which taken by itself may appear to have inconsequential value. Taken altogether and properly correlated, however, this information represents significant advances in that science of fluid mechanics which is pertinent to axial-flow compressors. It was the opinion of the NACA Subcommittee on Compressors and Turbines and others in the field that it would be appropriate to assimilate and correlate this information, and to present the results in a single report. Such a compilation should be of value to both neophytes and experienced designers of axial-flow compressors. Realizing the necessity and importance of a publication of this type, the NACA Lewis laboratory began reviewing and digesting existing data. This report represents the current status of this effort.

This chapter outlines the general objectives and the scope of the design report and indicates the chapters in which each specific phase of compressor design information is discussed. The general compressor design problem and the approach usually taken to accomplish its solution are indicated. The various aspects of compressor design to be treated in the over-all compendium are outlined, as well as the specific sequence in which they will be presented.

Because axial-flow compressors are most extensively used in the field of aircraft propulsion, and because this field requires the highest degree of excellence in compressor design and performance, the attention in this over-all report has been focused primarily on the problems pertinent to the axial-flow compressor of turbojet or turbo-

691-564 O-65-2

prop engines. The results presented, however, should be applicable to any class of axial-flow compressors.

DESCRIPTION OF AXIAL-FLOW COMPRESSOR

The basic function of a compressor is to utilize shaft work to increase the total or stagnation pressure of the air. A schematic drawing of an axial-flow compressor as installed in a turbojet engine is shown in figure 1. In the general configuration, the first row of blades (inlet guide vanes) imparts a rotation to the air to establish a specified velocity distribution ahead of the first rotor. The rotation of the air is then changed in the first rotor, and energy is thereby added in accordance with Euler's turbine equation. This energy is manifested as increases in total temperature and total pressure of air leaving the rotor. Usually accompanying these increases are increases in static pressure and in absolute velocity of the air. A part, or all, of the rotation is then removed in the following stator, thus converting velocity head to static pressure. This stator also sets up the distribution of airflow for the subsequent rotor. The air passes successively through rotors and stators in this manner to increase the total pressure of the air to the degree required in the gas-turbine engine cycle. As the air is compressed, the density of the air is increased and the annular flow area is reduced to correspond to the decreasing volume. This change in area may be accomplished by means of varying tip or hub diameter or both.

In this compression process certain losses are incurred that result in an increase in the entropy of the air. Thus, in passing through a compressor, the velocity, the pressure, the temperature, the density, the entropy, and the radius of a given particle of air are changed across each of the blade rows. The compressor design system must provide an adequate description of this flow process.

HISTORICAL BACKGROUND

The basic concepts of multistage axial-flow-compressor operation have been known for approximately 100 years, being presented to the French Academie des Sciences in 1853 by Tournaire (ref. 1). One of the earliest experimental axial-flow compressors (1884) was obtained by C. A. Parsons by running a multistage reaction-type turbine in reverse (ref. 2). Efficiencies for this type of unit were very low, primarily because the blading was not designed for the condition of a pressure rise in the direction of flow. Beginning at the turn of the century, a number of axial-flow compressors were built, in some cases with the blade design based on propeller theory. However, the efficiency of these units was still low (50 to 60

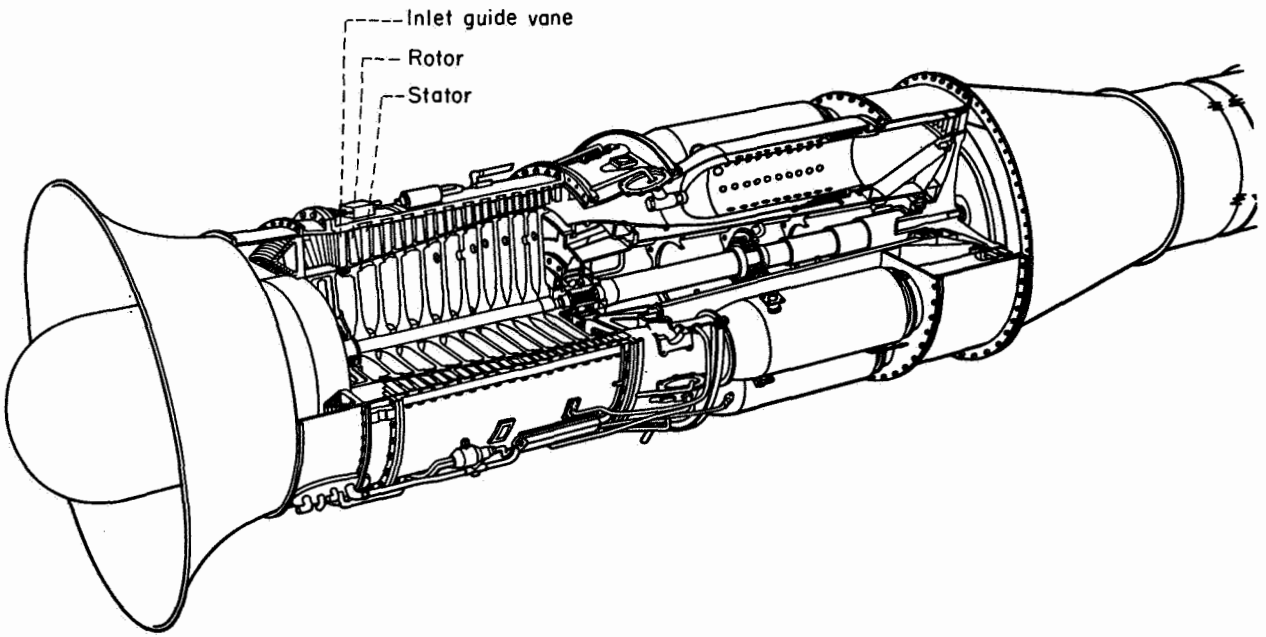

FIGURE 1.—Axial-flow compressor in turbojet engine.

percent). Further development of the axial-flow compressor was retarded by the lack of knowledge of the underlying principles of fluid mechanics.

The advances in aviation during the period of World War I and the rapidly developing background in fluid mechanics and aerodynamics gave new impetus to research on compressors. The performance of axial-flow compressors was considerably improved by the use of isolated-airfoil theory. As long as moderate pressure ratios per stage were desired, isolated-airfoil theory was quite capable of producing compressors with high efficiency (ref. 3, e.g.). Compressors of this class were used in such machinery as ventilating fans, air-conditioning units, and steam-generator fans.

Beginning in the middle 1930's, interest in the axial-flow compressor was greatly increased as the result of the quest for air superiority. Efficient superchargers were necessary for reciprocating engines in order to increase engine power output and obtain improved high-altitude aircraft performance. With the development of efficient compressor and turbine components, turbojet engines for aircraft also began receiving attention. In 1936 the Royal Aircraft Establishment in England began the development of axial-flow compressors for jet propulsion. A series of high-performance compressions was developed, culminating in the F.2 engine in 1941 (ref. 4). In Germany, research such as that reported in reference 5 ultimately resulted in the use of axial-flow compressors in the Jumo 004 and the B.M.W. 003 turbojet engines. In the United States, aerodynamic research results were applied to obtain high-performance axial-flow units such as that reported in reference 6. In the development of all these units, increased stage pressure ratios were sought by utilizing high blade cambers and closer blade spacings. Under these conditions the flow patterns about the blades began to affect each other, and it became apparent that the isolated-airfoil approach was inadequate. Aerodynamic theory was therefore developed specifically for the case of a lattice or cascade of airfoils. In addition to theoretical studies, systematic experimental investigations of the performance of airfoils in cascade were conducted to provide the required design information.

By 1945, compressors of high efficiency could be attained through the employment of certain principles in design and development (refs. 2 and 7). Since that time, considerable research has been directed at extending aerodynamic limits in an attempt to maximize compressor and gas-turbine performance. One of the major developments in this direction has been the successful extension of allowable relative inlet Mach numbers without accompanying sacrifices in efficiency (ref. 8). The subject of allowable blade loading, or blade surface diffusion, has also been attacked with a degree of success (ref. 9). Accompanying improvements such as these have been an increasing understanding of the physics of flow through axial-flow compressor blading, and corresponding improvements in techniques of aerodynamic design. Therefore, in view of the rapid advances in recent years, it appears appropriate to summarize the present state of the art of compressor design.

COMPRESSOR DESIGN APPROACH

The flow through the blading of an axial-flow compressor is an extremely complicated three-dimensional phenomenon. The flow in the compressor has strong gradients in the three physical dimensions (axial, radial, and circumferential), as well as time. Viscosity effects in compressors are significant and must be accounted for. In general, the design control problem becomes more critical as the level of compressor performance is increased. In order to provide ease of application, the compressor design system must reduce these complications and establish rational and usable procedures.

Because of the complexity of the problem, no complete solution is currently available for the three-dimensional, time-unsteady, viscous flow through an axial-flow compressor. In the main, designers have resolved these difficulties by making approximations that permit the use of two-dimensional techniques. These approximations are usually based on the assumptions of (1) blade-element flow and (2) axial symmetry.

The blade-element approach assumes that flow in the blade-to-blade or circumferential plane can be described by considering the flow about blade profiles formed by the intersection of a flow surface of revolution and the compressor blading (fig. 2).

Axial symmetry assumes that an average value can be utilized to represent the state of the air in the blade-to-blade plane. Equations describing

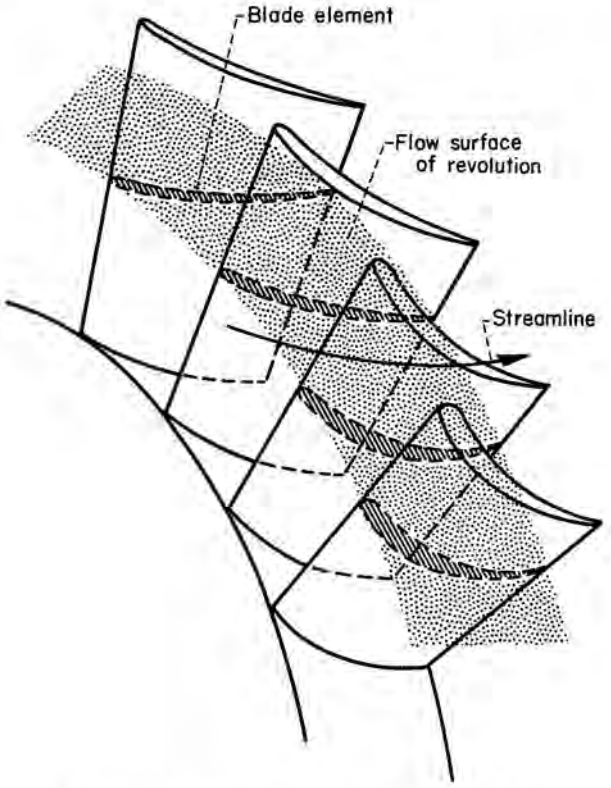

FIGURE 2.—Flow in circumferential plane.

radial variations of these average values may then be written for continuity, energy addition, and equilibrium in the hub-to-tip or meridional plane (fig. 3). In essence, then, a combination of two-dimensional solutions in the two principal planes (circumferential and meridional) is used to approximate the complete three-dimensional flow.

In applying this approach to compressor design, second-order corrections are used to account for three-dimensional variations from this simplified flow picture. Experimentally obtained data are utilized to account for effects such as those arising from viscosity, time-unsteady flow, and blade-row interactions. Empirical limits are established for such aerodynamic factors as maximum permissible Mach number and blade loading.

No rigorous theoretical justification of this simplified design approach can be made. It appears sufficient to state that comparatively excellent compressors can be and have been designed by simplified approaches such as these. In the absence of a more complete three-dimensional solution to the design problem, this quasi-three-dimensional approach has achieved general acceptance in the field.

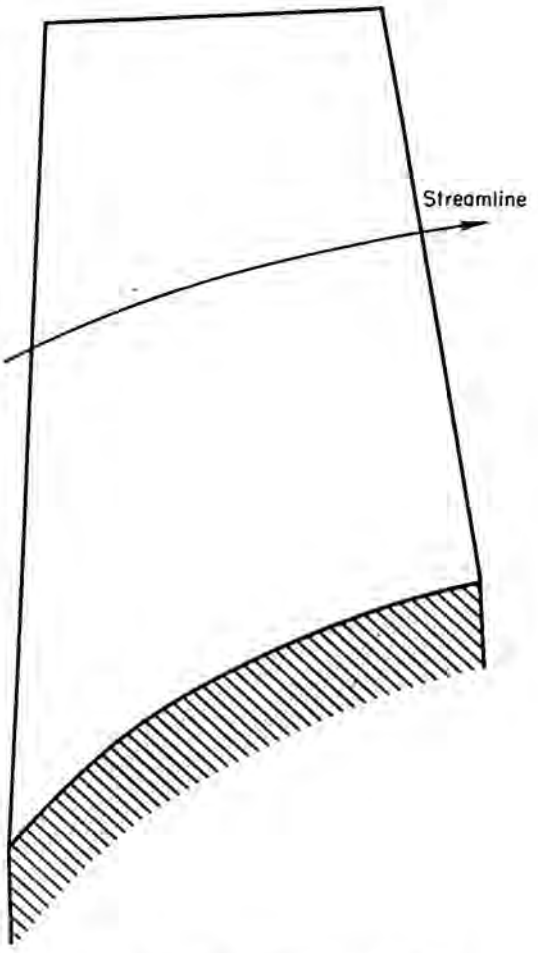

FIGURE 3.—Flow in meridional plane.

In practice, the aerodynamic design of a multistage axial-flow compressor may be considered to consist of three principal phases:

(1) Determination of stage-velocity diagrams for design-point operation
(2) Selection of stage blading
(3) Determination of off-design performance

The first part of the design involves the determination of the various air velocities and flow angles from hub to tip at the inlet and outlet of each blade row, to best achieve the design-point requirements of the compressor (i.e., pressure ratio and weight flow). The annular configuration (variation of hub and tip contours through the compressor) is determined. Next, the blading is selected

to satisfy the design-point velocity diagrams and to obtain high efficiency. Basically, this selection requires knowledge of loss and turning characteristics of compressor blade elements. With the compressor geometry established, the final step is the estimation of the performance characteristics of the compressor over a range of speeds and flows. In view of the importance of off-design operation, this procedure may be iterated so as to properly compromise design-point operation and the range requirements of the engine.

A more complete discussion of the compressor design system adopted for this over-all report is given in chapter III. The generalities of the concepts involved have been given merely to clarify the general approach to the problem.

OBJECTIVES OF DESIGN REPORT

The desire to provide a sound compressor design system has formed the basis for most research on axial-flow compressors. As a result, in this country and abroad, design concepts and design techniques have been established that will provide high-performance compressors. In general, these various design systems, although they may differ in the manner of handling details, utilize the same basic approach to the problem. This over-all report is therefore dedicated to summarizing and consolidating this existing design information. This effort may be considered to have three general objectives:

(1) To provide a single source of compressor design information, within which the major (representative) contributions in the literature are summarized

(2) To correlate and generalize compressor design data that are presently available only in many different forms and in widely scattered reports

(3) To indicate the most essential avenues for future research, since, in a summarization of this type, the missing elements (and their importance to the design system) become readily apparent

In this compressor report, an effort is made to present the data in a fundamental form. To illustrate the use of these data, a representative design procedure is utilized. However, since the design information is reduced to basic concepts, it can be fitted into any detailed design procedure

SCOPE OF DESIGN REPORT

Because of the complexity of the compressor design problem, even the simplest design system necessarily includes many different phases. In order to summarize existing compressor information as clearly and logically as possible, this over-all compendium is divided into chapters, each concerning a separate aspect of compressor design. The degree of completeness of these chapters varies greatly. In some cases, rather complete information is available and specific data are given that can be fitted into detailed compressor design procedures. In other cases, the information is not yet usable in design. The chapters may give only a qualitative picture of the problem, or they may merely indicate the direction of future research. Those aspects of the compressor problem which are considered pertinent are included, however, regardless of the present applicability of the information.

The following discussion provides an over-all perspective of the material covered in this compressor design compendium. Each chapter is summarized briefly, and the relation of each to the over-all report is indicated.

In order to provide proper emphasis in the design summarization, it is desirable to establish and evaluate the essential characteristics of compressors. Chapter II accomplishes this objective by first evaluating engine requirements with respect to airplane performance. These required engine characteristics are then used to identify essential requirements of the compressor. Characteristics of the compressor that are directly related to engine performance, such as compressor pressure ratio, efficiency, airflow capacity, diameter, length, and weight, are discussed. Other considerations in compressor design, including off-design requirements and the relation of the compressor to the inlet diffuser, combustor, turbine, and jet nozzle, are discussed. Compressor design objectives, based on these considerations, are summarized; these objectives indicate the direction in which compressor designs should proceed.

Chapter III provides a general description of the compressor design system that has been adopted for this report on the aerodynamic design of axial-flow compressors. The basic thermodynamic equations are given, and the simplifications commonly introduced to permit the solution of these equations are summarized. Representative ex-

perimental data are presented to justify these simplifications. This chapter thus provides a valid simplified model of the flow, which is the real basis of a design system. The elements of the resulting design system are then individually summarized; basic equations and techniques are given. Finally, the limitations of this adopted system are pointed out, and promising directions for future research are indicated.

The literature on plane potential flow in cascades is next reviewed (ch. IV). Many of the methods are evaluated within the bounds of limited available information on actual use. Some of the methods that have been used successfully are presented in detail to illustrate the mathematical techniques and to indicate the nature of the actual computation. The potential-flow theories discussed include both the design and analysis problems and consider both high-solidity and low-solidity applications. Compressibility is considered, but effects of viscosity are ignored.

A necessary adjunct to this subject of two-dimensional potential flow is the consideration of two-dimensional viscous effects, presented in chapter V. In this chapter, the problem of boundary-layer growth in the calculation of two-dimensional flow about compressor blade profiles is reviewed. A qualitative picture of boundary-layer behavior under various conditions of pressure gradient, Reynolds number, and turbulence normally encountered in two-dimensional blade-element flow is presented. Some typical methods for computing the growth and separation of laminar and turbulent boundary layers are presented. Analyses for determining the total-pressure loss and the defect in circulation are discussed.

Because of recognized limitations of theoretical calculations such as those presented in chapters IV and V, experimental blade-element data are generally required by the designer. The available experimental data obtained in two-dimensional cascade are surveyed and evaluated in chapter VI. These data (for conventional compressor blade sections) are presented in terms of significant parameters and are correlated at a reference incidence angle in the region of minimum loss. Variations of reference incidence angle, total-pressure loss, and deviation angle with cascade geometry, inlet Mach number, and Reynolds number are investigated. From the analysis and the correlations of the available data, rules and relations are evolved for the prediction of blade-profile performance. These relations are developed in simplified form readily applicable to compressor design procedures.

Because of modifying effects (wall boundary layers, three-dimensional flows, etc.), blade-element characteristics in an annular cascade can be expected to differ from those obtained in two-dimensional cascades. Chapter VII attempts to correlate and summarize available blade-element data as obtained from experimental tests in three-dimensional annular cascades (primarily rotors and stators of single-stage compressors). Data correlations at minimum loss are obtained for blade elements at various radial positions along the blade span. The correlations are compared with those obtained from two-dimensional cascades (ch. VI). Design rules and procedures are recommended, and sample calculation procedures are included to illustrate their use.

As discussed in the preceding paragraphs, chapters IV to VII deal with the two-dimensional blade-element aspect of design. The design problem in the meridional or hub-to-tip plane is introduced and summarized in chapter VIII. This meridional-plane solution presumes the existence of the required blade-element data to satisfy the velocity diagrams that are established. The general flow equations are presented, together with the simplifying assumptions used to determine the design velocity distribution and flow-passage configuration. Techniques for accounting for effects of viscosity (particularly for wall boundary layers) are described. The application of these design techniques is clarified by a sample stage design calculation.

Since procedures for determining the design velocity distribution and flow-passage configurations in the meridional plane are usually iterative, it is desirable to have approximate techniques available to expedite this process of stage design. The equations for radial equilibrium, continuity, energy addition, efficiency, and diffusion factor, as well as vector relations, are presented in chart form in chapter IX. An example of the application of the chart technique to stage design is included.

In addition to the design-point problem, the compressor designer is vitally concerned with

the prediction of compressor performance over a range of flow conditions and speeds. Three techniques for estimating compressor off-design performance are presented in chapter X. The first method establishes the blade-row and over-all performance by means of the integration of blade-element characteristics. The second method utilizes generalized stage performance curves and a stage-by-stage calculation. The third method, which is based on the over-all performance characteristics of existing compressors, may be used to estimate the complete performance map of a new compressor if the compressor design conditions are specified. The advantages and limitations of each of these three off-design analysis techniques are discussed.

Chapter XI is the first of a group of three concerning the unsteady compressor operation that arises when compressor blade elements stall. The field of compressor stall (rotating stall, individual blade stall, and stall flutter) is reviewed. The phenomenon of rotating stall is particularly emphasized. Rotating-stall theories proposed in the literature are reviewed. Experimental data obtained in both single-stage and multistage compressors are presented. The effects of this stalled operation on both aerodynamic performance and the associated problem of resonant blade vibrations are considered. Methods that might be used to alleviate the adverse blade vibrations due to rotating stall are discussed.

Another unsteady-flow phenomenon resulting from the stalling of compressor blade elements is compressor surge. It may be distinguished from the condition of rotating stall in that the net flow through the compressor and the compressor torque become time-unsteady. Some theoretical aspects of compressor surge are reviewed in chapter XII. A distinction is made between surge due to abrupt stall and surge due to progressive stall. Experimental observations of surge in compressor test facilities and in jet engines are summarized.

The blade-element approach to the prediction of off-design performance (as presented in ch. X) is essentially limited to the unstalled range of operation. Because of the complexity of the flow phenomenon when elements stall, no quantitative data are available to permit a precise and accurate synthesis of over-all compressor performance in this range. A prerequisite to the complete solution of this off-design problem, however, is a qualitative understanding of the phenomena involved. An analysis of the part-speed operating problem in high-pressure-ratio multistage axial-flow compressors is presented in chapter XIII. The principal problems considered are poor low-speed efficiency, multiple-valued performance characteristics at intermediate speeds, and poor intermediate-speed surge or stall-limit characteristics. The effects of compromising stage matching to favor part-speed operation are studied. Variable-geometry methods for improving part-speed performance are discussed.

The design approach adopted for this series of reports is based essentially on two-dimensional concepts, assuming axial symmetry and blade-element flow. With the continuing trend toward increasing requirements in compressors, however, a condition may be reached where this simplified approach may no longer be adequate. Therefore, chapter XIV is devoted to a summarization of those existing design methods and theories that extend beyond the simplified-radial-equilibrium axisymmetric design approach. Design procedures that attempt to remove the two-dimensionalizing restrictions are presented. Various phases of three-dimensional flow behavior that assume importance in design are discussed, including radial flows, the over-all aspects of secondary flows, and time-unsteady effects.

As pointed out in chapter XIV, secondary flows represent one of the most critical aspects of the three-dimensional design problems. In view of the growing importance of this subject, existing literature on secondary flows and three-dimensional boundary-layer behavior is summarized in chapter XV. The material is discussed from two aspects: (1) the principal results obtained from experimental studies, and (2) the theoretical treatment of the problem. The experimental phase is directed at providing a qualitative insight into the origin and nature of the observed secondary-flow phenomena. The theoretical results include a summary and evaluation of both the nonviscous and the boundary-layer approaches.

Errors in blade-element design can seriously affect over-all compressor performance, since these errors not only cause deviations from desired blade-row performance, but also alter the inlet conditions to the next blade row. The effects of

errors in the three basic blade-element design parameters (turning angle, total-pressure loss, and local specific mass flow) on compressor performance are analyzed in chapter XVI. The results are presented in the form of formulas and charts. These charts may be used to indicate those design types for which the design control problem is most critical and to estimate the limits in performance that can be anticipated for design data of a given accuracy. Typical design cases are considered, and significant trends are discussed. A second phase of this chapter concerns accuracy of experimental measurements. Proper interpretation and analysis of experimental data require that measurements be precise. This chapter presents a systematic evaluation of the effect of measurement errors on the measured compressor performance. These results, which are also presented in chart form, can be used to estimate the required accuracy of instrumentation.

One of the most important aspects of gas-turbine engine design, particularly for applications where high power output and wide operating range are required, is that of compressor and turbine matching. The existing literature on compressor and turbine matching techniques, which can be used to compromise properly the aerodynamic design of the compressor and turbine to achieve the best over-all engine, is summarized in chapter XVII. Both single-spool and two-spool engines are considered. For equilibrium operation, the basic matching technique, which involves the superposition of compressor and turbine maps, is presented, as well as a simplified and more approximate method. In addition, a simple technique for establishing an engine operating line on a compressor map is reviewed. An available technique for matching during transient operation is also discussed. The use of this method permits engine acceleration characteristics and acceleration time to be approximated for either single-spool or two-spool engines.

CONCLUDING REMARKS

The subsequent chapters in this report summarize available information on the aerodynamic design of axial-flow compressors. It is recognized that many techniques have been proposed for describing the flow in an axial-flow compressor and for accounting for the complex flow phenomena that are encountered. Obviously, consideration of all of these techniques is impossible. However, the available literature in the field is reviewed extensively, and the material presented is considered to be representative and pertinent. In general, the attempt is made to present the information in its most basic form, so that it may be fitted into any generalized design system.

Because of the many difficult and involved problems associated with compressor design, very few of these underlying problems are treated with finality. In some cases, the problem is only partly defined. Nevertheless, many successful designs (by present standards, at least) have been made with the use of this information. The voids in the information clearly indicate the research problems for the future.

CHAPTER II

COMPRESSOR DESIGN REQUIREMENTS

By Robert O. Bullock and Ernst I. Prasse

The important requirements of axial-flow compressors for aircraft gas-turbine engines and the reasons for these requirements are reviewed. Attention is first directed to the over-all requirements of the engines themselves; then the desired properties of compressors are examined.

Cycle analyses of the turbojet and turboprop engines are presented to illustrate the effects of compressor pressure ratio and efficiency on engine performance. The significance of high flow capacity in compressors is indicated. The compromises in compressor design dictated by aerodynamic design limitations in the compressor itself as well as aerodynamic and structural design limitations in other components are investigated. The pertinent off-design problems resulting from the necessity of matching the compressor with the inlet and with the turbine over a range of flight conditions are enumerated, and some available methods of coping with these problems are discussed. From these studies, the basic objectives of a compressor design system are evolved.

INTRODUCTION

The information presented in this report is primarily concerned with the problems encountered in designing axial-flow compressors for gas-turbine engines used in aircraft propulsion. In order to enumerate these problems, the important characteristics required of such compressors should be defined. Reviewing these requirements is the object of this chapter.

A compressor, being only one component of an engine, must have characteristics consonant with those required of the engine. The requirements of an engine, in turn, are dictated by the demands of the airplane. Before the desired properties of a compressor can be given, therefore, the interrelations between an airplane and its engines must be examined. Similarly, the important compressor requirements are found from a study of the interrelations between the engine and its compressor. In the strictest sense, all these interrelations are obtained only after a detailed study of many airplane-engine designs and flight paths. Fortunately, however, broad design objectives may be indicated by a more cursory analysis such as that used in the present report.

What an airplane requires of its engine is viewed from generalized flight situations to obtain the broad objectives for engine design. The important engine variables such as specific weight, specific fuel consumption, and thrust per unit of frontal area are thus defined. The relative importance of these engine performance variables is then examined with regard to the flight conditions to which the airplane will be subjected.

Compressor characteristics having a direct bearing on engine performance are then discussed. Attention is given to compressor efficiency, pressure ratio, and flow capacity and their quantitative effects on specific fuel consumption, size and airflow capacity of engine components downstream of the compressor, and turbine aerodynamic limits. Other important considerations in compressor design are discussed, including the mutual problems of compressor, turbine, combustor, and inlet diffuser, for both design and off-design conditions. Exact quantitative relations are developed whenever this can readily be done; otherwise, qualitative results are presented and representative examples are used to underline the trends.

Present compressor design objectives, based on the requirements indicated by the analyses of this report, are summarized. These objectives indicate the direction in which compressor designs should proceed.

SYMBOLS

The following symbols are used in this chapter:

A	area, sq ft
B	engine-weight parameter (eq. (7b))

C_{fr}	coefficient of skin friction
C_j	jet-nozzle velocity coefficient
C_m	coefficient of maneuver
c_p	specific heat at constant pressure, Btu/(lb)(°R)
D	diffusion factor (eq. (29))
$\mathcal{D}$	diameter
d	drag, lb
E	pressure-ratio parameter (eq. (20))
$eshp$	equivalent shaft power, hp
F	thrust, lb
$F(sfc)$	thrust specific fuel consumption, lb/(hr)(lb)
f	fuel-air ratio
G	pressure-ratio parameter (eq. (16))
g	acceleration due to gravity, 32.17 ft/sec^2
H	total or stagnation enthalpy, Btu/lb
H_f	fuel heating value, Btu/lb
J	mechanical equivalent of heat, 778.2 ft-lb/Btu
k	fraction of gross airplane weight taken by structural weight and useful load, $(W_{st}+W_u)/W_{g,i}$
L	lift, lb
l	length, ft
M	Mach number
N	rotational speed, rpm
P	total or stagnation pressure, lb/sq ft
p	static or stream pressure, lb/sq ft
Q	pressure-ratio parameter (eq. (13))
R	gas constant, 53.35 ft-lb/(lb)(°R)
$\mathcal{R}$	range of flight, ft
r	radius
sfc	power specific fuel consumption, lb/hp-hr
T	total or stagnation temperature, °R
U	rotor speed, ft/sec
V	air velocity, ft/sec
W	weight
w	weight flow, lb/sec
α	airplane acceleration in direction of flight, ft/sec^2
β	air angle, angle between air velocity and z-axis, deg
Γ	turbine blade metal density, lb/cu ft or lb/cu in.
γ	ratio of specific heats
δ	ratio of total pressure to NASA standard sea-level pressure of 2116 lb/sq ft
ϵ	angle between thrust axis and direction of flight, deg
η	efficiency
θ	ratio of total temperature to NASA standard sea-level temperature of 518.7° R
ρ	density, lb/cu ft
ρV	air weight flow per unit flow area, (lb/sec)/sq ft
σ	solidity, ratio of chord to spacing
τ	turbine blade centrifugal stress, psf or psi
ψ	turbine blade taper factor
ω	angular velocity of rotor, radians/sec

Subscripts:

ad	adiabatic
B	combustor
C	compressor
d	design value
e	engine
eff	effective
F	frontal
f	fuel
g	gross
h	hub
i	airplane takeoff condition or that after refueling
j	jet nozzle
M	mechanical power
min	minimum
n	nacelle
$n\text{-}fr$	nacelle-friction
PT	power turbine
pr	propulsive
ref	reference
sl	NASA standard sea-level conditions
st	structure
T	turbine
t	tip
u	useful
w	wetted
x	arbitrary engine station
z	axial direction

Stations in engines (fig. 9):

0	free stream
1	compressor inlet
2	combustor inlet
3	turbine inlet
4	turbine discharge for turbojet engine
5	turbine discharge for turboprop engine
6	exhaust-nozzle exit

Superscripts:

conditions relative to rotor blade

— denotes average over flight path

EFFECTS OF ENGINE CHARACTERISTICS ON AIRPLANE PERFORMANCE

The suitability of an engine for aircraft propulsion is frequently judged by three quantities—the specific weight, the thrust specific fuel consumption, and the thrust per unit frontal area. While it is patently desirable for engines to have low values of the first two quantities and high values of the third, it frequently happens that the best possible values of all these quantities cannot be obtained simultaneously. Some important requirements for low thrust specific fuel consumption, for example, are incompatible with those for either low specific weight or high thrust per unit of frontal area. Moreover, some of the requirements for low specific weight may be different from those for high thrust per unit frontal area. Thus, the design of an engine and its components is always a compromise in which one feature of engine performance is favored over another. The direction and degree of the compromise depend, among other things, on the design and the intended use of the airplane.

The best compromise is, of course, pinpointed only after detailed studies of a number of definite airplane and engine designs. On the other hand, some basic knowledge of the way the design and mission of an airplane affect these compromises may be obtained from a more general study. Some of the over-all results outlined by such a study are discussed in this section. The significance of specific weight is first examined. The role of thrust specific fuel consumption is then reviewed, and the relative importance of specific weight and thrust specific fuel consumption is noted. Some effects of the drag associated with the engine installation are then indicated. Finally, other engine features that affect the design and performance of an airplane are discussed.

ENGINE WEIGHT

Specific engine weight is one of the important factors determining how much of the load-carrying capacity of an airplane is consumed by engine weight. Since specific engine weight is defined by W_e/F, the required ratio of engine weight to airplane gross weight for any specific flight condition is

$$\frac{W_e}{W_g}=\left(\frac{W_e}{F}\right)\left(\frac{F}{W_g}\right) \tag{1}$$

where F in W_e/F represents the thrust the engine can produce, and the same symbol in F/W_g stands for the thrust demanded by the airplane. The two thrusts, of course, must always be equal. Both the thrust produced by the engine and the thrust demanded by the airplane vary with flight altitude and speed.

Since the thrust of a given engine varies with altitude and speed, the value of W_e/F must also vary. An example of this variation in a turbojet engine is shown in figure 4, where specific weight is plotted against altitude for flight Mach numbers of 0.8 and 2.0. A point is also shown for corresponding sea-level static conditions. For the purpose of generalization, the specific weights are divided by the specific weight for a flight Mach number of 0.8 at sea level. It may be noted that specific weight is approximately doubled for every 15,000-foot increase in altitude in the stratosphere. This variation is inversely proportional to the change in air density. Increasing

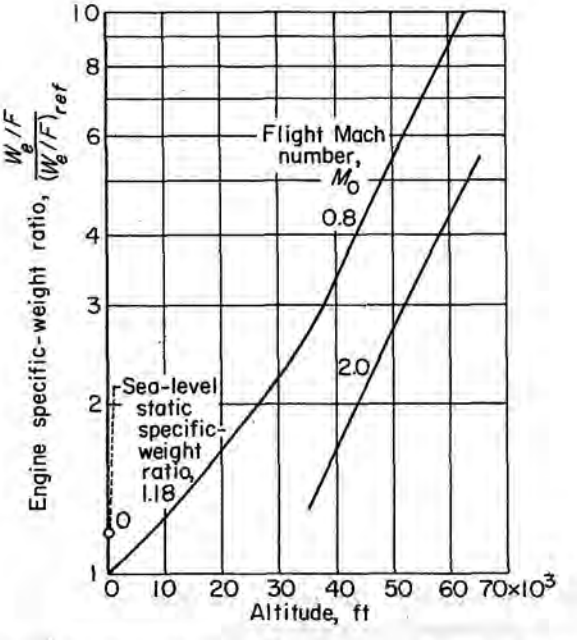

FIGURE 4.—Typical variation of turbojet-engine specific weight with altitude at constant engine mechanical speed. Reference condition: Altitude, sea level; flight Mach number, 0.8.

the flight Mach number from 0.8 to 2.0 also increases the density of the air in the engine because of the effects of ram. In this example, the specific weight is about halved for this increase in flight Mach number.

The curve for the flight Mach number of 0.8 is also more or less applicable to turboprop engines. The sea-level static value of specific weight for these engines, however, is usually much lower than that for the jet engine; its value depends as much on the selection of the propeller as on the engine itself.

The term F/W_g, which represents the thrust required for a unit gross weight, is a function of a number of variables. The trends may be conveniently studied by the following procedure: At any point in flight, the thrust required of the engines is determined by the relations

$$F\cos\epsilon = d + W_g\frac{\alpha}{g}$$

$$L = C_m W_g - F\sin\epsilon$$

where ϵ is the angle between the thrust axis and the direction of flight, d is the dissipative drag force, $W_g\alpha/g$ is the component of body force in the direction of flight, and $C_m W_g$ is the component of body force perpendicular to the direction of flight. These expressions may be combined to give

$$\frac{C_m + \frac{L}{d}\frac{\alpha}{g}}{\frac{L}{d}\cos\epsilon + \sin\epsilon} = \frac{F}{W_g} \tag{2}$$

where L/d is the ratio of the aerodynamic lifting force to the drag force. When the airplane is in level flight and moving with a constant velocity, then $C_m=1$ and $\alpha=0$. Moreover, when the thrust axis is along the direction of flight, then $\epsilon=0$. Under these conditions, equation (2) becomes

$$\frac{F}{W_g} = \frac{1}{\frac{L}{d}} \tag{2a}$$

For the sake of simplicity, the complete form of equation (2) is expressed by analogy as

$$\frac{F}{W_g} = \frac{1}{\left(\frac{L}{d}\right)_{eff}} \tag{2b}$$

Because $(L/d)_{eff}$ is a function of a large number of variables, its trends cannot be generally plotted as a function of altitude and flight Mach number alone without leaving some misleading impressions. The trends described in the following paragraphs may be noted, however.

As the design altitude of the airplane increases, the maximum attainable value of L/d tends to increase. This trend results from increases in the aspect ratio of the wings and from the fact that the fuselage drag becomes a smaller portion of the total drag. High values of L/d may be obtained with subsonic airplanes during level flight. Values in the neighborhood of 20 are not uncommon, and values approaching 30 have been sought. Airplanes designed for high values of L/d with subsonic flight, however, would have very poor values of L/d at supersonic flight. In airplanes designed exclusively for supersonic flight, values of L/d approaching 6 have been observed in some model tests, and reasonably higher values might be obtained in the future. Again, the value of L/d may increase with altitude. In general, an airplane designed exclusively for supersonic flight would have undesirably low values of L/d at subsonic speeds.

When reasonably good performance is desired at both subsonic and supersonic speeds, the attainable values of L/d must be compromised for both regimes. For subsonic speeds, the value of L/d may be expected to be slightly more than 10. The corresponding value of L/d for supersonic flight may be of the order of 3 or lower. The possible increase in L/d with design altitude is again noted for both regimes.

At takeoff conditions, the value of $(L/d)_{eff}$ can become very low for all types of airplanes. With vertical takeoff, the thrust of the engine must overcome the acceleration due to gravity; the value of F/W_g in equation (2b) must then be greater than unity. The magnitude of $(L/d)_{eff}$ is therefore less than unity. Less stringent takeoff conditions permit the value of $(L/d)_{eff}$ to be somewhat improved. For an ordinary takeoff, the value of $(L/d)_{eff}$ may be of the order of 4.

A high-maneuverability requirement also reduces the value of $(L/d)_{eff}$. A 2g turn, for example, makes the value of C_m equal 2 in equation (2), and $(L/d)_{eff}$ could be reduced by more than 50 percent.

A study of the combined effects of specific engine weight and $(L/d)_{eff}$ on W_e/W_g may now be made by combining equations (1) and (2b) to give

$$\frac{W_e}{W_g}=\frac{\frac{W_e}{F}}{\left(\frac{L}{d}\right)_{eff}} \tag{1a}$$

Since the gross weight at any instant equals the initial weight minus the fuel expended ($W_g=W_{g,i}-\Delta W_f$), equation (1a) may also be written as

$$\frac{W_e}{W_{g,i}}=\frac{\frac{W_e}{F}}{\left(\frac{L}{d}\right)_{eff}}\left(1-\frac{\Delta W_f}{W_{f,i}}\frac{W_{f,i}}{W_{g,i}}\right) \tag{1b}$$

The initial gross weight of the airplane is the sum of the structural weight, useful weight or payload, initial fuel weight, and engine weight:

$$W_{g,i}=W_{st}+W_u+W_{f,i}+W_e \tag{3}$$

Using this equation to eliminate $W_{g,i}$ in the right side of equation (1b) (setting $W_{st}+W_u=kW_{g,i}$) gives

$$\frac{W_e}{W_{g,i}}=\frac{\frac{W_e}{F}}{\left(\frac{L}{d}\right)_{eff}}\left[\frac{1-\frac{\Delta W_f}{W_{f,i}}(1-k)}{1-\frac{\Delta W_f}{W_{f,i}}\frac{\frac{W_e}{F}}{\left(\frac{L}{d}\right)_{eff}}}\right] \tag{4}$$

Some trends of this relation are shown in figure 5, where $W_e/W_{g,i}$ is plotted against $(W_e/F)/(L/d)_{eff}$. One of the curves of this figure applies to conditions at or shortly after takeoff, where $\Delta W_f/W_{f,i}\approx 0$ and $W_e/W_{g,i}\approx(W_e/F)/(L/d)_{eff}$. The other four curves apply to the case where $\Delta W_f/W_{f,i}=0.4$; that is, after 40 percent of the fuel weight has been expended. These curves successively represent the condition where $k=(W_{st}+W_u)/W_{g,i}=0.3$, 0.4, 0.5, and 0.6.

For conditions at or shortly after takeoff, the magnitude of $W_e/W_{g,i}$ is independent of k and varies linearly with $(W_e/F)/(L/d)_{eff}$. When $\Delta W_f/W_{f,i}=0.4$, the assumption that $W_e/W_{g,i}$ is proportional to $(W_e/F)/(L/d)_{eff}$ is again a good approximation as long as $(W_e/F)/(L/d)_{eff}$ is 0.2 or smaller for $k=0.6$. Compared with the takeoff value of $W_e/W_{g,i}$, however, $W_e/W_{g,i}$ is reduced about 12 percent for $k=0.6$ and 30 percent for $k=0.3$. For the same critical flight conditions (a given value of $(W_e/F)/(L/d)_{eff}$), the required engine weight decreases as $\Delta W_f/W_{f,i}$ is increased and as k is decreased. Near the end of the flight, equation (4) becomes

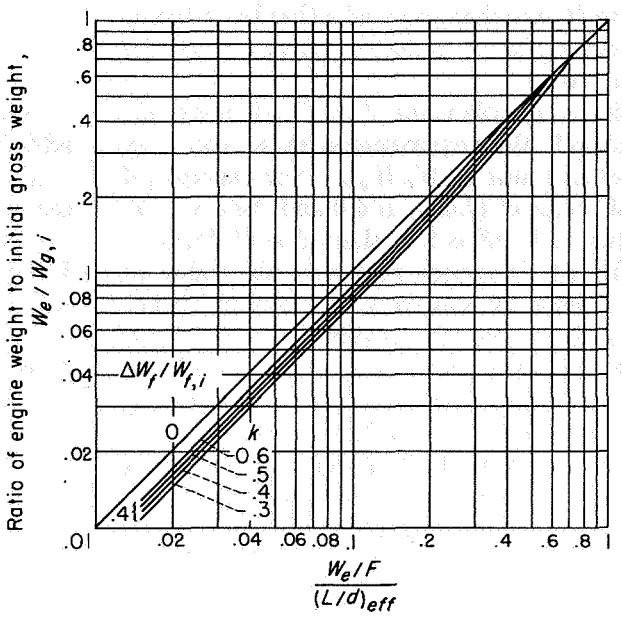

FIGURE 5.—Graphical representation of equation (4).

$$\frac{W_e}{W_{g,i}}=\frac{\frac{W_e}{F}}{\left(\frac{L}{d}\right)_{eff}}\frac{k}{1-\frac{\frac{W_e}{F}}{\left(\frac{L}{d}\right)_{eff}}}$$

For reasonably small values of $(W_e/F)/(L/d)_{eff}$, the required value of $W_e/W_{g,i}$ is then approximately k times its required value at takeoff for the same magnitude of $(W_e/F)/(L/d)_{eff}$.

The value of $W_e/W_{g,i}$ required in an airplane is determined by the values of W_e/F, $(L/d)_{eff}$, and $\Delta W_f/W_{f,i}$ at the critical flight condition. The value of the right side of equation (4) here is the maximum encountered for the flight. At all other flight conditions for the aircraft, the value of $W_e/W_{g,i}$ is, of course, the same, and the requirements

of equation (4) are then satisfied either by reducing F by throttling or by reducing $(L/d)_{eff}$ below its attainable value.

Since the attainable value of $(L/d)_{eff}$ is relatively low at takeoff, the requirements at takeoff may determine the value of $W_e/W_{g,t}$. For example, if the takeoff value of $(L/d)_{eff}$ is 4.0 and the sea-level static value of W_e/F is 0.4, the value of $W_e/W_{g,t}$ is 0.10 (fig. 5). Suppose now that the value of $(L/d)_{eff}$ becomes 20 shortly after takeoff. Since $W_e/W_{g,t}$ is unchanged, the required value of W_e/F is 2.0 (fig. 5). The value of F must be reduced either by throttling the engine or by increasing the flight altitude. The value of W_e/F of 2.0 corresponds to a value of $(W_e/F)/(W_e/F)_{ref}$ of about 5.9 (fig. 4). For the flight Mach number of 0.8, the ordinate of figure 4 is 5.9 at the altitude of about 52,000 feet. As long as the flight is below this altitude, the takeoff condition would govern the selection of engine weight in this particular example. Suppose, however, that the airplane (with $k=0.5$) must achieve the altitude of 63,000 feet and the Mach number of 0.8 after 40 percent of the fuel is expended. If the takeoff value of W_e/F is still 0.4, the value of W_e/F at the required flight condition is now 3.4. Moreover, if the value of $(L/d)_{eff}$ is still 20, the required value of $W_e/W_{g,t}$ is 0.145. Since $W_e/W_{g,t}$ only had to be 0.10 at takeoff, the condition at 63,000 feet would now determine the required engine weight. Notice that $W_{f,t}/W_{g,t}$ would have to be reduced by 0.045 in order to compensate for the increased engine weight if k remains at 0.5. At the same time, however, the takeoff requirements can be made more stringent; $(L/d)_{eff}$ can be reduced to 2.76 if the structural strength of the airplane is adequate.

A requirement of supersonic flight may decide the value of $W_e/W_{g,t}$, because the attainable value of $(L/d)_{eff}$ is comparatively low. Although supersonic flight itself tends to decrease W_e/F (fig. 4), this trend may be offset by the need for making the engines operate at high flight altitudes. (High altitudes may be desired to make $(L/d)_{eff}$ as high as possible, to obtain a reasonable level of wing loading for takeoff and landing, and to reduce aerodynamic heating.) The low value of $(L/d)_{eff}$ combined with the high values of W_e/F at high altitudes results in high values of $W_e/W_{g,t}$.

Consider the case where $k=0.5$ and $(L/d)_{eff}=4.0$ for level flight at the Mach number of 2.0. If the value of W_e/F is again 0.4 at static sea-level conditions, it would have the value of 1.2 at the altitude of about 56,000 feet. In order to meet these conditions after 40 percent of the fuel is exhausted, $W_e/W_{g,t}$ must be 0.27 (fig. 5). An additional requirement of high maneuverability ($C_m>1$) would have to be answered by an added increase in engine weight. Even if the value of C_m is only 1.25, then $(L/d)_{eff}$ becomes 3.2 and $W_e/W_{g,t}$ is increased to 0.35. Only 15 percent of the gross weight could then be allotted for fuel.

This brief sampling shows how engine weight depends on the conditions of flight. Of particular interest is the increase in $W_e/W_{g,t}$ associated with increases in flight altitude and Mach number. It is under these conditions that reductions in W_e/F are most appreciated. In the first of the preceding examples (subsonic flight at comparatively low altitudes), the value of $W_e/W_{g,t}$ was 0.1 for $W_e/F=0.4$ at sea-level static conditions. A 50-percent reduction in specific engine weight would reduce $W_e/W_{g,t}$ by 0.05. This saving in weight could be distributed among useful weight, fuel weight, and structural weight. For the last example, on the other hand, such a reduction in specific engine weight would reduce $W_e/W_{g,t}$ by 0.19. A much larger weight movement is available to the other parts of the airplane. The fuel weight, for example, could be more than doubled. To meet the requirements for high altitude or supersonic flight, every effort should be made to make W_e/F as small as possible.

ENGINE EFFICIENCY

The previous discussion was centered about the size of engines needed to meet certain thrust requirements. Of equal importance is the weight of fuel required to meet the various range requirements demanded of the airplane. The range requirements may be examined with the aid of the familiar Breguet range equation, which can be written as

$$\mathcal{R}=-JH_f\left(\frac{\overline{L}}{d}\right)_{eff}\bar{\eta}_e \ln\left(1-\frac{W_{f,t}}{W_{g,t}}\right) \qquad (5)$$

where the bars denote average values over the entire flight path. This expression is modified by using equation (3); it then becomes

$$\mathcal{R}=-JH_f\left(\frac{\overline{L}}{d}\right)_{eff}\bar{\eta}_e \ln\left(k+\frac{W_e}{W_{g,t}}\right) \qquad (5a)$$

Since $W_e/W_{g,i}$ is determined from equation (4) at the most critical flight condition, equation (5a) may be written as

$$\mathcal{R}=-JH_f\left(\frac{L}{d}\right)_{eff}\bar{\eta}_e \ln\left\{1-\left[\frac{1-k-\dfrac{\dfrac{W_e}{F}}{\left(\dfrac{L}{d}\right)_{eff}}}{1-\dfrac{\dfrac{W_e}{F}}{\left(\dfrac{L}{d}\right)_{eff}}\dfrac{\Delta W_f}{W_{f,i}}}\right]\right\} \tag{6}$$

It is immediately noted that the range of flight is proportional to the average efficiency of the engine and the heating value of the fuel used. In other words, the weight of fuel required for a given mission is inversely proportional to both the heating value of the fuel and the engine efficiency. The range is also proportional to the average value of $(L/d)_{eff}$ over the entire flight path. Finally, the range is proportional to the function in the brackets.

The trends of this function are illustrated in figure 6. The abscissa of this figure is $(W_e/F)/(L/d)_{eff}$ at the most critical flight condition of the airplane. The ordinate is the calculated range divided by the range when $(W_e/F)/(L/d)_{eff}=0.1$, $k=0.5$, and $\Delta W_f/W_{f,i}=0$. The curves represent conditions where k is again 0.3, 0.4, 0.5, and 0.6,

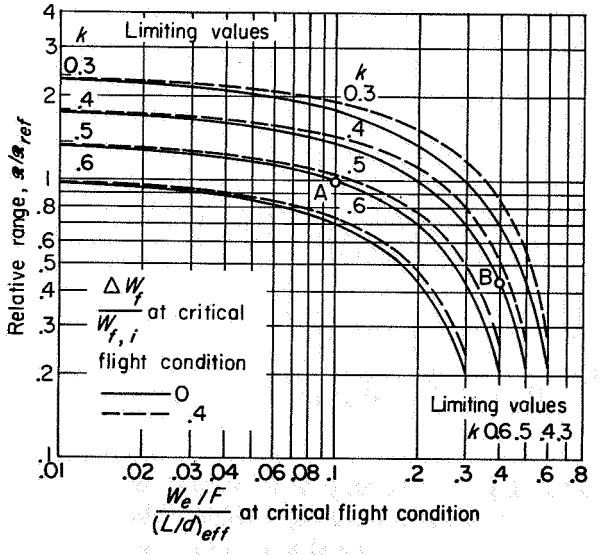

FIGURE 6.—Graphical representation of equation (6).

and where $\Delta W_f/W_{f,i}$ is 0 and 0.4 at the critical flight condition. These curves show that there is always an incentive for making $(W_e/F)/(L/d)_{eff}$ as low as possible, but the need for low specific engine weights becomes more imperative as $(W_e/F)/(L/d)_{eff}$ increases above 0.1. This statement is particularly true for the higher values of k and for situations where the critical flight condition is reached before an appreciable amount of fuel is used.

With respect to range, therefore, light engines are required whenever high-altitude flight is required; when stringent takeoff conditions are imposed; when a high degree of maneuverability is demanded; or when high supersonic flight speeds must be attained. Notice in this connection that high design flight altitudes may permit the attainment of relatively high values of $(L/d)_{eff}$ and range, and that low values of W_e/F are required for this accomplishment.

As previously noted, it frequently happens that some of the design requirements for light weight are incompatible with some of the requirements for high efficiency. As shown by equation (6), the range is directly proportional to the average efficiency during flight. Decreases in engine weight that unduly prejudice the efficiency are therefore unwelcome. At point A of figure 6, a decrease in specific engine weight of 10 percent improves the range about 3 percent, if there is no change in $(L/d)_{eff}$ or $\bar{\eta}_e$. If, however, the efficiency also decreased 3 percent, there would be no change in range. At this point, then, the efficiency would not be upset in order to obtain trifling improvements in engine weight. At point B, on the other hand, a 10-percent reduction in specific engine weight increases the range by about 23 percent. In this case a 23-percent reduction in engine efficiency is equivalent to a 10-percent reduction in specific engine weight. Significant reductions in efficiency could be tolerated here to obtain moderate reductions in engine weight.

A comparison of the relative effects of a small change in efficiency and a small change in specific engine weight may be directly obtained by differentiating equation (6) with respect to $\bar{\eta}_e$ and W_e/F. The values of k and $(L/d)_{eff}$ are assumed to be fixed, along with the value of $\Delta W_f/W_{f,i}$, since these

are the values at the most critical flight conditions, which determine $W_e/W_{g,t}$:

$$\frac{\frac{\partial(\mathcal{R})}{\mathcal{R}}}{\frac{\partial(\bar{\eta}_e)}{\bar{\eta}_e}}=1 \tag{7a}$$

$$\frac{\frac{\partial(\mathcal{R})}{\mathcal{R}}}{\frac{\partial\left(\frac{W_e}{F}\right)}{\frac{W_e}{F}}}=\frac{\frac{W_e}{F}}{\left(\frac{L}{d}\right)_{eff}}\frac{1-\frac{\Delta W_f}{W_{f,t}}(1-k)}{\left[1-\frac{\Delta W_f}{W_{f,t}}\frac{\frac{W_e}{F}}{\left(\frac{L}{d}\right)_{eff}}\right]^2}B\ln B \tag{7b}$$

where

$$B=1-\frac{1-k-\frac{\frac{W_e}{F}}{\left(\frac{L}{d}\right)_{eff}}}{1-\frac{\frac{W_e}{F}}{\left(\frac{L}{d}\right)_{eff}}\frac{\Delta W_f}{W_{f,t}}}$$

The implications of this equation are shown in figure 7, where the ordinate is

$$-\frac{\frac{\partial(\mathcal{R})}{\mathcal{R}}}{\frac{\partial\left(\frac{W_e}{F}\right)}{\frac{W_e}{F}}}\text{ or }-\frac{\frac{\partial(\bar{\eta}_e)}{\bar{\eta}_e}}{\frac{\partial\left(\frac{W_e}{F}\right)}{\frac{W_e}{F}}}$$

and the abscissas and parameters are the same as those in figure 6.

For a long-range airplane, where $(W_e/F)/(L/d)_{eff}$ may be of the order of 0.05, a 1-percent increase in efficiency increases the range 1 percent (eq. (7a)); a 7-percent decrease in specific engine weight is necessary to obtain the same range increase if $k=0.5$ (fig. 7(a)). If high-altitude requirements cause W_e/F to be doubled, the 1-percent increase in efficiency is about equivalent to a 3-percent decrease in specific weight. For supersonic flight, with $(W_e/F)/(L/d)_{eff}=0.33$, $k=0.5$, and $\Delta W_f/W_{f,t}=0.4$, a 1-percent increase in efficiency is equivalent to a ½-percent decrease in specific engine weight (fig. 7(b)). A maneuverability requirement of $C_m=1.25$ increases $(W_e/F)/(L/d)_{eff}$ to 0.413. Here, 1-percent change in efficiency is equivalent to about 0.2-percent change in specific engine weight. If the required altitude is increased by 15,000 feet, however, specific engine weight must be reduced, regardless of the consequences, because the required engine weight would be so large that there would be no room for fuel.

When engine efficiency must be compromised with specific engine weight, the design and intended use of the airplane determine the direction and the degree of the compromise. When range is the main objective and $(L/d)_{eff}$ and the required weight of fuel are large, some liberties can be taken with specific engine weight to favor efficiency. There is the provision, of course, that the loss in attainable altitude does not reduce the value of $(L/d)_{eff}$ by a significant amount. At the other extreme, when the combination of high flight speeds, high altitudes, and maneuverability make $(L/d)_{eff}$ low and tend to make W_e/F high, the compromise must favor specific engine weight.

THRUST PER UNIT FRONTAL AREA

Part of the drag d of the airplane results from the drag of the inlet supplying the engine with air and from the drag of the nacelle or that part of the fuselage housing the engine. If this drag is denoted by d_n, then

$$d=d_n+d_0$$

Equation (2) could then be written as

$$\frac{C_m+\frac{L}{d_0}\frac{\alpha}{g}}{\frac{L}{d_0}\left(\cos\epsilon-\frac{d_n}{F}\right)+\sin\epsilon}=\frac{F}{W_g}$$

The term on the left side is again denoted by $1/(L/d)_{eff}$. For small values of ϵ, the following can be written:

$$\frac{C_m+\frac{L}{d_0}\frac{\alpha}{g}}{\frac{L}{d_0}}=\frac{F}{W_g}\left(1-\frac{d_n}{F}\right)=\frac{F}{W_g}\left(1-\frac{d_n}{A_F}\frac{1}{\frac{F}{A_F}}\right)$$

When d_n/A_F is high, obtaining low values of d_n/F requires high values of F/A_F. Since the highest values of d_n/A_F are usually obtained at supersonic flight conditions, large values of F/A_F are particularly desired for supersonic flight.

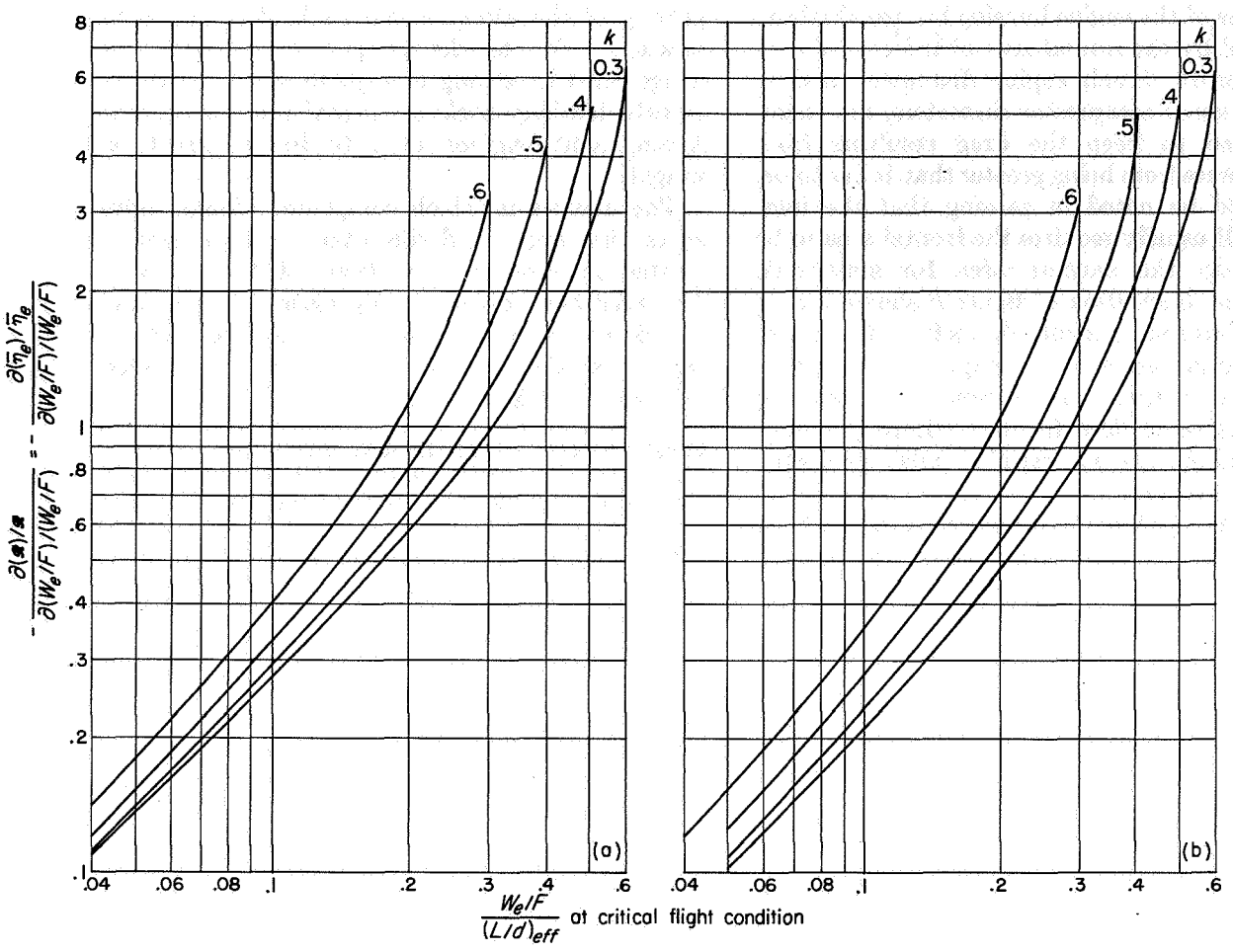

(a) $\Delta W_f/W_{f,i}$ at critical flight condition, 0. (b) $\Delta W_f/W_{f,i}$ at critical flight condition, 0.4.

FIGURE 7.—Graphical representation of equation (7b).

The drag of the inlet mainly consists of an "additive drag" (ref. 10), a drag resulting from the pressure forces acting on the outer curved portion of the inlet (fig. 8), and the drag resulting from friction. In some cases, for supersonic flight, it may be desirable to bypass some of the air entering the inlet to the outside. In this case a "bypass" drag is added. The "additive" and "bypass" drags depend on the matching of the inlet with the engine, which is discussed in more detail in a later section.

The drag resulting from pressure forces depends on the difference between the maximum frontal area of the engine housing and the open area of the inlet. It also depends on the slope and curvature of the outer surface of the inlet. The open area of the inlet depends on the mass-flow requirements

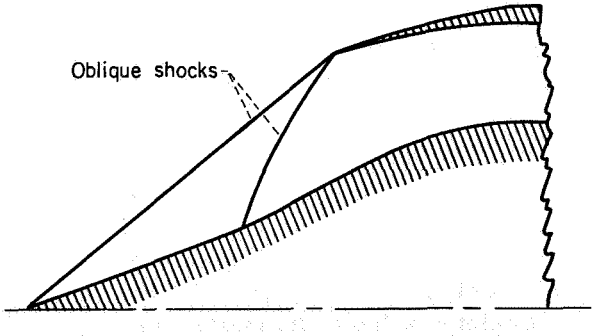

FIGURE 8.—Representative supersonic inlet.

of the engine and the speed of flight; its order of magnitude is given by

$$A=\frac{w_1}{(\rho_0 V_0)_{min}}$$

where $(\rho_0 V_0)_{min}$ is the minimum value of $\rho_0 V_0$ anticipated for steady flight. The maximum

frontal area of the engine housing has usually been determined by the frontal area of the engine with its accessories. Small engine diameters, and in particular small compressor diameters, are therefore desired to keep the drag resulting from pressure forces from being greater than it has to be.

It should be noted in passing that the inlet design itself usually requires the frontal area to be greater than the capture area for supersonic flight. The illustration of figure 8 shows such a design. This requirement follows from the necessity of meeting certain area requirements within the inlet and from the necessity of avoiding abrupt changes in flow direction within the inlet. Some requirements of variable inlet geometry aggravate this trend.

Most of the rest of the drag associated with an engine installation is due to friction. An estimate of the magnitude of the friction drag is given by the formula

$$d_{n\text{-}fr}=C_{fr}(\tfrac{1}{2}\gamma p_0 M_0^2 A_w) \qquad (8)$$

As shown in reference 11, a value of C_{fr} of 0.00168 is in agreement with available data. At a Mach number of 1.0 at 35,000 feet, this formula then becomes

$$d_{n\text{-}fr}=1.84\,\mathcal{D}_e l_e$$

In the interest of keeping this drag low, both the diameter $\mathcal{D}$ and the length l of the engine should be small. In particular, small compressor lengths and diameters are desired.

Another component of drag is that resulting from the pressure forces at the rear end of the engine. This drag is much more closely related to other engine components than it is to the compressor, however, and it is therefore dismissed from further consideration.

OTHER ENGINE REQUIREMENTS

Besides affecting airplane drag, the length and diameter of the engine may affect the structural weight of the airplane. In particular, long engines require a long and fairly rigid fuselage, which adds weight to the airplane without noticeably improving the lift-drag ratio.

Engine weight also affects the structural weight and other properties of the airplane, because the concentration of weight in the engine must be supported by the airplane. In fuselage installations, for example, the design of the airplane can be unfavorably compromised to keep the center of gravity of the airplane and its load in the right location. For nacelle or pod installation, the wings must be strong enough to support the engines for landing shocks or other violent maneuvers. Again, light engines tend to lessen structural weight.

The manner in which compressor design influences the length and diameter of the engine is treated in subsequent sections of this chapter. The relations between compressor diameter and the diameters of the other components of the engine are studied and some of the factors involved in engine length are enumerated.

EFFECTS OF COMPRESSOR PRESSURE RATIO, COMPRESSOR EFFICIENCY, AND FLIGHT CONDITIONS ON ENGINE PERFORMANCE

For a specified performance of its components, the efficiency and specific thrust of an engine are calculated by cycle analyses (refs. 12 and 13). The analysis presented here is similar to that of these references. Sketches of typical turbojet- and turboprop-engine installations with numerical stations are shown in figure 9. (Note that the condition of the engine gases after the work needed to drive the compressor has been extracted from the turbine can be indicated at station 4 of the turboprop engine, and that station 5 is at the discharge of the final turbine. For the turbojet engine, stations 4 and 5 coincide.)

The efficiency of each component is fixed in this analysis. The effect of compressor pressure ratio is examined for a range of flight conditions and turbine-inlet temperatures. The gas charts of reference 14 were used for determining gas properties.

ASSUMPTIONS USED IN CYCLE ANALYSES

The following values were assumed for the several variables involved in the cycle analyses of both the turboprop and the turbojet engine:

Flight Mach number, M_0	Inlet-diffuser total-pressure recovery, P_1/P_0
0	0.87
.8	.98
2.0	.90
3.0	.60

Compressor adiabatic efficiency, $\eta_{ad,C}$	0.88
Combustion efficiency, primary burner, η_B	0.98

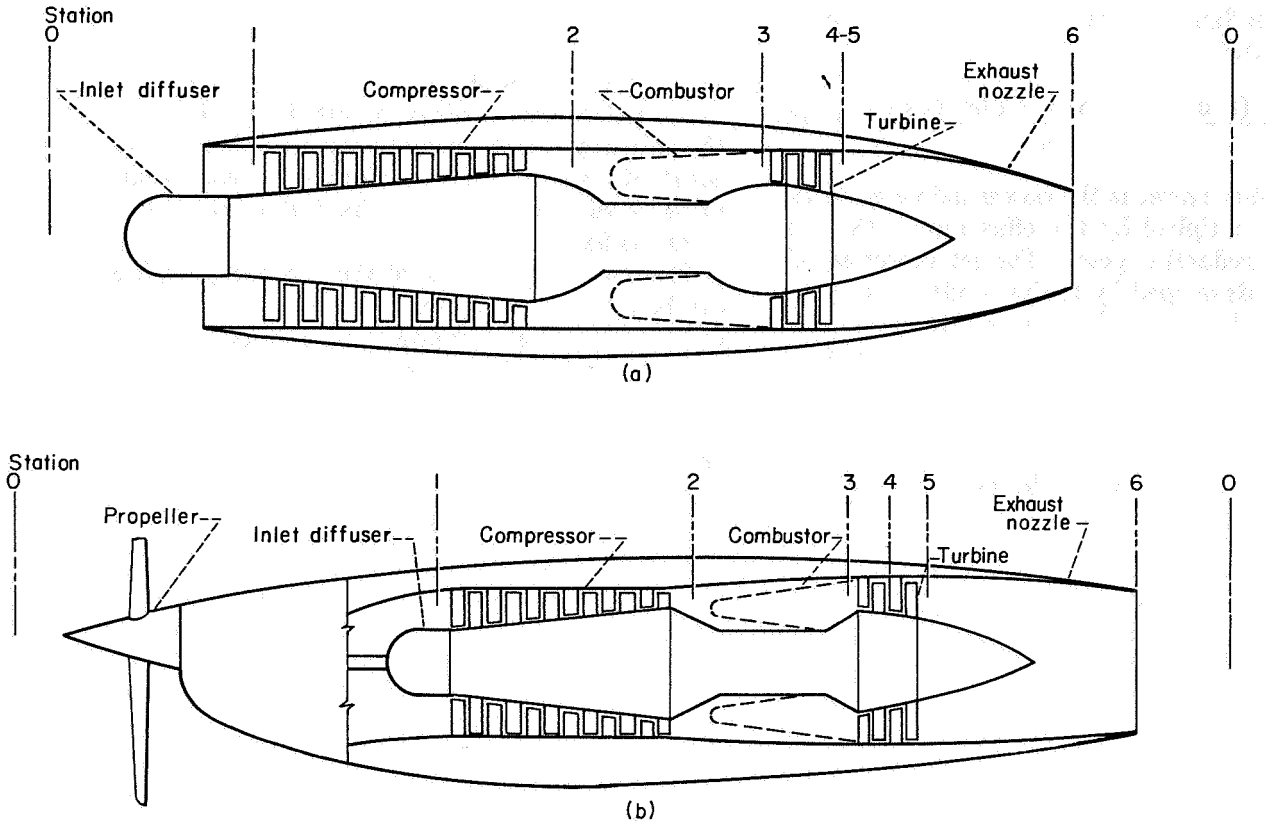

(a) Turbojet engine
(b) Turboprop engine

FIGURE 9.—Sketches of turbojet- and turboprop-engine configurations showing stations used in analysis.

Heating value of fuel, H_f, Btu/lb	18, 570
Hydrogen-carbon ratio of fuel	0. 167
Temperature of fuel injected as a liquid, T_f, °R	600
Total-pressure ratio across primary burners, P_3/P_2	0. 95
Turbine adiabatic efficiency, $\eta_{ad,T}$	0. 90
Exhaust-nozzle velocity coefficient, C_j	0. 98

No accounting was made for turbine cooling or other cooling that might be necessary at the high temperature levels. For the afterburning turbojet engine, the combustion efficiency of the afterburner was 0.95, the total-pressure ratio across the afterburner was 0.95, and the afterburner-outlet total temperature was 3500° R.

For the turboprop engine, the combined propeller and gearbox efficiency was assumed to be 0.86. In addition, the division of power between the propeller and jet was assumed to be such that the pressure ratio P_5/p_0 was 1.087 to obtain a reasonable nozzle area for the sea-level static case. For the other flight conditions considered, P_5/p_0 was assumed equal to P_1/p_0, a condition approximating that for maximum power.

The selected value of compressor efficiency appears to be attainable up to at least a compressor pressure ratio of 12. The efficiency of the turbine is high compared with the values observed in engine tests. It is comparable, however, to experimental efficiencies observed with uniform inlet conditions on cold-air turbines.

EFFECTS OF COMPRESSOR PRESSURE RATIO AND FLIGHT CONDITIONS ON TURBOPROP-ENGINE PERFORMANCE

Cycle analysis of a turboprop engine yields the power delivered to the propeller, the thrust developed by the jet nozzle, and the fuel burned per pound of engine air. To put the total developed power of the propeller-jet combination on a common basis, it is necessary to use the propeller propulsive efficiency η_{pr}. A power specific fuel consumption *sfc* may then be determined.

For level flight, thrust F is related to developed power by the equation

$$F=\frac{\text{(Propeller power)}+\text{(Jet power)}}{V_0} \tag{9}$$

The propeller power is the power delivered to the propeller multiplied by the efficiency of the propeller and reduction gear. The jet power equals the thrust developed by the jet multiplied by the airplane flight speed V_0. Hence, the thrust may be related to quantities obtained directly from cycle analysis by writing equation (9) as

$$F=\eta_{pr} \times\frac{[\text{(Power delivered to propeller)}+(\text{Jet power}/\eta_{pr})]}{V_0} \tag{10}$$

The term in brackets is defined as the equivalent shaft power *eshp* of the engine, which depends to some extent on the combined propeller-gearbox efficiency η_{pr}. Since the jet power is usually small compared with the propeller power, the equivalent shaft power is essentially unaffected by minor changes in this efficiency; therefore, the results are expressed in terms of equivalent shaft power. Equation (9) is not applicable to the static sea-level case, since $V_0=0$. For this condition, the equivalent shaft power is simply the power delivered by the power turbine, and the value of the thrust depends on the propeller selection.

Curves showing specific equivalent shaft power $eshp/w_1$ against power specific fuel consumption *sfc* and over-all engine efficiency η_e, with compressor total-pressure ratio P_2/P_1 and turbine-inlet total temperature T_3 as parameters, are presented in figure 10. Specific fuel consumption is used as the main variable for the abscissas because this term is more generally used than engine efficiency. These two quantities are related by the equation

$$\eta_e=\frac{(550)\,(3600)}{H_f J(sfc)}$$

The efficiency is practically independent of the heating value of the fuel, while the specific fuel consumption is inversely proportional to the fuel heating value. Figures 10 (a) and (b) represent sea-level flight at Mach numbers of 0 and 0.8, respectively, while figure 10(c) represents conditions for a flight Mach number of 0.8 in the stratosphere. In figure 11, the curves of figure 10 are repeated, except that compressor pressure ratio is replaced by enthalpy rise in the compressor ΔH_C as one parameter. This parameter is used because the enthalpy rise in a compressor tends to be more constant over a range of flight conditions than pressure ratio when the mechanical speed of the engine is fixed.

The general properties of the turboprop engine can be noted from figures 10 and 11. The turboprop engine is fundamentally capable of developing high shaft efficiency or low specific fuel consumption. The net efficiency of the engine is the product of the shaft efficiency and the efficiency of the reduction gears and the propeller. The shaft efficiency at a given turbine-inlet temperature increases with flight speed, because ram efficiently increases the cycle pressure ratio. Shaft efficiency also increases with altitude up to the tropopause, because the inlet-air temperature is reduced and the engine total-temperature ratio T_3/T_1 is increased. The specific power of the engine follows similar trends.

The actual power developed by the engine at various flying conditions is the product of specific power and the mass flow of air through the engine. The mass flow of air, in turn, depends on the value of $w\sqrt{\theta}/\delta$ of the compressor and the total pressure and temperature at the compressor inlet. The way the value of $w\sqrt{\theta}/\delta$ changes with flight conditions depends on the characteristics of the compressor and the value of the equivalent speed $N/\sqrt{\theta}$. One observed variation of $w\sqrt{\theta}/\delta$ with $N/\sqrt{\theta}$ is shown in figure 12. In this figure the ratio of $w\sqrt{\theta}/\delta$ to its design (sea-level) value is plotted against the ratio of $N/\sqrt{\theta}$ to its design value. This curve represents the general trend, although the specific values change from one compressor design to another.

At a flight Mach number of 0.8 in the stratosphere, the value of $\sqrt{\theta}$ is about 0.92. For a constant value of mechanical speed N, the value of $w\sqrt{\theta}/\delta$ is of the order of 106 percent of its sea-level value. At an altitude of 40,000 feet and a flight Mach number of 0.8, the value of $\delta/\sqrt{\theta}$ is 0.300. The weight flow through the engine is thus about 32 percent of its sea-level value (including the effects of the assumed diffuser recoveries). For a compressor enthalpy rise of 110 Btu per pound and a turbine-inlet temperature of 2000° R, the power developed by an engine

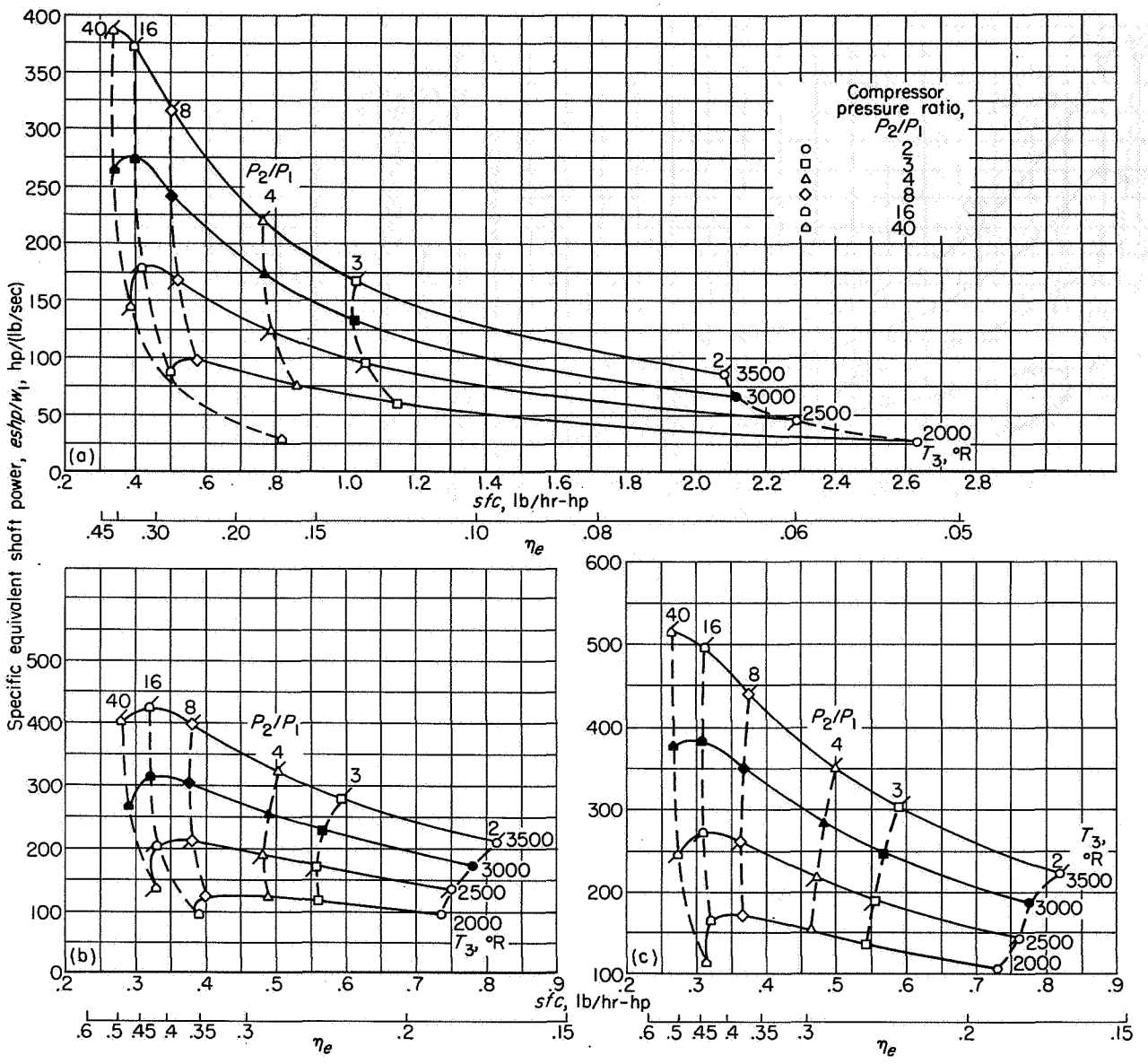

(a) Altitude, sea level; flight Mach number, 0.
(b) Altitude, sea level; flight Mach number, 0.8. (c) Altitude, stratosphere; flight Mach number, 0.8.

FIGURE 10.—Thermodynamic performance of turboprop engines (compressor pressure ratio as a parameter).

under these conditions is about 55 percent of its value at sea-level static conditions.

Because of the low power at high altitudes, the specific weight of turboprop engines (including the propeller) may vary between 1.5 and 3.0 at 40,000 feet. When flying at sea level, the corresponding specific weights are about half these values. At takeoff, the specific weights depend on propeller design as well as on engine design; values of specific weights under 0.2 are practical, however.

When the takeoff problem is secondary, one of the principal design problems is exploiting the inherently high efficiency of the engine. The selection of the compressor enthalpy rise or pressure ratio is then governed by the requirement of high efficiency. The desired value of either of these quantities depends on the turbine-inlet

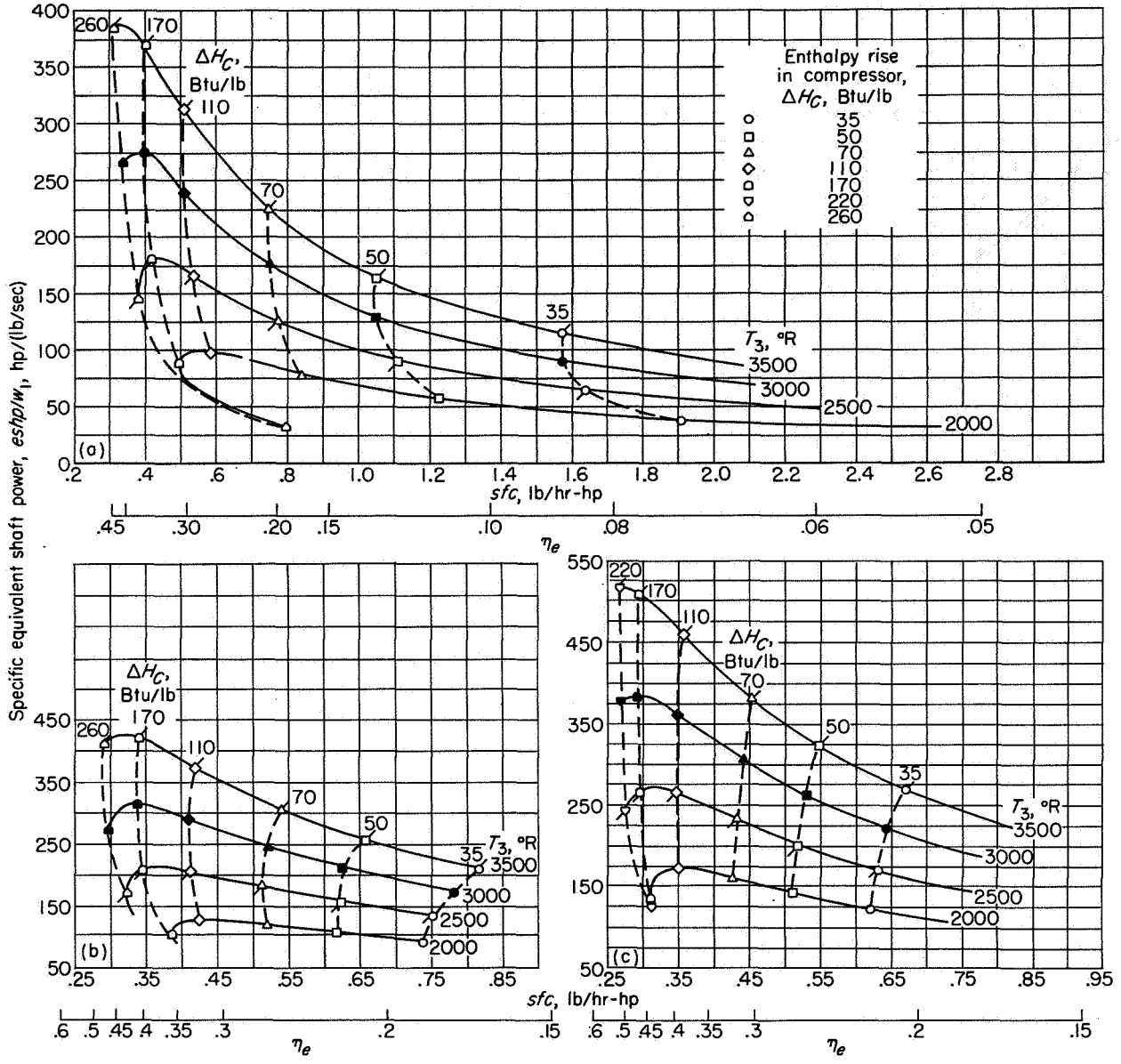

(a) Altitude, sea level; flight Mach number, 0.
(b) Altitude, sea level; flight Mach number, 0.8. (c) Altitude, stratosphere; flight Mach number, 0.8.

FIGURE 11.—Thermodynamic performance of turboprop engines (enthalpy rise in compressor as a parameter).

temperature, the flight speed, and the altitude. However, flight speed and altitude do not greatly affect the desirable value of enthalpy rise; and an enthalpy rise ΔH_C of 170 Btu per pound gives approximately maximum efficiency for 2000° R turbine-inlet temperature for the three flight conditions considered. The corresponding compressor pressure ratios are about 13 for a flight Mach number of 0.8 at sea level, 16 for sea-level static conditions, and 22 for a flight Mach Number of 0.8 in the stratosphere.

Engine weight may be adversely affected by these high compressor pressure ratios, but this trend is at least partially overcome by increasing the turbine-inlet temperatures. Although an important fraction of the engine weight is fixed by the weight of the gearbox and propeller (which depend on the maximum output required of the

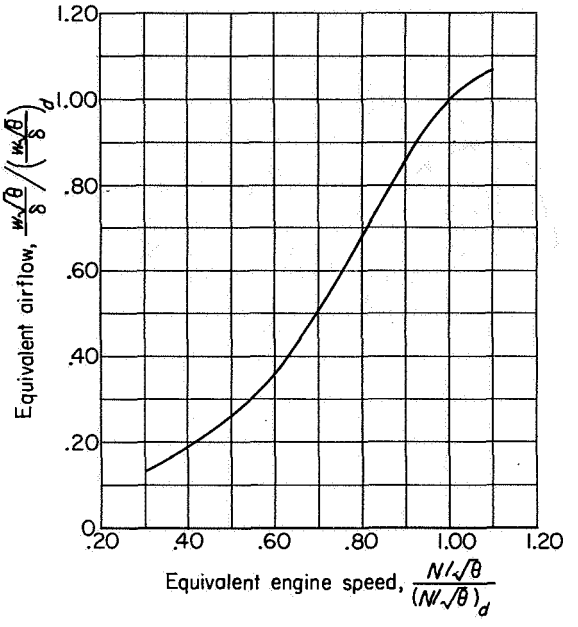

FIGURE 12.—Representative variation of equivalent airflow with equivalent speed.

engine), attractive gains are offered by using high turbine-inlet temperature together with the corresponding high pressure ratios. Employing turbine cooling for this purpose may reduce the indicated gains by a small amount but would not alter the general trend of the curves.

On the basis of this discussion, compressor design information must cover the problem of designing compressors for pressure ratios of 16 or higher. Although compressor efficiency has not yet been discussed, it is obvious that high levels of efficiency are required to obtain the highest levels of engine efficiency. While compressor weight may be of relatively minor importance at low design pressure ratios, it can represent a large portion of the engine weight when designs are made for the higher pressure ratios. Minimizing compressor weight for these conditions, without hurting the engine efficiency, is therefore an important design objective.

EFFECTS OF COMPRESSOR PRESSURE RATIO AND FLIGHT CONDITIONS ON TURBOJET-ENGINE PERFORMANCE

Some results of the cycle analysis of the turbojet engine are given in figures 13 to 15. Figure 13 presents specific thrust F/w_1 plotted against thrust specific fuel consumption $F(sfc)$ or over-all engine efficiency η_e, with compressor total-pressure ratio P_2/P_1 and turbine-inlet total temperature T_3 as parameters, for a nonafterburning engine. Thrust specific fuel consumption instead of over-all engine efficiency is again used as the main abscissa because it is a more familiar term and because the efficiency of a turbojet engine is always zero for static conditions. The relation between $F(sfc)$ and η_e is given by

$$\eta_e = \frac{3600 V_0}{H_f J \times F(sfc)}$$

The efficiency is again practically independent of the heating value of the fuel, while $F(sfc)$ is almost inversely proportional to it. Figures 13 (a) and (b) represent sea-level altitude for flight Mach numbers of 0 and 0.8, respectively. Figures 13 (c), (d), and (e) represent conditions in the stratosphere for flight Mach numbers of 0.8, 2.0, and 3.0, respectively. Figure 14 is identical with figure 13, except that lines of constant compressor total-pressure ratio are replaced by lines of constant enthalpy rise in the compressor ΔH_C. Figure 15, finally, is a carpet plot depicting the same engine variables as figure 13, for an afterburning turbojet engine with an afterburner-outlet total temperature of 3500° R. The carpet plot is used to spread the curves apart. The auxiliary curves show the relation between thrust specific fuel consumption and efficiency.

The thermodynamic efficiency of a turbojet engine (over-all efficiency divided by propulsive efficiency) is just as high as that of a turboprop. It also follows the same trends. The propulsive efficiency of the turbojet engine, which is approximately given by

$$\eta_{pr} = \frac{2V_0}{V_j + V_0} = \frac{1}{\frac{Fg}{w}\left(\frac{1}{2V_0}\right) + 1} \qquad (11)$$

cannot be independently controlled, however. At subsonic flight speeds, the propulsive efficiency is of the order of 0.50 or less, and the over-all engine efficiency is therefore low compared with that of the turboprop. At supersonic flight speeds, the propulsive efficiency increases because of the lower values of F/w and the higher values of V_0. The thermodynamic efficiency of the engine increases at the same time because of the greater cycle pressure ratios resulting from ram. The net result is an increase in the attainable over-all efficiency with increasing flight Mach number.

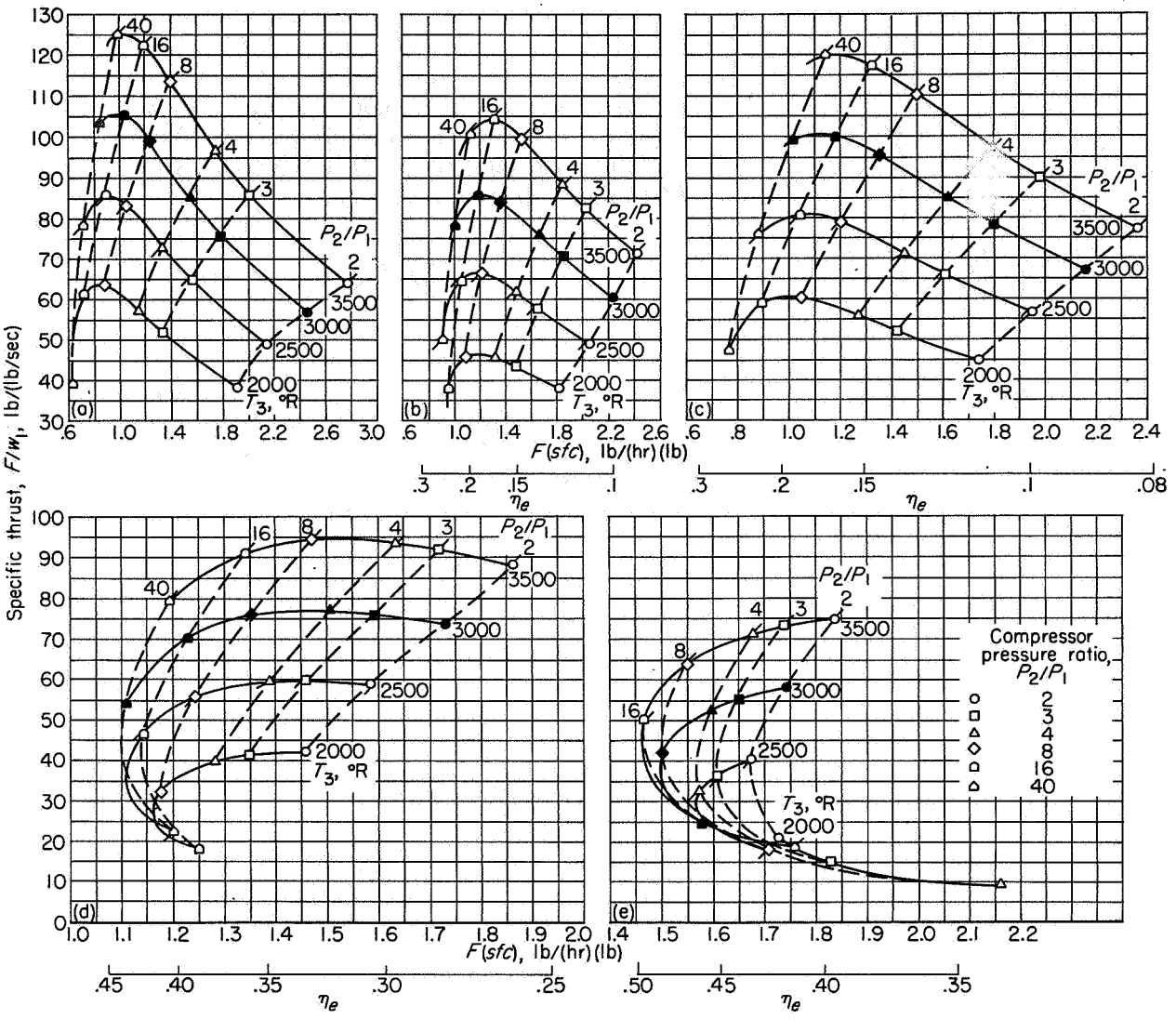

(a) Altitude, sea level; flight Mach number, 0. (b) Altitude, sea level; flight Mach number, 0.8.
(c) Altitude, stratosphere; flight Mach number, 0.8.
(d) Altitude, stratosphere; flight Mach number, 2.0. (e) Altitude, stratosphere; flight Mach number, 3.0.

FIGURE 13.—Thermodynamic performance of nonafterburning turbojet engines (compressor pressure ratio as a parameter).

By the same token, the specific thrust of a nonafterburning turbojet engine in a subsonic airplane is inherently lower than that of a turboprop. For two otherwise identical engines flying at a given flight speed and altitude, the ratio of the specific thrust of a turboprop engine to that of a turbojet engine is directly proportional to the ratio of their respective propulsive efficiencies. The turbojet engine is unencumbered by a gearbox and propeller, however, so that its specific weight in level flight is about half that of the turboprop. This comparison is considerably different at takeoff, where the thrust and power coefficients of the propeller play a dominant role.

Subsonic flight.—As previously noted, the weight flow through the engine at a flight Mach number of 0.8 and an altitude of 40,000 feet may be about 32 percent of the weight flow at sea-level static conditions, for a constant-mechanical-speed engine. The thrust produced by the nonafterburning engine at this altitude flight condition is about 30 percent of its sea-level static

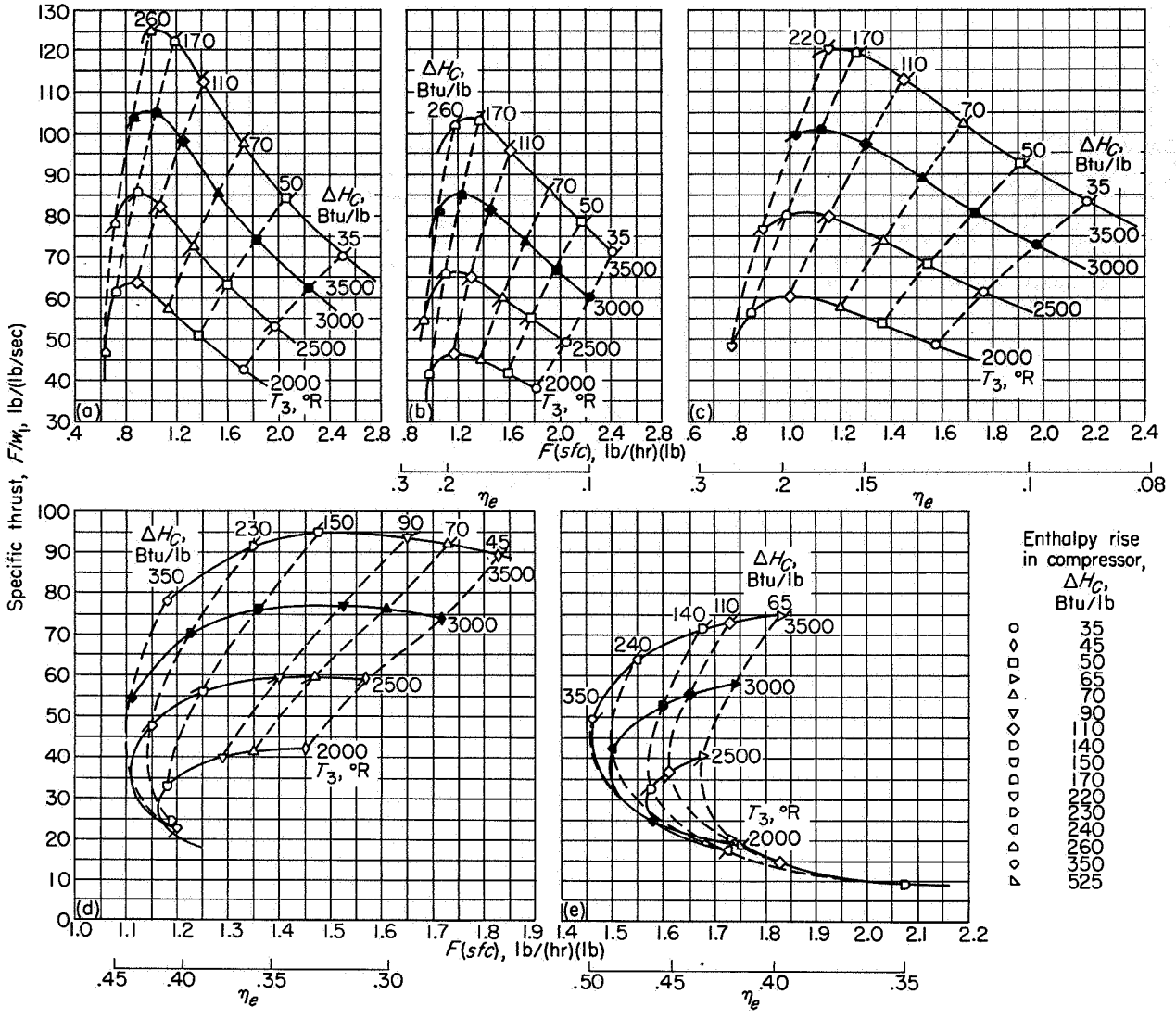

(a) Altitude, sea level; flight Mach number, 0. (b) Altitude, sea level; flight Mach number, 0.8.
(c) Altitude, stratosphere; flight Mach number, 0.8.
(d) Altitude, stratosphere; flight Mach number, 2.0. (e) Altitude, stratosphere; flight Mach number, 3.0.

FIGURE 14.—Thermodynamic performance of nonafterburning turbojet engines (enthalpy rise in compressor as a parameter).

value for a turbine-inlet temperature of 2000° R and a compressor enthalpy rise ΔH_C of 110 Btu per pound. A turbojet engine having a specific weight of 0.4 at sea level thus has a specific weight of about 1.3 at this altitude condition.

If a subsonic turbojet engine has about half the efficiency and about half the specific weight of a turboprop engine, it is profitably used when the ordinate of figure 6 is more than doubled by reducing $(W_{ef}/d)_e(L/F)/_f$ by 50 percent. For example, reducing $(W_e/F)/(L/d)_{eff}$ from 0.4 at point B to 0.2 increases the ordinate from 0.44 to 1.0. The same critical flight conditions are met, and the net improvement in range is about 14 percent. At point B, however, a 1-percent decrease in specific engine weight is equivalent to a 2.2-percent increase in efficiency (fig. 7(a)). At the new point (for the turbojet engine) a 1-percent decrease in specific weight is equivalent to only a 0.65-percent increase in efficiency. Even though

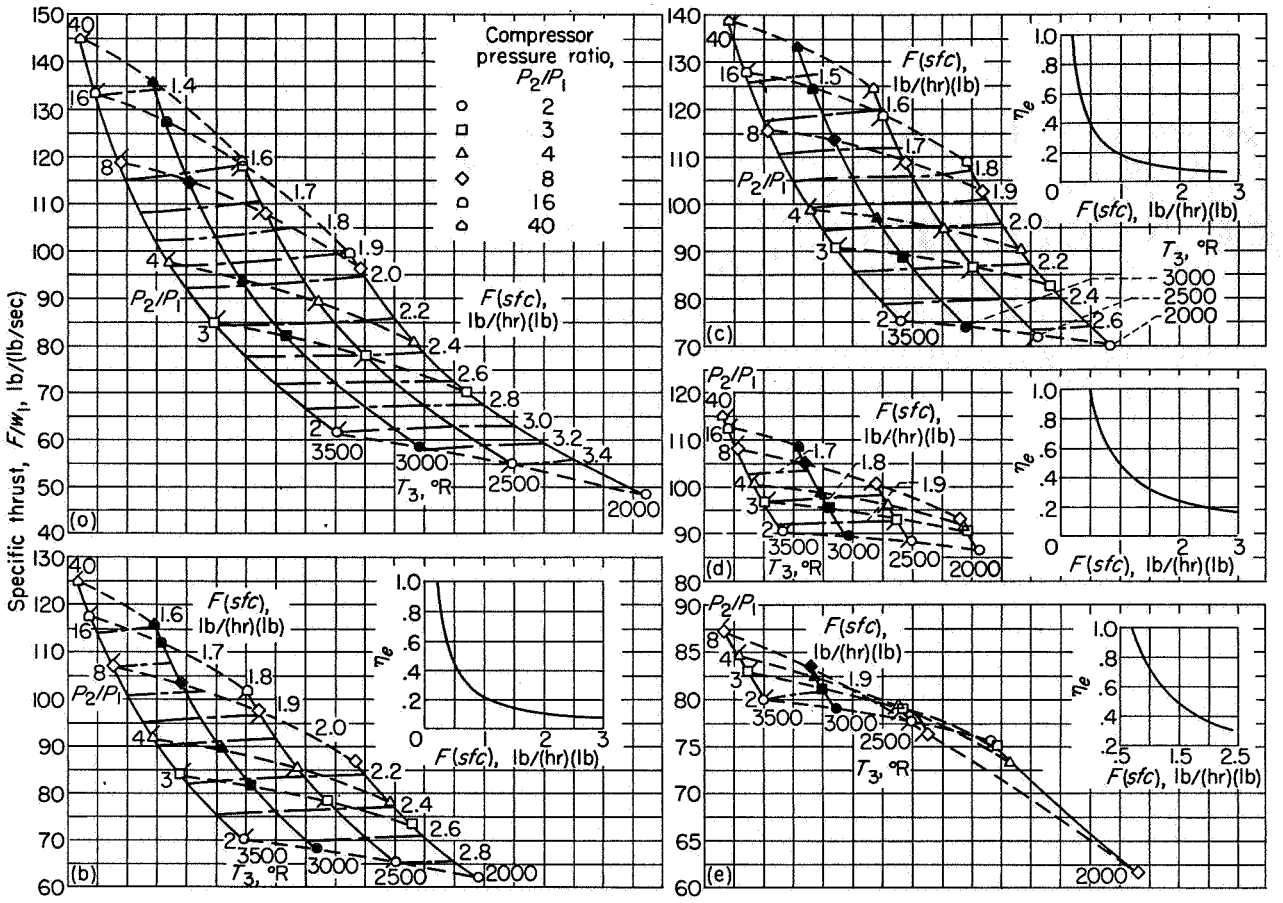

(a) Altitude, sea level; flight Mach number, 0.
(b) Altitude, sea level; flight Mach number, 0.8.
(c) Altitude, stratosphere; flight Mach number, 0.8.
(d) Altitude, stratosphere; flight Mach number, 2.0.
(e) Altitude, stratosphere; flight Mach number, 3.0.

FIGURE 15.—Thermodynamic performance of afterburning turbojet engines.

the lighter and less efficient turbojet engine is more suitable for the flight than the turboprop engine, improvements in its efficiency are now somewhat more desirable than improvements in specific weight. Compressor pressure ratios greater than that for maximum specific thrust are thus desired. For the conditions of figure 13(c), pressure ratios of 16 or higher might be indicated. The rate at which the compressor weight increases with pressure ratio is the governing factor, however, in the selection of pressure ratio. Design information permitting the development of high pressure ratios with lightweight compressors is thus necessary, just as it was for the turboprop engine.

When the high thrust levels are required for only a short time or for a short distance, the use of afterburning is advantageous. Comparison of figure 15(c) with figure 13(c) shows that the specific thrust can be increased 50 to 100 percent by afterburning. At the same time, however, the engine efficiency is reduced by the order of 50 percent. If the use of afterburning is limited to a short period of time, the extra weight of fuel expended is small and the average efficiency is only slightly reduced. The reduction in the critical value of W_e/F is sufficient to more than overcome this loss in efficiency, and an increase in the range results. Referring to figures 6 and 7, the value of $(W_e/F)/(L/d)_{eff}$ is now decided by the afterburning condition. The mean efficiency, however, is practically that at the nonafterburning conditions. Because of the low value of engine specific weight at the critical flight condition,

further improvements should favor a small increase in the average efficiency rather than a further decrease in specific engine weight. There is the provision, of course, that the critical condition is the one desired and not compromised to favor range to begin with.

Employing an afterburner may increase the engine weight from 10 to 30 percent. The specific engine weight is consequently not reduced in proportion to the increase in specific thrust. Because it offers resistance to the flow, the afterburner also decreases engine efficiency even when it is not burning fuel. Moreover, its added length increases nacelle drag, moves the center of gravity of the engine rearward, and increases the structural weight of the airplane. The net gains from its use are thus less than those indicated by the simple calculations of specific thrust.

Supersonic flight.—The turbojet engine, by itself, is capable of providing the thrust for takeoff, climb, and acceleration to Mach numbers between 2 and 3. It is therefore being seriously considered for this range of supersonic flight. At the flight Mach number of 2.0 in the stratosphere, the value of $N/\sqrt{\theta}$ is 86 percent of its sea-level value for a constant-speed engine. It is 69 percent of its sea-level value at the flight Mach number of 3.0. The corresponding values of $w\sqrt{\theta}/\delta$ are about 80 and 50 percent of their sea-level values (fig. 12). With the previously assumed inlet recoveries at an altitude of 55,000 feet, the associated values of $\delta/\sqrt{\theta}$ are about 0.5 and 1.4. Under these conditions, the weight flow of air at a flight Mach number of 2.0 is approximately 40 percent of that at sea level; at $M_0=3.0$, it is about 70 percent of its sea-level value.

The ratio of the developed thrust for these flight conditions to that at sea level depends on the enthalpy rise or pressure ratio of the compressor as well as the turbine-inlet and afterburner-exit temperatures. If the static sea-level pressure ratio is 8, if the turbine-inlet temperature is 2000° R, and if the afterburner-outlet temperature is 3500° R, then the specific thrust at a flight Mach number of 2 is about the same as that for sea-level static conditions for the afterburning engine. At 55,000 feet and the Mach number of 2, the total thrust would be about 40 percent of its sea-level value. If the specific weight of the afterburning engine were 0.3 at sea level, its specific weight at 55,000 feet and a Mach number of 2 would be about 0.75. For values of $(L/d)_{eff}$ of the order of 3, $(W_e/F)/(L/d)_{eff}$ becomes 0.25. At 70,000 feet $(W_e/F)/(L/d)_{eff}$ is increased to 0.50. The range of flight is thus drastically curtailed by the combination of high specific engine weights and low values of $(L/d)_{eff}$ (fig. 6). With lighter engines, higher altitudes are available and larger values of $(L/d)_{eff}$ might be obtained. Even at the same value of $(W_e/F)/(L/d)_{eff}$, a greater range would then be obtained if $(L/d)_{eff}$ is increased (eq. (6)). Emphasis is thus placed on low engine weights for this type of flight condition. As indicated in equation (7a), however, engine efficiency is of equal importance and must not be unduly prejudiced by efforts to reduce specific engine weight.

In order to obtain low specific weights at flight Mach numbers of the order of 2, the use of afterburning engines is attractive. According to figures 15 (d) and (e), high pressure ratios and high turbine-inlet temperatures would be desired for afterburning engines, since the highest specific thrust and efficiency are thereby attained. This desire is tempered, however, by the weight problems at the high pressure ratios and the problems associated with the use of high turbine-inlet temperatures. At lower turbine-inlet temperatures, there is a maximum desirable pressure ratio. At higher or lower pressure ratios, both the specific thrust and efficiency decrease. At a flight Mach number of 2, the pressure ratio for the highest specific thrust and efficiency is about 8 for a turbine-inlet temperature between 2000° and 2500° R. The corresponding pressure ratio at sea level for a constant-mechanical-speed engine is about 14.

High turbine-inlet temperatures without afterburning are also attractive at the flight Mach number of 2 (fig. 13(d)). Although the specific thrust is reduced from the afterburning case, the engine efficiency is increased. Moreover, the afterburning engine is penalized by the engine and airframe weight penalties previously discussed. These effects may more than counterbalance the loss in specific thrust. The pressure ratios desired for the nonafterburning engine are, of course, higher than for the afterburning engine.

At the high flight Mach number of 3, the required compressor pressure ratios are low. With a turbine-inlet temperature of 2000° R, a pressure ratio of the order of 2 is desired for

either an afterburning or nonafterburning engine (figs. 13(e) and 15(e)). This value corresponds to a pressure ratio of about 4 at sea level. Since the resulting subsonic performance is poor, higher turbine-inlet temperatures must be used to realize the advantages of the higher compressor pressure ratios. At the turbine-inlet temperature of 2500° R, the desirable pressure ratio lies between a value of 3 and 4 at the high flight Mach numbers. For constant-mechanical-speed engines, the corresponding sea-level pressure ratios are between 8 and 12. The necessity for lightweight compressors developing this order of pressure ratio at sea level is again apparent.

OTHER ENGINE CYCLES

There are many thermodynamic cycles suggested for aircraft propulsion. The ducted-fan or bypass engine, for instance, is an intermediate engine between the turboprop and the turbojet engines. The desired characteristics of the main compressor and fan are thus expected to be similar to the ones just outlined. The design data required are consequently the same. Similarly, the design data would be applicable to the design of other low-pressure-ratio compressors such as those used in the turborocket.

EFFECTS OF COMPRESSOR EFFICIENCY ON ENGINE PERFORMANCE

The effect of a change in compressor efficiency on the results of the preceding section can be estimated by the following considerations. At a given flight speed and altitude, the enthalpy rise due to ram is fixed, as is the temperature T_1 (fig. 9). With a given inlet recovery, the ram pressure ratio P_1/p_0 is constant. For a given enthalpy rise in the compressor, the combustor-inlet temperature T_2 is fixed. The compressor total-pressure ratio P_2/P_1 is then a function of compressor efficiency only. The turbine-inlet temperature T_3 is given a fixed value as is the combustor pressure ratio P_3/P_2. Since the work done by the turbine approximatley equals the enthalpy rise through the compressor, the turbine-outlet temperature T_4 is fixed. For a given turbine efficiency, the turbine pressure ratio P_4/P_3 is also fixed. Since the output and efficiency of the engine ultimately become functions of T_4 and P_4/p_0, the effect of compressor efficiency is examined by noting its effect on $P_4/p_0=P_2/P_1$ times a constant.

Compressor efficiency is defined by the equation

$$\eta_{ad,C}=\frac{\left(\frac{P_2}{P_1}\right)^{\frac{\gamma_C-1}{\gamma_C}}-1}{\frac{\Delta H_C}{T_1 c_p}} \tag{12}$$

Rearranging this expression and differentiating it, while holding the value of $\Delta H_C/T_1c_p$ constant, yield the following result:

$$\frac{\mathrm{d}\left(\frac{P_2}{P_1}\right)}{\frac{P_2}{P_1}}=Q\frac{\mathrm{d}\eta_{ad,C}}{\eta_{ad,C}} \tag{13a}$$

where

$$Q=\frac{\gamma_C}{\gamma_C-1}\frac{\left(\frac{P_2}{P_1}\right)^{\frac{\gamma_C-1}{\gamma_C}}-1}{\left(\frac{P_2}{P_1}\right)^{\frac{\gamma_C-1}{\gamma_C}}} \tag{13b}$$

The effect of a percent change in compressor total-pressure ratio on the total pressure P_x at any point in the engine downstream of the compressor is thus

$$\frac{\mathrm{d}\left(\frac{P_x}{p_0}\right)}{\frac{P_x}{p_0}}=\frac{\mathrm{d}\left(\frac{P_2}{P_1}\right)}{\frac{P_2}{P_1}}=Q\frac{\mathrm{d}\eta_{ad,C}}{\eta_{ad,C}} \tag{14}$$

Turboprop engine.—For a turboprop engine, neglecting the contribution of the jet, the mechanical energy ΔH_M developed in a complete expansion of the engine gases through the power turbine is given by

$$\Delta H_M=\eta_{ad,PT}T_4c_p\left[1-\left(\frac{p_0}{P_4}\right)^{\frac{\gamma_T-1}{\gamma_T}}\right] \tag{15}$$

and

$$\frac{p_0}{P_4}=\frac{1}{\frac{P_1}{p_0}\frac{P_4}{P_1}}$$

For given values of compressor pressure ratio P_2/P_1 and engine temperature ratio T_3/T_1, the value of P_4/P_1 may be found from figure 16. (In this figure, the quantity P_4/P_1 is plotted against P_2/P_1 with T_3/T_1 as a parameter. These data are a byproduct of the cycle calculations of the previous section. For a constant value of specific

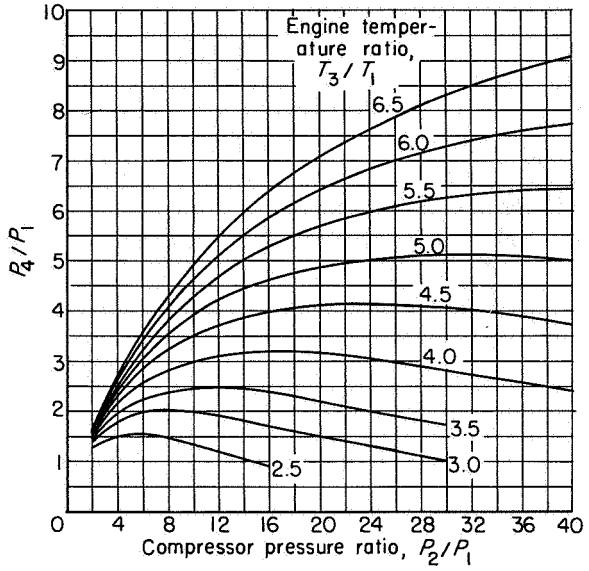

FIGURE 16.—Chart for estimating total pressure behind turbines driving compressors.

heat and γ, these curves would be independent of the flight condition. Actually, the variations in these quantities cause these curves to vary about ± 6 percent from the values shown over the entire range of flight conditions considered. The important trends of the curves are not affected, however.) Since the ram pressure ratio P_1/p_0 is also known, p_0/P_4 may be determined.

Differentiating equation (15) and utilizing equation (14) while holding $(\eta_{ad,PT} T_4 c_p)$ constant yield

$$\frac{d(\Delta H_M)}{\Delta H_M} = G \frac{d\eta_{ad,C}}{\eta_{ad,C}} \tag{16a}$$

where

$$G = \frac{\gamma_T - 1}{\gamma_T} \frac{\left(\frac{p_0}{P_4}\right)^{\frac{\gamma_T - 1}{\gamma_T}}}{1 - \left(\frac{p_0}{P_4}\right)^{\frac{\gamma_T - 1}{\gamma_T}}} Q \tag{16b}$$

Equation (16a) shows the general effect of a small change in compressor efficiency on the power output of a turboprop engine. Since this equation was derived with the assumption of a constant heat input to the engine, the percent change in power output is the same as the percent change in engine efficiency or specific fuel consumption.

Figure 17 shows the quantity G from equations (16) plotted against compressor total-pressure

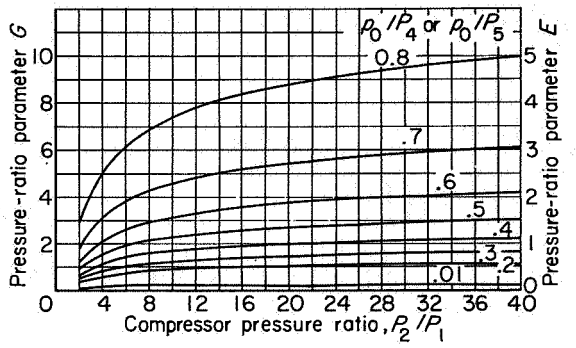

FIGURE 17.—Variation of parameters G and E with compressor pressure ratio (eqs. (16) and (20)).

ratio P_2/P_1, with the ratio p_0/P_4 as a parameter. In the calculation of this figure, values for γ_C and γ_T of 1.4 and 1.3, respectively, were assumed. Examination of figure 17 reveals that G is large when both P_2/P_1 and p_0/P_4 are large. For these conditions, the power output and efficiency of a turboprop engine are sensitive to small changes in compressor efficiency (eq. (16)).

For a turboprop engine developing a pressure ratio of 16 while flying at a Mach number of 0.8 in the stratosphere, a 1-percent decrease in compressor efficiency reduces the power and engine efficiency by a little less than 1 percent. The results of figures 16 and 17 also show that the effect of compressor efficiency diminishes slightly as turbine-inlet temperature is increased. Since compressor pressure ratio for a given enthalpy rise decreases as the efficiency decreases, a drop in compressor efficiency decreases the pressure ratios for both maximum specific power and maximum engine efficiency.

Turbojet engine.—In the case of a turbojet engine, a small change in compressor efficiency affects the total pressure P_5 in the jet nozzle, which in turn affects the jet velocity and the thrust. The magnitude of these effects may be examined as follows. The jet velocity V_j is expressed in terms of the jet-nozzle pressure ratio p_0/P_5 as

$$V_j = C_j \sqrt{2 T_5 c_p g J \left[1 - \left(\frac{p_0}{P_5}\right)^{\frac{\gamma_T - 1}{\gamma_T}}\right]} \tag{17}$$

Differentiating this equation while holding the

quantity $C_j\sqrt{2T_5c_pgJ}$ constant provides the relation

$$\frac{dV_j}{V_j}=\frac{\gamma_T-1}{2\gamma_T}\frac{\left(\frac{p_0}{P_5}\right)^{\frac{\gamma_T-1}{\gamma_T}}}{1-\left(\frac{p_0}{P_5}\right)^{\frac{\gamma_T-1}{\gamma_T}}}Q\frac{d\eta_{ad,c}}{\eta_{ad,c}} \tag{18}$$

using equation (14). The specific thrust F/w_1 is related to the jet velocity V_j by

$$\frac{F}{w_1}=\frac{(1+f)V_j-V_0}{g} \tag{19}$$

Then $d(F/w_1)=(1+f)dV_j/g$, assuming a constant fuel-air ratio f, and hence

$$\frac{d\left(\frac{F}{w_1}\right)}{\frac{F}{w_1}}=\frac{E}{1-\frac{V_0}{(1+f)V_j}}\frac{d\eta_{ad,c}}{\eta_{ad,c}} \tag{20a}$$

where

$$E=\frac{\gamma_T-1}{2\gamma_T}\frac{\left(\frac{p_0}{P_5}\right)^{\frac{\gamma_T-1}{\gamma_T}}}{1-\left(\frac{p_0}{P_5}\right)^{\frac{\gamma_T-1}{\gamma_T}}}Q \tag{20b}$$

using equations (18) and (19). The expression for the parameter E is seen to be half the value of G if the power-turbine pressure ratio p_0/P_4 is replaced by the jet-nozzle pressure ratio p_0/P_5. Figure 17 may therefore be used to evaluate E for given values of P_2/P_1 and p_0/P_5 by taking $E=G/2$. The value of p_0/P_5 is determined from figure 16 in the same way that p_0/P_4 is found for the turboprop engine.

Equation (20a) shows the effect of a percent change in compressor efficiency on the specific thrust of a turbojet engine. As in the case of the turboprop engine, the percent change in specific thrust may be taken as equal to the corresponding percent change in engine efficiency or thrust specific fuel consumption.

For the static case ($V_0=0$), the effect of a percent change in compressor efficiency on either specific thrust or efficiency can be determined directly by evaluating E from figure 17. Equations (20) and figure 17 show that for this case specific thrust or engine efficiency is sensitive to small changes in compressor efficiency when both P_2/P_1 and p_0/P_5 are large. This situation for the turbojet engine, as for the turboprop engine, corresponds to high compressor pressure ratios and low turbine-inlet temperatures. Figure 13(a) shows that these conditions are required for high values of engine efficiency. When engine efficiency is highly important at sea-level static conditions, therefore, high compressor efficiencies are necessary.

When a reasonably high flight speed is involved, the ratio $V_0/(1+f)V_j$ cannot be ignored. Notice, however, that the denominator of the coefficient of $d\eta_{ad,c}/\eta_{ad,c}$ in equation (20a) can be written as

$$1-\frac{V_0}{(1+f)V_j}=1-\frac{1}{\frac{F}{w_1}\frac{g}{V_0}+1}$$

If F/w_1 is 80 pounds per pound per second at a flight Mach number of 3, the value of this expression is about 0.5, and the coefficient of $d\eta_{ad,c}/\eta_{ad,c}$ in equation (20a) approaches the value of G. If F/w_1 is 60 pounds per pound per second at a flight Mach number of 0.8, this expression has the value of about 0.7.

For the subsonic airplane, in which the compressor pressure ratio is of the order of 16, a percent decrease in compressor efficiency reduces the specific thrust and engine efficiency by a little less than 1 percent for constant enthalpy rise in the compressor. Since the ratio T_3/T_1 is low for supersonic flight, the value of P_4/P_1 is low (fig. 16). On the other hand, the value of P_1/p_0 is high, and a percent decrease in compressor efficiency reduces the thrust and efficiency by the order of only 0.5 percent.

It is again noted that a reduction in compressor pressure ratio accompanies a decrease in efficiency for this analysis. The optimum pressure ratio for either maximum specific thrust or minimum specific fuel consumption, therefore, decreases as compressor efficiency decreases.

EFFECTS OF COMPRESSOR PRESSURE RATIO, FLOW CAPACITY, AND EFFICIENCY ON FRONTAL AREA OF OTHER ENGINE COMPONENTS

Compressor pressure ratio, flow capacity, and efficiency play a prominent role in determining the relative frontal areas of the engine components. The frontal areas of these components are also involved in engine weight. In this discussion, only the internal frontal area is considered. This area is defined by πr_t^2, where r_t is the radius to the internal surface of the casing of the component

under consideration. Of interest now is the ratio of the internal frontal area of a component to that of the compressor.

The flow area A of any component is determined by stipulating the weight flow and either a maximum velocity V or a Mach number M at the entrance or exit of the component. These maximum values may be either absolute or found from experience; in either case, undesirably high losses result from attempting to exceed these limits. The required flow area may be expressed in terms of the velocity V by the equation

$$A=\frac{w\sqrt{RT}}{\sqrt{\gamma g}\,\frac{VP}{\sqrt{\gamma gRT}}\left(1-\frac{\gamma-1}{2}\frac{V^2}{\gamma gRT}\right)^{\frac{1}{\gamma-1}}} \tag{21a}$$

or in terms of the Mach number M by

$$A=\frac{w\sqrt{RT}\left(1+\frac{\gamma-1}{2}M^2\right)^{\frac{\gamma+1}{2(\gamma-1)}}}{MP\sqrt{\gamma g}} \tag{21b}$$

When the values of w and M or V are given, the annular area is determined by the total pressure and temperature at the point considered. The internal frontal area is related to the annular area A by the equation

$$A=A_F\left[1-\left(\frac{r_h}{r_t}\right)^2\right]$$

Since the weight flow through a conventional engine is essentially constant, the ratio of the frontal area of any component to the frontal area of the compressor is given by

$$\frac{(A_F)_x}{(A_F)_C}=\frac{\left(\frac{w}{A_F}\right)_C}{\left(\frac{w}{A_F}\right)_x}$$

The equivalent weight flow per unit frontal area $w\sqrt{\theta}/A_F\delta$ of the compressor or of any other engine component may be expressed by substituting

$$A=A_F\left[1-\left(\frac{r_h}{r_t}\right)^2\right]$$

$$P=p_{sl}\delta$$

$$T=T_{sl}\theta$$

into equations (21a) and (21b). The results are

$$\frac{w\sqrt{\theta}}{A_F\delta}=\sqrt{\frac{\gamma g}{R}}\,\frac{V}{\sqrt{\gamma gRT}}\left(1-\frac{\gamma-1}{2}\frac{V^2}{\gamma gRT}\right)^{\frac{1}{\gamma-1}}\left[1-\left(\frac{r_h}{r_t}\right)^2\right]\frac{p_{sl}}{\sqrt{T_{sl}}} \tag{22a}$$

$$\frac{w\sqrt{\theta}}{A_F\delta}=\sqrt{\frac{\gamma g}{R}}\,M\left(1+\frac{\gamma-1}{2}M^2\right)^{-\frac{\gamma+1}{2(\gamma-1)}}\left[1-\left(\frac{r_h}{r_t}\right)^2\right]\frac{p_{sl}}{\sqrt{T_{sl}}} \tag{22b}$$

Notice that, when $V/\sqrt{\gamma gRT}$ or M is small, these equations are approximated by

$$\frac{w\sqrt{\theta}}{A_F\delta}=\frac{V}{\sqrt{T}}\left[1-\left(\frac{r_h}{r_t}\right)^2\right]\frac{p_{sl}}{R\sqrt{T_{sl}}} \tag{22a'}$$

$$\frac{w\sqrt{\theta}}{A_F\delta}=M\left[1-\left(\frac{r_h}{r_t}\right)^2\right]\sqrt{\frac{\gamma g}{R}}\,\frac{p_{sl}}{\sqrt{T_{sl}}} \tag{22b'}$$

At a value of $V/\sqrt{\gamma gRT}$ of 0.2, the error is about 2 percent. For the same value of M, the error is about 2.4 percent. A quantitative evaluation of equations (22) may be obtained from figures 18 and 19. In figure 18(a), $w\sqrt{\theta}/A_F\delta$ is plotted against $V/\sqrt{\gamma gRT}$, with the hub-tip radius ratio r_h/r_t as a parameter and with $\gamma=1.4$. Figure 18(b) is the same, except that $\gamma=1.3$. In figure 19 the flow Mach number M replaces $V/\sqrt{\gamma gRT}$ as the abscissa.

When the given or allowable flow Mach number is known, together with the ratio of the inner to the outer radius, the value of $w\sqrt{\theta}/A_F\delta$ may be determined from figure 19. The ratio of the required frontal area of any component to that of the compressor may be expressed as

$$\frac{(A_F)_x}{(A_F)_C}=\frac{\left(\frac{w}{A_F}\right)_C}{\left(\frac{w}{A_F}\right)_x}=\frac{\left(\frac{w\sqrt{\theta}}{A_F\delta}\right)_C}{\left(\frac{w\sqrt{\theta}}{A_F\delta}\right)_x}\left(\frac{P_1}{P_x}\sqrt{\frac{T_x}{T_1}}\right) \tag{23}$$

The value of the last term in parentheses in equation (23) may be determined from figure 20 for the combustor inlet. For the turbine discharge this term may be evaluated from figure 21. The data for these figures were obtained as a byproduct

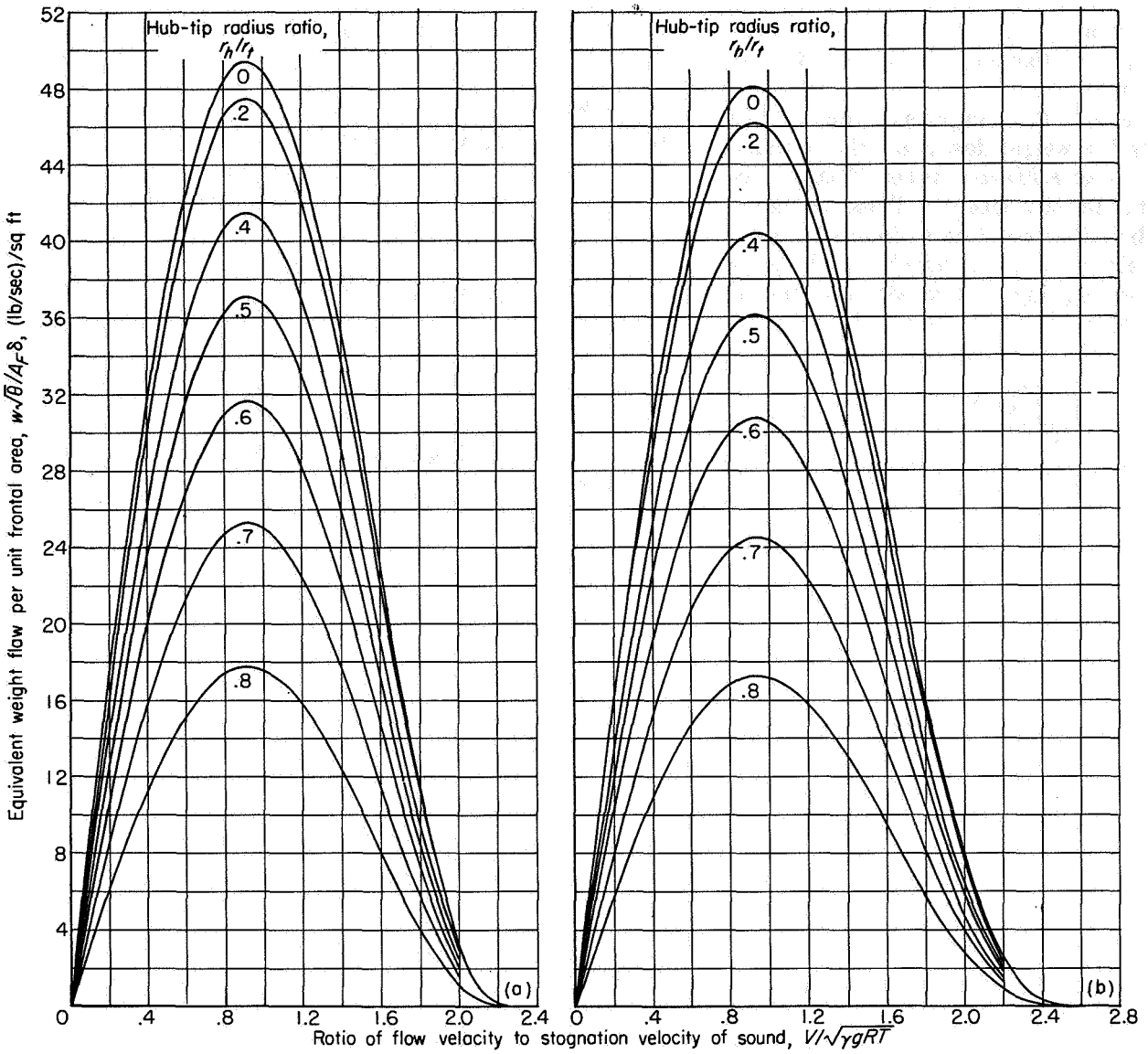

(a) Ratio of specific heats, 1.4.

(b) Ratio of specific heats, 1.3.

FIGURE 18.—Variation of equivalent weight flow per unit frontal area with $V/\sqrt{\gamma grT}$ for several values of hub-tip radius ratio.

of the cycle analyses previously presented. While figure 20 exactly represents the condition for the given assumptions, figure 21 is subject to the same error discussed in connection with figure 16. The value of $(P_1/P_x)\sqrt{T_x/T_1}$ at other engine stations can be calculated readily with the aid of these curves. If the flow velocity rather than the flow Mach number is of interest, the total-temperature ratio across the component must be known in order to determine $V/\sqrt{\gamma gRT}$, which is the abscissa of figure 18. These total-temperature ratios may also be evaluated from figure 20 for the combustor inlet and from figures 16 and 21 for the turbine outlet.

COMPARISON OF FRONTAL AREAS FOR SUBSONIC FLIGHT

Consider the situation for a flight Mach number of 0.8 in the stratosphere with a compressor pres-

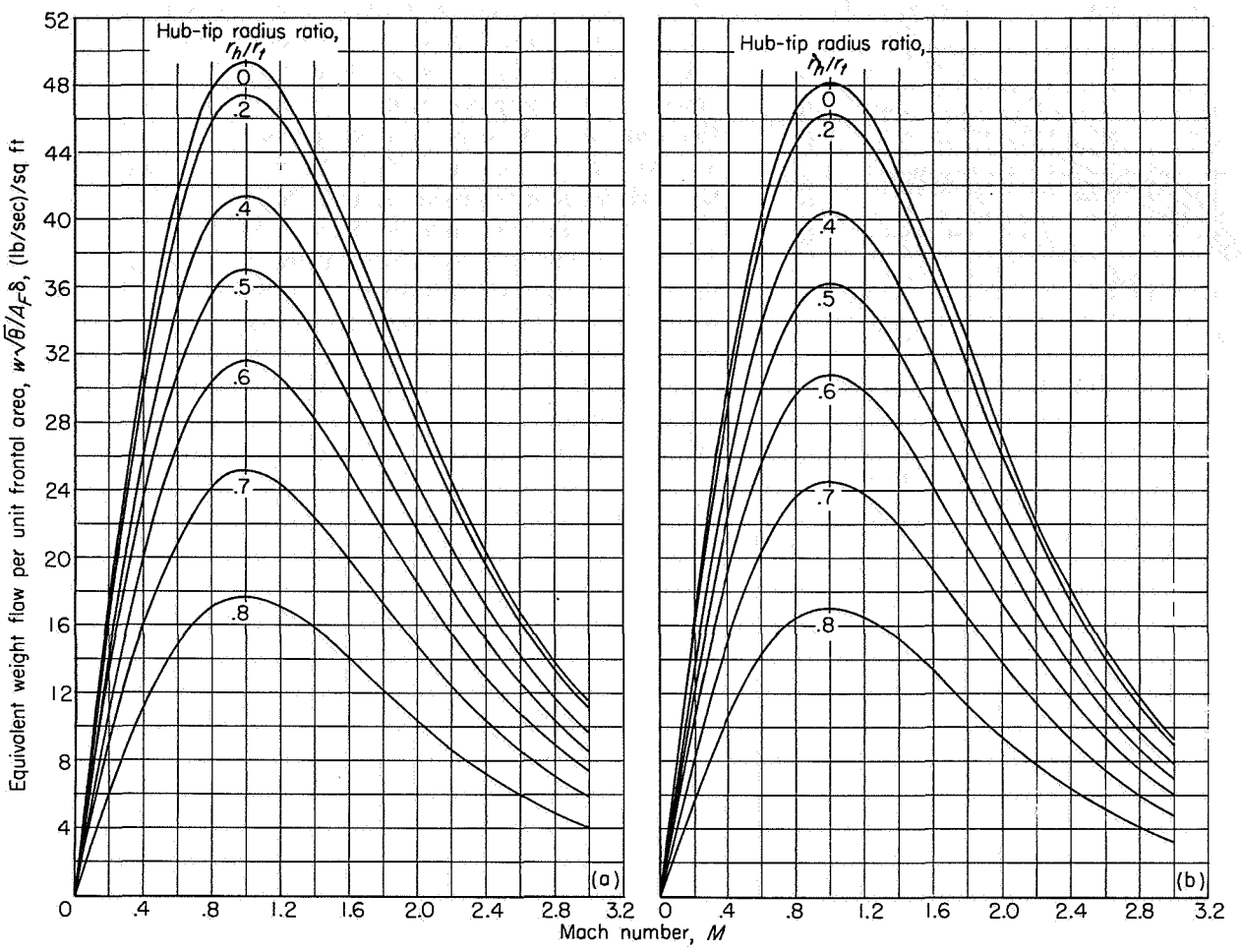

(a) Ratio of specific heats, 1.4.

(b) Ratio of specific heats, 1.3.

FIGURE 19.—Variation of equivalent weight flow per unit frontal area with Mach number for several values of hub-tip radius ratio.

sure ratio of 16. Assume $w\sqrt{\theta}/A_F\delta$ of 30 pounds per second per square foot for the compressor and a turbine-inlet temperature of 2000° R. Component efficiencies are those used in the cycle analyses previously presented.

Engine inlet.—Although it is not affected by compressor pressure ratio, the area of the inlet is also of interest and will be considered first. For reasonably high flight speeds, the internal frontal area of the inlet is equal to or greater than that of the free-stream tube passing the required mass flow. Assuming the internal inlet area to be equal to the free-stream area (the capture area), the value of $w\sqrt{\theta}/A_F\delta$ for the inlet is given by figure 19(a) with M=free-stream Mach number and r_h/r_t=0. With a pressure recovery of 0.98, the ratio of the inlet frontal area to compressor internal frontal area is 0.62. This ratio is directly proportional to both the total-pressure recovery of the inlet diffuser and the flow capacity of the compressor.

Combustor.—In determining the size of the combustor, the average velocity in the annulus is frequently taken as a critical factor, although Mach number is probably just as applicable. The magnitude of the velocity influences combustion efficiency as well as the pressure drop through the combustor. For a limiting velocity of 150 feet per second and r_h/r_t of 0.4, the internal frontal area of the combustor is 43 percent of the compressor internal frontal area. This number is inversely proportional to the limiting velocity

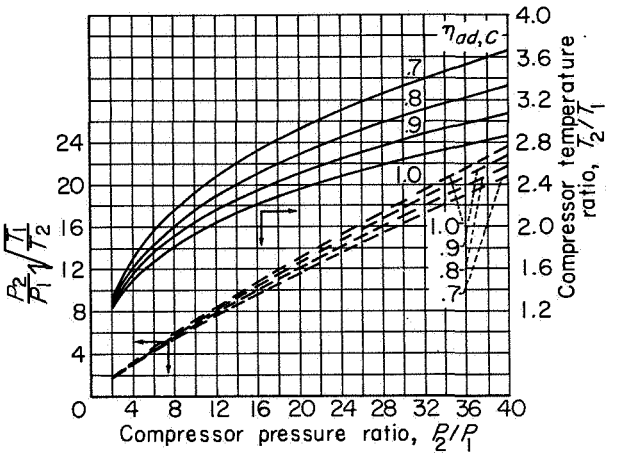

FIGURE 20.—Chart for estimating total pressure and temperature behind compressor; $\tau_C=1.4$.

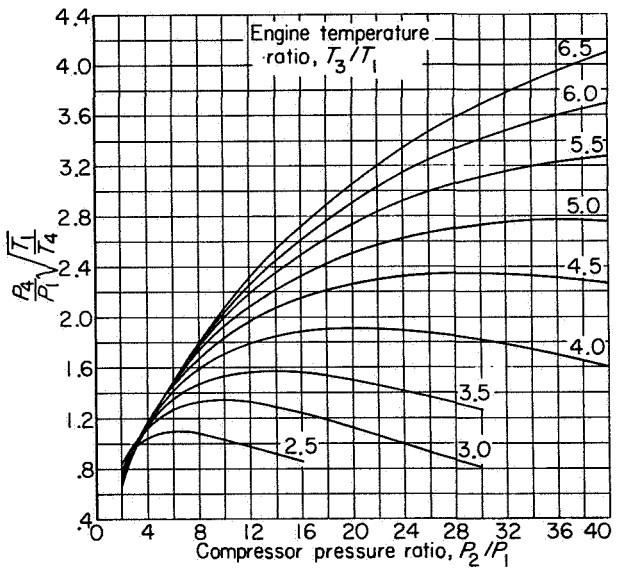

FIGURE 21.—Chart for estimating equivalent weight flow behind turbines driving compressors.

(eqs. (22a′) and (23)). It increases as compressor pressure ratio decreases; at a pressure ratio of 8, the internal frontal area of the combustor is 70 percent of that of the compressor, other conditions being the same. This ratio is again proportional to the flow capacity of the compressor.

Turbine.—For the turbine, the axial Mach number at the turbine outlet is decisive. This Mach number should be less than about 0.7 to avoid the limiting loading discussed in reference 15. For a leaving Mach number of 0.6 and a hub-tip radius ratio of 0.6, the ratio of the internal frontal area of the turbine to that of the compressor is 0.54. With leaving Mach numbers of 0.5 and 0.4, the respective ratios are 0.61 and 0.72. Decreasing the compressor pressure ratio increases this number. At a compressor pressure ratio of 8 it is 0.70 instead of 0.54. Again, increasing the turbine-inlet temperature to 2200° R ($T_3/T_1=5.0$) decreases this number from 0.54 to 0.50. For a fixed turbine-inlet temperature, a reduction in compressor-inlet temperature increases T_3/T_1 with an attendant reduction in this internal-frontal-area ratio.

The flow capacity of the turbine is controlled by the stresses in the turbine blades and the required work output of the turbine, as well as the Mach number at the turbine exit. This effect is outlined in reference 16 and given detailed study in reference 17. Briefly, the permissible annular flow area A is proportional to the allowable centrifugal stress τ at the blade root according to the equation

$$A=\frac{2\pi\tau g}{\omega^2\Gamma\psi}$$

where ψ is a taper factor defined as the ratio of the actual root centrifugal stress to the centrifugal stress in a blade having a constant spanwise cross-sectional area. Combining this relation with equation (21b) and noting that $U_t=r_t\omega$ provide the result

$$\frac{wU_t^2}{A_x g}\frac{\Gamma}{\tau}=\frac{2P}{\psi\sqrt{T}}\sqrt{\frac{\gamma g}{R}}M\left(1+\frac{\gamma-1}{2}M^2\right)^{-\frac{\gamma+1}{2(\gamma-1)}} \quad (24)$$

If reference values of compressor tip speed U_t, τ, and Γ are assigned and attention is focused on the turbine, equation (24) becomes

$$\left(\frac{w\sqrt{\theta}}{A_x\delta}\right)_1\frac{\Gamma}{\Gamma_{ref}}\frac{\tau_{ref}}{\tau}\left(\frac{U_t}{U_{t,ref}}\right)^2 = \frac{2}{\psi}\frac{P_4}{P_1}\sqrt{\frac{T_1}{T_4}}\sqrt{\frac{\gamma g}{R}}M_4\left(1+\frac{\gamma-1}{2}M_4^2\right)^{-\frac{\gamma+1}{2(\gamma-1)}} \left(\frac{p_{s1}}{\sqrt{T_{s1}}}\frac{\tau_{ref}}{\Gamma_{ref}}\frac{g}{U_{t,ref}^2}\right) \quad (25)$$

for a constant weight flow throughout the engine. A quantitative study of equation (25) is obtained from figure 22, in which a set of curves showing the left side of this equation as a function of

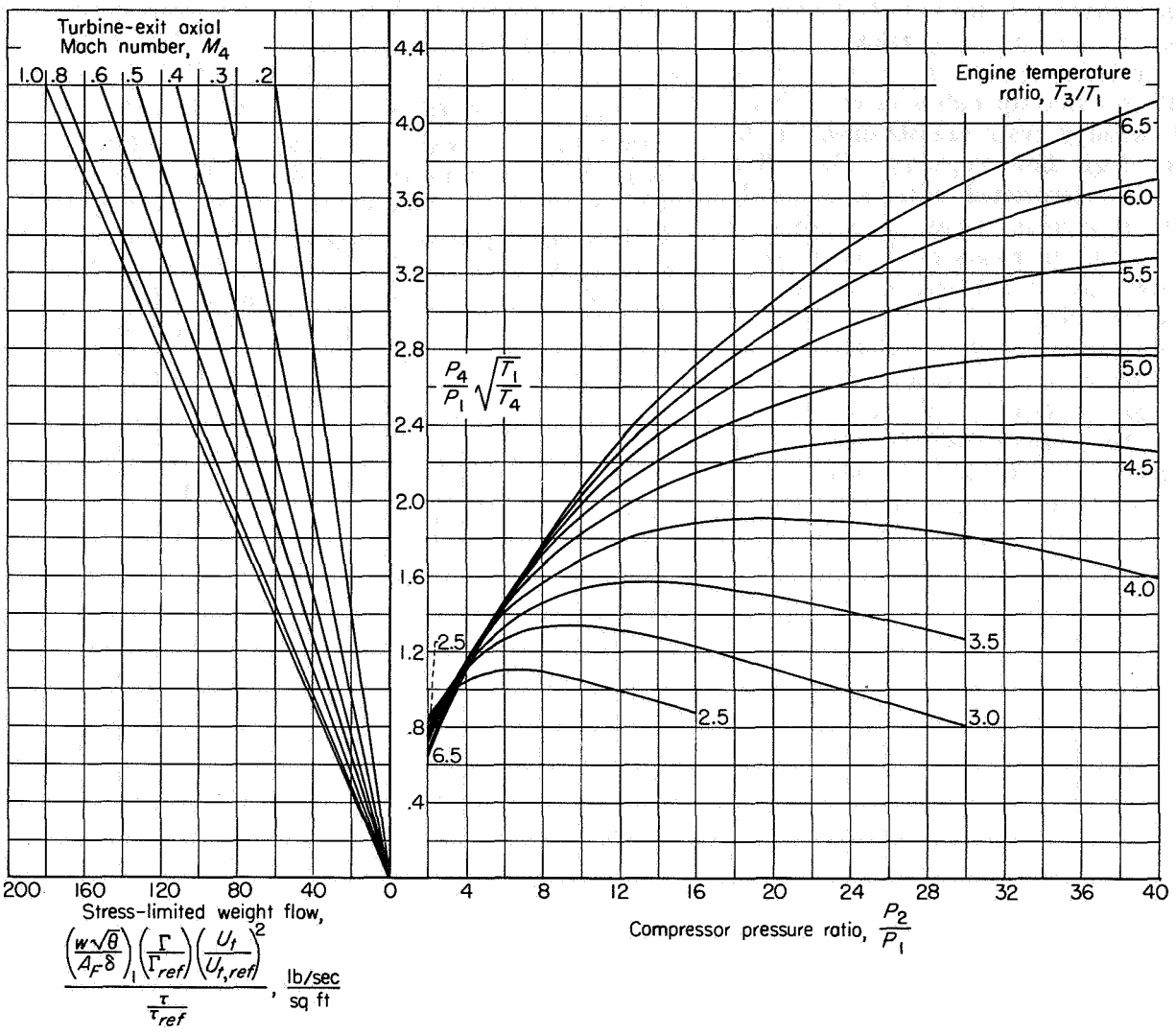

FIGURE 22.—Stress-limited airflow and tip speed for compressor or turbine (eq. (25)).

$(P_4/P_1)\sqrt{T_1/T_4}$ and M_4 is adjoined to the curves of figure 21. The following values were assumed in the calculations for this figure, with appropriate units where necessary: $\gamma=1.3$, $\psi=0.6$, $U_{t,ref}=1000$ feet per second, $\tau_{ref}=30{,}000$ pounds per square inch, and $\Gamma_{ref}=0.3$ pound per cubic inch.

When Γ, τ, and U_t assume their reference values, the left side of equation (25) is identically $w_1\sqrt{\theta_1}/A_F\delta_1$, the flow capacity of the compressor as limited by turbine stress. For the reference condition, the permissible values of $w_1\sqrt{\theta_1}/A_F\delta_1$ are considerably higher than those assumed in the previous study. The assumed hub-tip radius ratios are thus well within those permitted by the assumed stress limits and compressor flow capacities. Higher compressor speeds or lower turbine stress limits would, of course, reduce the compressor flow capacity permitted.

The relation between the work output of the turbine and the flow capacity of the compressor may be examined in a similar gross way. As a rule of thumb, the maximum output of a turbine stage is determined by the quantity $J\Delta H/(\omega r_h)^2$, which is inversely proportional to the square of the blade- to jet-speed ratio. An upper limiting value (of about 2) may be assigned to this quantity, and the permissible enthalpy drop

in a stage is given when the speed of rotation is known. Only a small enthalpy drop is obtained with the low rotative speeds and at the hub of turbines with low hub-tip radius ratios; accordingly, small enthalpy drops are obtained for the conditions of high flow capacity. High flow capacity is thus associated with a relatively large number of turbine stages. High rotative speeds and large hub-tip ratios, on the other hand, reduce the flow capacity but tend to decrease the number of turbine stages.

Afterburner.—At the inlet to the afterburner, a limiting velocity is again used for the same reasons that govern its use in the primary combustor. For the present example the limiting velocity is assumed to be 550 feet per second. With this limit, the ratio of the internal frontal area of the afterburner to that of the compressor is 0.58, ($r_h/r_t=0$). Changing the cycle pressures and temperature will vary this number in about the same proportions as those given for the turbine.

Nozzle.—The area of the jet nozzle depends on the amount of afterburning, the amount of supersonic expansion in the nozzle, and whether or not an ejector is employed. With sonic velocities at the nozzle exit and no afterburning, the area ratio is 0.29. Altering the cycle will change this number somewhat in proportion to the corresponding turbine areas.

It appears that a compressor having a flow capacity of 30 pounds per square foot ($=(w\sqrt{\theta}/A_F\delta)_C$) could have the largest internal frontal area of all the components in an engine for subsonic flight. Since the area ratios are proportional to compressor equivalent flow capacity, there is a strong incentive to make the flow capacity of the compressor as high as possible. The maximum value of compressor flow capacity is 49.4 pounds per second per square foot (fig. 18(a)), however, so that all the other components could presumably have a smaller frontal area than the compressor when the high pressure ratios required for good engine efficiency are used.

COMPARISON OF FRONTAL AREAS FOR SUPERSONIC FLIGHT

For a given mass flow, the free-stream-tube area increases with Mach number in the supersonic regime. The temperature at the compressor inlet increases and that at the compressor outlet thus also increases with flight Mach number. Both the values of P_2/P_1 and T_3/T_1 are generally lower for supersonic flight than they are for subsonic flight. As a result, the values of P_4/P_1 and $(P_4/P_1)\sqrt{T_1/T_4}$ are reduced (figs. 16 and 21). For a given value of $(w\sqrt{\theta}/A_F\delta)_C$, the value of $(A_F)_x/(A_F)_C$ therefore increases with flight Mach number (eq. (23)). As shown in figure 12, however, the flow capacity of the compressor also decreases with flight Mach number when the mechanical speed of the engine is fixed (since θ increases with flight Mach number). This behavior decreases the value of $(A_F)_x/(A_F)_C$.

In order to examine these trends, consider the situation at flight Mach numbers of 2 and 3 in the stratosphere. Let the respective values of P_2/P_1 be 8 and 4, and let the turbine-inlet temperature be 2500° R for both cases. Assume, moreover, that $(w\sqrt{\theta}/A_F\delta)_C$ is 30 pounds per second per square foot for the compressor at sea level.

At the flight Mach number of 2, the equivalent flow capacity of the compressor may drop to 24 ((lb/sec)/sq ft) for constant engine speed. With an inlet recovery of 0.90, the ratio $(A_{F_0}(/A_F)_C$ becomes 0.74. At the flight Mach number of 3 and a recovery of 0.6, the value of $(w\sqrt{\theta}/A_F\delta)_C$ is 15 pounds per second per square foot and $(A_F)_0/(A_F)_C=0.77$. Notice that this number applies only to the internal capture area. As indicated in figure 8, the actual frontal area of the inlet may be substantially larger than this.

With a limiting average combustor velocity of 150 feet per second, the ratio of the internal frontal area of the combustor to that of the compressor is 0.70 at the flight Mach number of 2 ($r_h/r_t=0.4$). It is 0.88 at the flight Mach number of 3. This value is almost inversely proportional to compressor pressure ratio for a given flight condition.

If the hub-tip radius ratio of the turbine is 0.6 and the leaving Mach number is 0.6, the ratio of the internal frontal area of the turbine to that of the compressor is 0.62 at the flight Mach number of 2 and 0.58 at the flight Mach number of 3. Increasing either the compressor pressure ratio or turbine-inlet temperature decreases this ratio in inverse proportionality to the resulting change in $(P_4/P_1)\sqrt{T_1/T_4}$ shown in figure 21. Notice that the assumed flow capacity of the compressor is low enough to satisfy the turbine stress requirements of figure 22 for the reference conditions.

Again using an afterburner-inlet velocity of 550 feet per second, the ratio of the internal frontal area of the afterburner to that of the compressor is found to be 0.77 at the flight Mach number of 2. At the flight Mach number of 3, it is 0.71. These values are again almost inversely proportional to $(P_4/P_1)\sqrt{T_1/T_4}$, and changes in compressor pressure ratio and turbine-inlet temperature will change this ratio following the trends shown in figure 21.

The area of the nozzle again depends on the factors previously mentioned. It is noted, however, that for complete expansion the outlet area of the nozzle is 92 percent of the internal frontal area of the compressor at the flight Mach number of 2. At the flight Mach number of 3, the area ratio for complete expansion is 1.14. When the nozzle area equals the frontal area of the compressor, the jet velocity V_j is reduced about 2.5 percent, with a resulting loss of thrust of about 1.5 percent compared with the complete-expansion case. Although the developed thrust is decreased slightly by limiting the expansion, the actual thrust minus drag is probably increased. Internal plugs on an ejector have been recommended frequently when large nozzle pressure ratios are developed. In these cases, the actual flow area is effectively less than the internal frontal area.

For the example chosen, the compressor has a greater frontal area than either the primary combustor or the turbine. The flow through the compressor is much less than its natural capacity, however; and a 20- to 100-percent increase in the flow capacity of the compressor at supersonic flight speeds could easily be obtained by some means or another. Thus, engines could be designed in which the compressor diameter is smaller than that of any other component in the engine. If the increase in flow capacity is obtained by increasing the mechanical speed with flight Mach number, so as to reduce the severity of the drop in $N/\sqrt{\theta}$, then turbine stress problems arise (eq. (25)). On the other hand, if the value of N is sufficiently low to avoid this difficulty, the enthalpy drop per turbine stage is low, and a large number of turbine stages is required. Therefore, the selection of compressor flow capacity is frequently based on a number of considerations other than frontal area. Design information is required, however, to permit designs as close as possible to the natural limit of 49.4 pounds per second per square foot of frontal area. This high value could then be used when it is desired.

EFFECTS OF COMPRESSOR EFFICIENCY ON SIZE OF COMPONENTS DOWNSTREAM

Compressor efficiency also affects the size of engine components downstream of the compressor. The magnitude and interrelation of these effects are estimated by the following technique. When the weight flow w and the velocity or Mach number are given, the annular flow area is seen by equations (21) to be determined by the total pressure P and the total temperature T at the point considered.

Presuppose a fixed enthalpy rise in the compressor and a given fuel flow so as to make the total temperature T at any point in the engine independent of the compressor efficiency and pressure ratio. Equation (14) then shows how a small change in compressor efficiency affects the total pressure at any point in the engine downstream of the compressor. Holding w, T, and V or M constant and differentiating either equation (21a) or (21b) with respect to A and P give

$$\frac{dA}{A}=-Q\frac{d\eta_{ad,C}}{\eta_{ad,C}} \tag{26}$$

utilizing equation (14). A curve showing the parameter Q as a function of P_2/P_1 for $\gamma_C=1.4$ is shown in figure 23. This curve indicates that the sensitivity of the flow area of the components downstream of the compressor to small changes in compressor efficiency is greatest when the compressor total-pressure ratio P_2/P_1 is high. Under these conditions, the frontal area of the components behind the compressor is usually low. When the components behind the compressor

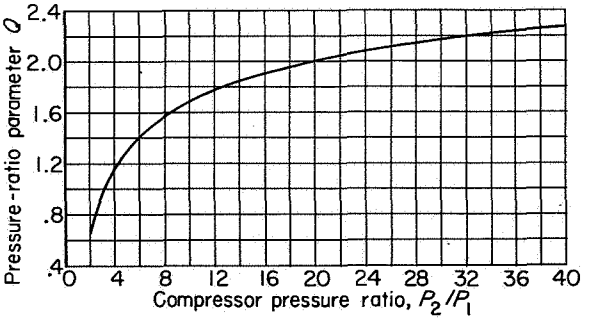

FIGURE 23.—Variation of parameter Q with compressor pressure ratio (eqs. (13) and (26)); $\gamma_C=1.4$.

decide the frontal area, however, low compressor efficiency can be costly with respect to size as well as engine efficiency and specific thrust.

FACTORS DETERMINING COMPRESSOR FLOW CAPACITY AND WEIGHT

FLOW CAPACITY

The flow capacity selected for a compressor represents a compromise among several factors that also control engine weight. Some of these factors are discussed in the next main section of this chapter. For the moment it is sufficient to note that, among other things, the flow capacity depends on the rotational speed of the engine. Two causes of this dependency, turbine blade stress and turbine work, were outlined in the previous section. A similar limit involving stress in the compressor blades could also be deduced. The stress in the turbine blades is frequently the governing factor, however, because of the elevated temperatures.

Another factor making the flow capacity depend on the speed of rotation arises from aerodynamic causes in the compressor itself. At the present state of the design art, dictates of efficiency limit the Mach number relative to the compressor blades. This Mach number may be written as

$$M_1'=M_1 \cos \beta_1 \sqrt{1+\left(\frac{U}{V_1 \cos \beta_1}-\tan \beta_1\right)^2} \quad (27)$$

The equivalent weight flow per unit of flow area at any radius is, however,

$$\frac{w\sqrt{\theta}}{A\delta}=\sqrt{\frac{\gamma g}{R}} M_1 \cos \beta_1 \left(1+\frac{\gamma-1}{2} M_1^2\right)^{-\frac{\gamma+1}{2(\gamma-1)}} \frac{p_{s1}}{\sqrt{T_{s1}}} \quad (28)$$

Because of other considerations, the value of β_1 is usually made as small as possible, and even negative values of β_1 may be desired. With a given value of β_1 and a limiting value of M_1, the flow capacity is critically dependent on the wheel speed U, decreasing as the wheel speed increases.

If, now, the wheel speed is independently determined, the maximum flow capacity of the compressor is automatically stipulated either by the limitations of blade stress or by the limitations of compressor blade Mach number. At low compressor pressure ratios and low ratios of turbine-inlet to compressor-inlet temperature, turbine blade stress tends to be the deciding factor. At higher levels of these quantities, with cooled turbines, compressor blade Mach number becomes the critical item. In order to overcome this latter limitation, considerable attention must be given to the problem of efficiently coping with high Mach numbers relative to the compressor blades.

The radial distribution of $w\sqrt{\theta}/A\delta$, as well as the hub-tip radius ratio, is required to determine the net equivalent flow capacity of the compressor. The radial-distribution problem is treated in chapter VIII. It will not be discussed here except to note that the flow capacity can be affected by the distribution. The hub-tip radius ratio is affected by two factors: (1) the problem of attaching the blades to the disks, which is chiefly a mechanical problem, and (2) the aerodynamic problem of designing the blades near the hub. The gains in flow capacity are small when the hub-tip radius ratio is reduced below about 0.35 (see figs. 15 and 16), and it is at the lower values of hub-tip radius ratio that the attachment and aerodynamic design problems may become serious. Below some value of hub-tip radius ratio, therefore, the possible gains in weight flow per unit of frontal area could be too small to justify the effort and expense required to obtain them.

LAYOUT AND WEIGHT

Some of the problems associated with the size and weight of a compressor are illustrated with the aid of a schematic drawing of a representative current compressor and its diffuser (fig. 24). The pressure ratio, turbine-inlet temperature, and weight flow of air of the engine associated with this compressor are presumably determined from preliminary design studies. The speed of rotation is also assumed to have been selected from this study. The flow capacity of the compressor is then fairly well defined, either by stress or aerodynamic considerations.

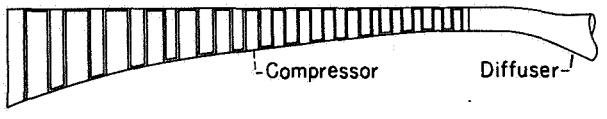

FIGURE 24.—Typical current layout of axial-flow compressor and exit diffuser.

The number of stages required by the compressor is determined by the pressure ratio or enthalpy rise that each stage can produce. At the present time, the permissible enthalpy rise per stage may be approximately expressed by

$$\Delta H=\frac{2\sigma V_1' U}{J}\left(D+\frac{V_2'}{V_1'}-1\right) \qquad (29)$$

where D is a measure of the blade loading as presented in reference 9. The enthalpy rise in a stage is thus directly proportional to the blade speed and to the stage-inlet velocity relative to the rotor. Obtaining high flow capacity by reducing the blade speed increases the number of stages required to obtain a given enthalpy rise. This result is similar to that previously noted for the turbine.

The enthalpy rise in a stage also depends on the relative velocity ratio V_2'/V_1' across the stage. If D has a limiting value of 0.4, changing V_2'/V_1' from 1 to 0.9 reduces the enthalpy rise in the stage by 25 percent. The limitations imposed by this velocity ratio affect the layout and the number of stages required by a compressor. In order to meet the velocity requirements in the combustor, the axial component of air velocity is sometimes reduced by a factor of 5 or more between the compressor inlet and the combustor. Avoiding excessive losses in the diffusing section behind the compressor requires that a considerable part of this deceleration be absorbed in the compressor. Since

$$\frac{V_2'}{V_1'}=\frac{V_{z,2}}{V_{z,1}}\frac{\cos\beta_1'}{\cos\beta_2'}=\left(\frac{V_{z,2}}{V_{z,1}}\right)\times\text{a number less than 1.0}$$

the ratio V_2'/V_1' must be appreciably less than 1.0 in the majority of the blade rows. The enthalpy rise per stage is thus restricted, and the number of stages is greater than that required if $V_{z,2}/V_{z,1}$ could be greater.

Continuously decreasing the axial velocity through the compressor also causes V_1' to be continuously reduced. The enthalpy rise per stage is consequently much less in the latter stages of the compressor than it is in the early ones. Obtaining a reasonable enthalpy rise in the latter stages thus requires the use of fairly high blade speeds, even if the inlet flow capacity of the compressor is prejudiced. Moreover, the casing diameter at the rear stages is usually kept large to obtain these high blade speeds. Continuity requirements then dictate the use of small blade heights to the detriment of efficiency.

The number of compressor stages and the compressor layout shown in figure 24 were determined by these principles. As a result of this particular layout, an awkward flow passage is required to connect the compressor to the combustor. Moreover, the bulk and weight of the compressor are large.

The length of each stage is decided by the axial clearance required and the chord length of the blades themselves. The spacing is usually set by mechanical tolerances and the location of the thrust bearing. The chord length of the blades is frequently determined by arbitrarily limiting the bending stress at the blade root. The bending moment normally used to calculate the stress is that caused by the steady aerodynamic forces on the blade. Because of the dangers of blade vibration, however, a large factor of safety is used, and the calculated steady-state bending force is well below the value that the blade can withstand. The blade chords, and hence the engine length, are thus greater than required by aerodynamics for steady-state stresses. (At high altitudes, however, large blade chords may be required to avoid poor performance at low Reynolds numbers. More information is required on this subject before definite statements can be made.)

Because of the large diameter and high internal pressure at the outlet, the casing is heavy. For the type of mechanical design shown in figure 24, a considerable amount of weight is also associated with the rear disk, which has a large diameter. If the metal in this solid disk had to resist only the stresses created by centrifugal force, the thickness could be considerably less than that actually used. Its weight would then be relatively small. It must, however, be stiff enough to be manufactured readily and handled without danger of warping. The disk must also be stiff enough to withstand the axial force resulting from the pressures acting on the disk face. These forces increase with the diameter of the disk and with compressor pressure ratio.

For a given Mach number limit, increasing the design weight flow through the compressor by reducing the design rotative speed reduces the diameter of the compressor and hence reduces the weight of an individual disk and a unit length of casing. On the other hand, the number of

stages is increased. More disks and a longer casing length are needed. It would appear that, for a given limitation between flow capacity and speed, there are optimum values of these quantities that yield the minimum compressor weight. As previously noted, the same reasoning applies to the turbine.

The size and length of the other engine components are fairly independent of the actual design of the compressor after the pressure ratio and flow capacity are given. An exception to this statement might be the diffuser between the compressor and combustor, but this element should be considered to be part of the compressor itself.

Since the Mach number relative to the compressor blades has an important bearing on the flow capacity of the compressor and the number of stages required, the highest permissible Mach number level should be used in design. This statement is particularly true of the inlet stages, where the Mach numbers naturally tend to be the highest. Important improvements of these stages have been made in recent years (see refs. 8 and 18). As a result, higher airflow capacity can be combined with high stage pressure ratios.

Identifying the true loading limit of a blade has also been given attention. The coarser the definition of the loading limit, the greater is the aerodynamic factor of safety that must be employed. The design pressure ratio of a stage thus suffers. While reference 9 and equation (29) are definite advancements in this direction, there is still considerable room for improvement.

Although the number of stages is reduced through the use of high Mach numbers and accurately defined loading limits, the over-all length tends to remain the same if the bending-stress limits are unaltered. The higher pressure ratios result partially from larger blade forces, which in turn cause larger bending moments at the blade roots. With a fixed allowable bending-stress limit, the chord length of the blades increases as the stage pressure ratio increases. Recent observations have shown, however, that blade vibrations are primarily the result of rotating stall (ref. 19). Blade wakes and the pressure fields of fixed obstacles may have contributory effects, but these sources can be avoided or otherwise treated by appropriate design. These investigations have also shown that vibration induced by rotating stall can be eliminated or mitigated by such methods as interstage bleed and variable stators. As indicated in reference 20, ramps at the inlet are also useful for evading the blade-vibration problem. Through the use of this type of equipment, the hazards of blade vibration are relieved. The permissible bending stresses can be raised, and marked reductions in chord length are possible. Reducing the chord length and the number of stages reduces compressor length and offers significant reductions in compressor weight.

The necessity of adding stages to a compressor just to reduce the axial velocity is a problem that needs more attention. It is possible that too great a penalty is being paid for the lack of complete information about the pressure loss in diffusers and combustion chambers.

As indicated in reference 21, a basic combustor parameter governing pressure loss may be the velocity in the secondary-air passage. An important variable governing the efficiency of a diffuser is the ratio of the maximum surface velocity before deceleration to the minimum surface velocity after deceleration. If the minimum velocity were that in the secondary-air passage of the combustor and the ratio of maximum to minimum surface velocity were given, the velocity entering the diffuser could not be greater than the product of the allowable secondary-air velocity and the allowable velocity ratio. If the diffuser passage causes local velocity maximums and minimums, however, the inlet velocity must be less than the otherwise allowable value. Potential-flow methods, such as those proposed in reference 21, afford a means of eliminating unnecessary maximums and minimums in the surface velocities.

Figure 25, which is taken from reference 21 illustrates a diffuser designed along these lines. An insert controls the flow area in the passage between the compressor outlet and the secondary-air passage of the combustor. The rate of change of this area has the major effect in controlling the rate of diffusion. Gentle curvatures are used to minimize the undesirable gradients due to curvature. Deceleration of the primary air is efficiently obtained by the stagnation of the air ahead of the insert. Such a device should permit higher velocities at the compressor outlet and should tend to shorten the diffuser length. These higher velocities could be used to enable the rear compressor stages to develop greater pressure ratios. On

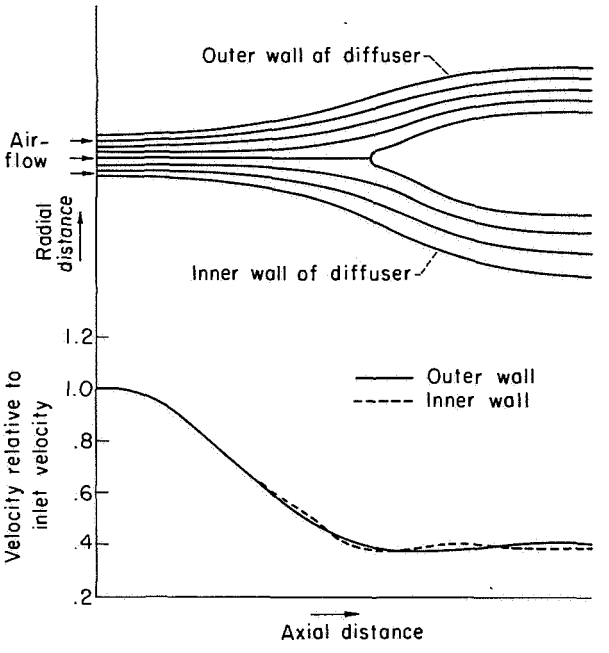

FIGURE 25.—Streamlines and velocity distributions in symmetric diffuser with continuous diffusion between compressor and combustor (ref. 21).

the other hand, the diameter of the casing (and hence blade speed) could be reduced between the inlet and outlet of the compressor without increasing the number of stages over those presently required. In the latter case, a lighter casing may result and the diameter and weight of the disks are reduced. The pressure forces on the disks are also reduced, and the disks may be thinner. Because of the greater radial length of the blades in the rear stages, higher efficiencies may be obtained.

A schematic drawing of a compressor in which the compressor design incorporates the ideas suggested is shown in figure 26. The pressure ratio and weight flow are the same as for figure 24. Higher rotative speeds and flow capacities result from raising the permissible blade Mach number. For this layout, the turbine stresses are higher than those normally used, but it was assumed that turbine cooling can be used to obtain the necessary strength in the turbine blades. The diameter of the compressor and the number of compressor stages are reduced. Interstage bleed and a ramp are assumed to eliminate the vibrations caused by rotating stall, and small blade chords are used. The controlled diffusion without reacceleration in the diffuser permits comparatively high velocities

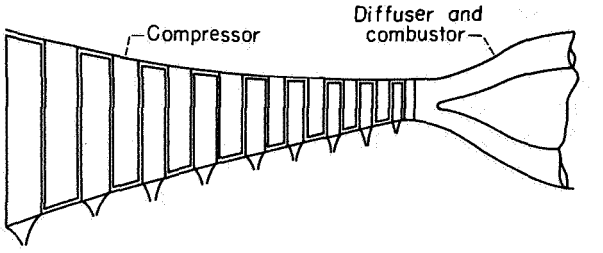

FIGURE 26.—Possible layout of axial-flow compressor and exit diffuser.

at the compressor discharge. These high velocities, together with the high rotative speed, permit the casing diameter to be reduced as shown without any untoward effects on length.

This arrangement is in no sense a recommended one. It merely serves to indicate how several critical aerodynamic factors can greatly influence the shape and weight of a compressor and the weight of the associated engine. The optimum arrangement depends, of course, on the mechanical design and the materials used. Although these factors are not given any other consideration in this report, advances in mechanical design and materials are as important as advances in aerodynamics. For example, obtaining the required disk stiffness with lightweight disks is an important mechanical problem. Improving the strength-weight ratio of materials is obviously another.

COMPRESSOR REQUIREMENTS

DESIGN POINT

The preceding discussions have indicated many of the over-all design-point requirements of compressors. High efficiency is shown to be important for several reasons. The thrust and efficiency of the engine increase with compressor efficiency, particularly with high compressor pressure ratios or low ratios of turbine-inlet to compressor-inlet temperature. The diameters of the components downstream of the compressor decrease as compressor efficiency increases. Moreover, the number of compressor and turbine stages required for a given compressor pressure ratio decreases as compressor efficiency increases.

High airflow capacity is also an important compressor attribute. When the maximum fron-

tal area of the engine is controlled by compressor diameter, high flow capacity is required to reduce nacelle drag. High flow capacity is also a factor in minimizing specific engine weight.

One of the most important requirements of compressors concerns engine weight. The weight of the compressor itself must be small, and its design must not prejudice the weight of the other components. For those flight conditions which are critical to specific engine weight, this requirement is obvious; it is also an important factor when high engine efficiency appears to the critical item. High engine efficiency is invariably associated with high compressor pressure ratio, particularly for subsonic flight. The full benefits of this high pressure ratio cannot be realized, however, when the increase in engine weight is out of proportion to the increase in engine efficiency.

Obtaining relatively lightweight engines and compressors requires each element to be operated near the limit of its aerodynamic and structural capacity. The dead weight carried must be a minimum. The compressor blades must tolerate large relative Mach numbers so that high flow capacity and high relative speeds can be realized. Provisions must be made for eliminating the sources of blade vibrations so that the thickness and chord length of the blades can be small. The diffuser at the compressor outlet must permit high entering velocities in order to obtain the maximum output from the rear stages of the compressor.

Another important factor in compressor design concerns the mating of flow passages. Aerodynamically clean passages are required for transitions between the inlet diffuser and the compressor inlet, and between the compressor discharge and the combustor. Abrupt increases in the flow area or in the curvature of the passages invite undesirable losses. These losses may immediately result from separation of the flow. The losses, on the other hand, may appear in the downstream components as the result of the thick boundary layers (or distortions) developed in the transition passages. Notice that, by the same token, thick boundary layers from any source entering or leaving the compressor are objectionable because they represent potential sources of loss.

These general requirements are necessary ingredients for efficient lightweight designs. The best design within the limits of these quantities results from a cut-and-try procedure in which several tentative, equivalent aerodynamic designs are made and their estimated weights compared.

OFF-DESIGN CONSIDERATIONS

The preceding general comments apply to any operating condition, but they are particularly directed at the design point of the engine and its compressor. The design point refers to a particular flight condition and engine operating condition where the engine components and subcomponents are deliberately matched to achieve certain desired engine characteristics. Besides meeting its obligations at this point, however, the compressor must be able to provide suitable performance at other operating conditions imposed upon it. It must permit the engine to be started readily and accelerated rapidly to its design speed. It must also provide satisfactory performance over a range of engine speeds, pressure ratios, and weight flows when varying flight conditions require them.

The exact nature of these off-design requirements depends on the type of engine and on the design of the components themselves. The general off-design problems are very similar for all engines, however, and the general requirements of the associated compressor can be obtained from the study of the problems of a typical one-spool turbojet engine. The particular problems of other engine types, such as the two-spool turbojet engine and the turboprop engine, are then indicated.

The study of the off-design conditions requires an investigation of the matching of the compressor to the other engine components. The techniques for this investigation are discussed in chapter XVII, and the following results were obtained through the use of these procedures.

ONE-SPOOL TURBOJET ENGINE

The off-design requirements of a compressor are conveniently shown on the compressor performance map in figure 27(a). In the usual representation, compressor pressure ratio is plotted against equivalent weight flow $w\sqrt{\theta}/\delta$. Lines of constant equivalent speed $N/\sqrt{\theta}$ and constant efficiency are parameters. The stall-limit (or surge) line represents the highest pressure ratio attainable at a given equivalent weight flow. The break in this line represents the region where the stall-limit line is not well defined because of multivalued characteristics of the compressors

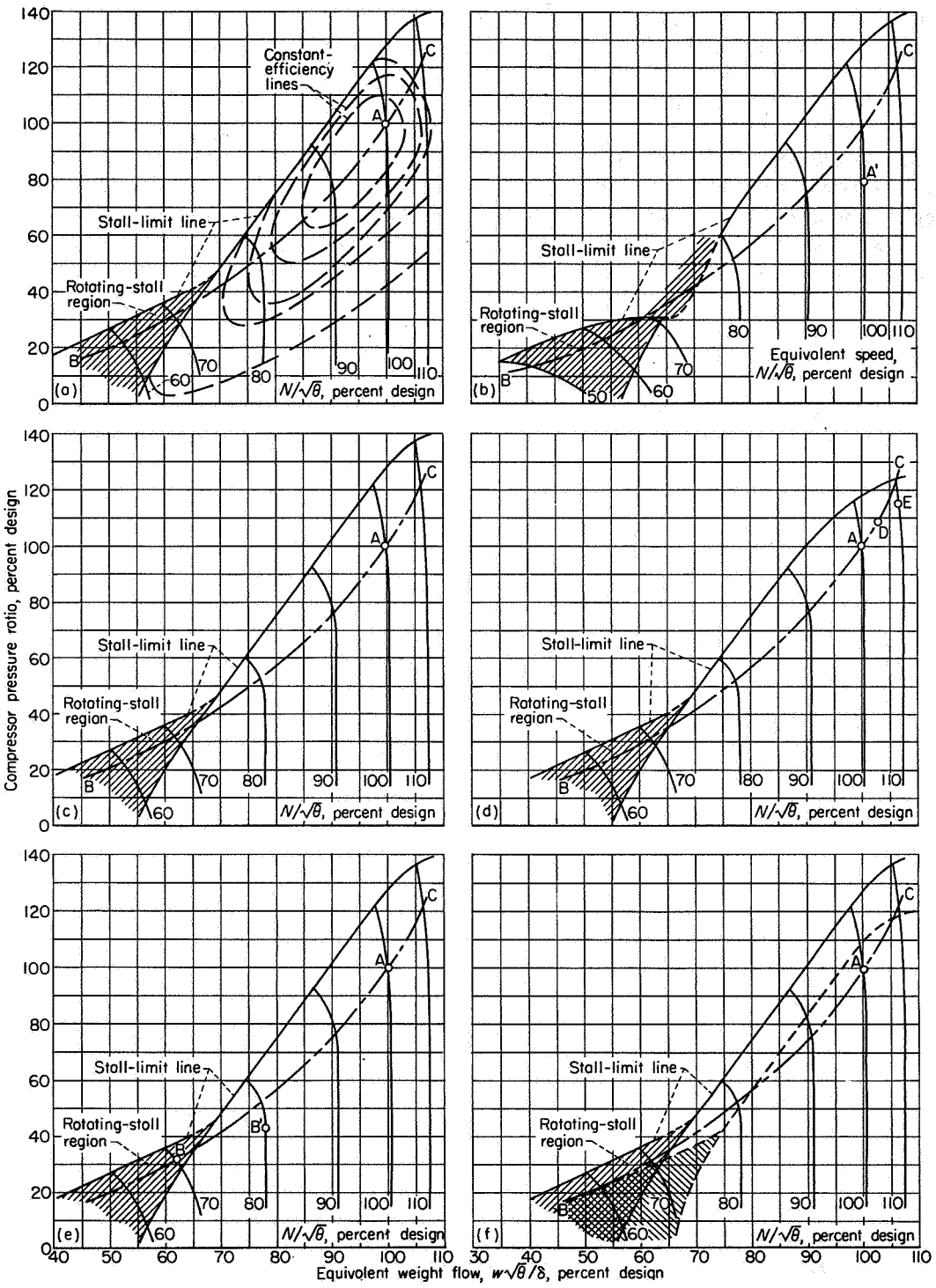

(a) Operating line for sea-level static conditions. (b) Sea-level static operating line intersecting stall-limit line.

(c) Operating line for fixed engine mechanical speed over range of flight Mach numbers. (d) Operating line intersecting stall-limit line at low flight speeds in stratosphere.

(e) Change in operating point resulting from increasing engine speed and opening exhaust nozzle. (f) Effect of inlet flow distortions.

FIGURE 27.—Compressor maps for various operating conditions

(ch. XIII). The shaded area of the map represents a region where one or more of the individual blade rows are stalled; here rotating stall and the attendant dangers of blade vibration may be prevalent (ch. XI).

In the ensuing discussions of off-design performance, the pressure ratio, equivalent speed, and equivalent weight flow are expressed as percentages of their design-point values. Thus, point A of figure 27(a), where the pressure ratio, equivalent speed, and equivalent weight flow are denoted by 100 percent, represents the design point of this particular compressor.

For any operating condition of the engine, the corresponding point on the compressor performance map is given when any two of the following variables are stipulated: the equivalent compressor weight flow, the equivalent compressor speed, and the ratio of turbine-inlet to compressor-inlet temperature. Frequently one of these variables is known directly and the others are functions of the flight Mach number, the recovery of the inlet diffuser, the amount of afterburning, and the jet-nozzle area.

Engine acceleration.—With a fixed jet-nozzle area, the compressor equilibrium operating points may lie along the line BC of figure 27(a) for sea-level static conditions. The principal off-design problems here pertain to blade vibrations and engine acceleration in the low-equivalent-speed regions. Blade vibrations may occur anywhere in the shaded region; and, for the time being at least, this danger appears to be inevitable unless some variable feature is incorporated into the compressor design. Such devices as outlet or interstage bleed, variable inlet guide vanes and stators, or ramps have been used, or suggested, to circumvent the vibration problem.

For the purpose of discussion, the problem of engine acceleration may be conveniently measured by the difference between the pressure ratio of the stall-limit line and that of the equilibrium operating line at a given equivalent weight flow. This difference is called the stall margin. When the stall margin is large, the turbine-inlet temperature, and hence the torque of the turbine, can be appreciably increased without encountering the stall limit. Rapid accelerations are then possible. When the stall margin is small, the acceleration rate is also small unless such devices as an adjustable jet nozzle, interstage bleed (refs. 22 and 23), or variable inlet guide vanes and stators are used. When the operating line intersects the stall-limit line (fig. 27(b)), the stall margin is negative, and such devices are necessary if design-speed operation is to be reached. An alternative to using these variable features is to relocate the design point to A′ of figure 27(b). This procedure is equivalent to making the compressor too big and too heavy for the pressure ratio it is required to produce (in particular, the rear stages are too lightly loaded); it is thus an undesirable remedy.

The reason that some compressors have good and others poor stall margins is not completely understood. Irrational design practices have contributed to the problem. Otherwise, the available stall margin usually becomes less as the design pressure ratio increases. Compromising the design so that the best compressor performance is sought at, say, 90-percent speed (lower design pressure ratio) has been suggested to help the low-speed stall margin. The benefits obtained by this procedure are usually small, however, and this type of design tends to put the compressor in jeopardy at higher speeds. Since some devices are desired anyway to deal with blade vibrations, it is reasonable to extend their use to increase the stall margin and not compromise the design of the compressor too much to combat the acceleration problem.

Varying flight speeds.—As previously indicated, the compressor operating point is a function of a number of variables. The general trend of operation over a range of flight speeds, however, may be indicated by line BC of figure 27(c). Along this line, the mechanical speed of the engine is constant. Point C thus corresponds to small values of θ_1 (low inlet temperatures resulting from low flight Mach numbers in the stratosphere). On the other hand, point B corresponds to large values of θ_1 (high flight Mach numbers). Specifically, values of $(N/\sqrt{\theta_1})/(N/\sqrt{\theta_1})_d$ of 0.7, 0.8, 0.9, 1.0, 1.1, and 1.13 correspond, respectively, to flight Mach numbers of 2.93, 2.30, 1.79, 1.28, 0.71, and 0.45 in the stratosphere for constant mechanical speed.

At flight Mach numbers below 1.28 in the stratosphere, the equivalent speed of the compressor is above its design value. The Mach number of the flow relative to the blades near the compressor inlet is higher than that assumed in design. Moreover, the matching of the com-

pressor stages is upset. These effects combine to reduce the efficiency of the compressor and to reduce the slope of the stall-limit line at the higher equivalent speeds. Besides reducing the efficiency of the engine, this drop in compressor efficiency moves the equilibrium operating line upwards. If the design of the compressor is compromised too much to favor low-speed engine acceleration, the compressor efficiency and slope of the stall-limit line may both drop so rapidly that the operating line intersects the stall line at a slight overspeed (fig. 27(d)). In this event, the rotative speed of the engine may have to be reduced so that the operation is at point D. Instead, the area of the jet nozzle may be increased in order to move the operating point to E. Either procedure causes the performance to decrease, and the latter procedure is ineffective when the turbine is at or beyond the point of limiting loading.

Avoiding these efficiency and stall-limit difficulties requires that considerable attention be given to the high-equivalent-speed operating condition during design. Either the design should be made for the assumed overspeed condition, or the design should be reviewed at this condition. Some approximate methods of making this review are presented in chapter X.

With high flight Mach numbers (above 1.28), the equivalent speed of the compressor is lower than its design value. If the flight Mach number is high enough, the compressor efficiency and stall-limit problems plaguing low-equivalent-speed operation reappear. Again, such devices as interstage bleed and variable inlet guide vanes and stators might be helpful, since they actually improve compressor performance in this regime. Variable inlet guide vanes and stators, however, frequently tend to reduce compressor weight flow at the high Mach numbers to the detriment of thrust. Interstage bleed, however, might be useful if the problems of handling the bleed air in flight are not too complicated.

An alternative, however, is to increase the rotative speed of the engine, at least to some extent, as the flight Mach number increases. If the compressor is normally required to operate at 70 percent of its design speed, increasing the mechanical speed 14 percent moves the operating point almost to the 80-percent-speed line. If the area of the jet nozzle is increased so that the turbine-inlet temperature is constant, the operating point shifts from B to B′ in figure 27(e). Not only is the operating point removed from the stall-limit line, but the compressor handles more weight flow and the engine develops more thrust.

Because of the higher flow rate, the flow capacity of the turbine must be higher for this kind of operation. The higher required flow capacity increases the stresses in the turbine for a given rotative speed (fig. 22). For a given turbine stress limit, therefore, the speed at the compressor design point is lower than it would otherwise be. One or more additional compressor stages may be required to attain the original design-point pressure ratios if this is considered necessary. The specific weight of the engine at the original design point is then increased. Whether or not the greater thrust at the high Mach numbers more than compensates for the increase in engine weight depends on the actual design and flight plan. However, the potential benefits from this kind of operation make it worthy of detailed consideration in the initial design studies.

There may be good reasons, however, for actually reducing the pressure ratio required at design speed for this type of engine. Not only is the number of stages reduced, but the internal pressure forces are lowered and the specific thrust is increased. A lighter engine is then obtained. In this case, the reduced engine speed at the low flight Mach numbers offers a saving in engine weight at the expense of engine efficiency for this flight condition. At the high flight Mach numbers, however, the higher thrust and lighter weight combine to offer significant increases in altitude and flight speed.

Reynolds number effects.—At high flight altitudes and low flight speeds, the Reynolds number of the flow through the inlet stages of a compressor becomes so low that their performance is often impaired. Two-dimensional-cascade data (ch. VI) indicate that this is a universal trend. The performance of such a cascade invariably deteriorates when the Reynolds number, based on blade chord, decreases below about 100,000. This behavior is attributed to laminar separation (ch. V). Some concurring evidence is also provided by investigations of multistage compressors, either by bench tests or as part of an engine.

In spite of these over-all performance data, the actual effect of Reynolds number on compressor performance is not completely known. The re-

sults of the two-dimensional-cascade data are not directly valid, because the behavior of their boundary layers is believed to be different from that of a blade row (ch. XV). Over the greater part of a blade row the boundary layer may be expelled by centrifugal forces before it separates. Moreover, a much higher level of turbulence is expected in a compressor, which tends to alter the influence of Reynolds number (ch. V). What are the significant characteristic lengths and velocities remains an unanswered question.

Compressor bench tests at low Reynolds numbers have not been completely conclusive, because the results are frequently contaminated by uncontrolled leakage of air from the atmosphere to the low-pressure regions in the compressor, and by heat transfer. The difficulty of obtaining accurate data at low pressures and small pressure differences adds to the confusion. These difficulties are also encountered in engine tests. Moreover, the latter results naturally include the effect of Reynolds number on the other engine components, as well as the effects of changes in the matching of the components.

In order to meet the Reynolds number problem it may be necessary to use one engine, with a big compressor, instead of two. Increasing only the chord lengths of the early stages has been advocated, but there is no guarantee that this remedy will do anything but add weight to the engine. As an alternative, a lower level of performance in the early stages may be anticipated and the matching of the rest of the stages modified accordingly. This procedure would prevent a small decrease in performance of the early stages from being amplified in the rest of the compressor. There is an urgent need for reliable and applicable data in the near future.

Inlet flow distortions.—Uniform flow at the inlet is the usual assumption in compressor design, and extreme precautions are taken to assure uniform flow at the inlet during bench tests of a compressor. Severe inlet flow distortions, however, are encountered in flight. These distortions may result from many sources. They may occur when the airplane is flying at a high angle of attack. They may result from disturbances created by the engine inlet. Distortions may also result from disturbances created by other parts of the airplane or armament fire in the vicinity of the inlet. At high supersonic speeds, current inlets invariably create disturbances resulting from nonuniform shock waves and from shock and boundary-layer interactions. Sharp curvatures in the inlet ducting also contribute to these distortions.

When distortions are present, the performance of the compressor usually deteriorates. As shown in figure 27(f), the stall-limit line drops (dashed line), and the shaded region (rotating stall) moves to the right. Design speed, overspeed, and underspeed performance suffer. In order to avoid compressor-stall difficulties, the operating line must be dropped.

Because of the penalties incurred by inlet flow distortions, a large amount of effort is being devoted to eliminating them. The eventual result of this work is unknown. At the higher equivalent speeds (low flight Mach numbers), the compressor must be designed to produce a greater pressure ratio than that available when distortions are present. The engine is either heavier than it otherwise needs to be, or else the efficiency is low. At the lower equivalent speeds (high flight Mach numbers) the compressor-stall and blade-vibration difficulties may be so severe that constant-mechanical-speed operation is impossible. Increasing the mechanical speed of the engine with flight Mach number, as discussed in connection with figure 27(e), alleviates this problem.

Inlet matching problem.—The characteristics of the inlet over the intended range of flight Mach numbers must be recognized in designing the compressor and selecting the type of engine operation. The matching problem, discussed in reference 24, is briefly reviewed here. At a given supersonic flight Mach number, an ideal matching of the engine and inlet is achieved when a flow pattern similar to that shown in figure 28(a) is produced. The flow ahead of the minimum inlet area is decelerated by one or more oblique shocks. It then passes through the minimum area with reduced supersonic velocities. A normal shock just behind the minimum area causes the Mach numbers to be reduced to high subsonic values. Thereafter, the flow is gradually decelerated to the velocity required by the compressor. This is the flow situation that occurs at critical inlet operation. (Notice that a compressor designed for high axial Mach numbers requires little subsonic diffusion in the inlet.)

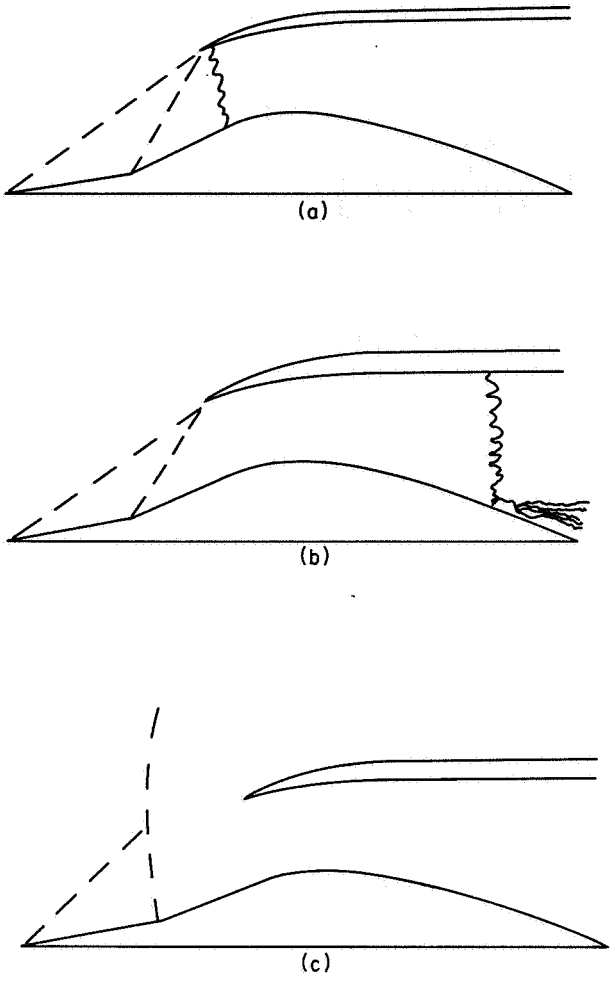

(a) Critical operation.
(b) Supercritical operation.
(c) Subcritical operation.

FIGURE 28.—Shock-wave configurations on engine inlets.

If it happens that the value of $w_1\sqrt{\theta_1}/\delta_1$ ideally delivered to the compressor with this flow pattern is lower than that required by the compressor, the value of δ_1 must decrease. (The weight flow itself cannot increase, and θ_1 is determined only by the flight Mach number and altitude.) What happens physically is that the normal shock moves downstream as shown in figure 28(b). The Mach number ahead of the shock is thus increased, and the pressure loss through the shock is increased. The shock automatically positions itself so that the loss in pressure through it is exactly that required to make $w_1\sqrt{\theta_1}/\delta_1$ conform with that required by the compressor. The inlet operation is then supercritical. The thrust and engine efficiency are reduced, and the flow ahead of the compressor becomes disturbed.

On the other hand, if the ideally delivered value of $w_1\sqrt{\theta_1}/\delta_1$ is too great for the compressor, the value of w_1 must decrease. Either the Mach number immediately ahead of the minimum area, or the total pressure of the flow ahead of the minimum area, or both, must decrease. In this case, the shocks ahead of the minimum area deflect part of the flow around the inlet (fig. 28(c)). The operation of the inlet is then subcritical. The shocks also decelerate the inlet flow, usually with comparatively high recoveries. The over-all recovery of the diffuser is consequently not impaired too drastically. The deflection of the flow, however, does cause an additional drag (ref. 10), which can appreciably reduce airplane performance. This flow condition is also frequently accompanied by an unsteady-flow phenomenon known as "buzz."

Over a range of flight Mach numbers, the inlet flow capacity of a fixed-geometry inlet follows the trend shown in figure 29. The equivalent weight flows are those for critical operation. With a fixed mechanical speed of the engine, the equivalent weight flow demanded by the compressor is also shown. To the left of the intersection of these curves, the inlet wants to supply less air than the compressor requires. It is thus forced to operate supercritically, with the attendant loss in total-pressure recovery. To the right of the intersection, the inlet wants to supply more air than the compressor can use. It then operates subcritically, with the attendant increase in nacelle drag.

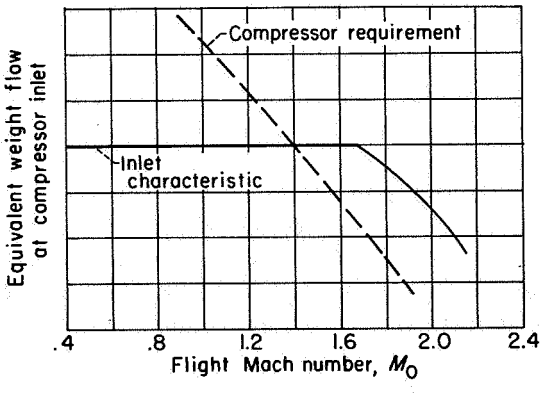

FIGURE 29.—Engine and inlet matching requirements.

The unhappy alternatives of accepting either large pressure losses or large drags at off-design conditions has stimulated research on variable-geometry inlets and on methods of bleeding air from a point between the minimum area of the inlet and the face of the compressor. While considerable improvements in inlet and engine performance have been demonstrated, much work remains to be done to obtain an inlet that is both mechanically and aerodynamically desirable.

In some instances, the severity of this problem can be reduced by modifications in compressor design and engine operation. In theory, the engine curve of figure 29 can be made to coincide with any desired inlet curve by appropriately adjusting compressor equivalent speed with the flight Mach number. Essentially constant equivalent speed is required over the flight Mach number range where the inlet curve is flat. Beyond the break in the curve, the equivalent speed would decrease with Mach number. The change in equivalent speed with Mach number depends on the characteristics of the inlet and compressor. (In this connection, it is noted that the rate of change in compressor airflow with speed appears to decrease as the inlet axial Mach number increases.) This type of engine operation is not inconsistent with that described in connection with figure 27(e).

The degree to which compressor design and engine operation can accommodate the inlet depends on the attendant changes in specific engine weights, engine efficiency, and engine frontal area that can be tolerated. Again, the decision must be based on the intended design and use of the airplane. The engine and airplane must be an integrated unit rather than separate entities.

TWO-SPOOL TURBOJET ENGINE

In the two-spool turbojet engine, the pressure ratio is developed in two separate and independently driven compressors. The upstream compressor is called the outer compressor; the downstream compressor, the inner compressor. Since the design pressure ratio of each compressor is less than that of the equivalent one-spool compressor, fewer difficulties might be expected with the slope and the discontinuities of the stall-limit line.

Because of the higher pressure of the air entering the inner-spool compressor, the value of $w\sqrt{\theta}/\delta$ there is less than that at the outer compressor; the diameter of the inner-spool compressor may thus be decreased. The higher air temperature permits the use of higher blade speeds for a given limit in the relative blade Mach number. Notice that the value of $P/\sqrt{T}$ downstream of the inner turbine is higher than that for the other turbine. According to equation (24), the tip speed of the inner turbine, or compressor, can be increased if the other design factors are fixed. The higher compressor blade speeds thus are also consistent with the turbine blade stress limitations. With uncooled blades, the allowable stress limits are lower for the inner turbine because of the higher temperature; less marked increases in wheel speed are then offered. The smaller diameters and higher blade speeds of the inner spools in any event offer possible reductions in engine size and weight.

Because of the complicated interrelations between the two compressors, the two turbines, and the other engine components, the trends of the operating lines are not as readily exposed as they are for one-spool engines. The important trends are indicated, however, in references 25 to 27, and the following discussion and the associated figures are taken from these reports.

Representative performance maps and operating lines for the outer and inner compressors, respectively, are shown in figures 30 (a) and (b). In this example, the ratio of the design pressure ratio of the outer compressor to that of the inner compressor is 0.75. The trends described, however, are fairly independent of this ratio. The operating line represents the conditions where the inner-turbine-inlet temperature is constant, the mechanical speed of the outer-spool compressor is constant (at its design value), and the flight Mach number is varying. At any flight Mach number, therefore, the equivalent speed of the outer compressor and the engine temperature ratio (ratio of inner-turbine-inlet to outer-compressor-inlet temperature) are defined. These two variables are sufficient to define the operating point of each component of the over-all compressor-turbine unit completely, as for the one-spool engine. The points A, B, and C on the map, respectively, represent the conditions for sea-level takeoff and for flight Mach numbers of 0.9 and 2.8 in the stratosphere.

Outer compressor.—The performance map and operating line of the outer compressor are shown

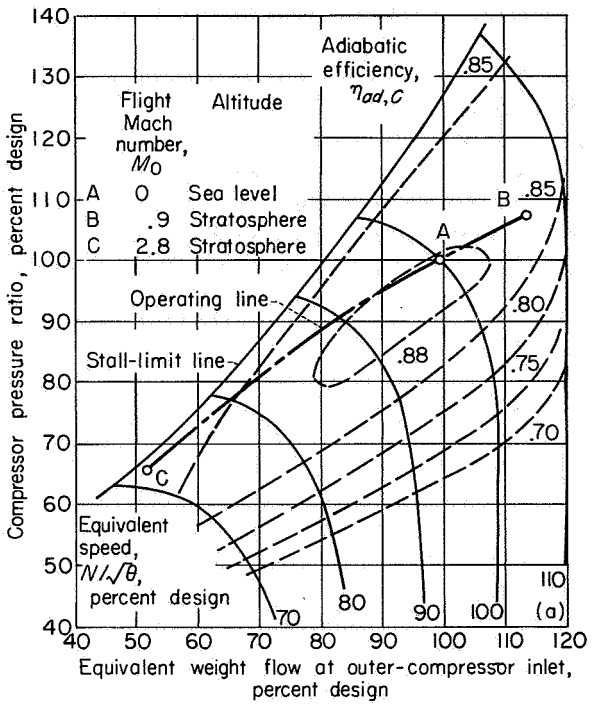

(a) Outer-compressor performance map.

FIGURE 30.—Off-design compressor performance in two-spool turbojet engine (ref. 26).

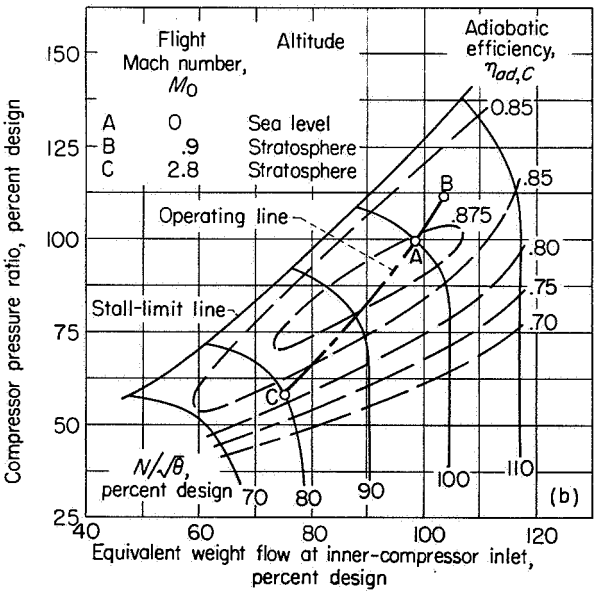

(b) Inner-compressor performance map.

FIGURE 30.—Concluded. Off-design compressor performance in two-spool turbojet engine (ref. 26).

in figure 30(a). At low flight Mach numbers or high engine temperature ratios, a large stall margin appears. The operating line tends to move towards the stall-limit line at low engine speeds. For the example illustrated, the slope of the stall-limit line increases with the equivalent speed. With a more critical compressor design, however, this trend may be reversed. At the high flight Mach numbers or low engine temperature ratios, the operating line approaches the stall-limit line. This behavior is similar to that of one-spool compressors. The equilibrium operating line at sea-level static conditions describes a similar trend.

With the possible exception of the overspeed problems, the outer spool experiences the same sort of difficulties that a one-spool engine encounters under off-design conditions. This statement includes the difficulties associated with Reynolds number and inlet distortions. The possible remedies are also similar, except that bleeding air between the two compressors might be substituted for interstage bleed. These remedies could, however, result in a greater reduction in thrust for the two-spool engine than they do for a single-spool engine.

Inner compressor.—The operating line of the inner compressor differs from that of the outer compressor in two respects: The slope of the operating line is greater, and the change in equivalent speed for a given change in flight conditions is less. For equilibrium operation, the principal stall-limit problem arises at the high equivalent speeds of the inner spool (low flight Mach numbers or high engine temperature ratios). This problem responds to the same treatment indicated for the similar problem of the one-spool compressor, but, again, the thrust penalties may make the solution an undesirable one.

An important point to note is that higher-than-equilibrium engine temperature ratios momentarily move the operating point of the inner compressor towards the stall-limit line, even though the surge margin is increased when equilibrium is finally attained. This higher-than-equilibrium temperature is required for engine acceleration. Bleeding air between the two compressors to assist the outer spool may also narrow the stall margin of the inner spool. For transient conditions, therefore, the benign indications of the equilibrium operating line may be deceiving.

As the inner compressor is started from rest, its front stages are inevitably stalled. The at-

691-564 O-65-5

tendant rotating stall may induce vibrations in the blades. Similarly, rotating stalls developed by the outer compressor may induce vibrations in the inner compressor. In addition, the rotating stalls originating in the outer compressor may impair the performance of the inner compressor and lower the stall-limit line. The published data are too meager to settle this point definitely, but the apparent wide stall margin of the inner compressor may disappear during engine acceleration as a result of these phenomena.

The inner compressor itself may not be subject to any Reynolds number problems, as both the density and the turbulence are relatively high. It can, however, amplify any deterioration in performance encountered by the outer compressor. The solution of this problem is again subject to speculation, but it should yield to the same treatments that may be found for the one-spool compressor.

Inlet distortions may affect the performance of the inner compressor because the inner compressor amplifies changes in the performance of the outer spool. A wide margin between the operating line and the stall-limit line is therefore desired. This requirement may be particularly needed at the high equivalent speeds where the stall margin is the smallest.

TURBOPROP ENGINE

In general, the design and off-design requirements of compressors for turboprop engines are similar to those of the turbojet engine. Since high compressor pressure ratios are desired for the turboprop engine, the stall margin and vibration problems at low speeds cannot be overlooked. Variable stator blades, interstage bleed, or some similar device may be absolutely necessary to obtain satisfactory engine acceleration at the low speeds and still use the pressure-ratio capacity of the compressor at high speeds.

At the design point, the efficiency of the engine should be the maximum obtainable for continuous operation. Practically speaking, this point then represents the maximum power that the engine can develop under continuous operation. Higher power can be obtained for brief periods by increasing the pressure ratio and speed of the compressor. When the compressor is coupled to the propeller, the compressor speed can be controlled independently by adjusting the pitch of the propeller blades. When the propeller is independently driven by its own turbine, the speed of the compressor depends on the turbine-inlet temperature and the power delivered to the propeller. The best location of the compressor operating point at the high power condition depends on the characteristics of the propeller, the stress margin of the engine components, and the characteristics of the airplane. The stall margin required at design or higher speeds thus depends on individual studies of the engine and its intended service. As a rule, however, the required margin is no greater than that required of subsonic jet-engine compressors (see ref. 28).

Except for starting and acceleration, operating the compressor below the design pressure ratio has been thought to be undesirable because of the incurred loss in engine efficiency. An exception to this principle has been made for takeoff and low-altitude flight. The pressures and power developed are so high that engine weight is decided by the low-altitude operating conditions. While high sea-level power is desired for rapid takeoff and climb, the sea-level output and compressor pressure ratio of a turboprop engine can be kept considerably below their maximum values without seriously hurting airplane performance. The resulting decrease in specific engine weight at altitude improves the altitude performance and range of the airplane. Although compressor speed is reduced at sea level for this type of operation, the reduction in most cases is small enough to avoid the stall and blade-vibration difficulties associated with low-speed operation.

Because of its high specific power, the airflow required by the engine is small. The diameter and blade chords of the compressor are also small. The compressor is therefore more susceptible to Reynolds number problems at high flight altitudes. As before, this problem can only be pointed out. Its definition and cure require much research.

CONCLUDING REMARKS AND SUMMARY OF COMPRESSOR DESIGN OBJECTIVES

The final specifications for a compressor gradually emerge from a detailed study of a number of engine and airplane layouts. The design-point pressure ratio, flow capacity, and rotative speed of the compressor represent a compromise that is established only after extensive preliminary studies have been made of various engine and

airplane designs for a given mission or missions. These tentative values may be subsequently modified for selecting the best method of meeting the various off-design conditions encountered. The weight, complexity, and efficiency or drag penalties associated with the available techniques for varying the geometry or performance of components are involved in this decision.

Regardless of the final specifications, the compressor should produce the required pressure ratio with high efficiency. It should, moreover, be subjected to the highest aerodynamic loading and Mach number allowed by available knowledge.

The resulting design should not require extensive development. The performance estimates at the design and off-design points must therefore be reasonably accurate. Moreover, mechanical problems arising from aerodynamic sources, such as blade vibrations, must be anticipated and the design made so that these problems can be either overcome or successfully evaded. Finally, with respect to manufacturing, the component parts should be as few in number as possible and their shape should be simple.

The material presented in the subsequent chapters is the result of research specifically aimed at realizing the objectives set forth in the previous paragraphs. Because of the importance of light and compact designs for aircraft, attention is paid to many problems that may not be so important in other fields of application. This point of view does not limit the usefulness of the information. Many successful designs, by present standards at least, have been made in a wide variety of commercial fields with this information.

CHAPTER III

COMPRESSOR DESIGN SYSTEM

By Robert O. Bullock and Irving A. Johnsen

A general description is presented for the compressor design system that has been adopted for this report on the aerodynamic design of axial-flow compressors. The basic thermodynamic equations are given, and the simplifications commonly introduced to permit the solution of these equations are summarized. Representative experimental data are presented to justify these simplifications. Thus, a valid simplified flow model (which is the real basis of a design system) is provided. The individual elements of the design system and the basic calculations required to execute the aerodynamic design of a compressor are summarized. The improvements in knowledge required to make compressor design a truer science and promising directions of future research are indicated.

INTRODUCTION

The problem of designing axial-flow compressors ultimately becomes the problem of accurately calculating the flow through compressor blade rows. In order to be accurate and have the greatest range of applicability, these calculations should be based on the fundamental laws of motion as much as possible. At the same time, they should be of such a nature that they can be made readily with available computing techniques and equipment.

To be strictly accurate, the fundamental theory should account for the fact that the motion of the air has components in the three physical dimensions. It must also account for the effects of viscosity as well as time-unsteady motion. By assessing each particle of air with these requirements, the differential equations of motion may be derived. The Navier-Stokes equations are, for example, obtained from this procedure. Although they are of great theoretical interest, these equations themselves are of little use in compressor design. They cannot yet be solved to express the flow through the complicated flow passages formed by the blades, the hub, and the casing.

In order to obtain more tractable methods of analysis, various techniques have been devised that combine simplified theories with empirical data. The simplifications made to the equations of motion are essentially the same as the simplifications that have been developed for airfoil analyses. The foundations of the simplified theories are thus the time-steady equations of the motion of an inviscid gas. In this attack, it is tacitly assumed that any important effects of viscosity and time-unsteady flow can be treated as correction factors and that the effects of viscosity are confined to thin boundary layers. The important flow properties not directly given by the simplified equations of motion must be obtained empirically.

The simplified equations, together with the empirical data required to calculate the flow with a reasonable degree of accuracy, constitute a framework for analysis or a design system. The techniques presented in references 29 to 33 are representative of such a system. It is the purpose of the present series of reports to derive an up-to-date design framework and to review the extensive published analytical and experimental results that are the building blocks for this framework. The function of this particular chapter is to coordinate the subsequent chapters by summarizing the important ideas presented in them. Therefore, the following are reviewed: (1) the important ideas underlying the design system, (2) some experimental investigations directed at examining these ideas, (3) the design system and the basic calculations required to execute the aerodynamic design of a compressor, and (4) the improvements in knowledge required to make compressor design a truer science.

The basic thermodynamic equations are first presented, and the general goals of aerodynamic flow analyses are outlined. The equations of

motion for an inviscid time-steady flow are introduced. The problem of solving these equations is then discussed. Some of the commonly used simplifications are presented, and the experimental data necessary to justify these simplifications are noted. Some rather obvious ways of treating the important viscous effects are indicated, and the experiments required both to evaluate these methods and to supply the necessary empirical data are enumerated. Some causes of time-unsteady flows and the approach used to account for them are then presented.

Representative experiments that answer the questions raised in the foregoing analyses are then reviewed. These results provide a valid simplified model of the flow, which is the real basis of a design system. In developing this model, the results of experiments with the simplest conceivable flows are first considered. The effects of complicating flows are then discussed one by one whenever possible. The scope of the investigations is the range over which data are available.

The elements of the resulting design system are then individually summarized. The basic equations and techniques are given. The interrelations among the various elements are pointed out, but no attempt is made to prescribe an actual sequence for their use. In this manner, the structure of a compressor design system is provided, within which the individual designer may work with considerable freedom.

Finally, the shortcomings of the previously outlined approaches are enumerated, and the direction of future research is discussed. Some promising though unproved techniques of analysis are mentioned.

SYMBOLS

The following symbols are used in this chapter:

a_a	stagnation velocity of sound
$\mathcal{C}$	curvature of meridional streamline, see fig. 64
c	chord length, see fig. 32
D	diffusion factor, defined by eq. (54)
$\mathcal{F}_c$	centrifugal force due to curvature of meridional streamline, see fig. 64
$\mathcal{F}_{fr,r}$	radial component of frictional force
$\mathcal{F}_R$	centrifugal force due to rotation of air about axis of compressor
g	acceleration due to gravity, 32.17 ft/sec^2
H	total or stagnation enthalpy per unit mass
I	modified total enthalpy, $H-\omega(rV_\theta)$, see eqs. (39) and (48b)
i	incidence angle, angle between inlet-air direction and tangent to blade mean camber line at leading edge (see fig. 32), deg
J	mechanical equivalent of heat, 778.2 ft-lb/Btu
K_{bk}	weight-flow blockage factor, implicitly defined in eq. (53a)
M	Mach number
P	total or stagnation pressure
p	static or stream pressure
R	gas constant, 53.35 ft-lb/(lb)(°R)
r	radius
S	entropy per unit mass
ΔS	entropy increase in stream tube between inlet and outlet of a blade row
s	blade spacing, see fig. 32
T	total or stagnation temperature
t	static or stream temperature
V	air velocity
w	weight flow
z	distance along compressor axis
α	angle of attack, angle between inlet-air direction and blade chord ($\alpha=\beta_1-\gamma°$, see fig. 32), deg
β	air angle, angle between air velocity and axial direction (see fig. 32), deg
$\Delta\beta$	turning angle, $\beta_2-\beta_1$ (see fig. 32), deg
Γ	circulation, rV_θ
γ	ratio of specific heats
$\gamma°$	blade-chord angle, angle between blade chord and axial direction (see fig. 32), deg
δ	boundary-layer thickness, see fig. 42
$\delta°$	deviation angle, angle between outlet-air direction and tangent to blade mean camber line at trailing edge (see fig. 32), deg
ϵ	angle between tangent to streamline projected on meridional plane and axial direction (fig. 64), deg
ζ	vorticity
η	efficiency
θ	angular distance
μ	viscosity

ρ	mass density
σ	solidity, ratio of chord to spacing
φ	blade camber angle, difference between angles of tangents to mean camber line at leading and trailing edges (see fig. 32), deg
ω	angular velocity of rotor
ω_{air}	angular velocity of air for solid-body rotation
$\bar{\omega}$	total-pressure-loss coefficient, see eq. (58)

Subscripts:

ad	adiabatic
h	hub
i	initial or reference position
id	ideal
m	arithmetic mean
p	polytropic
r	radial direction
t	tip
z	axial direction
θ	tangential direction
1	station at inlet to blade row
2	station at blade-row exit

Superscript:

′	relative to rotor

FUNDAMENTAL CONCEPTS UNDERLYING DESIGN SYSTEM

EQUATIONS OF THERMODYNAMICS

The design or analysis problem may be stated as the problem of determining how the shape of a blade row alters the thermodynamic flow properties and velocities of each particle of gas flowing through it. The changes in the total (or stagnation) state as well as the changes in the static state of the gas are of interest.

In order to avoid unnecessary complications in the thermodynamic equations, it has usually been the custom to assume that the entire flow may be subdivided into individual tubes of flow that maintain their identity. Another assumption is that there are no important effects of heat transfer into or out of these tubes of flow. (In the discussion of experimental data, it will be shown that these assumptions usually do not cause serious errors.) By virtue of these assumptions, the change in the total enthalpy or total temperature in the stream tube of the gas is equated to the mechanical energy transferred to it by the compressor rotors. The changes in both the total and static states of a gas can then be expressed in terms of the component velocities.

Flow through stators.—Since no energy is added to the flow by the stators, the total enthalpy and total temperature of a stream tube of the flow through stators are constant:

$$H_1=\frac{\gamma}{\gamma-1}gRT_1=\frac{\gamma}{\gamma-1}gRT_2=H_2 \tag{30}$$

From the definition of total and static states, this equation may be written as

$$H_1=\frac{\gamma}{\gamma-1}gRt_1+\frac{1}{2}V_{r,1}^2+\frac{1}{2}V_{z,1}^2+\frac{1}{2}V_{\theta,1}^2$$

$$=\frac{\gamma}{\gamma-1}gRt_2+\frac{1}{2}V_{r,2}^2+\frac{1}{2}V_{z,2}^2+\frac{1}{2}V_{\theta,2}^2=H_2 \tag{31}$$

This equation relates the change in static temperature to the changes in the individual components of velocity.

If there is an increase in entropy through a stream tube (e.g., from friction or an interchange of heat within the stream tube itself), the total pressure changes according to the equation

$$\frac{P_2}{P_1}=e^{-\frac{J}{R}\Delta S} \tag{32}$$

When the change in entropy, or total pressure, is known, the changes in static pressure and density corresponding to the changes in static temperature may be determined. Static pressures are related by the equation

$$\frac{p_2}{p_1}=\left(\frac{t_2}{t_1}\right)^{\frac{\gamma}{\gamma-1}}\frac{P_2}{P_1} \tag{33}$$

The densities are then related to the pressures and temperatures by the gas law

$$p=\rho gRt \tag{34}$$

or

$$\frac{\rho_2}{\rho_1}=\frac{p_2}{p_1}\frac{t_1}{t_2} \tag{35}$$

Equations (34) and (35) may, of course, also be used to relate the total conditions of state.

If the changes in the velocity components and the entropy in a stream tube are known, the resulting changes in static temperature, total and static pressure, and total and static density can be determined.

Flow through rotors.—Since the rotors do work on the gas, the enthalpy of a tube of flow changes through the rotor according to Euler's turbine equation:

$$H_2-H_1=\omega(r_2V_{\theta,2}-r_1V_{\theta,1}) \tag{36}$$

or

$$\frac{\gamma}{\gamma-1}gRt_1+\frac{1}{2}V_{r,1}^2+\frac{1}{2}V_{z,1}^2+\frac{1}{2}V_{\theta,1}^2-\omega r_1V_{\theta,1} =\frac{\gamma}{\gamma-1}gRt_2+\frac{1}{2}V_{r,2}^2+\frac{1}{2}V_{z,2}^2+\frac{1}{2}V_{\theta,2}^2-\omega r_2V_{\theta,2} \tag{37}$$

Notice that the changes in V_θ due to casing friction are ignored in these equations.

Since a stationary observer could not observe continuous tubes of flow through a rotor, recourse is frequently made to relative flow conditions, where the observations are theoretically made from the rotor itself. Continuous stream tubes can then be distinguished. The relative velocities are related to the absolute velocities by the equations

$$\left.\begin{aligned}V_r'&=V_r\\V_z'&=V_z\\V_\theta'&=V_\theta-\omega r\end{aligned}\right\} \tag{38}$$

(V_θ' is usually negative in the compressor case in the sense that ωr is positive.) Equation (36) then becomes

$$I_1=H_1'-\tfrac{1}{2}\omega^2r_1^2=H_2'-\tfrac{1}{2}\omega^2r_2^2=I_2 \tag{39}$$

where

$$H'=\frac{\gamma}{\gamma-1}gRT'=\frac{\gamma}{\gamma-1}gRt+\frac{1}{2}(V_r')^2+\frac{1}{2}(V_z')^2+\frac{1}{2}(V_\theta')^2 \tag{40}$$

When only the flow ahead of and behind the rotor is of interest, the use of relative quantities is not necessary; in this case equation (37) may also be applied to relate the changes in total and static temperatures with the changes in the individual components of velocity.

The corresponding changes in total pressure are given by

$$\frac{P_2}{P_1}=\left(\frac{T_2}{T_1}\right)^{\frac{\gamma}{\gamma-1}}e^{-\frac{J}{R}\Delta S}=\left(\frac{T_2}{T_1}\right)^{\frac{\gamma}{\gamma-1}\eta_p} =\left[1+\left(\frac{T_2}{T_1}-1\right)\eta_{ad}\right]^{\frac{\gamma}{\gamma-1}} \tag{41}$$

$$\frac{P_2'}{P_1'}=\left(\frac{T_2'}{T_1'}\right)^{\frac{\gamma}{\gamma-1}}e^{-\frac{J}{R}\Delta S} \tag{42}$$

(The magnitude of ΔS for absolute quantities is the same as for relative quantities.) The resulting change in static pressure is given by

$$\frac{p_2}{p_1}=\left(\frac{t_2}{t_1}\right)^{\frac{\gamma}{\gamma-1}}\frac{\frac{P_2}{P_1}}{\left(\frac{T_2}{T_1}\right)^{\frac{\gamma}{\gamma-1}}}=\left(\frac{t_2}{t_1}\right)^{\frac{\gamma}{\gamma-1}}\frac{\frac{P_2'}{P_1'}}{\left(\frac{T_2'}{T_1'}\right)^{\frac{\gamma}{\gamma-1}}} \tag{43}$$

The corresponding density changes may be determined by equations (34) and (35).

With these relations, the changes in total and static states of a gas can be determined when the changes in the velocity components, the entropy, and the radius of the stream tube (measured from the axis) can be estimated. The concepts discussed in the rest of this section were developed with the idea of making these estimates.

ANALYSIS OF TIME-STEADY AND INVISCID FLOW

As will be shown in chapter XIV, the three-dimensional equations of motion of even time-steady and inviscid flow are much too complicated for general use at the present time. Coping with all the three-dimensional gradients in the motion and properties of the gas is too big a problem for routine analysis. An inviting simplification appears, however, when the radial components of velocity in a blade row are small enough to be ignored.

Equations ignoring radial velocity.—Stationary blade row: Ignoring the radial components of velocity is tantamount to assuming that a streamline of the flow lies on the surface of a right circular cylinder (fig. 31). If this surface and its streamlines are developed into a plane, the streamlines

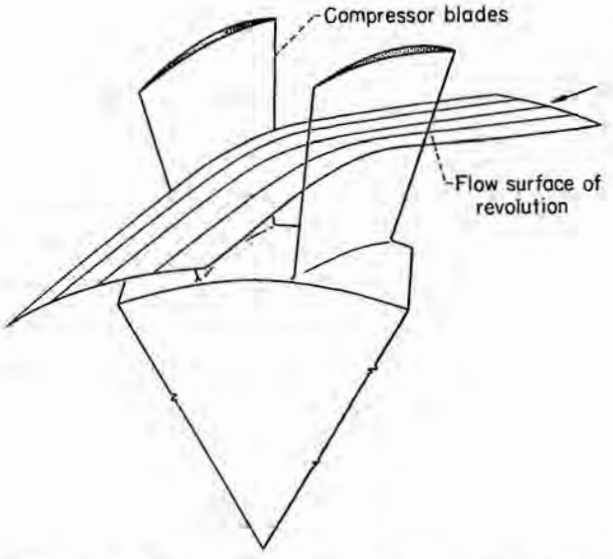

FIGURE 31.—Sketch of flow surface and streamlines when assumed flow lies on the surface of a right circular cylinder.

through a two-dimensional cascade of airfoils are obtained (fig. 32).

When the radial velocity is ignored, the equation of continuity (reviewed in ch. XIV) becomes

$$\frac{\partial(\rho V_\theta)}{r\partial\theta}+\frac{\partial(\rho V_z)}{\partial z}=0 \tag{44}$$

The basic equations for the radial, axial, and tangential components of vorticity are, respectively,

$$\frac{\partial V_z}{r\partial\theta}-\frac{\partial V_\theta}{\partial z}=\zeta_r \tag{45}$$

$$\frac{1}{r}\frac{\partial(rV_\theta)}{\partial r}-\frac{\partial V_r}{r\partial\theta}=\zeta_z \tag{46}$$

$$\frac{\partial V_r}{\partial z}-\frac{\partial V_z}{\partial r}=\zeta_\theta \tag{47}$$

If the inviscid flow is originally without vorticity, it will remain this way; ζ_r is then zero. Since r is assumed to be constant along a streamline, equations (44) and (45) then represent the flow through a two-dimensional cascade of airfoils. Figure 32 is thus again shown to represent the flow at a given radius for the assumed conditions of figure 31.

If V_r as well as ζ_z is zero, equation (46) becomes

$$\frac{1}{r}\frac{\partial(rV_\theta)}{\partial r}=0$$

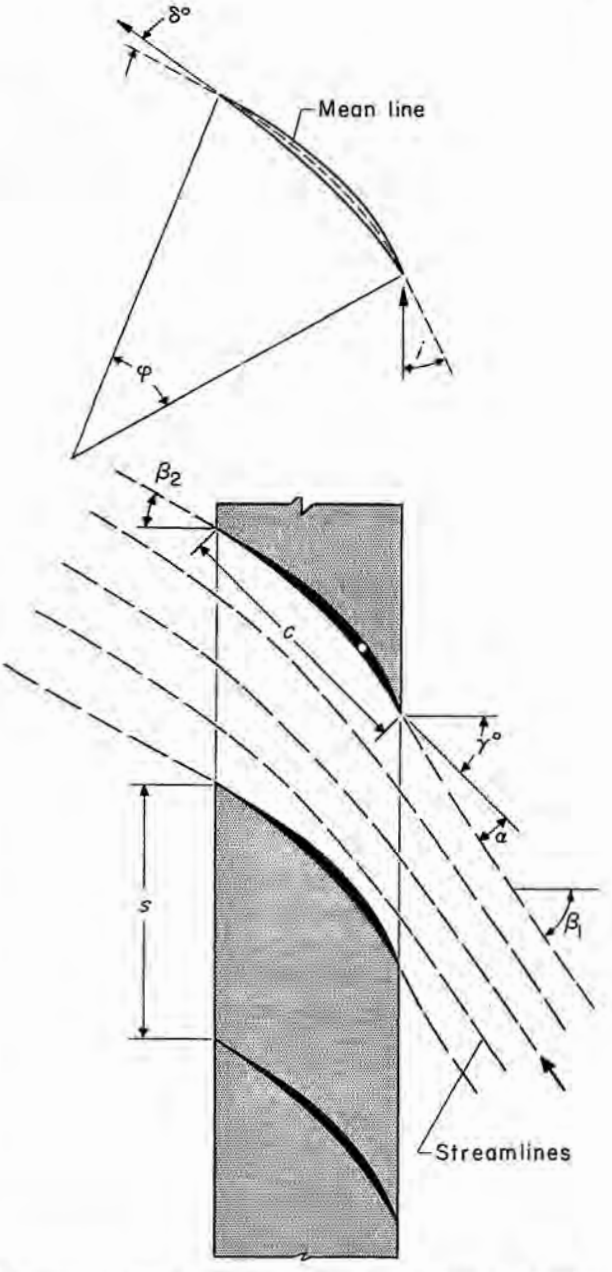

FIGURE 32.—Sketch of two-dimensional cascade showing streamlines and nomenclature.

and $rV_\theta=\Gamma=$constant along a radial line. This distribution of tangential velocity is known as free-vortex flow. Similarly, equation (47) becomes

$$\frac{\partial V_z}{\partial r}=0$$

and $V_z=$constant along a radial line.

Besides these relations, equation (378b) (ch. XIV) must also be satisfied. This equation may be written as, neglecting any radial forces exerted by the blades,

$$\frac{\partial H}{\partial r}-t\frac{\partial S}{\partial r}=V_\theta\zeta_z-V_z\zeta_\theta \tag{48}$$

If radial flows are neglected, this equation becomes

$$\frac{\partial H}{\partial r}-t\frac{\partial S}{\partial r}=\frac{V_\theta}{r}\frac{\partial(rV_\theta)}{\partial r}+V_z\frac{\partial V_z}{\partial r} \tag{48a}$$

When ζ_z and ζ_θ are zero, then the right side of this equation must be zero. The left side of this equation must also be zero—a condition which is realized when there are no radial gradients in enthalpy or entropy.

It may be noted that equation (48) is also applicable when the axial and tangential components of vorticity are not zero. For the condition of no radial flow, one component of vorticity (say ζ_z) may be stipulated by the radial variation of V_θ (eq. (46)). If the radial variations in enthalpy and entropy are also given, then the radial variations in V_z are determined by equations (47) and (48).

Rotating blade rows: In order to utilize steady-flow equations in rotors, the flow in rotors is referred to a coordinate system that rotates at rotor speed. The velocities in the rotating coordinate system (the relative velocities) are related to the absolute velocities by equations (38), which are rewritten here as

$$\left.\begin{aligned} V_r&=V'_r\\ V_z&=V'_z\\ V_\theta&=V'_\theta+\omega r \end{aligned}\right\} \tag{38}$$

Again $V'_r=0$; the relative velocities are then directly substituted for the absolute velocities in equation (44), and

$$\frac{\partial(\rho V'_\theta)}{r\partial\theta'}+\frac{\partial(\rho V'_z)}{\partial z}=0 \tag{44a}$$

The corresponding equations for the radial, axial, and tangential components of vorticity are

$$\frac{\partial V'_z}{r\partial\theta'}-\frac{\partial V'_\theta}{\partial z}=\zeta'_r=\zeta_r \tag{45a}$$

$$\frac{1}{r}\frac{\partial(rV'_\theta)}{\partial r}-\frac{\partial V'_r}{\partial\theta'}=\zeta'_z=\frac{1}{r}\frac{\partial(rV_\theta)}{\partial r}-\frac{\partial V_r}{\partial\theta}-2\omega=\zeta_z-2\omega \tag{46a}$$

$$\frac{\partial V'_r}{\partial z}-\frac{\partial V'_z}{\partial r}=\zeta'_\theta=\zeta_\theta \tag{47a}$$

If the radial flows and absolute vorticity are again assumed to be zero, equations (44a) and (45a) become the equations of a two-dimensional cascade. This simplification of flow equations is thus applicable to rotors as well as stators.

Equation (46a) may then be integrated along a radial line to become

$$rV'_\theta=\Gamma-\omega r^2=r(V_\theta-\omega r)$$

In order to meet the requirements of no tangential gradients in the radial flow through a rotor, the absolute flow along a radial line must be defined by

$$rV_\theta=\Gamma$$

This is the same requirement previously derived for stators. The tangential velocity distributions for rotors and stators are thus compatible. Similarly, the integration of equation (47a) shows the compatibility of axial velocity, namely,

$$V_z=\text{constant}$$

As shown in chapter XIV (eq. (378c)), the equation analogous to equation (48a) is

$$\frac{\partial I}{\partial r}-t\frac{\partial S}{\partial r}=\frac{V'_\theta}{r}\frac{\partial(rV_\theta)}{\partial r}+V_z\frac{\partial V_z}{\partial r} \tag{48b}$$

where, according to equation (39),

$$I=H'-\tfrac{1}{2}\omega^2r^2=H-\omega rV_\theta=H-\omega^2r^2-\omega rV'_\theta$$

If H and rV_θ are constant along a radial line, then I is also constant along a radial line. If the entropy is also constant along a radial line, equation (48b) is satisfied for free-vortex flows. Equation (48b), like equation (48), may be used when the vorticity components are not zero. The procedure involved is similar to that previously outlined.

When radial flows do not have important effects, the analysis of flow in a blade row is relatively simple. The three-dimensional problem for both

stators and rotors is broken down into the two-dimensional-cascade problem and the separate problem of determining the radial distribution of the flow. It is, of course, practically impossible to eliminate radial flows completely. Because of the simplification offered by this type of approach, however, it has been deemed advisable to seek and study those designs in which the radial flows are small. Attention is therefore directed to the study of the causes of radial flows in a blade row. The question concerning admissible radial flows is temporarily deferred to the review of experimental data.

Causes of radial flows.—Changes in radial density gradients: One cause of radial flows is the change in the radial density gradient between the inlet and the outlet. If the radial velocities are zero, the hydrodynamic equation of equilibrium (eq. (377), ch. XIV) becomes

$$\frac{1}{\rho}\frac{\partial p}{\partial r}=\frac{V_\theta^2}{r}$$

If $V_\theta=\Gamma/r$ and there are no radial gradients in entropy (i.e., $p=C\rho^\gamma$), this equation may be solved to read

$$\frac{\gamma}{\gamma-1}C\rho^{\gamma-1}=\left(\text{constant}-\frac{\Gamma^2}{2r^2}\right)$$

A change in Γ through a blade row therefore makes the radial distribution of density behind the blade row different from that in front of it. Figure 33 shows a representative change in the radial distribution of density for a blade row through which Γ is increased from 150 to 300 feet squared per second. Also shown in this figure is the change in $r\rho V_z$.

Continuity of mass flow requires the following equation to be satisfied in a stream tube:

$$\int_{r_{t,1}}^{r_{t,1}}\rho_1 V_{z,1} r\,dr=\int_{r_{t,2}}^{r_{t,2}}\rho_2 V_{z,2} r\,dr \qquad (49)$$

where the subscripts 1 and 2 refer to conditions far enough upstream and downstream of the blade row that V_r is practically zero and any circumferential gradients have disappeared; and r_t and r_t refer to the radius of a given streamline and that of the tip (or casing), respectively, (see fig. 34). Notice, however, that equation (49) is valid even when V_r is finite.

In the vicinity of the tip, $r\rho V_z$ has a greater value behind the blade row than in front of it (fig. 33). The distance (r_t-r_t) between two adjacent streamlines near the tip is therefore expected to decrease as $r\rho V_z$ increases if r_t is constant. As shown by streamline A of figure 34, this trend does occur and the streamline moves radially outward. (This drawing actually represents the projection of the flow on a plane through the axis. This representation is conventionally called the flow lines in the meridional plane.) A radial component of velocity, as indicated by the slope of the dashed streamline, must therefore exist within the blade row. Near the hub, on the other hand, the value of $r\rho V_z$ decreases through the blade row, and the distance between streamline B and the hub is greater behind the blade row than in front of it. In this case, the motion of the streamline is again radially outward, and radial components of velocity must again exist within the blade row.

Even for ideal conditions, therefore, where the tangential and axial components of velocity upstream and downstream of the blade row satisfy the requirements for no radial velocities, some radial flow must take place within the blade row. The magnitudes of the radial flows increase with the change in Γ through the blade row and with the corresponding change in $r\rho V_z$.

Blade thickness distribution: Another source of radial flow is the radial distribution of blade thickness. Some aspects of this problem are discussed in reference 34. Ahead of the blade row, a cross section of the stream surface in a plane normal to the axis would look like that shown in figure 35(a). A streamline of the flow between two adjacent blades lies within the area of the sector bounded by A–A and B–B. Because of blade thickness, these lateral boundaries are changed to C–C and D–D within the blade row (figs. 35 (b) and (c)). If C–C and D–D are also radial lines (fig. 35(b)), the area of each of the original stream tubes is reduced uniformly along the radius. The radial position of the streamlines then tends to remain unchanged. In the more usual case, the lines C–C and D–D are not radial lines; then, as indicated in figure 35(c), the flow would be deflected outwards with respect to that of figure 35(a). The areas of the original stream tubes are not uniformly reduced, and some radial adjustment of the streamlines is required to

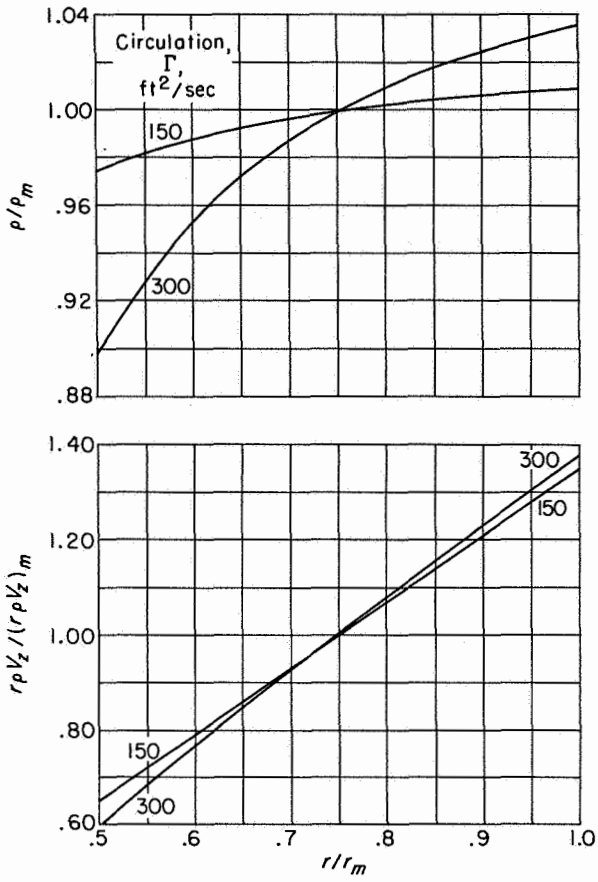

FIGURE 33.—Changes in distributions of ρ and $r\rho V_z$ due to change in Γ through blade row.

compensate for this. Some notion of the resulting flows is given in reference 34. This reference indicates that radial flow starts ahead of the blade row, as shown in figure 36. A maximum radial displacement occurs within the blade row, and thereafter a radially inward flow begins and continues downstream of the blade row.

Radial component of blade force: Still another source of radial flow is the radial component of blade force. This concept is reviewed in chapter XIV. The turning of the air at any point in a blade row is the result of tangential forces originating on the surface of a blade. The direction of these forces, however, must be perpendicular to the corresponding blade surfaces. If the surfaces are inclined to the radius, a radial component of force is imposed on the flow, and radial flows may thereby be induced. Since the forces on the high-pressure surface of the blade are dominant, the radial movements of the flow depend on the angle

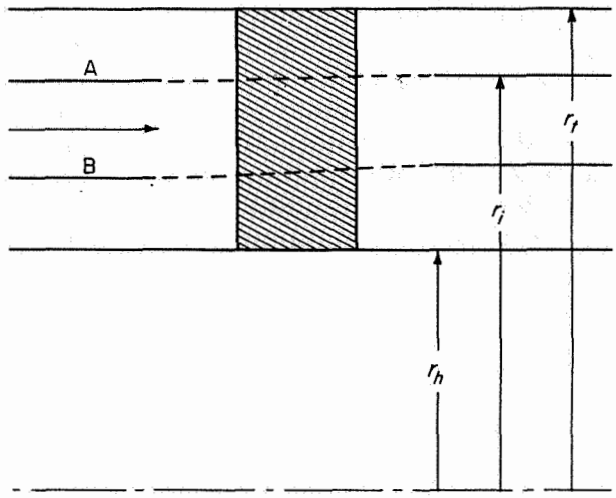

FIGURE 34.—Radial shift of streamlines due to change in radial density gradient through a blade row.

between this surface and a radial line. Depending upon how the blade elements are radially alined, inward or outward radial velocities could be generated. In the blade of figure 37(a), the predominant force is radially outward; so is the radial component of the flow. For figure 37(b), in which the shape of the individual cascade elements at each radius is the same as that of figure 37(a), the flow would be first inward, then outward.

Non-free-vortex flow: In order to alleviate some problems arising from Mach number limits, such as those described in reference 35, tangential velocity distributions differing from the free-vortex type are frequently used. One type of tangential velocity distribution that tends to overcome these difficulties is given by the equation

$$V_\theta = \omega_{air} r + \frac{\Gamma}{r} \tag{50}$$

where both ω_{air} and Γ are constant. Other distributions could also be used, but this type permits a simple discussion of nonvortex distributions. Suppose now that uniform flow entered a row of blades designed to produce this distribution at the outlet. Since the flow is originally without vorticity, equation (46) becomes

$$2\omega_{air} - \frac{\partial V_r}{r\partial\theta} = 0$$

and tangential variations in radial velocity are thus introduced.

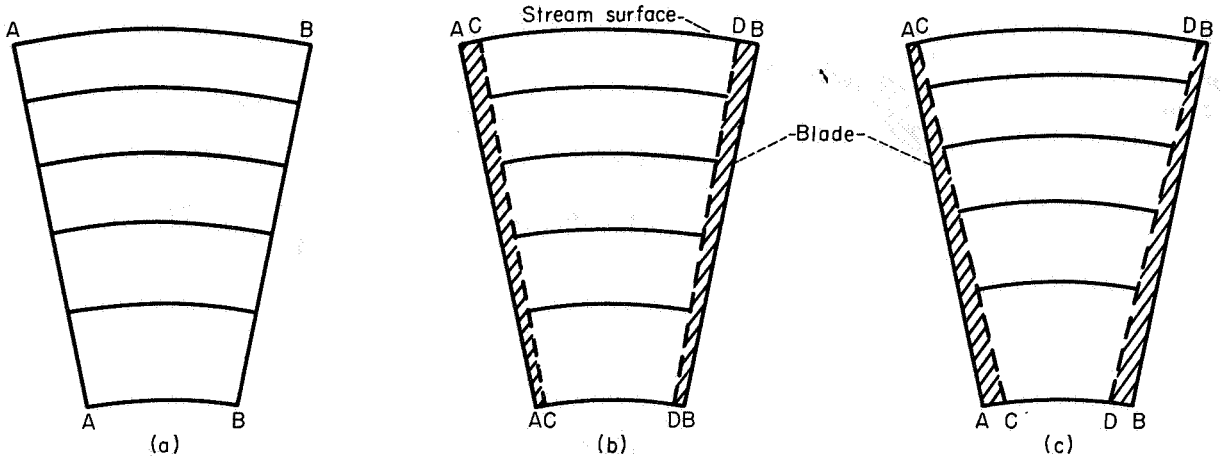

(a) Zero blade thickness. (b) Radial blade surfaces. (c) Tapered blades.

FIGURE 35.—Effect of blade thickness on radial location of stream surfaces.

The resulting flows can be visualized by dividing V_θ into three parts,

$$V_\theta = V_{\theta,a} + V_{\theta,b} + V_{\theta,c}$$

where

$$\frac{1}{r}\frac{\partial(rV_{\theta,a})}{\partial r} = 0$$

$$\frac{1}{r}\frac{\partial(rV_{\theta,b})}{\partial r} = 2\omega_{atr}$$

$$\frac{1}{r}\frac{\partial(rV_{\theta,c})}{\partial r} - \frac{\partial V_r}{r\partial\theta} = -2\omega_{atr}$$

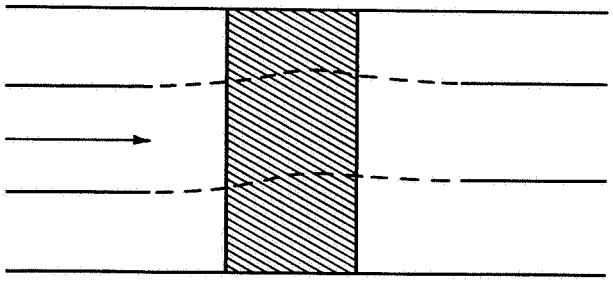

FIGURE 36.—Radial shift of streamlines due to blade thickness.

The velocity $V_{\theta,a}$ is that required for free-vortex flow. The circumferential-plane streamlines for the condition of no through flow are shown in figure 38(a). The velocity $V_{\theta,b}$ represents the rotation of a solid body, and the corresponding streamlines are shown in figure 38(b). The flow determined by $V_{\theta,c}$ is more complex. No general solution to this flow has been found, but solutions for several particular conditions are presented in reference 36. The streamlines for two of these solutions are shown in figure 38(c). In general, both $V_{\theta,c}$ and V_r must vary in the tangential direction. This trend is suggested by figure 38(c). It is evident that the velocity defined by equation (50) really cannot exist at every circumferential position. Equation (50), however, is approximated at every circumferential position when the blades are close enough together that the actual circumferential changes in V_θ and V_r are very small. The velocity $V_{\theta,c}$ might then be ignored. The change in V_r along the circumference could also be ignored. In this event, one could write

$$V_\theta = V_{\theta,a} + V_{\theta,b} = \omega_{atr} r + \frac{\Gamma}{r}$$

The resulting streamlines are those of figure 38(a) combined with figure 38(b).

The vorticity represented by this flow, however, is $2\omega_{atr}$. This result means that vorticity must be added to the flow by the blade row. Such a thing cannot be done in an ideal fluid, because the

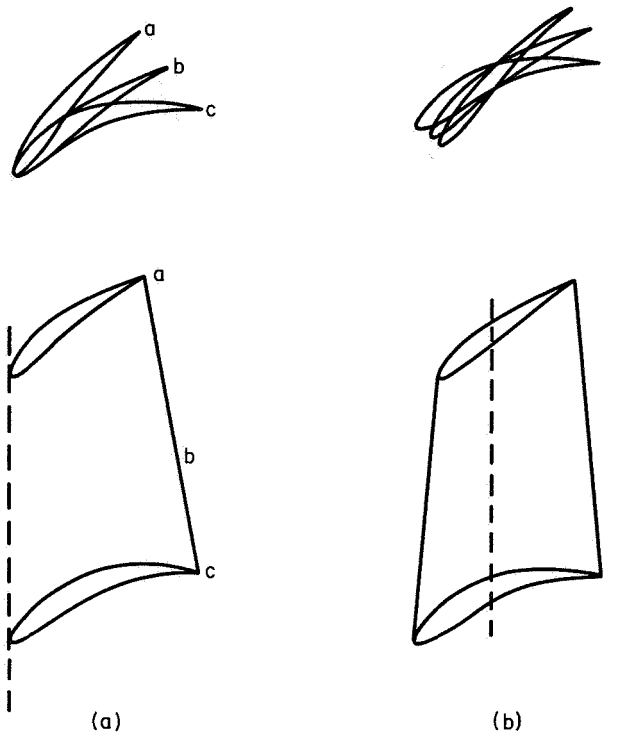

(a) Radial line through leading edge. (b) Radial line through center of gravity.

FIGURE 37.—Various radial alinements of compressor blade elements having the same radial distribution of cascade elements.

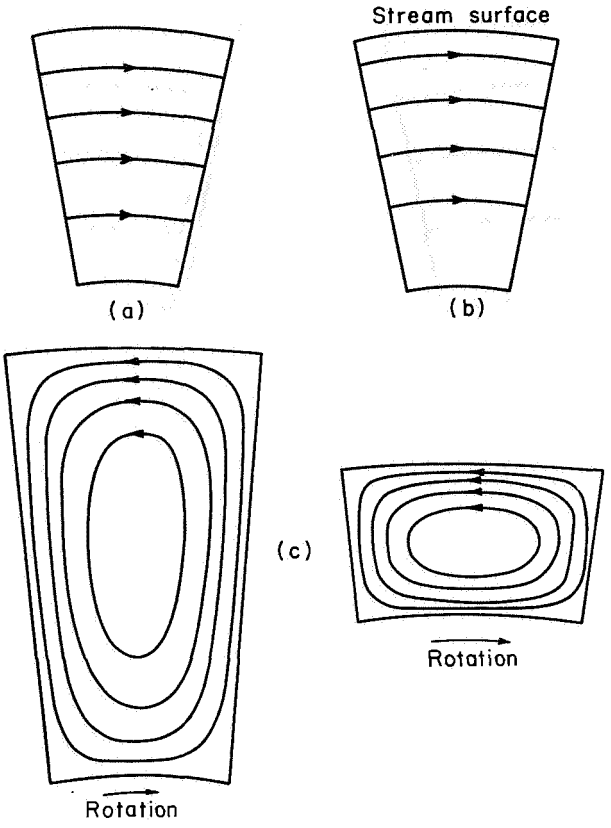

(a) Free-vortex rotation. (b) Solid-body rotation. (c) Eddy flow (ref. 36).

FIGURE 38.—Circumferential-plane streamlines for no through-flow.

vortex lines would extend downstream of the blades and they would be confined to infinitesimally thin sheets. Between them, the flow would be irrotational. Since these vortex sheets actually enclose the wakes in a real fluid, they eventually do permeate the entire flow field by the mixing of the wakes with the rest of the flow. Accordingly, for a reasonably close spacing between the blades, the entire flow could be assumed to have an axial component of vorticity of $2\omega_{air}$ downstream of a blade row, even though the upstream vorticity is zero. (For a further discussion of this point, see ref. 5.)

In this event, equation (46) may be used, and

$$\frac{1}{r}\frac{\partial(rV_\theta)}{\partial r}=2\omega_{air}=\zeta_z$$

Equation (48) can then be written as

$$\frac{\partial H}{\partial r}-t\frac{\partial S}{\partial r}=2\omega_{air}V_\theta-V_z\zeta_\theta \qquad (48c)$$

With uniform enthalpy and entropy, equation (48c) is written

$$V_z\zeta_\theta=2\omega_{air}V_\theta$$

By using equation (47), this equation becomes

$$2\omega_{air}V_\theta+V_z\frac{\partial V_z}{\partial r}=V_z\frac{\partial V_r}{\partial z}$$

Here again, radial flows are required, since $\partial V_r/\partial z$ cannot, in general, be zero. In many designs, these radial flows are far from negligible within a blade row and may be considerably more severe than those previously discussed. Far enough downstream of the blade row, the radial flow must disappear. Some studies of these flows are reviewed in chapter XIV.

For other radial distributions of tangential components of velocity, other equations must be used to describe the flow. The important point to

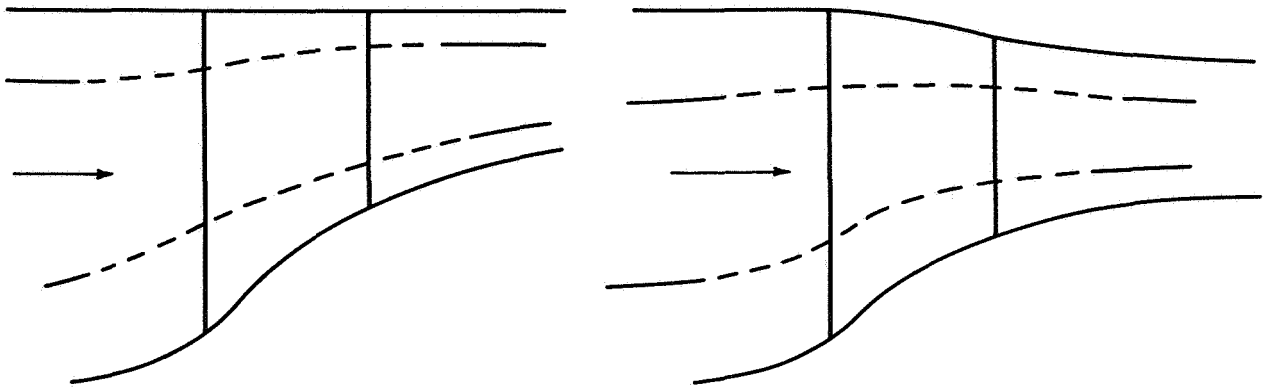

FIGURE 39.—Radial shift of streamlines due to hub and casing curvature.

note, however, is that additional radial flows tend to be introduced whenever the distribution is not that of a free vortex. These radial flows not only exist within the blade row but also may be found upstream and downstream of it.

Shape of hub and casing: Some radial flows must exist in the vicinity of the hub and casing when the slope is not zero (fig. 39). Such configurations usually cannot be avoided because of the exigencies of other considerations (blade surface velocity diffusion, attainable total-pressure ratio, etc.), which are discussed later in this chapter. The magnitude of the radial flows within and without the blade rows naturally increases as the slope of the boundaries increases.

Effect of radial flows on stream surface configuration.—As previously shown, the simplifying assumption of no radial flow presumes the streamlines of the flow to lie on the surfaces of right circular cylinders (fig. 31). The radial flows resulting from the changes in radial density gradients, the blade thickness distribution, and the radial component of blade force make these streamline surfaces undulate and twist as shown by comparing the upper surface of figure 40(a) with the lower surface. The additional disturbances encountered when rV_θ is not constant along a radial line and when annulus walls converge are indicated in figure 40(b). The increased twisting of the surfaces results from the flows shown in figure 38(c) (left side).

Experimental data required.—Although the magnitudes of these radial flows can sometimes be estimated by mathematical analyses, their actual effects on the performance of a blade row must eventually be measured by experiment. The deflections of the air at a given radius of a blade row and those of a two-dimensional cascade having identical geometry and inlet conditions may be compared; the agreement between the two sets of results is a measure of the usefulness of the simple concepts obtained by ignoring radial flows. Similarly, a comparison of the measured radial distributions of flow with those given by equations (46) to (48) (with $V_r=0$) provides another test of these concepts. The representative experimental data subsequently presented are examined from these points of view to show that, in many cases, the simple equations just derived provide an accurate estimate of the main flow.

ANALYSIS OF VISCOSITY PROBLEM

Two-dimensional-cascade elements.—Following the procedures used in other fields of aerodynamics, compressor design and analysis techniques assume that the important effects of viscosity are

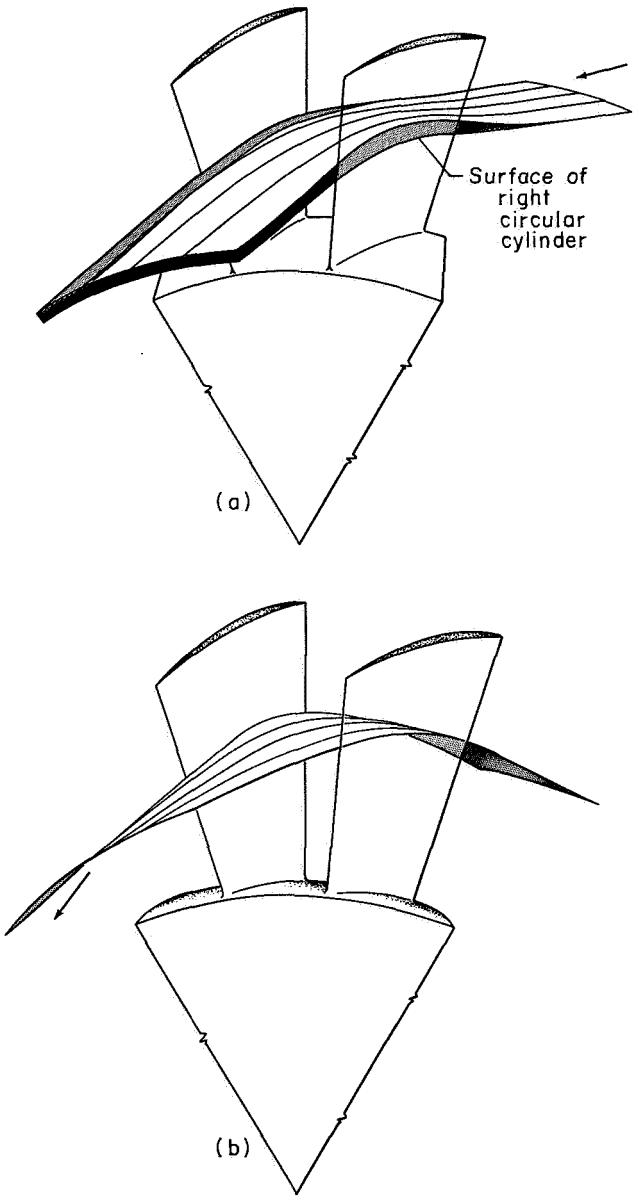

(a) Free-vortex design.
(b) Non-free-vortex design with converging annulus area.

FIGURE 40.—Warping of stream surfaces through a blade row.

confined to thin boundary layers and to blade wakes. For the cascade elements (defined in fig. 32), the boundary layers are indicated by the shaded areas immediately in contact with the blades in figure 41(a). Beyond the trailing edge of the blade, the boundary layers are shed as wakes. Within the shaded areas of the figure, the retarded flow of the wakes is mixed with the rest of the flow. The shaded areas, therefore, become wider in the direction of the flow. Far enough downstream, complete mixing would occur and the flow would be homogeneous.

A representative example of the velocity variation within a boundary layer is shown in figure 41(b), which presents the velocity distribution along a line A–A in figure 41(a). Between points a and b of figure 41(b), the effects of viscosity are small, because the velocity gradients are relatively small. Between the blade surfaces and points a or b, however, the velocity gradients are severe and viscous effects are dominant. Besides the indicated change in velocity, the total pressure, the entropy, and even the total temperature also vary. The static pressure, however, is likely to be approximately constant through the boundary layer.

One of the most important effects of viscosity is that it retards the relative flow in the boundary layers. (In making this statement, it is implied that the flow is viewed from the coordinate system attached to the blades. For stators, such a coordinate system is stationary, as previously noted; for rotors, it moves at blade speed.) Because of the low relative flow, the boundary layer may be almost replaced by a region of no flow for inviscid-flow analyses. Effectively, then, the boundary layer changes the aerodynamic shape of the blades, a phenomenon which must be recognized in interpreting inviscid-flow analyses. Although some methods of partially correcting inviscid-flow analyses for these changes in boundary conditions have been developed, it has usually been more practicable to use experimental results as a source of two-dimensional-cascade data (ch. VI). Two-dimensional-cascade inviscid-flow theory (ch. IV) may then be used to correlate these data.

Important data derived from two-dimensional-cascade experiments are the deflections or turning angles as functions of blade shape and inlet flow conditions. The turning angles are given by

$$\Delta\beta=(\beta_1-\beta_2)=\left[\tan^{-1}\frac{V_{\theta,1}}{V_{z,1}}-\tan\frac{V_{\theta,2}}{V_{z,2}}\right]$$

When the turning angle is known, the change in V_θ is a function of the change in V_z. Also of

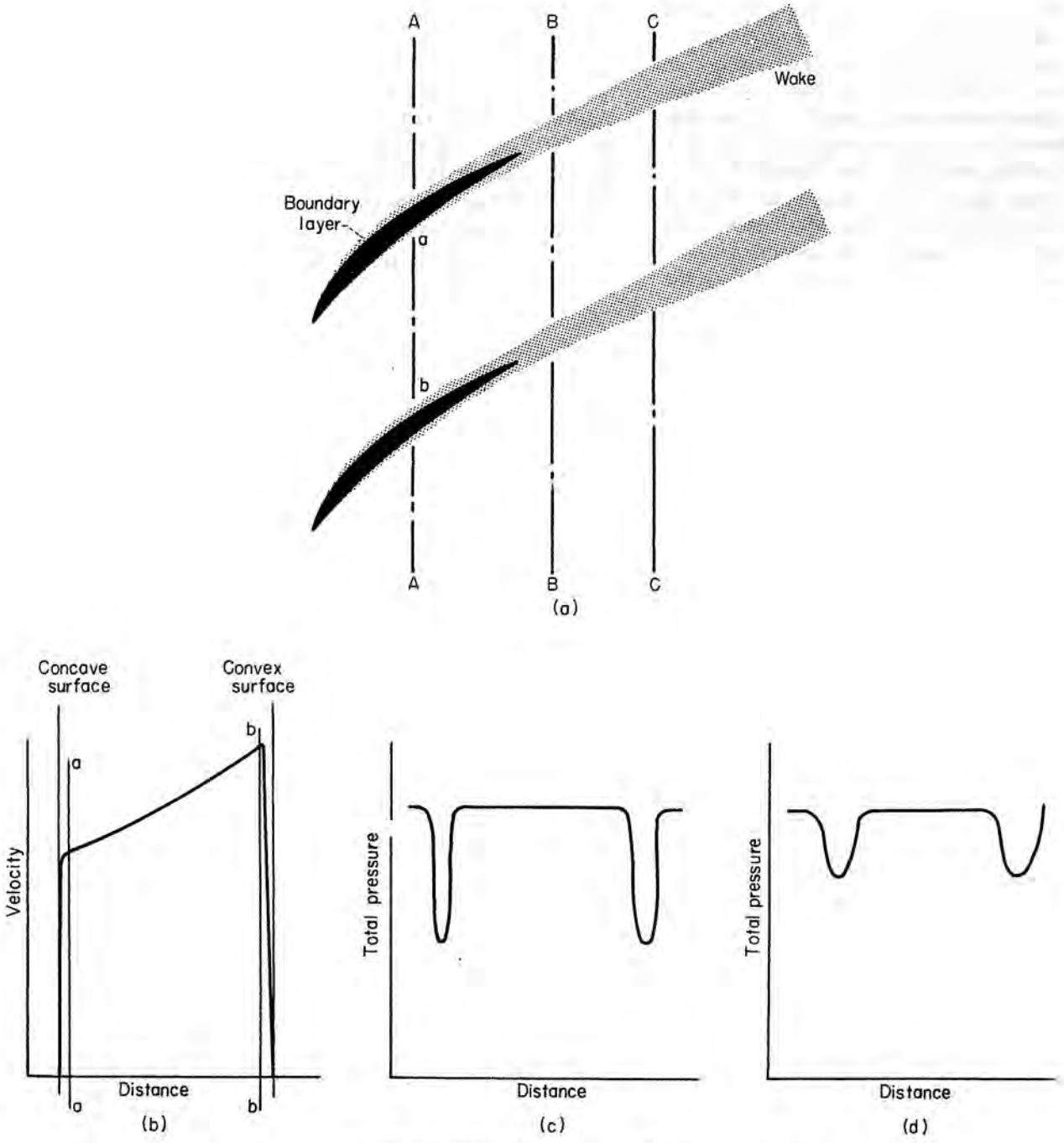

(a) Sketch of boundary layers and wakes.
(b) Velocity distribution along A–A. (c) Total-pressure distribution along B–B.
(d) Total-pressure distribution along C–C.

FIGURE 41.—Boundary layers and wakes formed by cascade elements.

importance are the losses in the relative total pressure suffered in the boundary layer, because these represent part of the over-all change in entropy.

It is noted that all changes in flow properties occurring in the boundary layer are passed on to the wakes, which are eventually mixed with the rest of the flow. The distribution of losses as

691-564 O-65-6

indicated by total pressure behind a two-dimensional cascade thus varies in two dimensions. Along the line B–B of figure 41(a), the distribution of total pressure resembles that shown in figure 41(c). Farther downstream, along C–C, the total-pressure distribution is more uniform (fig. 41(d)). Rigorously coping with the loss distributions is not practical at the present time. An average flow condition behind the blade row is therefore sought. Such an average is also required when unsteady flows are prevalent, as discussed in the later section on Treatment of Time-Unsteady Flows.

The best way of averaging the flow conditions behind a two-dimensional cascade is not established at the present time. Discussions on this point in reference 37 indicate that one method of averaging is probably as good as another as long as the trailing-edge boundary layers are thin and the flow Mach numbers are subsonic. Since these conditions are satisfied at the design point of many compressors, no case has yet been made for a particular method of averaging.

Hub and casing boundary layers in compressor blade rows.—The hub and casing boundary layers are indicated by the shaded areas of figure 42(a). The corresponding radial distributions of the circumferentially averaged total pressure ahead of and behind a blade row are shown in figure 42(b). Between a_1 and b_1 of this figure the total pressure at the inlet is practically constant. Beyond these lines, it drops rapidly. The distance from the hub to a_1 (fig. 42(b)) is indicative of the boundary-layer thickness at the hub of the inlet. The distance from the casing to b_1 (fig. 42(b)) indicates the boundary-layer thickness at the casing. Similarly, the lines a_2 and b_2 represent the extent of the boundary layer at the outlet. The boundary layer is also indicated by the distribution of circumferentially averaged axial velocity at the inlet and outlet of a row of blades (fig. 42(c)).

Reference to figure 42(b) shows that the circumferentially averaged losses between a_1–b_1 and a_2–b_2 can be small. (The difference between inlet and outlet total pressure is a measure of the loss.) Within this area the flow properties might be considered to be a function of the two-dimensional cascade, where the circumferentially averaged losses are usually quite small. In these cases, little error in the state of this main flow is introduced even by assuming the flow to be isentropic. Beyond these lines, at the blade ends, the circumferentially averaged losses are more severe. Since the flows causing these end losses have no counterpart in a truly two-dimensional cascade, loss data and flow-angle data from such cascades are expected to be useless in the vicinity of the hub and casing. Therefore, pertinent data must preferably come from the blade row itself.

This retarded flow in the hub and casing boundary layers poses an important problem in design. The nature of this problem may be studied from the following considerations.

The requirements of continuity may be expressed by the following equations:

$$w=2\pi\int_{r_{h,1}}^{r_{t,1}}\rho_1 V_{z,1} r_1\,dr_1=2\pi\int_{r_{h,2}}^{r_{t,2}}\rho_2 V_{z,2} r_2\,dr_2 \quad (51)$$

where

$$\rho=\frac{P}{gRT}\left(1-\frac{\gamma-1}{2\gamma}\frac{V_z^2+V_r^2+V_\theta^2}{gRT}\right)^{\frac{1}{\gamma-1}} \quad (52)$$

This expression is derived from equations (31), (33), and (34). The various flow quantities here must be the circumferentially averaged values ahead of and behind a blade row. For the flow behind a blade row, equations (51) and (52) may be combined to read

$$w=2\pi\int_{r_{h,2}}^{r_{t,2}}\frac{P_2 V_{z,2}}{gRT_2}\left(1-\frac{\gamma-1}{2\gamma}\frac{V_{z,2}^2+V_{r,2}^2+V_{\theta,2}^2}{gRT_2}\right)^{\frac{1}{\gamma-1}} r_2\,dr_2 \quad (53)$$

If the circumferentially averaged flow properties were known as a function of radius between the hub and casing, it would be a simple matter to use equation (53) to relate the hub and tip radii to the mass flow. Unfortunately, computing the extent of the boundary layer and the distribution of flow within it remains an unsolved problem except for extremely simple flow situations. Therefore, methods of making reasonable allowances for it have been sought.

When the circumferentially averaged flow between a-a and b-b of figure 42 is known,

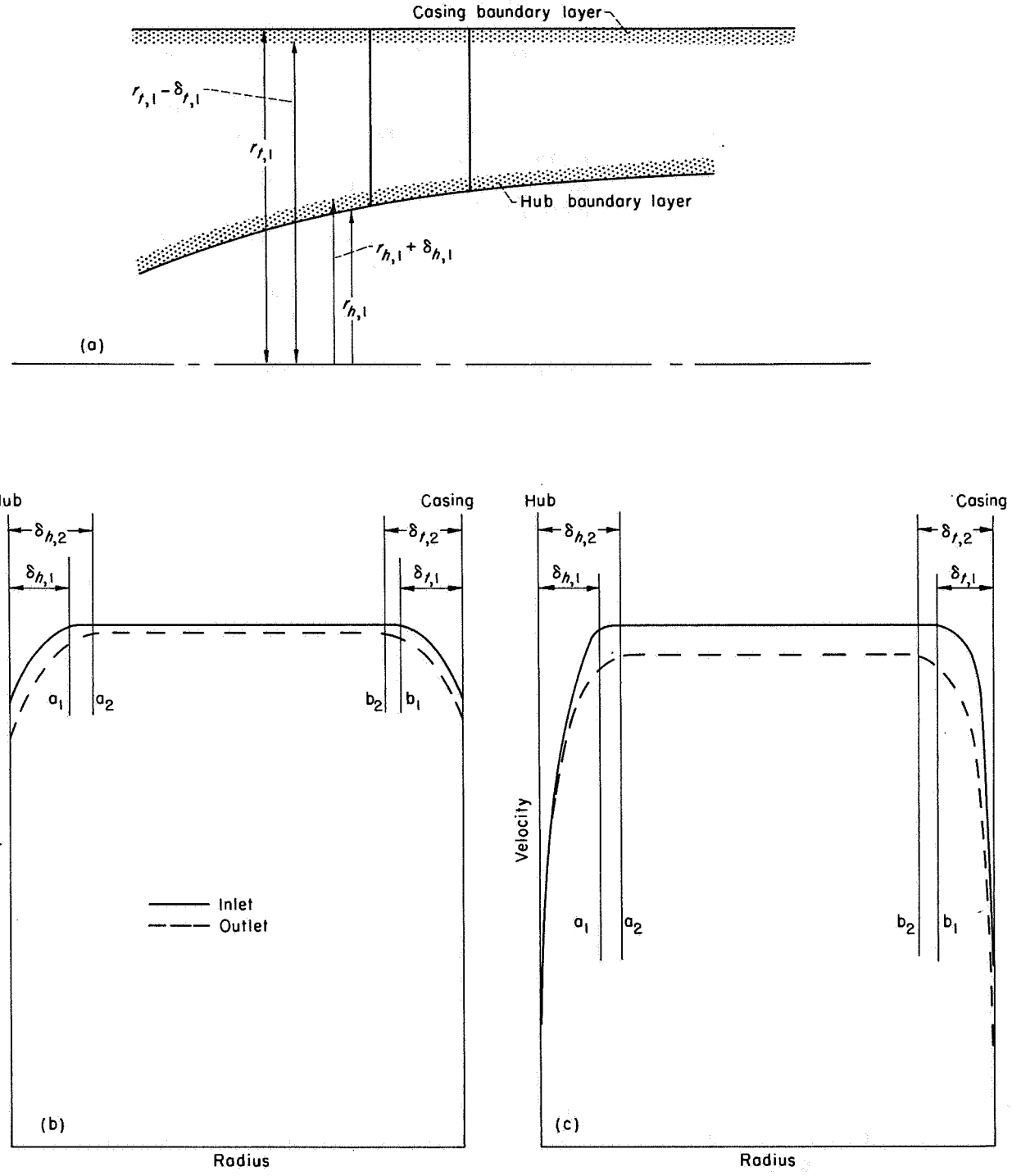

(a) Sketch of boundary layers.
(b) Total-pressure distribution. (c) Velocity distribution.

FIGURE 42.—Boundary layers at hub and casing.

equation (53) may be written as

$$w=2\pi\int_{(r_{h,2}+\delta_{h,2})}^{(r_{t,2}-\delta_{t,2})}\frac{P_2V_{z,2}}{gRT_2}\left(1-\frac{\gamma-1}{2\gamma}\frac{V_{z,2}^2+V_{r,2}^2+V_{\theta,2}^2}{gRT_2}\right)^{\frac{1}{\gamma-1}}r_2\,dr_2+\left[\int_{r_{h,2}}^{(r_{h,2}+\delta_{h,2})}\frac{P_2V_{z,2}}{gRT_2}\left(1-\frac{\gamma-1}{2\gamma}\frac{V_{z,2}^2+V_{r,2}^2+V_{\theta,2}^2}{gRT_2}\right)^{\frac{1}{\gamma-1}}r_2\,dr_2+\int_{(r_{t,2}-\delta_{t,2})}^{r_{t,2}}\frac{P_2V_{z,2}}{gRT_2}\left(1-\frac{\gamma-1}{2\gamma}\frac{V_{z,2}^2+V_{r,2}^2+V_{\theta,2}^2}{gRT_2}\right)^{\frac{1}{\gamma-1}}r_2\,dr_2\right]$$

The first integral is readily evaluated from data. The last two integrals, within the brackets, represent the relatively small mass flow through the space-consuming boundary layers. For lack of a better way of coping with these two integrals, they have usually been assumed to be adequately handled by the factor K_{bk} in the equation

$$w=2\pi K_{bk}\int_{r_{h,2}}^{r_{t,2}}\frac{P_2V_{z,2}}{gRT_2}\left(1-\frac{\gamma-1}{2\gamma}\frac{V_{z,2}^2+V_{r,2}^2+V_{\theta,2}^2}{gRT_2}\right)^{\frac{1}{\gamma-1}}r_2\,dr_2 \quad (53a)$$

where the blockage factor K_{bk} is a function of the design of the blade row, the inlet flow, and the position of the blade row in the compressor. The quantities P_2, $V_{z,2}$, $V_{r,2}$, and $V_{\theta,2}$ are taken as those in the main flow. However, an estimated average value of total pressure over the entire flow passage (including the boundary layer) might also be used; in this case a different value of K_{bk} would be necessary.

As long as the boundary layers are really thin, one technique is probably as good as another. If the boundary-layer correction itself amounts to 1 or 2 percent, a 20-percent error in the correction amounts to only 0.2 or 0.4 percent in the estimate for a single blade row. Notice, however, that the compounding effects in a multistage compressor might make even this error excessive. When the boundary layers become thick, greater accuracy is needed. When the flow resembles fully developed pipe flow, this method of accounting for viscous effects may leave something to be desired. It should also be noted, moreover, that, when the boundary layers are relatively thick, a consistent system of handling the boundary layers is especially imperative. Serious errors can result, for example, if one system is used to estimate P_2 and another to select the correction factor K_{bk}.

In addition to complicating the continuity relation, the existence of wall boundary layers could make the determination of average total pressure and total temperature difficult. It may be noted that the total pressures and total temperatures of the boundary layers may appreciably differ from those in the main stream. The problem of correctly averaging the total pressure and total temperature thus arises. A technique similar to that just discussed for continuity suggests itself. Correction factors, when they are required, could be applied to the main flow to estimate the mass-averaged quantities. These correction factors are again functions of the blade design, the inlet flow, and the position of the blade row in the compressor.

Loading limits.—Any flow device using a diffusion process will have a limiting diffusion at which the flow breaks down. This flow breakdown, or separation, can be directly attributed to the boundary layers; they do not have enough momentum to overcome the adverse static-pressure gradient accompanying the diffusion. In the usual compressor design, the velocity diffusion required on the blade surface increases as the ideal turning in a blade row increases. The intensity of this diffusion is frequently taken as a measure of the blade loading. The condition at which serious flow separation begins to occur is therefore called the loading limit.

The details determining the loading limit are still imperfectly understood. This statement is true even for relatively simple flow devices, and this situation is therefore not uniquely familiar to compressors. One of the important variables involved seems to be the ratio of the required static-pressure rise to an appropriate velocity pressure (refs. 9 and 38). The shape of the blades, the inlet flow conditions, and the required downstream flow conditions are thus expected to be involved in the loading limit. It should be noted

that the previously discussed radial shifts in the streamlines also influence the diffusion; this effect is particularly noteworthy for non-free-vortex distributions and at Mach numbers in the neighborhood of 1.00, where slight changes in streamtube distribution can cause large changes in velocity distribution. Some important differences between the loading limits of blade rows and those of corresponding two-dimensional cascades may therefore be anticipated. Since the demands of aircraft encourage the use of compressors with highly loaded blades (ch. II), at least some loading-limit information is a vital necessity. Experiments on actual blade rows are again the only positive source of data.

Experimental data required.—There are a number of questions relating to viscosity that can only be answered by experiment. The losses and loading limits of two-dimensional cascades over a range of blade shapes and inlet flow conditions are of interest. Data for various blade rows and inlet flow conditions in the actual compressor are required to evaluate the usefulness of the loss and loading-limit data obtained from two-dimensional cascades. Data are also required to establish the effect of staging on the losses suffered and the loading limits.

Data are required for the performance of the hub and tip sections of the blades as well as for those in the main flow regions. Because of the increased viscous effects in the wall regions, the turning-angle data, loss data, and loading-limit data can be quite different from those obtained under ideal two-dimensional-flow conditions.

Some examples of the studies required are given in the section of this chapter devoted to experimental data. Representative turning-angle, loss, and loading-limit data are first presented for two-dimensional cascades. The trends of these variables in various compressor blade rows and under various conditions are then noted. The relative thicknesses of the hub and tip boundary layers are discussed.

TREATMENT OF TIME-UNSTEADY FLOWS

Time-unsteady flows must exist in a compressor, because both stationary and rotating blade rows are used. Even for ideal flow conditions, as previously noted, the flow in a stator can be steady only when the motion is referred to a coordinate system that is also stationary. Similarly, a coordinate system moving at rotor speed must be used for the rotor. From a purely theoretical point of view, the flow through a rotor is therefore always unsteady with respect to uniform flow in a stator, and vice versa.

Moreover, time-steady circumferential variations in the flow ahead of or behind a rotor cause the flow in the preceding or following stator to be time-unsteady irrespective of the coordinate system used. Similarly, time-steady circumferential variations with respect to the rotor induce inevitable time-unsteady flows in the preceding and succeeding stators. It may also be noted that time-unsteady flows are also inevitable when either rotating stall (ch. XI) or surge (ch. XII) occurs.

Circumferential variations in the flow behind a blade row, and thus unsteady flows in the following blade row, are encountered even when the flow is completely inviscid. Some circumferential gradients in the flow persist for some distance upstream and downstream of even an ideal two-dimensional cascade. Similar circumferential gradients are associated with the types of flow presented in figure 38(c).

Additional circumferential gradients are brought about by the blade wakes (fig. 41). These gradients are made even more complicated by the fact that a fluctuating pressure field ahead of a blade row periodically changes the character of the wakes leaving the previous blade row. As a result of all these phenomena, both the rotor and stator are beset by complex unsteady flows. Notice that any two adjacent blade rows, one rotating and the other stationary, experience the same sort of disturbances.

Because of these time-unsteady components of the flow, average values of flow properties leaving one blade row have been used to represent the inlet flow to the next blade row. In this way, the unsteady-flow problem is rather arbitrarily reduced to a steady-flow problem. As discussed in chapter XIV, some theoretical considerations indicate that additional time-unsteady effects may be of importance. How vital these effects are must eventually be determined by experimental data.

The validity of this treatment of unsteady flow can also be judged by experimental data. Com-

paring the performance of isolated blade rows with those subjected to unsteady flows provides the basis for this evaluation. This problem is considered in the discussion of experimental data presented in the following section.

REPRESENTATIVE EXPERIMENTAL DATA SUPPORTING DESIGN CONCEPTS

Many of the questions that have been raised about the simplified flow concepts in the previous section have been answered by the published results of a large number of experiments and analyses. Some representative examples of these experiments and the indicated conclusions are presented in this section. Through this review, a qualitative picture of the flow is established that becomes the basis of a design system. Moreover, the results presented indicate the classes of assumptions and calculation techniques that may be used with a reasonable degree of confidence. The areas where design information must be tempered by intuition and judgment are also spotlighted.

Before presenting the data on actual compressor blade rows, attention is first focused on the aerodynamic properties of the two-dimensional cascade, since this type of reference data is the basis for many of the developed procedures. Typical data from inlet guide vanes are then reviewed. For inlet guide vanes with free-vortex flow distribution, the assumption of no radial flow is examined under conditions where the radial flows and viscous effects may be reduced as much as possible and the unsteady-flow effects are completely eliminated. The effects of changes in radial density gradients, of blade thickness distribution, of blade force, and of the hub slopes are noted. Radial flows resulting from non-free-vortex flow distributions are then examined.

Representative data obtained from rotating blades are also reviewed. The effects of blade rotation, over and above the effects considered for inlet guide vanes, are thus evaluated. Some effects of unsteady flows and the mixing of wakes are noted from the results of tests of both stationary and rotating blades.

Several significant results obtained from experiments on multistage compressors are next reviewed. These data indicate the validity of the simplified flow concepts under adverse, but typical, conditions. They also provide a basis for indicating important missing gaps in available knowledge.

For each experiment, the turning-angle data are presented and the loss or efficiency data are noted. Flow conditions in the main flow are discussed. The influence of the hub and tip boundary layers are also noted. Comments are made about the indicated effects of radial flows and unsteady flows. The significant knowledge derived from these classes of experiments is then summarized by outlining a model of the flow that can be used for design.

TWO-DIMENSIONAL CASCADES

Aerodynamic behavior.—Five quantities determine the aerodynamic behavior of a cascade with ideal flow. One of these is the shape of the blades, which is usually expressed in terms of the distribution of thickness and camber. Another quantity is the orientation of the blades with respect to the cascade axis; this orientation may be defined by the blade-chord angle $\gamma°$ (fig. 32). The third quantity is the solidity ($\sigma=c/s$), although the pitch-chord ratio, the reciprocal of this number, is sometimes used. With these three quantities, the geometry of the cascade of blades is defined. The fourth quantity identifies the direction of the flow ahead of the cascade. The relative inlet-air angle β_1' is frequently used for this purpose. Finally, the relative Mach number of the flow at some point must be known. This quantity is also usually referred to the relative inlet flow. Theoretically speaking, all details of the flow of an ideal inviscid fluid can be determined from these data.

For real flows, the factors involving friction are also pertinent. The Reynolds number of the relative flow thus becomes an important item. The Reynolds number is usually based on the properties of the inlet flow, using the chord length as the characteristic dimension. The factors involved are the turbulence of the incoming flow and the condition of the airfoil surfaces (see chs. V and VI). Because of the complicating effects of friction, the most reliable cascade data are derived from experiment rather than analysis.

Types of experimental data observed.—One of the most important pieces of cascade data required is the deflection of the flow ($\beta_1-\beta_2$), since deflecting the flow is the main purpose of the cascade. Al-

though analytical techniques have been developed and are occasionally used for determining this deflection (ch. IV), the greatest amount of data is obtained by experiment. A typical sample of the experimental data is shown in figure 43, which was obtained from reference 39. These data were obtained for fixed values of blade shape, solidity, and inlet-air angle. The blade angle was varied, the magnitude of the variation being described by the angle of attack $\alpha=\beta_1-\gamma°$. The deflection, or turning angle, is measured by the angle $\Delta\beta=\beta_1-\beta_2$.

The losses incurred by the cascade may be described in a variety of ways. In reference 39 the loss is measured by a drag coefficient; an average total-pressure loss or an average entropy increase could also have been used. (Notice that the drag coefficient is independent of the position of the downstream measurement and that no averaging techniques are required. The total-pressure loss and the increase in entropy, however, depend on the axial position of the measurements, the Mach number of the flow, and the method of averaging.) Of particular importance are the regions where the loss rises rapidly; the rapid rise in loss and the accompanying droop in the turning-angle curve indicate the point of flow separation or the loading limit of the cascade. For the particular family of blade shapes discussed in reference 39, it has been possible to correlate the loading limit by the following equation, developed in reference 9:

$$D=\left(1-\frac{V_2}{V_1}\right)+\frac{\Delta V_\theta}{2\sigma V_1} \qquad (54)$$

All the blades reached their loading limit at a value of D of approximately 0.6. This equation is simply an empirical means of estimating

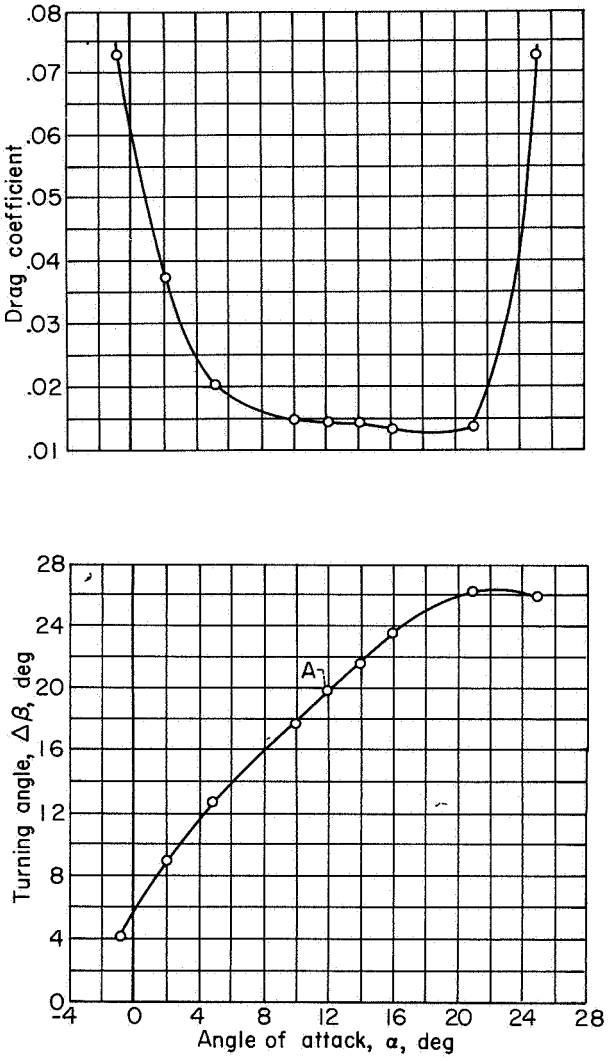

FIGURE 43.—Drag and turning-angle distribution for cascade combination. Blade section, NACA 65–(12)10; inlet-air angle, 45°; solidity, 1.0 (ref. 39).

$$\frac{\text{Downstream static pressure—Minimum static pressure on blade surfaces}}{\text{Maximum velocity pressure on blade surface}} \qquad (55)$$

Since it was derived for one family of blades, it is not expected to be univerally applicable. It does, nevertheless, provide an indication of the loading limit as good as or better than many other recommended empirical rules. A more fundamental approach would utilize equation (55) with the actual velocity and pressure data (see ref. 38).

Other details of the flow within a blade row may also be partially examined by studying the velocity distribution about a cascade element. The results of a typical experimental measurement in a two-dimensional cascade are shown in figure 44. The velocity distribution presented corresponds to the operating condition indicated by point A in figure 43. These data are valuable for interpreting over-all results, since comparing these data with similar measurements in a compressor blade row provides a means of comparing the internal flows.

The data described thus far were obtained at low inlet Mach numbers, the operating condition

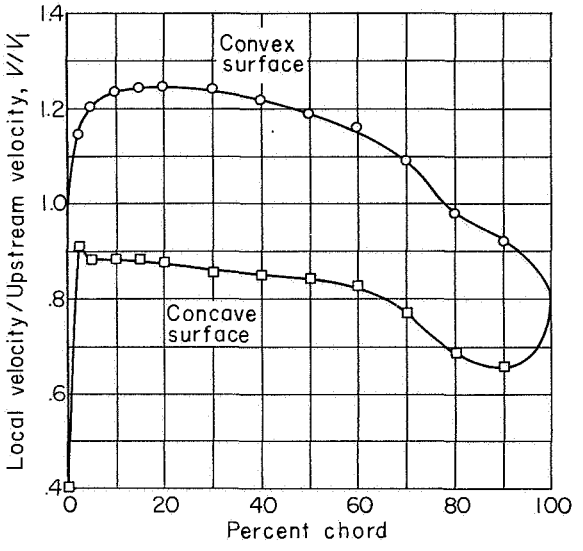

FIGURE 44.—Blade surface velocity distribution for cascade combination. Blade section, NACA 65-(12)10; inlet-air angle, 45°; solidity, 1.0 (ref. 39).

for most published cascade data. Increasing the inlet Mach number in two-dimensional-cascade rigs has the effect shown in figure 45, which was obtained from data of reference 40. As the Mach number increases, the range of angle of attack decreases. When the Mach number becomes high enough, the cascade is choked and the flow deteriorates to such an extent that the cascade is completely ineffective. The behavior of the flow at high Mach numbers is shown by the schlieren photographs of figure 46, which is taken from reference 41. The strong shocks that have developed cause the boundary layer to separate at all angles of attack. This type of data indicates an interrelation between loading limit and flow Mach number.

These results represent the principal knowledge obtained from numerous tests of two-dimensional cascades. As previously noted, the turning-angle data obtained are of primary interest. When the observed turning angle in an actual blade row agrees with that observed in two-dimensional cascades, credence may be given to the simple equations obtained by ignoring radial flows in that type of blade row. The relatively inexpensive two-dimensional cascade can then be used as an important source of design turning-angle data.

INLET GUIDE VANES

Tests of inlet guide vanes alone have been invaluable for studying and developing flow concepts and theory. In the laboratory setup, the flow ahead of inlet guide vanes has no tangential component of velocity, so that the inlet guide vanes have the function of creating a preconceived distribution of tangential velocity. When tested alone, the inlet guide vanes are exposed to essentially time-steady flow; therefore, time-unsteady-flow effects are eliminated. Moreover, the flow velocity behind the guide vanes is usually greater than that in front; thus, many adverse effects of viscosity arising from unfavorable pressure gradients are avoided. Inlet guide vanes, therefore, provide an excellent vehicle for studying the effects of radial flows brought about by the changes in radial density gradients through a blade row, by the radial distributions of blade thickness, by the radial components of blade force, by the slope of the hub or casing, and by nonvortex distributions of tangential velocity.

A typical setup used to conduct flow investigations is schematically shown in figure 47. Measurements are made ahead of and behind the blade row to determine the velocities and state properties of the air at these two stations. Sufficient data are taken behind the blade row to determine the radial gradients of the circumferentially averaged

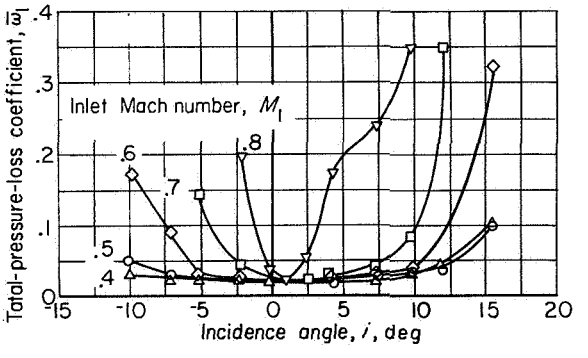

FIGURE 45.—Effect of inlet Mach number on loss characteristics of cascade blade sections (ref. 40).

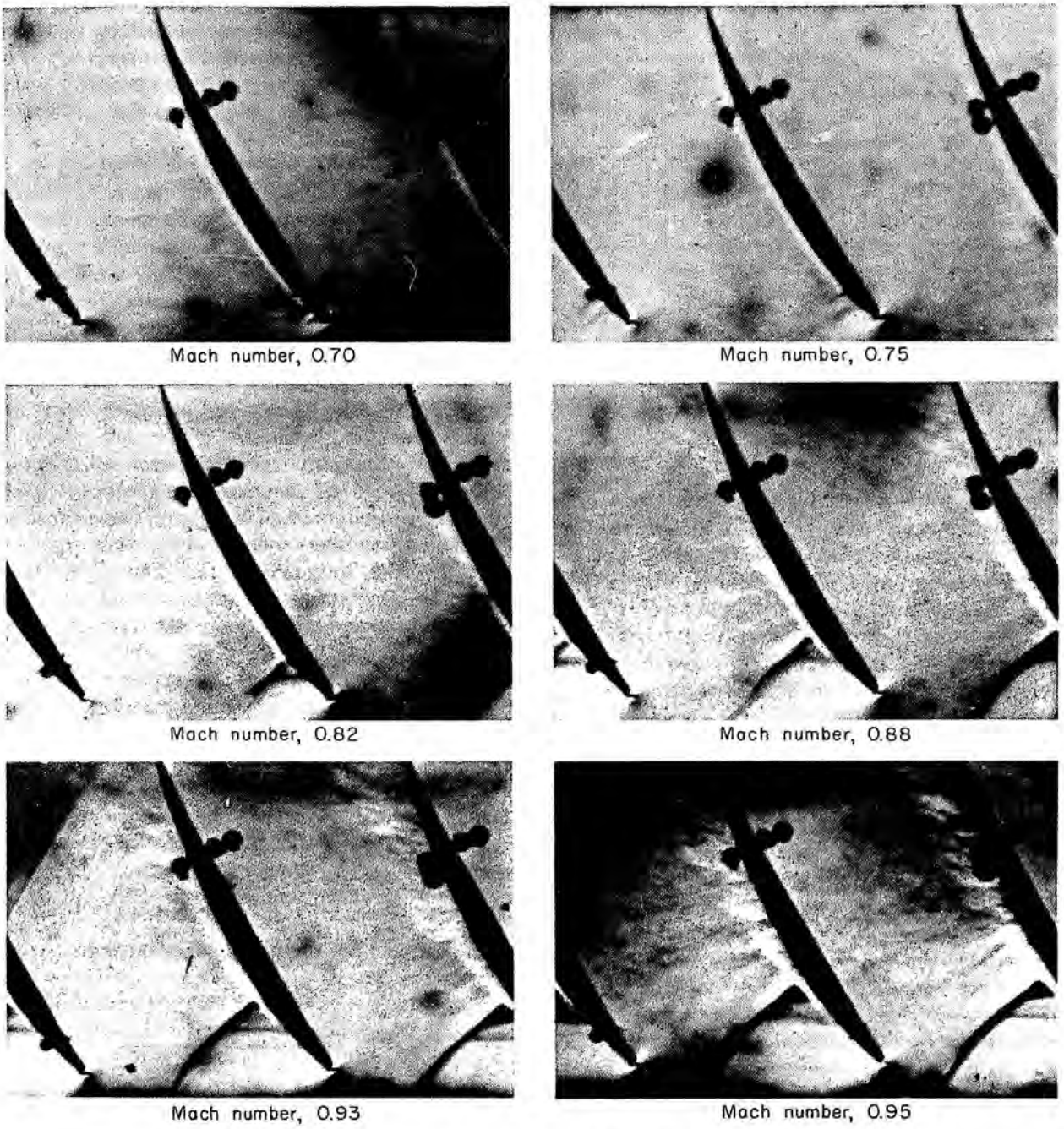

FIGURE 46.—Schlieren photographs for a range of Mach number.

properties of the main flow. Ahead of the blade row, precautions are taken to ensure a uniform distribution of the flow. Complete uniformity cannot, of course, be achieved in the hub and casing boundary layers, where the radial variation of entropy and the tangential component of vorticity are not zero. Care is taken, however, to make these boundary layers as thin as possible.

Free-vortex flow.—A representative result of an investigation with free-vortex blades is shown in

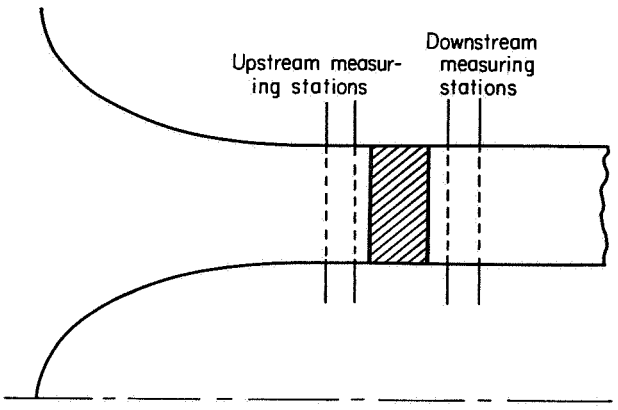

FIGURE 47.—Schematic diagram of an inlet-guide-vane test rig.

figure 48, which was obtained from reference 42. (The experimental setup was essentially the same as that shown in fig. 47.) In figure 48, the observed turning angle of the cascade elements of the blade row is compared with the turning angle that the same cascade elements would have in a two-dimensional cascade. As indicated in this figure, the observed turning was substantially the same as that of the corresponding two-dimensional cascade. The order of magnitude of the radial flows in this blade row is just about the same as that in many conventional compressors having free-vortex subsonic blade rows. There are strong indications, therefore, that the radial flows themselves have relatively minor effects, if any, on the turning angle at subsonic Mach numbers. Some discrepancies are noted in the vicinity of the blade ends. Those differences within the boundary layers are not unexpected, but the observed boundary layers were thin enough for these variations to be disregarded. The circulation gradients, or vorticity, within the boundary layer do, however, induce some deviations in the main flow. As shown in reference 43, these deviations are sometimes significant; however, they can be accurately treated by the technique reported therein.

The radial distribution of circumferentially averaged flow was also studied in reference 42. In general, the flow was fairly accurately described by equation (48a). An important point to note, however, is that the flow Mach numbers were not very close to 1.0, and the values of the local Mach numbers were therefore not extremely sensitive to small changes in the area of the stream tubes. At Mach numbers nearer 1.0, a small change in stream-tube area accompanying radial flows may give different results.

The loss data reported in reference 42 show that the average losses in total pressure were small. This trend agrees with two-dimensional-cascade data. In the hub and casing boundary layers, the losses increase; and eventually, of course, all the dynamic pressure is lost at the hub and casing surfaces. The main thing to notice with respect to losses is that radial flows themselves do not necessarily create large additional losses. The important losses, when the blades are operated within their loading limits, appear near the hub or casing. Probably the most important effect of these losses is the fact that they occupy space without transporting much mass. The correction K_{bk} in equation (53a) is thus an important quantity that depends on loss data. Therefore, two-dimensional-cascade loss data do not tell the whole story; data from actual blade rows are required to complete the loss picture.

Non-free-vortex flow.—Several investigations have been made with inlet guide vanes designed to establish the type of flow described by equation (50). Except for the type of velocity distribution created, these blade rows are physically similar to many of the free-vortex blades that have been tested. Studies of the non-free-vortex blade rows, therefore, provide a means of studying the effects of radial flows resulting from the radial gradients in circulation.

In figure 49 are shown representative data from

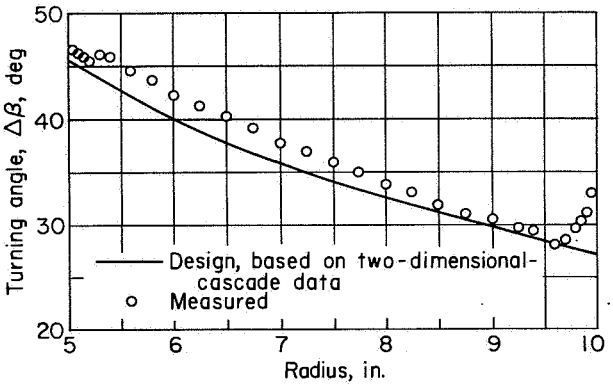

FIGURE 48.—Comparison of measured and design turning angles for free-vortex guide vanes (ref. 42).

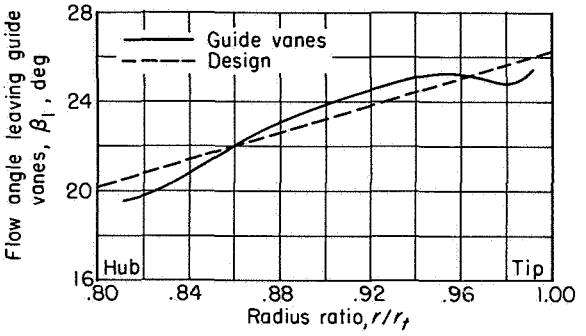

FIGURE 49.—Comparison of measured and designt urning angles for non-free-vortex guide vanes (ref. 44).

a test of inlet guide vanes designed for wheel-type rotation ($\Gamma=0$ in eq. (50)). These data are taken from reference 44. The average flow angles at the exit of the inlet guide vanes agree fairly well with those obtained from two-dimensional-cascade considerations. The effect of radial flows themselves is again quite small, if there is any effect at all. The other effect of circulation gradients, as reported in reference 43, cannot be completely ignored, however; and the correction techniques developed in this reference are frequently necessary for refining the analysis. But, when the radial gradient of tangential velocity is correctly established, the radial distribution of through flow usually agrees with the distribution expressed by equation (49a) (with radial flows ignored). The finite values of both ζ_z and ζ_θ required for axisymmetric flow are apparently suitable; the complicating flows shown in figure 38(c) seem to have little effect on the radial distribution of the circumferentially averaged flow.

The loss data available are similar to those obtained with free-vortex blade rows. Almost negligibly small losses are impressed on the main flow. The important losses again appear at the blade ends. Even here, the losses themselves are not as serious as their blockage effects are. The important loss information to be obtained is that required to evaluate K_{bk} in equation (53a) (or some similar function).

ROTORS AND SINGLE-STAGE COMPRESSORS

A large number of investigations have been made with rotors alone, rotors with inlet guide vanes, and complete stages formed from inlet guide vanes, rotors, and downstream stators. Tests of rotors alone have many of the same aims as the tests of inlet guide vanes—to study the net effects of radial flows. In addition, the effects of rotation that are not accounted for in simplified theories are investigated. Tests of inlet guide vanes and rotors examine the effects of unsteady flow and other phenomena for interferences between rotating and stationary blade rows that are otherwise neglected. Tests of a complete stage add the effects of another blade row.

A representative schematic layout for testing a complete stage is shown in figure 50. As with the inlet-guide-vane investigations, care is exercised to have thin hub and casing boundary layers at the inlet. Circumferentially uniform flow without distortion at the inlet of the first blade row is also sought. Enough measurements are taken upstream and downstream of each blade row to obtain an accurate picture of the behavior of the cascade elements at several radii. These data also enable the radial distribution of flow to be compared with that indicated by simple theory.

Free-vortex rotor blade rows.—A representative investigation of a free-vortex rotor with axial inflow is presented in reference 45. The observed turning-angle data are compared with those of the corresponding two-dimensional cascades in figure 51 for three radial positions: (a) near the tip,

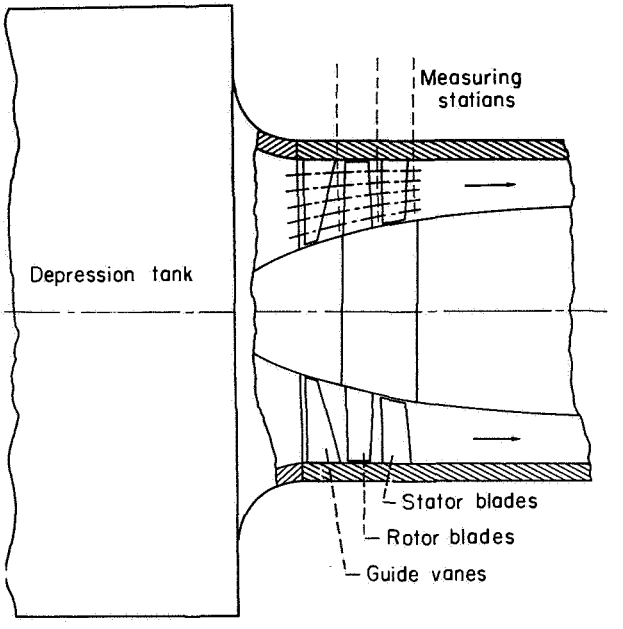

FIGURE 50.—Schematic layout of compressor stage.

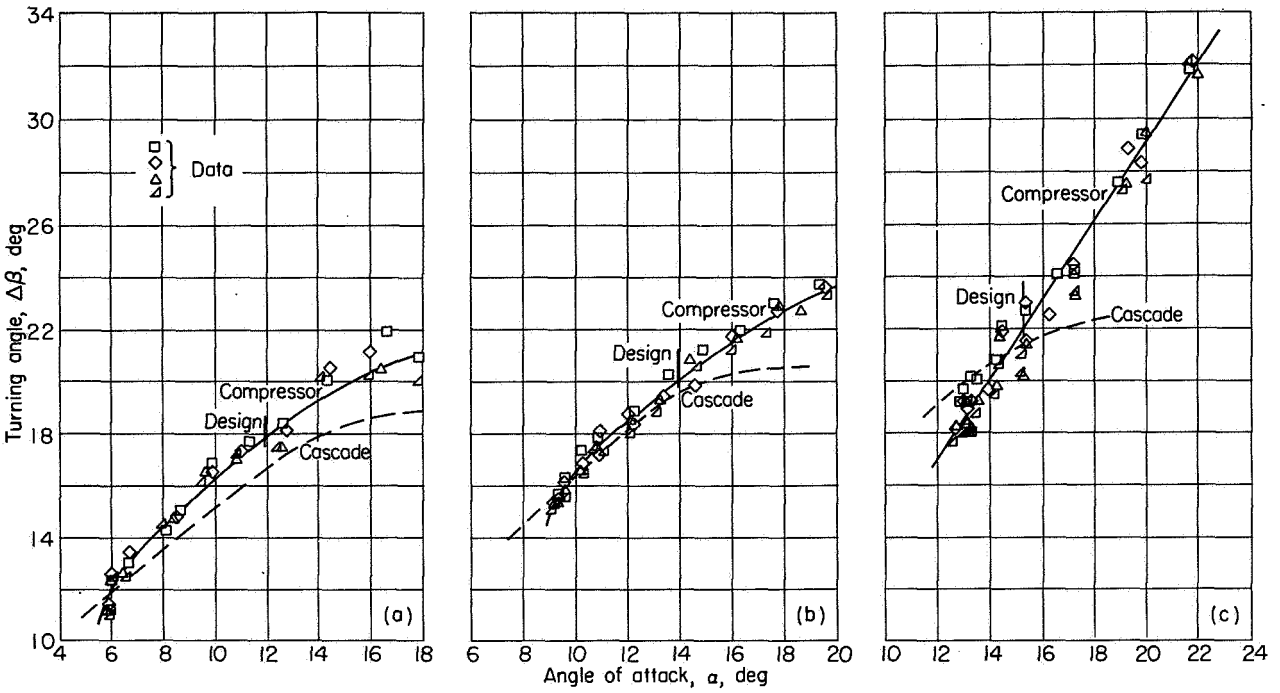

(a) Near rotor tip. (b) At midspan. (c) Near rotor hub.

FIGURE 51.—Compressor rotor and cascade turning angles (ref. 45).

(b) at the center of the span, and (c) near the hub. As shown in figure 51(a), the observed turning at the tip is slightly higher than that of the corresponding two-dimensional cascade. The rate of change of turning with angle of attack is about the same for both, however. At midspan (fig. 51(b)), the agreement in turning angle is good at low angles of attack. With high angles of attack, the turning through the rotor is greater than that indicated by two-dimensional-cascade data. The faired turning-angle curve for the data at the rotor hub (fig. 51(c)) has a steeper slope than the corresponding cascade curve. In this respect, the flow about the blade near the hub is comparable to ideal two-dimensional flow. Apparently this section can operate at much higher angles of attack than cascade data would indicate. In the vicinity of the design angle of attack of the cascade, the difference in turning is small.

In this particular investigation, the pressure distribution about the blades was also measured at the same time. These data are compared with those of the corresponding cascade in figure 52. At the hub and midspan, the agreement is excellent, except for some irregularity of the cascade curves between the 40- and 80-percent-chord points on the upper surface. The irregularities, however, are attributed to laminar separation (see ch. V), which may have occurred during the cascade tests but which did not occur during the rotor blade tests. The agreement near the tip is not quite so good, but there apparently are no pronounced effects of radial flows in the main stream.

These and other similar data indicate that the flow around the blade elements of a rotating row is reasonably the same as that in the two-dimensional-cascade counterpart except at the blade ends. In the main flow, the anticipated enthalpy rise is realized as long as flow separation is avoided.

In the boundary layer at the tip, however, the energy added by the rotor is usually higher than that anticipated from two-dimensional-cascade data. The total-temperature distribution indicated in figure 53 is fairly representative. There is always some scattering in the rotor data, which might be attributed to radial and time-unsteady flows as well as to instrument errors. The higher

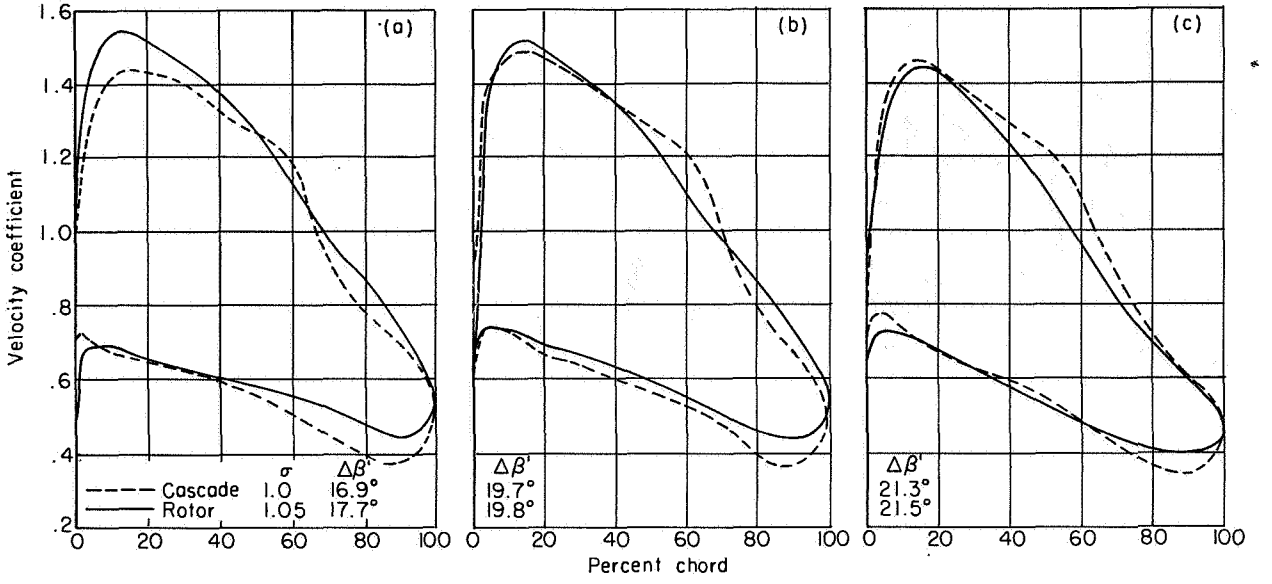

(a) Near rotor tip. Angle of attack, 12.2°.
(b) At midspan. Angle of attack, 14.1°; solidity, 1.183. (c) Near rotor hub. Angle of attack, 15.3°; solidity, 1.355.

FIGURE 52.—Compressor rotor and cascade pressure distributions. Relative inlet-air angle, 60°.

energy addition at the blade ends may be expressed in terms of a higher turning angle; however, a gross correction for the higher temperature rise is probably just as good as any other at the present time.

As was the case with inlet guide vanes, the rotor loss or efficiency is not always comparable with that of the corresponding two-dimensional cascade. A typical radial distribution of compressor rotor blade-element efficiency is shown in figure 53. Losses increase rapidly near the casing, and the loading limit frequently appears at lower values of D (eq. (54)) than suggested by two-dimensional-cascade data. It must be emphasized, however, that the changes in the absolute total pressure do not follow a simple trend. They depend on the relative magnitudes of the temperature rise as well as the loss in relative total pressure (see eqs. (41) and (42)).

The problem of accurately correlating the net effects of the flows in the hub and casing boundary layers is still somewhat confused. As proposed in the previous section on Analysis of Viscosity Problem, the space-consuming properties of the boundary layer can frequently be correlated by factor K_{bt} in equation (53a). In using this factor, a fictitious mass flow for ideal flow conditions is computed or assumed and the result is multiplied

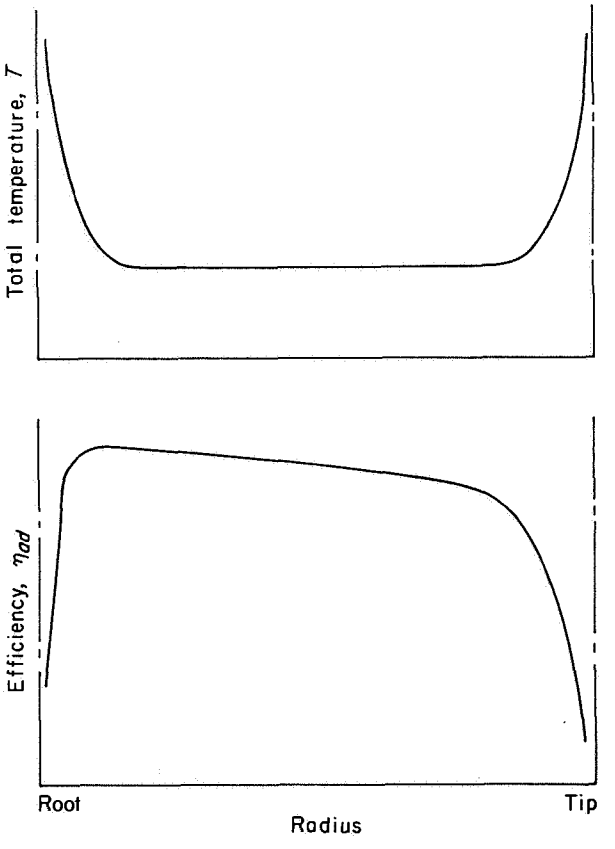

FIGURE 53.—Radial distribution of total temperature and efficiency through compressor rotor.

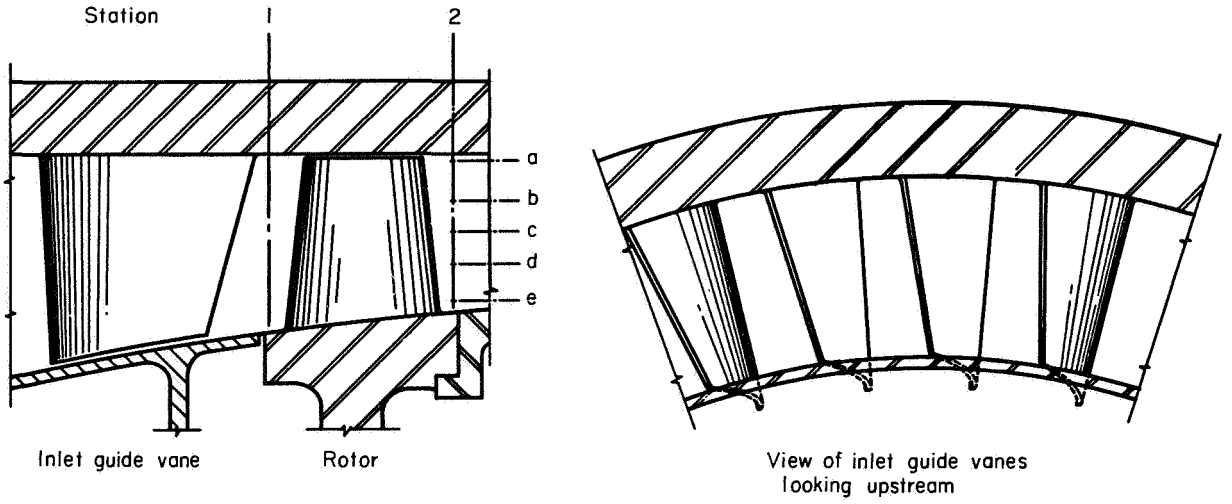

FIGURE 54.—Schematic layout for tests of inlet guide vanes and rotor (ref. 44).

by K_{bk} to obtain the true mass flow. Similarly, the ideal temperature rise and total pressure could be estimated by analyzing the ideal flow and then multiplying the result by an empirical correction factor. Satisfactory answers to these problems are still to be found. Except for their effects on blockage, the variations in total temperature and pressure at the blade tips are usually either ignored or are treated together as part of the over-all efficiency.

Investigations of the type just described have been extended to rotors with inlet guide vanes and to complete single stages. The results of these investigations are comparable with those indicated previously. As far as could be determined, the unsteady flows introduced by the alternate stationary and rotating blade rows had little effect on the turning angle of the blade row; the turning over a large part of the annulus was primarily decided by the corresponding two-dimensional-cascade variables. Moreover, the losses were not drastically increased by unsteady flows in the normal operating conditions.

Non-free-vortex blade rows.—An investigation was conducted on a setup consisting of inlet guide vanes and a rotor to study the effect of circulation gradients on the performance of a rotor and stator. The inlet guide vanes, the performance of which is presented in reference 44 and in figure 49, were designed to established a solid-body type of rotation ($\omega_{atr} \neq 0$, $\Gamma = 0$ in eq. (50)). No change in ω_{atr} was then required of the rotor; instead, the value of Γ was increased through the rotor. The arrangement of the inlet guide vanes and rotor reported in reference 44 is shown in figure 54. The large pitch of the inlet guide vanes suggests that the warping of the flow surfaces (fig. 40(b)) must be more than negligible. Notice also that the gap between the inlet guide vanes and the rotor is small. It is doubtful whether complete readjustment of the flow (that ideally occurring at an infinite distance downstream of the vanes) could have taken place at the rotor inlet. The radial distribution of flow at the rotor inlet might be in question, and severe time-unsteady flows might be anticipated.

As previously noted, the average flow angle at the exit of the inlet guide vanes alone agreed fairly well with that anticipated from two-dimensional blade-element considerations (fig. 55). The presence of the rotor may have had some additional influence on the flow angle, and some of this discrepancy might be attributed to time-unsteady flow. The major cause of the differences, however, is believed to be minor changes in the average radial distribution of flow due to the presence of the rotor. Even this effect is not excessive, however. Therefore, it has generally been ignored in practice, and equation (48a), obtained by ignoring radial flows, is usually quite accurate for this type of design.

The average turning through the rotor (fig. 56) was observed at the five radial positions indicated in figure 54. At radial position a, the observed turning was slightly higher than that of the corresponding two-dimensional cascade. At the

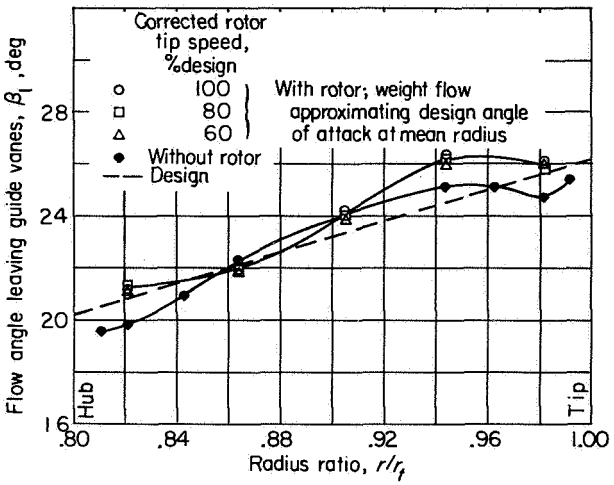

FIGURE 55.—Radial variation of flow angle leaving inlet guide vanes with and without rotor (ref. 44).

low angles of attack, the trends of the two curves are similar. The flow at the tip section of the blade apparently separated at a slightly lower angle of attack than cascade data would indicate.

In this particular type of flow distribution, the static-pressure rise near the casing is higher than that for the corresponding two-dimensional cascade. If equation (55) is a criterion for the loading limit, this premature separation is expected. The rise in turning following the dip in the curve is not related at all to normal two-dimensional-cascade performance.

At the other radial positions, the agreement is surprisingly good. Moreover, the trends observed are the same as those observed with free-vortex flow. The hub regions appear to be capable of operating at much higher angles of attack than the corresponding two-dimensional cascades. At those angles of attack where the data may be compared, the turning of the rotor is somewhat lower than that of the two-dimensional cascade. The similarity of these trends to those of rotors alone suggests that the effect of unsteady flows is relatively trivial.

The loss problem appears not to differ from that of the free-vortex designs. Only small losses are imposed on the active flow. The problem introduced by the boundary layers is principally that of boundary-layer blockage, although the different total temperatures and pressures in the boundary layers introduce complications that confuse the theory if not the flow. Losses cannot be predicted from two-dimensional-cascade data with sufficient accuracy to correlate actual blade-row data.

Transonic blade rows.—Recent investigations on free-vortex rotors (see refs. 8 and 18, e.g.) demonstrate the feasibility of obtaining high efficiency from rotors in which the Mach numbers at the tips are as high as 1.35. The turning angle of the blade elements at these higher Mach numbers cannot be compared with similar two-dimensional-cascade data, because usable two-dimensional cascades for transonic flows are yet to be developed. The compressor blade-element data that have been obtained, however, seem to lend themselves to the same correlation techniques that have been developed for two-dimensional-cascade data (ch. VI). It may be inferred from these data, for the time being at least, that radial flows themselves do not seriously affect the turning angle in the main-flow regions of the blade row.

Studies of the radial distribution of the circumferentially averaged flow properties indicate that equation (48a) or (48b) is not entirely adequate for the types of blade rows investigated. Reliable solutions to this problem have not yet been found, but the treatment discussed in the last section of this chapter offers some promise.

The loss picture is not different from that in subsonic blade rows, except that low losses are obtained only over a very narrow range of inlet flow angles at high Mach numbers. The viscous-flow regions near the hub and tip frequently have different total-pressure and total-temperature changes from those of the main flow. Their principal effect is again that of blocking part of the flow area. Whether the flow is subsonic or transonic is immaterial with regard to the factor K_{bk} in equation (53a), if the loading limits are not exceeded. The loading limit of the blade row, as indicated by the value of D, is about the same as that for conventional subsonic blade rows. The allowable values of D near the casing of the rotor appear to be lower than those elsewhere on the blade row.

MULTISTAGE COMPRESSORS

A representative example of the performance of the blade rows of a multistage compressor is shown in references 46 to 48. A schematic layout of this unit is shown in figure 57. This compressor was designed (see ref. 46) for finite values of both ω_{atr}

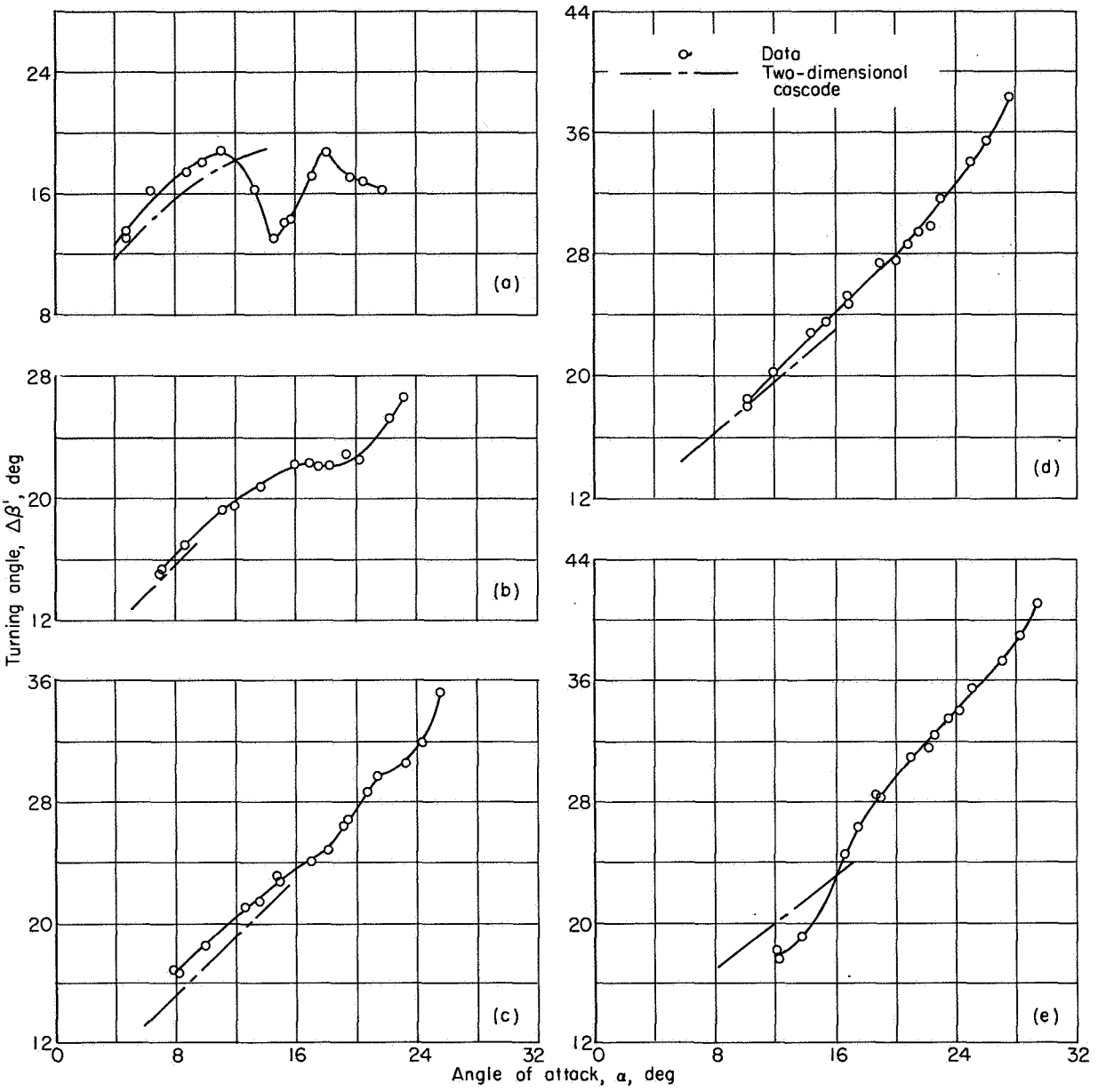

(a) Near casing.
(b) Between casing and mean radius.
(c) At mean radius.
(d) Between mean radius and hub.
(e) Near hub.

FIGURE 56.—Variation of turning angle across rotor blades with angle of attack at design speed (ref. 44).

and Γ (eq. (50)). Strong radial flows and time-unsteady flows are thus expected to be prevalent, particularly in the latter stages.

In reference 48 data for the performance of the first, fifth, and tenth stages are presented. Only the fifth and tenth stages are discussed here, however, since the flow entering the first stage is similar to that in single stages, and the results are similar to those previously presented.

Performance of fifth stage.—In spite of the fact that the hub and casing boundary layers seem to have ample opportunity to thicken, the flow distribution entering the fifth rotor at design speed (see fig. 58) was almost that expected for ideal

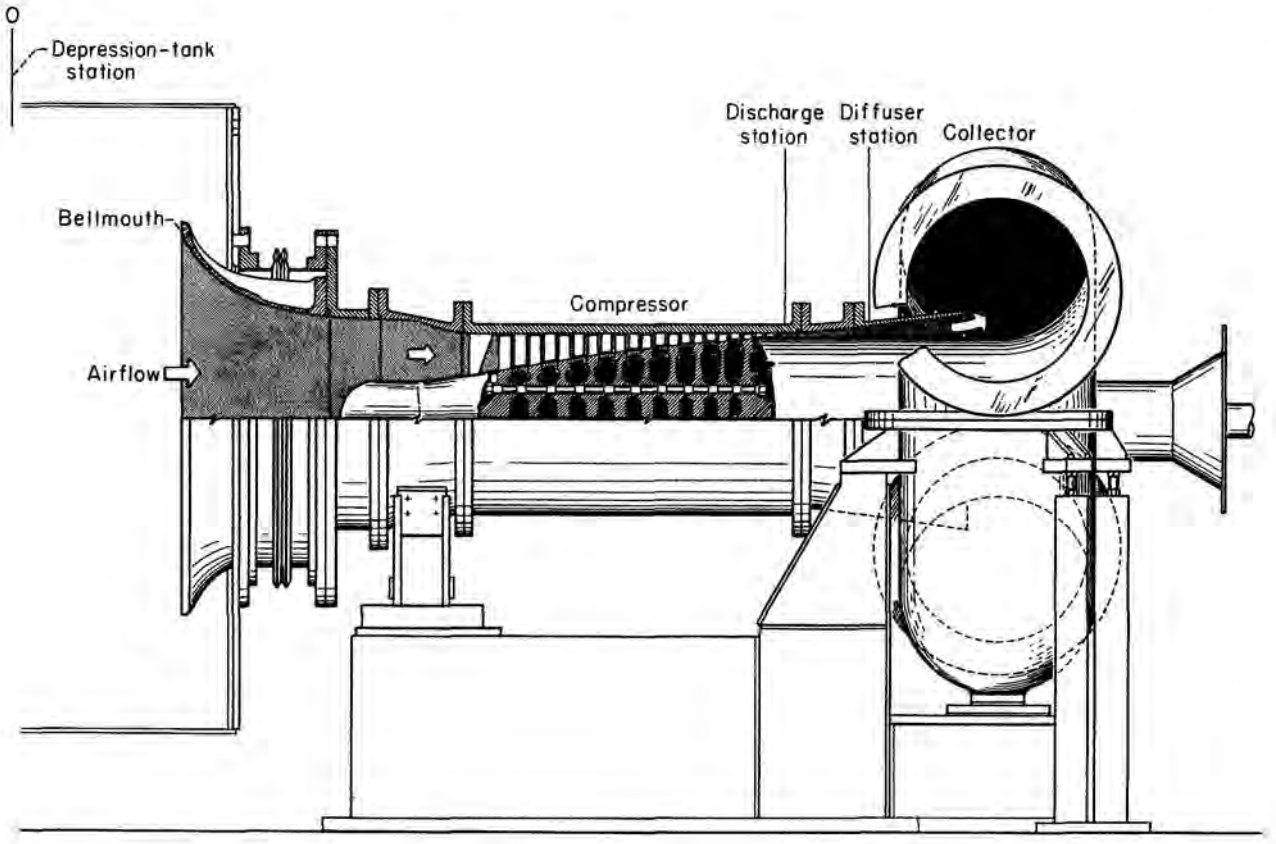

FIGURE 57.—Cross section of 10-stage axial-flow compressor, inlet bellmouth, and discharge collector (ref. 47).

flow, which was the basis for design computations. The observed turning angles through the rotor are shown for several radial positions in figure 59. Near the tip, the turning-angle data suggest that the blade is stalled; the loading limit is apparently exceeded even though the angle of attack and the value of D are within the limits of good two-dimensional-cascade performance. At the next two radial positions, good agreement with cascade data is found. At the two lowest radii (closest to the hub), the turning angle is somewhat below that obtained in two-dimensional cascades. These trends are similar to those presented in figures 51 and 56.

The turning-angle data for the following stator are presented in figure 60. The agreement with cascade data is fairly satisfactory, particularly near the design angle of attack. The tip (outer radius) of the stator appears to have a greater range of useful operation than is indicated by two-dimensional-cascade data. This trend, which is opposite to that of rotors, is fairly common for stators.

These results suggest that the turning angle of the main flow is not significantly affected by the wakes introduced by the upstream blade rows. The effect of the unsteady flows created in this compressor is apparently within the accuracy of instrumentation.

Qualitative observations of the losses in the main flow indicate that no unexpected developments have occurred. The main point of concern is the apparent premature stalling at the rotor blade tip. As previously indicated, this phenomenon is frequently observed, and the loading limits near the extremities of a blade row are frequently much different from those in the corresponding two-dimensional cascades. An important point to notice, however, is shown in figure 61. Because of the poor flow created by the rotor, significant entropy gradients were found in the entire flow field behind the fifth stage. In other words, thick hub and casing boundary layers appeared. When the observed entropy gradients were used in equation (48a), reasonably good correlation between the observed and computed axial velocity

691-564 O-65-7

distribution was found. If the entropy gradients were ignored, however, the correlation was not only poor but misleading. This experience shows the importance of recognizing entropy gradients when the boundary layers are thick. This point is elaborated in reference 49.

Performance of tenth rotor.—In contrast to the flow conditions at the entrance to the fifth rotor, the flow ahead of the tenth rotor was quite different from design (fig. 62). The axial velocity is lower than the design value at all radii. Instead of being fairly uniform, as designed, the velocity distribution is parabolic. The boundary layers at the hub and casing resemble those of fully developed pipe flow. The design values of absolute flow angles β_1 are realized near the center of the passages; at the hub and casing they tend to be high. The resulting relative angles of attack on the rotor blades are higher than the design values at all radii, the greatest angles occurring at the hub.

In spite of the difference between the design and observed inlet conditions, the observed turning angle at a given angle of attack (fig. 63) is surprisingly similar to the corresponding turning angle of the two-dimensional cascade. The trend is the same as that observed in investigations of single blade rows and single stages. This result is consistent over a wide range of compressor tip speeds and operating points at a given speed. These and similar tests indicate that the turning angle of a cascade element in a blade row is just about completely determined by the corresponding two-dimensional-flow conditions. The one important qualification is that the cascade element must not be stalled. Two-dimensional-cascade data are not always a reliable source of stalling data, however.

The poor flow distribution at the rotor inlet caused the over-all losses to be rather high. How this flow can be estimated properly in design remains an unanswered problem. Both intuition and judgment are still required to estimate the appropriate values of K_{bt} and P in equation (53a).

The radial distribution of the flow is adequately described by equation (48a). All the terms must be used in this equation, because the enthalpy and entropy gradients permeate the entire flow instead of being confined to thin boundary layers. Accurate estimates of the radial gradients in enthalpy and entropy would thus be necessary to make accurate designs, if this type of flow cannot otherwise be avoided.

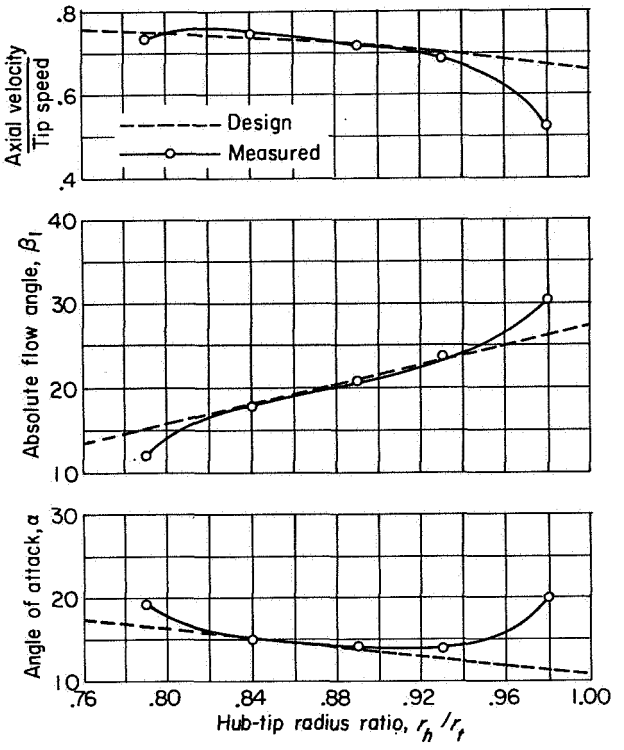

FIGURE 58.—Radial distribution of flow properties entering fifth rotor row of 10-stage compressor (ref. 48).

SIGNIFICANCE OF RESULTS

The results of experiments like those presented show that many features of the flow can be correlated with the aid of a few simple concepts. As long as the loading limits are not exceeded, the flow through a blade row may be divided into two regions. One of these regions is the main flow, where the viscous effects are comparatively small. In the other region, the velocity gradients are steep and the viscous effects are large.

Main-flow region.—In the main-flow region, the deflection of the flow at a given radius obeys about the same laws that govern the deflection in a two-dimensional cascade having the same geometry and inlet flow conditions. Two consistent differences are noted, however: (1) At a given angle of attack the turning angle is usually slightly higher near the casing of a rotor than that of the corresponding two-dimensional cascade. (2) Near the hub of a rotor the rate of change of turning with angle of attack is greater than that of the two-dimensional cascade.

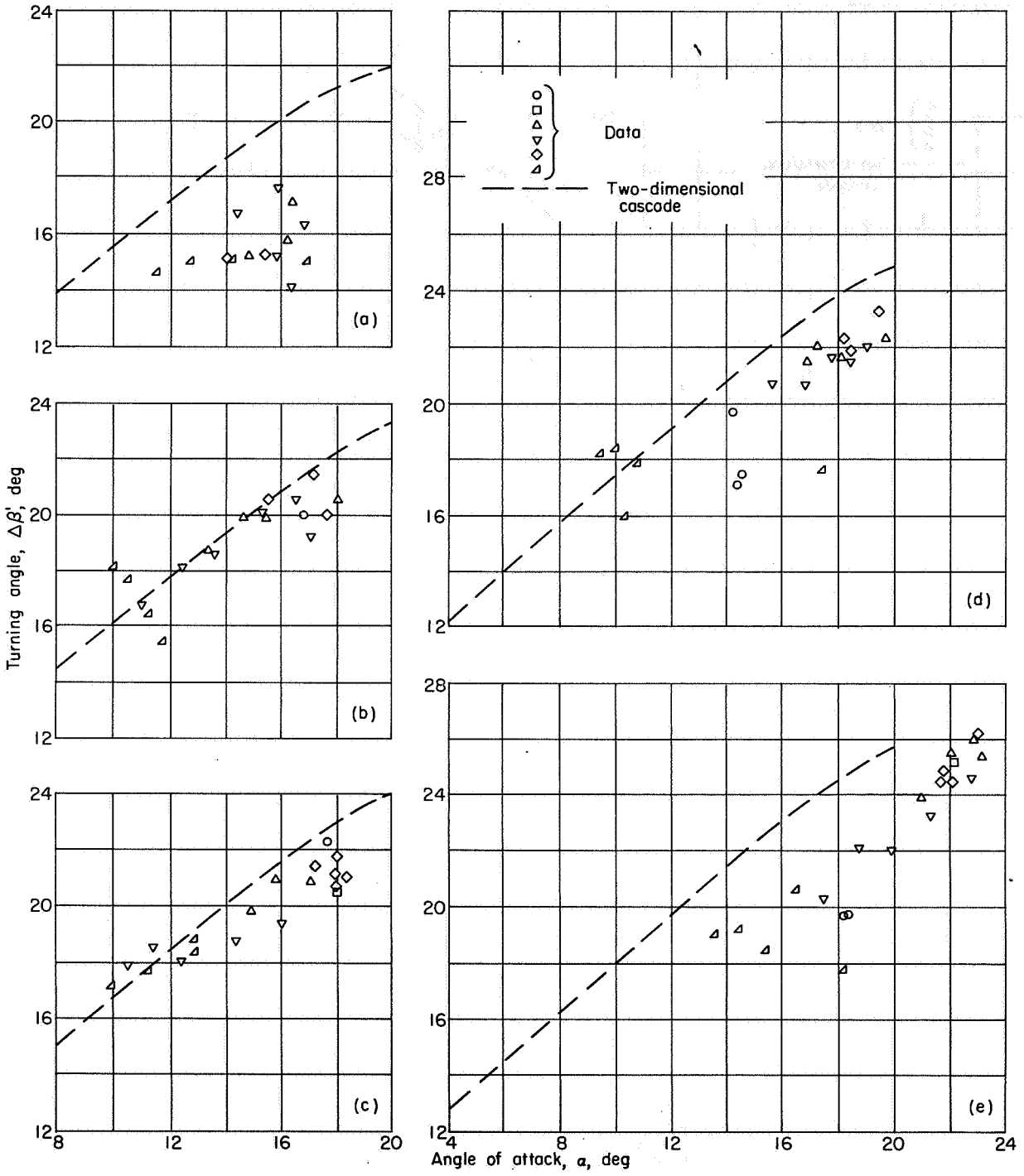

(a) Near casing.
(b) Between casing and mean radius.
(c) Near mean radius.
(d) Between mean radius and hub.
(e) Near hub.

FIGURE 59.—Variation of fifth-rotor turning angle with angle of attack at five radial positions (ref. 48).

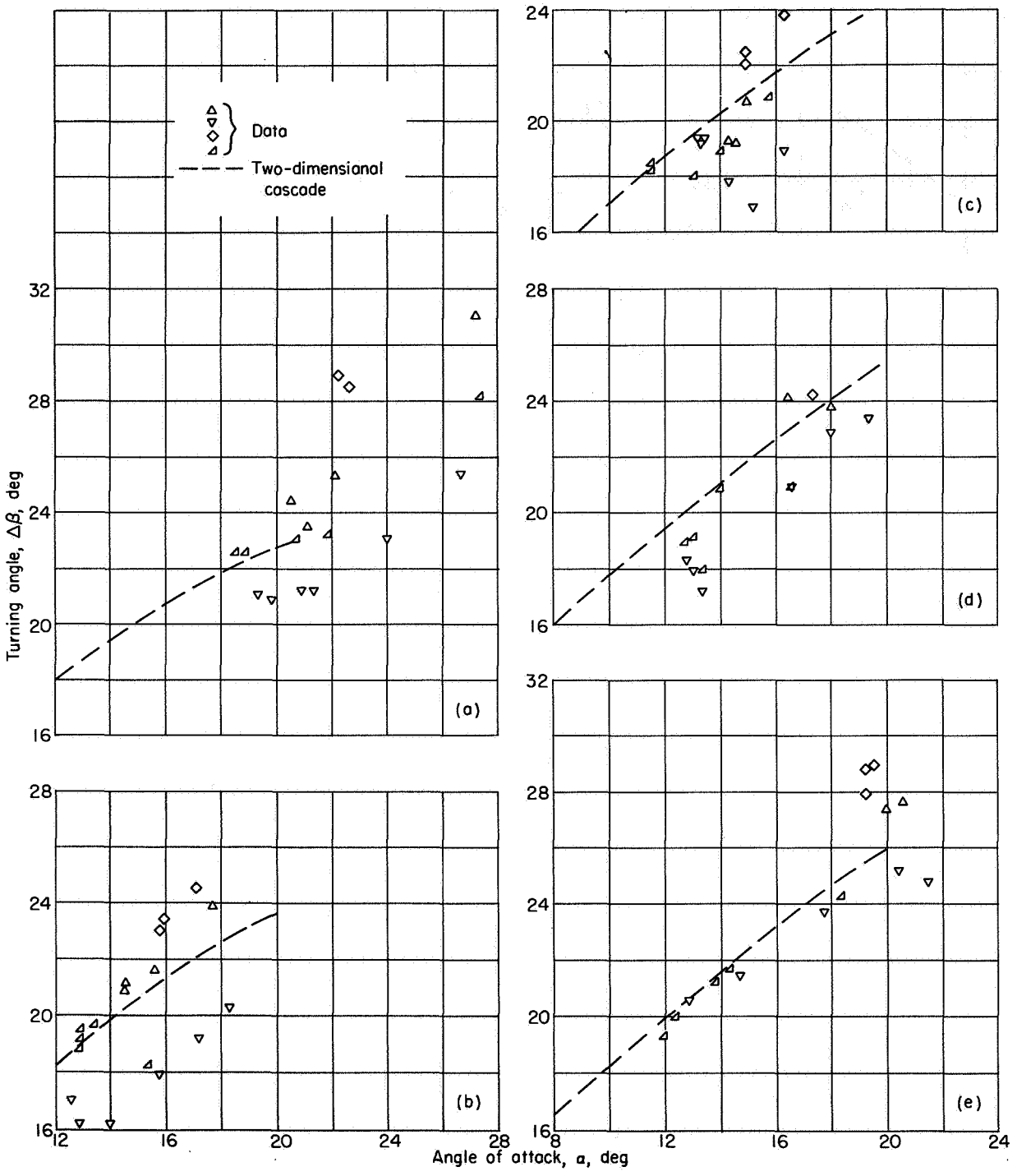

(a) Near casing.
(b) Between casing and mean radius.
(c) Near mean radius.
(d) Between mean radius and hub.
(e) Near hub.

FIGURE 60.—Variation of fifth-stator turning angles with angle of attack at five radial positions (ref. 48).

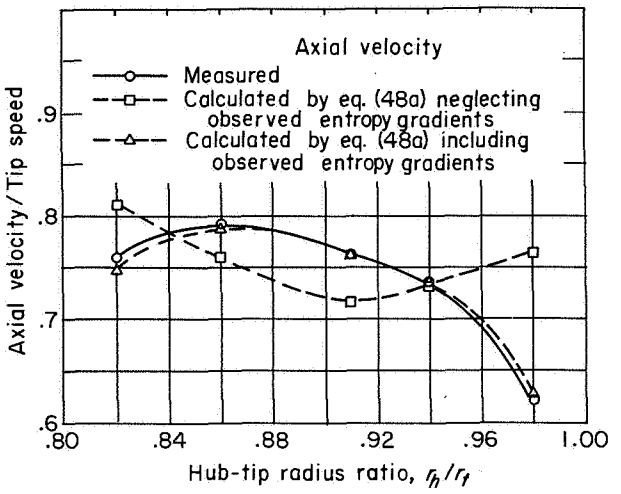

FIGURE 61.—Axial velocity distribution after fifth stage of 10-stage compressor (from ref. 48).

In the previous discussion, the governing flow has been assumed to be parallel to the axis of the blade row. These and other data may also be used to show that no accuracy is sacrificed when the cascade element and the governing flow are assumed to lie along a conical surface (fig. 64). This device is frequently useful when there is a pronounced radial shift in the streamlines through a blade row.

The radial distribution of flow ahead of and behind subsonic blade rows is quite accurately described by equation (49a), the form obtained by neglecting radial flows. As long as the boundary layers are rather thin, the entropy-gradient term is ignored. When thicker boundary layers are encountered, the entropy gradients must be recognized. For some transonic blade rows, this technique leaves something to be desired. In these cases, it is believed that techniques similar to those used in turbines and mixed-flow compressors may be useful. In these more erudite analyses, only axial symmetry is assumed, and the radial-distribution problem is treated as part of a two-dimensional-flow problem involving axial and radial gradients. This point is discussed in more detail in the last section of this chapter.

To a first approximation, the losses encountered by the main flow may be ignored if the design is not too critical. Recognition of the losses in the main flow, however, may be made by using two-dimensional-cascade loss data. In order to obtain greater accuracy, the losses measured from similar

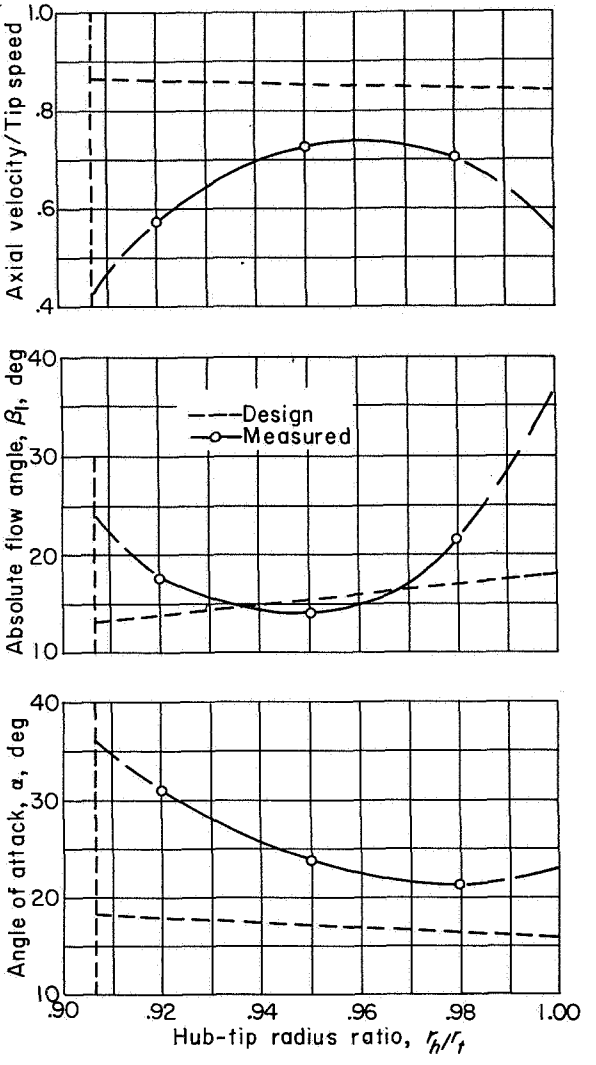

FIGURE 62.—Radial distribution of flow properties entering tenth rotor row of 10-stage compressor (ref. 48).

blade rows in similar flow environments should be used. The losses would then also be a function of the radial positions of the cascade element.

Of vital importance is the question of loading limits and Mach number limits. Although the diffusion factor of equation (54) is far from the perfect criterion of blade loading, it does offer some guide for selecting the deflection required of a blade row. When the static-pressure rise near the casing of a rotor is of the order of that of the corresponding two-dimensional cascade, the limiting value of D for the rotor tip seems to be about 0.35. When the static-pressure rise is higher than that for the corresponding two-dimensional flow, lower values of D seem to be necessary. The

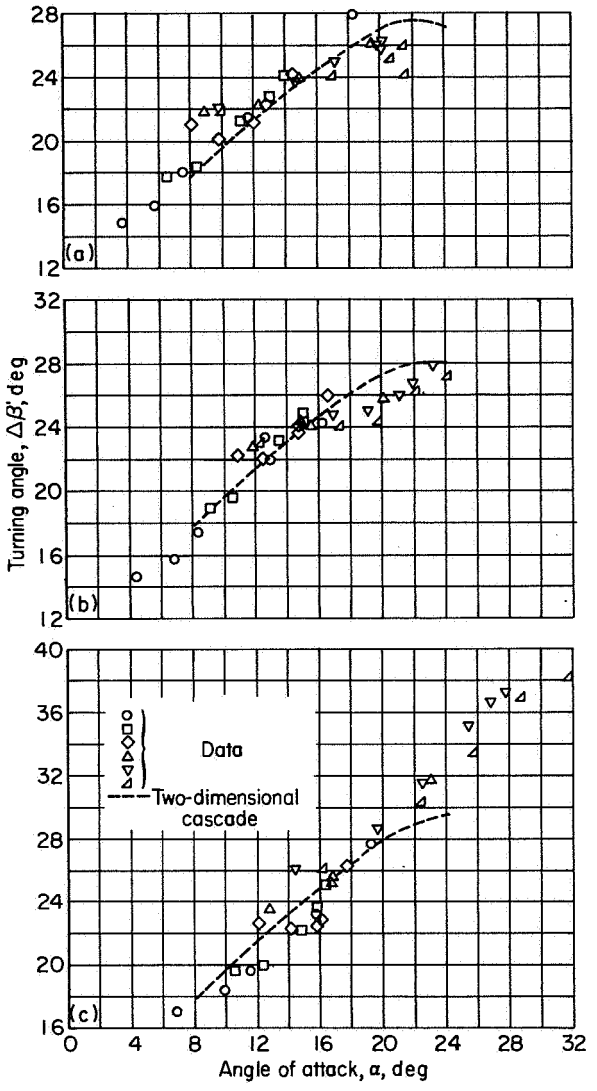

(a) Near casing.
(b) Near midspan.
(c) Near hub.

FIGURE 63.—Variation of tenth-rotor turning angle with angle of attack at three radial positions (ref. 48).

selection, for the time being, must be left to the judgment of the designer. If development time is to be minimized, low values of D are to be favored, even though the number of blade rows may be increased.

Up to Mach numbers at least as high as 1.35 there appears to be no fundamental reason for prescribing a Mach number limit. As the design Mach number is increased, however, more and more attention must be paid to the details of the flow. Defining and accounting for the important

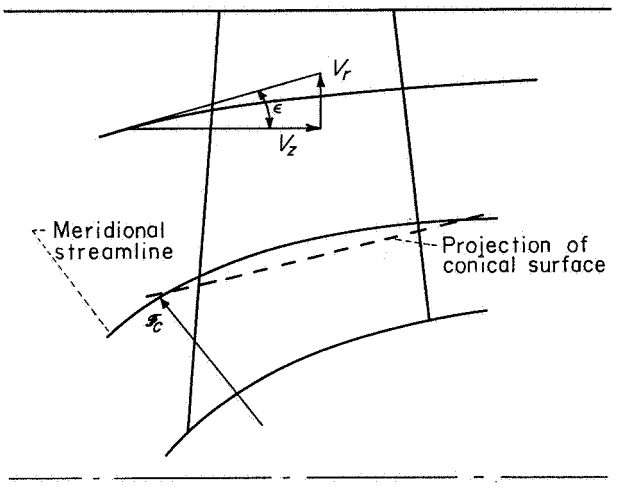

FIGURE 64.—Sketch showing typical projection of streamlines on meridional plane.

details is not yet a science, however; there have been too few successful designs above the Mach number of 1.2 to clarify the problem. Up to the Mach number of 1.2, however, the design problem does not appear to be much more complicated than the problem of executing a subsonic design.

For design, then, the main flow at the inlet of a blade row may be known or assumed. The main flow downstream of the blade row may be stipulated, if it can be prescribed within known loading limits, and if the distribution meets the requirements of equation (48) or its equivalent. Two-dimensional-cascade data or the equivalent may then be used to select blades to obtain the required deflection of the main flow.

Viscous-flow region.—Between the main flow and the hub and between the main flow and the casing is the second flow region, where viscous forces dominate the motion. The laws governing the movement of flow in this region are very imperfectly understood. Since the actual mass flow in these regions is often small, the areas usually contribute little to the mass-averaged enthalpy. Therefore, this effect is usually either ignored or given partial recognition by the use of gross correction factors. By the same token, the losses at the blade ends offer only a small contribution to the local mass-averaged loss. Significant additional losses may result from subsequent mixing, however. One important factor that cannot be ignored is the space-consuming property of these viscous-flow regions. This problem is discussed in the section on Analysis of Viscosity

Problem, where the use of the correction factor K_{bk} is suggested. Methods of accurately estimating K_{bk} have not yet been developed, however, and frequently an educated guess is the best technique available. It is the lack of information on this problem that has led to serious errors in estimating the flow in the latter stages of many compressors. This point is developed more fully in the following paragraphs.

Accuracy of estimate of state of air.—Many of the difficulties encountered in development have resulted from the fact that the flow towards the rear of the compressor is different from that anticipated in design. A common experience has already been mentioned in connection with figure 62. In this particular instance, the magnitude of the velocity is lower than the design value at all radii. In other compressors, however, the opposite behavior has been observed, the average velocity being higher than its design value. The high angles of attack shown in figure 62 increase the turning through the rotor; the enthalpy rise through the rotor is then increased, and the performance of the following rotor blade row deteriorates. The difference between the design and observed values of the average axial velocity is one of the principal reasons for this result. The error in turning angle owing to different radial gradients in flow properties may have contributed to the problem, but these effects are usually small (fig. 63) and in any event are masked by differences in the average velocity.

Errors in estimating the axial velocity can frequently be attributed to small errors in estimating the various terms in equation (53a). Suppose, for example, that the effective thicknesses of the hub and casing boundary layers after the first stage of a compressor are smaller than those anticipated; that is, K_{bk} is actually greater than the value used in design. If the estimated increase in enthalpy and total pressure in the main flow are otherwise accurately predicted, the axial velocity actually obtained after the stage is lower than that anticipated (eq. (53a)). (Notice that the same result would occur if K_{bk} were correctly predicted but the efficiency of the blade row or the turning angle of the cascade elements were underestimated in design.)

The angle of attack on the blade elements of the next rotor row is too high as a result of the low axial velocity. The turning angle is increased, and the energy addition is higher than its design value. (This trend of energy addition with turning angle is required by the relations expressed in eqs. (39) to (40)). If the efficiency and the value of K_{bk} for this stage were correctly estimated, the total pressure of the leaving flow would be too high and the axial velocity further reduced from its design value. Repeating this trend of error from stage to stage eventually causes an important error in the estimated axial velocity to result from only a small error in estimating the blockage effects of the hub and casing boundary layers. Of course, the same kind of result is obtained if the efficiency happens to be higher than the design value.

A qualitative indication of these trends is shown in figure 65. The dashed lines of figure 65(a) represent a design distribution of axial velocity and efficiency through the blade rows. A typical trend of the observed values of these quantities is shown by the solid lines. Because of the lower-than-

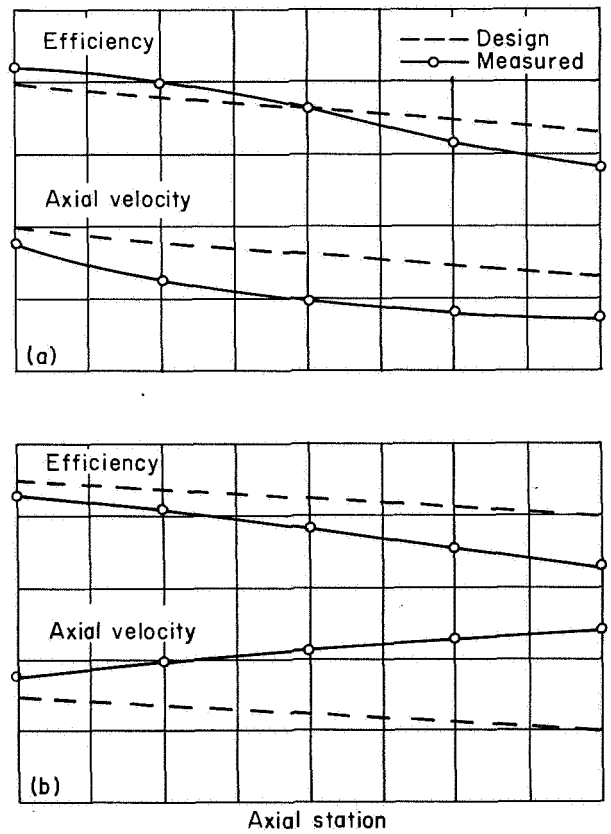

(a) Case I.
(b) Case II.

FIGURE 65.—Axial distribution of efficiency and axial velocity in multi-stage axial-flow compressors.

estimated boundary-layer thicknesses or the higher-than-estimated efficiencies obtained in the front stages of the compressor, the annular area for these stages is greater than it should have been. If the flow ahead of the compressor were that designed, the axial velocity leaving the front stages would be too low. Towards the middle of the compressor, the observed axial velocity would be so much less than its design value that the angle of attack on the blade rows would cause the stage efficiency to suffer and the boundary-layer blockage to increase. Flow separation might even occur. The axial velocity thereafter would not decrease as rapidly as before. It might still stay lower than the design value, however; and in any event the efficiency of the compressor always becomes low enough or the flow distribution distorted enough for the air to fill the passage made for it.

The opposite trend in axial velocity distribution occurs when the efficiency is lower or the boundary-layer thickness is greater than the design value. As indicated in figure 65(b), if the design mass flow were obtained, the axial velocity leaving the first stage would then be too high. The subsequent energy rise and pressure ratio would be too low, and the axial velocity would increase with respect to its design value. The axial velocity would eventually become so high that the angle of attack on the blade rows would be too low for efficient performance, and the efficiency would drop still further. In the extreme case, the velocity would become so high that the rear stages would be choked. In this case the mass flow is limited, so that the axial velocity in the front stages may be reduced below that shown.

As a matter of fact, experience indicates that, while the trends of figure 65 are observed, the flow usually adjusts itself so that the middle stages operate at about the optimum angles of attack; the front stages deviate in one direction about as far as the rear stages do in the other. In this way the excessive losses due to high angles of attack at one end of the compressor are about equal to those resulting from low angles of attack at the other end.

It should be noted that an overestimated value of K_{bk} in equation (53a) is just as bad as an underestimated value. The same thing may be said of the estimated blade-row turning and the total-pressure loss or efficiency.

The inability to estimate K_{bk} correctly is the principal reason that most successful compressors have required at least some development. There is an urgent need for better design information on these problems. The present difficulty is not due to the fact that the problems have not been recognized. Instead, the difficulty lies in obtaining the required data. Multistage data are required because efficiency and boundary-layer thickness are, among other things, functions of the axial position, which, in turn, partially determines the distribution of flow ahead of a blade row. Actual measurement of the blockage in numerous compressors is of little value, since the blockage adjusts itself to the design anyway. The blockage that is required for maximum efficiency, which is really the blockage desired, remains undetermined. Systematic readjustments in the annular area or the blade setting of a number of compressors will probably be required before correct estimates of the minimum required blockage area (that for highest blade-row efficiency) can be made. In the meantime, some development effort must be expended to exploit the merits of a given design fully.

SYSTEM ADOPTED FOR DESIGN AND RESEARCH

The preceding discussions have presented the techniques that have been useful for describing the important features of the three-dimensional time-unsteady motion of the viscous fluid through an axial-flow compressor. They have also indicated the general approaches that have been utilized in compressor design. These design procedures simplify the three-dimensional aspect of the problem by considering the main flow to be described essentially by two-dimensional solutions in two principal planes, thus making the problem mathematically tractable.

First, the blade-element approach is used. That is, the flow in the blade-to-blade or circumferential plane is treated by considering flow about the developed blade profiles formed by the intersection of flow surfaces of revolution and the compressor blading (fig. 32). The performance of such a blade element in the main flow is then described by a circumferentially averaged value of (1) turning and (2) loss; these data are obtained experimentally, preferably under conditions similar to

those existing in the compressor. Thus, effects such as those arising from viscosity, time-unsteady flow, and blade-row interactions are accounted for in a gross manner. Losses may be treated as functions of cascade geometry of the blade element, inlet Mach number, diffusion factor, radial position of the blade element, and axial position of the blade row. Turning may be treated as a function of cascade geometry, loss, Mach number, and radial position of the blade element. On the basis of available experimental data, limits are suggested for certain critical design parameters such as Mach number and blade loading.

Secondly, under the assumption of axial symmetry, the average quantities in the blade-to-blade plane are used to describe the distribution of the flow in the hub-to-casing or meridional plane (fig. 64). Equations representing the radial variation of this average state of the air are written for continuity, energy addition, and radial equilibrium. In this system, certain difficulties are created by the hub and casing boundary layers. It is eventually hoped that reliable estimates of the state of the air can be made at all radial positions, even within the wall boundary layers. For the present, however, the meridional-plane analysis is based on the main-flow region (A_1–B_1 of fig. 42), and the effects of wall boundary layers are accounted for by applying gross corrections.

In essence, then, a combination of two-dimensional solutions in the two principal planes (circumferential and meridional) is used to approximate the complete three-dimensional flow. Comparatively excellent compressors have been and can be designed by this approach, if the essence of the derived technique is used in its entirety and if the data are not extrapolated too far.

It is recognized that this quasi-three-dimensional design procedure can be an oversimplification of the problem, particularly as performance is extended to higher levels. However, this simplified flow model has been adopted for this series of reports on the basis that (1) it correlates experimental data as well as the more complicated systems that have been tested; (2) it provides adequate compressor designs, at least up to current levels of performance; (3) it has received general acceptance in the field; and (4) no practical and tested three-dimensional design procedure is yet available.

In practice, the design system can be considered to consist of three principal phases:

(1) Design-point solution in the meridional plane: As previously indicated, this phase of the problem is based on the assumption of axial symmetry. The problem is reduced to a two-dimensional system, in which only radial and axial variations are considered, by assuming circumferential averages to represent the flow at all points along the meridional-plane streamline. In many cases, the problem may be further reduced by ignoring the axial gradients as well. Equations describing radial variations of these average values are written to account for equilibrium, continuity, and energy addition. For a given flow distribution ahead of a blade row, a quantity like the radial distribution of tangential velocity may be selected. Another quantity such as the axial velocity at the casing (required for a certain loading limit) may also be selected. The radial distribution of the axial component of velocity may then be calculated. Velocity diagrams (fig. 66) may be then constructed at each of several radii to depict the air velocities and flow angles at the entrance and discharge of each blade row. The functions of the blade elements are thus given.

(2) Blade selection: This phase of the problem is based currently on the concept of blade-element flow, with the flow limited to the surfaces of a

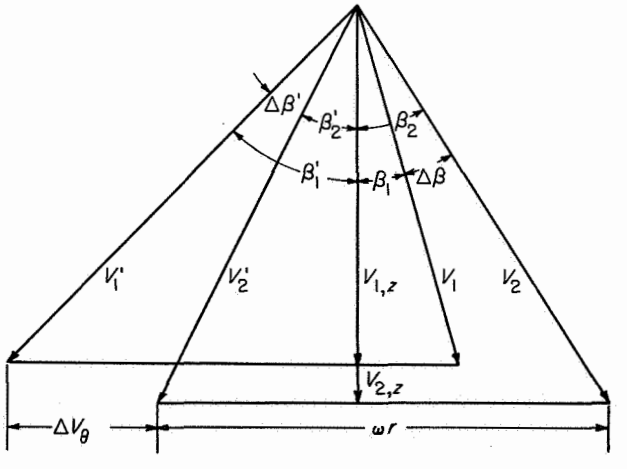

FIGURE 66.—Typical rotor velocity diagram for a cascade element.

cone that approximates the surface of revolution generated by rotating the meridional-plane streamline (for the circumferentially averaged flow) about the axis (fig. 64). Blade elements must then be selected that are consistent with the average conditions established in the meridional-plane analysis. This requires a knowledge of loss and turning characteristics of compressor blade elements. This information is usually provided by correlated empirical data, which are obtained from both two-dimensional cascades and from actual blade rows.

(3) Off-design performance: With the compressor blading and geometry established, the final phase of design is the estimation of the performance characteristics of the compressor over a range of speeds and flows. A rigorous solution to this "analysis" problem involves the use of the relations previously established in the meridional and blade-to-blade planes.

As might be inferred from the preceding brief description, such a design system is not direct in the sense that a single step-by-step procedure will result in the desired compressor. For example, because of the large number of factors involved in design (including matching with other engine components), the optimum compressor for any application is obtained only after a series of compromises among these various factors. Obtaining the required off-design characteristics usually necessitates a trial-and-error screening of a number of alternative designs. Therefore, this chapter does not attempt to outline a complete systematic step-by-step design procedure. Instead, the various elements entering into the design system that must be considered in the design process are summarized and interrelations are pointed out. The actual sequence in which these elements are then utilized is left to the individual designer. In the following discussion, the design concepts are grouped under the three principal phases previously listed.

DESIGN-POINT SOLUTION IN MERIDIONAL PLANE

Over-all specifications.—As indicated in chapter II, the specifications for an axial-flow compressor in an aircraft gas-turbine engine cannot be stipulated in an arbitrary fashion. Preliminary design studies and combined engine and airplane analyses are usually needed before the requirements are sufficiently explicit to define the design. Based on these preliminary studies, the following data may be given:

(1) Design weight flow
(2) Design over-all pressure ratio
(3) Design equivalent speed
(4) Desired level of efficiency
(5) Range of operation for which a high level of efficiency must be obtained
(6) Inlet and outlet diameters
(7) Maximum velocity of air at compressor outlet
(8) Desired length and weight
(9) Some idea of velocity distortions likely to be encountered at inlet

In the process of design, adjustments in some of these initial specifications are necessary when they are not completely compatible.

Velocity diagrams.—Initially, the meridional-plane solution is directed at determining the velocity diagrams throughout the compressor for the design operating conditions. In the past, analyses have been made in the attempt to establish the most desirable radial distribution of velocity diagrams for aircraft gas-turbine application. For example, reference 35 showed that, for given Mach number and lift-coefficient limitations, the use of a symmetrical velocity diagram at all radii would produce higher mass-flow and pressure ratios than the free-vortex type of diagram. With the use of blade-element theory based on incompressible airfoil concepts and with the assumption of constant axial velocity across the blade row, it was also shown that the symmetrical velocity diagram at all radii was also optimum with respect to profile efficiency.

With advances in the field, such as the raising of Mach number limits (ref. 41) and the establishment of more significant parameters for blade loading (ref. 90), specific velocity-diagram types begin to lose their significance. Research results have shown that satisfactory performance can be achieved for a wide range of velocity diagrams. Although specific velocity-diagram types may still be used because of the resulting convenience in design calculations, the present trend in compressor design is toward a greater freedom in their choice.

For example, raising the Mach number limitations has made free-vortex velocity diagrams attractive because of their simplicity. The design can be further simplified by specifying zero inlet

and exit whirl in each compressor stage. With constant work input from hub to tip, as is frequently specified in compressor designs, calculating the radial distribution of the velocity diagram becomes a rather simple process. High-performance compressors have been obtained through the use of this design approach (refs. 50 and 51).

Design equations.—In order to satisfy the aerodynamic and thermodynamic requirements for the circumferentially averaged flow in the meridional plane, a number of the previously given equations are used. The enthalpy change brought about by a blade row in a tube of flow is given by the energy equation:

$$H_2-H_1=\frac{\gamma}{\gamma-1}gR(T_2-T_1)=\omega(r_2V_{\theta,2}-r_1V_{\theta,1}) \quad (36)$$

or

$$\frac{T_2}{T_1}=1+\frac{(\gamma-1)\omega r_1}{a_{a,1}^2}\left(\frac{r_2}{r_1}V_{\theta,2}-V_{\theta,1}\right) \quad (36a)$$

If the inlet flow conditions are known, for example, and the outlet tangential velocity is assumed, the temperature ratio T_2/T_1 may be computed. An assumed radial distribution of tangential velocity at the outlet thus determines the outlet radial distribution of enthalpy. The associated radial distribution of axial velocity between blade rows must satisfy equation (49), which is frequently called the equilibrium equation since it may be derived from the consideration of the radial equilibrium of forces:

$$\frac{\partial H}{\partial r}-t\frac{\partial S}{\partial r}=V_\theta\zeta_z-V_z\zeta_\theta \quad (48)$$

where

$$\zeta_z=\frac{1}{r}\frac{\partial(rV_\theta)}{\partial r}-\frac{\partial V_r}{r\partial\theta} \quad (46)$$

and

$$\zeta_\theta=\frac{\partial V_r}{\partial_z}-\frac{\partial V_z}{\partial r} \quad (47)$$

For axial symmetry with no radial flows, equation (48) assumes the following form:

$$\frac{dH}{dr}-t\frac{dS}{dr}=\frac{V_\theta}{r}\frac{d(rV_\theta)}{dr}+V_z\frac{dV_z}{dr} \quad (48a)$$

By integration, this equation becomes

$$V_z^2-V_{z,t}^2=2(H-H_t)-(V_\theta^2-V_{\theta,t}^2)-2\int_{r_t}^{r}\frac{V_\theta^2}{r}dr-2\int_{r_t}^{r}t\frac{dS}{dr}dr \quad (56)$$

The velocity V_z at any radius is then expressed in terms of $V_{z,t}$, the velocity at any reference point (e.g., the hub). By interchanging the limits of integration, the casing radius could be used as a reference point.

Another relation between V_z and V_θ is given by the continuity equation:

$$w=2\pi K_{bk}\int_{r_h}^{r_t}\frac{PV_z}{gRT}\left(1-\frac{\gamma-1}{2\gamma}\frac{V_z^2+V_r^2+V_\theta^2}{gRT}\right)^{\frac{1}{\gamma-1}}r\,dr \quad (53b)$$

Notice that $V_z^2+V_r^2=V_z^2\sec^2\epsilon$ (fig. 64). With a known value of ϵ, the value of V_z may now be determined at any radius. For example: A value of $V_{z,t}$ may be tentatively assumed; equation (56) then enables the corresponding values of V_z to be found at various radii; substituting the known values of V_θ and the tentative values of V_z into equation (53b) determines the resulting mass flow w as a function of r_h and r_t. If r_t is given, r_h is then found. If the values of r_h and r_t are independently given, the mass flow calculated may differ from the known value; another trial value of V_t is then assumed, and the procedure is repeated. In making this calculation, a value of K_{bk} must be selected. For this and other details in these calculations, see chapter VIII.

The static temperature at various radii at the outlet may now be determined by

$$\frac{\gamma}{\gamma-1}gRt=\frac{\gamma}{\gamma-1}gRt+\frac{1}{2}V_r^2+\frac{1}{2}V_z^2+\frac{1}{2}V_\theta^2 \quad (37a)$$

If V_z is known, V_r may be estimated to be $V_z\tan\epsilon$ (see fig. 64).

The change in the total pressure of a stream tube through a blade row may be estimated by one or another form of the following equation:

$$\frac{P_2}{P_1}=\left(\frac{T_2}{T_1}\right)^{\frac{\gamma}{\gamma-1}}e^{-\frac{J}{R}\Delta S}=\left(\frac{T_2}{T_1}\right)^{\frac{\gamma}{\gamma-1}\eta_p}=\left[1+\left(\frac{T_2}{T_1}-1\right)\eta_{ad}\right]^{\frac{\gamma}{\gamma-1}} \quad (41)$$

Estimates may be made of η_p or η_{ad} to determine P_2/P_1. Or, the change in the relative total pressure may be estimated and the entropy change determined from

$$\frac{P_2'}{P_1'}=\left(\frac{T_2'}{T_1'}\right)^{\frac{\gamma}{\gamma-1}}e^{-\frac{J}{R}\Delta S} \quad (42)$$

where

$$\frac{\gamma}{\gamma-1} gRT' = \frac{\gamma}{\gamma-1} gRt + \frac{1}{2} V_r^2 + \frac{1}{2} V_z^2 + \frac{1}{2} (V_\theta - \omega r)^2 \tag{40a}$$

Notice that V_r may frequently be used in the thermodynamic equations even though it is effectively ignored in other correlations and equations. By using the entropy change in equation (41), the change in total pressure of a stream tube through a blade row is estimated. Notice that different efficiencies and entropy rises are required when the average change in total pressure over the entire blade row is desired.

The change in the static pressure of each stream tube may now be determined by the equation

$$\frac{p_2}{p_1} = \left(\frac{t_2}{t_1}\right)^{\frac{\gamma}{\gamma-1}} \frac{\frac{P_2}{P_1}}{\left(\frac{T_2}{T_1}\right)^{\frac{\gamma}{\gamma-1}}} \tag{43}$$

The total pressures in this equation must be those in the given stream tube ahead of and behind the blade row. The associated change in density is finally given by

$$p = \rho g R t \tag{34}$$

or

$$\frac{\rho_2}{\rho_1} = \frac{p_2}{p_1} \frac{t_1}{t_2} \tag{35}$$

Average values of energy addition for entire blade row.—In order to determine mass-flow-averaged values of pressure and temperature (or efficiency) at the discharge of a compressor blade row, the contributions of the boundary layer must be accounted for. As previously discussed, a precise integration from wall to wall is not possible, because of a lack of knowledge of the conditions within the boundary layer. In the main-flow region, however, all the conditions of state may be presumed to be known. A possible technique for accounting for the effects of wall boundary layers is to write the equations as if the main-flow conditions prevailed across the entire annular height, and to utilize modifying coefficients (based on the experimental data) to correct for the defects in the boundary layer. As previously noted, this technique is similar to that used for satisfying continuity. A detailed discussion of techniques available for establishing mass-averaged values of pressure, temperature, or efficiency is given in chapter VIII.

Blade loading.—In the preceding sections, relations have been presented that permit the designer to determine velocity diagrams. In general, designers establish these velocity diagrams on the basis of optimizing such performance characteristics as specific mass flow, stage pressure ratio, and efficiency. Unfortunately, the conditions for obtaining maximum values of all three factors are not usually compatible. Therefore, the designer must consider the selected values of the design parameters on the basis of their effect on each of the several factors describing compressor performance. Blade loading is one of the primary aerodynamic factors influencing this performance that must be selected in the process of determining compressor velocity diagrams. It is apparent that large values of ΔV_θ are desirable with respect to obtaining a large pressure ratio per stage (eqs. (36) and (41)). In the past, the concept of maximum lift coefficient as used in isolated-airfoil design has been also applied to compression to estimate the maximum blade turning angle, or loading limit, for which high efficiency may be obtained (e.g., the $C_L\sigma$ limit of ref. 35). It has been recognized, however, that the lift coefficient is not completely adequate as a measure of loss variation and of loading limits in a compressor.

An improved approach to the problem is one previously outlined. It considers the pressure distribution about a two-dimensional blade element in cascade and its influence on boundary-layer growth and separation. References 9 and 38 show that loading parameters based on the diffusion on the suction surface provide improved criteria for loss and for limiting loading. The diffusion factor as proposed in reference 9 is given for the case of a rotor with no radius change as

$$D = \left(1 - \frac{V_2'}{V_1'}\right) + \frac{\Delta V_\theta'}{2\sigma V_1'} \tag{54}$$

A discussion of diffusion limits, as well as empirical loss correlations based on available experimental data, is given in chapters VI and VII. Notice that, for a given value of $\Delta V_\theta'$ and a given value of D, the corresponding value of V_2' is automatically determined. This value could be used as a guide for selecting $V_{z,t}$ in equation (56), or, instead, $V_{z,t}$ could be independently scheduled and $V_{\theta,t}$ determined.

Relative Mach number.—Another important aerodynamic factor that has been discussed previously is the Mach number relative to rotor blade elements. As a result of the demand for high stage pressure ratios and high mass-flow capacity, the trend in compressor design has been toward higher compressor relative Mach numbers. The earliest attempts (ref. 52) to utilize these high relative Mach numbers led to large sacrifices in efficiency. However, with an improved understanding of the physics of flow over compressor blading (ref. 41), the gains associated with high Mach numbers have been achieved without corresponding reductions in efficiency. High performance has been demonstrated in multistage axial-flow compressors utilizing local relative entrance Mach numbers above 1.0 (refs. 51 and 53). Mach numbers up to 1.35 have been successfully utilized in single-stage units (ref. 18). It it generally accepted that this high level of relative Mach number can be maintained in compressors if proper consideration is given to the accompanying value of diffusion factor and to the form and thickness of the blade profiles. For routine design purposes, Mach numbers up to 1.2 may be contemplated. For higher Mach numbers, more refined techniques must be used.

Reynolds number.—Compared with the effects of loading and Mach number, the effect of Reynolds number on compressor performance is of secondary importance for the current types of aircraft. Reynolds number in a compressor is usually expressed in terms of blade chord $\rho Vc/\mu$, and the effect of a reduction in Reynolds number is to reduce the pressure ratio, weight flow, and efficiency of the compressor. This reduction in performance depends basically on the development of the boundary layer over the airfoil surfaces, the magnitude of the effect depending on the magnitude of Reynolds number, the turbulence level, and the pressure gradients in the flow. Discussions of Reynolds number effects are included in chapters V, VI, and VII. Although Reynolds number has been largely ignored in the past, it may play an important role in establishing the size of the compressors in high-altitude aircraft.

Axial velocity.—In a multistage axial-flow compressor, the axial velocity at the inlet is usually fixed by the mass flow per unit frontal area and the compressor hub-tip ratio. The axial velocity at the compressor exit is usually fixed by the diffuser and combustor requirements. The exact scheduling of axial velocity between these points is largely a function of blade-row design. Large reductions of axial velocity across any one blade element should be avoided whenever possible, since, for a given value of $\Delta V\theta'$, the diffusion factor is thereby increased.

Hub and tip contours.—In a multistage axial-flow compressor, configurations are possible in which the tip diameter, the hub diameter, or both, vary from stage to stage through the compressor. As pointed out in reference 35, a progressive increase in tip diameter is desirable with regard to maintaining high pressure ratios per stage and keeping the relative Mach number below a given value. However, the weight flow per unit frontal area is reduced. Furthermore, an increase in tip diameter results in reduced annular heights (for a given flow area) and reduced aspect ratios (for a given blade chord). Consequently, tip-clearance and annulus losses are probably larger for the increased tip diameter than for a comparable constant-tip-diameter design. Moreover, the high relative Mach numbers that may now be used tend to reduce many of the advantages cited in reference 36.

Constant-hub- or constant-tip-diameter designs offer some advantage with respect to fabrication and therefore are frequently used. However, there is increasing evidence that a configuration with a decreasing tip diameter may provide the best compressor layout, even though it may require one or two more stages for a given over-all pressure ratio. With respect to aerodynamics, the increased annular heights near the exit may also offer higher efficiencies.

Thus, the final selection of the configuration in the meridional plane is seen to depend to a large degree on the application being considered. Again, this is a phase of design in which the designer has considerable freedom; at least, several designs should be evaluated to establish an optimum for a given application.

BLADE SELECTION

The basic principle of compressor blade selection is that, if the blade element turns the air through the required angle with the predicted loss, the desired blade-row velocity diagrams will be closely achieved. The selection of blade

sections and settings for a given turning may be obtained from two-dimensional-cascade testing (ch. VI and refs. 39 and 54) or from blade-element measurements made in rotating or stationary annular cascades (ch. VII). Loss data are usually based on measurements made in the actual compressor environment (ch. VII). By using data such as these, elements are selected to obtain the desired turning with a minimum loss and to provide a maximum range of operation. The complete blade is built up from the blade-element profiles determined at several selected stations along the radial height of the passage.

Blade profile.—Basic blade shapes for compressor application are usually obtained by (1) establishing a mean line and (2) imposing a thickness distribution on this mean line. This method of designation is a carryover from isolated-airfoil experiences. It should be noted that the mean line and thickness distribution do not have the same significance in cascades as they did in isolated airfoils. Mean lines may be based on geometric shapes (e.g., circular- or parabolic-arc) or on prescribed loading distributions (NACA A_{10}). The mean-line shape is then scaled to give any desired camber. Thickness distributions are similarly determined; two popular thickness distributions are the NACA 65-series and the British C.4. Variations in absolute blade thicknesses are obtained by proportionally scaling the basic thickness distribution.

In the past, only a limited number of basic blade shapes have been used in compressor design, primarily because of the lack of adequate cascade data. In the United States, the NACA 65-series blade section has found the greatest application. In England, the blades with circular and parabolic mean lines have been used extensively. With the recent trend toward high Mach number applications, however, blade sections such as the double circular arc (ref. 55) and the modified 65-series blades (ref. 54) have received the most attention. All these common denominators for developing blade families are rather synthetic. The aerodynamic significance of geometric blade shapes changes so much with solidity and blade angle that some implied correlations are misleading.

Blade-element data.—The basic parameters selected in this report for the description of flow about compressor blade elements are

(1) Incidence angle i (angle between inlet airflow direction and tangent to mean line at leading edge, fig. 32)
(2) Deviation angle $\delta°$ (angle between outlet airflow direction and tangent to mean line at trailing edge, fig. 32)
(3) Total-pressure-loss coefficient $\overline{\omega}'$

Incidence angle has been selected as the basic directional approach parameter rather than angle of attack, since incidence angle is independent of blade camber and therefore provides a more significant description of flow around the blade leading edge. Deviation angle is selected as a measure of the blade guidance capacity; turning angle can then be determined by the relation

$$\Delta\beta=\varphi+i-\delta° \tag{57}$$

The loss coefficient is defined as

$$\overline{\omega}'=\frac{(P_2')_{id}-P_2'}{P_1'-p_1}=\left(\frac{P_2'}{P_1'}\right)_{id}\left\{\frac{1-\dfrac{\dfrac{P_2'}{P_1'}}{\left(\dfrac{P_2'}{P_1'}\right)_{id}}}{1-\left[\dfrac{1}{1+\dfrac{\gamma-1}{2}(M_1')^2}\right]^{\frac{\gamma}{\gamma-1}}}\right\} \tag{58}$$

where $(P_2'/P_1')_{id}$ is

$$\left(\frac{P_2'}{P_1'}\right)_{id}=\left\{1+\frac{\gamma-1}{2}\frac{(\omega r_2)^2}{\gamma g R T_1'}\left[1-\left(\frac{r_1}{r_2}\right)^2\right]\right\}^{\frac{\gamma}{\gamma-1}} \tag{59}$$

Blade-element characteristics are presented in terms of these turning and loss parameters in chapters VI and VII. In chapter VI, the data are correlated for blades in a two-dimensional low-speed cascade; in chapter VII, the data are given for blade elements of single-stage rotors and stators.

In the latter case, data are presented as functions of the radial position of the element. Through the use of this type of experimental data, obtained in the actual compressor environment, it is hoped that the important effects of three-dimensional flows will be accounted for. This concept is probably valid if the design under consideration does not deviate too greatly from the conditions under which the data were obtained.

Chord length and number of blades.—The aerodynamic design normally establishes the desired value of the cascade solidity. The actual selection of the chord length and number of blades then involves a consideration of a large number of factors, including blade-chord Reynolds number, weight, available length, blade root choking, blade root fastening, steady-state stresses, vibratory stresses, and manufacturing problems. Over and above many of these factors is the fact that the curvature of the hub and casing changes with chord length. This factor is discussed in the section REQUIRED IMPROVEMENTS IN ANALYSES.

OFF-DESIGN ANALYSIS

With the compressor flow channel and the blading established, the final phase of compressor design is the estimation of the performance of the compressor over a range of speeds and flows. Basically, the same relations and data are required for a thorough treatment of this problem. This blade-element type of solution, however, necessitates a rather complete knowledge of the blade-element flow, radial equilibrium, boundary-layer growth, blade-row interactions, radial mixing, and so forth. Unfortunately, this type of information is limited, and the prediction of compressor performance on the basis of the integration of blade-element characteristics is probably limited to operating points close to design. In particular, this technique always breaks down when a stalled condition occurs in the blade rows and may break down sooner owing to the lack of appropriate data concerning the behavior of K_{bk} and loading limits in the latter stages of a compressor.

Other simpler and more approximate approaches to the prediction of off-design performance have been developed. In particular, a stacking technique that utilizes certain generalized stage performance curves has been used effectively in the qualitative study of off-design operating problems. A discussion of those techniques which are available for prediction of off-design performance of multistage compressors is given in chapter X.

REQUIRED IMPROVEMENTS IN ANALYSES

As previously noted, there are three areas in which a better understanding of the flow is required in order to improve design techniques. One area encompasses the problem of estimating the radial distribution of flow in compressors of advanced design. The second area concerns the problem of treating the boundary layers at the hub and casing. The third area deals with the problem of estimating loading limits. Some of the work that has been done to clarify these problems is discussed in this section. While none of the work is far enough advanced to be included in a recommended design system, some phases can be useful for refining the design calculations. In other cases, the work has progressed only far enough to partially identify the real underlying problems.

RADIAL DISTRIBUTION OF FLOW

The problem of accurately estimating the radial distribution of the flow in compressors of advanced design may be appreciated from the following considerations. In order to obtain high flow capacity and short length, the first rotor of advanced multistage compressors may look more like those shown in figures 67 (a) and (b) than that shown in figure 67(c), which represents current practice. The higher pressure ratios in the new designs require a greater change in the annular area through the blade row, and the chord length will be as small as possible. In order to obtain high airflow capacity, the new designs will have lower hub-tip ratios and higher axial velocities.

Because of these differences in geometry, the curvature of the streamlines of figure 64 will be greater for the new designs. In flowing through

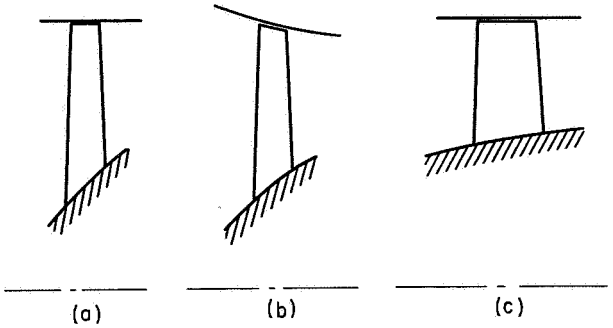

(a) Advanced design. (b) Advanced design. (c) Current design.

FIGURE 67.—Schematic drawing of several compressor-inlet stages.

the stream tubes, the air exerts a centrifugal force:

$$\mathcal{F}_c = C V_z^2$$

The large curvatures and high axial velocities make $\mathcal{F}_c$ have the same order of magnitude as

$$\mathcal{F}_R = \frac{V_\theta^2}{r}$$

which is the centrifugal force resulting from the rotation of the air about the compressor axis. (Eqs. (48a) and (48b) are essentially based on the premise that $\mathcal{F}_c$ is low enough in comparison with $\mathcal{F}_R$ to be ignored.) Since $\mathcal{F}_R$ has been found to be quite important (it is a dominant term in eq. (48a)), it follows that $\mathcal{F}_c$ must also be taken into account in the new designs.

An indication of the problems encountered by neglecting curvature is obtained from reference 57. An investigation was made of a single-stage compressor with an inlet hub-tip ratio of 0.4 and an inlet axial velocity that was intended to be constant along the radius. Tests showed, however, that the inlet axial velocity actually had the variation shown in figure 68. The ordinate in this figure is the ratio of the measured axial velocity to that at the mean radius. While the difference between the design and observed velocities did not seriously affect the average performance of this particular rotor, it did upset the flow in the neighborhood of the casing. Both the angle of attack and the blade loading can be critically upset by this order of error, and the multistaging effects become undesirable.

Some methods of including the effects of streamline curvature in the flow analysis have been developed for mixed-flow compressors (ref. 58). These methods are similar to those attributed to Flügel in reference 59 (vol. I). Substantial improvements in the design performance of these compressors immediately resulted from the use of this technique (refs. 60 and 61). It enabled the designer to eliminate adverse or impossible flow situations that would otherwise be unknown. The method has also been extended to turbines (ref. 62). As shown in references 63 to 65, techniques such as this had to be used when the curvature of the hub and the axial velocities were high. Otherwise, the measured velocity distribution differed so much from that designed that poor performance was inevitable. In other

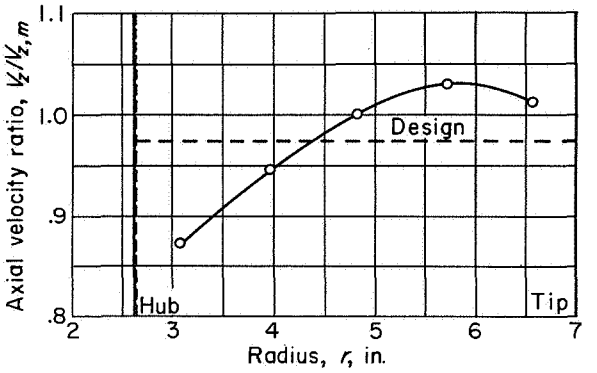

FIGURE 68.—Inlet axial velocity distribution for compressor of reference 57.

instances, premature choking within the blade row could be recognized and avoided in design only by using such an analysis.

The extent to which these methods can be used in axial-flow compressors is unknown. The small chord length compared with the blade spacing and the span makes some of the necessary assumptions rather tenuous. Perhaps some of the techniques reviewed in chapter XIV may have to be used. One critical problem is that of estimating the circumferentially averaged flow distribution through the blade row for flows at high Mach numbers. Some hope is offered by the approximate methods of reference 18. In particular, the method used for designing the Mach 1.35 rotor in reference 18 may be of value, crude though it is. More work along these lines is necessary.

HUB AND CASING BOUNDARY LAYERS

One of the greatest limitations of current design techniques is the fact that the flows in the hub and casing boundary layers cannot be correlated against anything definite. The importance of this problem has been the impetus for a considerable amount of research, both in the field of compressors and in the allied field of turbines. The results of preliminary studies suggest that the key to the problem may be an understanding of secondary flows. Some noteworthy advances in this understanding are described in the following paragraphs.

Secondary flows of blade boundary layer and wakes.—Detailed studies of the flow distribution in annular stators (ch. XV) reveal that some of the losses at the blade ends may be created or trans-

ported there by secondary flows. One type of secondary flow arises from the requirement of radial equilibrium (eq. (377), ch. XIV):

$$-\frac{1}{\rho}\frac{\partial p}{\partial r}=V_r\frac{\partial V_r}{\partial r}+V_\theta\frac{\partial V_r}{r\partial\theta}+V_z\frac{\partial V_r}{\partial z}-\frac{V_\theta^2}{r}-\mathcal{F}_{fr,r}$$

Within the boundary layers and wakes of a blade row, the pressures and pressure gradients are approximately the same as those in the adjacent potential-flow streams. In the type of stators normally used, the value of V_r is small in the main stream, and the values of V_θ and V_z are lower in the boundary layer and wakes than they are in the main stream. Unless $\mathcal{F}_{fr,r}$ is also large, the derivatives of V_r must increase (in the absolute sense), and V_r may thus assume moderately high values. When the boundary layers are thin, the value of $\mathcal{F}_{fr,r}$ throughout the entire boundary layer may be high enough to prevent large radial movements of the flow. When the boundary layers are thick, however, the frictional forces are relatively low. The boundary layer on the stator blades then flows from a region of high pressure to one of low pressure—that is, toward the hub. Since the value of $\mathcal{F}_{fr,r}$ is small in the wakes, the fluid in the wakes also moves toward the hub. Physical evidence of this flow is presented in chapter XV.

In rotors, on the other hand, the boundary layers and wakes travel radially outward. Since the tangential velocity of the blades is greater than that of the main stream, the value of V_θ in the boundary layer exceeds that of the main stream. The sign of the derivatives of V_r is thus reversed.

Existing evidence, such as that reviewed in chapter XV, suggests that a considerable portion of the losses near the casing of a rotor and near the hub of a stator may be attributed to losses created at some other point of the blade and transported to these regions. Besides just being there, the boundary layers at the blade ends may disturb the flow enough to induce flow separation and thereby create additional losses. Conversely, the movement of boundary layers away from the rotor hubs and stator tips may permit these regions to operate at conditions that would be impossible for their two-dimensional counterparts. This reasoning could partially explain why the cascade elements of rotor hubs and stator tips can sometimes operate at higher angles of attack than their two-dimensional counterparts.

Cross-channel flows and passage vortex formation.—Secondary flow also describes a movement of the boundary layer on the hub or casing. The flow is from the high-pressure side of one blade to the low-pressure side of the adjacent blade (fig. 69(a)). The phenomenon is fundamentally the same as that for the radial flows just described. The transverse pressure gradients in the main flow are again greater than those which the slowly moving boundary layers can support. Part of these gradients are resisted by friction and the rest tend to accelerate the flow to the low-pressure region. The experiments reviewed in chapter XV show that the boundary layers move across the passage and then roll up into a vortex (fig. 69(b)). It is conceivable that this movement of boundary layer may cause the flow near the suction surface of the blade ends to be more easily separated than the corresponding flow in ideal two-dimensional cascades.

Flow in blade end regions with clearance.—Other secondary flows result from the clearance between the blades and the adjacent wall. If the blades and the wall are stationary, air flows through the clearance space from the high- to the low-pressure side. It then rolls up as a vortex (fig. 70(a)). If the wall is moving with respect to the blades (such as an unshrouded rotor tip or stator hub), the blades may also scrape the boundary layer from the walls: a vortex similar to that of figure 70(b) is then formed near the pressure side of the blades.

Mixing of hub and casing boundary layers with main flow.—After the boundary-layer distributions are established behind a blade row (e.g., a rotor), the following blade row (in this case a stator) tends to mix them with the main flow. This behavior is clearly shown in reference 66. Figure 71(a), taken from this reference, shows the measuring stations and radial positions of measurements taken to determine the radial distribution of the efficiency of the rotor and the corresponding radial distribution of efficiency of rotor and stator. An example of the efficiency distribution is shown in figure 71(b). Because the rotor was severely loaded (large D), the rotor efficiency dropped rapidly in the vicinity of the outer radius. Measurements after the stator, however, indicated that the over-all efficiency at the outer radius was higher than that measured after the rotor. At the inner radii, the efficiency

691-564 O-65-8

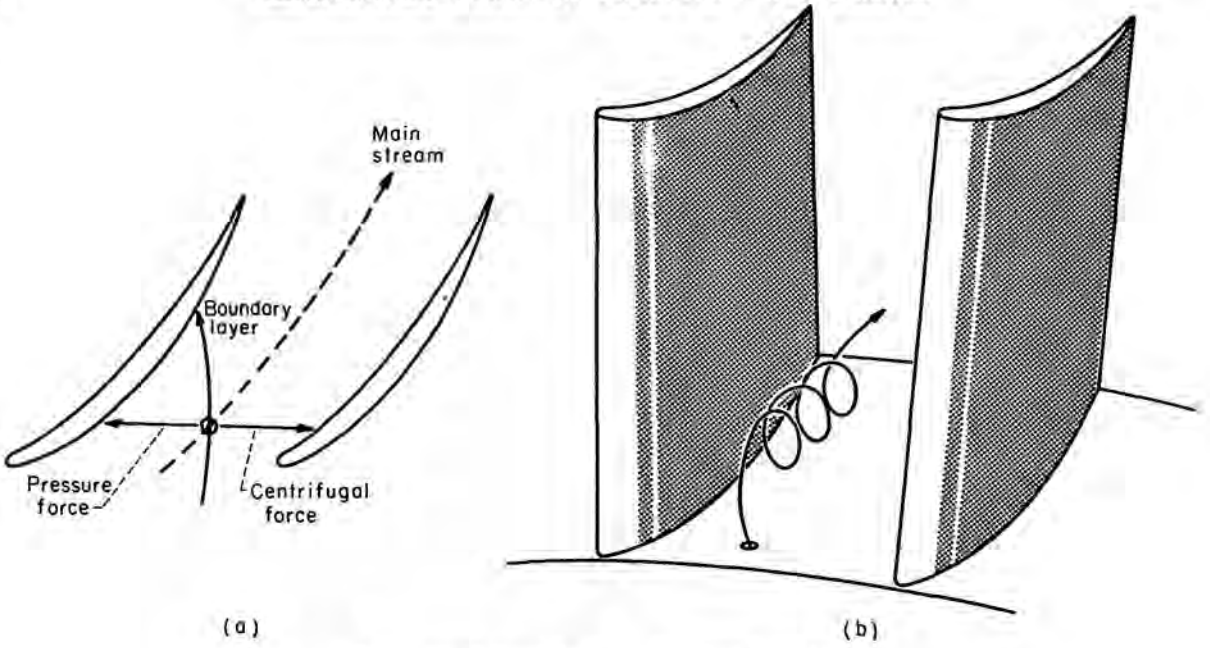

(a) Cross-channel flow. (b) Corner vortex.

FIGURE 69.—Secondary flow resulting from boundary layer on annulus walls.

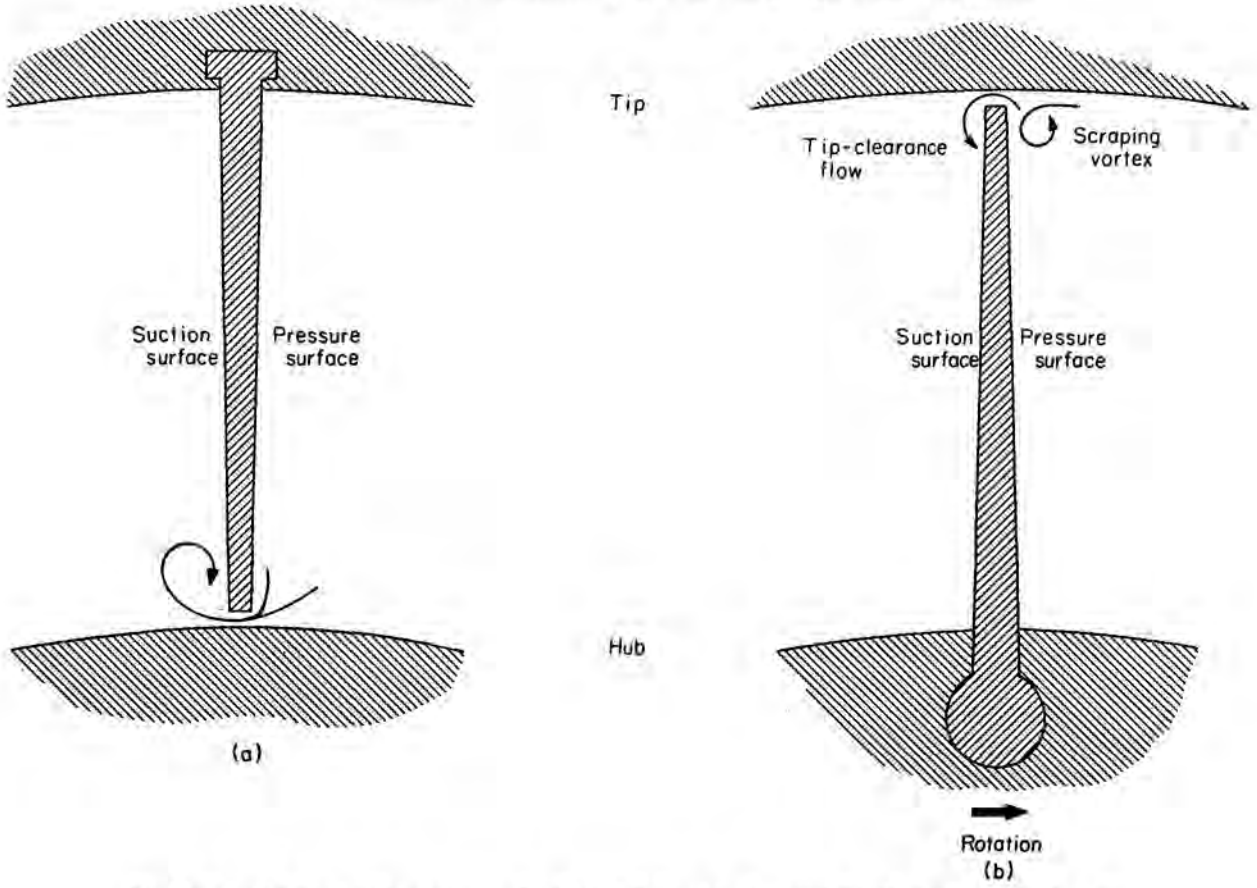

(a) No relative motion (stator). (b) Relative motion between blade and casing (rotor).

FIGURE 70.—Secondary flow in blade end-clearance region.

was much lower. The increase in efficiency at the outer radius can only be explained by a radially inward movement of the thick boundary layer as the flow passes through the stator. This movement also helps to explain the low efficiency of the air leaving the stator at the inner radii. Because of the different boundary-layer motions in a rotor and stator, a stator tends to mix up the boundary-layer distributions set up by a rotor, and vice versa. Although the energy added to the main flow by the hub and casing boundary layers usually does not noticeably increase the enthalpy of the main flow, these wayward movements of the boundary layer make the correlation of losses a difficult problem. Among other things, the losses transported by the boundary layer to a given radius must be separated from those created at that radius. The losses created must, in turn, be divided into those which are inherent at the radius in question and those which are induced or allayed by the inward or outward flux of the boundary layer. To date, no satisfactory technique has been found for separating these losses. At present, perhaps the best alternative is to continue to report the observed losses as a function of four quantities: the aerodynamic loading of the blade element, which involves relative Mach number and something akin to the diffusion factor; the geometry of the cascade element; the radial position of the element with respect to the hub and tip; and the distribution of flow ahead of the blade row.

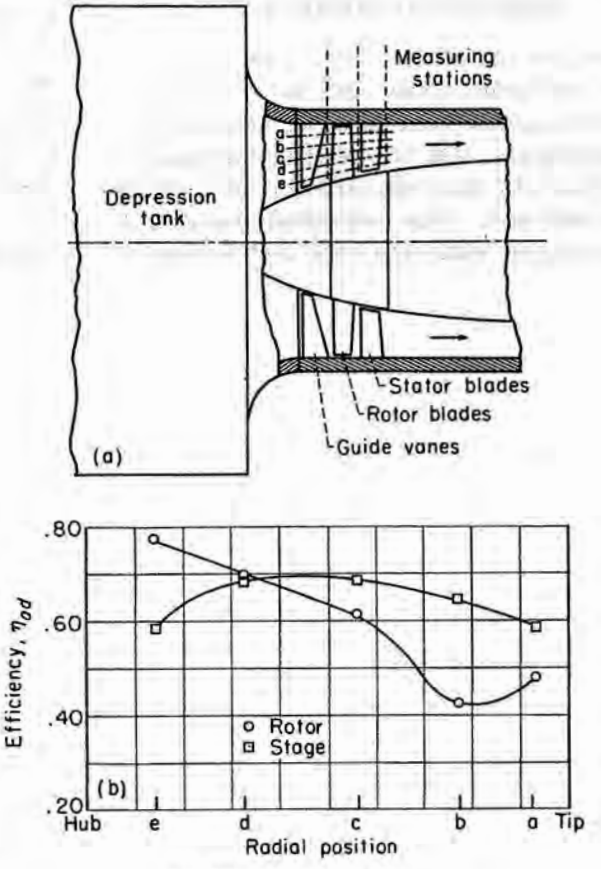

(a) Measuring stations.
(b) Efficiency variation.

FIGURE 71.—Measuring stations and radial variation of efficiency for compressor A of reference 66.

LOADING LIMITS

The analyses presented in references 9 and 38 suggest that the loading limits of a two-dimensional cascade can be quite ably described. Experience in actual blade rows, however, indicates that the loading limit of a cascade element depends upon the location of the element. Cascade elements near the casing of a rotor seem to stall at lower loadings than those near the center of the span or near the hub. There are also some indications that the hub regions of a stator are critical. Moreover, the condition of the hub and casing boundary layers is suspected to play an important role in determining the loading limit of the nearby cascade elements.

Because of the importance of the problem of loading limits, a large amount of work is being devoted to it. One of the questions to be answered is whether or not the ideas expressed by equation (55) are the important ones. Another important question is concerned with estimating the various terms of this equation. Still a third problem is the determination of the way the inlet flow conditions influence the loading parameter.

Improving the understanding of these loading limits is another incentive for continued effort in the study of ideal flows and the study of boundary layers. Reasonably simple yet accurate methods of estimating the critical velocities about various cascade elements are required. The interrelation between boundary-layer behavior and the pressure gradients created by the main flow must be better understood. Intensive efforts, both theoretical and experimental, will probably be required to pinpoint the answers within a tolerable range.

CONCLUDING REMARKS

A general picture of the flow characteristics of axial-flow compressors has been developed, indicating those features that must be considered in the design process. On the basis of this qualitative description of flow, the structure of a design system is outlined. The individual elements of the design system, including basic techniques and equations, are summarized. Also noted are some of the important gaps in knowledge, where art must be substituted for science. This information provides a design system and summarizes much of the work presented in the succeeding chapters. This general treatment is expanded in these chapters to provide specific design data that describe the techniques of application in detail.

CHAPTER IV

POTENTIAL FLOW IN TWO-DIMENSIONAL CASCADES

By WILLIAM H. ROUDEBUSH

The complexity of the flow of a fluid through a rotating blade row makes a direct theoretical attack on the general problem very difficult. However, the flow through axial-flow compressors, at least near the mean radius, is often sufficiently close to a mathematically two-dimensional flow that valuable results can be achieved by using two-dimensional theory.

An extensive review is presented of the literature concerning plane potential flow in cascades. No method of determining the flow is preferable under all conditions. The nature of the individual problem and the computing equipment available will dictate the method to be used. Some of the available techniques for solving the two basic problems, design and analysis, are evaluated: and several of the methods that have been used satisfactorily are presented in considerable detail.

The potential-flow cascade theories to be discussed are indicated by author in the chart on page 102, which is arranged with regard to general regions of applicability. The divisions are not absolute and can serve only as a general guide. The asterisks denote those authors whose methods are presented in detail in this chapter.

INTRODUCTION

Compressor design techniques should always reflect the current basic knowledge of airflow. Time limitations may prevent a designer from using refined theoretical methods in individual design problems, but the simplifying assumptions made should be based on a sound theory. Unfortunately, the flow through a rotating blade row is very complex. The three-dimensional potential-flow equations, representing a highly idealized flow and a substantial simplification of the true problem, still cannot be solved satisfactorily. The added difficulties of boundary-layer buildup and displacement, separation, tip-clearance effects, compressibility effects, unsteady flow, and local regions of supersonic flow make compressor design one of the very difficult practical engineering problems.

Since a complete solution is not currently obtainable, another approach must be used. Historically, a problem of this nature is treated by making simplifying assumptions. Chapter III indicates that flow through an axial-flow compressor can be represented in many important instances by a combination of essentially two-dimensional solutions. Generally speaking, one of these solutions is from hub to shroud and the other is from blade to blade.

Within the limitations discussed in chapter III, the change in radius of a particle passing through a compressor blade row can be assumed small, and the two-dimensional blade-to-blade flow surface is taken as cylindrical. This cylindrical surface can be developed into an infinite plane cascade. The theoretical determination of the potential flow about such a cascade is treated in the present paper. Some of the methods considered are not restricted to plane flows, as will be indicated in the discussion.

The exact theoretical treatment of two-dimensional-cascade flow is not a simple problem, and past investigators have relied heavily on experimental cascades to obtain basic flow information. Early experimental cascades, however, did not successfully achieve two-dimensional flow. The data obtained in different cascades exhibited a considerable lack of uniformity, primarily as a result of using blades of small aspect ratio in different tunnel geometries without adequate boundary-layer bleed. It was difficult to separate the essential characteristics of the two-dimensional flow about a given blade system from the characteristics introduced into the flow by the individuality of the particular cascade operation. As a result, comparison of early experimental and theoretical results was not always practicable.

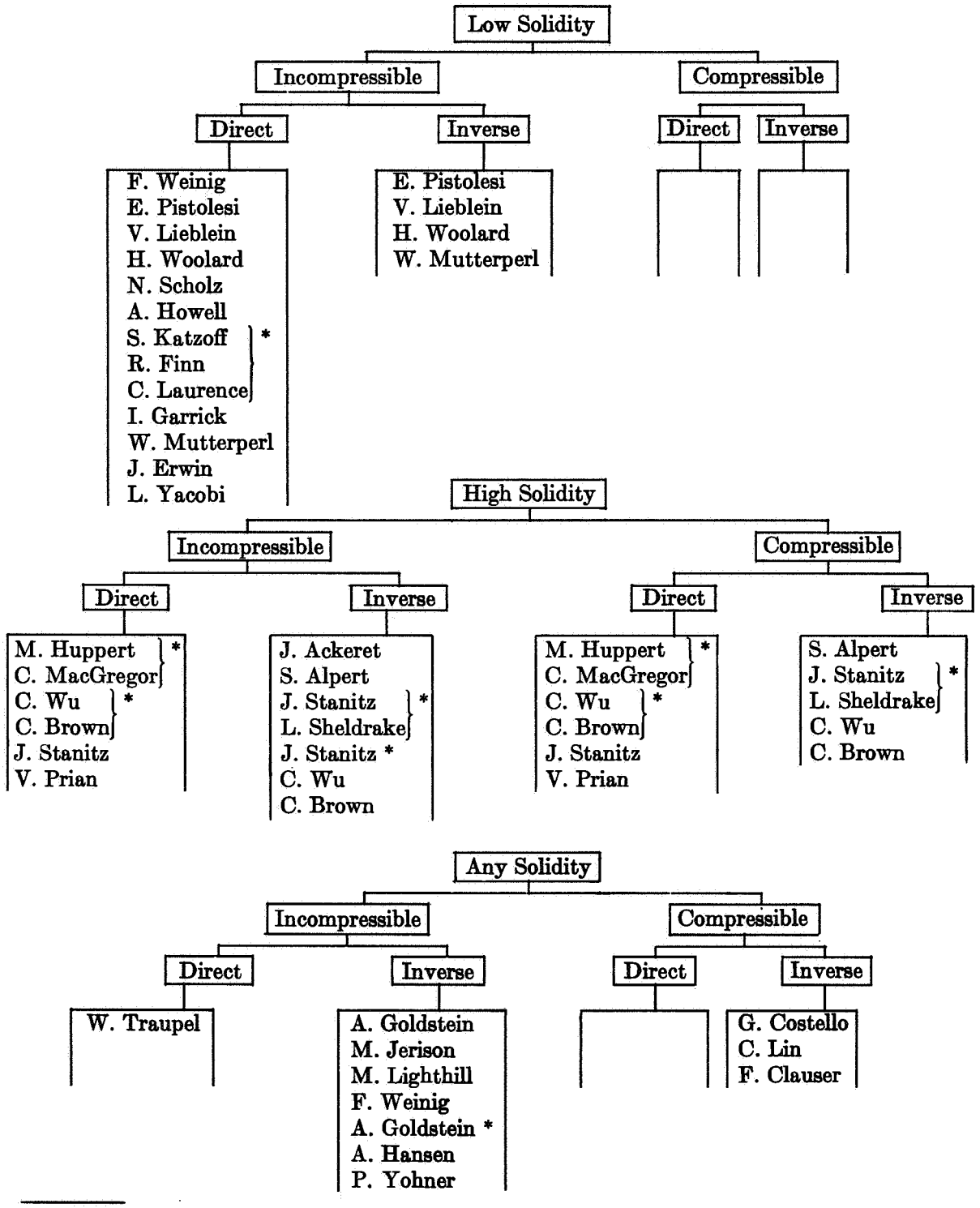

*Methods presented in detail in this chapter.

This situation has been corrected in recent cascades by the development of successful boundary-layer controls. A close approximation of two-dimensionality has been obtained, and accurate data are now available (see ch. VI). Therefore, it has become possible and highly desirable to interpret experimental cascade results in the light of theoretical analyses. In the future development of axial-flow compressors, more accurate predictions of turning angles and loss characteristics will probably be required over a wider range of operating conditions. A careful coordination of theory and experimental data may make possible accurate extrapolation of present data and should also provide a guide to future experimentation. Research on the off-design problems, in particular, can profitably employ this coordinated approach.

The flow of a viscous fluid through a cascade cannot yet be determined in its general form. However, since the effects of the viscosity are concentrated, in many cases, at the blade surfaces, the problem can be treated by boundary-layer theory. In this event the flow outside a narrow region at the boundaries is practically irrotational. Potential-flow calculations often provide reasonable pressure distributions, although they completely ignore viscosity. At times when thick boundary layers or separation exists or when knowledge of loss is desired, the potential-flow solution does not alone suffice. Even then, however, the pressure distribution obtained from the potential-flow calculation is indispensable for boundary-layer computation by existing methods. For these reasons the two-dimensional potential-flow solutions provide what is probably the most important single theoretical tool for analyzing the flow through an axial-flow compressor.

A survey of the large body of existing plane potential-flow theory may help to increase its present application. Although the theory has attained a high degree of completeness, the time involved in obtaining exact solutions is considerable. A reduction in time may be anticipated if the methods are used and understood and if attempts are made to adapt them to modern computing equipment in the most practical manner. There are also simplified approximate solutions that save time and may be quite worthwhile. Often the range of application of such methods is quite restricted; and accurate results in certain regions, such as the leading edge, are sometimes unobtainable. Subsequent examination may reveal, however, that some of these approximations are substantially valid in the region of interest to designers of axial-flow compressors.

An extensive review of the literature on the potential flow about cascades is presented herein. Many of the methods are evaluated within the bounds of limited available information on actual use. No method is universally applicable. The individual nature of a particular problem and the computing equipment available are large factors in determining the method of solution to be used. Some of the methods that have been used successfully are presented in detail to illustrate the mathematical techniques and to indicate the nature of the actual computation.

SYMBOLS

The following symbols are used in this chapter:

a	speed of sound
$\hat{b}$	dimensionless blade thickness
$\mathcal{C}$	curvature
c	chord length
c_p	specific heat at constant pressure
c^*	characteristic length of thin blade for small-perturbation theory
D	height of water surface
E	electric-field strength
$\pm e^K$	locations of singularities in circle plane
g	acceleration due to gravity, 32.17 ft/sec^2
h	mapping function defined by eqs. (72) to (75)
h_1	real part of h
h_2	imaginary part of h
h^*	mapping function corrected to satisfy closure conditions
I	electric-current density
l	distance along streamline
l_{le}	leading-edge stagnation point
$l_{te,P}$	trailing edge approached from pressure surface
$l_{te,s}$	trailing edge approached from suction surface
l^*	function relating corrected distance about blade perimeter to circle central angle
M	Mach number
m	plate thickness
P	total or stagnation pressure
p	static or stream pressure

q	velocity in compressible medium
$\bar{q}$	vector velocity in compressible medium
$\tilde{q}$	disturbance velocity in small-perturbation theory
R	electrical resistance
r	radius
s	blade spacing
$\hat{s}$	dimensionless blade spacing
T	total or stagnation temperature
t	static or stream temperature
v	velocity in incompressible medium
$\bar{v}$	vector velocity in incompressible medium
$\hat{v}$	velocity in cascade plane expressed as function of circle plane coordinates
$\hat{v}^*$	velocity in cascade plane expressed as function of circle plane coordinates corrected for closure condition
$\tilde{v}$	disturbance velocity in small-perturbation theory
W	complex potential function
w	complex velocity
Δw	rate of mass flow
$\hat{w}$	complex velocity in cascade plane expressed as function of circle-plane coordinates
x	abscissa in cascade plane
$\bar{x}$	axial length of region of validity of solutions by ref. 136
$\hat{x}$	dimensionless distance along x-axis
y	ordinate in cascade plane
$\hat{y}$	dimensionless distance along y-axis
z	complex variable in cascade plane
β	angle between air velocity and x-axis
Γ	circulation
γ	ratio of specific heats
γ°	blade-chord angle, angle between blade chord and x-axis (fig. 72)
δ_x	increment in x-direction
δ_y	increment in y-direction
ζ	complex variable in plane of mapping circle
η	imaginary part of ζ
Λ	constant in affine transformation (117)
μ	angle made by tangent to blade profile and x-axis
$\hat{\nu}$	thickness ratio, $\hat{b}/\hat{s}$
ξ	real part of ζ
ρ	density
σ	solidity, ratio of chord to spacing
Φ	potential function
$\acute{\Phi}$	electric potential function
$\tilde{\Phi}$	disturbance potential function
φ	central angle in mapping circle plane
φ_{le}	angle corresponding to leading-edge stagnation point
$\varphi_{te,P}$	angle corresponding to trailing edge approached from pressure surface
$\varphi_{te,s}$	angle corresponding to trailing edge approached from suction surface
Ψ	stream function
$\hat{\Psi}$	electric-current function
ψ	pressure coefficient
Ω	specific resistance

Subscripts:

a	stagnation conditions
add	additional
add_s	additional due to sources
add_v	additional due to vortices
av	arithmetic average of values at suction and pressure surfaces
C	compressible
$\mathcal{C}$	curvature
c	compensating
c_s	compensating due to sources
c_v	compensating due to vortices
cr	critical
d	disturbance
d_s	disturbance due to sources
d_v	disturbance due to vortices
inc	incompressible
l	arbitrary position along potential line
le	leading edge
m	mean of upstream and downstream conditions
max	maximum
o	isolated airfoil
P	pressure surface
r	radial direction
s	suction surface
te	trailing edge
x	direction of x-axis
y	direction of y-axis
z	in cascade plane
Γ	circulatory
ζ	in mapping circle plane
θ	tangential direction
Σ	total
1	upstream at infinity
2	downstream at infinity

GENERAL CONSIDERATIONS

Potential-flow theory, as it pertains to two-dimensional cascades of blades, is concerned with two basic problems, referred to as "direct" and "inverse." In the direct (or analysis) problem, the geometry of a cascade and a characteristic velocity (usually $\bar{v}_1$, the velocity vector far upstream, or $\bar{v}_m$, the mean free-stream velocity vector; see fig. 72) are given. A solution yields the velocity distribution in the region of the cascade. For the inverse (or design) problem, the velocity distribution on the surface of a cascade blade is given along with the vector velocities far upstream and far downstream. A solution, if one exists, gives the geometry (blade shape, chord angle, spacing) of the cascade.

In solving either the direct or inverse problem, an important distinction exists in the underlying approach. From figure 72 it can be seen that the flow about the cascade is given from a knowledge of the flow between streamlines bb and dd as a result of the periodicity of the flow pattern in the direction of the y-axis. Similarly, a knowledge of the flow field between streamlines aa and cc constitutes a complete solution. When the cascade flow field is considered to be made up of sections of the type bbdd, the cascade is pictured as an infinite array of isolated bodies. On the other hand, when sections of the type aacc are considered, the cascade appears as an infinite array of adjacent channels.

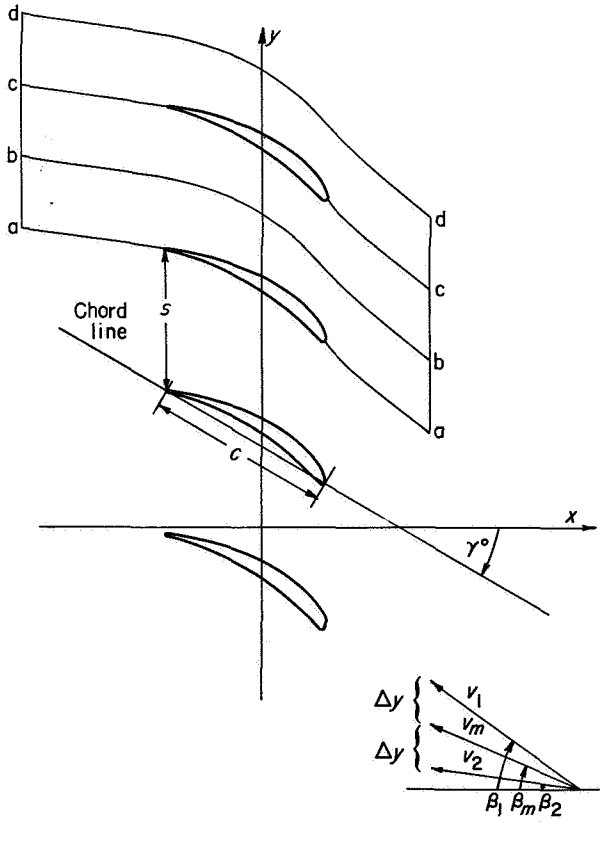

FIGURE 72.—Two-dimensional cascade.

As a result of these two basic points of view, different mathematical techniques are employed in the two cases. Either point of view is theoretically applicable for a given cascade. However, the mathematical techniques employed in the "isolated-body" approach become clumsy and tedious as the effects of the neighboring blades on each other become large. Similarly, the "channel-flow" approach works well only when the neighboring cascade blades exert an appreciable guidance on the fluid. Hence, the cascade solidity σ (ratio of chord length to spacing) determines the point of view that should be adopted for a given cascade. The solutions considered are divided into "low-solidity" and "high-solidity" methods, where each of these distinctions is subdivided into its relation to the direct and inverse problems. It must be noted that the classification by solidity is not rigid, but may depend on such factors as cascade stagger angle, experience with the technique, and the computational equipment available.

Although few of the methods of solution have been widely used, in most instances some solutions have been obtained by the author of the method. In some cases, experimental cascades have been investigated and compared with the theoretical results. Some authors have compared their solutions with other theoretically obtained solutions.

While the ultimate objective of any theoretical method is to design or analyze an actual cascade, there exists a practical difficulty in appraising a theoretical method by comparison with an actual cascade. Such an evaluation is indecisive, since the fluid has been divested of at least some of its natural properties by the mathematician. Therefore, the most reasonable test of a given theoretical method is comparison with an exact known theoretical solution. Such exact solutions do exist comparable to the Joukowski airfoils of isolated-airfoil theory. If this comparison is good, the new method is satisfying its function by predicting the flow of an idealized fluid. Determining the

flow relations that actually exist about the experimental counterpart of a theoretically determined cascade is an entirely different problem, which has not been adequately investigated.

In this chapter an attempt is made to discuss and, to some extent, to evaluate many of the theoretical methods available to the designer. Experimental data are not used for purposes of evaluation for the reasons given in the preceding paragraph. Three design methods (two for high solidity and one for low solidity) and three analysis methods (two for high and one for low solidity) are presented in detail.

LOW-SOLIDITY CASCADES

Almost all the available work on low-solidity cascades has been done on incompressible flow because of the intractability of the nonlinear equations involved in the compressible-flow problem. The assumption of constant density is justifiable for a considerable range of low Mach number flows. When sonic speeds are approached in regions of the flow field, the effects of density variation are, of course, pronounced. If shock waves occur, qualitative as well as quantitative errors may be introduced. Therefore, some methods of treating compressible flows and correcting incompressible-flow solutions for the effects of compressibility are discussed following the sections concerning the direct and inverse problems.

THE DIRECT PROBLEM

The pattern for solution of the direct problem has developed along two distinct lines. The first approach is to find a conformal mapping of the cascade onto a simple geometric shape, such as a straight line or a circle. The flow about the simple shape is readily determined, and the mapping function is applied to yield the desired flow about the original body. This method of solution has been of considerable mathematical interest for many years.

The second approach to the problem is based on the following fact: The effect of a solid body on the fluid surrounding it can be closely approximated by replacing the body with a carefully chosen system of flow singularities (sources, sinks, vortices). The characteristics of these singularities are well-known, and their effect on the uniform flow can be obtained.

By way of introduction to the cascade problem, the history of the application of these two approaches to the isolated-airfoil problem is discussed briefly in the following section.

Isolated airfoils.—Early significant results concerning the flow of fluid about an isolated airfoil were achieved by Kutta and Joukowski. The theory was extended and improved by von Kármán, Trefftz, von Mises, and many others (see ref. 67). This is an exact theory of special airfoil shapes that are obtained from a circle by simple conformal transformations. The airfoils thus obtained are not superior aerodynamically to many others, and a method to analyze the flow about arbitrary wing profiles was considered necessary.

A significant contribution to the problem was made by Munk (ref. 68), who presented a technique for determining the over-all characteristics of the flow about a thin, slightly cambered airfoil of otherwise arbitrary shape. The mapping $z=\zeta+1/\zeta$ is used to transform the thin airfoil (actually the camber line) into a near-circle in the ζ-plane. The near-circle is transformed into an exact circle resulting in a simple integral equation for determining the stagnation point of the flow about the exact circle. When the location of the stagnation point is known, the circulation (and consequently the lift) can be determined about the circle and hence about the airfoil. The technique is improved and utilized by Glauert in reference 69, where several comparisons are made with experimental data.

In 1923, Birnbaum (ref. 70) applied a method of singularities to the same problem. The thin airfoil is replaced by a continuous distribution of vortices along the mean camber line. This method, which is applicable to the inverse as well as the direct problem, is set forth in detail by Glauert in his text on airfoil theory (ref. 71). Glauert uses the trigonometric series

$$2v\left(A_0 \cot\frac{\theta}{2}+\sum_{n=1}^{\infty} A_n \sin n\theta\right)$$

for the distribution of vorticity. The abscissa x of the airfoil is related to θ by

$$x=\frac{c}{2}(1-\cos\theta)$$

The constants A_n are determined by the shape of the camber line. The first term of the expression

for the vorticity distribution represents the distribution on a straight-line airfoil, and the sine terms compensate for the curvature of the thin airfoil. This expression has been used in cascade work as well as in isolated-airfoil theory.

In later work along these lines, source and sink distributions were added by Allen (ref. 72) to approximate the effect of airfoil thickness. However, since the solution still applied only to thin airfoils of small camber, a more general solution was desired.

In 1931, Theodorsen (ref. 73) and Theodorsen and Garrick (ref. 74) produced an exact solution to the direct problem of two-dimensional, incompressible flow about an airfoil of arbitrary shape. A Joukowski transformation is used to map the airfoil into a near-circle. The mapping of the near-circle into an exact circle then leads to an integral equation, solved by an iteration process. (The numerical evaluation of the cotangent integral in the Theodorsen method is considered in refs. 75 and 76.) This general solution had considerable significance both in the impetus it gave to the work on the airfoil problem and in its direct application to later work on cascades of airfoils. A consideration of conditions sufficient to assure convergence of the iteration process of Theodorsen appears in reference 77.

Cascades.—The development of the theory of flow about cascades of blades is similar to the development of the isolated-airfoil theory. Particular cascades, corresponding to the so-called "theoretical airfoils" of the isolated-airfoil theory, were developed (refs. 78 and 79). Solutions were also found for cascades of thin, slightly cambered, but otherwise arbitrary, blades. Finally, solutions for general blade shapes were obtained of a more or less exact nature.

In 1935, a comprehensive text on the theory of turbomachines was presented by Weinig (ref. 80), in which was introduced and demonstrated the concept that every cascade has a corresponding straight-line cascade that is equivalent insofar as it produces the same turning and has the same circulation. Methods for approximately determining the equivalent-line cascade are given, and the foundations are laid for exact solutions to the general cascade problem. The theory of equivalent-line cascades will not be discussed herein, since it does not give information about local conditions on the blade surfaces. The more general theory will be mentioned later in its connection with other methods that have been developed from it.

In 1937, Pistolesi (ref. 81) extended the work of Birnbaum and Glauert to cascades of thin blades. This work is significant theoretically, but the complexity in the case of a staggered cascade makes computation difficult. In addition, the inherent limitation to thin, lightly loaded blades is an undesirable restriction in present-day design. This technique has been extended by V. Lieblein (ref. 82) to include the effect of thickness distribution. The approximations made in this analysis become increasingly inexact with higher camber and greater thickness. A closer examination of such approximate methods may indicate that they are reasonably valid in the ordinary range of compressor blade shapes. If this should be the case, such methods will become important because of the savings in time realized over the more exact methods.

An approximate theory of practical interest has been developed by Erwin and Yacobi (ref. 83), utilizing the principle of superposition common in isolated-airfoil theories. The local velocity on the cascade blade surface is taken to be the sum of the average velocity in the passage and incremental velocities due to thickness, camber, and angle of attack. The average velocity is determined from area change through the cascade, and the incremental velocities are related to corresponding incremental velocities on an isolated airfoil of the same shape. The relation is determined empirically in the report, but could probably be determined theoretically as well. This method provides solutions to the direct cascade problem quite rapidly when the characteristics of the corresponding isolated airfoil are known.

Other approximate methods, using a technique employing singularities, have been presented by Woolard (ref. 84) and Scholz (ref. 85). Results obtained in reference 84 show fair agreement with results obtained by the more exact method of reference 86 for NACA 4412 airfoils in a cascade of nearly unit solidity over a range of angle of attack.

In 1941, Howell (ref. 87) produced an exact solution to the general problem, employing the method of conformal mapping. A cascade, located in the z-plane, is transformed into a distorted airfoil n the z_1-plane by the equation

$z_1 = \tanh z$. The distorted airfoil is then transformed into a near-circle by two successive Joukowski transformations. Finally, the near-circle is transformed into an exact circle by using conjugate Fourier series. Since four transformations are involved, the work is necessarily lengthy. However, a detailed computational layout and some suggestions for decreasing the labor involved are available in reference 88, and a number of theoretical solutions are obtained for a cascade with a solidity slightly greater than 1.0. In reference 87 theoretical results are compared with experimental data for a cascade with a solidity of 0.85.

Howell's method appears to give reasonable and consistent results for solidities as high as 1.0. Higher solidities could be used, but the shape obtained in the first transformation would be distorted and the amount of labor would be increased. It is estimated in reference 88 that a complete solution for several angles of attack can be made in 3 weeks. If only the deviation angle is required, the time is reduced. Some further simplifications of the method are given in reference 89.

In 1944, Garrick (ref. 90) presented a solution using the well-known mapping (refs. 91 and 92) of a straight-line cascade into a circle. By means of this transformation, a cascade is mapped into a near-circle, and finally the near-circle is mapped into an exact circle. A computational procedure is given, and an example is worked out. As in the case of Howell's solution, the computations are lengthy.

A different approach was presented by Traupel (ref. 93), who mapped the flow field of the cascade onto the interior of an internally concave closed curve. A minimum of four transformations is generally required, and the computer must exercise a certain amount of skill and judgment in the selection of some of the transformations. Using Green's second formula, the author arrived at an integral equation that he solved by an iterative procedure. No comparison with other results is made in the report, although an example is computed. The method is mentioned also in connection with an experimental investigation on internal-combustion prime movers in reference 94.

Mutterperl (refs. 95 and 96) mapped the arbitrary cascade directly onto a straight-line cascade. Although the method does reduce computational time, some difficulty has been encountered at the Lewis laboratory in obtaining accurate numerical results. It is difficult to determine when the results have converged to a valid solution. This method was used in an investigation by Resnick and Green (ref. 97), but the validity of the pressure distributions obtained cannot be determined.

An exact solution, using a continuous distribution of vortices on the perimeter of a cascade of blades, was developed by Katzoff, Finn, and Laurence (ref. 86). With the velocity distribution of an arbitrary isolated blade known, the velocity distribution about the blade in cascade can be accurately determined with reasonably little computation, and can be approximated in even less time. Experience enables the user to compare the greater accuracy obtainable at any step of the solution with the attendant cost in computational time. Comparison of a solution by this method with one for a cascade about which the ideal flow is known exactly shows good agreement (fig. 73).

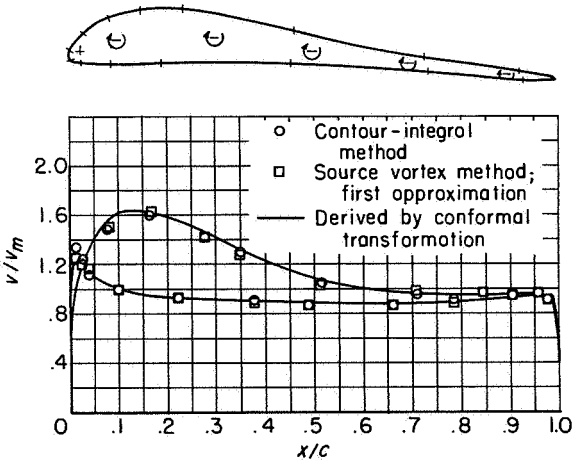

FIGURE 73.—Comparison of velocity distribution for blade shown, computed by methods of reference 86, with exact solution known from actual conformal-mapping function.

In reference 98 a comparison is made of experimental results and theoretical results obtained by the Katzoff, Finn, and Laurence method. As an example of the magnitude of agreement between experiment and theory when good two-dimensional-cascade data are available, a typical figure from reference 98 is presented (see fig. 74). The disagreement is due largely to the use of the Kutta

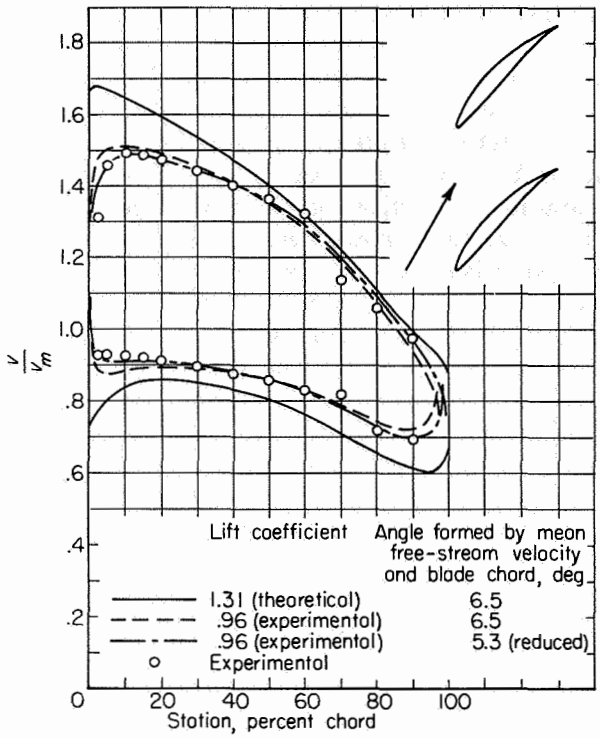

FIGURE 74.—Comparison of experimental and theoretical velocity distribution on airfoil in cascade. Airfoil, NACA 65–(12)10; inlet-air angle, 60°; blade-chord angle, 45.9°; solidity, 1.0 (ref. 98).

condition for establishing the branch point of the flow, as indicated in the figure by the results obtained when the experimental lift coefficient is used instead to determine circulation. Finally, very good agreement is obtained by reducing the angle of attack slightly. Although this reduction in angle was made arbitrarily to obtain good agreement, it can be justified qualitatively on the basis of boundary-layer formation on the blade surface.

The method of Katzoff, Finn, and Laurence (ref. 86) is developed in the following section in greater detail as an illustration of an adequate method for solving the direct problem for a low- or medium-solidity cascade. (Solutions are presented in the literature for solidities up to 1.5.) The mathematics involved is not complicated. This method is advantageous in that it can be used as an approximate method with any desired degree of accuracy.

Solution of low-solidity direct problem.—In the direct problem, the geometry of the cascade (blade shape, cascade chord angle $\gamma°$, and solidity $\sigma=c/s$) and the mean free-stream velocity v_m (i.e., vector average of the velocities far upstream and far downstream of the cascade) are given (see fig. 72). The problem is to find a flow with mean free-stream velocity $\bar{v}_m$, having the blade profiles as partial streamlines and leaving the blades at a fixed point. In the case of a sharp trailing edge, the Kutta condition places this point at the trailing edge. If the trailing edge is rounded, the position of the trailing-edge stagnation point must be prescribed from an empirical knowledge of this type of flow.

The cascade will be considered to consist of a central blade (the one containing the origin) and a lattice of external, or interference, blades. The solution obtained will be a superposition of flows, derived by first treating the central blade as an isolated body in the mean free stream of the cascade and then finding the interference flow due to the presence of the external blades. Such a superposition of solutions is possible because of the linear and homogeneous character of the equations governing a two-dimensional, irrotational, and incompressible flow.

The total complex potential function $W_\Sigma=\Phi_\Sigma + i\Psi\hat{\Sigma}$ will be composed of the following parts:

(1) The function $W_o=\Phi_o+i\Psi_o$ of the flow about the isolated central blade oriented as in the cascade with respect to the mean free-stream velocity. Since the blade profile forms part of a streamline, Ψ_o will be zero on the blade.

(2) The interference flow function $W_d=\Phi_d+i\Psi_d$ representing a distribution of isolated singularities along the mean camber lines (or a continuous distribution of vortices along the profiles) of the infinitely many external blades. The central-blade profile will not be a streamline in this flow.

(3) The function $W_c=\Phi_c+i\Psi_c$ of the compensating flow necessary to make the central-blade profile a streamline in the disturbance flow; $\Psi_c=-\Psi_d$ on the blade. This flow function is analytic exterior to the central blade.

(4) The function $W_\Gamma=\Phi_\Gamma+i\Psi_\Gamma$ of the circulatory flow, which causes the compensating flow to leave the blade at the trailing edge. Since the blade profile forms part of a streamline, $\Psi_\Gamma=0$ on the blade in this flow.

The problem of finding the flow about an isolated profile in a free stream is well-known and will be considered as already having been solved

for this application. An extensive treatment can be found in references 73 and 74. The potential distribution, as well as the mapping function of the central blade onto a circle (derived from the isolated-profile computation), is assumed in what follows. The presentation given herein of the cascade solution is concerned only with finding the disturbance effects of the external blades on the central blade.

For purposes of demonstrating the technique, the assumption is made that the final velocity distribution about the cascade is already known. The applicability of an iteration process will be indicated later. Using the known velocity distribution and blade shape, the first step is to represent the external blades by singularities arranged on the mean camber lines at intervals measured along the chords. A good approximation can usually be obtained with two sources, three sinks, and five vortices. A guide to the location of these singularities is given later. To evaluate the effect on the central blade of these infinite rows of singularities, the chart (first appearing in ref. 99) shown in figure 75 is used. This chart represents an infinite row of vortices (or sources) of unit strength placed a unit distance apart with the central vortex omitted. A drawing of the cascade blade is now prepared, with chord length chosen to give the proper solidity when used with the graph. To find the effect on the central blade of an infinite row of vortices, located at a point x on each exterior blade, the drawing of the central blade is placed with the point x on the origin of the graph and with the blade properly oriented with respect to the y-axis. The values of the stream function and potential function can be read from the graph at selected points on the central-blade profile. The values indicated on the graph must be multiplied by the vortex strength at the position being considered. If the singularity involved is a source, the lines marked Ψ become $-\Phi$ and those marked Φ become Ψ. A sink is regarded as a negative source. In this manner, the effect of each infinite row of singularities is found at certain prescribed points on the central blade. Adding all these contributions gives Φ_d and Ψ_d.

Although the use of isolated singularities distributed along the mean camber line is clearly an approximation, the results obtained in this manner are usually so accurate that no other technique is required. In instances where some doubt may exist concerning the accuracy of results thus obtained, a somewhat different approach is available for finding the disturbance flow. It has been shown (ref. 100) that a cascade of blades in a uniform stream can be represented exactly by a continuous distribution of vortices on the perimeter of each blade, where the vortex strength per unit length at each point is equal to the velocity of the flow about the blade at that point. With this result in view, the blade model is placed with a point of its contour on the origin, and the effects are computed as in the preceding discussion. At each point the vortex strength is $v\ dl$, where dl is an increment of the airfoil arc length. The velocity is taken as positive on the suction surface and negative on the pressure surface; that is, the velocity is taken as positive in the positively oriented arc-length direction (see fig. 76).

The disturbance flow function is then given at a point $z_0=x_0+iy_0$ on the central blade by

$$\left.\begin{aligned}\Phi_d(z_0)&=\oint \Phi\cdot v(z)\ dl\\ \Psi_d(z_0)&=\oint \Psi\cdot v(z)\ dl\end{aligned}\right\} \tag{60}$$

where Φ and Ψ are the values read at z_0 from the chart (note that these values are for vortices of unit strength and unit spacing) when the origin is at z on the central blade. The integration is performed over the blade profile. It is convenient to rewrite equations (60) as

$$\left.\begin{aligned}\Phi_d(z_0)&=\oint \Phi\cdot d\Phi_x(z)\\ \Psi_d(z_0)&=\oint \Psi\cdot d\Phi_x(z)\end{aligned}\right\} \tag{61}$$

From equations (61), Φ_d and Ψ_d are readily evaluated by plotting Φ and Ψ against Φ_x and integrating numerically or with a planimeter.

A disturbance flow has now been calculated yielding a Ψ_d and Φ_d distribution on the central-blade profile. To make this profile a streamline in the disturbance flow, a compensating flow W_c is now added such that $\Psi_c=-\Psi_d$ on the blade profile. It is necessary to compute the potential distribution Φ_c of which Ψ_c is the harmonic conjugate. This problem is greatly simplified, since the mapping of the central blade onto a circle is known

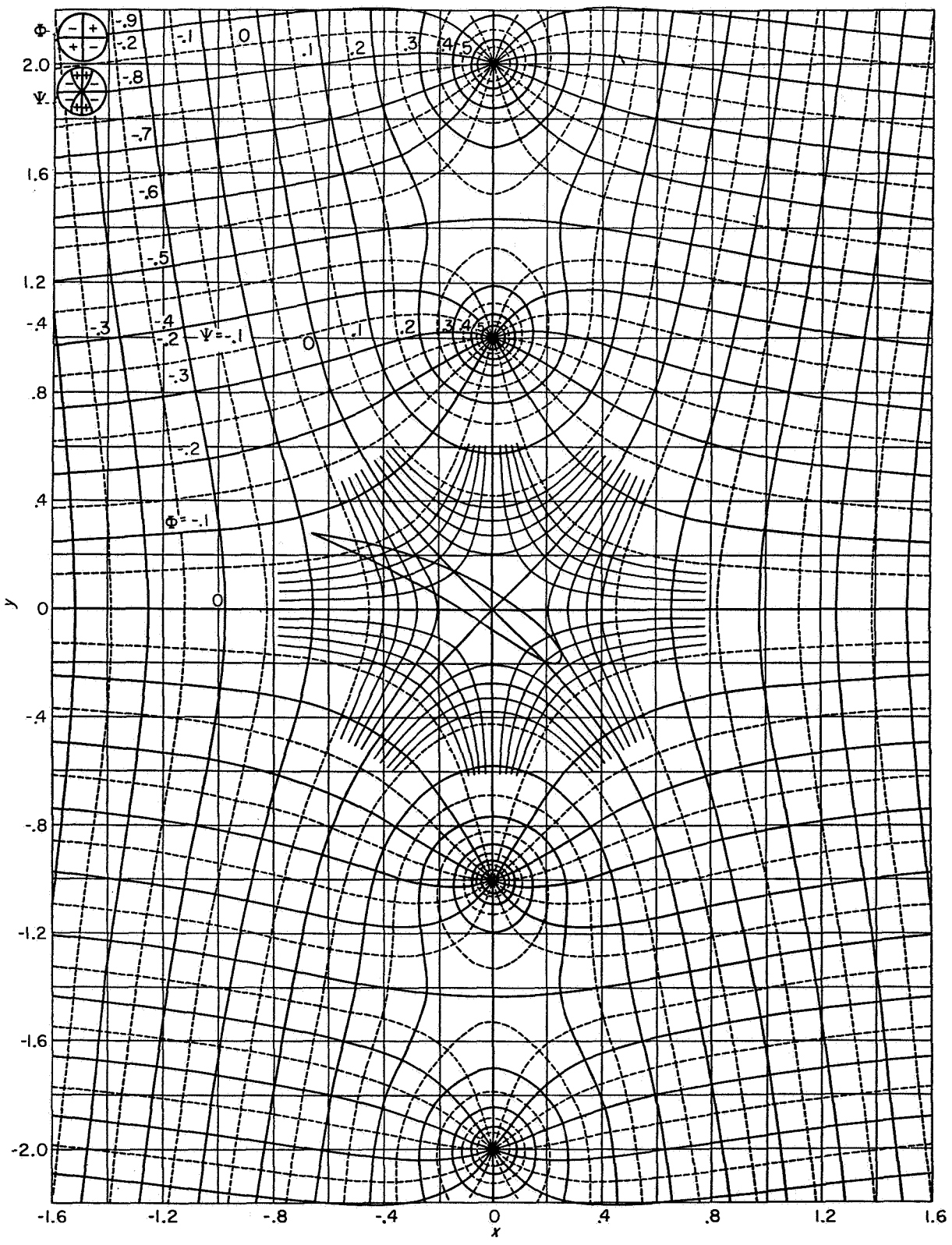

FIGURE 75.—Velocity potential and stream function for row of vortices of unit strength spaced at unit distance along the y-axis with central vortex omitted (ref. 99).

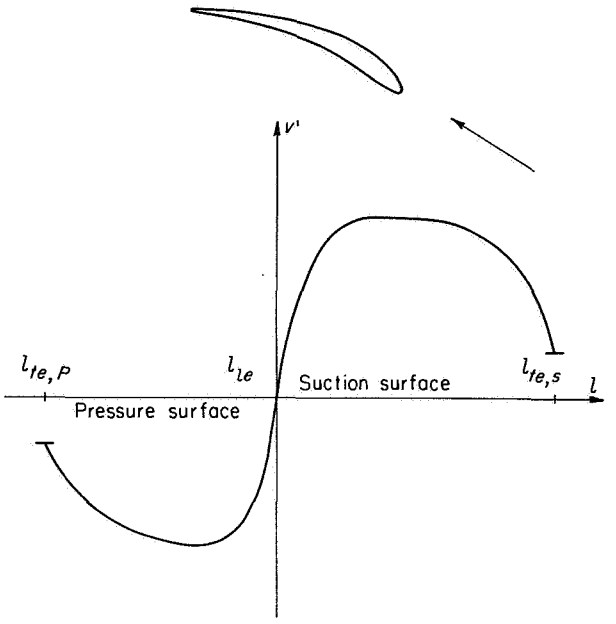

FIGURE 76.—Velocity distribution prescribed as function of arc length, with velocity taken as positive when velocity vector is in direction of increasing arc length.

from the initial computation of the flow about the isolated profile. The actual procedure is given in detail in reference 76 and will not be considered herein.

The flow $W_c=\Phi_c+i\Psi_c$ thus generated will have, in general, a value of $d\Phi_c/d\varphi$ unequal to zero at the trailing edge (φ is the central angle in the circle plane). In order to satisfy the Kutta condition, a vortex is added at the center of the circle with a strength

$$\Gamma_{add}=-2\pi\, d\Phi_c/d\varphi$$

The corresponding contribution to the potential function is $\Phi_\Gamma=(\Gamma_{add}/2\pi)\varphi$.

The complete potential function Φ_Σ is now obtained by summing the contributions Φ_o, Φ_d, Φ_c, and Φ_Γ obtained in the various stages of the solution. The final velocity distribution is obtained by differentiating Φ_Σ with respect to arc length on the blade profile.

The foregoing discussion was advanced on the assumption that the final velocity distribution was known initially. In the actual case, the velocity distribution about the isolated central blade may be taken as a convenient starting value. Adding the disturbance velocities calculated from this initial velocity distribution yields a distribution nearer the correct one. The disturbance effects are then recalculated on the basis of the corrected velocity, and so on. The rapidity of convergence will depend on the accuracy of the initial approximation. It is clear that for high-solidity cascades the initial approximation will be poor and slower convergence can be expected.

In the course of actual application, the authors of the method developed a technique for the iteration process that results in much faster convergence. As the iteration process is carried out, each change in the exterior singularities necessitates a change in the singularities within the central airfoil, that is, a change in W_c. In turn, this results in a change in W_Γ and a change in total circulation. In this sense, the change in circulation about the central blade can be attributed to changes made in the location and strength of the exterior sources and vortices. Then, if Γ_Σ is the total circulation and Γ_o the circulation about the isolated blade, the following equation is obtained:

$$\Gamma_\Sigma=\Gamma_o+\Gamma_{add_s}+\Gamma_{add_v} \tag{62}$$

where Γ_{add_s} and Γ_{add_v} are the additional circulations about the central blade attributable to the presence of the exterior sources and vortices, respectively. In actual practice, the value of Γ_{add_s} changes very little from one iteration to the next, and Γ_{add_v} is nearly proportional to the total circulation. Therefore, the following equation may be written instead of equation (62):

$$\Gamma_\Sigma\approx\Gamma_o+\Gamma_{add_s}+(\Gamma_\Sigma/\Gamma_o)\Gamma_{add_v}$$

or

$$\Gamma_\Sigma\approx\frac{\Gamma_o+\Gamma_{add_s}}{1-\dfrac{\Gamma_{add_v}}{\Gamma_o}} \tag{63a}$$

Values of Γ_Σ calculated from equation (63a) have proven to be considerably closer to the final correct value than those calculated from equation (62). Correspondingly, the potential function can be written

$$\Phi_\Sigma=\Phi_o+\Phi_{add_s}+\frac{\Gamma_\Sigma}{\Gamma_o}\Phi_{add_v} \tag{63b}$$

where Φ_Σ is now considered as the sum of Φ_o and Φ_{add}, where

$$\Phi_{add}=\Phi_d+\Phi_c+\Phi_\Gamma$$

The second iteration can be similarly adjusted:

$$\Gamma_{\Sigma_2}=\frac{\Gamma_o+\Gamma_{add_s}}{1-\frac{\Gamma_{add_v}}{\Gamma_{\Sigma_1}}} \tag{63c}$$

where the subscripts 1 and 2 refer to the first and second approximations, respectively. This modification is highly effective in obtaining rapid convergence. The additional complication of separating the effects of the vortices and sources is not great.

When an arrangement of isolated singularities is used (this is recommended by the author of the method almost without reservation), the proper number and location are largely a matter of experience. For solidities near 1.0, five vortices spaced at 0.1, 0.3, 0.5, 0.7, and 0.9 of chord length will probably give an adequate representation of the velocity distribution effects. The vortex strength at a given chord position is determined from the difference in potential on the upper and lower surfaces. For example, the difference in these potentials at 0.2 chord is approximately the vortex strength from the leading edge to the 0.2-chord position. This vorticity is assumed to be concentrated at the 0.1-chord position. The sum of the isolated vortex strengths must equal the total circulation about the blade.

In the example of reference 86, a source was placed at 0.025 chord and another midway between the leading edge and the position of maximum thickness. Sinks were placed at 0.5, 0.7, and 0.9 of the chord length. To determine the source strength, the average velocity v_{av} is defined as $(v_s+v_P)/2$, where v_s and v_P are the local velocities on the suction and pressure surfaces, respectively. The internal flow at each axial position is defined to be the product of the blade thickness at that position and the corresponding average velocity. The strength of a source or sink is then taken as the difference between the internal flow at a station midway between the location of the source in question and the preceding source and at a station midway between the location of the source in question and the following source. The total source strength must equal the total sink strength. The optimum arrangement of these singularities will differ with blade shapes, but a suitable arrangement should be evident.

The velocity distributions at other angles of incidence can be easily obtained by the method of conformal mapping. No knowledge of the actual mapping function is required; therefore, the off-design conditions can be readily obtained from the exact solution. The procedure for this computation is given in appendix A of this chapter and is applicable in any case of plane incompressible irrotational flow where a solution at one angle of attack is available. This characteristic of the incompressible-flow solution offers an advantage over the compressible-flow solutions for the same problem.

An outline of the general procedure to be used in applying the Katzoff, Finn, and Laurence method follows:

(1) Solve the problem of the isolated geometrically similar blade profile, oriented properly with respect to the mean free-stream velocity. The method of reference 74 or some related method yielding the blade mapping on a circle is used.

(2) Determine the location and strength of the singularities from considerations of cascade geometry and the isolated-blade solution, respectively.

(3) Determine Φ_{d_s}, Ψ_{d_s}, Φ_{d_v}, and Ψ_{d_v} from the chart in figure 75.

(4) Let $\Psi_{c_s}=-\Psi_{d_s}$ and $\Psi_{c_v}=-\Psi_{d_v}$ on the blade surface. Then determine Φ_{c_s} and Φ_{c_v} by the method of reference 76.

(5) Find Γ_{add_s} and Γ_{add_v} from the trailing-edge criterion. Find Γ_Σ from equation (63a) and Φ_Σ from equation (63b).

(6) Compute the final velocity distribution as the derivative of Φ_Σ with respect to arc length.

(7) Reevaluate the strength of the singularities in step (2) on the basis of the new velocity and potential distribution.

(8) Carry through all steps of the process again. If there exists a doubt concerning the accuracy of results obtained by using isolated singularities, replace these singularities by a continuous distribution in step (2) and carry out the remainder of the procedure.

(9) Continue the iteration until convergence is obtained. A second or third trial should be sufficient.

THE INVERSE PROBLEM

In the inverse problem for low solidities, as in the direct problem, the methods of conformal mapping and representation by singularities are used. Contrary to the direct problem, however,

691-564 O-65-9

the solidity often is not significant in the methods for solving the inverse problem. In particular, the method presented in detail in this section can be used for any solidity. This generality, where it exists, is indicated in the table contained in the SUMMARY.

Either the direct or the inverse problem can generally be solved by the method of singularities applied to thin blades, either isolated or in cascade. Therefore, the techniques developed by Birnbaum, Glauert, and Allen, mentioned previously in connection with the direct problem for isolated airfoils, and the solutions of the cascade problem by Pistolesi, Lieblein, and Woolard are applicable to the inverse problem as well.

The current use of higher cambered blades in compressors somewhat restricts the value of the approximate methods. Hence, this section is concerned chiefly with the more exact solutions, which have achieved a complete and convenient form in recent years.

Isolated airfoils.—In 1935, Betz (ref. 101) presented an approximate method for modifying the shape of an existing isolated airfoil to assure a predetermined change in the velocity distribution. Theodorsen also presented a method of modification based on his exact solution of the direct problem (ref. 102). More general methods have been given by Gebelein (ref. 103) and Peebles (ref. 104) using conformal mapping and by Goldstein and Jerison (ref. 100) using singularities. Other solutions of the isolated-airfoil design problem exist, but the foregoing illustrate the essential characteristics of a solution to the problem.

Cascades.—An approach to an exact solution of the cascade problem was given by Weinig (ref. 80). A complete solution by conformal mapping was developed and presented in a series of unpublished lectures by Arthur Goldstein. The computational procedure was given in considerable detail by Hansen and Yohner (ref. 105), and a theoretical solution was obtained. This method, considered to represent an accurate and reasonably fast solution to the problem, will be outlined later in some detail. There is no restriction on solidity.

A similar approach was given in 1945 by Lighthill (ref. 106), in which the velocities are not prescribed directly as a function of airfoil arc length but rather as a function of the central angle of the mapping circle. Hence, a certain amount of experience is required to obtain a desired velocity distribution on the cascade itself.

The method of Mutterperl (ref. 96), mentioned in connection with the direct problem, is applicable also to the inverse problem. As mentioned before, some results have indicated that the numerical answers might not always be reliable. If the accuracy can be improved, the method may find practical application.

All the inverse cascade methods considered so far have made use of conformal-mapping theory. A method of singularities was developed by Goldstein and Jerison (ref. 100), but they encountered some practical difficulty in the application of their technique in regions where the curvature of the blade surface is large, particularly in the leading-edge region of a thick blade. However, the solidity is not an important factor, and the method is considered to be quite useful for the design of thin blades.

Of the methods discussed, the conformal-mapping method of Goldstein has been selected for a detailed presentation. A report (ref. 105) is available on the computational procedure.

Solution of low-solidity inverse problem.—The low-solidity inverse problem is twofold: (1) to determine the flow about a unit circle that will have the desired characteristics when mapped into the cascade plane, and (2) to determine the mapping function and hence the blade coordinates. The problem is simpler than the corresponding direct problem in that no iteration is required. Furthermore, the solution is known to be exact, since no convergence is involved. A difficulty is introduced, however, by the fact that an arbitrarily selected velocity distribution may fail to result in a closed profile. In this event, the method to be described indicates the necessary change in the prescribed velocity distribution that will yield a closed profile. The suction-surface velocity distribution, usually the most critical, can be maintained as originally specified.

The following information must be given to obtain a solution: (1) the vector velocities infinitely far upstream and downstream of the cascade, and (2) the velocity distribution as a function of arc length on the contour of a blade. Velocities are considered positive in the positively oriented arc-length direction (fig. 76). Note that the arc length is increasing ($dl>0$) as the blade is traversed in a counterclockwise direction.

The following information is obtained in the solution: (1) the blade profile, and (2) the blade-chord angle $\gamma°$ and solidity σ.

In the following discussion the complex plane containing the cascade will be referred to as the $z=x+iy$ plane (or cascade plane). The complex plane containing the circle (fig. 77) will be referred to as the $\zeta=\xi+i\eta$ plane (or circle plane).

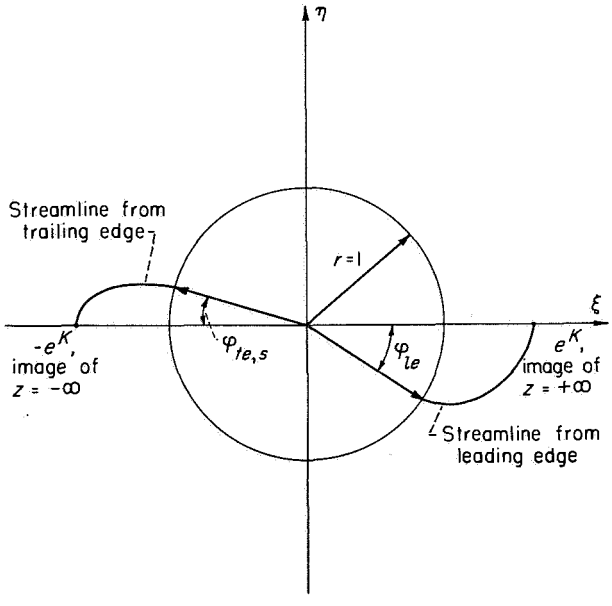

FIGURE 77.—Image of cascade in circle plane.

The most convenient mapping for this problem is one that takes the cascade into a unit circle with center at the origin. The points at $\pm\infty$ on a line normal to the y-axis are transformed into points $\pm e^K$, symmetrically located about the origin on the real axis (fig. 77). Such a mapping is discussed in considerable detail in references 80 and 91. Under a mapping of this kind, the complex potential function in the circle plane can be written (see ref. 80)

$$W_\zeta(\zeta)=\frac{v_m s}{2\pi}\left[e^{i\beta_m}\log_e\left(\frac{\zeta-e^K}{\zeta+e^K}\right)+e^{-i\beta_m}\log_e\left(\frac{\zeta-e^{-K}}{\zeta+e^{-K}}\right)\right]+\frac{\Gamma}{4\pi i}\log_e\left(\frac{\zeta^2-e^{-2K}}{\zeta^2-e^{2K}}\right)+\text{constant} \quad (64)$$

This equation is quite general and holds for an arbitrary cascade in the z-plane. The quantities v_m, β_m, s, Γ, and K are functions of the particular cascade to be mapped into the circle. When these quantities have been chosen properly for a given cascade, the flow about the circle will map back into the desired flow about the cascade. The symbols v_m, β_m, s, and Γ are the mean free-stream velocity, mean free-stream velocity angle, spacing, and circulation of the cascade, respectively; K is a measure of the location $\pm e^K$ of the singularities in the flow about the circle. All five of these quantities can be determined from the prescribed conditions in the inverse problem.

From the velocity diagram (fig. 72) it can be seen that

$$\beta_m=\tan^{-1}\left(\frac{\tan\beta_1+\tan\beta_2}{2}\right), \qquad -\frac{\pi}{2}<\beta_m<\frac{\pi}{2} \quad (65)$$

and

$$v_m=\frac{v_1\cos\beta_1}{\cos\beta_m} \quad (66)$$

The circulation is given by

$$\Gamma=\int_{l_{te,P}}^{l_{te,s}} v(l)\,dl \quad (67)$$

where $v(l)$ is the signed velocity on the cascade blade prescribed as a function of arc length (fig. 76). The blade spacing is given by

$$s=\frac{\Gamma}{v_1\sin\beta_1-v_2\sin\beta_2} \quad (68)$$

Determination of the constant K is somewhat more difficult and depends upon certain considerations of the potential functions. The range of the velocity potential (the difference between maximum and minimum values of the potential) on a cascade blade must equal the corresponding potential range on the circle. On the blade this range is computed as

$$\Delta\Phi_z=\Phi_z(l_{te,s})-\Phi_z(l_{te}) \quad (69)$$

where $l_{te,s}$ and l_{te} are identified in figure 76. From the simple relation connecting the potential distribution to the velocity distribution, Φ_z can be calculated as

$$\Phi_z(l)=\int_{l_{te,s}}^{l} v(l)\,dl$$

The velocity potential on the circle is given by

$$\Phi_\zeta=\text{Real}\,[W_\zeta(e^{i\varphi})] \quad (70)$$

where Real designates the real part, and φ is the central angle of the circle. Then,

$$\Delta\Phi_\zeta=\Phi_\zeta(e^{i\varphi_{te,s}})-\Phi_\zeta(e^{i\varphi_{le}}) \tag{71}$$

where $\varphi_{te,s}$ and φ_{le} are the values of φ (as yet unknown) corresponding to the trailing-edge and leading-edge stagnation points on the circle (see fig. 77). By the process of trial and error outlined in appendix A (described in detail in ref. 105), $\varphi_{te,s}$, φ_{le}, and K can be determined so that $\Delta\Phi_\zeta=\Delta\Phi_z$.

In this manner, the flow in the circle plane is determined uniquely for a prescribed set of conditions in the plane of the cascade (step (1) in the solution of the inverse problem). The function that conformally maps the cascade into the circle must yet be determined from the knowledge of velocities about the circle and about the cascade.

In appendix B of this chapter the following form of a general mapping function is developed:

$$\frac{dz}{d\zeta}=\frac{se^{-K}}{\pi}F(\zeta)e^{\frac{h(\zeta)}{F(\zeta)}} \tag{72}$$

where

$$F(\zeta)=\frac{\zeta^2(e^{2K}-e^{-2K})}{(e^{2K}-\zeta^2)(\zeta^2-e^{-2K})} \tag{73}$$

and

$$h(\zeta)=h_1(\xi,\eta)+ih_2(\xi,\eta) \tag{74}$$

The function $h(\zeta)$ is regular outside the unit circle, and

$$\lim_{\zeta\to\infty}\zeta h(\zeta)=0 \tag{75}$$

The function $z=z(\zeta)$, defined by equations (72) to (75), will map an arbitrary cascade into the unit circle so that the points far upstream and far downstream of the cascade are transformed into the points $\pm e^K$ in the circle plane. The function $h(\zeta)$ will determine the shape of the cascade. The problem is to determine $h(\zeta)$, and hence the blade shape, from the available information.

Let W_ζ and W_z represent the complex potential functions in the circle plane and cascade plane, respectively. Then, if $z=z(\zeta)$ is the desired mapping between the two planes,

$$W_z(z)=W_z(z(\zeta))=W_\zeta(\zeta) \tag{76}$$

Differentiating equation (76) gives a relation between the complex velocity conjugates w_z and w_ζ as follows:

$$w_\zeta(\zeta)=\frac{dW_\zeta}{d\zeta}=\frac{dW_z}{dz}\frac{dz}{d\zeta}=w_z(z)\frac{dz}{d\zeta} \tag{77}$$

If only the unit circle is considered, then $\zeta=e^{i\varphi}$, and it can be determined from equation (73) that $F(e^{i\varphi})$ is real. As a matter of convenience, all functions of $e^{i\varphi}$ are written simply as functions of φ in the following expressions. Combining equations (72) and (77) gives

$$\frac{w_\zeta(\varphi)}{w_z(l)}=\left(\frac{dz}{d\zeta}\right)_{\zeta=e^{i\varphi}}=\frac{se^{-K}}{\pi}F(\varphi)e^{\frac{h_1(\varphi)+ih_2(\varphi)}{F(\varphi)}} \tag{78}$$

where $w_z(l)$ indicates that w_z has now been expressed as a function of distance along the blade perimeter.

The value of the potential at any point on the blade is given by

$$\Phi_z(l)=\int_{l_{te,P}}^{l}v(l)\,dl \tag{79}$$

The values of $\Phi_\zeta(\varphi)$ are known to an additive constant from the real part of equation (64). The additive constant should now be chosen so that $\Phi_z(l_{te,P})=\Phi_\zeta(\varphi_{te,P})$. Then, equating the values of potential in the two planes gives a functional relation of l with φ, say $l=l(\varphi)$.

Now, by means of the function $l=l(\varphi)$, $w_z(l)$ can be written as a function of the central circle angle φ as follows:

$$w_z(l)=w_z(l(\varphi))=\hat{w}_z(\varphi) \tag{80}$$

where $\hat{w}$ denotes the velocity in the cascade plane expressed as a function of the circle-plane coordinates. Then the ratio of the velocities in the two planes can be written

$$\frac{w_\zeta(\varphi)}{\hat{w}_z(\varphi)}=\frac{v_\zeta(\varphi)e^{-i(\varphi+\pi/2)}}{\hat{v}_z(\varphi)e^{-i\mu}} \tag{81}$$

where v_ζ and v_z are signed velocities, and μ is the angle made by a tangent to the blade profile and the x-axis. Substituting equation (81) into equation (78) and taking the logarithms of both sides yield:

$$\log_e\left[\frac{v_\zeta(\varphi)}{\hat{v}_z(\varphi)}\right]+i(\mu-\varphi-\pi/2)=\log_e\left[\frac{se^{-K}}{\pi}F(\varphi)\right]+\frac{h_1(\varphi)}{F(\varphi)}+i\frac{h_2(\varphi)}{F(\varphi)} \tag{82}$$

Since $F(\varphi)$ is real, equating real and imaginary parts of equation (82) gives

$$h_1(\varphi)=F(\varphi)\,\log_e\left[\frac{\pi e^K}{sF(\varphi)}\,\frac{v_1(\varphi)}{\hat{v}_z(\varphi)}\right] \tag{83}$$

$$h_2(\varphi)=F(\varphi)\left(\mu-\varphi-\frac{\pi}{2}\right) \tag{84}$$

Equations (83) and (84) are the essential relations of the inverse solution. If h_1 and h_2 are determined, then h is known and the complete mapping of the cascade profile into the circle is known. Equation (83) gives h_1 as a function of the circle central angle φ. Since $h=h_1+ih_2$, it follows that h_2 is the harmonic conjugate of h_1. Therefore, h_2 can be found by one of the methods of harmonic synthesis, such as the one given in reference 76. When h_2 has been found as a function of φ, then μ is known as a function of φ from equation (84), and hence as a function of l.

Since $dx/dl=\cos\mu$ and $dy/dl=\sin\mu$ on the perimeter of the blade,

$$\left.\begin{aligned} x-x_{te,P}&=\int_{l_{te,P}}^{l}\cos\mu\,dl\\ y-y_{te,P}&=\int_{l_{te,P}}^{l}\sin\mu\,dl\end{aligned}\right\} \tag{85a}$$

or, more conveniently,

$$\left.\begin{aligned} x-x_{te,P}&=\int_{\varphi_{te,P}}^{\varphi}\frac{v_1(\varphi)}{\hat{v}_z(\varphi)}\cos\mu\,d\varphi\\ y-y_{te,P}&=\int_{\varphi_{te,P}}^{\varphi}\frac{v_1(\varphi)}{\hat{v}_z(\varphi)}\sin\mu\,d\varphi\end{aligned}\right\} \tag{85b}$$

Equation (85a) or (85b) gives the coordinates of the cascade blade and completes the solution, except for the case in which the cascade blades fail to close.

Equation (75) leads to the following conditions, necessary and sufficient for closure of the blades:

$$\int_{\varphi_{te,P}}^{\varphi_{te,s}}h_1(\varphi)\,d\varphi=\int_{\varphi_{te,P}}^{\varphi_{te,s}}h_1(\varphi)\sin\varphi\,d\varphi=\int_{\varphi_{te,P}}^{\varphi_{te,s}}h_1(\varphi)\cos\varphi\,d\varphi=0 \tag{86}$$

For an arbitrary velocity distribution this condition will not, in general, be satisfied. Suppose

$$\left.\begin{aligned}\int_{\varphi_{te,P}}^{\varphi_{te,s}}h_1(\varphi)\,d\varphi&=C_1\\ \int_{\varphi_{te,P}}^{\varphi_{te,s}}h_1(\varphi)\cos\varphi\,d\varphi&=C_2\\ \int_{\varphi_{te,P}}^{\varphi_{te,s}}h_1(\varphi)\sin\varphi\,d\varphi&=C_3\end{aligned}\right\} \tag{87}$$

Form a function $f(\varphi)$ such that

$$\left.\begin{aligned}\int_{\varphi_{te,P}}^{\varphi_{te,s}}f(\varphi)\,d\varphi&=-C_1\\ \int_{\varphi_{te,P}}^{\varphi_{te,s}}f(\varphi)\cos\varphi\,d\varphi&=-C_2\\ \int_{\varphi_{te,P}}^{\varphi_{te,s}}f(\varphi)\sin\varphi\,d\varphi&=-C_3\end{aligned}\right\} \tag{88}$$

From equations (87) and (88), it is seen that $h_1^*(\varphi)=h_1(\varphi)+f(\varphi)$ will satisfy the closure conditions. It should be noted that the conditions on $f(\varphi)$ are not severe and that the designer has considerable freedom in the selection. In particular, the velocity distribution on the suction surface can generally be maintained by a proper choice of $f(\varphi)$.

The changes caused by a change in $h_1(\varphi)$ require some consideration. From equation (83) it is seen that a change in $h_1(\varphi)$ causes a change in $\hat{v}_z(\varphi)$. That is, when considered as a function of the central circle angle, the cascade velocity has changed from $\hat{v}_z(\varphi)$ to some function $\hat{v}_z^*(\varphi)$. The function $\hat{v}_z^*(\varphi)$ is given by equation (83) as follows:

$$h_1^*(\varphi)=F(\varphi)\,\log_e\left[\frac{\pi e^K}{sF(\varphi)}\,\frac{v_1(\varphi)}{\hat{v}_z^*(\varphi)}\right] \tag{89}$$

Subtracting equation (89) from equation (83) and solving for $\hat{v}_z^*(\varphi)$ give

$$\hat{v}_z^*(\varphi)=\hat{v}_z(\varphi)e^{-f(\varphi)/F(\varphi)} \tag{90}$$

In the case of the blades that failed to close, $l(\varphi)$ is a function of φ such that

$$v_z(l)=v_z(l(\varphi))=\hat{v}_z(\varphi) \tag{91}$$

Similarly, a new relation $l^*(\varphi)$ must be found such that

$$v_z^*(l^*)=v_z^*(l^*(\varphi))=\hat{v}_z^*(\varphi) \tag{92}$$

Combining equations (91) and (92) and substi-

tuting from equation (90) yield

$$\frac{v_z(l)}{v_z^*(l^*)}=\frac{\hat{v}_z(\varphi)}{\hat{v}(\varphi)}=e^{\int (\varphi)/F(\varphi)} \tag{93}$$

It follows from equation (77) that

$$v_z(l)=v_f(\varphi)\frac{d\varphi}{dl} \tag{94}$$

Therefore, $l^*(\varphi)$ must be a function that satisfies the relation

$$v_z^*(l^*)=v_f(\varphi)\frac{d\varphi}{dl^*} \tag{95}$$

if the flow in the circle plane is to remain unaltered. Combining equations (94) and (95) and substituting from equation (93) give

$$dl^*=\frac{v_z(l)}{v_z^*(l^*)}\frac{dl}{d\varphi}d\varphi=e^{\int (\varphi)/F(\varphi)}\frac{dl}{d\varphi}d\varphi$$

or

$$l^*-l^*_{te,P}=\int_{\varphi_{te,P}}^{\varphi} e^{\int (\varphi)/F(\varphi)}\frac{dl}{d\varphi}d\varphi \tag{96}$$

These equations show the changes arising in the cascade velocity distribution as a result of changing $h_1(\varphi)$ to satisfy closure.

An outline for the general procedure to be used in applying the method follows:

(1) Prescribe a velocity distribution as a function of arc length about a cascade blade.

(2) Prescribe v_1, v_2, β_1, and β_2.

(3) Determine v_m, β_m, s, Γ, and K from equations (65) to (71) and appendix A.

(4) Determine $\Phi_z(l)$ from equation (79).

(5) Determine $\Phi_f(\varphi)$ as the real part of equation (64) plus an additive constant.

(6) Choose the arbitrary constant in equation (64) such that $\Phi_z(l_{te,P})=\Phi_f(\varphi_{te,P})$, and equate the potential functions yielding a relation $l=l(\varphi)$.

(7) Find $\hat{v}_z(\varphi)$ and, with $v_f(\varphi)$, solve equation (83) for $h_1(\varphi)$. Check for closure and make the necessary changes.

(8) By the method of reference 76, or some related method, find $h_2(\varphi)$ as the harmonic conjugate of $h_1(\varphi)$.

(9) Solve equation (84) for μ as a function of ϕ.

(10) Find the blade coordinates from equation (85b).

Appendix A can be used to analyze the resulting blade shape at all angles of incidence. A prescribed velocity distribution, the velocity distribution corrected to ensure closure, and the resulting blade shape are shown in figure 78 (from ref. 105).

COMPRESSIBILITY CONSIDERATIONS

Both the direct and inverse problems for low-solidity cascades have been discussed only for an incompressible fluid. The equations governing an incompressible two-dimensional flow are simple in form and, as has been shown, can be solved by complex-function theory. When the fluid density is permitted to vary, the ordinary formulations of the flow equations become nonlinear and very much more difficult to solve.

In high-solidity cascades, where a channel treatment is possible, the finite-difference techniques can be used. The relaxation method of Southwell (refs. 107 to 109) has been used to solve many difficult differential equations. Since the advent of high-speed digital computing machinery, the direct solution of a large number of simultaneous linear equations in a reasonable period of time has become feasible. Thus, a complicated differential equation can be represented over the flow domain by a set of linear finite-difference equations, which can be solved either by the relaxation method (usually done on a desk computing machine) or by a direct matrix solution on high-speed computing equipment.

In high-solidity cascades the physical boundaries of the flow favor a solution of the compressible-flow equations by finite-difference techniques. In the low-solidity cascades, however, the guidance exerted by the blades is less pronounced, and the proper satisfaction of boundary conditions is more difficult. Hence, for low-solidity cascades the problem of obtaining compressible-flow solutions still exists, at least for the direct problem. (A solution for compressible flow with a linear pressure-volume relation has been obtained for the inverse problem and is discussed later in this section.) In general engineering practice, two methods of attacking this problem are currently being used, the hodograph method and the small-perturbation method. These two important theories will be discussed in this section, where the following notation is used: v is the magnitude of velocity in an incompressible-flow field, and q is the magnitude of velocity in a compressible-flow field.

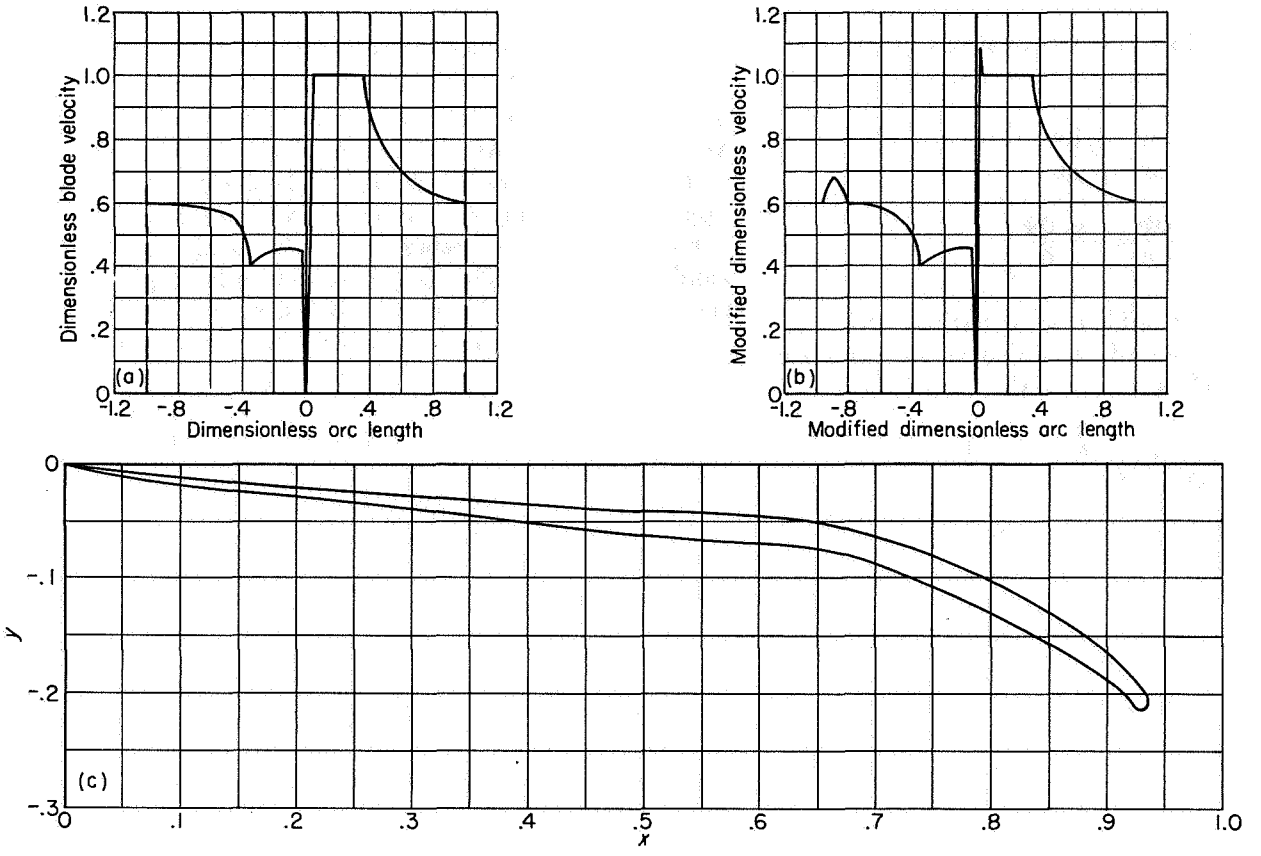

(a) Prescribed velocity distribution. (b) Modified velocity distribution to ensure closure. (c) Resulting blade shape.

FIGURE 78.—Prescribed velocity distribution used in blade design with velocity distribution modified for closure and resulting blade shape (obtained in ref. 105).

Hodograph method.—Although the equations relating the stream and potential functions of a two-dimensional compressible flow of an ideal fluid are, in general, nonlinear, they can be rewritten in terms of a new set of independent variables such that the equations become linear. This result was discussed extensively by Chaplygin (ref. 110) in 1902. For many years thereafter very little was done in this direction, probably because of the adequacy of the incompressible-flow solutions for interpreting low-speed flows. However, in more recent years it has become necessary to consider the effects of density variation in many applications. Under this impetus, the hodograph theory (investigation of flow in the velocity plane) has been advanced considerably and is still expanding. The essential advantage of the hodograph method is the linearization of the equations relating the stream and potential functions by a proper choice of independent variables. An important disadvantage is the difficulty in establishing boundary conditions in the hodograph plane to represent a given problem in the physical plane. In spite of this major handicap, however, important use has been made of the theory.

For incompressible flow, the following relations hold:

$$\left.\begin{aligned}\frac{\partial\Phi}{\partial x}&=\frac{\partial\Psi}{\partial y}\\ \frac{\partial\Phi}{\partial y}&=-\frac{\partial\Psi}{\partial x}\end{aligned}\right\} \tag{97a}$$

Equations (97a) can be rewritten with v and β replacing x and y as the independent variables (see e.g., ref. 111), where β is the inclination of the velocity vector to the x-axis:

$$\left.\begin{aligned}\frac{\partial\Phi}{\partial\beta}&=v\frac{\partial\Psi}{\partial v}\\ \frac{\partial\Phi}{\partial v}&=-\frac{1}{v}\frac{\partial\Psi}{\partial\beta}\end{aligned}\right\} \tag{98a}$$

For compressible flow the relations corresponding to equations (97a) can be written

$$\left.\begin{aligned}\frac{\partial\Phi}{\partial x}&=\frac{\rho_a}{\rho}\frac{\partial\Psi}{\partial y}\\ \frac{\partial\Phi}{\partial y}&=-\frac{\rho_a}{\rho}\frac{\partial\Psi}{\partial x}\end{aligned}\right\} \tag{97b}$$

As in the incompressible case, equations (97b) can be written in terms of the independent variables q and β, with M as the local Mach number:

$$\left.\begin{aligned}\frac{\partial\Phi}{\partial\beta}&=\frac{\rho_a}{\rho}\,q\,\frac{\partial\Psi}{\partial q}\\ \frac{\partial\Phi}{\partial q}&=-\frac{\rho_a}{\rho}\,\frac{1-M^2}{q}\,\frac{\partial\Psi}{\partial\beta}\end{aligned}\right\} \tag{98b}$$

Introducing the variables V and Q, defined by

$$\left.\begin{aligned}dV&=\frac{dv}{v}\\ dQ&=\sqrt{1-M^2}\,\frac{dq}{q}\end{aligned}\right\} \tag{99}$$

into (98a) and (98b), respectively, yields

$$\left.\begin{aligned}\frac{\partial\Phi}{\partial\beta}&=\frac{\partial\Psi}{\partial V}\\ \frac{\partial\Phi}{\partial V}&=-\frac{\partial\Psi}{\partial\beta}\end{aligned}\right\} \tag{100}$$

and

$$\left.\begin{aligned}\frac{\partial\Phi}{\partial\beta}&=\frac{\rho_a}{\rho}\sqrt{1-M^2}\,\frac{\partial\Psi}{\partial Q}\\ \frac{\partial\Phi}{\partial Q}&=-\frac{\rho_a}{\rho}\sqrt{1-M^2}\,\frac{\partial\Psi}{\partial\beta}\end{aligned}\right\} \tag{101}$$

Equations (101) can be simplified by the following considerations:

$$\frac{\rho_a}{\rho}\sqrt{1-M^2}=\left(1+\frac{\gamma-1}{2}M^2\right)^{\frac{1}{\gamma-1}}\sqrt{1-M^2}$$

For $\gamma=-1$, $(\rho_a/\rho)\sqrt{1-M^2}=1$. Although $\gamma=-1$ does not correspond to any actual fluid, this value causes the adiabatic pressure-volume relation $p(1/\rho)^\gamma=$constant to become linear in p and $1/\rho$. When a general linear relation between pressure and volume is assumed initially, the theory shows that $(\rho_a/\rho)\sqrt{1-M^2}=1$ in this case, also. Thus, a straight line can be taken to represent the pressure-volume relation instead of the usual curve. Early workers in this field (e.g., ref. 112) allowed the approximating line to be tangent to the adiabatic curve at a point corresponding to the stagnation condition $p=p_a$. This is a poor choice for high-speed flows. Von Kármán and Tsien (refs. 113 and 114) took the point of tangency to correspond to free-stream conditions, which better approximated the true curve in the region of greatest interest. With this approximation, equations (101) become

$$\left.\begin{aligned}\frac{\partial\Phi}{\partial\beta}&=\frac{\partial\Psi}{\partial Q}\\ \frac{\partial\Phi}{\partial Q}&=-\frac{\partial\Psi}{\partial\beta}\end{aligned}\right\} \tag{102}$$

Comparing equations (102) with equations (100) shows that a solution of the incompressible-flow equations (100) will be a solution of the quasi-compressible-flow equations (102) when the velocities are related (from eq. (99)) by

$$\frac{dv}{v}=\sqrt{1-M^2}\,\frac{dq}{q} \tag{103}$$

This relation integrates (with the help of the linear pressure-volume relation) to

$$q=\frac{4a_a^2v}{4a_a^2-v^2} \tag{104}$$

The density ratio becomes

$$\frac{\rho_a}{\rho}=\frac{4a_a^2+v^2}{4a_a^2-v^2} \tag{105}$$

The pressure coefficient for the incompressible flow is given by

$$\psi_{inc}=\frac{p-p_m}{\frac{1}{2}\rho_m v_m^2}=1-\frac{v^2}{v_m^2} \tag{106}$$

For compressible flow,

$$\psi_C=\frac{p-p_m}{\frac{1}{2}\rho_m q_m^2}=2\,\frac{a_m^2}{q_m^2}\left(1-\frac{\rho_m}{\rho}\right) \tag{107}$$

The pressure coefficients are related by the following equation (called the Kármán-Tsien relation):

$$\psi_C=\frac{\psi_{inc}}{\sqrt{1-M_m^2}+\dfrac{M_m^2}{\sqrt{1-M_m^2}+1}\,\dfrac{\psi_{inc}}{2}} \tag{108}$$

Hence, equations (104), (105), and (108) provide a compressible-flow solution when an incompressible-flow solution is known. It is evident, however, that the two solutions will not satisfy the same boundary conditions. Applying equations (104) and (105) will yield a solution for compressible flow about a cascade of somewhat different geometry. The correlation of the two flow fields is only approximately valid.

The relations presented herein as a simple means of approximating the effects of compressibility on a known incompressible-flow field are a byproduct of the hodograph theory. The aim of the theory in its complete form, to put the direct and inverse compressible-flow problems on a substantial theoretical foundation, has been realized to a certain extent. The inverse problem for cascades has been solved in its general form with the assumption of a linear pressure-volume relation by Costello (ref. 115); Costello, Cummings, and Sinnette (ref. 116); Clauser (ref. 117); and Lin (ref. 118). These theories are based upon earlier work by von Kármán (ref. 113), Tsien (ref. 114), and Lin (ref. 119). Reference 116 offers a detailed computational procedure for the use of Costello's method.

The direct problem has not reached the same state of development. Even in the case of an incompressible fluid flow, an iteration process is necessary. In the case of a compressible fluid flow, a trial-and-error iteration is possible. However, no systematic process for converging to a solution in the case of compressible flow about a body of arbitrary shape has been given.

The method of appendix A for finding velocity distributions at angles of incidence other than the one of the original solution does not hold in the compressible-flow case. This fact makes the incompressible-flow solution more valuable for some investigations. For this reason, and because of the difficulty in presenting the material concisely, the compressible-flow solution for the inverse problem is not presented in detail in this chapter. The reader is referred again to references 115 and 116.

Small-perturbation method. The equations governing the flow of a compressible fluid about a body can be linearized in the physical plane instead of the hodograph plane by making certain assumptions about the nature of the flow. These assumptions cause the equations only to approximate the actual flow. For slender bodies the approximation is generally good and the theory has proven to be useful.

Flows that differ only very little from the mean free-stream flow will be considered. The relations among the various velocity components can be seen in the following sketch. The assumption

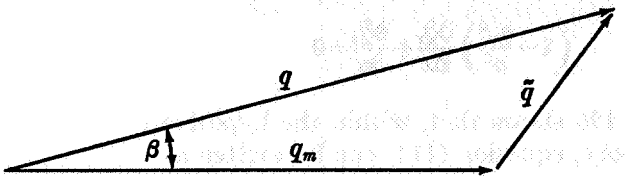

is made that second and higher powers of $\tilde{q}$ (disturbance velocity) or its components can be neglected and that derivatives of the disturbance-velocity components are approximately equal to the component over a characteristic length of the object in the flow field. These conditions are expressed

$$\tilde{q}^{\,n} \approx \tilde{q}_x^{\,n} \approx \tilde{q}_y^{\,n} \approx 0 \text{ for } n \geq 2 \tag{109}$$

$$\left.\begin{aligned} \frac{\partial \tilde{q}_x}{\partial x} \approx \frac{\partial \tilde{q}_x}{\partial y} \approx \frac{\tilde{q}_x}{c^*} \\ \frac{\partial \tilde{q}_y}{\partial x} \approx \frac{\partial \tilde{q}_y}{\partial y} \approx \frac{\tilde{q}_y}{c^*} \end{aligned}\right\} \tag{110}$$

where c^* is a characteristic length.

The actual velocities are related to the disturbance velocities by

$$\left.\begin{aligned} q_x = q_m + \tilde{q}_x \\ q_y = \tilde{q}_y \end{aligned}\right\} \tag{111}$$

Euler's equations of motion for a two-dimensional compressible steady flow with no external forces can be written

$$\left.\begin{aligned} q_x \frac{\partial q_x}{\partial x} + q_y \frac{\partial q_x}{\partial y} = -\frac{1}{\rho}\frac{\partial p}{\partial x} = -\frac{a^2}{\rho}\frac{\partial \rho}{\partial x} \\ q_x \frac{\partial q_y}{\partial x} + q_y \frac{\partial q_y}{\partial y} = -\frac{1}{\rho}\frac{\partial p}{\partial y} = -\frac{a^2}{\rho}\frac{\partial \rho}{\partial y} \end{aligned}\right\} \tag{112}$$

Combining equations (112), with the help of the continuity equation

$$\frac{\partial(\rho q_x)}{\partial x} + \frac{\partial(\rho q_y)}{\partial y} = 0$$

gives

$$q_x^2 \frac{\partial q_x}{\partial x} + q_x q_v \left(\frac{\partial q_x}{\partial y} + \frac{\partial q_v}{\partial x} \right) + q_v^2 \frac{\partial q_v}{\partial y} = a^2 \left(\frac{\partial q_x}{\partial x} + \frac{\partial q_v}{\partial y} \right) \tag{113}$$

By using the relations (111) and the hypotheses (109) and (110), equation (113) reduces to

$$\left(1 - \frac{q_m^2}{a^2} \right) \frac{\partial \tilde{q}_x}{\partial x} + \frac{\partial \tilde{q}_v}{\partial y} = 0 \tag{114}$$

Reference 120 shows that, within the hypotheses of this theory, equation (114) can be written as

$$(1 - M_m^2) \frac{\partial \tilde{q}_x}{\partial x} + \frac{\partial \tilde{q}_v}{\partial y} = 0 \tag{115}$$

or, introducing the disturbance velocity potential,

$$(1 - M_m^2) \frac{\partial^2 \tilde{\Phi}}{\partial x^2} + \frac{\partial^2 \tilde{\Phi}}{\partial y^2} = 0 \tag{116}$$

Now consider the transformation

$$x_t = x, \qquad y_t = y\sqrt{1 - M_m^2}, \qquad \tilde{\Phi}_t = \Lambda \tilde{\Phi} \tag{117}$$

Applying transformation (117) to equation (116) gives

$$\frac{\partial^2 \tilde{\Phi}_t}{\partial x_t^2} + \frac{\partial^2 \tilde{\Phi}_t}{\partial y_t^2} = 0 \tag{118}$$

the Laplace equation for the disturbance potential in an incompressible flow. At affinely corresponding points (under transformation (117)) in the two planes, the following expressions relate the velocity vectors and their angles:

$$\left.\begin{aligned} \tilde{v}_{x_t} &= \frac{\partial \tilde{\Phi}_t}{\partial x_t} = \Lambda \frac{\partial \tilde{\Phi}}{\partial x} = \Lambda \tilde{q}_x \\ \tilde{v}_{v_t} &= \frac{\partial \tilde{\Phi}_t}{\partial y_t} = \Lambda \frac{\partial \tilde{\Phi}}{\partial y} \frac{\partial y}{\partial y_t} = \frac{\Lambda}{\sqrt{1 - M_m^2}} \tilde{q}_v \\ \beta_t \approx \tan \beta_t &\approx \frac{\tilde{v}_{v_t}}{q_m} = \frac{\Lambda}{\sqrt{1 - M_m^2}} \frac{\tilde{q}_v}{q_m} = \frac{\Lambda}{\sqrt{1 - M_m^2}} \beta \end{aligned}\right\} \tag{119}$$

From equations (119) it can be seen that, at affinely corresponding points of the flow fields, the ratio of β_t to β is constant and equal to $\Lambda/\sqrt{1 - M_m^2}$. Hence, for flow about geometrically similar boundaries, $\Lambda = \sqrt{1 - M_m^2}$ and

$$\tilde{q}_x = \frac{1}{\sqrt{1 - M_m^2}} \tilde{v}_{x_t} \tag{120}$$

It can be shown under the hypotheses of the small-perturbation theory that the pressure coefficient can be written

$$\left.\begin{aligned} \psi_c &= -2 \frac{\tilde{q}_x}{q_m} \\ \psi_{inc} &= -2 \frac{\tilde{v}_{x_t}}{q_m} \end{aligned}\right\} \tag{121}$$

Using equations (120) and (121) gives

$$\psi_c = \frac{1}{\sqrt{1 - M_m^2}} \psi_{inc} \tag{122}$$

Equation (122) is referred to as the Glauert-Prandtl compressibility correction and corresponds to equation (108) in the hodograph theory. When these equations are applied to cascades of blades, the corresponding cascades in the two flow fields will have the same blade shape but different chord angles and solidities. The relations between the cascades are given by Woolard in reference 121. Pressures predicted from equations (108) and (122) are compared with actual experimental data in reference 122.

The compressibility corrections of either the Glauert-Prandtl or Kármán-Tsien methods are quite simple in application and have yielded satisfactory results for cascades by using the local Mach number at points in the blade passage instead of the mean free-stream Mach number (ref. 123). The local Mach number is derived from a one-dimensional analysis.

HIGH-SOLIDITY CASCADES

In general, the mathematical techniques applied successfully to low-solidity-cascade problems become increasingly tedious to apply as solidities rise above 1.0. Although the methods are not out of the question for solidities greater than 1.0, difficulties may be expected for the range of solidity from 1.0 to 1.5, and above 1.5 these difficulties are liable to be excessive. The lines of demarcation are not clear but vary with individual methods and prescribed conditions other than solidity.

As was indicated previously, various mathematical techniques are available for handling the problems of closely spaced cascades. The decisive factor in the employment of the channel-flow techniques is the advance knowledge of the approximate streamline patterns, which results from the considerable guidance of the fluid by closely spaced blades. This factor is most clearly demonstrated in the stream-filament and power-series-expansion techniques.

Much of the work in the field of closely spaced blades has been done for quasi-three-dimensional flows. The formulation of the equations in a manner suitable for solution is often only slightly more difficult for flow on a general surface of revolution than for plane cascade flow. In addition to this advantage, it is generally possible to consider compressible flows.

The literature in the field has grown so quickly that priorities are not easily established. No attempt is made here to cover the many variations of method in common use for closely spaced blades. Only the fundamental approaches of a few authors have been selected as representative of the basic techniques involved.

THE DIRECT PROBLEM

Probably the most widely used channel-flow technique is the stream-filament method (e.g., ref. 59 (vol. II, p. 992)). A simplification by Huppert and MacGregor (ref. 124), based on an assumed linear variation of streamline curvature, is presented in some detail in this section. The method is simple in theory and application, and solutions are obtained quickly. The major drawback is the failure of the method to provide accurate results in the immediate regions of the leading and trailing edges. In reference 124 results are obtained for a solidity as low as 1.42.

A rapid approximate solution is given by Stanitz and Prian in reference 125. The method is based on the principle of zero absolute circulation, with linear variation of velocity and velocity angle assumed in the direction of the y-axis. Results are obtained only on the blade surfaces and not throughout the channel. Although this method has definite limitations, it has been used successfully at the NACA Lewis laboratory. A counterpart for treating the inverse problem is discussed in some detail later in this chapter.

Another approach to an approximate solution is with a power-series expansion, as illustrated by the work of Wu and Brown (ref. 126). The same difficulty exists in solving for the leading- and trailing-edge regions as exists in the stream-filament method. The results obtained in reference 126 compare satisfactorily in the region of applicability with results obtained by a more exact procedure.

The application of relaxation and matrix solution techniques is indicated in this section, based upon considerations from another work by Wu and Brown (ref. 127). A more exact solution is obtainable by these methods than by the stream-filament or series-expansion methods. However, more time is required to obtain the more exact answers, the time element varying considerably with the type of computing equipment available. Accurate time estimates are not readily available, since experience in this field is still not great. For use of high-speed digital computing machinery, the setup time may be prohibitive unless a number of solutions is desired.

Stream-filament method.—The stream-filament technique is a natural approach to the flow problem. Briefly, the procedure is as follows: (1) Approximate the streamline positions using empirical data or intuition; (2) find a method of systematically improving the accuracy of the streamline arrangement. It will be shown that the velocities in the flow field can be computed, based on the assumed streamlines. This information can then be used to improve the streamline positions.

For two-dimensional irrotational flow, the rate of change of velocity in a direction normal to the streamlines is given by

$$\frac{dq}{dn}=-\frac{q}{r_{\mathcal{C}}}=-q\mathcal{C} \tag{123}$$

where dn is an increment in a direction normal to the streamline, $r_{\mathcal{C}}$ is the radius of curvature, and $\mathcal{C}$ is the curvature. This equation of motion and the continuity equation are the basic relations used in this stream-filament method.

The curvature is assumed to vary linearly with respect to n across the passage (ref. 124). Then,

$$\mathcal{C}=\mathcal{C}_s+\frac{\mathcal{C}_p-\mathcal{C}_s}{n_p}n=\mathcal{C}_s+\frac{\Delta\mathcal{C}}{n_p}n \tag{124}$$

On the suction surface, n is taken as zero. Differentiating equation (124) and substituting into equation (123) give

$$\frac{dq}{q}=-\frac{n_P}{\Delta\mathcal{C}}\mathcal{C}\,d\mathcal{C} \tag{125}$$

Integrating equation (125) gives

$$\frac{q}{q_l}=exp\left[-\frac{n_P}{2\Delta\mathcal{C}}(\mathcal{C}^2-\mathcal{C}_l^2)\right] \tag{126}$$

where the subscript l denotes an arbitrary position along the potential line. From equation (126) q is known at each point along the potential line if it is known at any point l. Noting that

$$\frac{\rho}{\rho_a}=\left(1-\frac{q^2}{2c_pT_a}\right)^{\frac{1}{\gamma-1}} \tag{127}$$

the continuity equation can be written

$$d(\Delta w)=\rho q\,dn=\rho_a q\left(1-\frac{q^2}{2c_pT_a}\right)^{\frac{1}{\gamma-1}}dn \tag{128}$$

where Δw is the mass flow per unit time. With the substitution

$$X=\frac{q^2}{2c_pT_a} \tag{129a}$$

equation (128) becomes

$$\frac{d(\Delta w)}{n_P\rho_a\sqrt{2c_pT_a}}=\sqrt{X}(1-X)^{\frac{1}{\gamma-1}}\frac{dn}{n_P} \tag{130}$$

Now let

$$(1-X)^{\frac{1}{\gamma-1}}=(1-X_l)^{\frac{1}{\gamma-1}}\left(1-\frac{X-X_l}{1-X_l}\right)^{\frac{1}{\gamma-1}} \tag{131}$$

where

$$X_l=\frac{q_l^2}{2c_pT_a} \tag{129b}$$

Equation (130) is the fundamental equation to be solved. A convenient technique of solution is afforded by the binomial expansion. Expanding equation (131) by the binomial series and keeping only the first two terms give

$$(1-X)^{\frac{1}{\gamma-1}}=(1-X_l)^{\frac{2-\gamma}{\gamma-1}}\left[1+X_l\left(\frac{2-\gamma}{\gamma-1}\right)-\frac{X}{\gamma-1}\right] \tag{132}$$

Now let

$$f=\sqrt{X_l}\,(1-X_l)^{\frac{2-\gamma}{\gamma-1}}\left[1+X_l\left(\frac{2-\gamma}{\gamma-1}\right)\right] \tag{133}$$

and

$$g=\frac{X_l^{3/2}}{\gamma-1}(1-X_l)^{\frac{2-\gamma}{\gamma-1}} \tag{134}$$

Using (133) and (134) in equation (132) yields

$$(1-X)^{\frac{1}{\gamma-1}}=\frac{f}{\sqrt{X_l}}-g\frac{X}{X_l^{3/2}} \tag{135}$$

Equation (130) becomes

$$\frac{d(\Delta w)}{n_P\rho_a\sqrt{2c_pT_a}}=\left[f\sqrt{\frac{X}{X_l}}-g\left(\frac{X}{X_l}\right)^{3/2}\right]\frac{dn}{n_P} \tag{136}$$

Let

$$\hat{\mu}=\frac{1}{\rho_a n_P\sqrt{2c_pT_a}}\int_0^{(\Delta w)_P}d(\Delta w)=\frac{(\Delta w)_P}{\rho_a n_P\sqrt{2c_pT_a}} \tag{137}$$

Integrating (136) and using (129a), (129b), and (137) yield

$$\hat{\mu}=\int_0^{n_P}f\frac{q}{q_l}\frac{dn}{n_P}-\int_0^{n_P}g\left(\frac{q}{q_l}\right)^3\frac{dn}{n_P} \tag{138}$$

Let

$$\left.\begin{aligned}J&=\int_{\mathcal{C}_s}^{\mathcal{C}_P}\exp\left[-\frac{n_P}{2\Delta\mathcal{C}}(\mathcal{C}^2-\mathcal{C}_l^2)\right]\frac{d\mathcal{C}}{\Delta\mathcal{C}}\\ K&=\int_{\mathcal{C}_s}^{\mathcal{C}_P}\exp\left[-\frac{3n_P}{2\Delta\mathcal{C}}(\mathcal{C}^2-\mathcal{C}_l^2)\right]\frac{d\mathcal{C}}{\Delta\mathcal{C}}\end{aligned}\right\} \tag{139}$$

Using (126) and (139), equation (138) becomes

$$\hat{\mu}=fJ-gK \tag{140}$$

or

$$f=\frac{gK}{J}+\frac{\hat{\mu}}{J} \tag{141}$$

For $\mathcal{C}_s>\mathcal{C}_P$ the integrals in (139) can be simplified by a change of variables. Using

$$k^2=\frac{-n_P\mathcal{C}^2}{2\Delta\mathcal{C}} \tag{142}$$

equations (139) become

$$\left.\begin{aligned} J&=\frac{exp(-k_l^2)}{\sqrt{-\frac{\Delta \mathcal{C} n_P}{2}}}\int_{k_P}^{k_s} exp(k^2)\,dk \\ K&=\frac{exp(-3k_l^2)}{\sqrt{-\frac{3\Delta \mathcal{C} n_P}{2}}}\int_{\sqrt{3}k_P}^{\sqrt{3}k_s} exp(3k^2)\,d\sqrt{3}k \end{aligned}\right\} \quad (143)$$

The values of k_s and k_P are fixed by the channel geometry, and $\int_0^x exp(x^2)\,dx$ is available in standard tables.[1]

It is clear at this point that the velocities at each location on a potential line are known when a reference velocity q_l is known (see eq. (126)). The value of q_l is conveniently taken at the point of average streamline curvature so that $X-X_l$ in the binomial expansion previously used is small. In equation (140) the quantities $\hat{\mu}$, J, and K are known from the mass-flow requirements and passage geometry, and f and g are functions of X_l alone for fixed values of γ. As shown in figure 79, f can be plotted against $\sqrt{X_l}$ and hence against g. In order to satisfy equation (141), f and g satisfy a straight-line relation with slope K/J and an f intercept of $\hat{\mu}/J$. This line is shown in figure 79. The intercept of this straight line with the curve for f against g yields the proper value of X_l, and hence q_l. All other velocities are now obtainable from equation (126).

An outline for the procedure to be used follows:

(1) Given a cascade as shown in figure 80, with upstream velocity prescribed, draw in upstream and downstream streamlines, continuing the blade channel. Draw in an orthogonal net of approximate streamlines and potential lines.

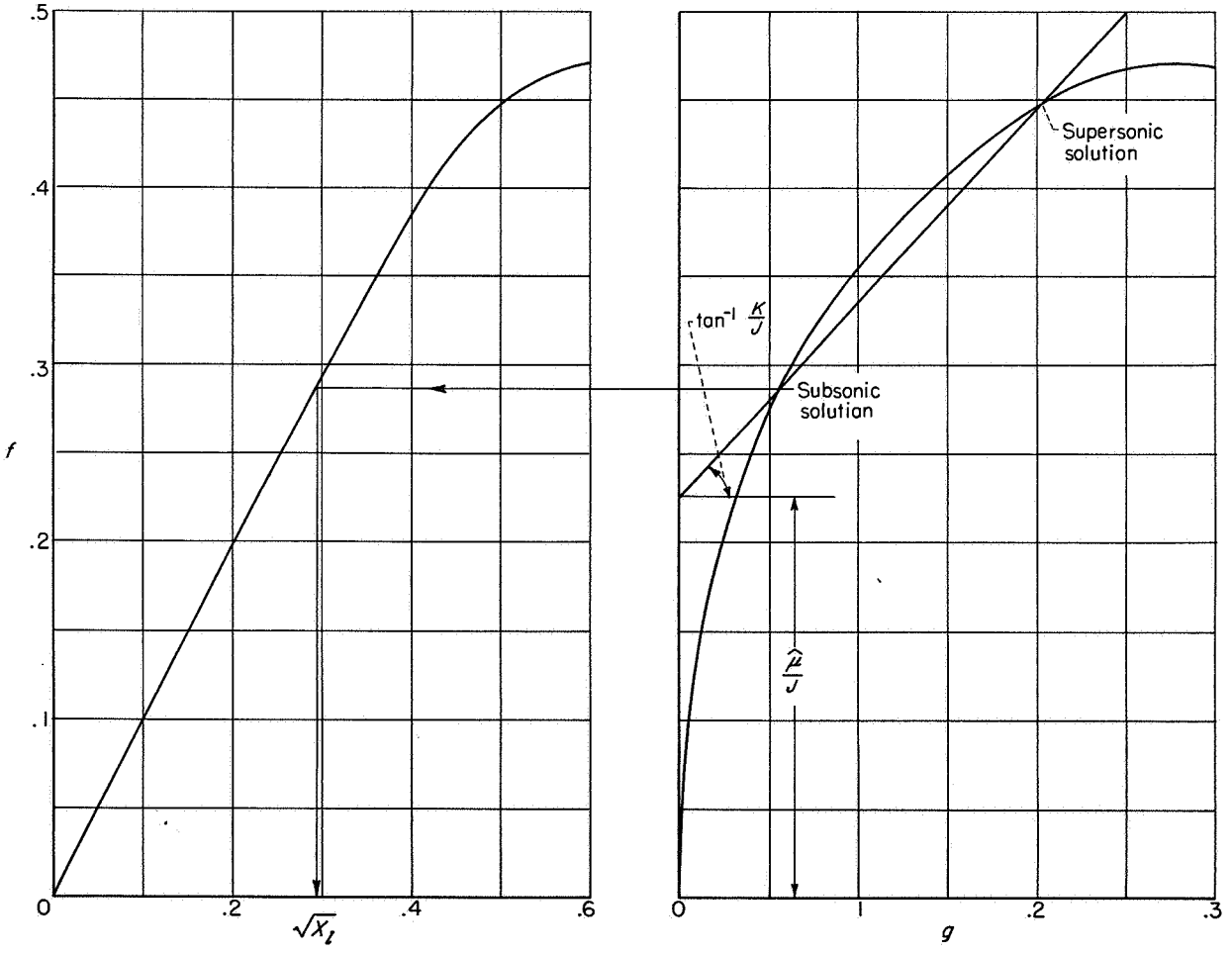

FIGURE 79.—Chart for determining average velocity in blade channel.

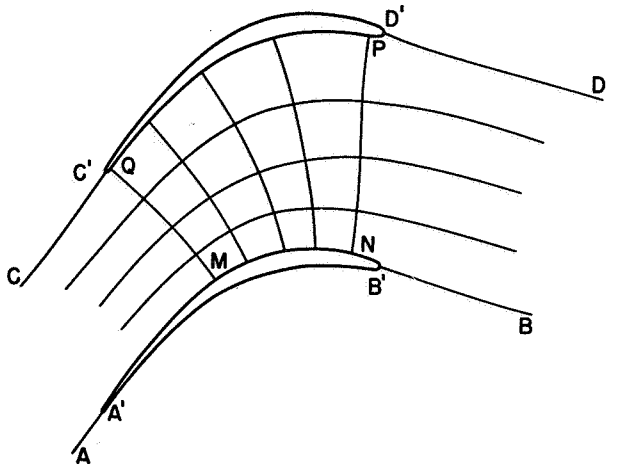

FIGURE 80.—High-solidity cascade showing streamlines and potential lines.

(2) Compute velocities at each node of the flow net. Since the streamlines AA′, B′B, CC′, and D′D are only approximate, good accuracy can be expected only in the region MNPQ of figure 80.

(3) Obtain the potential distribution along each streamline as a function of arc length l by integrating the velocity with respect to arc length. These values will be used in drawing new potential lines.

(4) New values of stream function are obtained by integrating ρq along the potential lines. These values are used in drawing new streamlines.

(5) An adjusted grid of potential lines and streamlines is drawn and new velocities are computed. The iteration is continued until convergence is obtained.

A solution obtained by this method in reference 124 for a turbine cascade is illustrated in figure 81. The solidity is 1.4 in the computed example. It must be noted, however, that solidity is not the only consideration for determining the applicability of the method. Blade thickness and stagger angle combine with solidity to determine the effective channel formed by adjacent blades. To apply the method successfully, it is necessary that a significant portion of the blade surface form part of the effective channel. In compressor designs this is often not the case, and care must be used in determining the applicability of the method.

Techniques are available to increase the region of validity of the stream-filament results. A solution can be obtained for two adjacent channels formed by three blades. The stagnation streamline attached to the center blade must be congruent to the other stagnation streamlines in the final result. This serves as a check on the assumed stagnation streamlines outside the blade region. An alternative check can be made on the validity of these assumed streamlines by integrating the velocity about a closed path in the region exterior to the blades and setting it equal to zero. Either of these techniques might require more accuracy than is obtainable by assuming a linear variation of curvature. If the actual measured curvatures are used, the additional work involved may be prohibitive.

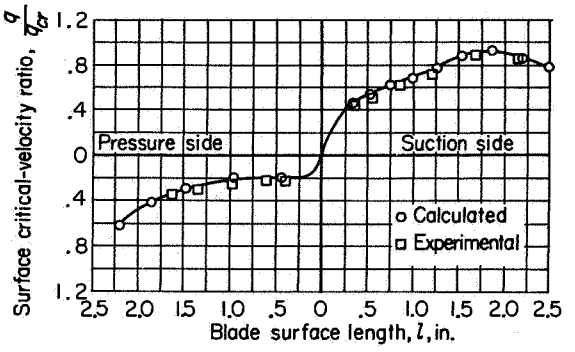

FIGURE 81.—Blade surface velocities at design conditions (ref. 124).

Relaxation and matrix solutions.—The technique presented herein is from reference 127. The basic differential equation is developed briefly, and the method of solving it is discussed in some detail.

The equation of continuity for a two-dimensional steady compressible flow is written

$$\frac{\partial(\rho q_x)}{\partial x}+\frac{\partial(\rho q_y)}{\partial y}=0 \tag{144}$$

Equation (144) will be satisfied if a stream function exists such that

$$\left.\begin{aligned}\frac{\partial \Psi}{\partial x}&=-\rho q_y\\ \frac{\partial \Psi}{\partial y}&=\rho q_x\end{aligned}\right\} \tag{145}$$

The equation arising from the condition of irrotational motion is given by

$$\frac{\partial q_x}{\partial y}-\frac{\partial q_y}{\partial x}=0 \tag{146}$$

Using equations (145) in equation (146) gives

$$\frac{\partial^2\Psi}{\partial x^2}+\frac{\partial^2\Psi}{\partial y^2}-\frac{1}{\rho}\left(\frac{\partial\rho}{\partial x}\frac{\partial\Psi}{\partial x}+\frac{\partial\rho}{\partial y}\frac{\partial\Psi}{\partial y}\right)=0 \quad (147)$$

Then, letting

$$B=\frac{-1}{\rho}\left(\frac{\partial\rho}{\partial x}\frac{\partial\Psi}{\partial x}+\frac{\partial\rho}{\partial y}\frac{\partial\Psi}{\partial y}\right) \quad (148)$$

equation (147) becomes

$$\frac{\partial^2\Psi}{\partial x^2}+\frac{\partial^2\Psi}{\partial y^2}+B=0 \quad (149)$$

Equation (149) is a nonlinear equation. If B were a known function of x and y, the equation would be linear. In the process of solution to be described herein, B will be treated as a known function of x and y in the first approximation. Then B will be adjusted from the results of the first approximate solution and will be held fixed while a second approximate solution is obtained, and so forth. That is, if a Ψ-distribution is known, B can be computed at each point in the field from this distribution. Then B will be held fixed at this set of values while new values of Ψ are computed from equation (149). Then B will be recalculated on the basis of the new Ψ values.

Equation (149) is the basic equation of the present analysis. There are two steps to the solution of this equation: (1) to replace the differential equation with a finite-difference equation, and (2) to solve the finite-difference equation at a representative set of points in the flow field.

Suppose a function $y=f(x)$ is known at $n+1$ values of x: $x_0, x_1, \ldots x_n$. It is assumed that $y=f(x)$ can be represented closely by a polynomial of degree n passing through the known points $(x_0, y_0), (x_1, y_1), \ldots (x_n, y_n)$. Such a polynomial P is given by (see ref. 128)

$$P_n(x)=\frac{(x-x_1)(x-x_2)\ldots(x-x_n)}{(x_0-x_1)(x_0-x_2)\ldots(x_0-x_n)}y_0 + \frac{(x-x_0)(x-x_2)\ldots(x-x_n)}{(x_1-x_0)(x_1-x_2)\ldots(x_1-x_n)}y_1+\ldots + \frac{(x-x_0)(x-x_1)\ldots(x-x_{n-1})}{(x_n-x_0)(x_n-x_1)\ldots(x_n-x_{n-1})}y_n \quad (150)$$

It is easily verified that this polynomial does pass through the required points. Furthermore, it is the only one that does, since $n+1$ points define an n^{th} degree polynomial uniquely. The polynomial $P_n(x)$ can be differentiated successively, the m^{th} derivative being written

$$P_n^m(x)=A_0y_0+A_1y_1+\ldots+A_ny_n \quad (151)$$

where the coefficients $A_0, \ldots A_n$ are seen to be functions of the order of the derivative, the degree of the polynomial representing the function, and the point at which the derivative is evaluated. Equations (150) and (151) are considerably simplified when the derivative is evaluated at one of the points $x_0, x_1, \ldots x_n$. They are further simplified when the intervals x_i-x_{i-1} are equal for $i=1, \ldots n$. The coefficients A^i are available in a table in reference 129 for derivatives up to the fourth order and for spacings such that the last interval on either end differs in length from the other intervals. (The tables for unequal intervals are very useful for writing the difference equations at curved boundaries where such unequal spacings do occur.) Polynomial representations up to the fourth degree are included, and an error term is given.

If it is assumed that the function Ψ can be represented by a polynomial over a small interval, equation (149) can be replaced by a finite-difference equation. In the nomenclature of reference 129, equation (149) can be written

$$\sum_{j=0}^{n}{}_n^2B_j^i\Psi^j+\sum_{k=0}^{n}{}_n^2B_k^i\Psi^k+B^i=0 \quad (152)$$

where B is a coefficient of Ψ corresponding to the coefficients A_n in equation (151). The presuperscript 2 of B represents the order of the derivative; the presubscript n is the degree of the polynomial representing Ψ. The postsuperscript i denotes the point at which the equation is being applied; the postsubscripts j and k indicate that the values of Ψ are taken along the x- and y-directions, respectively. To clarify this notion, a set of grid points is drawn in figure 82 in the neighborhood of a point P somewhere in the flow field. Suppose, for simplicity, that a second-degree polynomial is adequate to represent Ψ in the neighborhood of the point P. Then $n=2$ and, following the notation of figure 82, equation (152) can be written

$${}_2^2B_0^1\Psi^{j=0}+2{}_2^2B_1^1\Psi^{j=k=1}+{}_2^2B_2^1\Psi^{j=2} + {}_2^2B_0^1\Psi^{k=0}+{}_2^2B_2^1\Psi^{k=2}+B^1=0 \quad (153)$$

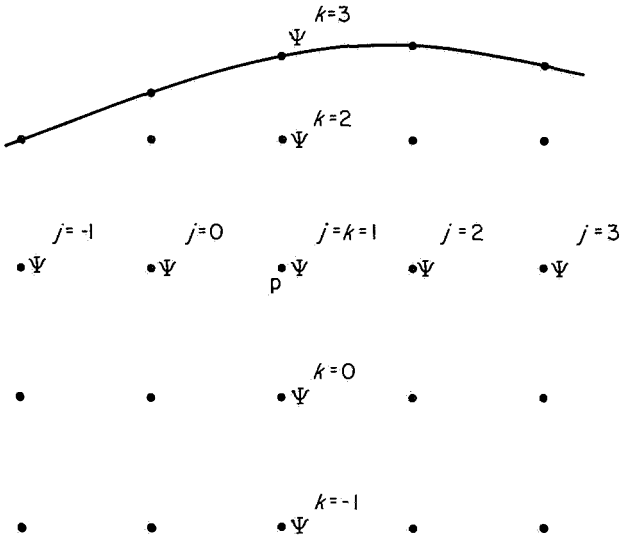

FIGURE 82.—A portion of grid used for finite-difference solution.

In this case the form of the coefficients ${}_2^2B_j^1$ and ${}_2^2B_k^1$ is quite simple over most of the flow region. At any point in the region that is surrounded by equally spaced points, equation (153) becomes

$$\Psi^{j=0}+\Psi^{j=2}+\Psi^{k=0}+\Psi^{k=2}-4\Psi^{j=k=1}+B^1=0$$

Only at the boundaries of the region where unequal spacing of the flow net occurs do the coefficients of equation (153) take different values.

Higher-degree polynomial representations could be used, resulting in more terms in equation (153). For example, a fourth-degree polynomial representation would involve additional terms containing $\Psi^{k=-1}$, $\Psi^{k=3}$, $\Psi^{j=-1}$, and $\Psi^{j=3}$ (fig. 82). In general, higher-degree polynomials substantially improve the approximation in regions of rapidly changing conditions. Increased accuracy can also be attained by decreasing the net size and hence increasing the number of points in the flow field at which a solution is found. Near the boundaries where unequally spaced grid points occur (e.g., where $\Psi=\Psi^{k=3}$ in fig. 82), the accuracy of the approximation often becomes critical, and higher-degree approximations or closer spacings are needed to achieve an accuracy comparable with that in other portions of the flow field. Additional points can be added in the course of solution if the accuracy of the results appears questionable.

Suppose the entire closed boundary ABFGCDHEA in figure 83 is fixed and the values of Ψ are known along this boundary. A network of equidistant points is placed on the flow field. The mesh size is taken sufficiently small that values of Ψ found at each point of the net will suffice to give a clear picture of the entire flow field. With the net size chosen, equation (153), or more generally equation (152), is used with the coefficients from reference 129 to determine a linear equation in the unknown values of Ψ at each nonboundary point of the net. It is clear that there will be N unknown values of Ψ if the net has N inner points (i.e., points which are not on the boundary). At each of these points a linear equation can be written involving some of the unknown values of Ψ. Thus, there is a system of N equations in N unknowns for determining the values of Ψ at each point.

Unfortunately, conditions along the entire boundary ABFGCDHEA in figure 83 are not known at the outset for a given cascade of blades and a given upstream vector velocity. The boundaries AB and CD, parallel to the y-axis, are located far enough upstream and downstream, respectively, that uniform flow across these boundaries can be reasonably expected. If it is discovered subsequently that uniform flow does not exist at these stations, they must be adjusted to positions farther removed from the blades. Two to three chord lengths from the blade edges is usually a sufficient distance. The lines AE and BF are drawn parallel to the upstream velocity vector; the lines GC and HD are drawn parallel to the downstream velocity vector. Satisfaction of the trailing-edge condition (Kutta condition in the case of a sharp trailing edge) cannot be achieved at the outset of the problem. Initially, the downstream velocity vector is assumed. After a solution has been obtained, the downstream flow angle can be adjusted to satisfy the trailing-edge condition and a second solution can be obtained.

With the geometry of the boundaries now fixed, the values of Ψ along these boundaries are considered. The stream function Ψ is constant along the blade surfaces, since these boundaries are streamlines in the flow. The value on the suction surface can be taken as zero, and the value on the pressure surface can be found from the required mass flow

$$\Psi_P-\Psi_s=\int_{y_s}^{y_P}\frac{\partial\Psi}{\partial y}\,dy=\int_{y_s}^{y_P}\rho q_x\,dy=\text{mass flow}$$

Outside the blade channel the boundaries are not

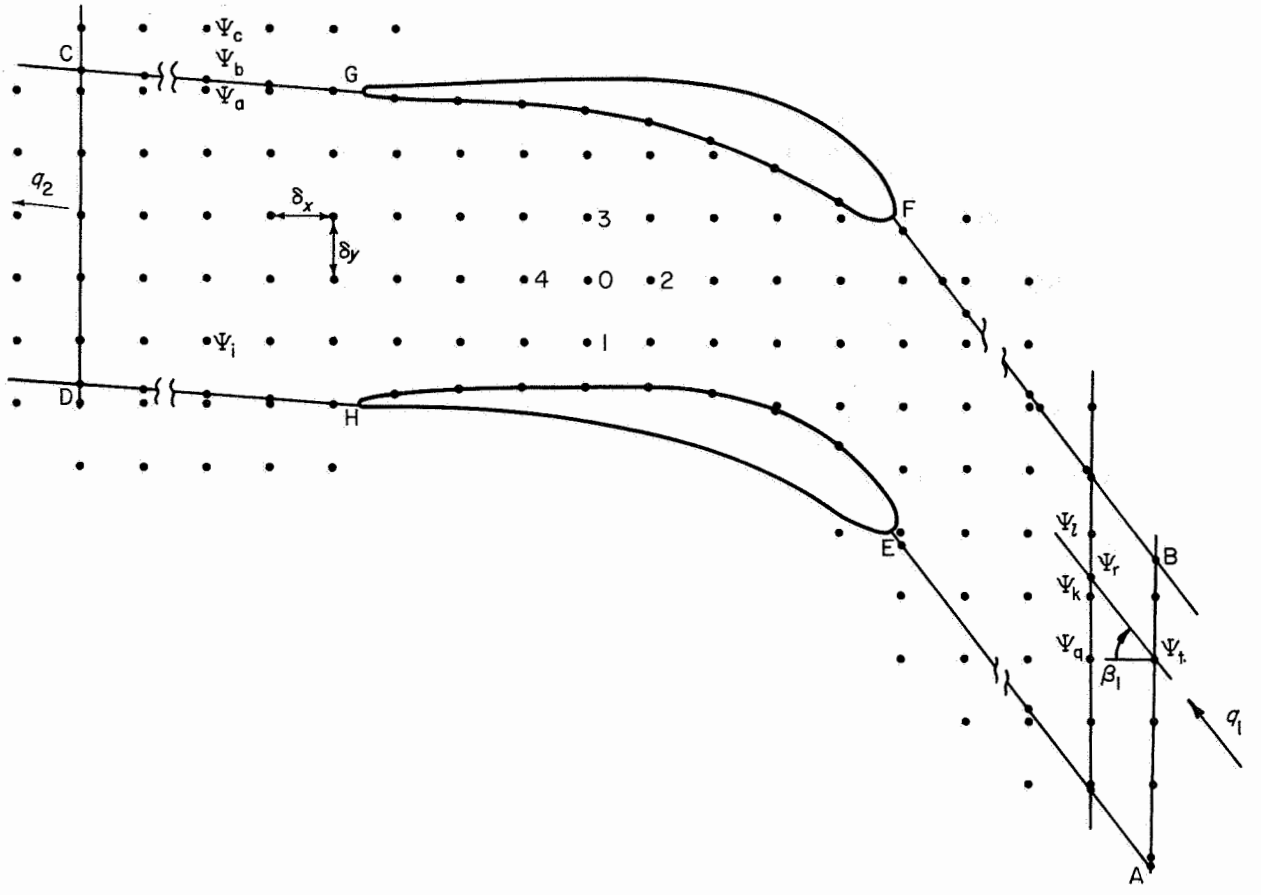

FIGURE 83.—Cascade channel showing grid points and boundary of solution.

streamlines, and the values of Ψ on these boundaries are neither constant nor known. However, since the flow is periodic in the direction of the y-axis (with period equal to the spacing of the blades), the values of Ψ need not be known. For example, consider the point at which $\Psi=\Psi_a$ in figure 83. Normally the boundary value Ψ_b would enter into the finite-difference expression about Ψ_a, but in this case Ψ_b is not known. Instead, the finite-difference expression about Ψ_a is written in terms of Ψ_c. Furthermore, $\Psi_c=\Psi_i+(\Psi_P-\Psi_s)$ because of the periodic nature of the flow: In this way the finite-difference expression about Ψ_a contains only values of Ψ at inner points. Thus, Ψ values have been determined everywhere except on the vertical boundaries.

To write the finite-difference expression about the point where $\Psi=\Psi_q$ in figure 83, the value of Ψ_t would normally be used. However, this value does not need to be known explicitly, since the following relation results from the linearity of Ψ:

$$\Psi_t=\Psi_r=\frac{2\delta_y-\delta_x \tan \beta_1}{2\delta_y}\Psi_q+\frac{\delta_x \tan \beta_1}{2\delta_y}\Psi_l$$

Since Ψ_q and Ψ_l are unknown values of Ψ at two inner points of the field, the finite-difference expression involving them is satisfactory for this solution. The same type of relation can be used at the downstream boundary.

A second method to satisfy these vertical boundary conditions is presented in reference 127. Although the second method is not as simple and accurate as the first, it has the advantage of not directly involving the inlet angle in the expressions for the boundary conditions. This characteristic is useful if the problem is being solved by matrices, for in that case other angles of inflow can be investigated with much less effort. This method will not be discussed further but can be found in detail in reference 127.

Suppose now that there are N inner grid points in the grid selected for the problem. Applying

691-564 O-65-10

equation (149) to each point yields N simultaneous linear equations in N unknowns. (The B' are not known and must be given an assumed value.) Now the problem is one of solving this set of simultaneous equations, by either a relaxation process (indirect) or a matrix process (direct). The latter process is too lengthy for hand computation when a reasonable number of grid points is used. Both methods are discussed in detail in references 129 and 130 and are indicated briefly in appendixes C and D of this chapter, respectively.

When the values of Ψ have been obtained at each interior point by some process, the nonlinear term B in equation (149) must be recalculated on the basis of these Ψ values. A second solution is then carried out. With the relaxation technique, it may be advantageous to recalculate the B' in the middle of a cycle if the changes in Ψ have been large. This is, of course, not possible in a matrix solution. In either case, the initial Ψ values estimated for relaxation and the B' values estimated for matrices should be as close as possible to the final answer to obtain rapid convergence. The question of convergence has not been considered mathematically. In most examples that have been carried out so far, convergence has occurred.

Some difficulty has been encountered at the Lewis laboratory in obtaining convergence at high subsonic Mach numbers when equation (147) is used. From equation (148) it is seen that B contains first derivatives of ρ and hence second derivatives of Ψ. More rapid convergence could be expected if all second-derivative terms in equation (149) were to be included in the operative part of the equation rather than in the field function B. As in reference 120, equation (147) can be rewritten as

$$\frac{\partial^2\Psi}{\partial x^2}\left[1-\left(\frac{\rho_a}{\rho a}\frac{\partial\Psi}{\partial y}\right)^2\right]+\frac{\partial^2\Psi}{\partial y^2}\left[1-\left(\frac{\rho_a}{\rho a}\frac{\partial\Psi}{\partial x}\right)^2\right]+2\left(\frac{\rho_a}{\rho a}\right)^2\frac{\partial^2\Psi}{\partial x\partial y}\frac{\partial\Psi}{\partial x}\frac{\partial\Psi}{\partial y}=0 \quad (154)$$

where $(\rho_a/\rho a)^2$ is a function of q and hence of $(\partial\Psi/\partial x)^2+(\partial\Psi/\partial y)^2$. Equation (154) is linearized by writing

$$A\frac{\partial^2\Psi}{\partial x^2}+B\frac{\partial^2\Psi}{\partial y^2}+C\frac{\partial^2\Psi}{\partial x\partial y}=0 \quad (155)$$

where

$$A=1-\left(\frac{\rho_a}{\rho a}\frac{\partial\Psi}{\partial y}\right)^2$$

$$B=1-\left(\frac{\rho_a}{\rho a}\frac{\partial\Psi}{\partial x}\right)^2$$

$$C=2\frac{\partial\Psi}{\partial x}\frac{\partial\Psi}{\partial y}\left(\frac{\rho_a}{\rho a}\right)^2$$

The coefficients A, B, and C are field functions (corresponding to B in eq. (149)) containing only first derivatives of Ψ. A complication is thus introduced into the coefficients of the finite-difference expressions, but convergence is expected to be more rapid.

The results of an example computed in reference 127 by the relaxation process and equation (148) for a turbine cascade are reproduced in figure 84. The method is easily adapted to a general surface of revolution (see ref. 127).

THE INVERSE PROBLEM

Since the physical boundaries of the flow channel (i.e., the blade surfaces) are not known for the inverse problem, the relaxation and matrix solutions have not been used in the physical plane. A method has been developed, however, by Stanitz (ref. 131) and by Stanitz and Sheldrake (ref. 132) to solve the equations governing the fluid motion when the stream and potential functions replace the Cartesian coordinates as independent varia-

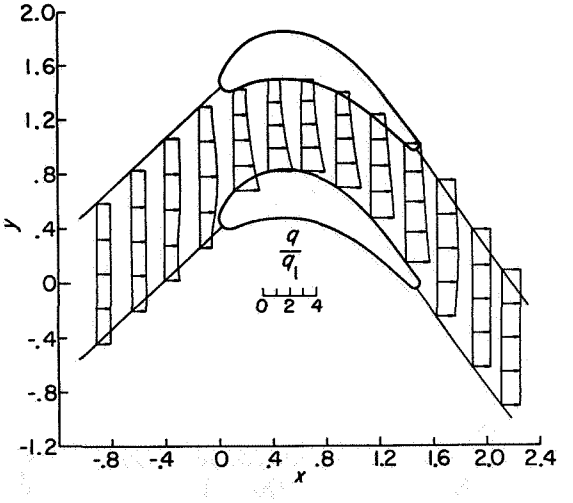

FIGURE 84.—Variation of magnitude of resultant velocity across channel for compressible-flow solution. Inlet Mach number, 0.42 (ref. 127).

bles. Relaxation and matrix techniques can be employed in this $\Phi\Psi$-plane.

Some simpler approximate techniques are available. Ackeret (ref. 133) replaced the cascade of closely spaced blades by a continuous distribution of vortices and sources, periodic in the direction of the y-axis. This infinite strip of singularities yields an approximate velocity distribution and approximate thickness. A blade shape is then computed. The method is iterative in nature but does not require as much time as the exact solutions. Sawyer employed this method to design a cascade (ref. 134) for testing purposes. The time required for the complete theoretical solution was approximately 40 hours.

In reference 135, Alpert developed a method for designing a channel when the shape of one wall is known and a velocity distribution is prescribed on that wall. Although this appears to overprescribe the problem, the author necessarily uses only a finite number of points in actually obtaining a solution. A solution progresses from one streamline to the next, away from the known wall. The method is easily and rapidly carried out with the aid of tables the author has prepared. An example is worked by this method, but no comparison with an exact theoretical solution is made.

The method of expansion by power series is presented by Wu and Brown in reference 126 for the inverse problem as well as the direct problem. The same limitations to the method apply as those discussed previously for the direct problem.

A rapid approximate method is presented by Stanitz in reference 136. The assumptions made in the method are realized to a sufficient degree in a closely spaced cascade, but the nose and tail sections cannot be included in the design. A comparison of the results obtained by the author with stream-filament solutions showed good agreement. It should be pointed out, however, that the method is essentially limited to angles of incidence such that the mean streamlines enter the blade channel with curvatures close to the mean blade curvature. This approximate design method, which enables a practical and rapid solution, is presented in some detail in the following section. The exact solution by relaxation in the $\Phi\Psi$-plane (refs. 131 and 132) is also presented.

Approximate method.—The design method to be presented (ref. 136) is not applicable in the immediate regions of the leading and trailing edges of the cascade blade, where the small radii of curvature of the blade sections invalidate the assumptions made in the method. When a pressure distribution is prescribed on the channel surfaces as a function of dimensionless distance $\hat{x}$ along the x-axis,[2] along with the upstream and downstream vector velocities, the solution will yield the channel shape in the region of validity.

Two important assumptions are made underlying the use of the method. At a given value of $\hat{x}$, it is assumed that (1) the mass-weight average flow direction is the same as the direction of the blade-element camber line, and (2) the mass-weight average velocity is equal to one-half the sum of the velocities prescribed on the suction and pressure surfaces.

The solidity σ can be defined as

$$\sigma=\frac{1}{\hat{s}} \tag{156}$$

Then the thickness ratio $\hat{\nu}$ is defined as

$$\hat{\nu}=\frac{\hat{b}}{\hat{s}} \tag{157}$$

The blade-element profile is determined from σ and from $\hat{\nu}$ and β as functions of $\hat{x}$. The method of this section is concerned with a determination of these quantities.

Consider an elemental strip of axial depth $d\hat{x}$. The tangential force on the strip of fluid can be equated to the rate of change in momentum in the tangential direction as follows:

$$\bar{x}(p_P-p_s)\,d\hat{x}=\Delta w\,dq_v \tag{158}$$

where Δw is the rate of mass flow in the channel formed by the two adjacent blades. Equation (158) can be written as

$$(p_P-p_s)\,d\hat{x}=\hat{s}\left(\frac{\Delta w}{\bar{x}\hat{s}}\right)dq_v \tag{159}$$

where $\Delta w/\bar{x}\hat{s}$ is the average rate of mass flow per unit area of the cascade channel. Then, from equations (156) and (159), it follows that

$$\sigma\int_{\hat{x}=0}^{\hat{x}=1}(p_P-p_s)\,d\hat{x}=\frac{\Delta w}{\bar{x}\hat{s}}\,(q_{v_2}-q_{v_1})$$

[2] All linear quantities are considered to be made dimensionless by division by $\bar{x}$, where $\bar{x}$ is the axial length of the assumed region of validity of the solution.

or

$$\sigma=\frac{\frac{\Delta w}{\bar{x}\hat{s}}(q_{v_2}-q_{v_1})}{\int_{\hat{x}=0}^{\hat{x}=1}(p_P-p_s)\,d\hat{x}} \tag{160}$$

The pressure p is determined from the prescribed velocity q and from given stagnation conditions by the equation

$$p=P\left(1-\frac{\gamma-1}{2a_a^2}q^2\right)^{\frac{\gamma}{\gamma-1}} \tag{161}$$

Since q_P and q_s are prescribed, p_P and p_s are calculable from equation (161), and σ is known from equation (160). With σ known, q_v can be calculated at any value of $\hat{x}$ from

$$q_v=q_{v_1}+\frac{\sigma\bar{x}\hat{s}}{\Delta w}\int_{\hat{x}=0}^{\hat{x}}(p_P-p_s)\,d\hat{x} \tag{162}$$

The average flow angle β is given by

$$\beta=\sin^{-1}\left(\frac{q_v}{q}\right)\qquad\frac{-\pi}{2}\leqq\beta\leqq\frac{\pi}{2} \tag{163}$$

where q is given by

$$q=\frac{q_s+q_P}{2} \tag{164}$$

Thus, from equations (160) to (164) the solidity and the β-distribution are obtainable. The value $\hat{\nu}$ will now be obtained from continuity considerations, whereby

$$\Delta w=\rho q(\hat{s}-\hat{b})\bar{x}\cos\beta$$

Since $\hat{b}=\hat{\nu}\hat{s}$,

$$\frac{\Delta w}{\bar{x}\hat{s}}=\rho q(1-\hat{\nu})\cos\beta$$

and

$$\hat{\nu}=1-\frac{\Delta w}{\rho q\bar{x}\hat{s}\cos\beta} \tag{165}$$

where the density is given by

$$\rho=\rho_a\left(1-\frac{\gamma-1}{2a_a^2}q^2\right)^{\frac{1}{\gamma-1}} \tag{166}$$

Applying the continuity requirement upstream and downstream of the cascade gives

$$\frac{\Delta w}{\bar{x}\hat{s}}=\rho_1 q_1\cos\beta_1=\rho_2 q_2\cos\beta_2 \tag{167}$$

This condition must be satisfied by the prescribed quantities q_1, q_2, β_1, and β_2.

Following is a step-by-step procedure for solving a given problem:

(1) Prescribe the quantities q_1, q_2, β_1, and β_2 so that equation (167) is satisfied.

(2) Prescribe q_s and q_P as functions of $\hat{x}$.

(3) Find $\Delta w/\bar{x}\hat{s}$ from equation (167).

(4) Find p_P and p_s as functions of $\hat{x}$ from equation (161).

(5) Find σ from equation (160).

(6) Find q_v from equation (162).

(7) Find q from equation (164).

(8) Find β from equation (163).

(9) Find $\hat{\nu}$ from equation (165).

(10) Compute the equation of the blade mean camber line from

$$\hat{y}=\int_0^{\hat{x}}\frac{q_v}{q\cos\beta}\,d\hat{x}=\int_0^{\hat{x}}\tan\beta\,d\hat{x}$$

(11) Distribute the blade thickness $\hat{b}$ symmetrically about the mean camber line.

(12) Fair in leading- and trailing-edge sections.

The preceding method is given in reference 136 in a form applicable to a general surface of revolution as well as to a plane cascade. Figure 85 shows the prescribed velocity distribution for a plane cascade computation (ref. 136) along with a stream-filament analysis of the final blade shape obtained.

Exact method.—As mentioned previously, the difficulty in applying the matrix and relaxation techniques for solving differential equations to the design problem arises from the fact that the physical boundaries are not known. In a report by Stanitz (ref. 131), the equations governing the motion of the fluid are written in terms of the $\Phi\Psi$-coordinates, for in these coordinates the boundary location is known. The assumptions made in this solution are that the flow is nonviscous, two-dimensional, and irrotational. The problem of designing an infinite channel will be treated first, and this problem will then be adapted to cascade design.

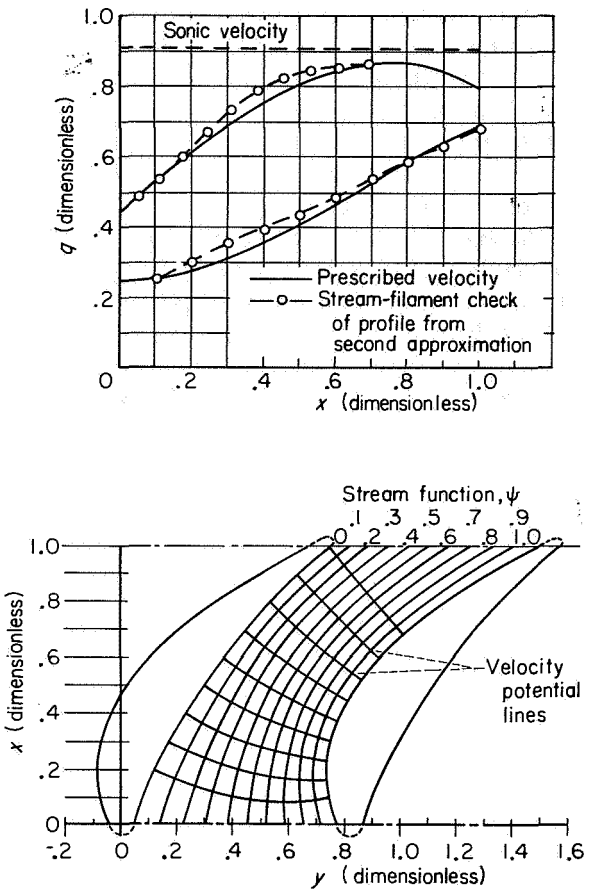

FIGURE 85.—Prescribed velocity distribution and resulting blade shape obtained by method of reference 136.

At each point in the channel, the velocity has a magnitude q and a direction β with the positive x-axis.

From the condition of continuity, a stream function Ψ can be defined such that

$$d\Psi=\rho q\, dn \tag{168}$$

Similarly, from the condition of irrotationality, a potential function Φ can be defined such that

$$d\Phi=q\, dl \tag{169}$$

where dl is an increment taken along a streamline and dn is an increment in a direction normal to the streamline. It is clear from equations (168) and (169) that Ψ is constant along a streamline and Φ is constant along a line normal to the streamlines (potential line). The channel boundaries in the physical plane (xy-plane) are streamlines in the flow. Hence, these lines will become constant values of Ψ in the transformed $\Phi\Psi$-plane (i.e., the curved channel in the xy-plane will become an infinite strip in the $\Phi\Psi$-plane). Furthermore, the distribution of velocity as a function of Φ along the boundaries is known, since the velocity

$$q=q(l) \tag{170}$$

is prescribed as a function of arc length in the physical plane; therefore, equation (169) integrates to give

$$\Phi=\Phi(l) \tag{171}$$

From equations (170) and (171),

$$q=f(\Phi) \tag{172}$$

Thus, the boundary conditions in the transformed plane are known, and only the equations governing the flow in the transformed plane are needed to complete the setup of the problem.

The continuity and irrotationality equations in the $\Phi\Psi$-plane are developed in reference 131 and are, respectively,

$$\frac{1}{\rho}\left(\frac{\partial \log \rho}{\partial \Phi}+\frac{\partial \log q}{\partial \Phi}\right)+\frac{\partial \beta}{\partial \Psi}=0 \tag{173}$$

$$\rho\frac{\partial \log q}{\partial \Psi}-\frac{\partial \beta}{\partial \Phi}=0 \tag{174}$$

Differentiating equations (173) and (174) with respect to Φ and Ψ, respectively, and combining to eliminate $\partial^2\beta/\partial\Phi\partial\Psi$ yield

$$\frac{\partial^2 \log \rho}{\partial \Phi^2}+\frac{\partial^2 \log q}{\partial \Phi^2}-\frac{\partial \log \rho}{\partial \Phi}\left(\frac{\partial \log \rho}{\partial \Phi}+\frac{\partial \log q}{\partial \Phi}\right)+\rho^2\frac{\partial \log q}{\partial \Psi}\frac{\partial \log \rho}{\partial \Psi}+\rho^2\frac{\partial^2 \log q}{\partial \Psi^2}=0 \tag{175}$$

This equation, together with the relation (166) between velocity and density, determines the distribution of $\log q$ in the $\Phi\Psi$-plane. Equation (175) can be solved by relaxation methods (appendix C) or matrix methods (appendix D). When the distribution of $\log q$ has been found throughout the channel for a given distribution of q along the boundaries, the distribution of β can be found along each streamline (constant Ψ) by integrating

equation (174):

$$\beta=\int_{\Psi}\rho\frac{\partial \log q}{\partial\Psi}\,d\Phi \tag{176}$$

The distribution of β can be found along each potential line from equation (173):

$$\beta=-\int_{\Phi}\frac{1}{\rho}\left(\frac{\partial \log \rho}{\partial\Phi}+\frac{\partial \log q}{\partial\Phi}\right)d\Psi \tag{177}$$

At each point in the xy-plane,

$$\left.\begin{aligned} dx&=dl\cos\beta\\ dy&=dl\sin\beta\end{aligned}\right\} \tag{178}$$

Using equations (178) with equations (168) and (169) gives

$$\left.\begin{aligned} x&=\int_{\Psi}\frac{\cos\beta}{q}\,d\Phi\\ x&=-\int_{\Phi}\frac{\sin\beta}{\rho q}\,d\Psi\\ y&=\int_{\Psi}\frac{\sin\beta}{q}\,d\Phi\\ y&=\int_{\Phi}\frac{\cos\beta}{\rho q}\,d\Psi\end{aligned}\right\} \tag{179}$$

Equations (179) give the relation between a point (x, y) in the physical plane and a point (Φ, Ψ) in the transformed plane. In this fashion, the shape of the physical channel that produces the prescribed velocity distribution is found.

This method is adapted in reference 131 to a flow governed by a linear pressure-volume relation. Solutions of two problems, having the same prescribed boundary conditions, are compared for a compressible flow and a linearized compressible flow. The resulting channels are quite similar. Under the assumption of a linearized compressible flow, the following equiation for the turning angle is given:

$$\Delta\beta=-\frac{1}{\Delta\Psi}\int_{-\infty}^{\infty}\Phi\left\{\left[\frac{\partial \log_e\left(\frac{q}{1+\sqrt{1+q^2}}\right)}{\partial\Phi}\right]_{\Delta\Psi}-\left[\frac{\partial \log_e\left(\frac{q}{1+\sqrt{1+q^2}}\right)}{\partial\Phi}\right]_{0}\right\}d\Phi \tag{180}$$

where the subscripts $\Delta\Psi$ and 0 refer to the channel boundaries. In the cascade design problem, equation (180) enables the designer to prescribe a velocity distribution that is consistent with the prescribed turning angle.

In figure 86 a cascade is shown with the stagnation streamline drawn in. The cascade can be formed by the "islands" between adjacent channels. The cascade design problem then becomes a problem in channel design. The channel design method considered in the preceding paragraphs does not allow zero velocities on the channel surfaces. This results in cusps on the leading and trailing edges of the islands, which must be rounded off to form a blade.

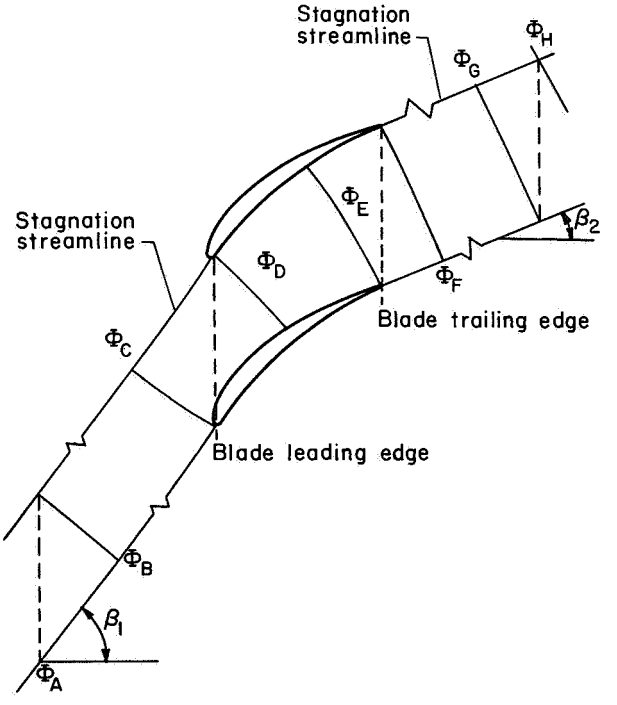

FIGURE 86.—Related potentials on cascade.

In applying the channel design method to a cascade design, it is necessary to determine the position of the leading and trailing edges on both suction and pressure surfaces in the $\Phi\Psi$-plane. From figure 86 it is seen that

$$\Phi_C-\Phi_A=\Phi_D-\Phi_B$$

from which

$$\Phi_D-\Phi_C=\Phi_B-\Phi_A \tag{181}$$

But conditions are uniform far upstream, so that

$$\Phi_B-\Phi_A=\frac{\Delta\Psi \tan \beta_1}{\rho_1}=\Phi_D-\Phi_C \qquad (182)$$

where $\Delta\Psi$ is the change in Ψ from one channel surface to the other. Similarly (see fig. 86),

$$\Phi_F-\Phi_E=\frac{\Delta\Psi \tan \beta_2}{\rho_2}=\Phi_H-\Phi_G \qquad (183)$$

Equations (182) and (183) determine the relative positions on the boundaries in the $\Phi\Psi$-plane that correspond to the leading and trailing edges of the blade, respectively.

The design procedure for a cascade of blades can now be formulated. A linear pressure-volume relation is assumed so that equation (180) can be used:

(1) Prescribe a cascade turning angle.

(2) Prescribe a velocity distribution.

(3) Adjust the velocity distribution so that equations (180), (182), and (183) are satisfied.

(4) Solve the resulting channel problem by the technique described in the preceding paragraphs.

An impulse cascade with 90° turning is investigated in reference 132. The prescribed velocity distribution on the suction surface and the final cascade obtained are presented in figure 87.

ANALOG TECHNIQUES

For many years attempts have been made to establish relations between the flow of compressible fluids and other physical problems that can be solved by nonanalytic techniques. Two physical problems have no mathematical individuality if the governing equations are the same (i.e., the same except for a possible change in nomenclature). This fact is utilized in the analogs considered in the present section.

As a result of the importance of experimental technique in most analog methods, such methods cannot be satisfactorily evaluated on the basis of theoretical correctness. In fact, the theory is generally of quite a simple nature, and the real problems involved are problems of operational technique. Because of this and because of the tremendous extent of the literature in this field, no attempt is made herein to evaluate individual contributions, some of which are discussed in references 137 to 148.

This section is concerned only with compressible flow. The incompressible-flow problem, resulting as it does in a Laplace equation, is the simpler to solve directly and to analogize. The basic theory is developed for several important types of analog that have been used successfully.

HYDRAULIC ANALOG

Consider the irrotational flow of water with a free surface over a horizontal plane. Bernoulli's equation for a stream filament of this flow can be written

$$p+\frac{\rho}{2}v^2+\rho gz=p_0+\frac{\rho}{2}v_0^2+\rho gz_0 \qquad (184)$$

The subscript 0 refers to conditions at a given point through which the filament passes, g is the acceleration due to gravity, and z is the coordinate in the vertical direction. If the flow emanates from a tank of sufficiently large volume, the velocity in the tank can be considered zero. Then, if the reference point is taken in the tank, equation (184) becomes

$$p+\frac{\rho}{2}v^2+\rho gz=P+\rho gz_0$$

or

$$v^2=\frac{2}{\rho}(P-p)+2g(z_0-z) \qquad (185)$$

A simplifying assumption is now made that the acceleration in the vertical direction at any point is negligible when compared with the acceleration due to gravity. This assumption (not always sufficiently realized, see ref. 137) leads to the relations

$$\left.\begin{aligned} P&=\rho g(D_0-z_0)\\ p&=\rho g(D-z)\end{aligned}\right\} \qquad (186)$$

where D is the height of the water surface. Using equations (186) in equation (185) yields

$$v^2=2g(D_0-D) \qquad (187a)$$

The maximum attainable velocity is given by

$$v_{max}=\sqrt{2gD_0} \qquad (188a)$$

Combining equations (187a) and (188a) yields

$$\left(\frac{v}{v_{max}}\right)^2=\frac{D_0-D}{D_0} \qquad (189a)$$

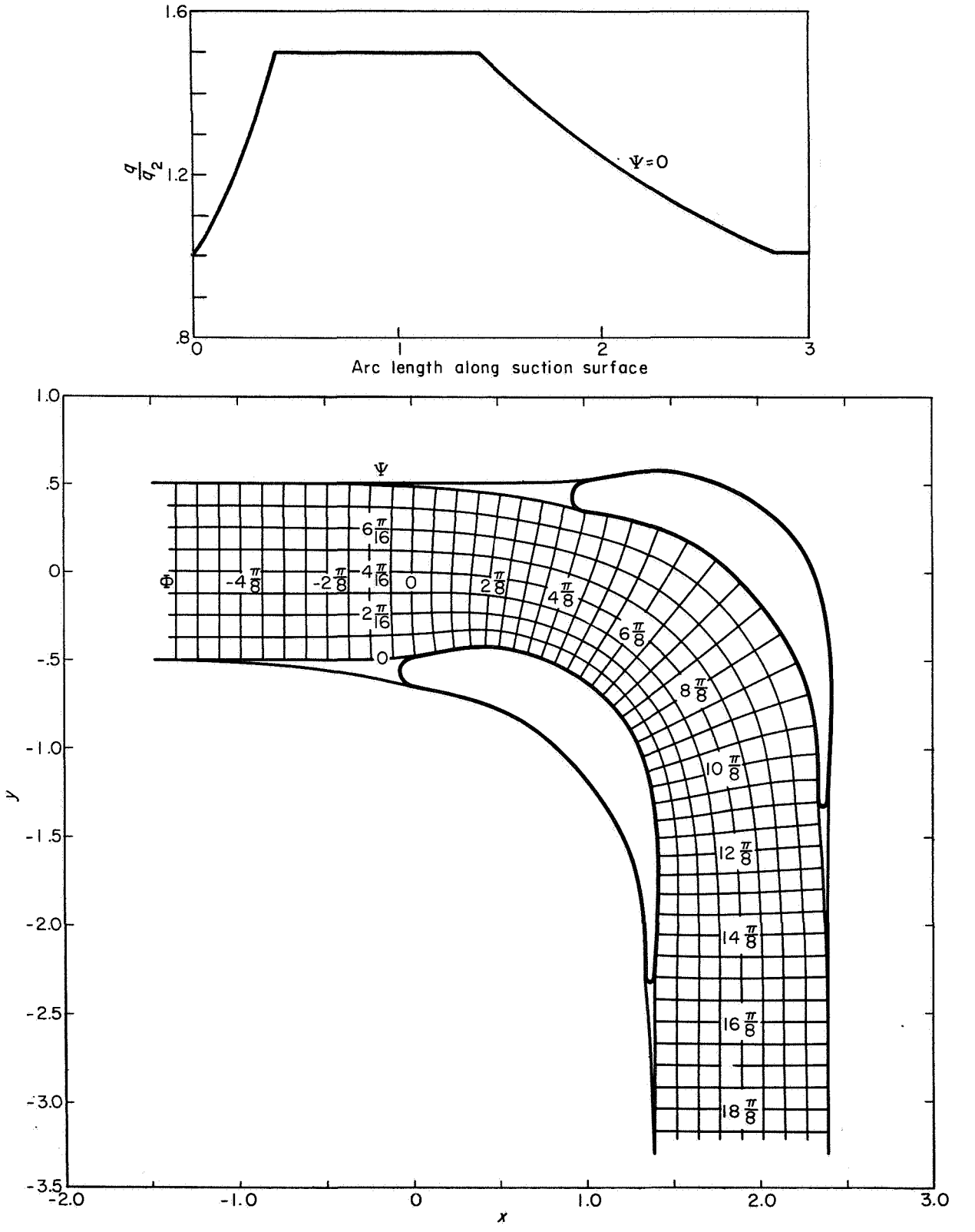

FIGURE 87.—Prescribed suction-surface velocity with resulting blade shape for impulse cascade with 90° turning (obtained by method of ref. 132).

The continuity equation for this flow is

$$\frac{\partial(Dv_x)}{\partial x}+\frac{\partial(Dv_y)}{\partial y}=0 \tag{190a}$$

The irrotationality condition is utilized as follows: From equation (187a), since the flow is essentially two-dimensional,

$$\left.\begin{aligned}\frac{\partial D}{\partial x}&=-\frac{1}{2g}\frac{\partial(v^2)}{\partial x}=-\frac{1}{g}\left(v_x\frac{\partial v_x}{\partial x}+v_y\frac{\partial v_y}{\partial x}\right)\\ \frac{\partial D}{\partial y}&=-\frac{1}{2g}\frac{\partial(v^2)}{\partial y}=-\frac{1}{g}\left(v_x\frac{\partial v_x}{\partial y}+v_y\frac{\partial v_y}{\partial y}\right)\end{aligned}\right\} \tag{191}$$

Equation (190a) is rewritten as

$$D\left(\frac{\partial v_x}{\partial x}+\frac{\partial v_y}{\partial y}\right)+v_x\frac{\partial D}{\partial x}+v_y\frac{\partial D}{\partial y}=0 \tag{192}$$

Then, substituting equation (191) into (192) yields

$$\frac{\partial v_x}{\partial x}\left(1-\frac{v_x^2}{gD}\right)+\frac{\partial v_y}{\partial y}\left(1-\frac{v_y^2}{gD}\right)-\frac{v_xv_y}{gD}\left(\frac{\partial v_x}{\partial y}+\frac{\partial v_y}{\partial x}\right)=0 \tag{193}$$

If the flow is irrotational, $\frac{\partial v_x}{\partial y}-\frac{\partial v_y}{\partial x}=0$ and a velocity potential $\Phi(x,y)$ exists such that

$$\left.\begin{aligned}v_x&=\frac{\partial\Phi}{\partial x}\\ v_y&=\frac{\partial\Phi}{\partial y}\end{aligned}\right\} \tag{194}$$

Using equations (194) in equation (193) yields

$$\frac{\partial^2\Phi}{\partial x^2}\left[1-\frac{\left(\frac{\partial\Phi}{\partial x}\right)^2}{gD}\right]+\frac{\partial^2\Phi}{\partial y^2}\left[1-\frac{\left(\frac{\partial\Phi}{\partial y}\right)^2}{gD}\right]-2\frac{\partial^2\Phi}{\partial x\partial y}\frac{\frac{\partial\Phi}{\partial x}\frac{\partial\Phi}{\partial y}}{gD}=0 \tag{195a}$$

These are the fundamental equations governing the flow of water under the conditions specified. They will now be compared with the fundamental equations governing the two-dimensional irrotational flow of a compressible fluid. The energy equation for the fluid flow can be written as

$$q^2=2gc_p(T-t) \tag{187b}$$

The maximum local velocity is given by

$$q_{max}=\sqrt{2gc_pT} \tag{188b}$$

Then,

$$\left(\frac{q}{q_{max}}\right)^2=\frac{T-t}{T} \tag{189b}$$

Therefore, if the velocity ratio of the gas flow is equated to the velocity ratio of the water flow, equations (189a) and (189b) yield

$$\frac{D_0-D}{D_0}=\frac{T-t}{T}$$

or

$$\frac{D}{D_0}=\frac{t}{T} \tag{196}$$

The continuity equation for the gas flow is written

$$\frac{\partial(\rho q_x)}{\partial x}+\frac{\partial(\rho q_y)}{\partial y}=0 \tag{190b}$$

Comparing equations (190a) and (190b) yields the further condition for the analogy that

$$\frac{\rho}{\rho_a}=\frac{D}{D_0} \tag{197}$$

For adiabatic isentropic flow, the temperature and density of the gas are related by

$$\frac{\rho}{\rho_a}=\left(\frac{t}{T}\right)^{\frac{1}{\gamma-1}} \tag{198}$$

An examination of equations (196) and (197) indicates that $\rho/\rho_a=t/T$ in the analogy, so that $\gamma=2$. Pressures are obtained from

$$\frac{p}{P}=\left(\frac{\rho}{\rho_a}\right)^\gamma=\left(\frac{\rho}{\rho_a}\right)^2=\left(\frac{D}{D_0}\right)^2 \tag{199}$$

This value of γ is not valid for any real gas. However, since many relations are not significantly affected by using a value of γ slightly different from the true value, it should be possible to obtain at least qualitatively correct results.

The potential-flow equation for the gas is

$$\frac{\partial^2\Phi}{\partial x^2}\left[1-\frac{\left(\frac{\partial\Phi}{\partial x}\right)^2}{a^2}\right]+\frac{\partial^2\Phi}{\partial y^2}\left[1-\frac{\left(\frac{\partial\Phi}{\partial y}\right)^2}{a^2}\right]-2\frac{\partial^2\Phi}{\partial x\partial y}\frac{\frac{\partial\Phi}{\partial x}\frac{\partial\Phi}{\partial y}}{a^2}=0 \tag{195b}$$

Comparison of equations (195a) and (195b) shows that

$$\frac{gD}{2gD_0}=\frac{a^2}{2gc_pT} \tag{200}$$

Thus, $\sqrt{gD}$ compares with the velocity of sound in the gas flow. It is known from the literature on hydraulics that $\sqrt{gD}$ corresponds to the speed of propagation of long surface waves. The ratio $v/\sqrt{gD}$ in liquid flow is seen to correspond to the Mach number q/a in gas flow. Liquid flows with $v/\sqrt{gD}<1$ are called "streaming" and with $v/\sqrt{gD}>1$ are called "shooting." The difference in the character of the equations governing subsonic and supersonic compressible flows exists also in the equations governing "streaming" and "shooting" incompressible flows.

Thus, utilization of the hydraulic analogy reduces the problem of finding compressible-flow properties of a gas to measuring depth in a liquid flowing under certain conditions. The chief advantage of the analogy is that it provides a relatively inexpensive way to investigate high-speed flow of compressible fluids. A photograph of an apparatus used successfully in applying the hydraulic analogy (ref. 137) is shown in figure 88.

MECHANICAL ANALOGS

For a two-dimensional compressible isentropic flow, the following equations are valid:

$$\frac{d\Phi}{dl}=q \tag{201}$$

$$\frac{d\Psi}{dn}=\rho q \tag{202}$$

$$\frac{\rho}{\rho_a}=\left[1-\frac{\gamma-1}{2}\left(\frac{q}{a_a}\right)^2\right]^{\frac{1}{\gamma-1}} \tag{203}$$

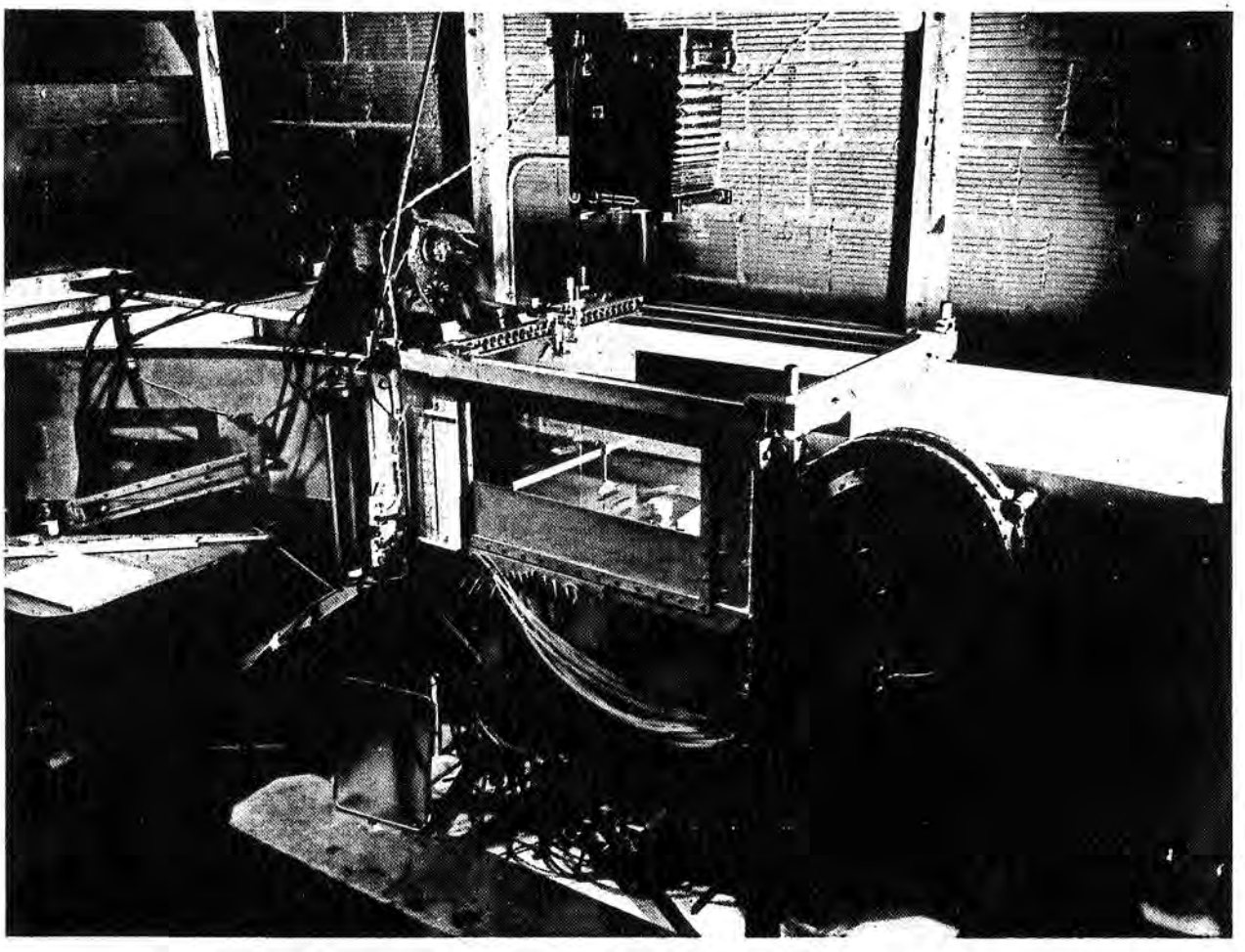

FIGURE 88.—Equipment used in water analogy (from ref. 137).

where the derivatives in equations (201) and (202) are taken in the direction of a streamline and a potential line, respectively.

For purposes of mechanical representation, it is assumed that the total differentials $d\Phi$ and $d\Psi$ in (201) and (202) can be replaced by finite increments of a size sufficiently small in comparison with the cascade. Equations (201) and (202) become, respectively,

$$\left.\begin{aligned}\Delta\Phi&=q\Delta l\\ \Delta\Psi&=\rho q\Delta n\end{aligned}\right\} \tag{204}$$

Then, from equations (203) and (204),

$$a_a\rho_a\frac{\Delta n}{\Delta\Psi}=\frac{a_a}{q}\frac{\rho_a}{\rho}=\frac{a_a}{q}\frac{1}{\left[1-\frac{\gamma-1}{2}\left(\frac{q}{a_a}\right)^2\right]^{\frac{1}{\gamma-1}}}$$

$$=a_a\frac{\Delta l}{\Delta\Phi}\frac{1}{\left[1-\frac{\gamma-1}{2}\left(\frac{\Delta\Phi}{a_a\Delta l}\right)^2\right]^{\frac{1}{\gamma-1}}} \tag{205}$$

giving the relation between $(a_a\rho_a\Delta n/\Delta\Psi)$ and $(a_a\Delta l/\Delta\Phi)$.

From equations (204),

$$\frac{a_a\rho_a\dfrac{\Delta n}{\Delta\Psi}}{a_a\dfrac{\Delta l}{\Delta\Phi}}=\frac{\dfrac{a_a\rho_a}{q\rho}}{\dfrac{a_a}{q}}=\frac{\rho_a}{\rho}$$

and it is clear that

$$a_a\rho_a\frac{\Delta n}{\Delta\Psi}=a_a\frac{\Delta l}{\Delta\Phi} \tag{206}$$

for stagnation conditions. Equation (205) is plotted for $\gamma=1.4$ in figure 89. This equation is quite general in application and relates Δn to Δl for the meshes of a streamline—potential-line network in a compressible-flow field. From equation (203) the pressure at any point of the flow field is given by

$$\frac{p}{P}=\left[1-\frac{\gamma-1}{2}\left(\frac{\Delta\Phi}{a_a\Delta l}\right)^2\right]^{\frac{\gamma}{\gamma-1}} \tag{207}$$

Similarly, the local Mach number can be determined as

$$M^2\left(a_a\frac{\Delta l}{\Delta\Phi}\right)^2=1+\frac{\gamma-1}{2}M^2 \tag{208}$$

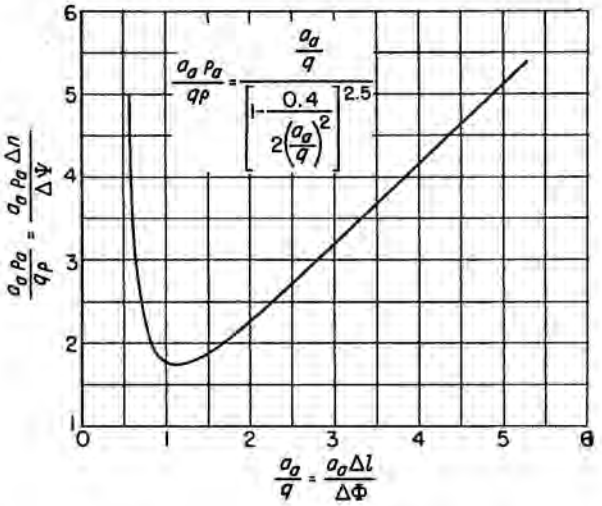

FIGURE 89.—Velocity—mass-flux reciprocal relation for $\gamma=1.4$.

These equations may be used in several ways to determine the flow about a cascade of blades. A description of the graphical method (flux plot) will indicate the general theory and clarify the mechanical analogies arising from it. The blades to be investigated are first drawn to a convenient scale. Three blades (and hence two passages) are used to provide a clearer picture of the flow in the leading-edge region and a check on the accuracy of the assumed stagnation streamlines. That is, the stagnation streamline attached to the central airfoil must have the same shape in the final solution as the outside stagnation streamlines. As a first approximation, the stream and potential lines are drawn for an incompressible flow, which divides the field net into nearly square meshes. (Strict accuracy is not necessary, since this is only a first approximation to the compressible flow.) The meshes are then corrected to a rectangular shape by the application of equations (204) and (205).

A word must be said here about the use of these equations in a given problem. Generally, the upstream conditions q_1 and β_1 will be given as well as the cascade geometry. When a drawing of the cascade has been made to a convenient scale, the spacing s can be measured. The total mass flow through a single passage is given by

$$\Delta w=s\rho_1 q_1\cos\beta_1 \tag{209}$$

and $\Delta\Psi$ is chosen as $\Delta\Psi=\Delta w/N$ where N is the desired number of incremental flow passages per

cascade passage. The value of N should be chosen to represent the best compromise between time and accuracy. Then, if Δl is taken equal to Δn at stagnation conditions, equation (206) yields

$$\Delta\Phi=\frac{\Delta\Psi}{\rho_a} \tag{210}$$

Thus, from a given set of inlet conditions, a given cascade drawing, and a desired number of streamlines per passage, values of $\Delta\Psi$ and $\Delta\Phi$ are determined. These values are constant over the flow field, so that equation (205) yields a fixed relation between Δn and Δl. As a practical measure, it is often convenient to make a plot of Δl against Δn for the particular problem being considered. Such a plot follows at once from figure 89 when values of $\Delta\Psi$ and $\Delta\Phi$ have been chosen. The stream and potential lines can then be adjusted (generally by an iteration process) to satisfy the known relation between Δn and Δl.

The flux plot has the advantage of requiring no unusual equipment. However, the erasure and redrawing of the many lines in the flow net in the successive iterations is a time-consuming operation. Simple mechanical means of alleviating some of the difficulties are discussed in the following paragraphs.

The condition of orthogonality can be nearly satisfied by using a net of wires and pins. The stream and potential lines of the flow are represented by thin spring steel wires. The nodes of the net are steel pins with holes drilled at right angles through them (see fig. 90). When the wires have been threaded through the pins, the network, under distortion to satisfy boundary conditions, will maintain orthogonality to a certain degree. The friction present will prevent a complete self-alinement of the network. The diameter of the pins and tolerance of the holes will result in some deviation from orthogonality.

The boundary conditions are satisfied by using pins with sharply pointed ends to secure the bounding streamlines in their proper locations. Special pins are used for stagnation streamlines.

For the case of an incompressible fluid, the meshes of the network must be square. A second orthogonal network, forming diagonals of the small squares, can be superimposed to satisfy this condition. The pins must be drilled to receive this second network as well as the first. Use of the second network results in more accurate curvilinear squares than could be achieved by measuring distances between midpoints of opposite sides.

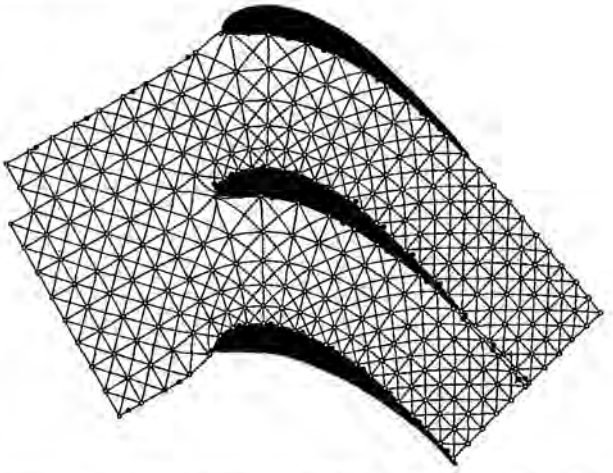

FIGURE 90.—Flow through adjacent channels by wire-mesh plotting (from ref. 140).

To facilitate the network adjustment in the case of compressible flow, a four-legged caliper has been devised by Sells (ref. 138). The spacing between one pair of legs is a function of the spacing between the other legs, and the functional relation is devised to maintain the width-to-length ratio of the small meshes of a compressible-flow net. This device was used successfully by the authors of reference 138.

Another mechanical method of adjustment (fig. 91) has been devised by Westphal and Dunavant (ref. 139). A few basic considerations must be noted relating to its construction. If $\Delta l=\Delta n$ at stagnation conditions, then, as pointed out earlier, $\Delta\Phi=\Delta\Psi/\rho_a$. In this case,

$$a_a\rho_a\frac{\Delta n}{\Delta\Psi}=a_a\frac{\Delta n}{\Delta\Phi} \tag{211}$$

By choosing $\Delta\Phi=a_a/2$, equation (211) yields

$$a_a\rho_a\frac{\Delta n}{\Delta\Psi}=2\Delta n \tag{212}$$

and also

$$a_a\frac{\Delta l}{\Delta\Phi}=2\Delta l \tag{213}$$

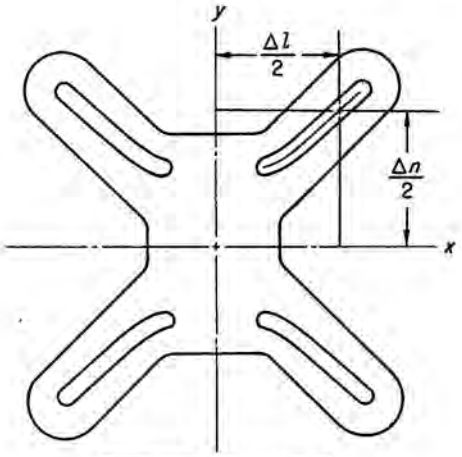

Cam ordinates	
$\frac{\Delta l}{2}$	$\frac{\Delta n}{2}$
0.2740	0.4318
.2750	.4322
.3000	.4360
.3250	.4435
.3500	.4580
.3750	.4730
.4000	.4905
.4250	.5083
.4500	.5370
.5000	.5683
.5500	.6108
.6000	.6555
.6500	.7008
.7000	.7465
.7500	.7932
.8000	.8408
.8405	.8795

FIGURE 91.—Mechanical device used to determin compressible flows (ref. 139).

Using equations (212) and (213) in equation (205) yields

$$\Delta n = \frac{\Delta l}{\left[1-\frac{\gamma-1}{2(2\Delta l)^2}\right]^{\frac{1}{\gamma-1}}} \qquad (214)$$

which is a universal relation between Δn and Δl for a fixed value of $\Delta\Phi$. To obtain this relation, it was necessary to give up the freedom of choosing $\Delta\Psi$, and hence $\Delta\Phi$, in each individual problem. In a given problem, equation (209) is used to determine $\Delta w/s$, and then s, from $\Delta\Psi$ and N. Then the cascade must be drawn to correspond to this value of s. Thus, in any given problem the scale of the drawing is uniquely determined by the inlet conditions, the desired number of streamlines per passage, and the fixed value of $\Delta\Phi$.

Figure 91 (from ref. 139) shows a slotted cam constructed to reproduce mechanically the functional relation given by equation (214). If the cams are placed over a network of pins and wires as shown in figure 92, the distance Δn will automatically require the distance Δl to be such that the proper relation, as expressed by equation (214), is preserved. In general procedure the wire net is fitted to the boundary conditions of a particular problem. Then the cams are placed over the pins beginning from a known portion of the flow field, usually far upstream. The alinement of the pins and wires is complete with the placement of the cams. Since additional measurements and corrections are not necessary, the procedure is fairly rapid.

The value $a_a/2$ was chosen for $\Delta\Phi$ to yield a reasonable cam size. Clearly, a value of $\Delta\Phi$ must be fixed in order to construct a cam of fairly universal applicability. The cam reported in reference 139 is valid for a range of Mach number from 0.3 to 1.0 and for stream-tube widths of 0.864 to 1.760 inches.

The time required for obtaining a solution for turbine cascades and nozzles by use of the cams is estimated in reference 139 to be about 8 hours. However, some difficulty was encountered in reference 140 in applying the wire-mesh method to a compressor cascade. This difficulty was attributed to the more poorly defined passage of the compressor cascade investigated as compared with the cascade of turbines.

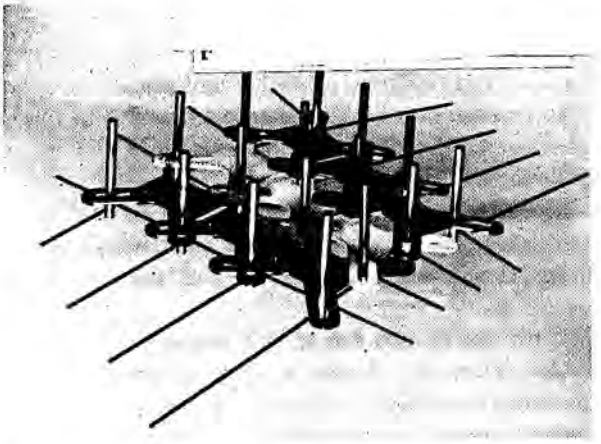

FIGURE 92. Cams and pins used to determine compressible flow (ref. 139).

ELECTRICAL ANALOGS

The flow of an electric current through a nearly flat plate is governed by the following equations:

$$\left.\begin{aligned} \frac{\partial\hat{\Phi}}{\partial x}&=-I_x\Omega & \frac{\partial\hat{\Phi}}{\partial y}&=-I_y\Omega \\ \frac{\partial\hat{\Psi}}{\partial x}&=-I_y m & \frac{\partial\hat{\Psi}}{\partial y}&=I_x m \end{aligned}\right\} \tag{215}$$

where $\hat{\Phi}$ is the electric potential, $\hat{\Psi}$ is an electric-current function, Ω is the specific resistance of the plate, I is the current density, and m is the thickness of the plate. The following relations hold for the irrotational flow of a nonviscous compressible fluid:

$$\left.\begin{aligned} \frac{\partial\Phi}{\partial x}&=q_x & \frac{\partial\Phi}{\partial y}&=q_y \\ \frac{\partial\Psi}{\partial x}&=-\rho q_y & \frac{\partial\Psi}{\partial y}&=\rho q_x \end{aligned}\right\} \tag{216}$$

A comparison of equations (215) and (216) indicates that an analogy exists if

$$\left.\begin{aligned} \Phi&=-\hat{\Phi} & \Psi&=\hat{\Psi} \\ q_x&=\Omega I_x & q_y&=\Omega I_y \\ \rho q_y&=I_y m & \rho q_x&=I_x m \end{aligned}\right\} \tag{217}$$

Then, from equations (217) it follows that

$$\rho=\frac{m}{\Omega} \tag{218}$$

If the flow pattern is known in any field of fluid flow, the velocity, and hence the density, is known at each point. Then, if the ratio of plate thickness to plate specific resistance at each point is made equal to the density at the corresponding point of the flow field, the lines of flow of the electric current will correspond to streamlines of the compressible fluid flow. Similarly, the lines of constant electric potential will correspond to potential lines of the flow field.

In the first approach to the use of this analogy, let Ω=constant. That is, choose a conducting substance of constant specific resistance. Then m must be varied to satisfy relation (218). A convenient way to construct a conducting sheet of constant specific resistance and varying thickness is to use a tank containing an electrolyte. The electrolyte must be shallow, and the bottom of the tank must be made of a substance easily deformed into a desired shape (see ref. 141). The tank must be constructed of a nonconducting material, as must be the object about which the flow is to be determined. An arrangement must be made to enable a potential difference to be created between points far upstream and far downstream.

To solve a compressible-flow problem with such an apparatus, the bottom of the tank is left flat for the first approximation. This corresponds to obtaining an incompressible-flow solution. A potential difference is applied, and the current lines and electric potential lines are determined. Various apparatus have been developed for this operation (see refs. 141 and 142). The current lines are then interpreted as streamlines, and a velocity field is determined. From the velocities obtained in this first approximation, densities are computed at each point of the flow field, and corresponding thicknesses of the electrolyte are determined from equation (218). This varying thickness of the electrolyte is achieved by deformation of the tank bottom. With the shape of the tank bottom thus adjusted, new current lines are determined and the entire process is repeated. If the procedure is a convergent one, the result will be the desired compressible flow about the object considered.

To avoid the problems involved in varying the shape of the tank bottom, a method is desirable wherein the thickness is held constant and the resistance is varied. A conducting material in which the resistance varies in the proper manner with the local current density would make this type of analog realizable. Although no such material is known at the present time, a discrete-point type of analog can be used to achieve a properly varying resistance. The details of such a treatment using a direct-current board are given in reference 138.

Equations (215) are rewritten as

$$\left.\begin{aligned} \frac{\partial\hat{\Phi}}{\partial x}&=-E_x & \frac{\partial\hat{\Phi}}{\partial y}&=-E_y \\ I_x&=\frac{E_x}{\Omega} & I_y&=\frac{E_y}{\Omega} \\ \frac{\partial\hat{\Psi}}{\partial x}&=-I_y & \frac{\partial\hat{\Psi}}{\partial y}&=I_x \end{aligned}\right\} \tag{219}$$

where E_x and E_y are the electric-field components, and I_x and I_y are now the electric-current components per unit thickness. The derivatives in equations (219) are now replaced by difference quotients of values of $\hat{\Phi}$ and $\hat{\Psi}$ at the nodes of a square lattice net with square mesh size δ. These difference equations then become the circuit equations for a network of resistances. The resistance R of each segment of the net is given by

$$\frac{R}{R_1}=\left[1-\frac{\gamma-1}{2}\left(\frac{E}{E_1}\right)^2\right]^{\frac{-1}{\gamma-1}} \tag{220}$$

The field strength E is given by

$$E=\left(\frac{1}{\delta}\right)\sqrt{(\Delta_x\hat{\Phi})^2+(\Delta_y\hat{\Phi})^2} \tag{221}$$

where Δ_x and Δ_y denote differences in the x- and y-directions, respectively. The network has the same geometrical boundaries as the flow field to be investigated.

As a first approximation in the solution of a compressible-flow problem, the resistances in the net are all taken equal. The voltages are then read at all the lattice points, and E is found from equation (221). The resistances are determined from equation (220) and incorporated into the network. New readings are then taken and a second set of resistances calculated. These resistances are incorporated into the system, and so forth. If the method converges, the result will be a finite-difference approximation to the flow of a compressible fluid.

CONCLUDING REMARKS

A survey of the literature on plane potential flow about cascades has been presented. The theories are classified according to their application to high-solidity or low-solidity cascades and according to whether the method solves the direct or the inverse problem. Several methods have been presented in considerable detail to illustrate acceptable solutions for the problems in the various classifications. These methods are considered to offer practical solutions, since they combine a reasonable amount of computing time with acceptable accuracy. The authors of these methods are Katzoff, Finn, and Laurence (ref. 86); Goldstein (unpublished lectures); Huppert and MacGregor (ref. 124); Wu and Brown (ref. 127); Stanitz (ref. 136); and Stanitz and Sheldrake (ref. 132).

APPENDIX A

VELOCITY DISTRIBUTION AT ARBITRARY ANGLE OF INCIDENCE

It is possible to map conformally an infinite cascade in the z-plane into a circle of radius 1 with center at the origin in the ζ-plane. The mapping can be chosen so that the points $\pm\infty$ in the z-plane map into the real points $\pm e^K$ in the circle plane (e.g., ref. 90). The complex potential function of the flow about the circle, which will have the desired singularities when mapped into the cascade plane, is given by

$$W_f(\zeta)=\frac{v_m s}{2\pi}\left[e^{i\beta_m}\log_e\left(\frac{\zeta-e^K}{\zeta+e^K}\right)+e^{-i\beta_m}\log_e\left(\frac{\zeta-e^{-K}}{\zeta+e^{-K}}\right)\right]+\frac{\Gamma}{4\pi i}\log_e\left(\frac{\zeta^2-e^{-2K}}{\zeta^2-e^{+2K}}\right)+\text{constant} \quad (64)$$

The constants v_m, β_m, s, Γ, and K are determined from the cascade being investigated. Suppose now that a solution is known for the cascade at some angle of incidence. Then v_m, β_m, s, and Γ are known quantities. If K can also be found, equation (64) will give the flow in the circle plane that corresponds to the flow in the cascade plane. Then, a conformal mapping is determined between points of the z-plane and points of the ζ-plane by equating values of the respective potential functions. Actually, the value of K can be determined by requiring that the two flow fields be related conformally and utilizing the condition of correspondence of potential values. Note that, on the circle, $\zeta=e^{i\varphi}$, and equation (64) becomes

$$W_f=\Phi_f=\frac{v_m s}{2\pi}\left[\cos\beta_m\log_e\left(\frac{\cos\varphi-\cosh K}{\cos\varphi+\cosh K}\right)+2\sin\beta_m\tan^{-1}\left(\frac{\sin\varphi}{\sinh K}\right)+\frac{\Gamma}{v_m s}\tan^{-1}\left(\frac{\tan\varphi}{\tanh K}\right)\right] \quad (A1)$$

Let $\Delta\Phi_f$ denote the change in potential from the leading-edge stagnation point φ_{le} to the trailing-edge stagnation point $\varphi_{te,s}$ along the upper portion of the circle (see fig. 77):

$$\Delta\Phi_f=\frac{v_m s}{2\pi}\left\{\cos\beta_m\log_e\left(\frac{\cos\varphi_{te,s}-\cosh K}{\cos\varphi_{te,s}+\cosh K}\,\frac{\cos\varphi_{le}+\cosh K}{\cos\varphi_{le}-\cosh K}\right)+2\sin\beta_m\left[\tan^{-1}\left(\frac{\sin\varphi_{te,s}}{\sinh K}\right)-\tan^{-1}\left(\frac{\sin\varphi_{le}}{\sinh K}\right)\right]+\frac{\Gamma}{v_m s}\left[\tan^{-1}\left(\frac{\tan\varphi_{te,s}}{\tanh K}\right)-\tan^{-1}\left(\frac{\tan\varphi_{le}}{\tanh K}\right)\right]\right\} \quad (A2)$$

where

$$-\frac{\pi}{2}<\tan^{-1}\left(\frac{\sin\varphi_{te,s}}{\sinh K}\right)<\frac{\pi}{2}$$

$$-\frac{\pi}{2}<\tan^{-1}\left(\frac{\sin\varphi_{le}}{\sinh K}\right)<\frac{\pi}{2}$$

and $\tan^{-1}\left(\frac{\tan\varphi_{te,s}}{\tanh K}\right)$ and $\tan^{-1}\left(\frac{\tan\varphi_{le}}{\tanh K}\right)$ are in the same quadrant as $\varphi_{te,s}$ and φ_{le}, respectively.

The stagnation points are found by differentiating (A1) and equating to zero. This results in the following equation for $\varphi_{te,s}$ and φ_{le}, which can be interpreted as a quadratic equation in $\sin\varphi$:

$$\sin\varphi\cos\beta_m+\cos\varphi\sin\beta_m\tanh K+\frac{\Gamma}{2v_m s}\sinh K=0 \quad (A3)$$

Since the two flow fields are to be related conformally, the potential difference $\Delta\Phi_z$ measured from the leading-edge stagnation point to the trailing edge of a cascade blade must equal the corresponding potential difference (as given by eq. (A2)) in the circle plane. The procedure for finding K is as follows:

(1) Assume several values of K.

(2) For each value of K, compute $\varphi_{te,s}$ and φ_{le} from equation (A3).

(3) Compute $\Delta\Phi_f$ from equation (A2) for each value of K.

(4) Plot $\Delta\Phi_f$ against K, and select the value of K for which $\Delta\Phi_f=\Delta\Phi_z$.

With this value of K, the flow function (64) is completely determined and velocity distributions at angles of incidence other than the one for the original solution can be considered.

If W_ζ and W_z denote the complex potential functions in the circle plane and the cascade plane, respectively, and $z=z(\zeta)$ is the desired mapping function, the following relations hold:

$$W_z(z)=W_z(z(\zeta))=W_\zeta(\zeta) \tag{76}$$

$$\frac{dW_\zeta}{d\zeta}=\frac{dW_z}{dz}\frac{dz}{d\zeta} \tag{A4}$$

or

$$w_z=w_\zeta\frac{d\zeta}{d_z}$$

where w_z and w_ζ denote the complex velocity conjugates in the cascade and circle planes, respectively. If only the blade perimeters and the unit circle are considered, equation (A4) becomes

$$v_z=\left|\frac{d\zeta}{dz}\right|_{boundary}\frac{d\Phi_\zeta}{d\varphi}=\left|\frac{d\zeta}{dz}\right|\frac{v_m s}{\pi}\left[\frac{\cos\beta_m\cosh K(\sin\varphi-\sin\varphi_{te,s})+\sin\beta_m\sinh K(\cos\varphi-\cos\varphi_{te,s})}{\cosh^2 K-\cos^2\varphi}\right] \tag{A5}$$

In order to satisfy the Kutta condition for a new value of β_m (corresponding to a new value of incidence angle), the flow must continue to leave the cascade blades at a point corresponding to $\varphi=\varphi_{te,s}$. Since the mapping function is unaltered, the velocity distribution for an arbitrary value of β_m (say β_m^*) is given by

$$(v_z)_{\beta_m^*}=(v_z)_{\beta_m}\left[\frac{\cos\beta_m^*\cosh K(\sin\varphi-\sin\varphi_{te,s})+\sin\beta_m^*\sinh K(\cos\varphi-\cos\varphi_{te,s})}{\cos\beta_m\cosh K(\sin\varphi-\sin\varphi_{te,s})+\sin\beta_m\sinh K(\cos\varphi-\cos\varphi_{te,s})}\right] \tag{A6}$$

After K and $\varphi_{te,s}$ have once been found for a given cascade, equation (A6) can be used to determine velocity distributions at any angles of incidence.

691-564 O-65-11

APPENDIX B

CASCADE MAPPING FUNCTION

The development of the cascade mapping function as presented herein is taken from unpublished lectures by A. Goldstein.

Consider an infinite cascade of blades in the $z=x+iy$ plane, oriented as in figure 72. If s is the blade spacing, the cascade can be mapped into a single closed curve by the function

$$z_1=e^{\frac{2\pi z}{s}} \tag{B1}$$

By the mapping theorem of Riemann, the exterior of this closed curve can be mapped conformally onto the exterior of a unit circle in the z_2-plane in such a way that

$$\lim_{z_2\to\infty} z_1(z_2)=\infty \tag{B2a}$$

and

$$\lim_{z_2\to\infty} \frac{dz_1}{dz_2}=A \tag{B2b}$$

where A is a real constant. Since the derivative of the function has no zeros outside the circle, the mapping function can be written

$$\frac{dz_1}{dz_2}=e^{f(z_2)} \tag{B3}$$

with conditions (B2a) and (B2b) satisfied.

The observation is now made that

When $z\to-\infty$, then $z_1\to 0$ and $z_2\to$ some point a (B4)

When $z\to+\infty$, then $z_1\to+\infty$ and $z_2\to+\infty$ (B5)

The unit circle in the z_2-plane can be mapped uniquely by a linear fractional transformation onto a unit circle in the ζ-plane with center at the origin and such that $+\infty$ and a in the z_2-plane map into e^K and $-e^K$, respectively (see ref. 149). This mapping can be written

$$z_2-\mathrm{a}=\mathrm{a}\,\frac{\zeta+e^K}{\zeta-e^K}\tanh K \tag{B6}$$

If z_1 is considered as a function ζ, certain conditions on $z_1(\zeta)$ must be fulfilled. From relations (B6) and (B5), $z_1(\zeta)$ has a pole of order 1 at $\zeta=e^K$. From relations (B6) and (B4), $z_1(\zeta)$ has a zero at $\zeta=-e^K$ of order 1. It is clear that the desired function has the form

$$z_1=\frac{\zeta+e^K}{\zeta-e^K}\,g(\zeta) \tag{B7}$$

where $g(\zeta)$ is regular for $|\zeta|>1$. Furthermore, $g(\zeta)\neq 0$ for $|\zeta|>1$, because, if $g(\rho)=0$ for some ρ such that $|\rho|>1$, then $z_1=0$ would correspond to two points, $\zeta=-e^K$ and $\zeta=\rho$. But this is not possible, since z_1 is a regular one-to-one function of ζ. Hence, equation (B7) can be rewritten

$$z_1=\frac{\zeta+e^K}{\zeta-e^K}e^{f(\zeta)} \tag{B8}$$

where $f(\zeta)$ is regular for $|\zeta|>1$. Then

$$\frac{dz_1}{d\zeta}=\frac{e^{f(\zeta)}}{(\zeta-e^K)^2}\left[(\zeta^2-e^{2K})f'(\zeta)-2e^K\right] \tag{B9}$$

From equations (B3) and (B6),

$$\frac{dz_1}{d\zeta}=\frac{dz_1}{dz_2}\frac{dz_2}{d\zeta}=\frac{-2e^{f(z_2)}\mathrm{a}e^K\tanh K}{(\zeta-e^K)^2} \tag{B10}$$

Equating (B9) and (B10) yields

$$(\zeta^2-e^{2K})f'(\zeta)-2e^K=-e^{(-f)}2\mathrm{a}e^K\tanh K$$
$$=-2e^Ke^{G(\zeta)} \tag{B11}$$

where G is defined by the relation

$$e^{G(\zeta)}=\mathrm{a}\tanh K e^{(-f)}$$

Then,

$$f'(\zeta)=2e^K\frac{1-e^{G(\zeta)}}{(\zeta-e^K)(\zeta+e^K)} \tag{B12}$$

But $f(\zeta)$, and hence $f'(\zeta)$, is regular for $|\zeta|>1$, so $1-e^{G(\zeta)}$ must have zeros at $\zeta=e^K$ and $\zeta=-e^K$. It follows that $G(\zeta)$ has zeros at $\zeta=e^K$ and $\zeta=-e^K$.

Then fron equations (B1), (B9), and (B11),

$$\frac{dz}{d\zeta}=\frac{dz}{dz_1}\frac{dz_1}{d\zeta}=\frac{s}{2\pi z_1}\frac{-2e^K e^{G(\zeta)} e f'(\zeta)}{(\zeta-e^K)^2}$$

$$=\frac{-se^K}{\pi}\frac{e^{G(\zeta)}}{(\zeta-e^K)(\zeta+e^K)} \quad \text{(B13)}$$

with the condition that $G(\zeta)$ is regular for $|\zeta|>1$, and $G(\pm e^K)=0$. Equation (B13) can be put into a more convenient form. Consider the function

$$h(\zeta)=F(\zeta)\left[G(\zeta)+\log_e\left(\frac{1-\frac{e^{-2K}}{\zeta^2}}{1-e^{-4K}}\right)\right] \quad \text{(B14)}$$

where

$$F(\zeta)=\frac{\zeta^2(e^{2K}-e^{-2K})}{(e^{2K}-\zeta^2)(\zeta^2-e^{-2K})} \quad (73)$$

Therefore, $h(\zeta)$ is regular for $|\zeta|>1$ and has a zero of order two at $\zeta\to\infty$. Substituting equation (B14) into equation (B13) gives

$$\frac{dz}{d\zeta}=\frac{se^{-K}}{\pi}F(\zeta)e^{\frac{h(\zeta)}{F(\zeta)}} \quad (72)$$

and the condition on $h(\zeta)$ can be expressed as

$$\lim_{\zeta\to\infty}\zeta h(\zeta)=0 \quad (75)$$

In a case where the cascade blade has a sharp trailing edge, the function $h(\zeta)$ will not be regular at the corresponding point on the mapping circle. As a result, the determination of h_2 from h_1 (where $h=h_1+ih_2$) is unduly complicated in the preceding form. The singularity can be factored out, however, and the computations simplified. The general mapping function (eq. (72)) then takes the following form:

$$\frac{dz}{d\zeta}=\frac{se^{-k}}{\pi}\left(1-\frac{\zeta_{te}}{\zeta}\right)^{\frac{1-\epsilon}{\pi}}\left(1-\frac{\zeta_{te}}{e^{2K}}\right)^{-\frac{1}{2}+\frac{\epsilon}{2\pi}}$$

$$F(\zeta)e^{\frac{h(\zeta)}{F(\zeta)}}\exp\left[\frac{e^K\left(\frac{1}{2}-\frac{\epsilon}{2\pi}\right)}{\zeta}\log\frac{e^K+\zeta_{te}}{e^K-\zeta_{te}}\right] \quad \text{(B15)}$$

where ϵ is the included trailing-edge angle and ζ_{te} is the point corresponding to the trailing edge. The function $h(\zeta)$ appearing in equation (B15) is regular on and outside the unit circle. For details of this computation, see reference 105.

APPENDIX C

RELAXATION CONSIDERATIONS

Consider the set of five grid points 0, 1, 2, 3, and 4 shown in figure 83. The number 0 denotes the central point at which the finite-difference equation, under consideration in this discussion, is written. The subscripts 0, 1, 2, 3, and 4 refer to the five points 0, 1, 2, 3, and 4. The finite-difference equation is written at 0 as

$$A_0\Psi_0+A_1\Psi_1+A_2\Psi_2+A_3\Psi_3+A_4\Psi_4+K_0=0 \quad \text{(C1)}$$

The coefficients A_i are known, and the nonlinear contribution K_0 is fixed from a previous approximate solution or from an assumed solution.

Equation (C1) is rewritten

$$A_0\Psi_0+A_1\Psi_1+A_2\Psi_2+A_3\Psi_3+A_4\Psi_4+K_0=R_0 \quad \text{(C2)}$$

where R_0 is called the residual at 0. When the correct values of Ψ_i are inserted in equation (C2), R_0 will be zero. If incorrect values of Ψ_i are used, R_0 will, in general, have a value different from zero.

When equation (C1) is applied to each of N points in the flow field, N simultaneous equations in N unknowns (Ψ_i) result. When values of Ψ_i ($i=0, 1, \ldots N$) are assumed, equation (C2) yields N residual values R_i ($i=0, 1, \ldots N$). The purpose of the relaxation process is to reduce these residuals to small values. From equation (C2) it is seen that R_0 can be reduced to zero by a new choice of Ψ_0, say Ψ_0', such that

$$\Psi_0'=\Psi_0-\frac{R_0}{A_0} \quad \text{(C3)}$$

This choice of a new Ψ_0' has an influence on other residuals. In this case, the residuals at points 1, 2, 3, and 4 in figure 83 are immediately affected. The finite-difference equations written at these four points each contain Ψ_0' multiplied by a coefficient that has been determined at the outset. Thus, it is seen that R_1, for example, is a function of Ψ_0 and subsequently of Ψ_0'. A change in Ψ_0 then must cause a corresponding change in R_1.

A simple way to carry out this process is to list the initial values of Ψ_i and R_i at each point on an oversized drawing of the flow field. Then a change in Ψ_i of $\Delta\Psi_i$ is recorded under Ψ_i at the point in question. Resulting changes ΔR_i are recorded at the respective points affected.

In this illustration, second-order polynomial representation (resulting in five values appearing in each difference equation) was used. The principle is the same for higher-order representations where more points are involved in each equation. Unequal spacing of points near the boundaries does not affect the general procedure. Residuals are systematically reduced over the entire flow field, usually beginning with the larger ones. As there is considerable interaction of effects, the residual at a given point may undergo many changes in the course of a solution.

There are many devices for obtaining rapid convergence that can be used to great advantage when employing relaxation methods (see ref. 109).

APPENDIX D

MATRIX CONSIDERATIONS

Applying equation (149) to each grid point in the flow field results in a collection of N linear equations in N unknowns. In a flow problem of this nature, so many points are required in the solution that matrices can be used to solve the equations only if high-speed computing equipment is available. Various matrix techniques are available in the literature. A brief outline of a method that has been used successfully in references 129 and 130 is presented herein.

The finite-difference equations are written in matrix form as follows:

$$[A]\{\psi\}=\{J\} \tag{D1}$$

where

$[A]$ square matrix of order N
$\{\Psi\}$, $\{J\}$ column matrices having N elements

The square matrix $[A]$ can be written as

$$[A]=[l][d][u] \tag{D2}$$

where

$[l]$ lower triangular matrix with unity on the diagonal
$[u]$ upper triangular matrix with unity on the diagonal
$[d]$ diagonal matrix

The matrices $[l]$ and $[d]$ can be combined into a lower triangular matrix $[L]$, and (D2) is then written

$$[A]=[L][u] \tag{D3}$$

If i denotes row and j denotes column, the elements of $[L]$ and $[u]$ can be written

$$L_j^i=A_j^i-\sum_{k=1}^{j-1} L_k^i u_j^k \qquad i\geq j \tag{D4}$$

$$\begin{aligned} L_1^i&=A_1^i \\ u_j^i&=\frac{A_j^i-\sum_{k=1}^{i-1} L_k^i u_j^k}{L_i^i} \qquad j>i \\ u_i^i&=1 \\ u_j^1&=\frac{A_j^1}{L_1^1} \end{aligned} \tag{D5}$$

It is seen from equations (D4) and (D5) that L_1^i can be found first from a knowledge of A_1^i. Then u_j^1 can be found from (D5), since $u_j^1=\frac{A_j^1}{L_1^1}$. Next, the second column of $[L]$ can be found and then the second row of $[u]$. In this manner, all elements of both matrices are known.

Now define a column matrix $\{Q\}$ such that

$$[L]\{Q\}=\{J\} \tag{D6}$$

It can be shown that

$$Q_i=\frac{J^i-\sum_{k=1}^{i-1} L_k^i Q^k}{L_i^i} \tag{D7}$$

$$Q_1=\frac{J^1}{L_1^1}$$

Hence, $[Q]$ can be found by finding Q^1, Q^2, . . . in successive order.

From (D3) and (D1),

$$[L][u]\{\Psi\}=\{J\} \tag{D8}$$

From (D6) and (D8),

$$[u]\{\Psi\}=\{Q\} \tag{D9}$$

Since $[u]$ is a known upper diagonal matrix and $\{Q\}$ is a known column matrix, $\{\Psi\}$ can be determined from Ψ_n, Ψ_{n-1}, . . . in successive order. In general,

$$\begin{aligned} \Psi^i&=Q^i-\sum_{k=n}^{i+1} u_k^i \Psi^k \\ \Psi^n&=Q^n \end{aligned} \tag{D10}$$

In this manner, the Ψ^i are found and the problem is solved. Suggestions for a computational layout designed for minimum time expenditures are made in reference 130.

CHAPTER V

VISCOUS FLOW IN TWO-DIMENSIONAL CASCADES

By WILLIAM H. ROUDEBUSH and SEYMOUR LIEBLEIN

Boundary-layer behavior on two-dimensional compressor blade sections is described, based on a review of available theory and experiment. The material is divided into two main sections, one presenting a qualitative discussion of boundary-layer behavior, and the other treating the quantitative aspects of boundary-layer theory as applied to cascade blades.

In the qualitative analysis, the general characteristics of laminar and turbulent boundary layers are reviewed. Instability and transition and their influence on boundary-layer behavior are discussed. An attempt is then made to construct a qualitative picture of blade losses determined over a wide range of Reynolds number, surface pressure gradient, and free-stream turbulence.

The section on quantitative boundary-layer theory discusses some approximate methods for computing the growth and separation of laminar and turbulent boundary layers. The loss in total pressure and defect in circulation resulting from blade boundary-layer growth are also considered.

INTRODUCTION

Considerable effort in the past several decades has been devoted to the determination of the two-dimensional potential or inviscid flow about airfoil and cascade sections. Comprehensive surveys of the state of potential-flow theory for two-dimensional cascades are presented in chapter IV and reference 150. These surveys indicate that the theory available for analysis of ideal two-dimensional flow, although not simple, is usable and has provided a firm understanding of the ideal flow on and around two-dimensional-cascade blade sections. A real fluid, however, is viscous, and it is well-known that the presence of viscosity exerts a considerable influence on the behavior of the flow.

The determination of the viscous flow about two-dimensional-cascade sections is considered important in the development of compressor flow theory for two reasons. First, it will aid in obtaining a basic understanding of the general nature of viscous-flow effects. Second, it will provide a background for the interpretation and correlation of experimental and theoretical cascade data. This is essential for the successful application of blade-element theory to compressor design (ch. III).

In fluid-flow theory, a complete representation of the two-dimensional viscous flow is given by the Navier-Stokes equations (ref. 151, pt. I). General exact solutions of these equations have not as yet appeared. The principal advances in viscous-flow solutions have come as a result of various approximations to the basic relations. The viscous-flow literature is covered extensively in reference 152, published in 1938. More recent literature is reviewed in reference 153. Compressible boundary-layer flow is surveyed in reference 154.

Concurrently with the development of boundary-layer theory, considerable experimental research on boundary-layer behavior has been conducted. These experiments not only provide empirical data necessary for obtaining approximate solutions to the boundary-layer equations, but also contribute to the establishment of a valuable qualitative picture of the behavior of boundary layers.

This chapter reviews the problem of determining viscous effects on the two-dimensional incompressible flow about compressor blade profiles in cascade. The material is divided into two major parts, entitled QUALITATIVE BOUNDARY-LAYER THEORY and QUANTITATIVE BOUNDARY-LAYER THEORY. In the first part, some of the more important terminology is presented, and general trends to be anticipated in real fluid flows are indicated. Laminar and turbulent boundary layers, instability, transition, and separation are discussed.

The general effects of Reynolds number on total-pressure loss for several levels of blade loading are evaluated qualitatively. In the second part, selected methods are presented for actually calculating laminar- and turbulent-boundary-layer growth and predicting separation. In addition, some consideration is given to the computation of the defect in circulation and the total-pressure loss caused by the growth of the blade surface boundary layers. The analysis indicates the extent to which current viscous-flow theory can predict the important phenomena involved in the flow of a real fluid about a two-dimensional cascade.

SYMBOLS

The following symbols are used in this chapter:

C_D drag coefficient
C_{fr} local friction coefficient
C_L lift coefficient
c chord length
H boundary-layer form factor, δ^*/θ^*
$\mathcal{I}$ turbulence intensity
i incidence angle, angle between inlet-air direction and tangent to blade mean camber line at leading edge, deg
L scale of turbulence
l^* characteristic length
n coordinate normal to blade surface
P total or stagnation pressure
$\Delta\overline{P}$ mass-averaged loss in total pressure
p static or stream pressure
q arbitrary constant
Re Reynolds number, $V_t l^*/\nu$
Re_c Reynolds number based on chord length, $V_1 c/\nu$
Re_δ Reynolds number based on boundary-layer thickness, $V_0\delta/\nu$
Re_θ Reynolds number based on boundary-layer momentum thickness, $V_0\theta^*/\nu$
s coordinate along direction of blade surface
s' distance along blade surface from leading to trailing edge
u s-component of velocity in boundary layer
V air velocity
V_t characteristic velocity
v n-component of velocity in boundary layer
x abscissa in cascade plane (fig. 94)
y ordinate in cascade plane (fig. 94)
α angle of attack, angle between inlet-air direction and blade chord, deg
β air angle, angle between air velocity and x-axis, deg
Γ turbulent-boundary-layer parameter, $(\Theta/V_0)(dV_0/ds)$
δ boundary-layer thickness
δ^* boundary-layer displacement thickness
ζ turbulent-boundary-layer parameter, $(C_{fr}/2)Re_\theta^q$
Θ turbulent-boundary-layer parameter, $\theta^* Re_\theta^q$
θ^* boundary-layer momentum thickness
λ Pohlhausen parameter, $(\delta^2/\nu)(dV_0/ds)$
μ viscosity
ν kinematic viscosity
ρ density
σ solidity, ratio of chord to spacing
τ time
$\hat{\tau}$ shear stress
$\hat{\tau}_w$ shear stress at wall
$\overline{\omega}$ total-pressure-loss coefficient

Subscripts:

cr critical
$f.p.$ flat plate
m mean of upstream and downstream conditions
n n-direction
ref reference
s s-direction
te trailing edge
tr transition
0 outer edge of boundary layer
1 upstream at infinity
2 downstream at infinity

QUALITATIVE BOUNDARY-LAYER THEORY

GENERAL CONSIDERATIONS

For an ideal fluid, the velocity tangent to a fixed surface is generally nonzero at the surface and (for small surface curvature) is nearly equal to the velocity at points near the surface, as shown in figure 93(a). A viscous fluid, however, adheres to the surface over which it is flowing, so that the velocity tangent to the surface is zero at the surface. The velocity near the surface rapidly increases and attains the value of the free-stream velocity at a short distance from the surface, as shown in figure 93(b). The region of flow in which the local velocity is retarded is referred to as the boundary layer. The static pressure across the boundary layer is nearly constant.

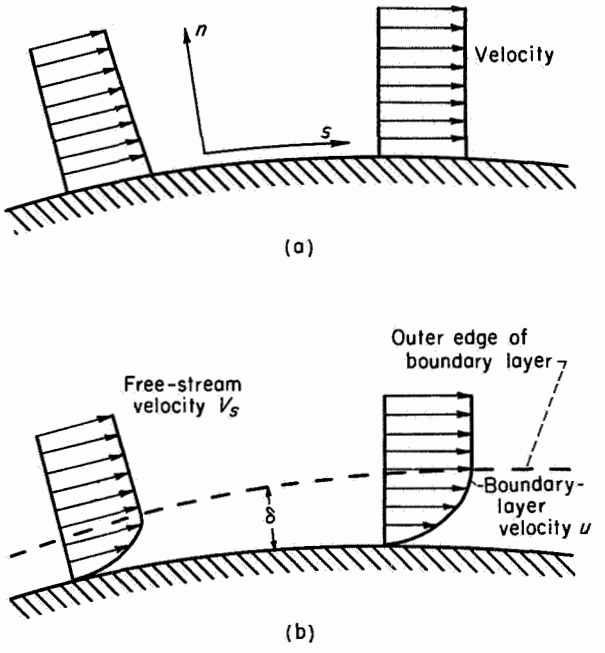

(a) Nonviscous flow.
(b) Viscous flow.

FIGURE 93.—Velocity profiles near a fixed boundary.

In two-dimensional-cascade flow, boundary layers develop on both the suction and pressure surfaces of the blade. These surface boundary layers then come together at the blade trailing edge and form the blade wake, as shown in figure 94. As the wake moves downstream, a mixing takes place between the wake and free stream and, through viscous action, the flow becomes uniform at some distance behind the blade trailing edge.

Although, in many practical problems, the blade surface boundary layer constitutes a small portion of the flow field, it plays a decisive part in the determination of the actual flow characteristics of the cascade. The effect of blade boundary-layer development on cascade losses is obvious, since the resulting wake formation contains a defect in total pressure. The surface boundary layers can also exert a strong influence on the surface pressure distribution and outlet-angle characteristics of the blade. If the boundary layer is very thin, the pressure distribution obtained from potential-flow calculations over the original body will be a good approximation to the actual distribution. As the boundary layer thickens, however, the actual pressure distribution will depart from the potential-flow determination. Under certain conditions, the boundary layer actually separates from the surface of the blade somewhere in advance of the trailing edge. In this event, the entire flow pattern about the cascade is altered by the displacement of fluid accompanying such separation, and the potential-flow solution about the original profile loses its significance almost completely.

It is evident, therefore, that a knowledge of general boundary-layer behavior is vital to the accurate prediction and interpretation of cascade flow characteristics. In the present section, the discussion is presented in the following order:

(1) Preliminary boundary-layer definitions and concepts
(2) Description of laminar boundary layer in some detail with particular emphasis on effects of Reynolds number
(3) Description of turbulent boundary layer and comparison with laminar layer
(4) Discussion of instability and transition with regard to their importance in cascade operation and data interpretation
(5) Combination of considerations (1) to (4) to form a qualitative picture of the loss spectrum as influenced by pressure gradient and Reynolds number variation

BOUNDARY-LAYER CONCEPTS

Types of boundary layers.—The two general types of boundary layer occurring on blade surfaces are designated laminar and turbulent. The boundary layer is initially laminar and usually becomes

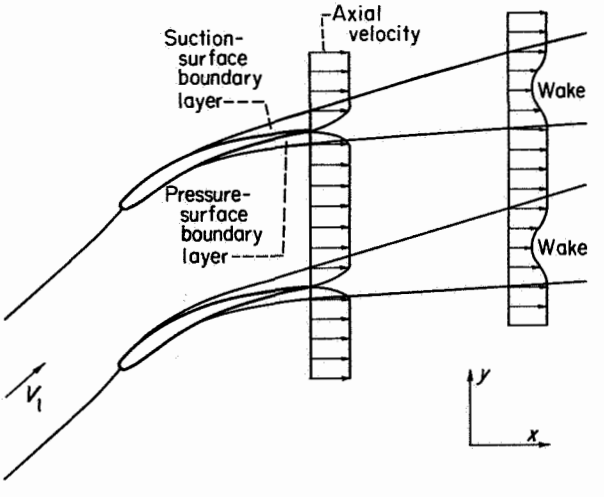

FIGURE 94.—Boundary layers and blade wake in two-dimensional-cascade flow.

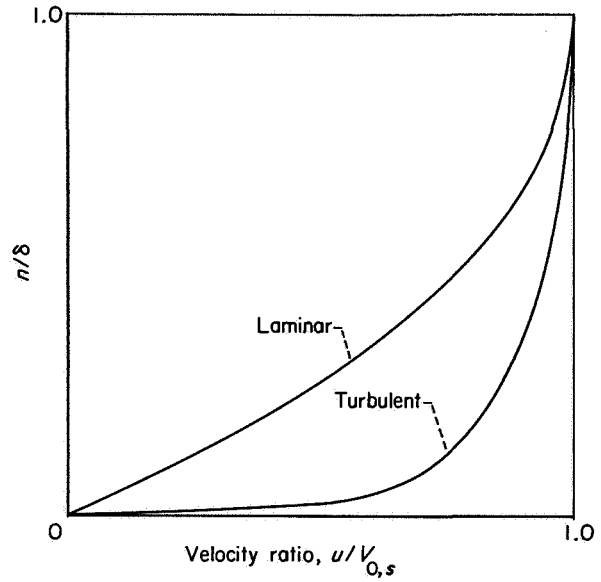

FIGURE 95.—Typical velocity profiles for laminar and turbulent boundary layers.

turbulent somewhere along the blade surface. The boundary layer is said to be in a laminar state if the flow, at any instant, can be represented as a sequence of layers, each layer tracing a path essentially tangent to the surface of the cascade blade. In this case, the velocity varies uniformly through the boundary layer from a value of zero at the blade surface to a value almost equal to the free-stream velocity at a short distance from the surface. The boundary layer in a turbulent state is characterized by a rapid random fluctuation with time of the velocity at any point and a large interchange of momentum. The velocity is again zero at the blade surface, and the mean velocity averaged with respect to time varies continuously through the boundary layer and attains a value approaching the free-stream velocity a short distance from the surface.

Typical velocity distributions through the boundary layer for the laminar and turbulent cases are illustrated in figure 95. The turbulent-flow velocities remain higher closer to the boundary because of the turbulent infiltration of high-energy particles into the boundary layer. In the laminar flow, the interchange of momentum is due only to the shear stress exerted between two neighboring layers of fluid. This difference between the two types is manifest when an adverse pressure gradient is impressed on the boundary layer by a deceleration of the main stream. A turbulent boundary layer often receives sufficient momentum influx to advance some distance against an adverse pressure gradient before separation occurs. The laminar boundary layer, on the other hand, with very little momentum influx, is unable to advance far into the face of a rising pressure. Eventually, in either case, the particles near the wall are slowed down to a stop and finally actually reverse their direction and begin to flow upstream (fig. 96). This results in separation of the through-flow from the blade surface.

In the range of Reynolds number and turbulence of conventional cascades and compressors, the boundary layer is laminar over the forward portion and turbulent over the rearward portion of the blade. Since the loss characteristics of these two boundary-layer regions are markedly different, the location and nature of the transition between the regions are significant in determining the magnitude of the resulting wake.

Boundary-layer parameters.—A definition of certain basic terms is prerequisite to any further discussion of boundary layers. The more important of these terms are defined in this section.

There are several boundary-layer thickness parameters that occur throughout the literature. The actual full physical thickness δ is taken to be the distance normal to a fixed surface wherein the velocity in the boundary layer attains some fixed percentage, say 99 percent, of the free-stream velocity. The boundary-layer velocity theoretically equals the free-stream velocity only at an infinite distance normal to the surface. However, for practical considerations, the two can usually be considered equal at a short distance δ from the surface (fig. 93(b)).

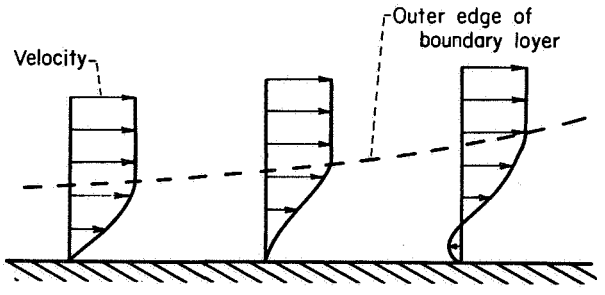

FIGURE 96.—Boundary-layer flow reversal in presence of adverse pressure gradient.

Since the velocity in the boundary layer goes to zero at the wall, the weight flow in the boundary-layer region is decreased. This decrease in weight flow can be expressed in terms of a length δ^*, called the displacement thickness, obtained by dividing the integrated defect in weight flow within the boundary layer by the free-stream velocity $V_{0,s}$ at the outer edge of the layer. For incompressible flow, this gives

$$\delta^*=\int_0^\delta \left(1-\frac{u}{V_{0,s}}\right) dn$$

in which the coordinate n is taken in a direction normal to the surface (similarly, the coordinate s represents distance in the direction of the surface, fig. 93(a)); u is the local velocity in the s-direction within the boundary layer; and $V_{0,s}$ is the velocity in the s-direction at the outer edge of the boundary layer.

In a similar manner, a momentum thickness θ^* is obtained to represent the corresponding decrease in momentum in the boundary layer. The momentum thickness is obtained by dividing the integrated defect in momentum by $V_{0,s}^2$ to give

$$\theta^*=\int_0^\delta \frac{u}{V_{0,s}}\left(1-\frac{u}{V_{0,s}}\right) dn$$

The momentum thickness in the wake is directly related (as shown in a later section) to the loss in total pressure across a cascade.

Another parameter frequently encountered is the boundary-layer form factor H, defined as the ratio of displacement thickness to momentum thickness:

$$H=\frac{\delta^*}{\theta^*}$$

The form factor appears as a parameter in approximate boundary-layer theory in the determination of the magnitude of the momentum thickness. It also gives a rough indication of the state of the boundary layer with regard to possible separation.

One of the most significant parameters characterizing boundary-layer behavior is the Reynolds number, a dimensionless parameter proportional to the ratio of inertial force to viscous force, given by

$$Re=\frac{V_t l^*}{\nu}$$

where V_t is a characteristic velocity of the flow, l^* is a characteristic length, and ν is the kinematic viscosity. In particular, V_t can be taken as the upstream velocity V_1 and l^* as the blade chord c to give what is called the body Reynolds number, or blade-chord Reynolds number, $Re_c=V_1 c/\nu$. In another formulation, the velocity can be taken to be the velocity V_0 at the outer edge of the boundary layer and the characteristic length as the momentum thickness θ^* to give the boundary-layer Reynolds number $Re_\theta=V_0\theta^*/\nu$, where Re_θ is a function of the particular location at which V_0 and θ^* are computed. As will be indicated later, Reynolds number exercises a considerable influence on the boundary-layer growth, instability, and transition.

Loss parameters.—In the flow about airfoil sections, friction exerts a tangential force that opposes the forward motion of the airfoil. The retarding component arising from the friction force is called the friction drag. In addition to friction, a retarding force component is also obtained from the normal pressure forces of the real flow. This force component is called the form drag. The total drag of the section, which is the sum of the friction and form drags, is called the profile drag. Ordinarily, the profile drag force is expressed as a drag coefficient C_D, defined as the drag force per unit span divided by a reference kinetic head and the chord length.

For the isolated airfoil, at a distance sufficiently far downstream that static pressure is uniform normal to the flow direction, the drag coefficient can be related to the momentum-thickness ratio θ^*/c by the following equation (ref. 155):

$$C_D=2\left(\frac{\theta^*}{c}\right)$$

The downstream wake momentum thickness appearing in this relation is directly related to the momentum thickness of the surface boundary layers at the blade trailing edge. An analogous approximate equation

$$C_D\approx 2\left(\frac{\theta^*}{c}\right)_{te}\frac{\cos\beta_m}{\cos\beta_{te}}\left[1+\frac{1}{2}\left(\frac{\theta^*}{c}\right)_{te}\frac{\sigma H_{te}^2}{\cos\beta_{te}}\right]$$

exists between the drag coefficient based on dynamic pressure in the free stream at the trailing

edge and on the trailing-edge wake momentum-thickness ratio of the cascade airfoil. Thus, the drag coefficient can be considered as a measure of the momentum-thickness ratio of the surface boundary layers for both isolated and cascade airfoils.

In compressor design and analysis, it has been found convenient to use a loss parameter based on the defect in total pressure across a blade element. A general compressor total-pressure-loss coefficient $\bar{\omega}$ has been defined (ref. 156) as

$$\bar{\omega}=\frac{\Delta\bar{P}}{\frac{1}{2}\rho V_{ref}^2}$$

where $\Delta\bar{P}$ represents the mass-averaged decrease in relative total pressure across the blade element, and $\frac{1}{2}\rho V_{ref}^2$ represents the dynamic pressure at some reference location. It is desirable, therefore, in the discussion of real cascade flow, to consider the effects of viscosity on the defect in total pressure. Since $\bar{\omega}$ depends on $\Delta\bar{P}$, the value changes with distance downstream of the trailing edge (because of turbulent mixing) and therefore depends, to some extent, on the location of the measuring station. The complete loss in total pressure is obtained at a station sufficiently far downstream that the flow has become uniform This is contrary to the case of drag coefficient, which is theoretically the same at any axial location downstream of the blade trailing edge.

For the two-dimensional cascade with incompressible flow, reference 156 shows that, if the static pressure is uniform across the blade spacing at the trailing edge, the total-pressure-loss coefficient for complete mixing $\left(\text{based on } \frac{1}{2}\rho V_{0,te}^2\right)$ is given approximately by

$$\omega\approx 2\left(\frac{\theta^*}{c}\right)_{te}\frac{\sigma}{\cos\beta_{te}}\left[1+\frac{1}{2}\left(\frac{\theta^*}{c}\right)_{te}\frac{\sigma H_{te}^2}{\cos\beta_{te}}\right]$$

Thus, the trailing-edge momentum thickness should be an indication of the complete loss in total pressure.

In view of the preceding discussion, the boundary-layer momentum thickness at the blade trailing edge is considered herein as the basic parameter reflecting qualitatively the total-pressure loss or the profile drag for an airfoil section.

LAMINAR BOUNDARY LAYER

A laminar boundary layer is always present on the forward portion of a cascade blade. The growth of the laminar layer (expressed as boundary-layer thickness δ) in the absence of a longitudinal pressure gradient (flat-plate flow) proceeds essentially according to the proportionality relation

$$\delta\propto\sqrt{\frac{\nu s}{V_1}} \tag{222}$$

where ν is kinematic viscosity, s is distance along the surface, and V_1 is the velocity far upstream. In the presence of a negative pressure gradient the boundary-layer thickness is somewhat less, and for a positive pressure gradient it is somewhat greater, than for the constant-pressure case of equation (222).

To relate equation (222) to a body in the flow field, let Re_c be the Reynolds number based on blade chord length (the length of the plate in the case of a flat plate). Then, equation (222) can be rewritten as

$$\frac{\delta}{c}\propto\frac{\sqrt{\frac{s}{c}}}{\sqrt{Re_c}} \tag{223}$$

where $Re_c=V_1c/\nu$. Therefore, δ/c varies inversely with the square root of the body Reynolds number for a given value of s/c.

The drag due to friction in the laminar flow depends on the integral of the local surface shear stress $\hat{\tau}_w$ and therefore on the velocity gradient at the wall $\left(\text{i.e., } \hat{\tau}_w=\mu\left(\frac{\partial u}{\partial n}\right)_{n=0}\right)$. For flat-plate flow, the drag coefficient varies with the body Reynolds number as

$$C_D\propto\frac{1}{\sqrt{Re_c}} \tag{224}$$

For accelerating flow the friction coefficient is greater (larger $\partial u/\partial n$ at wall, see fig. 97), and for decelerating flow the friction coefficient is smaller (smaller $\partial u/\partial n$), than for the flat plate; but in all cases a decreasing trend with body Reynolds number is observed.

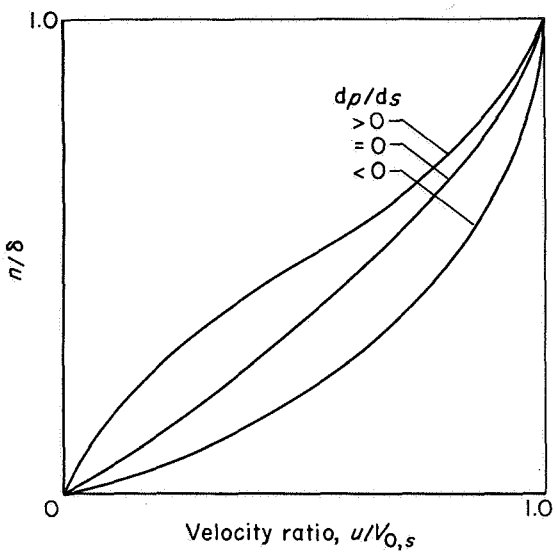

FIGURE 97.—Laminar-boundary-layer velocity distributions for different surface pressure gradients.

In the presence of a positive pressure gradient, the boundary-layer momentum is often insufficient to overcome the increase in pressure, and separation will occur. Specifically, separation occurs when the surface shear stress is zero (i.e., when $(\partial u/\partial n_{n=0}=0)$. According to simplified theory, the separation condition depends on the value of a flow parameter of the form

$$\lambda=\frac{\delta^2}{\nu}\frac{dV_0}{ds} \tag{225}$$

as in the Pohlhausen theory (ref. 157), or

$$m=\frac{-\theta^{*2}}{\nu}\frac{dV_0}{ds} \tag{226}$$

as in the Thwaites theory (to be discussed later). According to the Pohlhausen theory, separation occurs when $\lambda=-12$. As will be seen later, this is not entirely reliable, since the theory is least applicable in regions of rising pressure. Thwaites gives a value of $m=0.082$ for separation to occur. This criterion appears to be more valid than that of Pohlhausen. In any event, the location of the point of laminar separation is primarily characterized by a boundary-layer thickness and the local gradient of free-stream velocity. The location is unaffected by changes in blade-chord Reynolds number.

Now consider the laminar flow over a blade section at fixed angle of attack (fig. 98). The velocity distributions on the pressure and suction surfaces are indicated in the lower part of the figure. The laminar boundary layer grows along the surface until some point after the maximum velocity is reached. The laminar boundary layer then separates if a sufficiently severe pressure gradient occurs. The location of the separation point behind the point of peak velocity varies with the magnitude of the positive pressure gradient and is independent of the body Reynolds number (if the Reynolds number is low enough that transition to turbulent flow does not occur). With a separation of the laminar boundary layer, the free-stream velocity distribution is altered as indicated by the dashed line in figure 98, and an increase in form drag results. The magnitude of the form drag depends on the thickness of the profile at the point of separation and the camber of the airfoil. For a cascade airfoil, the variation of the free-stream velocity after the separation may be slightly different from that for the isolated airfoil because of the channel effect of adjacent blades.

The pronounced effect of the surface velocity gradient on the calculated location of the point of laminar separation is illustrated in figure 99 (obtained from ref. 151, pt. I) for a Joukowski profile. As the pressure gradient increases, the point of separation moves closer to the point of peak velocity. The different velocity gradients in the figure were achieved by varying the angle of attack of the airfoil.

TURBULENT BOUNDARY LAYER

In the range of turbulence and Reynolds number usually encountered in cascade blade rows, the laminar boundary layer generally becomes turbulent somewhere along the blade surface. It is chiefly because of this transition that practical compressors are realizable. The turbulent interchange of momentum between the free stream and the turbulent boundary layer increases the energy level in the boundary layer so that it can advance farther, without separating, in the face of a pressure rise than could a laminar boundary layer.

The turbulent-boundary-layer thickness develops (e.g., ref. 152), in the absence of a pressure gradient, as

$$\delta\propto\sqrt[5]{\frac{\nu s^4}{V_1}} \text{ or } \frac{\delta}{c}\propto\frac{\sqrt[5]{\frac{s^4}{c^4}}}{\sqrt[5]{Re_c}} \tag{227}$$

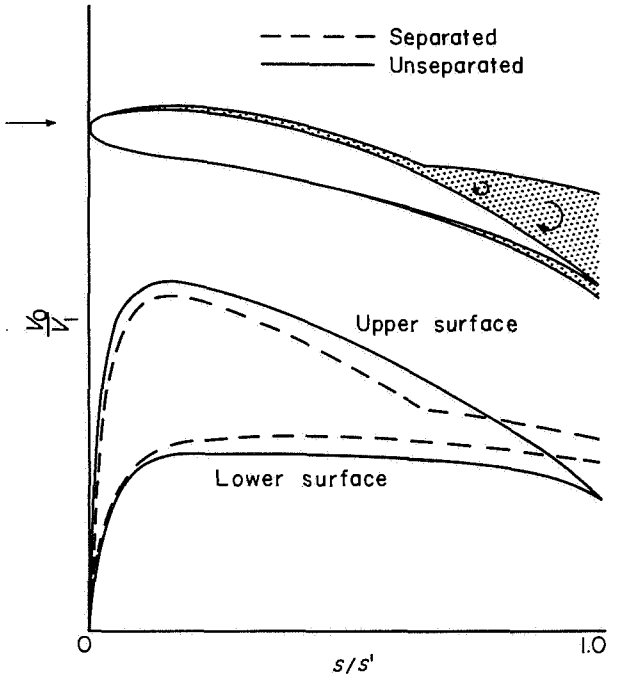

FIGURE 98.—Effect of separation on velocity distribution about an airfoil.

The turbulent δ is generally larger than the laminar δ for the same Re_c. This increased thickness contributes to a slightly larger form drag for the turbulent boundary layer than for an equivalent unseparated laminar layer (at the same Reynolds number).

In a laminar boundary layer the local shear stress is given throughout by $\hat{\tau}=\mu(\partial u/\partial n)$. This simple equation does not hold for the turbulent boundary layer because of the turbulent shear stresses present. The wall shear stress is given by $\hat{\tau}_w=\mu(\partial u/\partial n)_{n=0}$ in both cases, since a very thin laminar boundary layer, called a laminar sublayer, is always present between the turbulent layer and the wall. However, not enough is known of the velocity distribution in the laminar sublayer to enable the utilization of this expression to compute wall shear stress for the turbulent layer. As a result, the problem must be approached empirically.

From velocity profiles observed in pipe flow, the drag coefficient for a flat plate is found to vary inversely with the fifth root of Re_c:

$$C_D \propto \frac{1}{\sqrt[5]{Re_c}} \tag{228}$$

Experience shows that many factors such as boundary-layer form factor, Reynolds number, and pressure gradient (ref. 158) influence the magnitude of the shear stress. To date, many empirical relations have been established between local shearing stress and boundary-layer characteristics. One of the most recent is due to Ludwieg and Tillmann (ref. 159):

$$\frac{\hat{\tau}_w}{\frac{1}{2}\rho V_0^2}=0.246e^{-1.561H}Re_\theta^{-0.268} \tag{229}$$

where Reynolds number $Re_\theta=V_0\theta^*/\nu$, and H is the form factor. The empirical skin-friction formulas lead to the general conclusion that the turbulent skin-friction coefficient is greater than the laminar skin-friction coefficient for the same Reynolds number.

The condition that $\hat{\tau}_w=0$ defines the point of separation in both laminar- and turbulent-boundary-layer-flows. In the case of the turbulent-boundary-layer, the point at which $\hat{\tau}_w=0$ is determined from an empirical equation such as equation (229). In reference 160 this equation is used in conjunction with experimentally determined values of H and Re_θ to predict separation. It is clear that $\hat{\tau}_w$, in equation (229), never actually becomes zero. However, the decreasing trend is sufficiently pronounced as the separation point is approached that extrapolation to $\hat{\tau}_w=0$

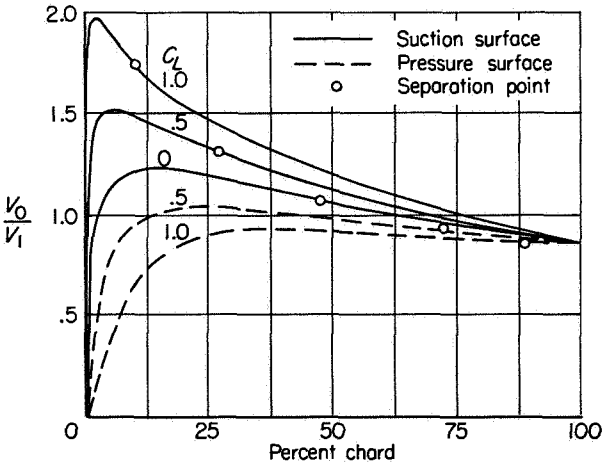

FIGURE 99.—Potential-theoretical velocity distribution showing calculated point of laminar separation for Joukowski profile J 015 for lift coefficients of 0, 0.5, and 1.0 (ref. 151, pt. I).

is possible. Figure 100 shows the results of such a calculation from reference 160.

For conventional two-dimensional compressor sections, several gross parameters have been developed to indicate whether separation is likely in certain areas of blade design (refs. 9 and 38). These parameters, based on the diffusion in velocity on the blade suction surface, involve consideration of only the peak and outlet suction-surface velocities or approximations to these velocities in terms of over-all (inlet and outlet) velocities and flow angles. Implicit in the work is the consideration that the boundary-layer history at the start of the diffusion and the velocity distributions along the surface are generally the same for conventional blade sections. Location of the point of separation, however, cannot be determined from these parameters.

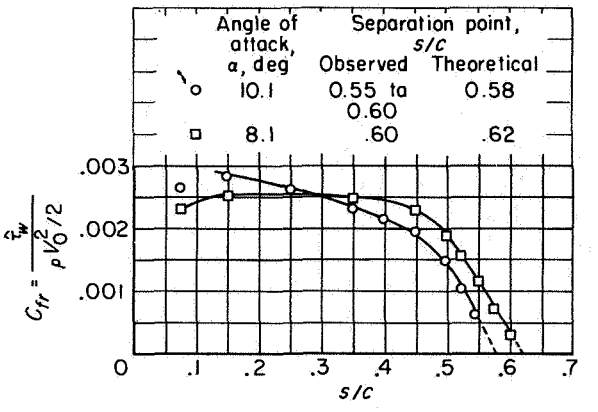

FIGURE 100.—Comparison of experimentally observed separation points with those obtained by extrapolating values of C_{fr} obtained from Ludwieg-Tillmann formula using experimental data of reference 174 for NACA airfoil section 65(216)–222 (approx.) (ref. 160).

TRANSITION

For conventional airfoil shapes, the initial laminar boundary layer, if it remains laminar, will separate at some point downstream of the pressure minimum. Depending on certain flow characteristics to be considered in this section, a transition to turbulent flow may occur at a point prior to the laminar separation point. In this event, the turbulent flow will remain attached for some distance farther along the blade surface. Such a transition will normally occur under ordinary cascade flow conditions. The region in which the transition to turbulent flow takes place is small and is conveniently thought of as a point, called the transition point.

The exact location and conditions under which the transition from a laminar to a turbulent boundary layer will occur are not currently predictable, and the question of transition constitutes a major problem in present-day boundary-layer research. Transition can result either from disturbances of finite magnitude such as free-stream turbulence, or from an instability of the laminar steady flow in which infinitesimal disturbances, under proper conditions, grow exponentially with respect to time. The length of travel or time before transition occurs depends on the rate of amplification of the disturbances and therefore on the particular flow conditions in and about the boundary layer.

Experiment shows (ref. 161) that transition occurs because of infinitesimal disturbance instability when the free-stream turbulence intensity is less than about 0.2 percent and when no other external disturbances are present. For free-stream turbulence greater than about 0.2 percent, which is generally the situation in cascade and compressor flow, the characteristics of the free-stream turbulence (scale and intensity) play a decisive role in effecting the transition. In any event, the transition phenomena can generally be related in terms of the Reynolds number and another parameter or parameters describing the characteristics of the disturbance (i.e., free-stream turbulence, surface roughness, etc.).

Infinitesimal-disturbance theory.—The first significant theoretical work on transition was concerned with the instability of the laminar boundary layer with respect to infinitesimal oscillations within the layer (e.g., ref. 151, pt. II). In a stable laminar boundary layer the disturbances are damped, while in an unstable boundary layer the disturbances are amplified. The point of division, called the neutral or instability point, depends on the origin of the disturbance. The existence of instability in a laminar boundary layer indicates that transition is possible but not necessarily present after the neutral point. The actual transition to a fully developed turbulent motion will occur some distance downstream of

the instability point, since a finite time is required for the oscillations to build to full strength and permeate the boundary-layer region.

According to this theory, an instability of the laminar boundary layer (i.e., an amplification of oscillations) results from (1) the presence of viscosity and (2) an inflection in the boundary-layer velocity profile normal to the surface. The theory further indicates that the instability point is a function of the boundary-layer Reynolds number; that is, below some value of Reynolds number infinitesimal oscillations are damped, while above this value oscillations are amplified. The instability value of the boundary-layer Reynolds number depends largely on the form of the velocity profile of the basic boundary-layer flow. This profile is determined primarily by the longitudinal pressure gradient of the flow. The greater the positive pressure gradient, the lower the boundary-layer Reynolds number at instability. In translating these results into terms of the blade-chord Reynolds number, the boundary-layer Reynolds number Re_δ can be expressed as

$$Re_\delta = \frac{V_0 \delta}{\nu} \frac{V_1}{V_1} \frac{c}{c} = Re_c \frac{V_0}{V_1} \left(\frac{\delta}{c}\right) \qquad (230)$$

Thus, in general, the closer the point in question to the blade leading edge (the smaller the value of δ/c), the larger the blade-chord Reynolds number necessary for the attainment of the instability value of the boundary-layer Reynolds number at that point. That is, the higher the blade-chord Reynolds number, the sooner will the instability condition occur. These considerations are illustrated graphically in figure 101, which shows the results of the calculation of the instability point for various blade-chord Reynolds numbers on the suction surface of a Joukowski airfoil at several angles of attack (from ref. 162). The effect of the increased surface pressure gradient and Reynolds number on the location of the instability point as angle of attack is increased is clearly indicated.

Finite-disturbance theory.—In a second general theory of transition (ref. 163), disturbances of finite magnitude are considered to be imposed on the laminar boundary layer from outside sources. In this case, the transition of the laminar boundary

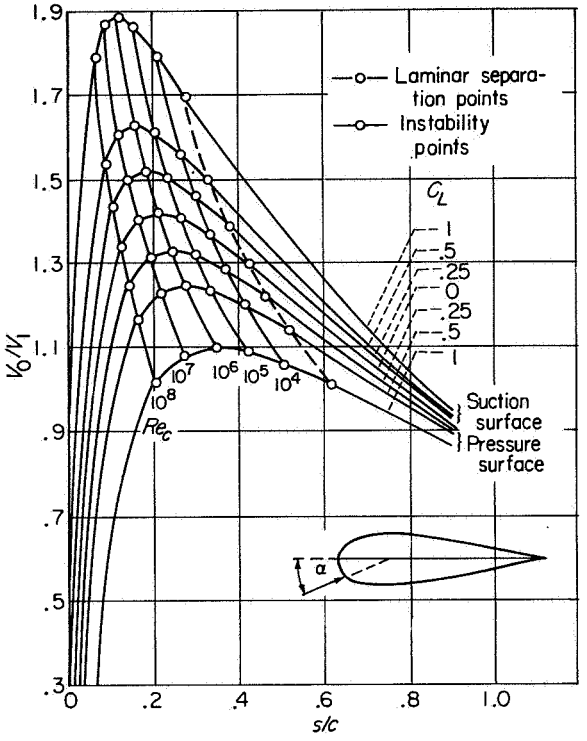

FIGURE 101.—Theoretical velocity distributions for J 025 airfoil at various values of lift coefficient (obtained by varying angle of attack) with instability and separation points calculated for various values of blade-chord Reynolds number (ref. 162).

layer depends on the characteristics of the imposed disturbance. The principal source of external disturbance is a function of the intensity and scale of free-stream turbulence according to the parameter $\mathcal{J}(l^*/L)^{1/5}$, where $\mathcal{J}$ is the intensity of the turbulence, L is the scale of the turbulence, and l^* is some characteristic dimension of the body such as chord length or diameter. The greater thef ree-stream turbulence parameter, the lower the magnitude of the critical Reynolds number. Intensity of turbulence is defined as the ratio of the root mean square of the disturbance velocity to the mean flow velocity. Scale of turbulence is a measure of the effective size of the turbulent eddies and has an inverse effect on the turbulence parameter. Experimental confirmation of this theory has been obtained by several investigators (refs. 164 and 165) in the study of the drag characteristics of spheres.

Flow about spheres.—In the development of

the boundary layer on cascade blade sections, a primary consideration is whether the transition occurs before or after the point of laminar separation. The effect of transition location on the loss characteristics of submerged bodies is graphically illustrated by the well-known flow around a sphere at a fixed turbulence level as represented in figures 102 and 103. At low Reynolds numbers, when no transition occurs, the laminar boundary layer separates and high profile drag results. When transition occurs before the point of laminar separation at high Reynolds numbers, the resulting turbulent boundary layer can tolerate a greater pressure gradient; separation of the turbulent layer is delayed, and a lower profile drag is observed. The Reynolds number at which the rather sudden change of drag characteristic occurs, called the critical Reynolds number of the sphere, corresponds to the point where the transition and separation coincide.

The drag characteristics of spheres have provided a means for evaluating the effects of free-stream turbulence on transition. As previously discussed, theory indicates that the critical Reynolds number will be a function of the turbulence parameter $\mathcal{J}(l^*/L)^{1/5}$. Experimental verification of this effect (ref. 164) is represented by figure 104, which illustrates the earlier transition associated with increasing free-stream turbulence. The turbulence correlation of figure 104 provides a means for identifying the free-stream turbulence level from the measured drag characteristics of spheres. The turbulence in a cascade tunnel is frequently expressed in terms of a turbulence factor, defined as the ratio of the critical Reynolds number at zero turbulence to the measured critical Reynolds number of the sphere (ref. 165).

The effective Reynolds number for a blade section, defined as blade-chord Reynolds number times turbulence factor of the tunnel, has been used to represent a transition parameter that

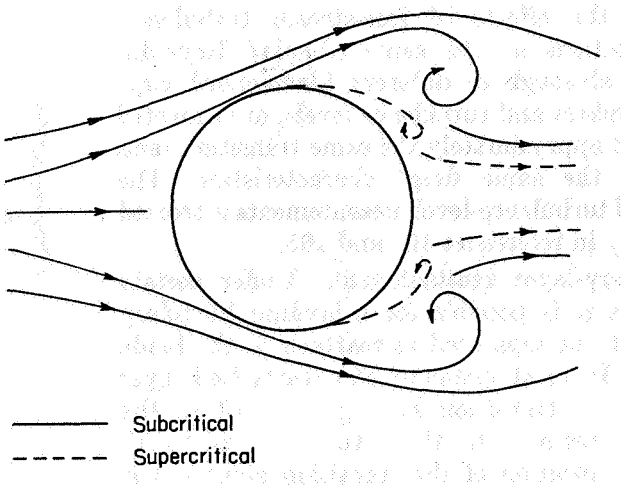

FIGURE 103.—Subcritical and supercritical flow around sphere (schematic, after ref. 151, pt. II).

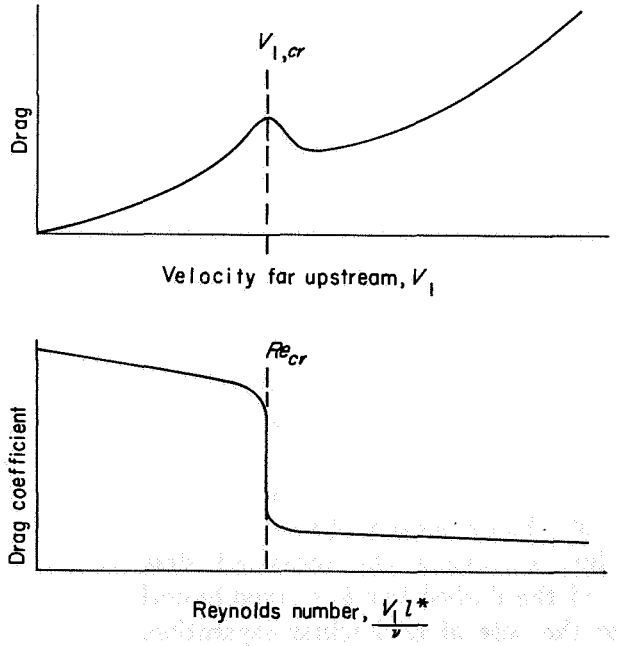

FIGURE 102.—Drag and drag coefficient of sphere in region of critical Reynolds number.

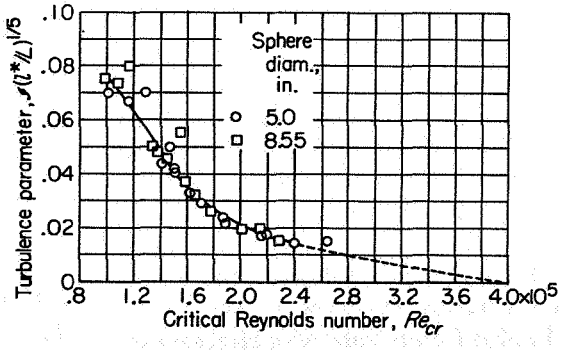

FIGURE 104.—Experimental variation of critical Reynolds number of spheres with turbulence factor; extrapolated to zero turbulence (data of ref. 164). Value of Re_{cr} for zero turbulence indicated to be between 3.85×10^5 (ref. 182) and 4.11×10^5 (ref. 165).

includes the effects of free-stream turbulence. Blade sections at the same effective Reynolds number, although of different blade-chord Reynolds numbers and turbulence levels, are expected to exhibit approximately the same transition (and therefore the same drag) characteristics. The subject of turbulence-level measurements is treated more fully in references 164 and 165.

Boundary-layer reattachment.—Under certain conditions it is possible for a laminar boundary layer that has separated to reattach to the blade surface. In most instances the reattached layer is turbulent, transition having occurred in the separated region. In these turbulent reattachments the location of the transition point is the principal determinant.

Generally speaking, the boundary-layer behavior is fairly well understood as long as the transition occurs either before the separation point or at a large distance downstream of the separation. In the former case a thickening of the boundary layer occurs in the region of transition as the flow passes to the turbulent state. In the latter case, the laminar boundary layer remains separated, and the flow breakaway and high form drag are observed. When transition occurs close behind the point of laminar separation, however, under certain conditions, the separated laminar boundary layer may reattach to the surface as a turbulent layer, forming a sort of bubble of locally separated flow. The reattached turbulent boundary layer is considerably thicker than if transition had occurred at that point without a previous laminar separation. The turbulent reattachment has been observed for both isolated and cascade airfoil sections. Detailed discussions of the nature of the separation bubble and the various factors influencing its characteristics are presented in references 39, 166, and 167 (pt. II). Various experimental methods of determining the extent and location of the laminar separation are discussed in references 166, 167 (pt. II), and 168.

Experimental variations of the boundary-layer momentum thickness, boundary-layer form factor, and pressure distribution observed in the region of the laminar bubble for an isolated-airfoil section (ref. 166) are illustrated in figure 105. A similar illustration of the pressure distribution on the suction surface of a cascade section with laminar separation bubble (ref. 39) is shown in figure

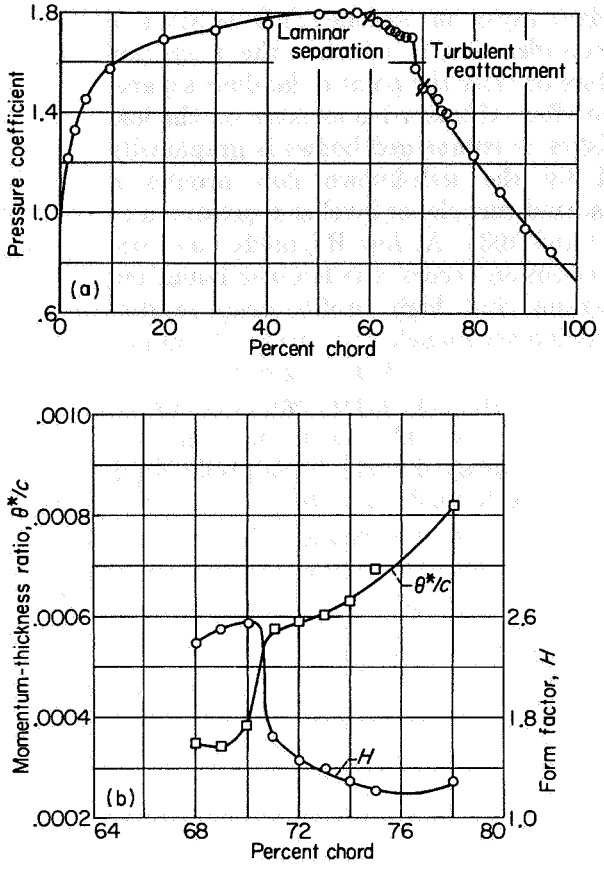

(a) Pressure distribution.
(b) Momentum thickness and form factor.

FIGURE 105.—Pressure distribution on NACA 66$_3$–018 airfoil at zero angle of attack and blade-chord Reynolds number of 2.4×10^6, and variation of momentum-thickness ratio and form factor in region of reattachment of locally separated flow (ref. 166).

106(a). The most detrimental effect of the laminar separation bubble is the rather sharp increase in momentum thickness associated with the turbulent reattachment. The effect of a suction-surface laminar separation bubble on the loss characteristics of a blade section is illustrated in figure 106(b), which presents the variation of drag coefficient C_D with angle of attack α for a typical cascade blade section (from ref. 39). The solid line represents the measured drag coefficient, and the dashed line is a hypothetical variation for the case of no laminar separation. A noticeable increase in the drag coefficient occurs in the low-loss range of operation.

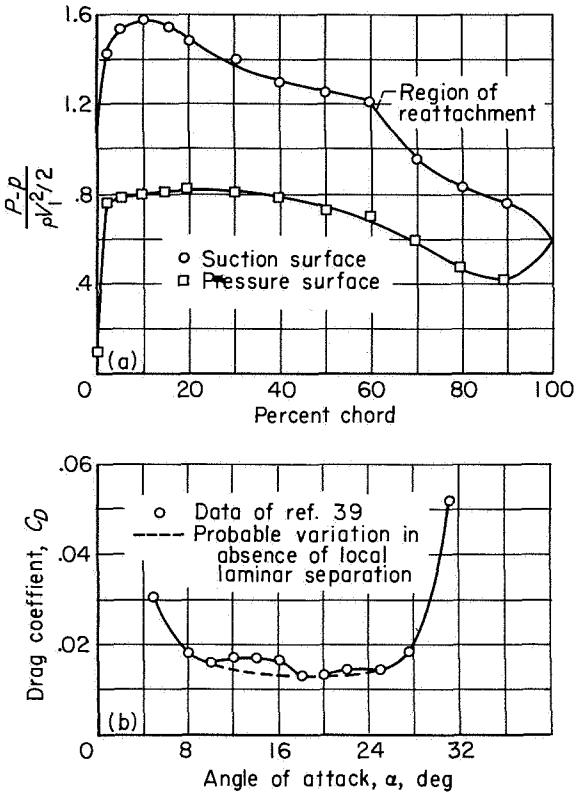

(a) Pressure distribution at 16.1° angle of attack.
(b) Variation of drag coefficient with angle of attack.

FIGURE 106.—Illustration of effect of local laminar separation on pressure distribution and drag characteristics for NACA 65–(12)10 airfoil in cascade. Inlet-air angle, 45°; solidity, 1.5.

Obviously, the occurrence of laminar separation bubbles will make the correlation of cascade data difficult. The effects of turbulence level and Reynolds number further increase the problem. Although the theory governing these effects is not complete, some qualitative ideas can be drawn from the foregoing descriptive material.

COMPOSITE LOSS VARIATIONS

The preceding sections have presented a qualitative picture of the characteristics of the three general regimes of boundary-layer development—the laminar region, the fully turbulent region, and the transition region. On the basis of available theory and experimental evidence, the manner in which each type of flow influences the resulting thickness of the boundary layer was indicated. On conventional cascade blade surfaces, all three boundary-layer regimes are known to exist. The momentum thickness of the boundary layer at the blade trailing edge depends on the extent of each flow regime. The momentum thickness at the blade trailing edge is a principal factor in the determination of the loss in total pressure of the cascade system. The prediction of the loss characteristics of a given cascade geometry thus involves an analysis of the composite effects of the boundary-layer regimes.

From the previous discussions, it is known that the principal factors affecting the boundary layer are the local surface pressure distribution, the blade-chord Reynolds number, and the free-stream turbulence level. It is desirable to construct a qualitative picture of the anticipated variation of boundary-layer momentum thickness on a blade surface over a wide range of Reynolds number, pressure distribution, and turbulence level. Such a composite plot will not only constitute an effective summary of the preceding theory as applied to blade sections, but may also be of interest in identifying desirable or undesirable areas of cascade operation.

The comparative variation of trailing-edge boundary-layer momentum thickness (actually the ratio θ^*/c) with blade-chord Reynolds number is presented qualitatively for several levels of pressure gradient in figure 107. Pressure distributions are considered ranging from zero pressure rise (no blade loading) to a severe pressure gradient (very high loading) resulting in a separation of the turbulent layer. The analysis is made for the flow along the convex (suction) surface of conventional compressor blade sections. The pressure distributions considered, therefore, contain a decreasing pressure over the forward portion of the blade and a rising pressure over the rearward portion.

The variation of trailing-edge momentum-thickness ratio is presented in figure 107 for a fixed low turbulence level (as normally encountered in low-turbulence cascade tunnels). It must be emphasized that the trends established are only qualitative and that no sufficient substantiating data are available. The values of Reynolds number at which the transition phenomena are indicated in figure 107 are not to be interpreted as accurate definitions of these regions. These values are largely unpredictable at this time.

Zero loading.—The limiting case of no blade surface pressure gradient can be represented by the boundary-layer flow along a flat plate. For

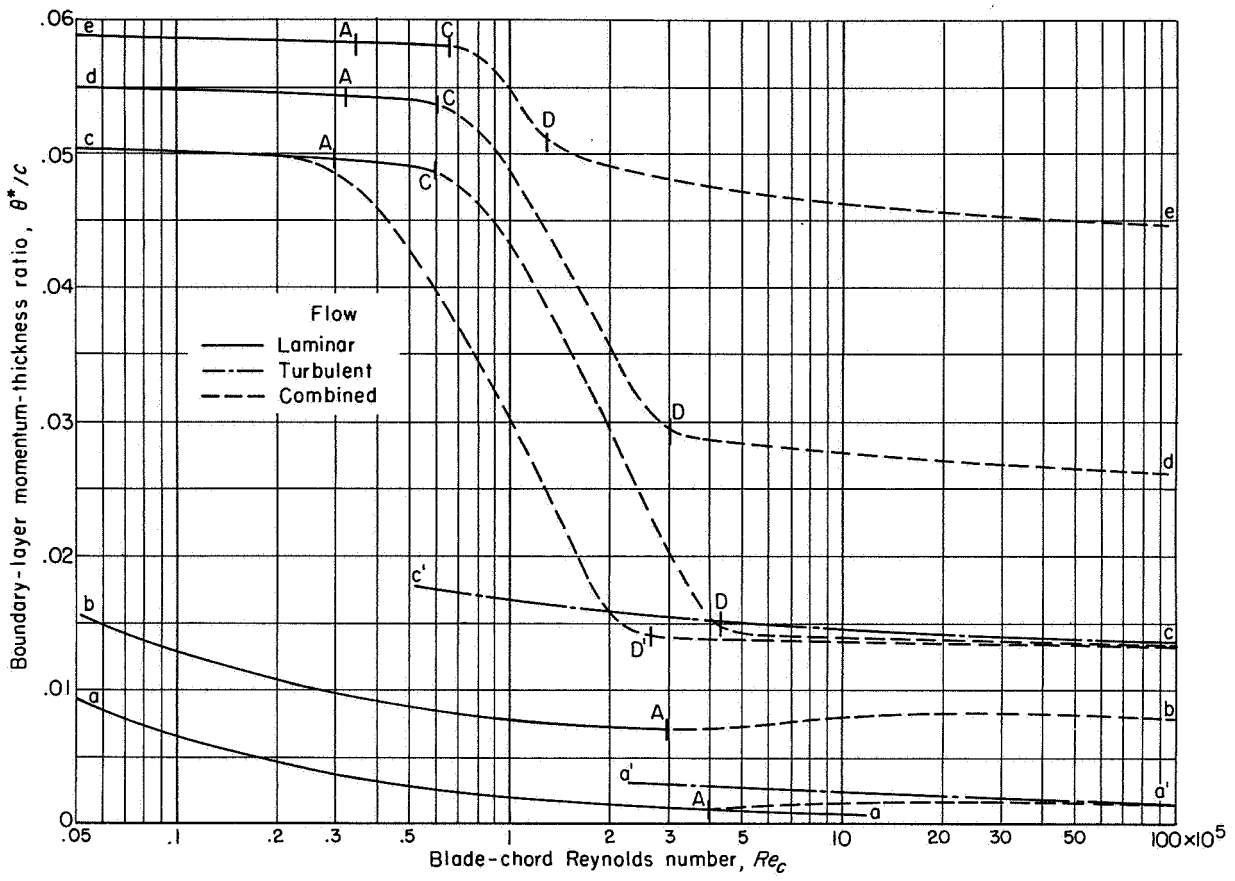

FIGURE 107.—Qualitative variation of trailing-edge momentum-thickness ratio with blade-chord Reynolds number for several levels of blade loading on conventional airfoils in cascade. (Not to be considered quantitatively correct.)

flat-plate flow, no separation occurs, and the two regimes of laminar and turbulent flow are described by the drag variations of equations (224) and (228), respectively. Curve a-a in figure 107 represents the momentum-thickness variation for laminar flow, and curve a′-a′ represents the variation for turbulent flow for the flat plate.

At low values of Re_c the boundary layer is entirely laminar, and θ^*/c decreases with increasing Re_c as shown by curve a-a. At some value of Re_c, indicated by A in the figure, Re_c becomes sufficiently large that transition from a laminar to a turbulent layer occurs at the trailing edge. This Reynolds number appears to yield the minimum boundary-layer thickness. With a further increase in Re_c, the transition moves forward from the trailing edge, and the boundary-layer thickness falls somewhere between the laminar and, turbulent curves (dashed portion). Finally, as the transition point approaches the leading edge the boundary layer will essentially assume the characteristics of the fully turbulent flow. [Strictly speaking, since the boundary-layer transition point actually arrives at the leading edge only at an infinite Reynolds number (in the absence of outside disturbance), the dashed transition curve will asymptotically approach the turbulent curve as Re_c approaches infinity.]

Increased turbulence will cause the boundary-layer transition phenomena to occur at lower values of Reynolds number and will therefore have the effect of shifting point A farther to the left on curve a-a. For zero pressure gradient, therefore, increased turbulence may increase the minimum boundary-layer momentum thickness.

Low loading.—The curve b-b in figure 107 represents the case of a very lightly loaded blade whose surface pressure gradient is such that laminar separation will not occur. In this case, the picture is much the same as for the flat plate, except that the boundary-layer thicknesses will generally be somewhat greater. It is also quite

possible that both the presence of a pressure gradient and the location of the minimum pressure will have some influence on the location of point A. However, it is not believed that these effects will be marked for the lightly loaded surface.

Moderate loading.—The boundary-layer thickness variations for a moderately loaded blade surface are illustrated by curve c-c in figure 107. The moderately loaded blade probably represents the major portion of current design experience. The blade loading in this case can be achieved by a blade with moderate camber operated at its best (minimum-loss) angle of attack, or by a section of smaller camber operated at a relatively high angle of attack.

At low Reynolds number, the adverse pressure gradient is sufficient to cause a separation of the laminar bondary layer somewhere downstream of the point of minimum pressure. A marked rise in the momentum loss compared with the low-loading case will therefore be obtained in the low Reynolds number range. The precise magnitude of the separated boundary-layer thickness depends on the shape and angle of attack of the blade. A separation point close to the leading edge would tend to produce a relatively large separated wake (form drag). Since the point of laminar separation is independent of Reynolds number, the laminar layer remains separated, and the high values of θ^*/c continue as Reynolds number is increased to point A. A slight decrease in θ^*/c in this high-loss region is to be expected, however, because of the thinning of the boundary layer upstream of the point of separation.

At a Reynolds number corresponding to the point A, the transition to turbulent flow would take place at the trailing edge if the laminar layer were still attached. Since the laminar layer has separated, there is no transition and the thickness continues high from A to C. With increasing Re_c, the transition point moves closer to the point of laminar breakaway. When the two points are sufficiently close together, the separated laminar layer may be infused with sufficient turbulence to reattach itself a short distance beyond the point of separation, resulting in a separation bubble. After reattachment starts at point C, the θ^*/c curve drops rather sharply with Reynolds number increase in the

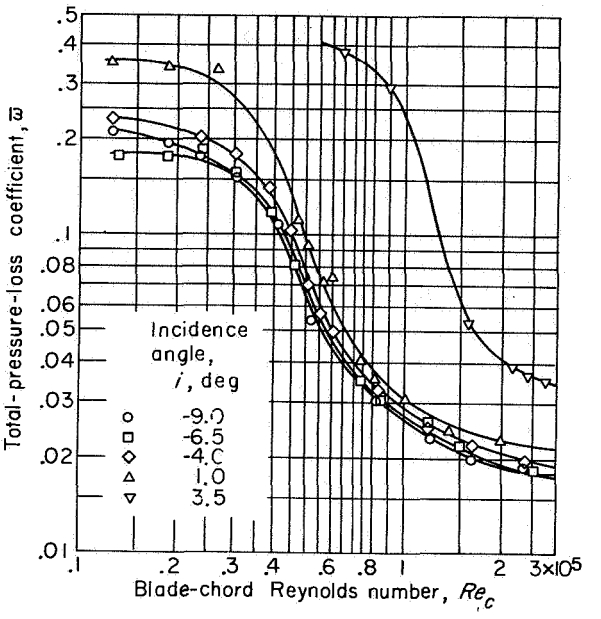

FIGURE 108.—Variation of total-pressure-loss coefficient with blade-chord Reynolds number for parabolic-arc blade 10C4/40 P40. Inlet-air angle, 28° to 40°; solidity, 1.333 (ref. 183).

region from C to D as the extent of the separation bubble decreases. Finally, the transition occurs right at the point of separation indicated by point D. Thereafter, the curve of θ^*/c tends to approach the variation of the fully turbulent flow (curve c'-c'). The rate at which the fully turbulent curve is approached will probably depend to a large extent on the chordwise location of the point of minimum pressure. (Since the blade is moderately loaded, the separation point is probably not far beyond the minimum-pressure point, and any further movement of the transition point will be slow.) An experimental illustration of the type of loss against Reynolds number curve represented by curve c-c in figure 107 is shown in figure 108 for a conventional cascade blade section at several angles of incidence.

In view of the many factors influencing the formation and extent of the separation bubble, it would appear possible to obtain a wide range of possible transition paths between laminar breakaway (below point C, fig. 107) and turbulent attachment (beyond point D). Also, if for some reason a separation bubble does not occur and attachment does not take place until the transition point and the laminar separation point essentially coincide (as in the case of the flow about

a sphere or cylinder), then the laminar breakaway region will extend farther out along the line A–C and a very sharp drop in boundary-layer thickness will be observed to D (as in the case of the sphere). Furthermore, the chordwise location of the minimum-pressure point will probably affect the location of the transition region. For example, if the minimum-pressure point occurs far back on the blade, the reattachment of the laminar layer will probably begin very shortly after the transition point first occurs on the blade. This would tend to reduce the flat portion of the curve between A and C, and probably also give a steeper drop in θ^*/c. (The magnitude of the loss of the separated laminar boundary layer would not, however, be as large as in the case of a forward pressure minimum.)

The preceding picture will be further complicated by considerations of varying turbulence levels. In general, however, it is probable that increased free-stream turbulence will cause an earlier boundary-layer transition and therefore tend to move the transition region of the curve to lower values of Reynolds number (c–D′–c). An experimental illustration of such an effect is presented in figure 109 in terms of the loss parameter $\overline{\omega}$. A further extension of the turbulent layer into the lower range of Reynolds number (extension along curve c′–c) may also be obtained by employing artificial means for tripping the boundary layer at the leading edge. Such measures, however, although extending the range of low loss to lower Reynolds numbers, probably result in an increase in the magnitude of the loss at higher Reynolds numbers.

High loading.—Curve d-d in figure 107 represents a highly loaded blade. As in the previous case, the laminar boundary layer separates at low values of Reynolds number. As Re_c increases, the transition point moves forward (starting at A) until it approaches the separation point. The laminar layer may then reattach (point C) and proceed as a turbulent layer. The momentum-thickness ratio then decreases as the extent of the laminar separation is reduced, as indicated by the dashed curve after point C. (The establishment of turbulent flow in the high-loading case may require actual coincidence of the transition and separation points, in which case the drop in θ^*/c after point C will be much steeper.)

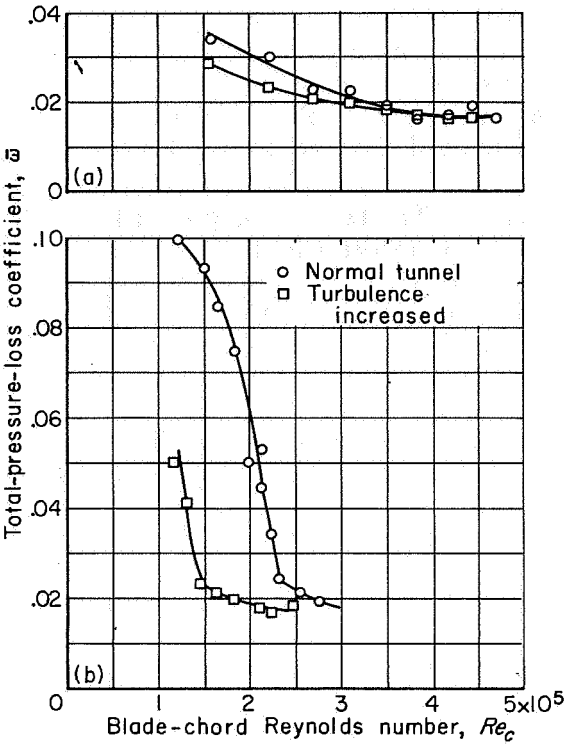

(a) NACA 65–(12)10 blade. Inlet-air angle, 45°; solidity, 1.5 (ref. 39).

(b) Lighthill blade, 50-percent laminar flow. Inlet-air angle, 45.5°; solidity, 1.0 (ref. 167, pt. I).

FIGURE 109.—Effect of blade-chord Reynolds number and free-stream turbulence on minimum-loss coefficient of cascade blade section in two-dimensional tunnel.

The surface pressure distribution is such, however, that the established turbulent layer will now separate at some point downstream of the transition. The resulting momentum-thickness ratio when the local laminar separation has disappeared (transition moves forward of the laminar separation) will then be greater, as indicated by point D, than for the corresponding condition in the moderately loaded blade. Then, as Reynolds number is increased and the boundary-layer characteristics upstream of the separation are improved, the turbulent boundary layer will be able to proceed farther into the adverse pressure gradient. Thus, with a resulting downstream movement of the turbulent separation, the trailing-edge boundary-layer thickness will decrease with increasing Reynolds number from point D on.

The actual magnitude of the loss in the presence of turbulent separation depends to a large extent

on the chordwise location of the point of turbulent separation. For separation close to the blade trailing edge, as represented by curve d-d, the increase of boundary-layer thickness will not be very great (level of curve D-d). If the separation occurs forward on the blade close behind the transition, as represented by curve e-e, the increase in thickness will be much greater (level of curve D-e).

Summary.—The previous considerations indicate that a considerable range of trailing-edge boundary-layer momentum thickness can be obtained from blade sections, depending on the surface pressure distribution, Reynolds number, and turbulence level. In two-dimensional-cascade research, therefore, it appears highly desirable to identify the range of operation of the blade sections in the general loss against Reynolds number spectrum. Actually, some effective Reynolds number should be considered so that turbulence level can also be included. Such identification can aid in determining the best regions of cascade operation and also be of use in correlating data from different tunnels. Furthermore, in view of the possible pronounced effect of the laminar breakaway at low Reynolds number, the question of Reynolds number effects might be a significant consideration in compressor design. Reduced Reynolds number in compressor design may arise for small-scale units and for operation at high altitude.

It must be repeated that the curves presented in figure 107 are only qualitative. The magnitude of loss and the values of Reynolds number indicated for the ranges of different loss characteristics are not to be interpreted as quantitatively correct. The precise wake momentum-thickness variations of a specific cascade geometry can currently be determined only by experiment.

QUANTITATIVE BOUNDARY-LAYER THEORY

GENERAL CONSIDERATIONS

Unfortunately, current ability to determine cascade boundary-layer behavior quantitatively falls below the ability to establish a qualitative picture. The principal difficulty in this respect lies in obtaining satisfactory solutions of the viscous-flow equations.

The complete viscous flow about cascade sections is generally considered to be described by the equations of Navier-Stokes and the continuity equation. For two-dimensional incompressible flow, neglecting body forces, these equations are written as follows (ref. 151, pt. I):

$$\left.\begin{aligned} &\frac{\partial u}{\partial \tau}+u\frac{\partial u}{\partial s}+v\frac{\partial u}{\partial n}=-\frac{1}{\rho}\frac{\partial p}{\partial s}+\nu\left(\frac{\partial^2 u}{\partial s^2}+\frac{\partial^2 u}{\partial n^2}\right)\\ &\frac{\partial v}{\partial \tau}+u\frac{\partial v}{\partial s}+v\frac{\partial v}{\partial n}=-\frac{1}{\rho}\frac{\partial p}{\partial n}+\nu\left(\frac{\partial^2 v}{\partial s^2}+\frac{\partial^2 v}{\partial n^2}\right)\\ &\frac{\partial u}{\partial s}+\frac{\partial v}{\partial n}=0 \end{aligned}\right\} \quad (231)$$

The last equation represents the condition of continuity. The Euler equations for nonviscous fluids can be obtained by setting the kinematic viscosity ν equal to zero. As long as the viscosity term is retained, however, no matter how small ν is taken to be, equations (231) remain of the second-order and are fundamentally different from the first-order equations governing the ideal fluid. This difference is reflected in the boundary conditions allowable in the two problems. For viscous flow, the resultant velocity is required to be zero at solid boundaries in the flow field. For nonviscous flow, only the component normal to the boundary is required to be zero.

The solution of equations (231) has not been found in any but the simple cases of laminar flow. A solution for the flow through an arbitrary cascade is not feasible at the present time. However, when the predominant viscous effects are confined to the boundary region, a simplifying approximation is possible. By considering the relative magnitudes (within the boundary layer) of the terms appearing in equations (231), that system of equations can be reduced (ref. 151, pt. I) to the following:

$$\left.\begin{aligned} &\frac{\partial u}{\partial \tau}+u\frac{\partial u}{\partial s}+v\frac{\partial u}{\partial n}=-\frac{1}{\rho}\frac{\partial p}{\partial s}+\nu\frac{\partial^2 u}{\partial n^2}\\ &\frac{\partial u}{\partial s}+\frac{\partial v}{\partial n}=0 \end{aligned}\right\} \quad (232)$$

where s is the coordinate along the blade surface, and n is the coordinate normal to the surface. The boundary layer is assumed sufficiently thin and the curvature of the surface sufficiently small that the pressure gradient normal to the

surface is negligible within the boundary layer; $\partial p/\partial s$ can then be determined from the potential flow outside the boundary layer. Equations (232) represent a significant simplification of equations (231) and have proved reliable in many flow problems. Unfortunately, these equations, also, are very difficult to solve in most cases of practical interest.

A decisive simplification in approach was made by von Kármán (ref. 169), who integrated the first of equations (232) with respect to n and thus replaced the boundary-layer equation with an integral condition that can be written in the following form:

$$\frac{\hat{\tau}_w}{\rho V_0^2}=\frac{d\theta^*}{ds}+\frac{\theta^*}{V_0}(2+H)\frac{dV_0}{ds} \qquad (233)$$

where V_0 is the velocity at the outer edge of the boundary layer and $\hat{\tau}_w$ is the surface shear stress. In this manner, the boundary-layer equations are required to be satisfied only in the mean instead of at each point along a normal to the surface in the boundary-layer region. Equation (233) has provided the basic equation for most of the general boundary-layer investigations.

Many theories have been developed from equation (233) for approximately solving the boundary-layer problem with pressure gradient for both laminar and turbulent flows. These theories, although not completely successful, provide some orderly means of attacking the problem for either the laminar or the turbulent boundary layer. The question of transition, however, remains relatively unanswered and constitutes a serious defect in current quantitative theory.

The present approach to the viscous-flow cascade problem requires that the potential flow about the cascade be determined first. The surface pressure distributions thus obtained are used to determine the boundary-layer characteristics from equation (233). The defect in total pressure resulting from the formation of the boundary layer can then be established. Potential-flow pressure distributions can serve as an initial basis for the boundary-layer calculation, since, as indicated previously, the viscous effects are generally restricted to the boundary layer and exert a negligible influence on the potential flow outside the layer. Under certain conditions, however (as in the case of a very thick boundary layer), the original blade potential flow may need to be adjusted for the effects of the boundary-layer development.

The subject of potential-flow calculation is covered in chapter IV. The present analysis is concerned with the computation of the boundary-layer characteristics. In the succeeding sections, two simple approximate methods, one for the computation of laminar boundary layers and the other for turbulent layers, are presented. The resulting defects in total pressure and circulation are also considered.

LAMINAR BOUNDARY LAYER

The approximate methods of solution available for laminar-boundary-layer flows are generally satisfactory for engineering use. The more recent methods (e.g., refs. 170 and 171) are so simple and accurate that little further work is being done on the problem. The technique presented here in some detail is due to Thwaites (ref. 171). It was developed from a comprehensive analysis of previously obtained solutions of laminar-boundary-layer flows. From the method, the distributions of θ^* and H can be accurately obtained and the point of laminar separation located.

The methods of Thwaites (ref. 171) and Loitsianskii (ref. 170) are both based initially on the simplified system of equations given by equation (232). For steady incompressible flow, since the static pressure is constant through the boundary layer, the first of equations (232) can be put in the form

$$u\frac{\partial u}{\partial s}+v\frac{\partial u}{\partial n}=V_0V_0'+\nu\frac{\partial^2 u}{\partial n^2} \qquad (234)$$

where $V_0'=dV_0/ds$ denotes the derivative with respect to s of the velocity V_0 at the outer edge of the boundary layer. With the help of the continuity equation (second of eqs. (232)), equation (234) can be written

$$\frac{\partial}{\partial s}[u(V_0-u)]+\frac{\partial}{\partial n}[v(V_0-u)]+V_0'(V_0-u)-\nu\frac{\partial^2(V_0-u)}{\partial n^2}=0 \qquad (235)$$

The developments in the two methods then differ in the subsequent handling of equation (235).

Thwaites' method.—In the method of reference 171, equation (235) is integrated through the

boundary layer from the wall ($n=0$) to the outer edge ($n=\delta$) to give ultimately

$$\frac{d\theta^*}{ds}+\frac{V_0'\theta^*}{V_0}(2+H)=\frac{\nu}{V_0^2}\left(\frac{\partial u}{\partial n}\right)_{n=0} \tag{236}$$

Equation (236) is the same as (233) with $\overset{\blacktriangle}{\tau}_w=\mu(\partial u/\partial n)_{n=0}$. Equation (236) is used by Thwaites in conjunction with the equation obtained from (234) by setting n equal to zero, namely

$$0=V_0V_0'+\nu\left(\frac{\partial^2 u}{\partial n^2}\right)_{n=0} \tag{237}$$

The quantities $(\partial u/\partial n)_{n=0}$, $(\partial^2 u/\partial n^2)_{n=0}$, and H appearing in equations (236) and (237) characterize the velocity distribution in the boundary layer. The first two terms indicate the behavior of the velocity in the significant region of the boundary layer at the wall, and $H=\delta^*/\theta^*$ indicates the over-all form of the distribution. The term $(\partial^2 u/\partial n^2)_{n=0}$ is given explicitly by equation (237) as equal to $-V_0V_0'/\nu$ and hence as a known function of s. If the relation between $(\partial u/\partial n)_{n=0}$ and $(\partial^2 u/\partial n^2)_{n=0}$ for a given flow is known, then $(\partial u/\partial n)_{n=0}$ is also known as a function of s through $-V_0V_0'/\nu$. If, furthermore, the relation between H and $(\partial^2 u/\partial n^2)_{n=0}$ is known for the given flow, H is also known as a function of s. Then, the momentum equation (236) can be integrated to obtain the distribution of θ^*. Such relations among $(\partial u/\partial n)_{n=0}$, $(\partial^2 u/\partial n^2)_{n=0}$, and H are obtained now by examining velocity distributions from known solutions.

The quantities l and m are defined as follows:

$$\left.\begin{aligned} l&=\frac{\theta^*}{V_0}\left(\frac{\partial u}{\partial n}\right)_{n=0}\\ m&=\frac{\theta^{*2}}{V_0}\left(\frac{\partial^2 u}{\partial n^2}\right)_{n=0}\end{aligned}\right\} \tag{238}$$

The definitions are constructed in this way to eliminate the effect of θ^* and V_0 on the partial derivatives. This allows l and m to depend only on the form of the velocity distribution. According to this preliminary analysis, the terms l and H are regarded as functions of m and are plotted as such for all theoretical laminar-boundary-layer velocity distributions available to Thwaites at the time of his work.

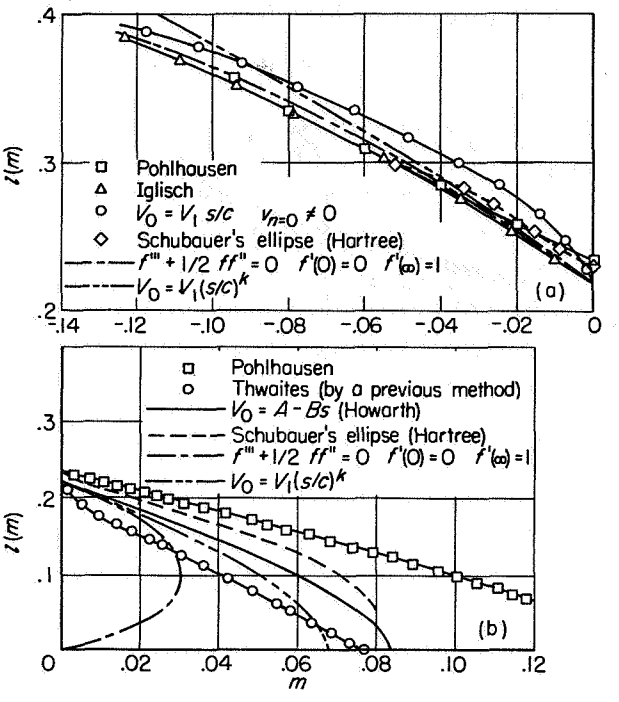

(a) $m<0$.
(b) $m\geqq 0$.

FIGURE 110.—Variation of $l(m)$ with m for theoretical velocity distributions (ref. 171).

The solutions used are identified in figures 110 and 111, where the derived functional relations are plotted. The values of l, H, and m are computed from the actual velocity distributions obtained in these solutions. The figures are divided into positive and negative values of m, corresponding respectively to decelerating and accelerating flow ($m=-V_0'\theta^{*2}/\nu$ from eqs. (237) and (238)). Figures 110(a) and 111(a) reveal a remarkable similarity for $m<0$ (accelerating flow) in the $l(m)$ and $H(m)$ curves for the variety of velocity distributions appearing in the wide range of solutions used.

On the other hand, figures 110(b) and 111(b) show that the agreement for $m\geqq 0$ (decelerating flow) is not nearly as good. The curve corresponding to the solution of the problem $f'''+\frac{1}{2}ff''=0$ is dismissed on the grounds that the problem it defines in this region is of no interest (i.e., blowing out through the boundary layer). The three exact solutions, Schubauer's ellipse (Hartree), $V_0=A-Bs$ (Howarth), and

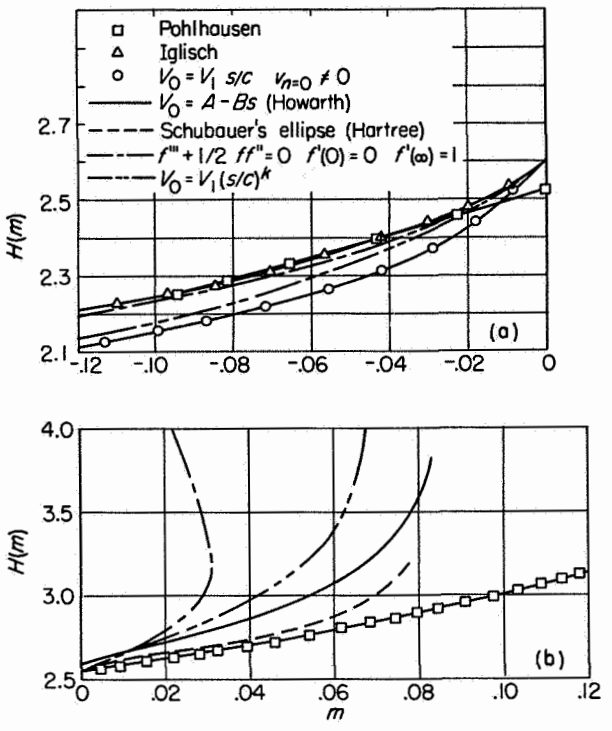

(a) $m<0$.
(b) $m \geq 0$.

FIGURE 111.—Variation of $H(m)$ with m for theoretical velocity distributions (ref. 171).

$V_0=V_1(s/c)^k$, are in reasonable agreement. Pohlhausen's approximate method gives values of $l(m)$, and, hence, values of skin friction, that are far too large. This explains the failure of the Pohlhausen method in regions of rising pressure.

As previously pointed out, the momentum equation can be integrated if the relations $l(m)$ and $H(m)$ are known for the problem at hand. The present method uses figures 110 and 111 to obtain universal curves that best fit the whole family of particular solutions. The curves thus obtained are tabulated in table I. Note that separation is taken to occur at $m=0.082$. This value is chosen arbitrarily to agree with the value for the ellipse, since the flow about an ellipse is similar to the flow about conventional airfoils.

With these functions tabulated, the analysis can proceed as follows. Substituting equations (238) into (236) and (237) gives

$$\frac{d\theta^*}{ds}=-(H+2)\frac{V_0'\theta^*}{V_0}+\frac{\nu l(m)}{V_0\theta^*} \tag{239}$$

TABLE I.—FUNCTIONS FOR THWAITES SOLUTION OF LAMINAR BOUNDARY LAYER (REF. 171)

m	$l(m)$	$H(m)$	$\mathcal{L}(m)$
0.082	0	3.70	0.938
.0818	.011	3.69	.953
.0816	.016	3.66	.956
.0812	.024	3.63	.962
.0808	.030	3.61	.967
.0804	.035	3.59	.969
.080	.039	3.58	.971
.079	.049	3.52	.970
.078	.055	3.47	.963
.076	.067	3.38	.952
.074	.076	3.30	.936
.072	.083	3.23	.919
.070	.089	3.17	.902
.068	.094	3.13	.886
.064	.104	3.05	.854
.060	.113	2.99	.825
.056	.122	2.94	.797
.052	.130	2.90	.770
.048	.138	2.87	.744
.040	.153	2.81	.691
.032	.168	2.75	.640
.024	.182	2.71	.590
.016	.195	2.67	.539
.008	.208	2.64	.490
0	.220	2.61	.440
−.016	.244	2.55	.342
−.032	.268	2.49	.249
−.048	.291	2.44	.156
−.064	.313	2.39	.064
−.080	.333	2.34	−.028
−.10	.359	2.28	−.138
−.12	.382	2.23	−.251
−.14	.404	2.18	−.362
−.20	.463	2.07	−.702
−.25	.500	2.00	−1.000

$$0=V_0V_0'+\frac{\nu V_0 m}{\theta^{*2}} \tag{240}$$

Substituting (240) into (239) gives

$$\frac{1}{\nu}\frac{V_0}{2}\frac{d\theta^{*2}}{ds}=m[H(m)+2]+l(m) \tag{241}$$

Then, defining $\mathcal{L}(m)$ to be

$$\mathcal{L}(m)=2\{m[H(m)+2]+l(m)\} \tag{242}$$

and substituting equation (242) into equation (241) give

$$\frac{V_0}{\nu}\frac{d\theta^{*2}}{ds}=\mathcal{L}(m) \tag{243}$$

The function $\mathcal{L}(m)$ is tabulated in table I.

The solution proceeds now by a direct integration of equation (243) to obtain the distribution of θ^*. Thereafter, the other properties of the boundary layer are obtained by using $l(m)$ and $H(m)$.

A very simple solution can also be obtained in a slightly different manner. The function $\mathcal{L}(m)$ is plotted against m in figure 112. It is found

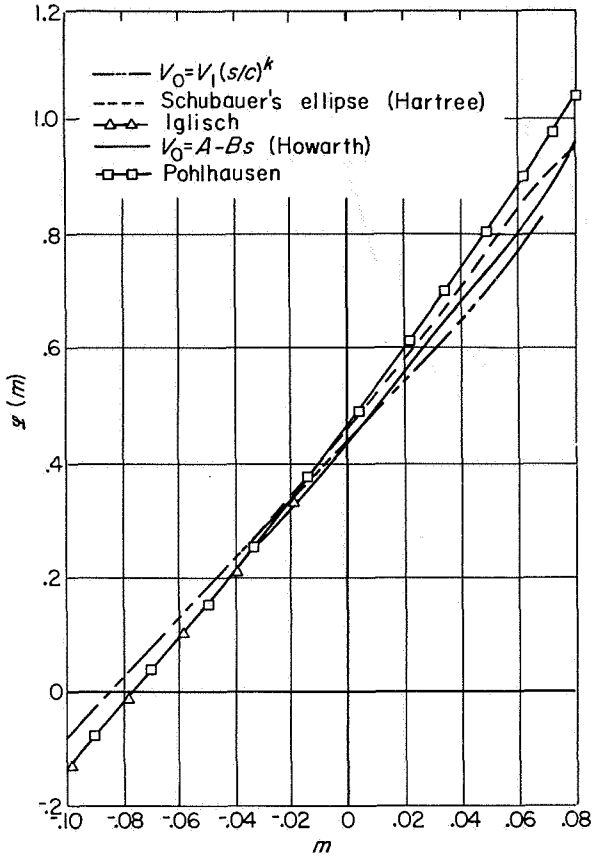

FIGURE 112.—Variation of $\mathscr{L}(m)$ with m for theoretical velocity distributions (ref. 171).

that $\mathscr{L}(m)$ can be approximated by a linear function of the form

$$\mathscr{L}(m)=0.45+6m \tag{244}$$

Equation (244) is then substituted into equation (243), which is integrated to give

$$\theta^{*2}=\frac{0.45\nu}{V_0^6}\int_0^s V_0^5\,ds \tag{245}$$

Therefore, with the potential-flow velocity distribution known, θ^{*2} can be obtained directly from equation (245). The distribution of m, and hence of $l(m)$ and $H(m)$, follows from θ^{*2}. In this way, all the significant boundary-layer parameters are obtained with very little effort.

To demonstrate the accuracy of the simple solution, Thwaites solved by the approximate method the flow given by $V_0=A-Bs$ and compared the results with the exact solution as given by Howarth. The results of these comparative calculations are given in figure 113. The parameters of principal interest, δ^*, θ^*, and $(\partial u/\partial n)_{n=0}$, are presented in a nondimensional form. The agreement between the approximate and exact solutions is satisfactory for all parameters. A similar comparison is made in reference 171 for the problem of Schubauer's ellipse. Both comparisons are discussed extensively in that reference.

Comparisons between experimental and calculated predictions of the point of laminar separation based on Thwaites' method are demonstrated for the isolated airfoil and cascade airfoil, respectively, in references 172 and 173. The fact that close agreement was obtained in the references between calculated and experimentally observed locations of the separation point indicates that the method may be satisfactory for prediction of the other boundary-layer characteristics.

Loitsianskii's method.—In reference 170 Loitsianskii presents a final equation similar to equation (245) but developed from a quite different approach. Equation (235) is multiplied by n^k and integrated through the boundary layer. The second and third integrals (i.e., $k=1$ and $k=2$) are also used. The three equations are solved simultaneously for three parameters characterizing the boundary-layer velocity distribution. In order to do this, a simple assumed velocity form in the boundary layer is used to evaluate certain of the integrals involved in the three equations. The final equations are (in the terminology of Thwaites)

$$\theta^{*2}=\frac{0.44\nu}{V_0^{5.5}}\int_0^s V_0^{4.5}\,ds$$

$$l(m)=0.22-1.85m-7.55m^2$$

$$H(m)=2.59+7.55m$$

These equations show that the method in application differs very little from that of Thwaites. Analytical expressions for $l(m)$ and $H(m)$ are used instead of the tabulated values used by Thwaites. In general, the values of Thwaites correspond more nearly to the values of $l(m)$ and $H(m)$ obtained from exact solutions. The differences, however, may not be significant.

TURBULENT BOUNDARY LAYER

The turbulent boundary layer is more difficult to treat theoretically than the laminar layer. The use of characteristic velocity forms, as in

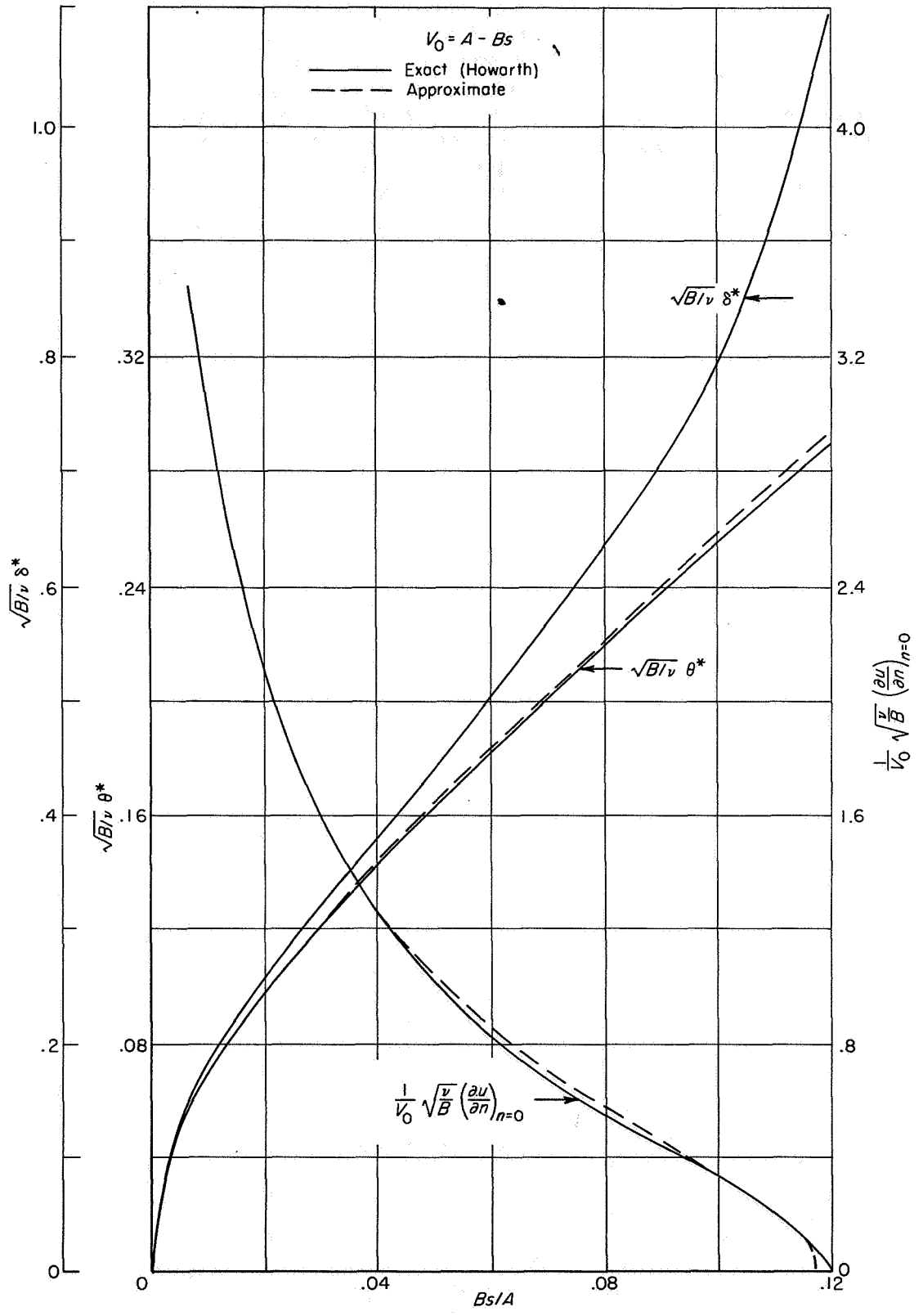

FIGURE 113.—Comparison of solutions obtained by approximate method of Thwaites with exact solutions (ref. 171).

many approximate methods for the laminar layer, has not proved satisfactory in the turbulent case. Furthermore, the shear stress is not given as a simple function $\mu(\partial u/\partial n)$ of the velocity distribution, except in the laminar sublayer. An additional difficulty is the determination of the proper value of H or δ^* at the point of transition. As a result of these difficulties, the best methods available for calculating the characteristics of a turbulent boundary layer are more tedious and less accurate than the method given for the laminar problem.

Since the turbulent boundary layer is preceded, on a blade, by a laminar layer, it is necessary first to determine the values of θ^* and H immediately after transition. These values, as well as the location of the transition point, are determined with the help of the computation of the preceding laminar boundary layer. Once these values are known, certain differential equations for θ^* and H can be solved to obtain the entire distribution.

In the technique of Maskell (ref. 160) presented here, the momentum thickness can be obtained simply and with acceptable accuracy. The determination of the distribution of the form factor H is more difficult. When θ^* and H have been obtained, the point of turbulent separation can be obtained accurately by the use of a skin-friction formula for turbulent flow given by Ludwieg and Tillmann (ref. 159).

Approach.—From the conservation of momentum in the boundary layer, the momentum equation can be developed for the turbulent case as

$$\frac{d\theta^*}{ds}=\frac{C_{fr}}{2}-(H+2)\frac{\theta^*}{V_0}\frac{dV_0}{ds} \tag{246}$$

where

$$C_{fr}=\frac{\hat{\tau}_w}{\frac{1}{2}\rho V_0^2} \tag{247}$$

and $\hat{\tau}_w$ is the friction stress for a turbulent boundary layer. It has always been observed that the distribution of θ^* calculated from equation (246) is not greatly affected by the way H varies with s. In fact, H can be taken as constant and reasonably accurate values of θ^* obtained in some cases. For this reason, Maskell proposes a simplification of equation (246) (based on the insensitivity to H) that enables that equation to be directly integrated for θ^*. Then, he uses the derived values of θ^*, in conjunction with an empirical differential equation in H, for obtaining values of H accurately. This approach is simpler than the well-known method of von Doenhoff and Tetervin (ref. 174), in which an empirical differential equation in H is constructed and solved simultaneously with equation (246). The results obtained for θ^* and H in the two methods are comparable. The method of Maskell recommends itself not only because of its simplicity but also because of its ability to predict separation with acceptable accuracy.

Momentum thickness.—The first part of the boundary-layer problem is to determine the momentum thickness. To do so, equation (246) is first written in the following form:

$$\frac{d\Theta}{ds}=(1+q)\left[\zeta-\left(H+\frac{2+q}{1+q}\right)\Gamma\right] \tag{248}$$

where

$$\left.\begin{aligned}\Theta&=\theta^* Re_\theta{}^q\\ \Gamma&=\frac{\Theta}{V_0}\frac{dV_0}{ds}\\ \zeta&=\frac{C_{fr}}{2}Re_\theta{}^q\end{aligned}\right\} \tag{249}$$

and q is an arbitrary constant that will be determined later. The friction coefficient C_{fr} is given by the formula

$$C_{fr}=0.246e^{-1.561H}Re_\theta{}^{-0.268} \tag{250}$$

which is developed in reference 159. This formula, which Maskell adopts for his method, is probably superior to previously used formulas for C_{fr}.

Equation (248) can be integrated directly if the right side can be approximated in the linear form $A+B\Gamma$. For flat-plate flow, dV_0/ds (and hence Γ) equals zero, and equation (248) becomes

$$\left(\frac{d\Theta}{ds}\right)_{f.p.}=(1+q)\zeta=A \tag{251}$$

Therefore, an approximation of equation (248) in the form $A+B\Gamma$ requires that $(1+q)\zeta$ be constant if the approximation is to agree in the simple case of flat-plate flow. The value of q required to make the ζ term constant in equation (251) is determined as indicated in the following paragraph.

The experimental variation of H with log Re_θ for a flat plate is illustrated in figure 114, along

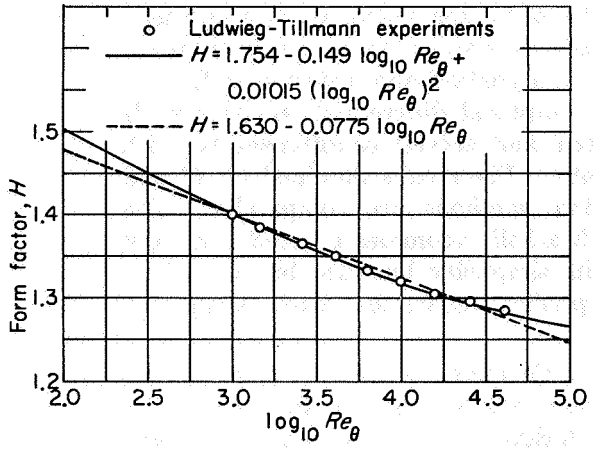

FIGURE 114.—Profile parameter H for flat-plate flow (ref. 160).

with two simple analytic approximations to the experimental data. The simplest approximation,

$$H = 1.630 - 0.0775 \log_{10} Re_\theta \qquad (252)$$

is used in this part of the analysis. Substitution of equations (252) and (250) in the definition of ζ (eq. (249)) gives

$$\zeta = 0.00965 Re_\theta^{q-0.2155} \qquad (253)$$

Therefore, taking $q = 0.2155$ in equation (253) gives a constant value of ζ as desired. With this value of q, equation (248) becomes

$$\frac{d\Theta}{ds} = 1.2155 [\zeta - (H + 1.823)\Gamma] \qquad (254)$$

The right side of equation (254) is now evaluated from experimental data and plotted against Γ to see whether an approximation of the form $A + B\Gamma$ will be satisfactory. These results, shown in figure 115, indicate that such a linear approximation should be adequate. The best approximation to the data is given by $A = 0.01173$, $B = 4.200$; and equation (254) becomes

$$\frac{d\Theta}{ds} = 0.01173 - 4.200\Gamma$$

which can be written as (from eq. (249))

$$\frac{d\Theta}{ds} + 4.200 \frac{\Theta}{V_0} \frac{dV_0}{ds} = 0.01173 \qquad (255)$$

The solution of (255) is then given by

$$(\Theta V_0^{4.200})_s - (\Theta V_0^{4.200})_{s_{tr}} = 0.01173 \int_{s_{tr}}^{s} V_0^{4.200}\, ds \qquad (256)$$

where s_{tr} is the starting point of the turbulent boundary layer. Equation (256) thus requires a simple integration for the calculation of the momentum thickness once the initial value of θ^* is known.

Form factor.—With the momentum thickness known, it becomes necessary to determine H accurately in order to ascertain δ^* and C_{f_r}. In order to determine H, Maskell develops an empirical differential equation. A considerable amount of data is used in the development, including zero and negative pressure-gradient data. The resulting equation must be divided into three parts to fit the available data accurately. The division is made in terms of the

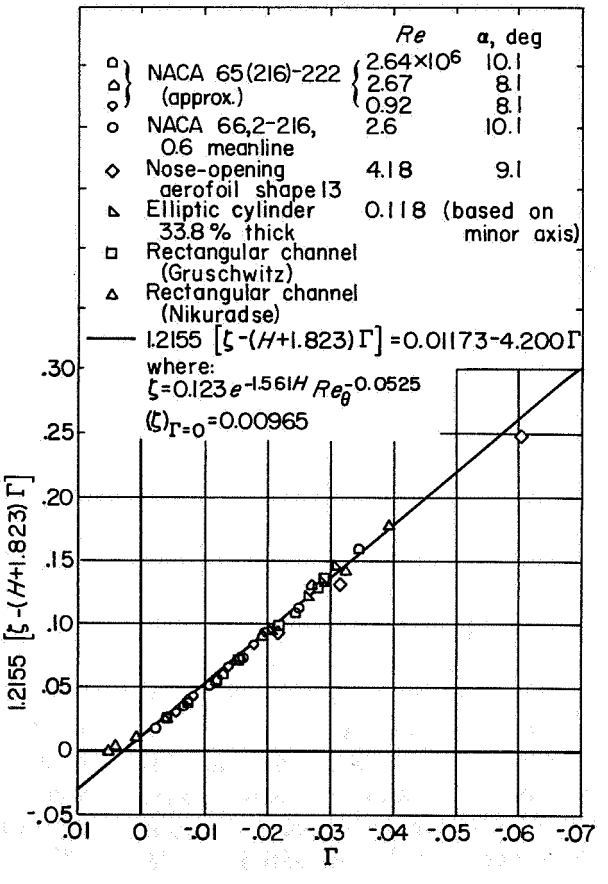

FIGURE 115.—Experimental values of function $1.2155 [\zeta - (H + 1.823)\Gamma]$

Γ range by $\Gamma=0$ and $\Gamma=\Gamma_t$, where Γ_t is itself a function of H. The following relation is obtained in reference 160:

$$\left.\begin{aligned} H&=1.754-0.149\log_{10}Re_\theta \\ &\quad +0.01015(\log_{10}Re_\theta)^2 \text{ for } \Gamma>0 \\ \frac{dH}{ds}&=\frac{1}{\theta^* Re_\theta^{0.268}}[\varphi-\Gamma(0.30H-0.32)] \\ &\quad \text{for } 0>\Gamma>\Gamma_t \\ \frac{dH}{ds}&=\frac{1}{\theta^* Re_\theta^{0.268}}[-0.15(H-1.2) \\ &\quad -\Gamma(0.30H-0.15)] \text{ for } \Gamma_t>\Gamma \end{aligned}\right\} \quad (257)$$

where

$$\Gamma_t=\frac{-0.15(H-1.2)-\varphi}{0.17} \quad (258)$$

and φ is given in figure 116. The portion of the curve for $H<1.4$ is given by $\varphi=-10^{-0.678H}(0.01399H-0.01485)$; for $H>1.6$, by $\varphi=-0.054H+0.0796$; and for $1.4<H<1.6$ the curve is faired.

Assuming the distribution of θ^* is now known, and also the value of H at transition, equations (257) and (258) can be solved step-by-step for the complete distribution of H. With H and θ^* known, C_{f_r} can be found from equation (250).

The point of turbulent separation is determined in the method from the variation of the friction coefficient ($C_{f_r}=0$ at separation). It is clear from its form that equation (250) cannot lead directly to a value of $C_{f_r}=0$. However, the calculated C_{f_r} curve falls off toward zero in such a way that an extrapolation to zero is easily made. Examples of the separation-point extrapolation are shown in figure 100.

Initial conditions.—The problem yet remaining is the proper determination of H and θ^* at the onset of turbulent flow. The velocity profile undergoes an abrupt change from laminar type to turbulent type. The initial value of θ^* is taken from the value occurring in the laminar computation at the point of transition. This is equivalent to assuming that the momentum thickness is continuous through the point of transition. Requiring continuity of the momentum thickness results in a discontinuity (i.e., rapid change) in displacement thickness and hence in H (ref. 175). The experimental data now available do not point clearly to a suitable means of determining

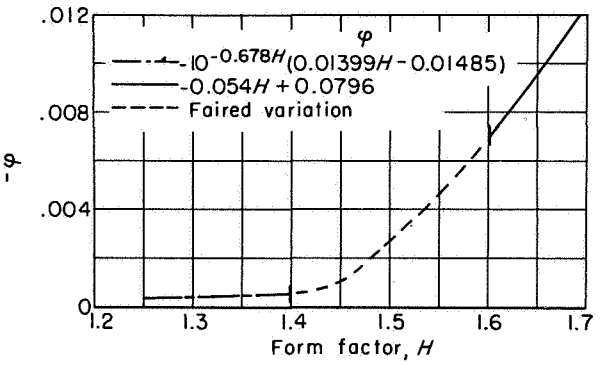

FIGURE 116.—Definition of φ as function of H (ref. 160).

the initial value of H. Maskell does recognize some systematic trend and presents an analysis leading to highly qualified relations for predicting the value of H at transition. For details of his development, see reference 160.

As an indication of the sensitivity of the calculation to the initial value of H, Maskell tried two widely different initial values and obtained the results shown in figure 117. In spite of the large difference in initial value, the computed curves of H are in fair agreement. The computed values of C_{f_r} are in even better agreement. These results, although not susceptible to the general interpretation that the calculations are insensitive to the value of H at transition, are encouraging.

Evaluation.—The accuracy of the method, given the location of the transition point, is demonstrated in several examples in reference 160. Figure 118, taken from reference 160, illustrates the computed boundary-layer characteristics for an NACA airfoil and compares the results with actual experimental data and with the results of the method of von Doenhoff and Tetervin. The agreement is generally satisfactory for the entire range of θ^*, H, and C_{f_r}. The agreement of the calculated separation point with the experimentally obtained separation point is also quite good.

TRANSITION

A major difficulty yet remaining in the computation of blade boundary layers is the successful prediction of the location of the transition point. This problem is in a very difficult realm of viscous-flow theory because of the close relation of the transition point to the Reynolds number and free-stream turbulence of the flow. The

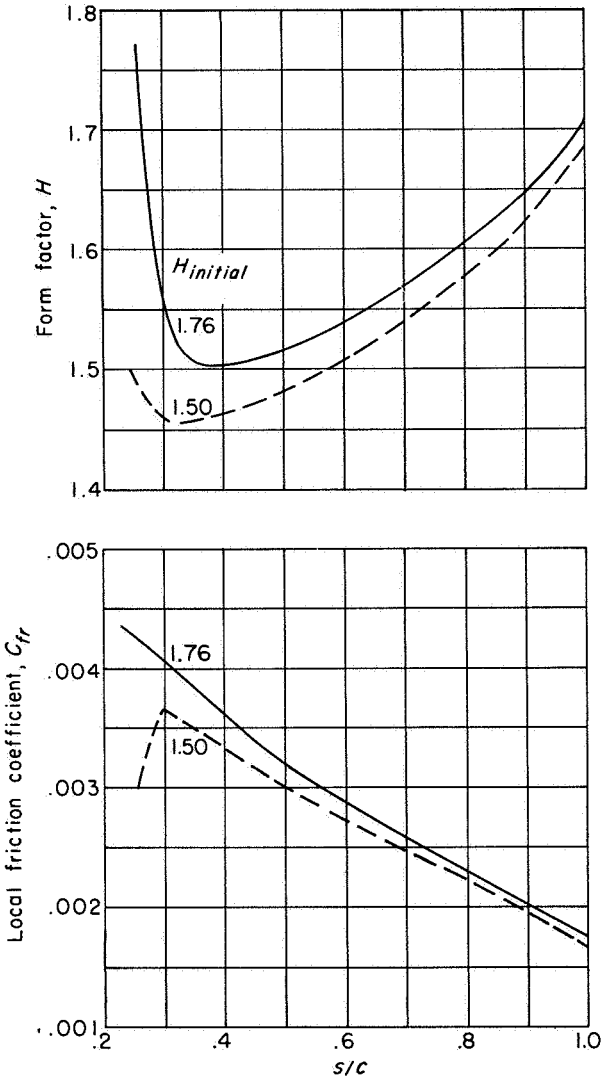

FIGURE 117.—Effect of initial value of H on calculated values of form factor and skin-friction coefficient in turbulent boundary layer on upper surface of airfoil section RAE 101. Blade-chord Reynolds number, 1.7×10^6; lift coefficient, 0.4 (ref. 160).

problem has been discussed qualitatively in a previous section. An indication of the errors that may result from mislocation of the transition point in the calculation of the drag coefficient of an isolated airfoil is given in figure 119. The figure presents a plot of the variation of calculated profile drag coefficient against distance of the transition point from the leading edge.

Although reliable criteria for transition-point location for general airfoil flow are not currently

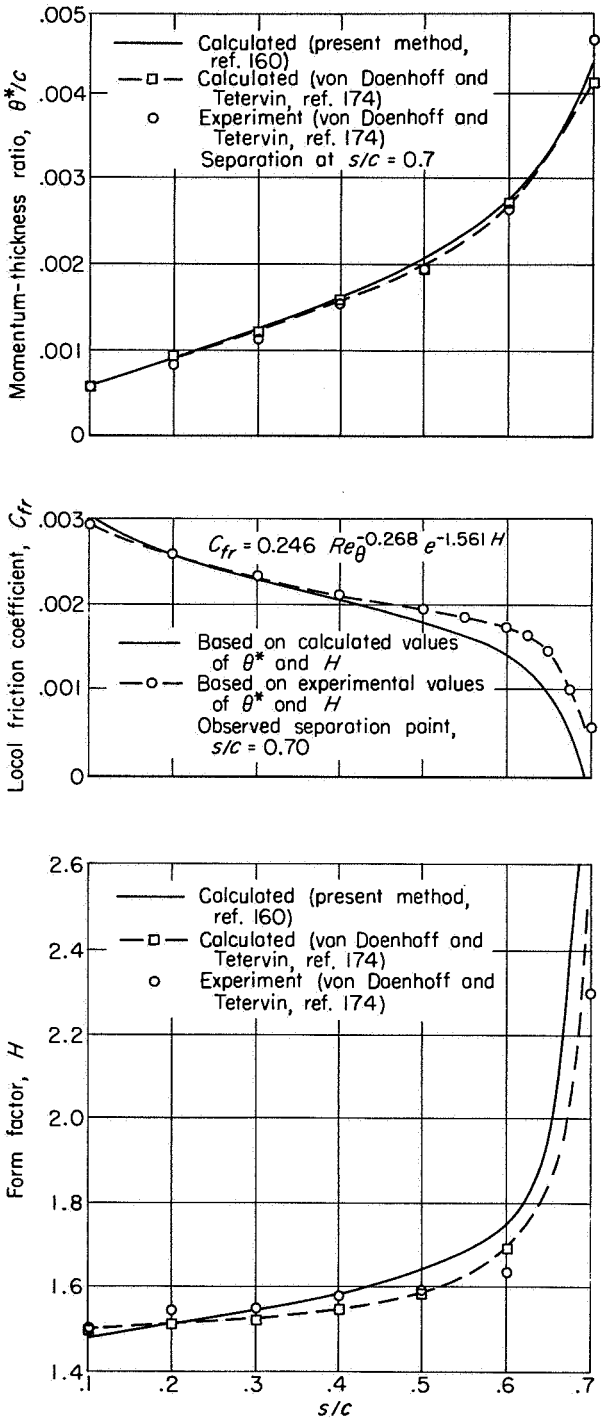

FIGURE 118.—Comparison of experimental and calculated distributions of boundary-layer parameters for NACA airfoil section 66,2–216. Blade-chord Reynolds number, 2.64×10^6; angle of attack, 10.1° (ref. 160).

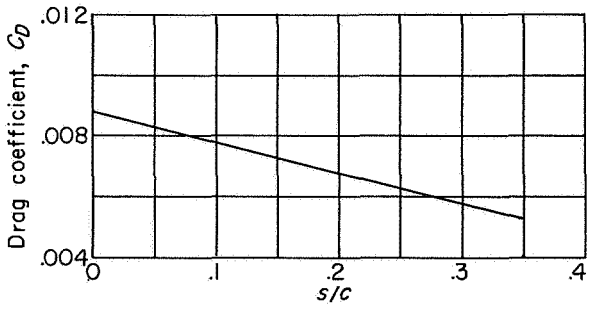

FIGURE 119.—Variation of profile drag with location of transition point for 14-percent-thick wing at blade-chord Reynolds number of 10^7 (ref. 155).

available, some work has been done along these lines. A low-turbulence investigation of an NACA $65_{(215)}$–114 airfoil in reference 176, for example, revealed that, for blade-chord Reynolds numbers ranging from 26×10^6 to 49×10^6, a criterion for transition based on boundary-layer Reynolds number can be satisfactorily established as $Re_\delta=8000$. ($Re_\delta=V_0\delta/\nu$, where δ is the normal distance from the airfoil surface to a point within the boundary layer where the velocity is equal to 0.707 of the velocity at the outer edge of the boundary layer.) These results were obtained for values of Reynolds number that are considerably higher than those encountered in conventional low-speed-cascade practice.

Much more work will have to be done on this problem before reliable criteria are determined for very general conditions of Reynolds number, turbulence, and pressure distribution. Until such criteria are available, theoretical boundary-layer calculations will probably have to concern themselves with a range of possible transition-point locations.

CIRCULATION DEFECT

Potential-flow calculations provide a tool for determining the surface velocity distribution and hence the circulation and air outlet angle of cascade blades. For a viscous fluid, the potential flow is altered because of the development of the boundary layer. For many practical blade shapes, the error in the velocity distribution obtained from potential-flow calculations about the original blade may be large. Figure 120, taken from reference 98, indicates the error in a typical cascade calculation. The theoretical potential-flow circulation is always greater than the actual circulation.

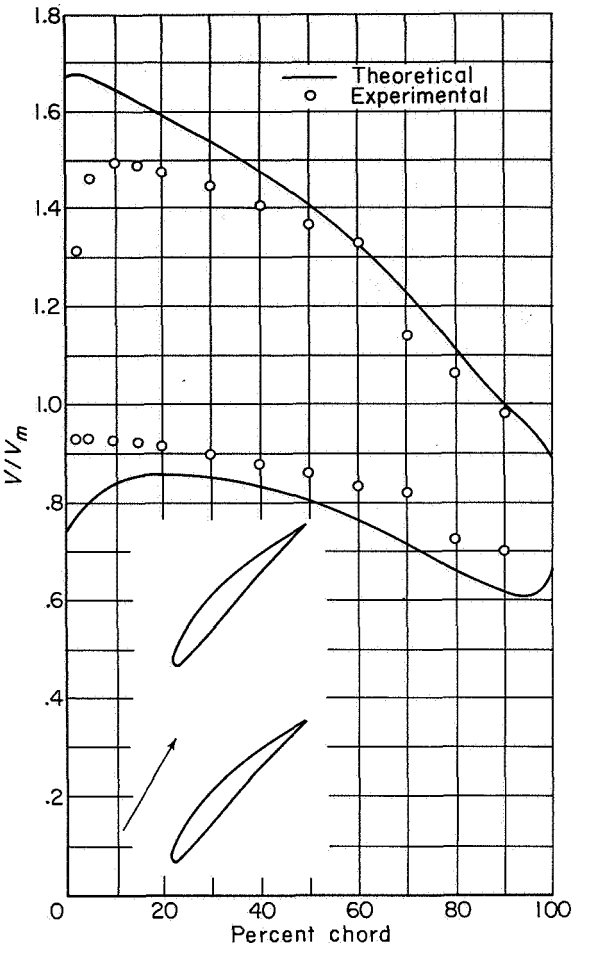

FIGURE 120.—Comparison of experimental and theoretical velocity distribution on airfoil in cascade. Airfoil, NACA 65–(12)10; inlet-air angle, 60°; angle of attack, 14.1°; angle of attack of mean vector velocity, 6.5°; turning angle, 18.6°; solidity, 1.0 (ref. 98).

References 98 and 177 found that, if the actual (real-flow) circulation of a given blade section could be predicted, the use of this actual value of circulation in the potential-flow calculation for the section would yield theoretical velocity distributions that agreed much better with the measured values. Two mechanisms of incorporating the actual circulation in the velocity-distribution calculation are discussed in reference 177. The first method neglects the Kutta condition and directly reduces the theoretical circulation to the actual

value obtained from measurements. By neglecting the Kutta condition an exact potential flow about the original airfoil is obtained, wherein the rear stagnation point occurs on the upper surface. The second method is to distort the airfoil by curving up the trailing edge until the theoretical lift, with the stagnation point at the trailing edge, equals the experimental lift.

The investigation also found that a small reduction in the angle of attack of the section in the theoretical calculation improved the agreement between calculated and observed velocities. An illustration of the effectiveness of the reduced circulation, with and without change in angle of attack, in providing a close comparison between theoretical and measured cascade velocity distributions is shown in figure 121. These results are interesting in that a simple procedure is established for satisfactorily incorporating the circulation decrement into the potential-flow velocity-distribution calculation, once that decrement is known.

The principal problem now is the determination of the actual circulation in the presence of boundary-layer growth. To date, no analytical or empirical data have appeared to permit the general estimation of actual circulation (or lift) for conventional cascade sections. An investigation of an analytical determination of the actual lift of isolated airfoil sections is presented in reference 178. A brief discussion of the method is included herein, since the concepts and procedures involved should be significant also for the cascade airfoil.

The analysis of reference 178 postulates that the presence of surface boundary layers will affect the potential flow about the airfoil in two principal ways. First, since the boundary layers tend to displace the main flow away from the surfaces of the airfoil, the effective shape of the airfoil will be altered according to the variation of the displacement thicknesses of the surface boundary layers. In general, with the boundary layer thicker on the upper than on the lower surface, an effective reduction in blade camber will result. In addition, a reduced angle of attack will result from altering the effective camber line.

The altering of the effective angle of attack possibly accounts for the general improvement in velocity-distribution comparisons (as in fig. 121) obtained when a slight reduction in angle of attack is included in the theoretical calculation.

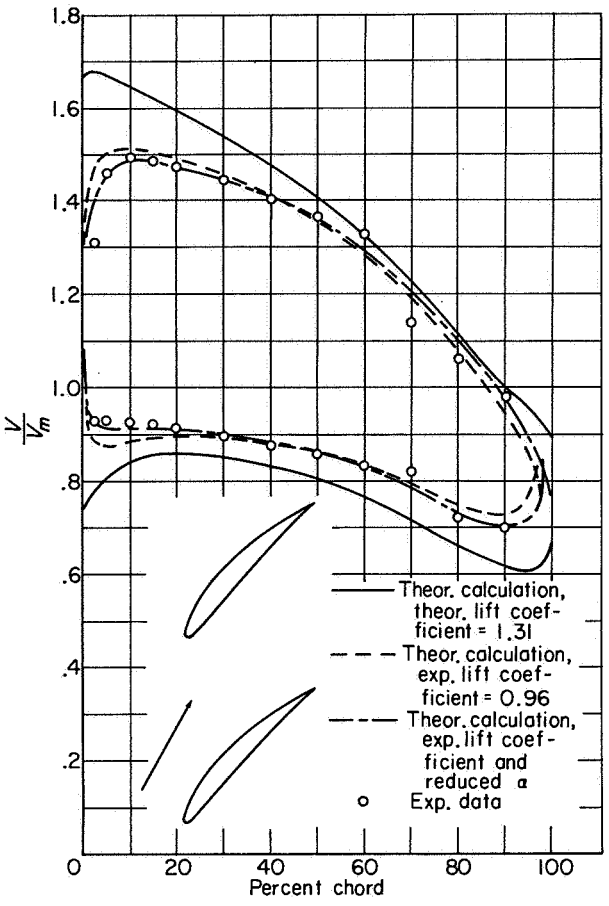

FIGURE 121.—Comparison of experimental velocity distribution with theoretical velocity distribution corrected for circulation and angle of attack on airfoil in cascade. Airfoil, NACA 65-(12)10; inlet-air angle, 60°; angle of attack, 14.1°; angle of attack of mean vector velocity, 6.5°; turning angle, 18.6°; solidity, 1.0 (ref. 98).

The second effect on circulation is the destruction of the Kutta condition at the trailing edge. Reference 178 replaces the Kutta condition with the theorem that, for steady motion, the rates of discharge of positive and negative vorticity into the wake at the trailing edge are equal. Methods of computing the reduction in circulation resulting from the change in profile shape and trailing-edge condition are presented in the reference. Results of calculations for two airfoil shapes show that a considerable portion of the difference between theoretical and actual lift can be predicted on the basis of these considerations. The results further show that the effective

altering of the profile shape contributed most to the lift defect.

The theoretical calculation of the lift defect resulting from an effective profile change will generally be more difficult for a cascade airfoil than for the isolated airfoil. Accordingly, the consideration of an empirical correlation between actual lift ratio and some significant boundary-layer thickness parameter may offer more immediate promise for cascade sections.

In view of the preceding discussion, it appears that an iteration process may prove necessary for some boundary-layer computation on airfoils in cascade. The procedure would be as follows:

(1) Compute potential velocity distribution.

(2) Compute boundary-layer development from (1).

(3) Compute circulation defect from boundary-layer characteristics (2).

(4) Recompute potential velocity distribution on the basis of corrected circulation (3).

(5) Continue iteration until process converges.

CALCULATION OF TOTAL-PRESSURE LOSS

In compressor design and performance analysis, it is desirable to determine the loss in total pressure incurred across a blade row. In the present section, a method is discussed for relating the total-pressure loss of a cascade section to the boundary-layer characteristics at the blade trailing edge. This makes possible, within the limits of the assumptions involved, the complete theoretical calculation of the cascade loss once the blade boundary-layer conditions have been established. The loss so determined represents the basic two-dimensional profile loss of the section.

If separation has not occurred, the flow field in the plane of the blade trailing edge will appear essentially as a core of potential (or free-stream) flow bounded by viscous layers adjoining the blade surfaces. A considerable portion of the complete loss in total pressure across a cascade is already realized in the viscous layers at the blade trailing edge. However, owing to the lack of uniformity of the velocity distribution in the wake (and also in the free stream), a turbulent mixing of the fluid takes place resulting in an additional loss in total pressure downstream of the blade trailing edge. The complete loss attributable to the cascade can only be measured at an axial position sufficiently far downstream to assure that uniformity has been achieved. Since the rate of dissipation of the wake depends on many factors, experimental loss data obtained at a fixed location for various cascade configurations will not be completely comparable unless properly interpreted in relation to the complete loss involved.

A notable achievement was made in the calculation of the complete loss for isolated airfoils by Squire and Young (ref. 155), who succeeded in relating the total drag to the boundary-layer state at the airfoil trailing edge. The cascade case was treated by Loitsianskii in references 179 and 180. With the assumption that conditions are nearly uniform in the plane of coalescence of the wakes from neighboring blades, the conditions far downstream are related to conditions at the plane of coalescence. Then, the conditions at the plane of coalescence, and consequently at the far-downstream position, are related to the trailing-edge boundary-layer characteristics.

More recently, simplified analyses have been presented in references 156 and 181. In these theories, losses far downstream again are related to the trailing-edge boundary-layer characteristics. This relation is easily and directly established by assuming free-stream conditions to be uniform tangentially in the plane of the trailing edge. Although this restriction is severe, it is likely that the theory can provide a simple guide to better understanding and estimating cascade loss data.

The assumptions and results of reference 156 are now presented briefly. Only the incompressible-flow case is considered. For purposes of this analysis, the velocity distributions in the tangential direction at various axial locations are assumed to occur as shown in figure 122. Far downstream of the blade row, the wake is ultimately dissipated and the flow is completely uniform in the tangential direction. The mass-averaged loss in total pressure is then (since free-stream total pressure in the plane of the trailing edge is taken equal to the inlet total pressure)

$$\Delta\overline{P}=P_1-P_2=P_{0,1}-P_2 \qquad (259)$$

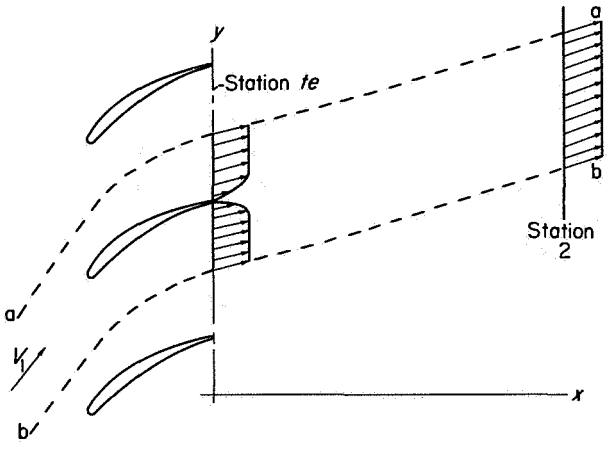

FIGURE 122.—Cascade flow indicating velocity distribution at trailing edge and after complete mixing has occurred (a–a and b–b are streamlines for a full blade spacing).

where subscripts 1 and 2 denote positions far upstream and far downstream of the blade row (fig. 122), and $P_{0,te}$ is the total pressure in the potential-flow region at the trailing-edge position.

From consideration of the Bernoulli equation, conservation of mass flow and of axial and tangential momentum over the control surface bounded by the dashed streamlines in figure 122, and the conventional definitions of displacement and momentum thickness, the loss coefficient is given by

$$\bar{\omega}=\frac{\Delta\overline{P}}{\frac{1}{2}\rho V_{0,te}^2}=2\left(\frac{\theta^*}{c}\right)_{te}\frac{\sigma}{\cos\beta_{te}}\left(1+\frac{1}{2}\left(\frac{\theta^*}{c}\right)_{te}\frac{\sigma}{\cos\beta_{te}}\right.$$

$$\left.\left\{H_{te}^2-\sin^2\beta_{te}\left[H_{te}-\frac{1}{1-\left(\frac{\theta^*}{c}\right)_{te}\frac{\sigma H_{te}}{\cos\beta_{te}}}\right]^2\right\}\right) \quad (260)$$

where, if desired, $V_{0,te}$ can be related to the inlet velocity V_1 through the expression

$$\frac{V_1}{V_{0,te}}=\frac{\cos\beta_{te}}{\cos\beta_1}\left[1-\left(\frac{\theta^*}{c}\right)_{te}\frac{\sigma H_{te}}{\cos\beta_{te}}\right]$$

In this manner, the loss involved in the flow from an upstream position to a position of complete dissipation of the wake is related to the boundary-layer characteristics at the trailing edge of the blade and to the cascade geometry. For a more detailed presentation of the development and some calculated results, see reference 156.

CONCLUDING REMARKS

It is apparent from the preceding analysis that the boundary-layer theory currently available is incapable of completely predicting the viscous flow about a two-dimensional cascade. However, the qualitative information provided by the theory can serve as a useful guide in obtaining and interpreting cascade data. Furthermore, some quantitative results can be obtained from the theory in its present state for a limited range of flow conditions and assumptions.

The principal conclusion reached from the qualitative evaluation of cascade boundary-layer behavior is the large sensitivity of the losses to blade-chord Reynolds number and free-stream turbulence. Apparently, a wide range of boundary-layer loss can be obtained for a conventional cascade geometry, depending upon Reynolds number and turbulence. The importance of the identification and evaluation of Reynolds number effects in cascade operation and data analysis is thereby indicated.

The primary shortcoming of quantitative evaluations is the inability of theory to predict the location and characteristics of the transition from laminar to turbulent flow. The computation for a completely laminar or completely turbulent boundary layer is acceptably simple and accurate. Widespread use of the quantitative calculations will follow the ability to locate the transition point successfully. This problem is so difficult theoretically that an attempt should be made to determine an empirical correlation valid for the limited variety of blade shapes currently in use.

The question of possible serious Reynolds number effects in compressor operation is raised in view of the large increases in loss that may be obtained at reduced Reynolds number because of laminar separation in the cascade flow. Reduced Reynolds numbers are encountered in compressors for small-size units and high-altitude operations. However, it is recognized that the viscous-flow phenomena in the compressor configuration are far more complex than in the cascade. First, the development of the boundary layers along the blade elements is complicated by the various spanwise boundary-layer motions and three-dimensional effects existing in compressor blade rows.

Secondly, the turbulence picture differs because of blade wakes and inlet flow distortions. Finally, there are other sources of Reynolds number effects in the development of the casing boundary layers and of the other three-dimensional effects. The observed loss characteristics in the compressor result from the various compressor viscous phenomena. Therefore, the extent to which cascade viscous-flow characteristics will be reflected in the compressor is questionable. The answers to these questions must be supplied by continued comparative research.

CHAPTER VI

EXPERIMENTAL FLOW IN TWO-DIMENSIONAL CASCADES

By SEYMOUR LIEBLEIN

Available experimental two-dimensional-cascade data for conventional compressor blade sections are correlated. The two-dimensional cascade and some of the principal aerodynamic factors involved in its operation are first briefly described. Then the data are analyzed by examining the variation of cascade performance at a reference incidence angle in the region of minimum loss. Variations of reference incidence angle, total-pressure loss, and deviation angle with cascade geometry, inlet Mach number, and Reynolds number are investigated.

From the analysis and the correlations of the available data, rules and relations are evolved for the prediction of the magnitude of the reference total-pressure loss and the reference deviation and incidence angles for conventional blade profiles. These relations are developed in simplified forms readily applicable to compressor design procedures.

INTRODUCTION

Because of the complexity and three-dimensional character of the flow in multistage axial-flow compressors, various simplified approaches have been adopted in the quest for accurate blade-design data. The prevailing approach has been to treat the flow across individual compressor blade sections as a two-dimensional flow. The use of two-dimensionally derived flow characteristics in compressor design has generally been satisfactory for conservative units (ch. III).

In view of the limitations involved in the theoretical calculation of the flow about two-dimensional blade sections (chs. IV and V), experimental investigations of two-dimensional cascades of blade sections were adopted as the principal source of blade-design data. Early experimental cascade results (e.g., refs. 184 to 186), however, were marked by a sensitivity to individual tunnel design and operation. This was largely a result of the failure to obtain true two-dimensional flow. Under these circumstances, the correlation of isolated data was very difficult. Some efforts were made, however, to correlate limited experimental data for use in compressor design (e.g., ref. 187). The British, in particular, through the efforts primarily of Carter and Howell, appear to have made effective use of their early cascade investigations (refs. 31 (pt. I) and 188 to 190).

In recent years, the introduction of effective tunnel-wall boundary-layer removal for the establishment of true two-dimensional flow gave a substantial impetus to cascade analysis. In particular, the porous-wall technique of boundary-layer removal developed by the NACA (ref. 191) was a notable contribution. The use of effective tunnel boundary-layer control has resulted in more consistent systematic test data (refs. 39, 54, 123, and 192 (pt. II)) and in more significant two-dimensional comparisons between theoretical and experimental performance (refs. 98, 167 (pt. I), and 193). With the availability of a considerable amount of consistent data, it has become feasible to investigate the existence of general relations among the various cascade flow parameters. Such relations curtail the amount of future experimental data needed and also result in more effective use of the data currently available.

Since the primary function of cascade information is to aid in the design of compressors, the present chapter expresses the existing cascade data in terms of parameters applicable to compressor design. Such expression not only facilitates the design of moderate compressors but also makes possible a rapid comparison of cascade data with data obtained from advanced high-speed compressor configurations. Since the bulk of the available cascade data has been obtained at low speed (Mach numbers of the order of 0.1), the question of applicability to such high-speed units is very significant. It is necessary to determine which flow parameters can or cannot be applied,

to what extent the low-speed data are directly usable, and whether corrections can be developed in those areas where the low-speed data cannot be used directly.

In this chapter, the available cascade data obtained from a large number of tunnels are reworked in terms of what are believed to be significant parameters and are correlated in generalized forms wherever possible. The performance parameters considered in the correlation are the outlet-air deviation angle and the cascade losses expressed in terms of blade-wake momentum thickness. The correlations are based on the variations of the performance parameters with cascade geometry (blade profile shape, solidity, chord angle) and inlet flow conditions. In view of the difficulties involved in establishing correlations over the complete range of operation of the cascade at various Mach number levels, the analysis is restricted to an examination of cascade performance at a reference incidence-angle location in the region of minimum loss.

The chapter is divided into four main sections: (1) a brief description of the two-dimensional cascade and of the parameters, concepts, and data involved in the analysis; (2) an analysis of the variation of the reference incidence angle with cascade geometry and flow conditions; (3) an analysis of the variation of total-pressure loss at the reference incidence angle; and (4) an analysis of the variation of deviation angle at the reference incidence angle.

SYMBOLS

The following symbols are used in this chapter:

A	flow area
b	exponent in deviation-angle relation
c	chord length
D	diffusion factor (based on over-all velocities)
D_{loc}	local diffusion factor (based on local velocities)
d	exponent in wake velocity-distribution relations
f	function
H	wake form factor, δ^*/θ^*
i	incidence angle, angle between inlet-air direction and tangent to blade mean camber line at leading edge, deg
i_o	incidence angle of uncambered blade section, deg
K_C	compressibility correction factor in loss equation
K_i	correction factor in incidence-angle relation
K_δ	correction factor in deviation-angle relation
M	Mach number
m, m_c	factors in deviation-angle relation
n	slope factor in incidence-angle relation
P	total or stagnation pressure
p	static or stream pressure
Re_c	Reynolds number based on chord length
s	blade spacing
t	blade maximum thickness
V	air velocity
y	coordinate normal to axis
z	coordinate along axis
α	angle of attack, angle between inlet-air direction and blade chord, deg
β	air angle, angle between air velocity and axial direction, deg
$\Delta\beta$	air-turning angle, $\beta_1-\beta_2$, deg
$\gamma°$	blade-chord angle, angle between blade chord and axial direction, deg
δ	wake full thickness
δ^*	wake displacement thickness
$\delta°$	deviation angle, angle between outlet-air direction and tangent to blade mean camber line at trailing edge, deg
$\delta_o°$	deviation angle of uncambered blade section, deg
θ^*	wake momentum-defect thickness
κ	blade angle, angle between tangent to blade mean camber line and axial direction, deg
ρ	density
σ	solidity, ratio of chord to spacing
φ	blade camber angle, difference between blade angles at leading and trailing edges, $\kappa_1-\kappa_2$, deg
$\overline{\omega}$	total-pressure-loss coefficient

Subscripts:

av	average
$i.e.$	incompressible equation
inc	incompressible
l	lower surface
max	maximum
min	minimum
ref	reference

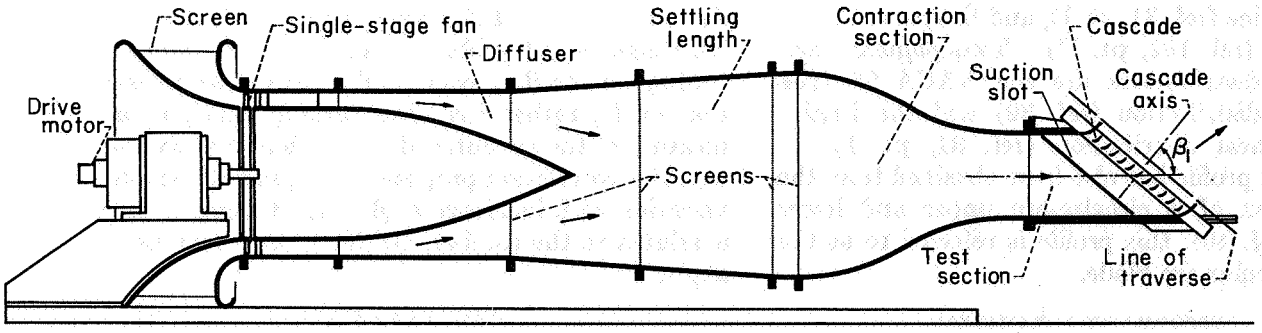

FIGURE 123.—Layout of conventional low-speed cascade tunnel (ref. 168).

sh	blade shape
t	blade maximum thickness
u	upper surface
z	axial direction
θ	tangential direction
0	free stream
1	station at cascade inlet
2	station at cascade exit (measuring station)
10	10 percent thick

PRELIMINARY CONSIDERATIONS

DESCRIPTION OF CASCADE

A schematic diagram of a low-speed two-dimensional-cascade tunnel is shown in figure 123 to illustrate the general tunnel layout. The principal components of the conventional tunnel are a blower, a diffuser section, a large settling chamber with honeycomb and screens to remove any swirl and to ensure a uniform velocity distribution, a contracting section to accelerate the flow, the cascade test section, and some form of outlet-air guidance. The test section contains a row or cascade of blades set in a mounting device that can be altered to obtain a range of air inlet angles (angle β_1 in figs. 123 and 124). Variations in blade angle of attack are obtained either by rotating the blades on their individual mounting axes (i.e., by varying the blade-chord angle $\gamma°$) while maintaining a fixed air angle or by keeping the blade-chord angle fixed and varying the air inlet angle by rotating the entire cascade. Outlet flow measurements are obtained from a traverse along the cascade usually between $\frac{1}{2}$ and $1\frac{1}{2}$ chord lengths behind the blade trailing edge at the blade midspan. In the analysis, blade outlet refers to the cascade measuring station.

In most cases, some form of wall boundary-layer control in the cascade is provided by means of suction through slots or porous-wall surfaces. Examples of different tunnel designs or detailed information concerning design, construction, and operation of the two-dimensional-cascade tunnel can be obtained from references 39, 122, 168, 191, and 194.

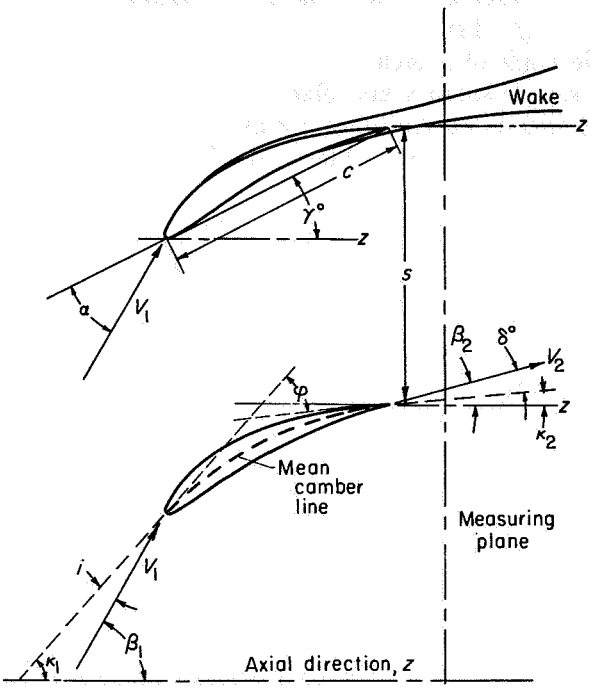

FIGURE 124.—Nomenclature for cascade blade.

Nomenclature and symbols designating cascade blade characteristics are given in figure 124. As in isolated-airfoil practice, cascade blade shapes are normally evolved by adding a basic thickness distribution to a mean camber line. The mean camber line (as indicated in fig. 124) represents the basic curvature of the profile. Some frequently used curvatures are the NACA (A_{10}) and related mean lines (refs. 39 and 123), the circular-

arc mean line (ref. 31, pt. I), and the parabolic-arc mean line (ref. 192, pt. II). Two popular basic thickness distributions are the NACA 65-series thickness distribution (ref. 39) and the British C.4 thickness distribution (ref. 31, pt. I). A high-speed profile has also been obtained from the construction of a circular-arc upper and lower surface (ref. 40); this profile is referred to as the double-circular-arc blade.

PERFORMANCE PARAMETERS

The performance of cascade blade sections has generally been presented as plots of the variation of air-turning angle, lift coefficient, and flow losses against blade angle of attack (or incidence angle) for a given cascade solidity and blade orientation. Blade orientation is expressed in terms of either fixed air inlet angle or fixed blade-chord angle. Flow losses have been expressed in terms of coefficients of the drag force and the defects in outlet total pressure or momentum. A recent investigation (ref. 156) demonstrates the significance of presenting cascade losses in terms of the thickness and form characteristics of the blade wakes.

In this analysis, the cascade loss parameters considered are the wake momentum-thickness ratio θ^*/c (ref. 156) and the total-pressure-loss coefficient $\bar{\omega}_1$, defined as the ratio of the average loss in total pressure across the blade to the inlet dynamic head. Cascade losses are considered in terms of $\bar{\omega}_1$, since this parameter can be conveniently used for the determination of compressor blade-row efficiency and entropy gradients. The parameter θ^*/c represents the basic wake development of the blade profile and as such constitutes a significant parameter for correlation purposes. Values of θ^*/c were computed from the cascade loss data according to methods similar to those presented in reference 156. The diffusion factor D of reference 9 was used as a measure of the blade loading in the region of minimum loss.

In the present analysis, it was necessary to use a uniform nomenclature and consistent correlation technique for the various blade shapes considered. It was believed that this could best be accomplished by considering the approach characteristics of the blade in terms of air incidence angle i, the camber characteristics in terms of the camber angle φ, and the air-turning characteristics in terms of the deviation angle $\delta°$ (fig. 124). As indicated in figure 124, these angles are based on the tangents to the blade mean camber line at the leading and trailing edges. The use of the deviation angle, rather than the turning angle, as a measure of the air outlet direction has the advantage, for correlation purposes, of a generally small variation with incidence angle. Air-turning angle is related to the camber, incidence, and deviation angles by

$$\Delta\beta=\varphi+i-\delta° \tag{57}$$

Incidence angle is considered positive when it tends to increase the air-turning angle, and deviation angle is considered positive when it tends to decrease the air-turning angle (fig. 124).

The use of incidence and deviation angles requires a unique and reasonable definition of the blade mean-line angle at the leading and trailing edges, which may not be possible for some blade shapes. The principal difficulty in this respect is in the 65-(A_{10})-series blades (ref. 39), whose mean-line slope is theoretically infinite at the leading and trailing edges. However, it is still possible to render these sections usable in the analysis by arbitrarily establishing an equivalent circular-arc mean camber line. As shown in figure 125, the equivalent circular-arc mean line is obtained by drawing a circular arc through the leading- and trailing-edge points and the point of maximum camber at the midchord position. Equivalent incidence, deviation, and camber angles can then be established from the equivalent circular-arc mean line as indicated in the figure. The relation between equivalent camber angle and isolated-airfoil lift coefficient of the NACA 65-(A_{10})-series mean line is shown in figure 126.

A typical plot of the cascade performance parameters used in the analysis is shown in figure 127 for a conventional blade section at fixed solidity and air inlet angle.

DATA SELECTION

In selecting data sources for use in the cascade performance correlations, it is necessary to consider the degree of two-dimensionality obtained in the tunnel and the magnitude of the test Reynolds number and turbulence level.

Two-dimensionality.—As indicated previously, test results for a given cascade geometry obtained from different tunnels may vary because of a fail-

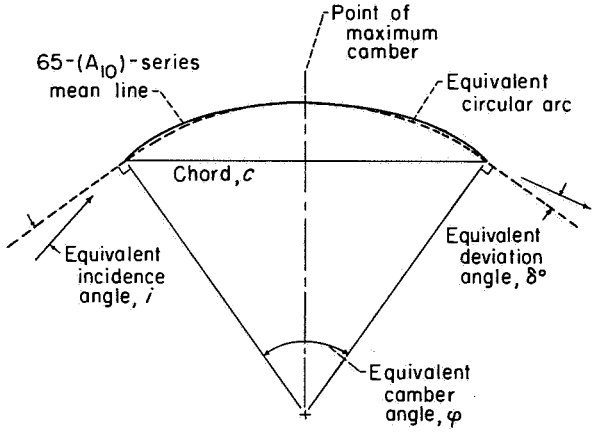

FIGURE 125.—Equivalent circular-arc mean line for NACA 65-(A_{10})-series blades.

ure to achieve true two-dimensional flow across the cascade. Distortions of the true two-dimensional flow are caused by the tunnel-wall boundary-layer growth and by nonuniform inlet and outlet flow distributions (refs. 191 and 168). In modern cascade practice, good flow two-dimensionality is obtained by the use of wall-boundary-layer control or large tunnel size in conjunction with a large number of blades, or both. Examples of cascade tunnels with good two-dimensionality are given by references 39 and 194.

The lack of good two-dimensionality in cascade testing affects primarily the air-turning angles and blade surface pressure distributions. Therefore, deviation-angle data were rejected when the two-dimensionality of the tunnel appeared questionable (usually the older and smaller tunnels). Practically all the cascade loss data were usable, however, since variations in the measured loss obtained from a given cascade geometry in different tunnels will generally be consistent with the measured diffusion levels (unless the blade span is less than about 1 or 2 inches and there is no extensive boundary-layer removal).

Reynolds number and turbulence.—For the same conditions of two-dimensionality and test-section Mach number, test results obtained from cascades of the same geometry may vary because of large differences in the magnitude of the bladechord Reynolds number and the free-stream turbulence. Examples of the effect of Reynolds number and turbulence on the losses obtained from a given blade section at fixed incidence angle are presented in figure 128. Similar pronounced effects are observed on the deviation angle. As discussed in chapter V, the loss variation with Reynolds number is associated primarily with a local or complete separation of the laminar boundary layer on the blade surfaces. The data used in the correlation are restricted to values of blade-chord Reynolds number from about 2.0×10^5 to 2.5×10^5 in order to minimize the effects of different Reynolds numbers. Free-stream turbulence level was not generally determined in the various cascade tunnels.

In some cases (refs. 39 and 195, e.g.), in tunnels with low turbulence levels, marked local laminar-separation effects were observed in the range of Reynolds number selected for the correlation. Illustrative plots of the variation of total-pressure-loss coefficient with angle of attack for a cascade with local laminar separation are shown in figure 129. In such instances, it was necessary to estimate the probable variation of loss (and deviation angle) in the absence of the local separation (as indicated in the figure) and use values obtained from the faired curves for the correlations.

The specific sources of data used in the analysis are indicated by the references listed for the various performance correlations. Details of the tunnel construction and operation and other pertinent information are given in the individual references.

APPROACH

In a correlation of two-dimensional-cascade data that is intended ultimately for use in compressor blade-element design, the variations of performance parameters should be established over a wide range of incidence angles. Experience shows (fig. 130) that the variation of loss with incidence angle for a given blade section changes markedly as the inlet Mach number is increased. Consequently, correlated low-speed blade performance at high and low incidence angles is not applicable at high Mach numbers. The low-speed-cascade performance is therefore considered at some reference point on the general loss-against-incidence-angle curve that exhibits the least variation in location and in magnitude of performance parameters as Mach number is increased.

The reference location herein is selected as the point of minimum loss on the curve of total-

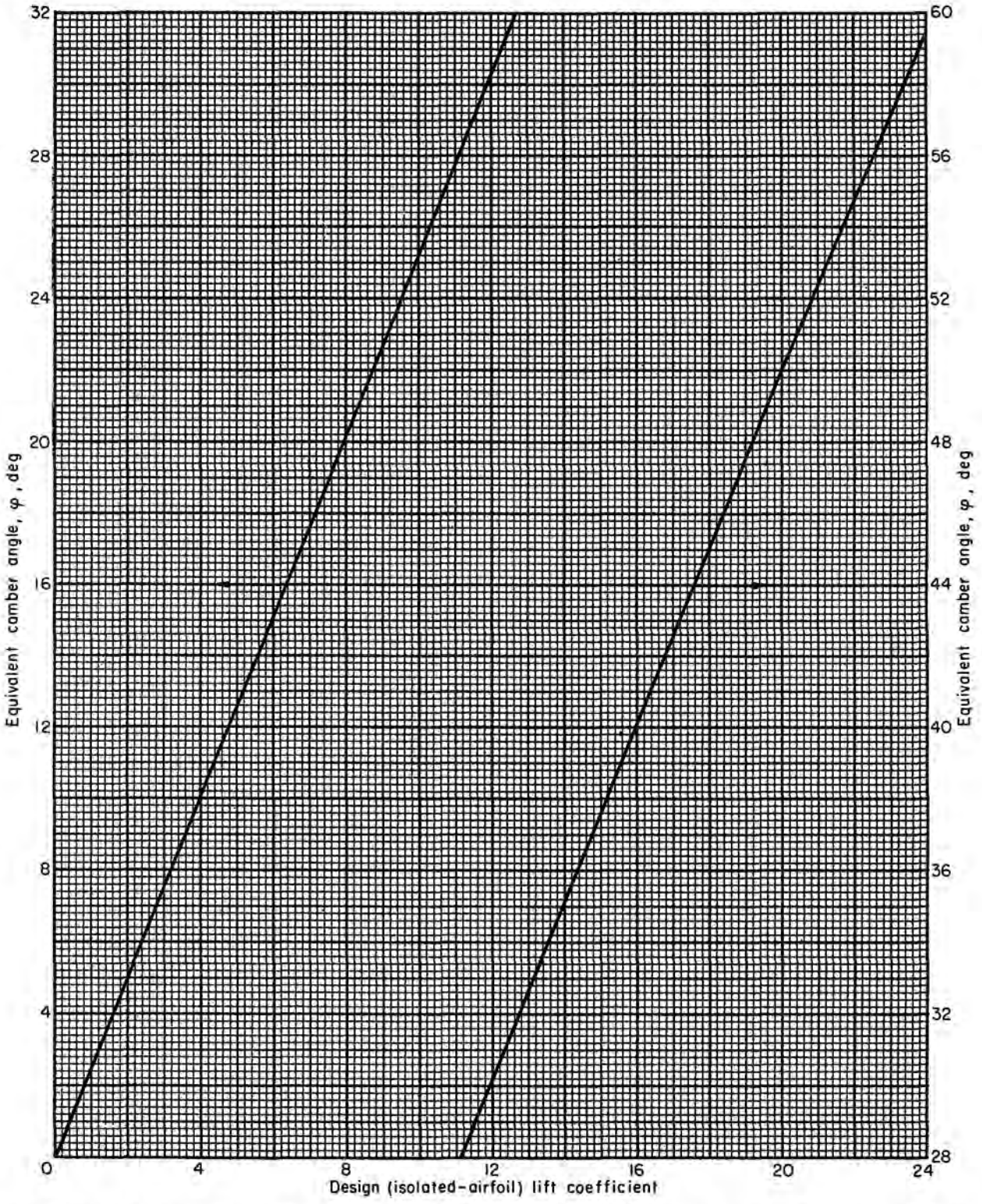

FIGURE 126.—Equivalent camber angles for NACA 65-($C_{l_0}A_{10}$) mean camber line as equivalent circular arc (fig. 125).

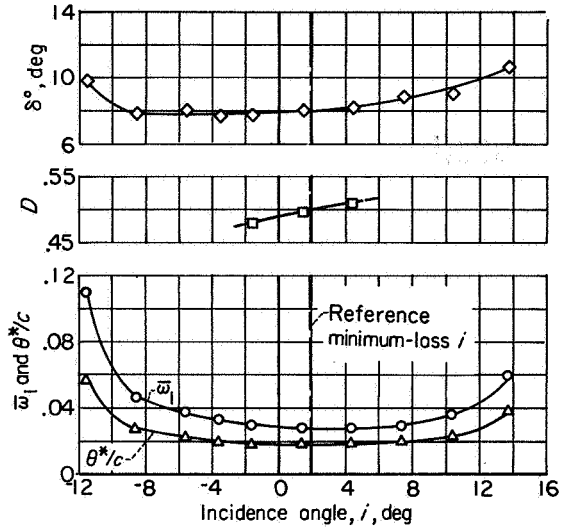

FIGURE 127.—Illustration of basic performance parameters for cascade analysis. Data obtained from conventional blade geometry in low-speed two-dimensional tunnel.

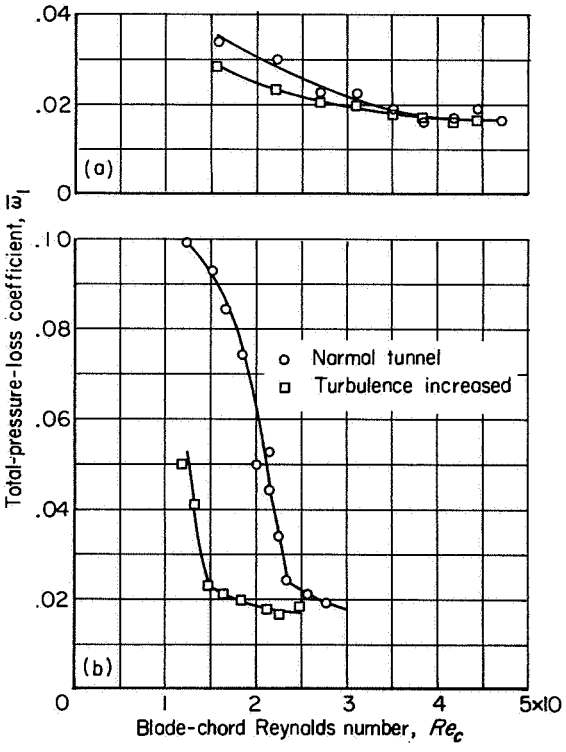

(a) NACA 65–(12)10 blade. Inlet-air angle, 45°; solidity, 1.5 (ref.39):
(b) Lighthill blade, 50 percent laminar flow. Inlet-air angle, 45.5°; solidity, 1.0 (ref. 167, pt. I).

FIGURE 128.—Effect of blade-chord Reynolds number and free-stream turbulence on minimum-loss coefficient of cascade blade section in two-dimensional tunnel.

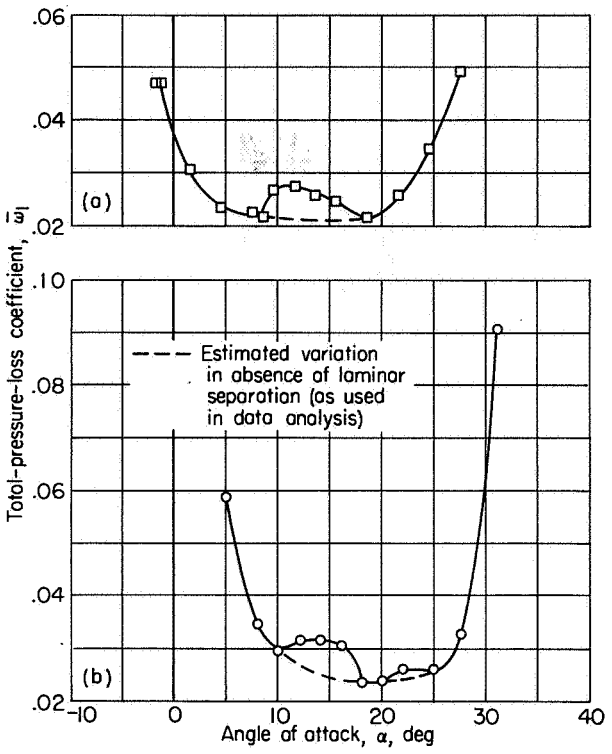

(a) NACA 65–810 blade. Inlet-air angle, 30°.
(b) NACA 65–(12)10 blade. Inlet-air angle, 45°.

FIGURE 129.—Loss characteristics of cascade blade with local laminar separation. Solidity, 1.5; blade-chord Reynolds number, 2.45×10^5 (ref. 39).

pressure loss against incidence angle. For conventional low-speed-cascade sections, the region of low-loss operation is generally flat, and it is difficult to establish precisely the value of incidence angle that corresponds to the minimum loss. For practical purposes, therefore, since the curves of loss coefficient against incidence angle are generally symmetrical, the reference minimum-loss location was established at the middle of the low-loss range of operation. Specifically, as shown in figure 131, the reference location is selected as the incidence angle at the midpoint of the range, where range is defined as the change in incidence angle corresponding to a rise in loss coefficient equal to the minimum value. Thus, for conventional cascade sections, the midrange reference location is considered coincident with the point of minimum loss. In addition to meeting the abovementioned requirement of small variation with inlet Mach number, the reference minimum-loss incidence

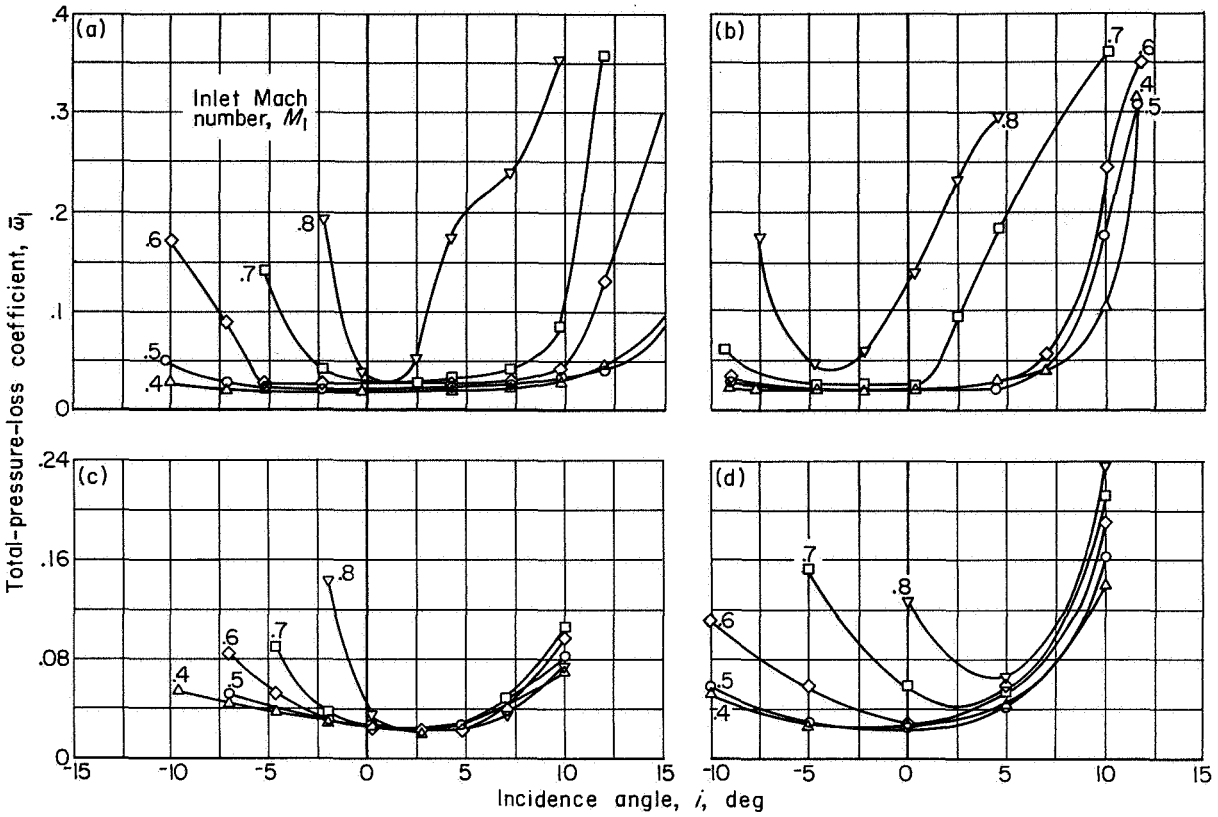

(a) C.4 Circular-arc blade. Camber angle, 25°; maximum-thickness ratio, 0.10; solidity, 1.333; blade-chord angle, 42.5° (ref. 40). (b) C.4 Parabolic-ard blade. Camber angle, 25°; maximum-thickness ratio, 0.10; solidity, 1.333; blade-chord angle, 37.6° (ref. 40). (c) Double-circular-arc blade. Camber angle, 25°; maximum-thickness ratio, 0.105; solidity, 1.333; blade-chord angle, 42.5° (ref. 40). (d) Sharp-nose blade. Camber angle, 27.5°; maximum-thickness ratio, 0.08; solidity, 1.15; blade-chord angle, 30° (ref. 205).

FIGURE 130.—Effect of inlet Mach number on loss characteristics of cascade blade sections.

angle (as compared with the optimum or nominal incidence settings of ref. 196 or the design incidence setting of ref. 39) requires the use of only the loss variation and also permits the use of the diffusion factor (applicable in region of minimum loss) as a measure of the blade loading.

At this point, it should be kept in mind that the reference minimum-loss incidence angle is not necessarily to be considered as a recommended design point for compressor application. The selection of the best incidence angle for a particular blade element in a multistage-compressor design is a function of many considerations, such as the location of the blade row, the design Mach number, and the type and application of the design. In general, there is no one universal definition of design or best incidence angle. The cascade

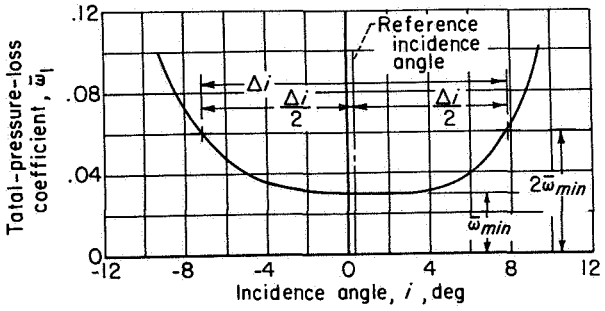

FIGURE 131.—Definition of reference minimum-loss incidence angle.

reference location is established primarily for purposes of analysis.

Of the many blade shapes currently in use in compressor design practice (i.e., NACA 65-series, C-series circular arc, parabolic arc, double

circular arc), data sufficient to permit a reasonably complete and significant correlation have been published only for the 65-(A_{10})-series blades of reference 39. Therefore, a basic correlation of the 65-(A_{10})-series data had to be established first and the results used as a guide or foundation for determining the corresponding performance trends for the other blade shapes for which only limited data exist.

Since the ultimate objective of cascade tests is to provide information for designing compressors, it is desirable, of course, that the structure of the data correlations represent the compressor situation as closely as possible. Actually, a blade element in a compressor represents a blade section of fixed geometry (i.e., fixed profile form, solidity, and chord angle) with varying inlet-air angle. In two-dimensional-cascade practice, however, variations in incidence angle have been obtained by varying either the inlet-air angle or the blade-chord angle. The available systematic data for the NACA 65-(A_{10})-series blades (ref. 39) have been obtained under conditions of fixed inlet-air angle and varying blade-chord angle. Since these data form the foundation of the analysis, it was necessary to establish the cascade performance correlations on the basis of fixed inlet-air angle. Examination of limited unpublished low-speed data indicate that, as illustrated in figure 132, the loss curve for constant air inlet angle generally falls somewhat to the right of the constant-chord-angle curve for fixed values of β_1 and $\gamma°$ in the low-loss region of the curve. Values of minimum-loss incidence angle for fixed β_1 operation are indicated to be of the order of 1° or 2° greater than for fixed $\gamma°$ operation. An approximate allowance for this difference is made

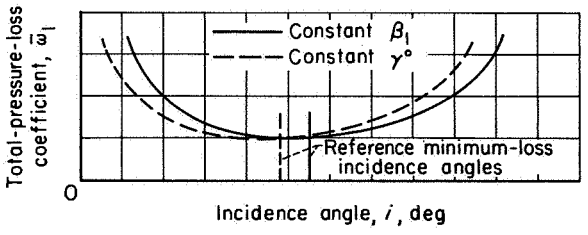

FIGURE 132.—Qualitative comparison of cascade range characteristics at constant blade-chord angle and constant inlet-air angle (for same value of β_1 in region of minimum loss).

in the use of reference-incidence-angle data from these two methods.

With the definition of reference incidence angle, performance parameters, and analytical approach established, the procedure is first to determine how the value of the reference minimum-loss incidence angle varies with cascade geometry and flow conditions for the available blade profiles. Then the variation of the performance parameters is determined at the reference location (as indicated in fig. 127) as geometry and flow are changed. Thus, the various factors involved can be appraised, and correlation curves and charts can be established for the available data. The analysis and correlation of cascade reference-point characteristics are presented in the following sections.

INCIDENCE-ANGLE ANALYSIS

PRELIMINARY ANALYSIS

In an effort to obtain a general empirical rule for the location of the reference minimum-loss incidence angle, it is first necessary to examine the principal influencing factors.

It is generally recognized that the low-loss region of incidence angle is identified with the absence of large velocity peaks (and subsequent decelerations) on either blade surface. For infinitely thin sections, steep velocity gradients are avoided when the front stagnation point is located at the leading edge. This condition has frequently been referred to as the condition of "impact-free entry." Weinig (ref. 80) used the criterion of stagnation-point location to establish the variation of impact-free-entry incidence angle for infinitely thin circular-arc sections from potential-flow theory. Results deduced from reference 80 are presented in figure 133(a). The minimum-loss incidence angle is negative for infinitely thin blades and decreases linearly with camber for fixed solidity and blade-chord angle.

While there is no definite corresponding i-inc dence-angle theory for thick-nose blades with rounded leading edges, some equivalent results have been obtained based on the criterion that the location of the stagnation point in the leading-edge region of a thick blade is the controlling factor in the determination of the surface velocity distributions. Carter, in reference 190, showed semitheoretically on this basis that optimum incidence angle (angle at maximum lift-drag ratio)

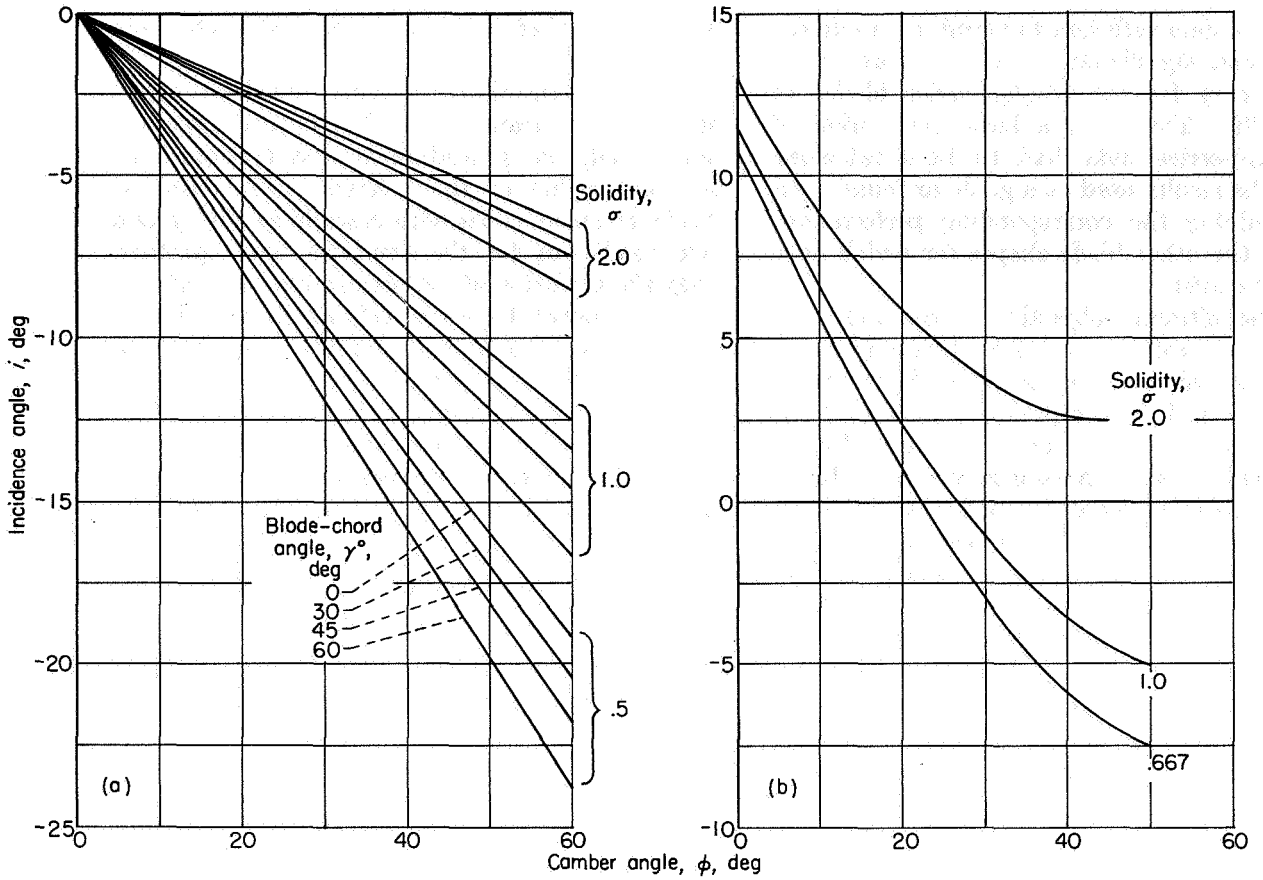

(a) "Impact-free-entry" incidence angle for infinitely thin blades according to potential theory of Weinig (ref. 80).
(b) "Optimum" incidence angle for 10-percent-thick C-series profiles according to semitheoretical developments of Carter *et al.* (refs. 190 and 196). Outlet-air angle, 20°.

FIGURE 133.—Variation of reference incidence angle for circular-air-mean-line blades obtained from theoretical or semitheoretical investigations.

for a conventional 10-percent-thick circular-arc blade decreases with increasing camber angle. The results of reference 190 were followed by generalized plots of optimum incidence angle in reference 196, which showed, as in figure 133(a), that optimum incidence angle for a 10-percent-thick C-series blade varies with camber angle, solidity, and blade orientation. (In these references, blade orientation was expressed in terms of air outlet angle rather than blade-chord angle.) The plot for an outlet-air angle of 20° is shown in figure 133(b). Apparently, the greater the blade circulation, the lower in magnitude the minimum-loss incidence angle must be. It is reasonable to expect, therefore, that the trends of variation of minimum-loss incidence angle for conventional blade sections will be similar to those established by thin-airfoil theory.

A preliminary examination of experimental cascade data showed that the minimum-loss incidence angles of uncambered sections ($\phi=0$) of conventional thicknesses were not zero, as indicated by theory for infinitely thin blades (fig. 133(a)), but always positive in value. The appearance of positive values of incidence angle for thick blades is attributed to the existence of velocity distributions at zero incidence angle that are not symmetrical on the two surfaces. Typical plots illustrating the high velocities generally observed in the inlet region of the lower (pressure) surface of thick uncambered blades at zero incidence angle are shown in figure 134. Apparently, an increase in incidence angle from the zero value is necessary in order to reduce the lower-surface velocity to a more equitable distribution that results in a minimum of the over-all loss. This

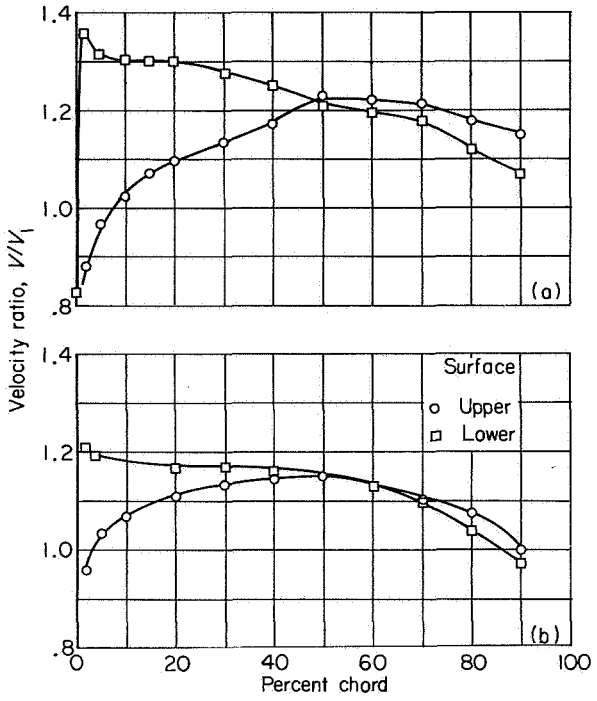

(a) Inlet-air angle, 60°; solidity, 1.5.
(b) Inlet-air angle, 30°; solidity, 1.0.

FIGURE 134.—Illustration of velocity distribution for uncambered blade of conventional thickness at zero incidence angle. Data for 65–(0)10 blade of reference 39.

zero-camber thickness effect will appear only for blade-chord angles between 0° and 90°, since, as indicated by the highly simplified one-dimensional model of the blade passage flow in figure 135, the velocity distributions at these limit angles are symmetrical.

The effect of blade thickness blockage on impact-free-entry incidence angle for straight (uncambered) blades of constant chordwise thickness in incompressible two-dimensional flow is investigated in reference 34. The results of reference 34 are plotted in terms of the parameters used in this analysis in figure 136. It is reasonable to expect that similar trends of variations of zero-camber reference minimum-loss incidence angle will be obtained for compressor blade profiles.

On the basis of the preceding analysis, therefore, it is expected that, for low-speed-cascade flow, reference minimum-loss incidence angle will generally be positive at zero camber and decrease with increasing camber, depending on solidity and blade-chord angle. The available theory also indicates that the variation of reference incidence angle with camber at fixed solidity and chord angle might be essentially linear. If so, the variations could be expressed in terms of slope

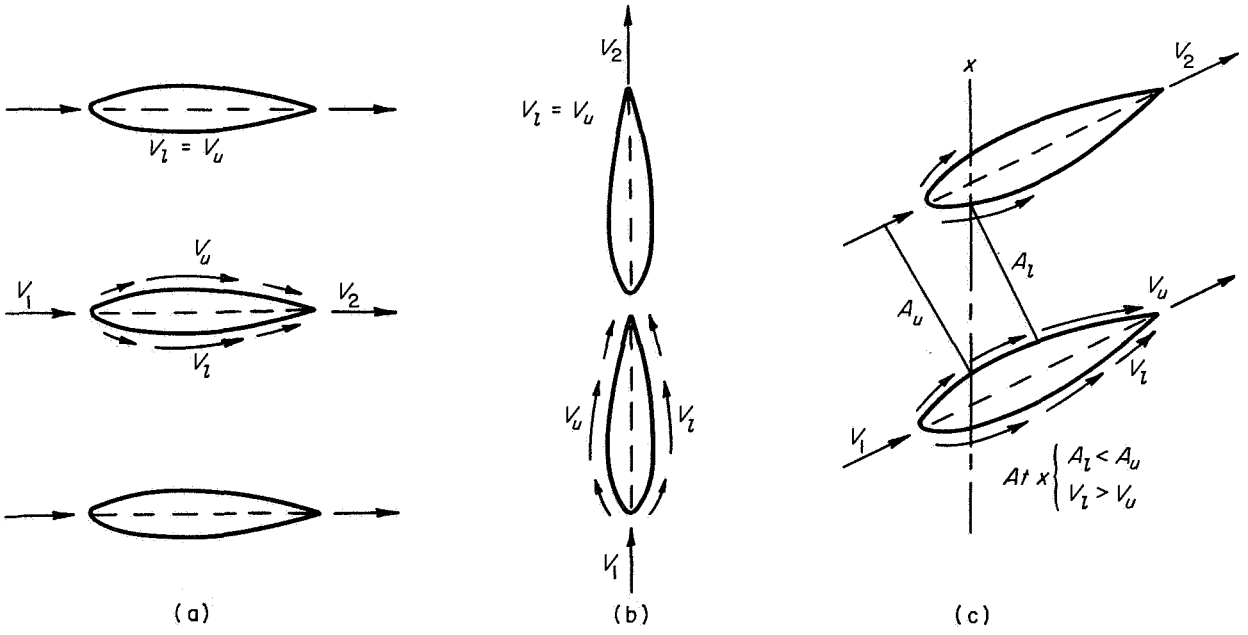

(a) $\gamma°=0°$. (b) $\gamma°=90°$. (c) $0°<\gamma°<90°$.

FIGURE 135.—Effect of blade thickness of surface velocity at zero incidence angle for uncambered airfoil section according to simplified one-dimensional model.

691-564 O-65-14

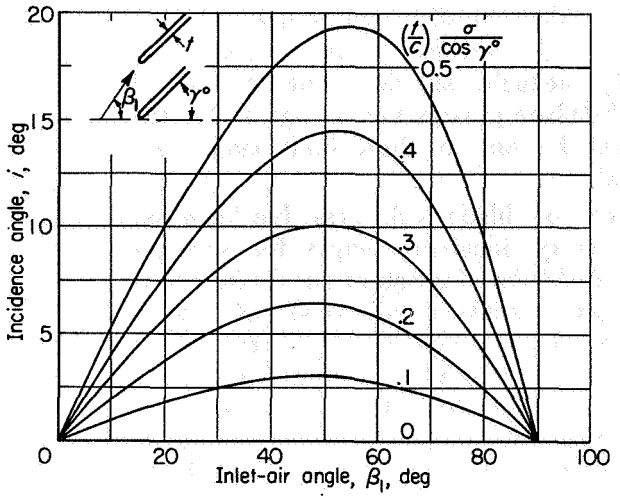

FIGURE 136.—Theoretical variation of "impact-free-entry" incidence angle for constant-thickness uncambered sections according to developments of reference 34.

and intercept values, where the intercept value represents the magnitude of the incidence angle for the uncambered section (function of blade thickness, solidity, and blade-chord angle). Reference minimum-loss incidence angle may also vary with inlet Mach number and possibly with Reynolds number.

DATA CORRELATIONS

Form of correlation.—Although preliminary theory indicates that blade-chord angle is the significant blade orientation parameter, it was necessary to establish the data correlations in terms of inlet-air angle, as mentioned previously. The observed cascade data were found to be represented satisfactorily by a linear variation of reference incidence angle with camber angle for fixed solidity and inlet-air angle. The variation of reference minimum-loss incidence angle can then be described in equation form as

$$i=i_o+n\varphi \qquad (261)$$

where i_o is the incidence angle for zero camber, and n is the slope of the incidence-angle variation with camber $(i-i_o)/\varphi$.

Since the existence of a finite blade thickness is apparently the cause of the positive values of i_o, it is reasonable to assume that both the magnitude of the maximum thickness and the thickness distribution contribute to the effect. Therefore, since the 10-percent-thick 65-series blades of reference 39 are to be used as the basis for a generalized correlation of all conventional blade shapes, it is proposed that the zero-camber reference incidence angle be expressed in the form

$$i_o=(K_i)_{sh}(K_i)_t(i_o)_{10} \qquad (262)$$

where $(i_o)_{10}$ represents the variation of zero-camber incidence angle for the 10-percent-thick 65-series thickness distribution, $(K_i)_t$ represents any correction necessary for maximum blade thicknesses other than 10 percent, and $(K_i)_{sh}$ represents any correction necessary for a blade shape with a thickness distribution different from that of the 65-series blades. (For a 10-percent-thick 65-series blade, $(K_i)_t=1$ and $(K_i)_{sh}=1$.)

The problem, therefore, is reduced to finding the values of n and i_o (through eq. (262)) as functions of the pertinent variables involved for the various blade profiles considered.

NACA 65-(A_{10})-series blades.—From the extensive low-speed-cascade data for the 65-(A_{10})-series blades (ref. 39), when expressed in terms of equivalent incidence and camber angles (figs. 125 and 126), plots of i_o and n can be deduced that adequately represent the minimum-loss-incidence-angle variations of the data. The deduced values of i_o and n as functions of solidity and inlet-air angle are given for these blades in figures 137 and 138. The subscript 10 in figure 137 indicates that the i_o values are for 10-percent maximum-thickness ratio. Values of intercept i_o and slope n were obtained by fitting a straight line to each data plot of reference incidence angle against camber angle for a fixed solidity and air inlet angle. The straight lines were selected so that both a satisfactory representation of the variation of the data points and a consistent variation of the resulting n and i_o values were obtained.

The deduced rule values and the observed data points compared in figure 139 indicate the effectiveness of the deduced representation. In several configurations, particularly for low cambers, the range of equivalent incidence angle covered in the tests was insufficient to permit an accurate determination of a minimum-loss value. Some of the scatter of the data may be due to the effects of local laminar separation in altering the range characteristics of the sections.

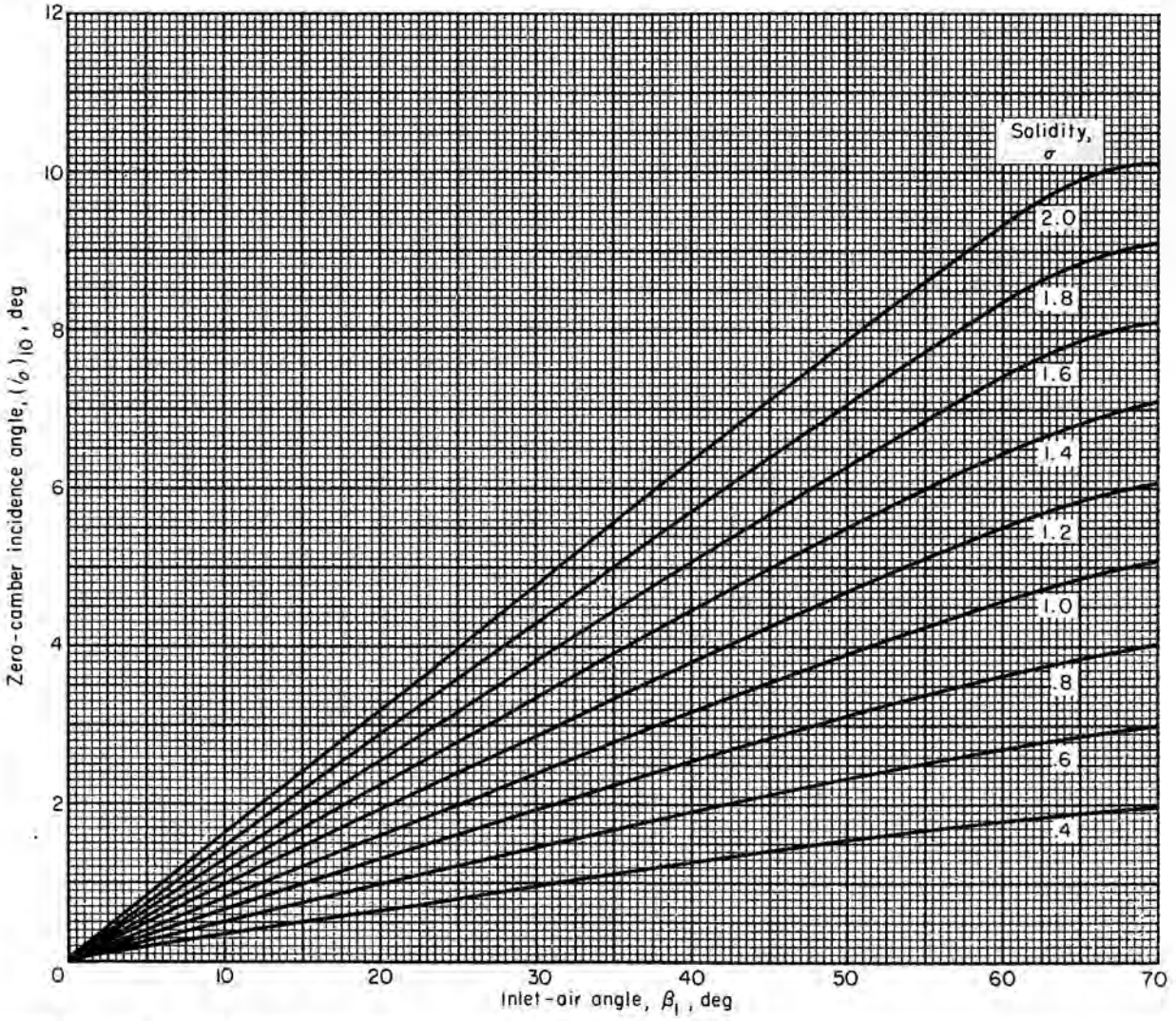

FIGURE 137.—Reference minimum-loss incidence angle for zero camber deduced from low-speed-cascade data of 10-percent-thick NACA 65-(A_{10})-series blades (ref. 39).

Although the cascade data in reference 39 include values of inlet-air angle from 30° to 70° and values of solidity from 0.5 to 1.5, the deduced variations in figures 137 and 138 are extrapolated to cover wider ranges of β_1 and σ. The extrapolation of i_o to zero at $\beta_1=0$ is obvious. According to theory (fig. 133), the value of the slope term does not vanish at $\beta_1=0$. In figure 138, therefore, an arbitrary fairing of the curves down to nonzero values of n was adopted as indicated. Actually, it is not particularly critical to determine the exact value of the slope term at $\beta_1=0$ necessary to locate the reference incidence angle precisely, since, for such cases (inlet guide vanes and turbine nozzles), a wide low-loss range of operation is usually obtained. The solidity extrapolations were attempted because of the uniform variations of the data with solidity. However, caution should be exercised in any further extrapolation of the deduced variations.

C-Series circular-arc blades.—The various thickness distributions used in combination with the circular-arc mean line have been designated C.1, C.2, C.3, and so forth (refs. 196 to 198). In general, the various C-series thickness distributions are fairly similar, having their maximum thickness located at between 30 and 40 percent of the chord length. The 65-series and two of

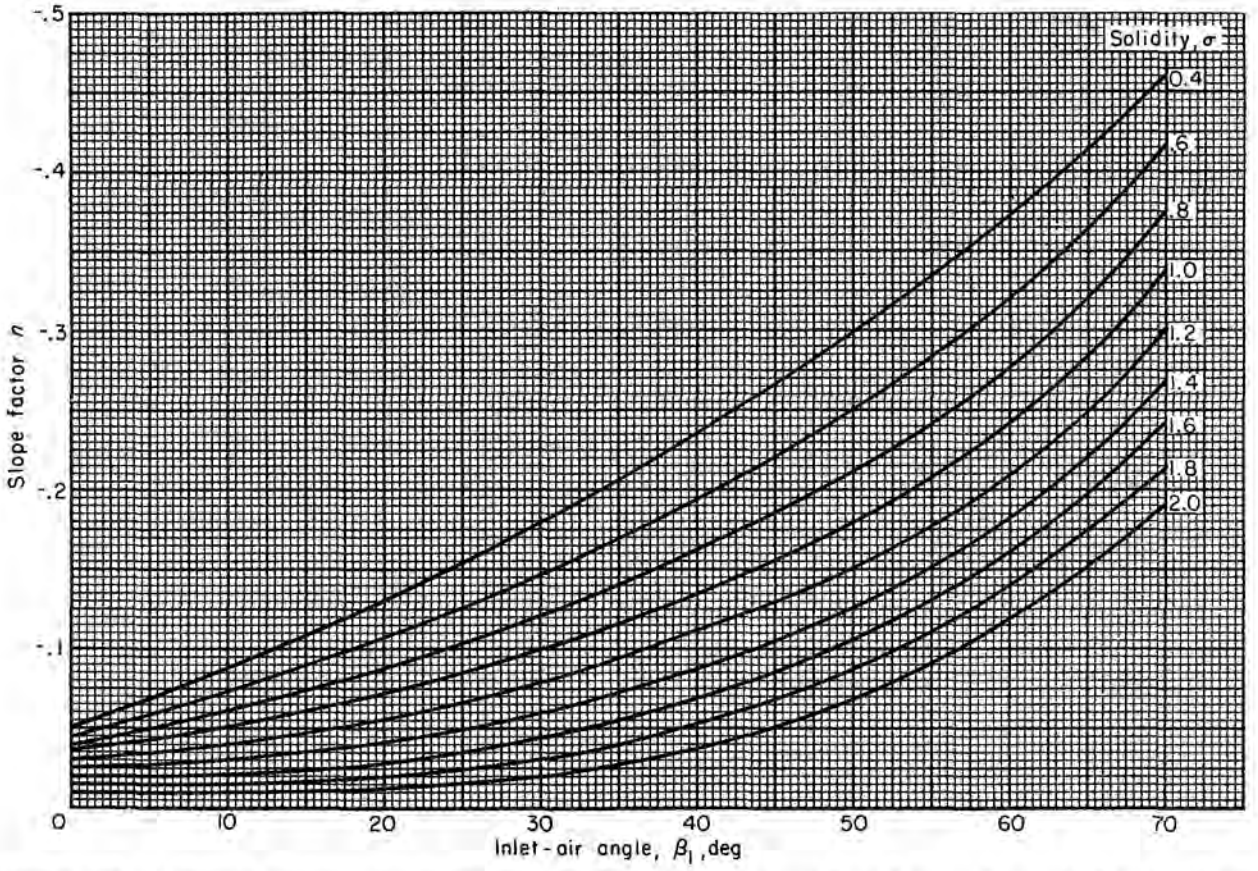

FIGURE 138.—Reference minimum-loss-incidence-angle slope factor deduced from low-speed-cascade data for NACA 65-(A_{10})-series blades as equivalent circular arcs.

the more popular C-series thickness distributions (C.1 and C.4) are compared on an exaggerated scale in figure 140. (The 65-series profile shown is usually thickened near the trailing edge in actual blade construction.)

In view of the somewhat greater thickness blockage in the forward portions of the C-series blades (fig. 140), it may be that the minimum-loss incidence angles for zero camber for the C-series blades are somewhat greater than those for the 65-series profiles; that is, $(K_i)_{sh}>1$. In the absence of any definitive cascade data, the value of $(K_i)_{sh}$ for the C-series profiles was arbitrarily taken to be 1.1. Observed minimum-loss incidence angles for an uncambered 10-percent-thick C.4 profile (obtained from ref. 192, pt. I) are compared in figure 141 with values predicted from the deduced $(i_o)_{10}$ values for the 65-series blade (fig. 137 and eq. (262)) with an assumed value of $(K_i)_{sh}=1.1$. (For 10-percent thickness, $(K_i)_t=1$.)

In view of the similarity between the 65-(A_{10})-series mean line and a true circular arc (fig. 125), the applicability of the slope values in figure 138 to the circular-arc mean line was investigated. For the recent cascade data obtained from tunnels having good boundary-layer control (refs. 167, (pt. I) and 199), a check calculation for the 10-percent-thick C.4 circular-arc blades using figures 137 and 138 with $(K_i)_{sh}=1.1$ revealed good results. For the three configurations in reference 199 tested at constant $\beta_1(\varphi=30°)$, the agreement between observed and predicted minimum-loss incidence angles was within 1°. For the one configuration in reference 167 (pt. I) tested at constant $\gamma°(\varphi=31°)$, the predicted value of minimum-loss incidence angle was 1.7° greater than the observed value. However, in view of the general 1° to 2° difference between fixed β_1 and fixed $\gamma°$ operation (fig. 132), such a discrepancy is to be expected. On the basis of these limited data, it appears that the low-speed minimum-loss incidence angles for the C-series circular-arc

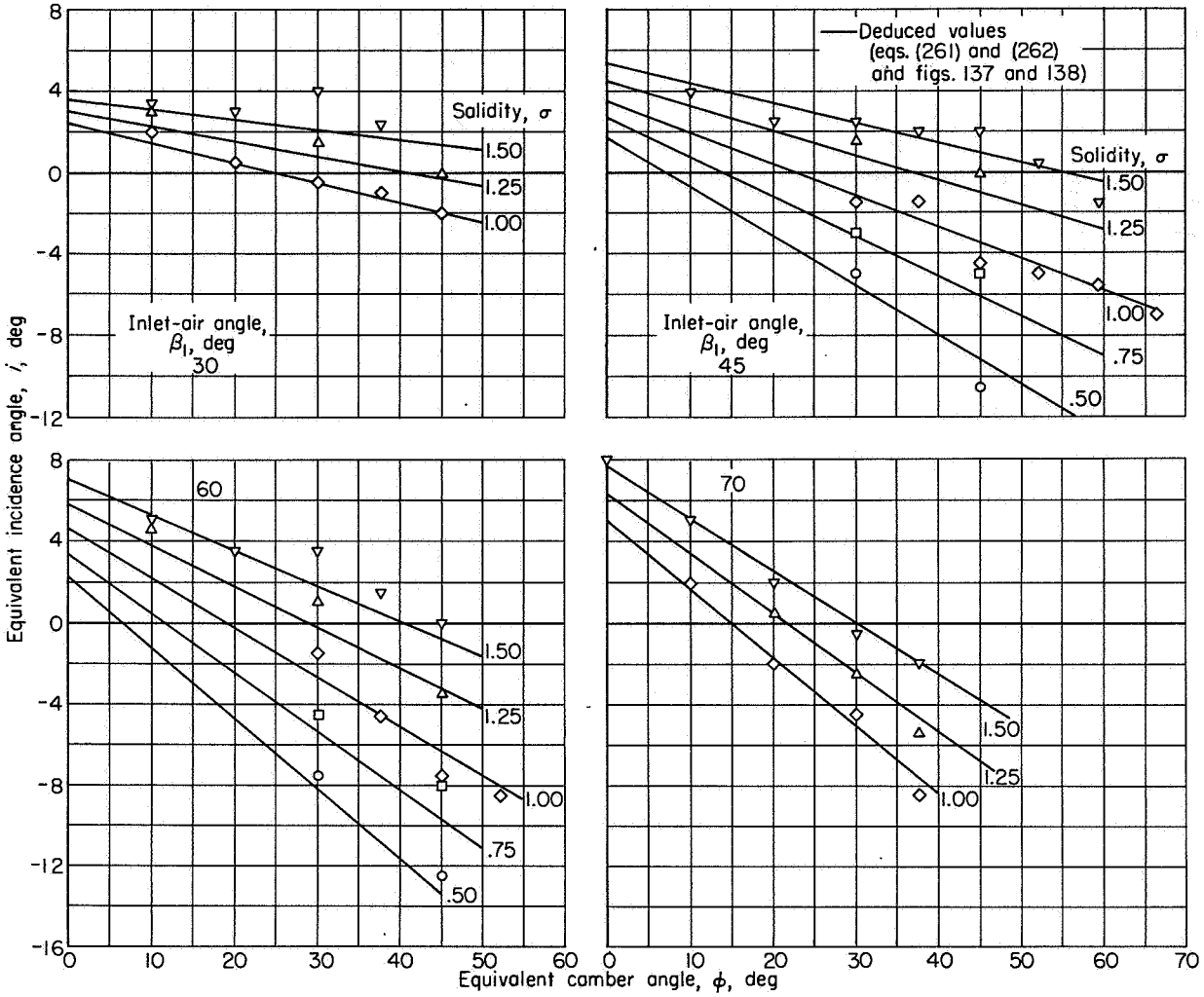

FIGURE 139.—Comparison of data values and deduced rule values of reference minimum-loss incidence angle for 65-(A_{10})10 blades as equivalent circular arc (ref. 39).

blade can be obtained from the i_o and n values of the 65-series blade with $(K_t)_{sh}=1.1$.

Double-circular-arc blades.—The double-circular-arc blade is composed of circular-arc upper and lower surfaces. The arc for each surface is drawn between the point of maximum thickness at midchord and the tangent to the circles of the leading- and trailing-edge radii. The chordwise thickness distribution for the double-circular-arc profile with 1-percent leading- and trailing-edge radius is shown in figure 140. Lack of cascade data again prevents an accurate determination of a reference-incidence-angle rule for the double circular arc. Since the double-circular-arc blade is thinner than the 65-series blade in the inlet region, the zero-camber incidence angles for the double-circular-arc blade should be somewhat different from those of the 65-series section, with perhaps $(K_t)_{sh}\leq 1$. It can also be assumed, as before, that the slope-term values of figure 138 are valid for the double-circular-arc blade. From an examination of the available cascade data for the double-circular-arc blade ($\varphi=25°$, $\sigma=1.333$, ref. 40; and $\varphi=40°$, $\sigma=1.064$, ref. 197), it appears that the use of figures 137 and 138 with a value of $(K_t)_{sh}=0.7$ in equations (261) and (262) results in a satisfactory comparison between predicted and observed values of reference incidence angle.

Other blades.—Similar procedures can be applied to establish reference-incidence-angle correlations for other blade shapes. Cascade data

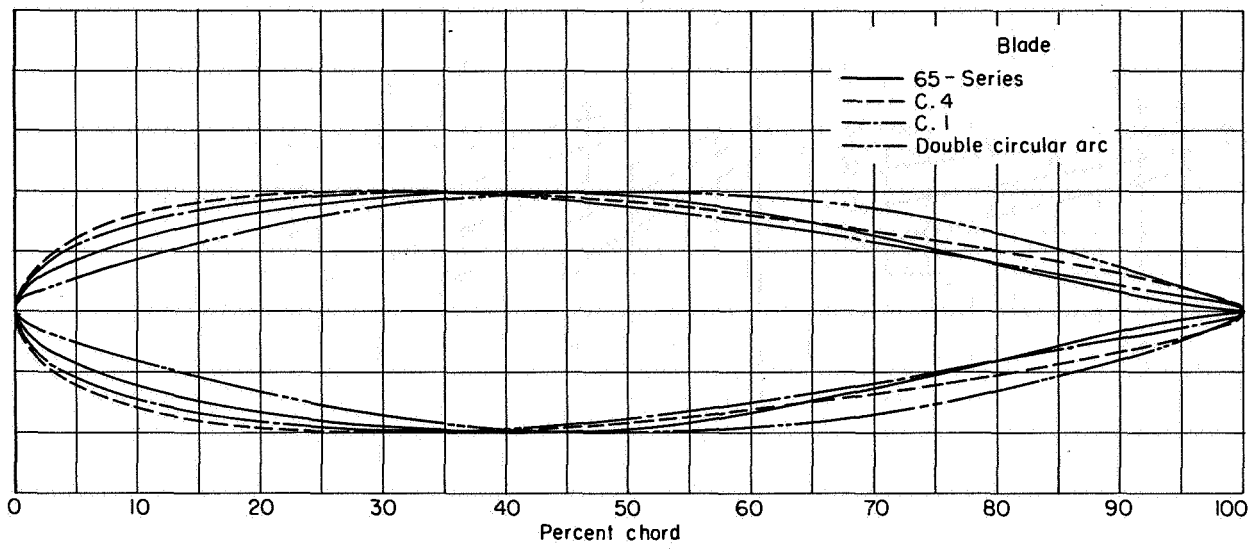

FIGURE 140.—Comparison of basic thickness distributions for conventional compressor blade sections.

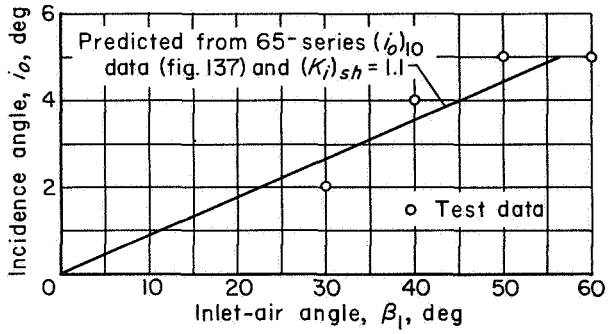

FIGURE 141.—Zero-camber minimum-loss incidence angle angle for 10-percent-thick C.4 profile. Solidity, 1.0 (ref. 192, pt. I).

are also available for the C-series parabolic-arc blades (refs. 40, 192, 200, and 201) and the NACA 65-(AI)-series blade (ref. 123); but, in view of the limited use of these forms in current practice, no attempt was made at this time to deduce corresponding incidence-angle rules for these blades.

Effect of blade maximum thickness.—As indicated previously, some correction (expressed here in terms of $(K_t)_i$, eq. (262)) of the base values of $(i_o)_{10}$ obtained from the 10-percent-thick 65-series blades in figure 137 should exist for other values of blade maximum-thickness ratio. According to the theory of the zero-camber effect, $(K_t)_i$ should be zero for zero thickness and increase as maximum blade thickness is increased, with a value of 1.0 for a thickness ratio of 0.10. Although the very limited low-speed data obtained from blades of variable thickness ratio (refs. 202 and 203) are not completely definitive, it was possible to establish a preliminary thickness-correction factor for reference zero-camber incidence angle as indicated in figure 142 for use in conjunction with equation (262).

Effect of inlet Mach number.—The previous correlations of reference minimum-loss incidence angle have all been based on low-speed-cascade data. It appears from limited high-speed data, however, that minimum-loss incidence angle will vary with increasing inlet Mach number for certain blade shapes.

The variations of minimum-loss incidence angle with inlet Mach number are plotted for several blade shapes in figures 143 and 144. The extension of the test data points to lower values of inlet Mach number could not generally be made because of reduced Reynolds numbers or insufficient points to establish the reference location at the lower Mach numbers. In some instances, however, it was possible to obtain low-speed values of incidence angle from other sources.

The blades of figure 143 show essentially no variation of minimum-loss incidence angle with inlet Mach number, at least up to a Mach number of about 0.8. The blades of figure 144, however, evidence a marked increase in incidence angle with Mach number. The difference in the variation of minimum-loss incidence angle with Mach number in figures 143 and 144 is associated with the

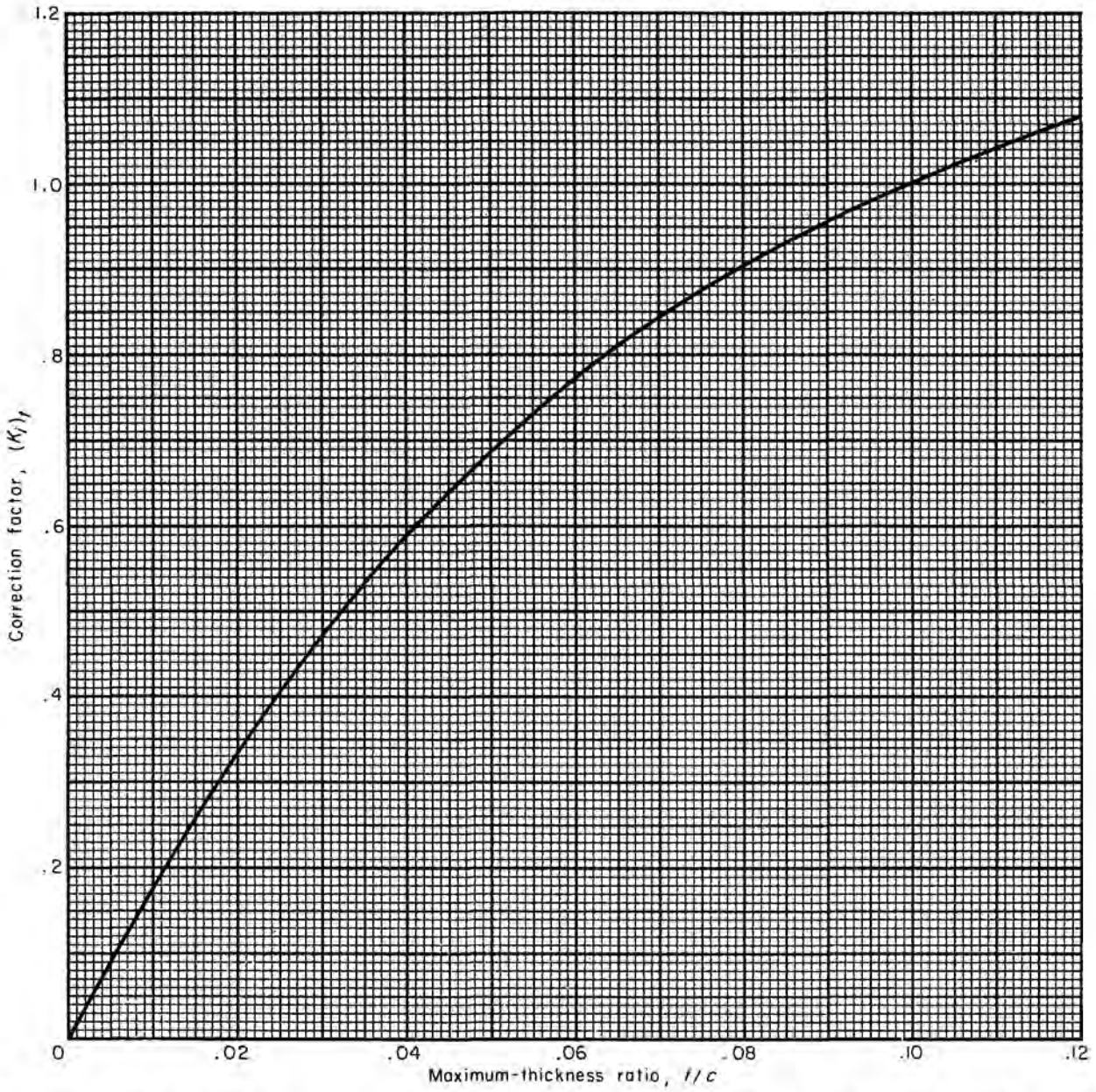

FIGURE 142.—Deduced blade maximum-thickness correction for zero-camber reference minimum-loss incidence angle (eq. (262)).

different way the general pattern of the loss variation changes with increasing Mach number for the two types of blades. For the thick-nose blades, as illustrated in figures 130 (a) and (b), the loss coefficient increases with Mach number at both the high and low incidence angles, thus tending to maintain the same point of minimum loss. For the sharp-nose blade, as illustrated by figures 130 (c) and (d), the increase in loss occurs primarily on the low-incidence-angle side; and a positive shifting of the minimum-loss incidence angle results. Data for other thick-nose sections in reference 201 show the rise in loss to occur at both ends of the curve, but plots of reference incidence angle against Mach number could not validly be

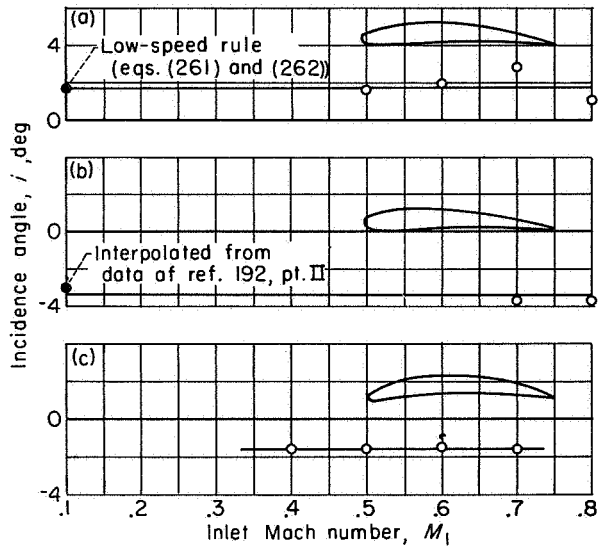

(a) C.4 Circular-arc blade. Camber angle, 25°; solidity 1.333; blade-chord angle, 42.5° (ref. 40).
(b) C.4 Parabolic-arc blade. Camber angle, 25°; solidity, 1.333; blade-chord angle, 37.5°; maximum camber at 40-percent chord (ref. 40).
(c) C.7 Parabolic-arc blade. Camber angle, 40°; solidity, 1.0; blade-chord angle, 24.6°; maximum camber at 45-percent chord (ref. 216).

FIGURE 143.—Variation of reference minimum-loss incidence angle with inlet Mach number for thick-nose sections. Maximum-thickness ratio, 0.10.

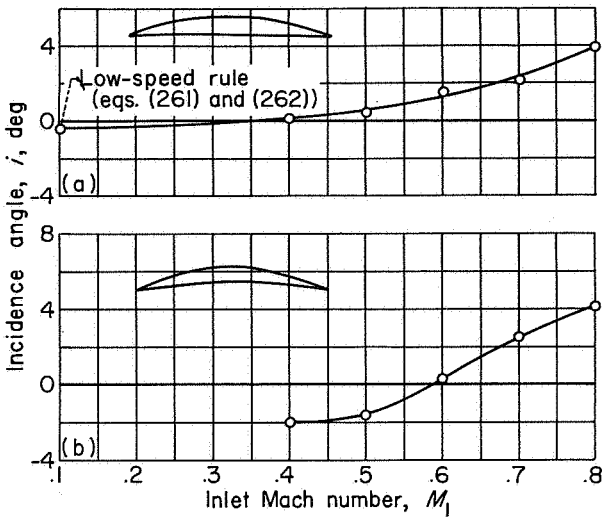

(a) Double-circular-arc blade. Camber angle, 25°; maximum-thickness ratio, 0.105; solidity, 1.333; blade-chord angle, 42.5° (ref. 40).
(b) Blade section of reference 205. Camber angle, 27.5°; maximum-thickness ratio, 0.08; solidity, 1.15; blade-chord angle, 30°; maximum thickness and camber at 50-percent chord.

FIGURE 144.—Variation of reference minimum-loss incidence angle with inlet Mach number for sharp-nose sections.

made for these blades because of evidence of strong local laminar-separation effects.

Since the most obvious difference between the blades in figures 143 and 144 is the construction of the leading-edge region, the data suggest that blades with thick-nose inlet regions tend to show, for the range of inlet Mach number covered, essentially no Mach number effect on minimum-loss incidence angle, while blades with sharp leading edges will have a significant Mach number effect. The available data, however, are too limited to confirm this observation conclusively at this time. Furthermore, for the blades that do show a Mach number effect, the magnitude of the variation of reference incidence angle with Mach number is not currently predictable.

SUMMARY

The analysis of blade-section reference minimum-loss incidence angle shows that the variation of the reference incidence angle with cascade geometry at low speed can be established satisfactorily in terms of an intercept value i_o and a slope value n as given by equation (261). Deduced values of i_o and n were obtained as a function of β_1 and σ from the data for the 10-percent-thick 65-(A_{10})-series blades of reference 39 as equivalent circular-arc sections (figs. 137 and 138). It was then shown that, as a first approach, the deduced values of $(i_o)_{10}$ and n in figures 137 and 138 could also be used to predict the reference incidence angles of the C-series and double-circular-arc blades by means of a correction $(K_t)_{sh}$ to the $(i_o)_{10}$ values of figure 137 (eq. (262)).

The procedure involved in estimating the low-speed reference minimum-loss incidence angle of a blade section is as follows: From known values of β_1 and σ, $(i_o)_{10}$ and n are selected from figures 137 and 138. The value of $(K_t)_t$ for the blade maximum-thickness ratio is obtained from figure 142, and the appropriate value of $(K_t)_{sh}$ is selected for the type of thickness distribution. For NACA 65-series blades, $(K_t)_{sh}=1.0$; and it is proposed that $(K_t)_{sh}$ be taken as 1.1 for the C-series circular-arc blade and as 0.7 for the double-circular-arc blade. The value of i_o is then computed from equation (262); and finally i is determined from

the blade camber angle according to equation (261).

It should be noted that the values of $(K_i)_{sh}$ given for the circular-arc blades are rather tenuous values obtained from very limited data. The use of the proposed values is not critical for good accuracy; the values were included primarily for completeness as a reflection of the anticipated differences in the blade thickness blockage effects. Further experimental data will be necessary to establish the significance of such a correction. Also, a marked increase in reference minimum-loss incidence angle with Mach number is to be expected for sharp-nose blade sections. The magnitude of the Mach number correction for these blades is currently unpredictable.

LOSS ANALYSIS

With the location of the low-speed reference minimum-loss incidence angle established for several conventional blade sections, the magnitude of the losses occurring at this reference position (fig. 127) will now be investigated. Accordingly, the nature of the loss phenomena and the various factors influencing the magnitude of the loss over a range of blade configurations and flow conditions are first analyzed. The available experimental loss data are then examined to establish fundamental loss correlations in terms indicated by the analysis.

PRELIMINARY ANALYSIS

Two-dimensional-cascade losses arise primarily from the growth of boundary layer on the suction and pressure surfaces of the blades. These surface boundary layers come together at the blade trailing edge, where they combine to form the blade wake, as shown in figure 145. As a result of the formation of the surface boundary layers, a local defect in total pressure is created, and a certain mass-averaged loss in total pressure is determined in the wake of the section. The loss in total pressure is measured in terms of the total-pressure-loss coefficient $\bar{\omega}$, defined generally as the ratio of the mass-averaged loss in total pressure $\overline{\Delta P}$ across the blade row from inlet to outlet stations to some reference free-stream dynamic pressure $(P_0-p_0)_{ref}$, or

$$\bar{\omega}_{ref}=\frac{\overline{\Delta P}}{(P_0-p_0)_{ref}} \tag{263}$$

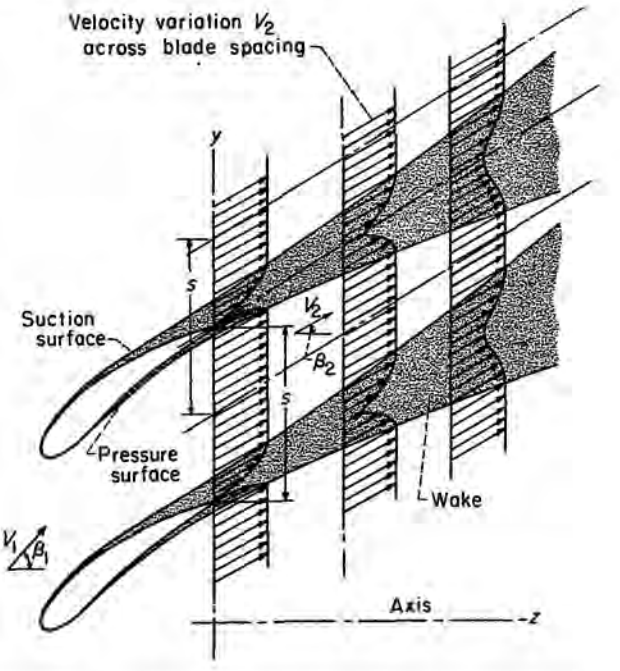

FIGURE 145.—Schematic representation of development of surface boundary layers and wake in flow about cascade blade sections.

For incompressible flow, P_0-p_0 is equal to the conventional free-stream dynamic pressure $\rho_0 V_0^2/2$. The total-pressure-loss coefficient is usually determined from consideration of the total-pressure variation across a blade spacing s (fig. 145).

A theoretical analysis of incompressible two-dimensional-cascade losses in reference 156 shows that the total-pressure-loss coefficient at the cascade-outlet measuring station (where the static pressure is essentially uniform across the blade spacing) is given by

$$\bar{\omega}_1=2\left(\frac{\theta^*}{c}\right)_2\frac{\sigma}{\cos\beta_2}\left(\frac{\cos\beta_1}{\cos\beta_2}\right)^2\left\{\frac{\frac{2H_2}{3H_2-1}}{\left[1-\left(\frac{\theta^*}{c}\right)_2\frac{\sigma H_2}{\cos\beta_2}\right]^3}\right\} \tag{264}$$

where $\bar{\omega}_1$ is the loss coefficient based on inlet dynamic head, θ^*/c is the ratio of wake momentum thickness to blade-chord length, σ is cascade solidity, β_2 is the air outlet angle, and H_2 is the wake form factor (displacement thickness divided by momentum thickness). The wake characteristics in equation (264) are expressed in terms of

conventional thickness in a plane normal to the wake (i.e., normal to the outlet flow) at the measuring station. Definitions of wake characteristics and variations in velocity and pressure assumed by the analysis are given in reference 156. The analysis further indicates that the collection of terms within the braces is essentially secondary (since H_2 is generally $\leq$ about 1.2 at the measuring station), with a magnitude of nearly 1 for conventional unstalled configurations. The principal determinants of the loss in total pressure at the cascade measuring station are, therefore, the cascade geometry factors of solidity, air outlet and air inlet angles, and the aerodynamic factor of wake momentum-thickness ratio.

Since the wake is formed from a coalescing of the pressure- and suction-surface boundary layers, the wake momentum thickness naturally depends on the development of the blade surface boundary layers and also on the magnitude of the blade trailing-edge thickness. The results of references 156, 202, and 204 indicate, however, that the contribution of conventional blade trailing-edge thickness to the total loss is not generally large for compressor sections; the preliminary factor in the wake development is the blade surface boundary-layer growth. In general, it is known (ch. V, e.g.) that the boundary-layer growth on the surfaces of the blade is a function primarily of the following factors: (1) the surface velocity gradients (in both subsonic and supersonic flow), (2) the blade-chord Reynolds number, and (3) the free-stream turbulence level.

Experience has shown that blade surface velocity distributions that result in large amounts of diffusion in velocity tend to produce relatively thick blade boundry layers. The magnitude of the velocity diffusion in low-speed flow generally depends on the geometry of the blade section and its incidence angle. As Mach number is increased, however, compressibility exerts a further influence on the velocity diffusion of a given cascade geometry and orientation. If local supersonic velocities develop at high inlet Mach numbers, the velocity diffusion is altered by the formation of shock waves and the interaction of these shock waves with the blade surface boundary layers. The losses associated with local supersonic flow in a cascade are generally greater than for subsonic flow in the same cascade. The increases in loss are frequently referred to as shock losses.

Cascade-inlet Mach number also influences the magnitude of the subsonic diffusion for a fixed cascade. This Mach number effect is the conventional effect of compressibility on the blade velocity distributions in subsonic flow. Compressibility causes the maximum local velocity on the blade surface to increase at a faster rate than the inlet and outlet velocities. Accordingly, the magnitude of the surface diffusion from maximum velocity to outlet velocity becomes greater as inlet Mach number is increased. A further secondary influence of Mach number on losses is obtained because of an increase in losses associated with the eventual mixing of the wake with the surrounding free-stream flow (ref. 37).

On the basis of the foregoing considerations, therefore, it is expected that the principal factors upon which to base empirical cascade-wake-thickness correlations should be velocity diffusion, inlet Mach number, blade-chord Reynolds number, and, if possible, turbulence level.

DATA CORRELATIONS

Velocity diffusion based on local velocities.— Recently, several investigations have been reported on the establishment of simplified diffusion parameters and the correlation of cascade losses in terms of these parameters (refs. 9, 38, and 156). The general hypothesis of these diffusion correlations states that the wake thickness, and consequently the magnitude of the loss in total pressure, is proportional to the diffusion in velocity on the suction surface of the blade in the region of the minimum loss. This hypothesis is based on the consideration that the boundary layer on the suction surface of conventional compressor blade sections contributes the major share of the wake in these regions, and therefore the suction-surface velocity distribution becomes the governing factor in the determination of the loss. It was further established in these correlations that, for conventional velocity distributions, the diffusion in velocity can be expressed significantly as a parameter involving the difference between some function of the measured maximum suction-surface velocity V_{max} and the outlet velocity V_2.

Reference 38 presents an analysis of blade-loading limits for the 65-(A_{10})10 blade section in terms of drag coefficient and a diffusion parameter given for incompressible flow by $(V_{max}^2-V_2^2)/V_{max}^2$.

Results of an unpublished analysis of cascade losses in terms of the momentum thickness of the blade wake (as suggested in ref. 156) indicate that a local diffusion parameter in the form given previously or in the form $(V_{max}-V_2)/V_{max}$ can satisfactorily correlate experimental cascade loss data.[2] The term "local diffusion parameter" is used to indicate that a knowledge of the maximum local surface velocity is required. The correlation obtained between calculated wake momentum-thickness ratio θ^*/c and local diffusion factor given by

$$D_{loc}=\frac{V_{max}-V_2}{V_{max}} \tag{265}$$

obtained for the NACA 65-(A_{10})-series cascade sections of reference 39 at reference incidence angle is shown in figure 146. Values of wake momentum-thickness ratio for these data were computed from the reported wake coefficient values according to methods similar to those discussed in reference 156. Unfortunately, blade surface velocity-distribution data are not available for the determination of the diffusion factor for other conventional blade shapes.

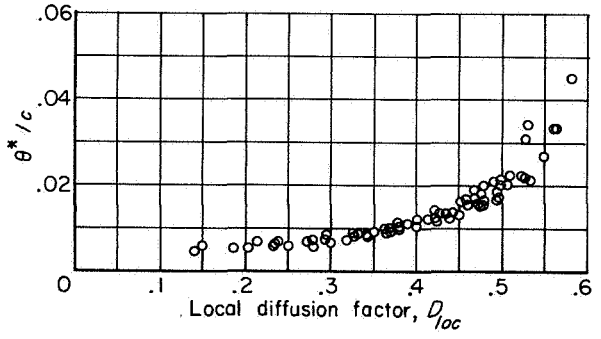

FIGURE 146.—Variation of computed wake momentum-thickness ratio with local diffusion factor at reference incidence angle for low-speed-cascade data of NACA 65-(A_{10})10 blades (ref. 39).

The correlation of figure 146 indicates the general validity of the basic diffusion hypothesis. At high values of diffusion (greater than about 0.5), a separation of the suction-surface boundary layer is suggested by the rapid rise in the momentum thickness. The indicated nonzero value of momentum thickness at zero diffusion represents the basic friction loss (surface shear stress) of the flow and also, to a smaller extent, the effect of the finite trailing-edge thickness. The correlation of figure 146 further indicates that wake momentum-thickness ratio at reference incidence angle can be estimated from the computed local diffusion factor for a wide range of solidities, cambers, and inlet-air angles. The loss relations of equation (264) and reference 156 can then be used to compute the resulting loss in the total pressure.

Velocity diffusion based on over-all velocities.—In order to include the cases of blade shapes for which velocity-distribution data are not available, a diffusion parameter has been established in reference 9 that does not require a specific knowledge of the peak local suction-surface velocity. Although originally derived for use in compressor design and analysis, the diffusion factor of reference 9 can also be applied in the analysis of cascade losses. The diffusion factor of reference 9 attempts, through several simplifying approximations, to express the local diffusion on the blade suction surface in terms of over-all (inlet or outlet) velocities or angles, quantities that are readily determined. The basis for the development of the over-all diffusion factor is presented in detail in reference 9 and is indicated briefly in figure 147. The diffusion factor is given by

$$D=\left(1-\frac{V_2}{V_1}\right)+\frac{\Delta V_\theta}{2\sigma V_1} \tag{54}$$

which, for incompressible two-dimensional-cascade flow, becomes

$$D=\left(1-\frac{\cos\beta_1}{\cos\beta_2}\right)+\frac{\cos\beta_1}{2\sigma}(\tan\beta_1-\tan\beta_2) \tag{266}$$

As in the case of the local diffusion factor, the diffusion factor of equation (266) is restricted to the region of minimum loss.

Cascade total-pressure losses at reference minimum-loss incidence angle are presented in reference 9 as a function of diffusion factor for the blades of reference 39. In a further unpublished analysis, a composite plot of the variation of computed wake momentum-thickness ratio with D at reference minimum-loss incidence angle was obtained from the available systematic cascade data (refs. 39 and 192) as shown in figure 148.[2] Blade maximum thickness was 10 percent in all

[2] A later analysis of cascade total-pressure losses is given in Analysis of Experimental Low-Speed Loss and Stall Characteristics of Two-Dimensional Compressor Blade Cascades by Seymour Liebein, NACA RM E57A28, 1957.

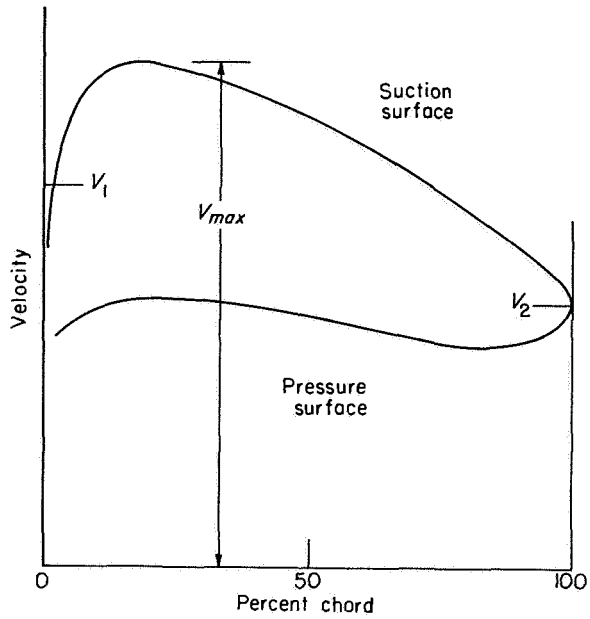

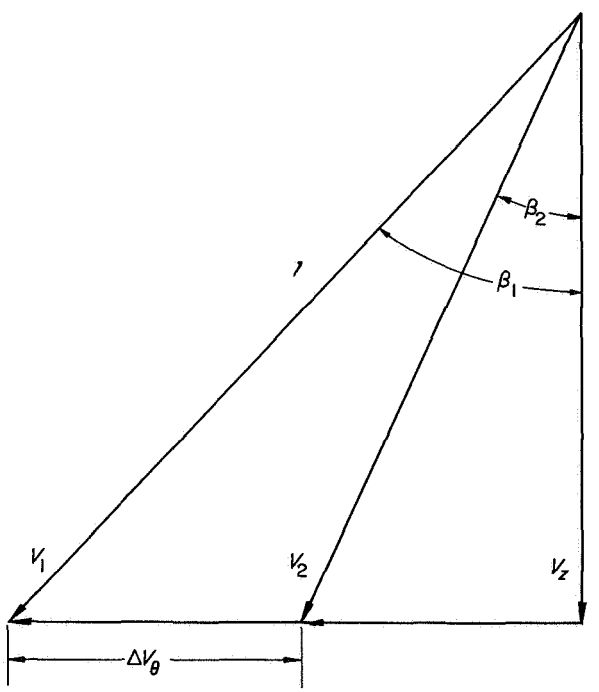

FIGURE 147.—Basis of development of diffusion factor for cascade flow from reference 9. $D \approx \frac{V_{max}-V_2}{V_{av}} \approx \frac{V_{max}-V_2}{V_1}$; $V_{max} \approx V_1 + f\left(\frac{\Delta V\theta}{\sigma}\right)$; thus, equations (54) and (266).

cases. A separation of the suction-surface boundary layer at high blade loading is indicated

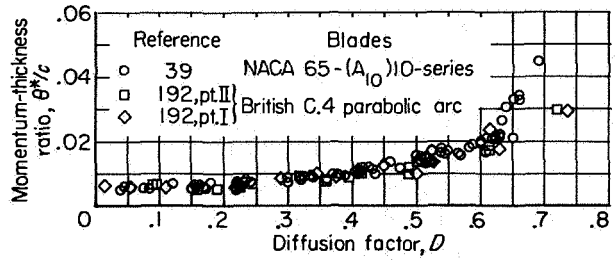

FIGURE 148.—Variation of computed wake momentum-thickness ratio with overall diffusion factor at reference incidence angle for low-speed systematic cascade data of references 39 and 192. Blade maximum-thickness ratio, 0.10; Reynolds number, $\approx 2.5 \times 10^5$.

by the increased rise in the wake momentum thickness for values of diffusion factor greater than about 0.6.

For situations in which the determination of a wake momentum-thickness ratio cannot be made, a significant loss analysis may be obtained if a simplified total-pressure-loss parameter is used that closely approximates the wake thickness. Since the terms within the braces of equation (264) are generally secondary factors, a loss parameter of the form $\bar{\omega}_1 \frac{\cos \beta_2}{2\sigma}\left(\frac{\cos \beta_2}{\cos \beta_1}\right)^2$ should constitute a more fundamental expression of the basic loss across a blade element than the loss coefficient alone. The effectiveness of this substitute loss parameter in correlating two-dimensional-cascade losses is illustrated in figure 149(a) for all the data for the NACA 65-(A_{10})-series blades of reference 39. (Total-pressure-loss coefficients were computed for the data from relations given in ref. 9.) A generalized correlation can also be obtained in terms of $\bar{\omega}_1 \frac{\cos \beta_2}{2\sigma}$, as shown in figure 149(b), but its effectiveness as a separation indicator does not appear to be as good. Such generalized loss parameters are most effective if the wake form does not vary appreciably among the various data considered.

Effect of blade maximum thickness.—Since an increase in blade maximum-thickness ratio increases the magnitude of the surface velocities (and therefore the diffusion), higher values of wake momentum-thickness ratio would be expected for thicker blades. From an analysis of limited available data on varying blade maximum-thickness ratio (refs. 202 and 203), it appears that the effect of blade thickness on wake momentum-thickness ratio is not large for conventional

cascade configurations. For example, for an increase in blade maximum-thickness ratio from 0.05 to 0.10, an increase in θ^*/c of about 0.003 at D of about 0.55 and an increase of about 0.002 at D of about 0.35 are indicated. The greater increase in wake θ^*/c at the higher diffusion level is understandable, since the rate of change of θ^*/c with D_{loc} increases with increasing diffusion (see fig. 146).

If blade surface velocity distributions can be determined, then the thickness effect will automatically be included in the evaluation of the resulting local diffusion factor. When an overall diffusion factor such as equation (54) is used, variations in blade thickness are not reflected in the corresponding loss prediction. However, in view of the small observed effect and the scatter of the original θ^*/c against D correlation of figure 148, it is believed that a thickness correction is unwarranted for conventional thickness ranges. However, the analysis does indicate that, for high diffusion and high solidity levels, it may be advisable to maintain blade thickness as small as practicable in order to obtain the lowest loss at the reference condition.

Thus, the plots of figures 146, 148, and 149 show that, when diffusion factor and wake momentum-thickness ratio (or total-pressure-loss parameter) are used as the basic blade-loading and loss parameters, respectively, a generalized correlation of two-dimensional-cascade loss data is obtained. Although several assumptions and restrictions are involved in the use and calculation of these parameters, the basic diffusion approach constitutes a useful tool in cascade loss analysis. In particular, the diffusion analysis should be investigated over the complete range of incidence angle in an effort to determine generalized off-design loss information.

Effect of Reynolds number and turbulence.—The effect of blade-chord Reynolds number and turbulence level on the measured losses of cascade sections is discussed in the section on Data Selection, in chapter V, and in references 39, 167 (pt. I), and 183. In all cases, the data reveal an increasing trend of loss coefficient with decreasing Reynolds number and turbulence. Examples of the variation of the total-pressure-loss coefficient with incidence angle for conventional compressor blade sections at two different values of Reynolds number are illustrated in figure

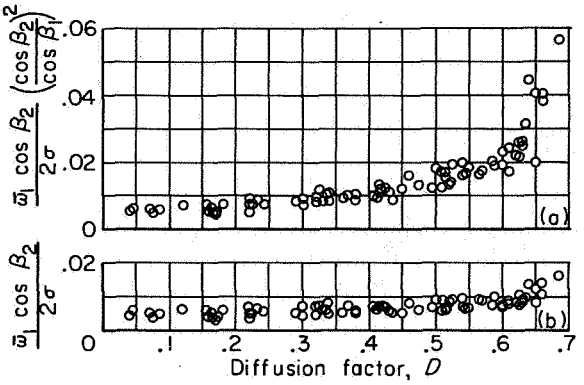

(a) Based on $\bar{\omega}_1 \left(\frac{\cos \beta_2}{\cos \beta_1}\right)^2$.

(b) Based on $\bar{\omega}_1$.

FIGURE 149.—Variation of loss parameter with diffusion factor at reference minimum-loss incidence angle computed from low-speed-cascade data of NACA 65-(A_{10})10 cascade blades (ref. 39).

150. Loss variations with Reynolds number over a range of incidence angles for a given blade shape are shown in figure 151. A composite plot of the variation of total-pressure-loss coefficient

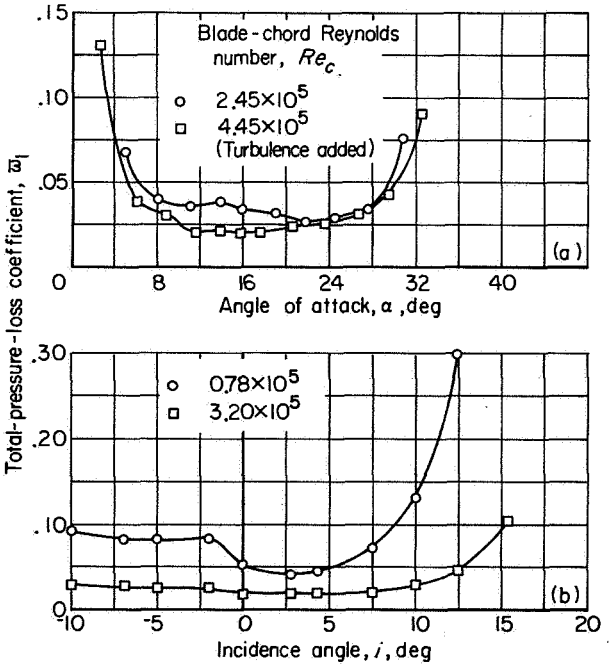

(a) 65-Series blade 65-(12)10. Solidity, 1.5; inlet-air angle, 45° (ref. 39).

(b) Circular-arc blade 10C4/25C50. Solidity, 1.333; blade-chord angle, 42.5° (ref. 40).

FIGURE 150.—Effect of Reynolds number on variation of loss with incidence angle.

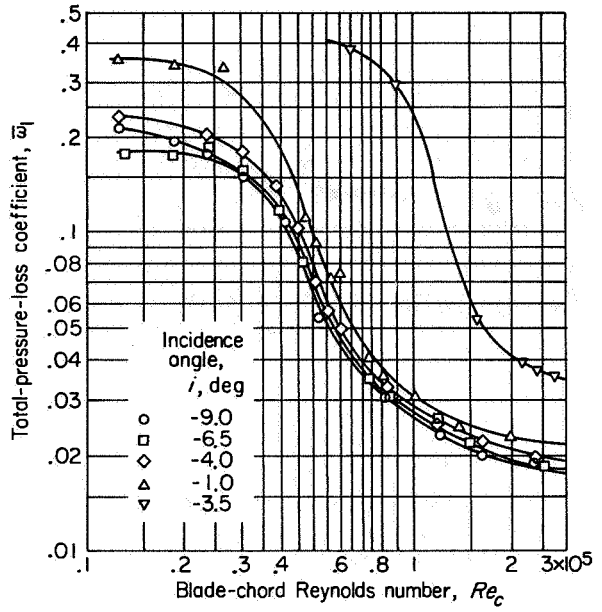

FIGURE 151.—Variation of total-pressure-loss coefficient with blade-chord Reynolds number for parabolic-arc blade 10C4/40 P40. Inlet-air angle, 28° to 40°; solidity, 1.333 (ref. 183).

at minimum loss with blade-chord Reynolds number for a large number of blade shapes is shown in figure 152. Identification data for the various blades included in the figure are given in the references. For the blades whose loss data are reported in terms of drag coefficient, conversion to total-pressure-loss coefficient was accomplished according to the cascade relations presented in reference 9. The effect of change in tunnel turbulence level through the introduction of screens is indicated for some of the blades.

It is apparent from the curves in figure 152 that it is currently impossible to establish any one value of limiting Reynolds number that will hold for all blade shapes. (The term limiting Reynolds number refers to the value of Reynolds number at which a large rise in loss is obtained.) On the basis of the available cascade data presented in figure 152, however, it appears that serious trouble in the minimum-loss region may be encountered at Reynolds numbers below about 2.5×10^5. Carter in reference 190 places the limiting blade-chord Reynolds number based on outlet velocity at 1.5 to 2.0×10^5. Considering that outlet Reynolds number is less than inlet Reynolds number for decelerating cascades, this quoted value is in effective agreement with the value of limiting Reynolds number deduced herein.

The desirability of conducting cascade investigations in the essentially flat range of the curve of loss coefficient against Reynolds number in order to enhance the correlation of data from various tunnels, as well as from the various configurations of a given tunnel, is indicated. Cascade operation in the flat range of Reynolds number may also yield a more significant comparison between observed and theoretically computed loss. Reynolds number and turbulence level should always be defined in cascade investigations. Furthermore, the development of some effective Reynolds number (ch. V) that attempts to combine the effects of both blade-chord Reynolds number and turbulence should be considered for use as the independent variable.

Effect of inlet Mach number.—In the previous correlations, attention was centered on the various factors affecting the loss of cascade blades for

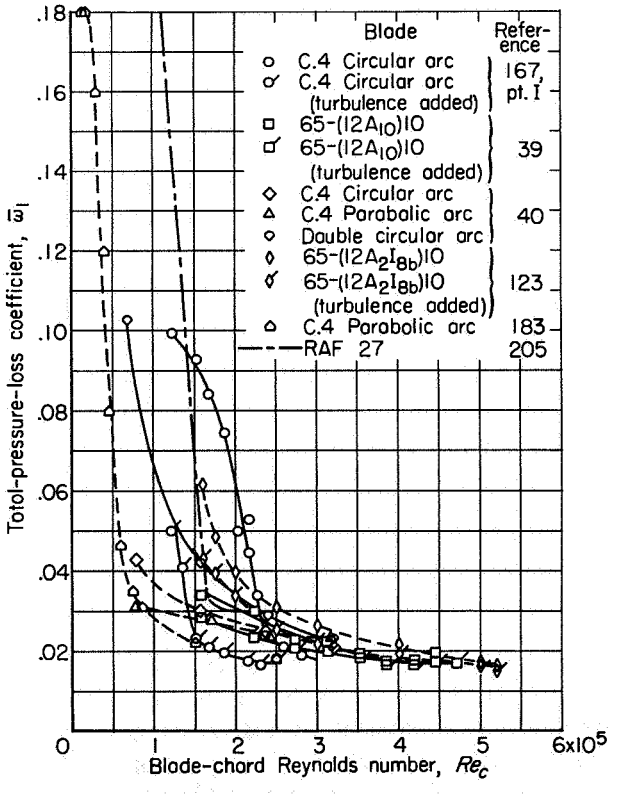

FIGURE 152.—Composite plot of loss coefficient against blade-chord Reynolds number in region of minimum loss for two-dimensional-cascade blade sections at low speed.

essentially incompressible or low Mach number flow. Tests of cascade sections at higher Mach number levels have been relatively few, primarily because of the large power requirements and operational difficulties of high-velocity tunnels. As a consequence, it has not been possible to establish any empirical correlations that will permit the estimation of Mach number effects for conventional blade sections. The limited available data indicate, however, that a marked rise in loss is eventually obtained as Mach number is increased.

A typical example of the variation of total-pressure-loss coefficient with inlet Mach number for a conventional cascade section at fixed incidence angle in the region of minimum loss is presented in figure 153(a). The inlet Mach number at which the sharp rise in loss occurs is referred to as the limiting Mach number. The variation of the wake profile downstream of the blade as Mach number is increased is shown in figure 153(b) to illustrate the general deterioration of the suction-surface flow. The flow deterioration is the result of a separation of the suction-surface boundary layer induced by shock-wave and boundary-layer interactions.

In view of the complex nature of the shock-wave development and its interaction effects, the estimation of the variation of minimum total-pressure loss with inlet Mach number for a given blade is currently impossible. At the moment, this pursuit must be primarily an experimental one. Schlieren photographs showing the formation of shocks in a cascade are presented in references 41, 205, and 206, and detailed discussions of shock formations and high-speed performance of two-dimensional-cascade sections are treated in references 41, 205, and 207 to 209. Cascade experience (refs. 40 and 205) and theory (refs. 41, 88, and 209) indicate that a location of the point of maximum thickness at about the 50-percent-chord position and a thinning of the blade leading and trailing edges are favorable for good high Mach number performance. The avoidance of a throat area within the blade passage is also indicated in order to minimize the effects of flow choking. Discussions of the choking problem are presented in references 203 and 208, and blade throat areas are given for several blade shapes in references 123 and 210 to 212. The effects of

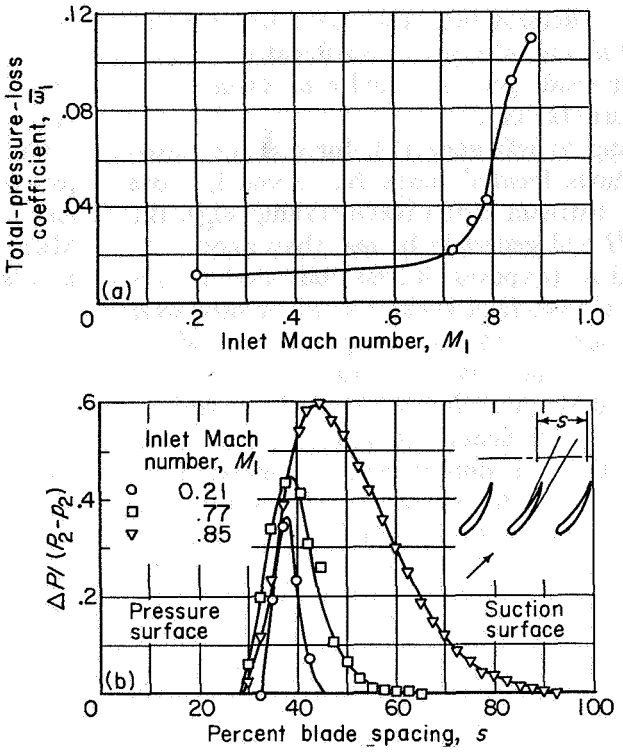

(a) Total-pressure-loss coefficient.
(b) Blade wake.

FIGURE 153.—Variation of cascade blade loss with inlet Mach number for NACA 65–($12A_{10}$)10 blade in region of minimum loss (ref. 122).

camber distribution on high Mach number performance are discussed extensively in the literature (refs. 123, 200, and 201). Results indicate that, for the range of blade shapes and Mach numbers normally covered, camber distribution does not have a large effect on maximum Mach number performance as obtained in the two-dimensional cascade.

SUMMARY

From the foregoing correlations and considerations, the low-speed loss in total pressure of conventional two-dimensional-cascade sections can readily be estimated. If blade surface velocity distributions are available, the suction-surface local diffusion factor D_{loc} is determined according to equation (265) and a value of θ^*/c is then selected from figure 146. In the absence of blade surface velocity data, the diffusion factor D is computed from over-all conditions by means of equation (54) and θ^*/c is selected from figure 148.

With θ^*/c determined, the total-pressure-loss coefficient is computed according to equation (264) from the cascade geometry and a pertinent value of wake form factor H.

According to reference 156, for cascade measuring stations located more than about ½ chord length downstream of the blade trailing edge, the value of H will generally be less than about 1.2. For practical purposes, it was indicated that a constant value of H of about 1.1 can be used over a wide range of cascade configurations and incidence angles for measuring stations located between ½ and 1½ chord lengths behind the trailing edge. Loss coefficients based on inlet dynamic head can then be determined, if desired, from equation (266). The estimation of losses based on the diffusion factor D can, for example, produce a value of solidity that results in the least computed loss coefficient for a given velocity diagram.

The accuracy of the results obtained from the prediction procedure outlined is subject to the limitations and approximations involved in the diffusion analysis and wake momentum-thickness correlations. Strictly speaking, the procedure gives essentially a band of probable loss values at the cascade measuring station about ½ to 1½ chord lengths downstream of the blade trailing edge for the reference-incidence-angle setting and Reynolds numbers of about 2.5×10^5 and greater at low speed (up to about 0.3 inlet Mach number). It should also be noted at this point that the loss values obtained in this manner represent the low-speed profile loss of the cascade section. Such loss values are not generally representative of the losses of the section in a compressor blade row or in a high-speed cascade.

A corresponding loss-estimation technique for high Mach number flow is currently unavailable because of the unknown magnitude of the compressibility effect on the wake momentum-thickness ratio of a given cascade geometry. Furthermore, both the wake form factor H and the relation between θ^*/c and $\bar{\omega}$ (given for incompressible flow by eq. (264)) vary with Mach number. For example, if the velocity variation in each leg of the wake is assumed to vary according to the power relation

$$\frac{V}{V_0}=\left(\frac{y}{\delta}\right)^d \qquad (267)$$

where δ is the thickness of the wake and d is some constant, then variations of H and θ^* and of the relation between θ^*/c and $\bar{\omega}$ with outlet free-stream Mach number can be established analytically to illustrate the nature of the compressibility effects.

Curves of the variation of the ratios of compressible to incompressible form factor H/H_{inc} and momentum thickness θ^*/θ^*_{inc} with outlet Mach number for various d values obtained from numerical integration of the wake parameters involved are shown in figures 154 and 155. Recently, the increasing trend of H with M_2 was substantiated experimentally at the NACA Lewis laboratory in an investigation of the wake characteristic of a turbine nozzle (unpublished data). Curves of the ratio of the integrated value of $\bar{\omega}$ obtained from a given value of θ^*/c in a compressible flow to the value of $\bar{\omega}$ computed from the same value of θ^*/c according to the incompressible relation of equation (264) are shown in figure 156. It should be noted that for compressible flow the denominator in the loss-coefficient definition (eq. (263)) is now given by $P-p$.

In summary, therefore, an accurate prediction of the variation of reference total-pressure loss with inlet Mach number for a given cascade

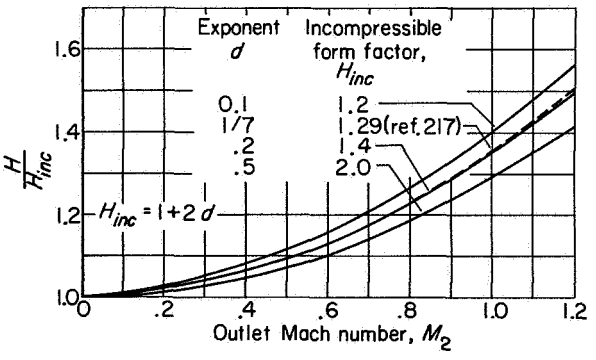

FIGURE 154.—Ratio of compressible to incompressible form factor for constant value of exponent in power velocity distribution.

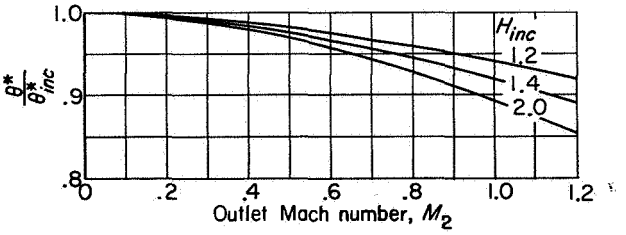

FIGURE 155.—Ratio of compressible to incompressible momentum thickness for constant full thickness and exponent for power velocity distribution.

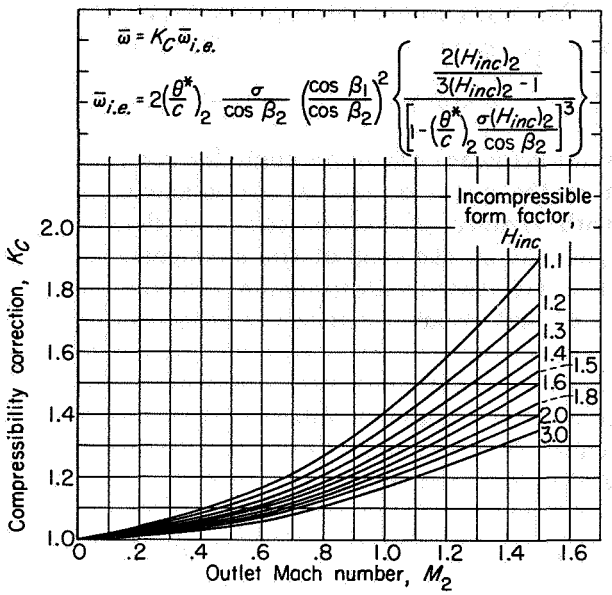

FIGURE 156.—Correction factor K_C for calculation of total-pressure-loss coefficient for compressible flow on basis of incompressible equation (264) as determined from model wake form with power velocity profile.

blade is currently impossible. At the moment, this pursuit is primarily an experimental one. Families of curves of wake momentum thickness and form factor against diffusion factor are required (with appropriate definitions for subsonic or supersonic flow) as in figure 146 or 148 for a wide range of inlet Mach number. Analytically, a simple compressible relation is needed between θ^*/c and $\bar{\omega}$ as a function of Mach number.

DEVIATION-ANGLE ANALYSIS

PRELIMINARY ANALYSIS

The correct determination of the outlet flow direction of a cascade blade element presents a problem, because the air is not discharged at the angle of the blade mean line at the trailing edge, but at some angle δ° to it (fig. 124). Since the flow deviation is an expression of the guidance capacity of the passage formed by adjacent blades, it is expected that the cascade geometry (camber, thickness, solidity, and chord angle) will be the principal influencing factor involved.

From cascade potential-flow theory (ref. 80, e.g.), it is found that the deviation angle increases with blade camber and chord angle and decreases with solidity. Weinig in reference 80 shows that the deviation angle varies linearly with camber for a given value of solidity and chord angle for infinitesimally thin blades at zero incidence. Furthermore, with deviation angle equal to zero at zero camber angle in this theory, it is possible to express the deviation angle as a ratio of the camber angle. Values of the ratio of deviation angle to camber angle for an infinitely thin circular-arc blade of small camber deduced from the theory of reference 80 are presented in figure 157 for a range of solidities and chord angles. The values in figure 157 are for the incidence angle for "impact-free entry" previously mentioned, which corresponds essentially to the condition of minimum loss.

The results of figure 157 show that, for a blade of zero thickness, the minimum-loss deviation angle is zero at zero camber angle. However, analysis indicates that this is not the case for blades of conventional thicknesses. A recent theoretical demonstration of the existence of a positive value of zero-camber deviation angle according to potential-flow calculations is given by Schlichting in reference 193. The computed variation of zero-camber deviation angle for a conventional 10-percent-thick profile at zero incidence angle as obtained in the reference is shown in figure 158.

It will be recalled from the discussion of the zero-camber minimum-loss incidence angle that, for the conventional staggered cascade ($0° < \gamma° < 90°$) with finite blade thickness set at zero incidence angle, a greater magnitude of velocity

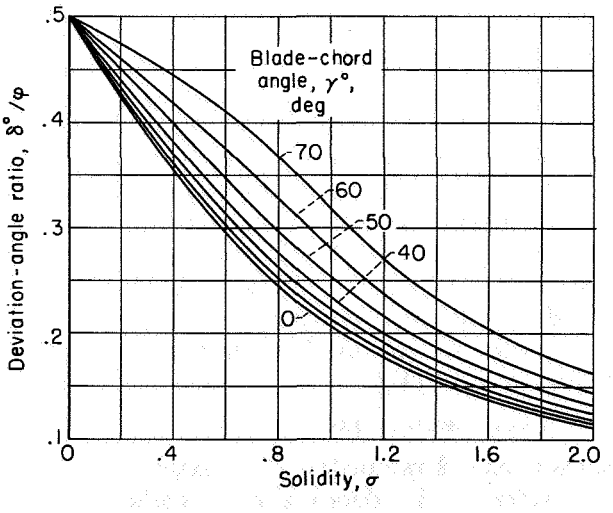

FIGURE 157.—Theoretical variation of deviation-angle ratio for infinitely thin circular-arc sections at "impact-free-entry" incidence angle according to potential theory of reference 80.

691-564 O-65-15

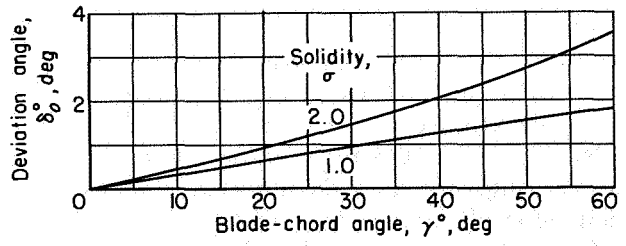

FIGURE 158.—Theoretical variation of deviation angle for conventional uncambered 10-percent-thick blade section at zero incidence angle as presented in reference 193.

occurs on the blade lower (concave) surface than on the upper (convex) surface (fig. 134). Such velocity distributions result in a negative blade circulation and consequently (as indicated by the solid vectors in fig. 159) in a positive deviation angle. Furthermore, since the deviation angle increases slightly with increasing incidence angle ($d\delta^\circ/di$ is positive in potential cascade flow), positive values of deviation angle will likewise be obtained at the condition of minimum-loss incidence angle (as illustrated by the dashed vectors in fig. 159). Since the zero-camber deviation angle arises from essentially a thickness blockage effect, the characteristics of the variation of minimum-loss zero-camber deviation angle with cascade geometry would be expected roughly to parallel the variation of the minimum-loss zero-camber incidence angle in figure 137. The low-speed reference-deviation-angle correlations may, therefore, involve intercept values as in the case of the reference-incidence-angle correlations.

In addition to the cascade-geometry factors mentioned, the low-speed deviation angles can also be affected by Reynolds number, turbulence, and Mach number. The thickened surface boundary layers resulting from low levels of Reynolds number and turbulence tend to increase the deviation angle. Variations in inlet Mach number can affect the deviation angle of a fixed two-dimensional-cascade geometry because of the associated changes in blade circulation, boundary-layer development, and outlet to inlet axial velocity ratio (compressibility effect on ρV_z).

DATA CORRELATIONS

Form of correlation.—Examination of deviation-angle data at reference incidence angle reveals that the observed data can be satisfactorily represented by a linear variation of reference deviation angle with camber angle for fixed solidity and air inlet angle. The variation of reference deviation angle can then be expressed in equation form as

$$\delta^\circ = \delta_o^\circ + m\varphi \tag{268}$$

where δ_o° is the reference deviation angle for zero camber, m is the slope of the deviation-angle variation with camber $(\delta^\circ - \delta_o^\circ)/\varphi$, and φ is the camber angle. As in the case of the analogous terms in the reference-incidence-angle relation (eq. (261)), δ_o° and m are functions of inlet-air angle and solidity.

The influence of solidity on the magnitude of the slope term m could also be directly included as a functional relation in equation (268), so that equation (268) could be expressed as

$$\frac{\delta^\circ - \delta_o^\circ}{\varphi} = \frac{m_{\sigma=1}}{\sigma^b} \tag{269}$$

where $m_{\sigma=1}$ represents the value of m (i.e., $(\delta^\circ - \delta_o^\circ)/\varphi$) at a solidity of 1, b is the solidity exponent (variable with air inlet angle), and the other terms are as before. It will be noted that equation (269) is similar in form to the frequently used deviation-angle rule for circular-arc blades originally established by Constant in reference 186 and later modified by Carter in reference 88. Carter's rule for the condition of nominal incidence angle is given by

$$\frac{\delta^\circ}{\varphi} = \frac{m_c}{\sqrt{\sigma}} \tag{270}$$

in which m_c is a function of blade-chord angle. Values of m_c determined from theoretical considerations for circular-arc and parabolic-arc mean lines (ref. 88) are shown in figure 160. In the

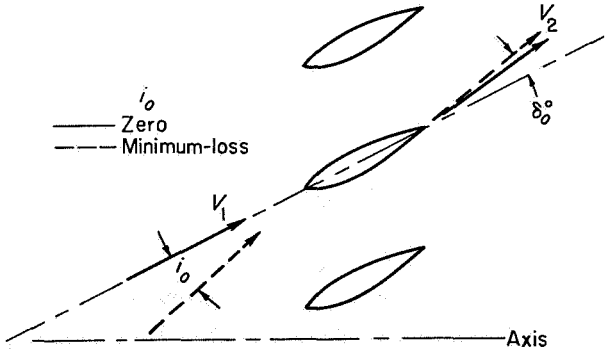

FIGURE 159.—Outlet flow direction for cascade of staggered uncambered blades.

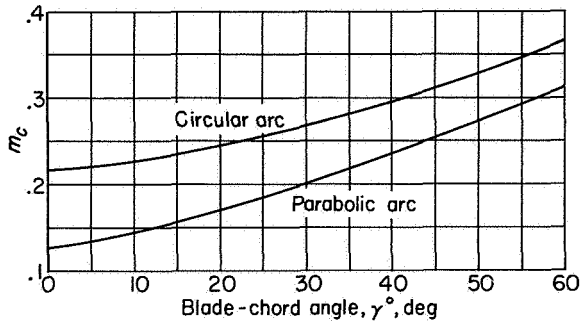

FIGURE 160.—Variation of factor m_c in Carter's deviation-angle rule (ref. 88).

ensuing correlations, both forms of the deviation-angle relation (eqs. (268) and (269)) are used, since each has a particular advantage. Equation (268), with m plotted as a function of β_1 and σ, is easier to use for prediction, especially if the calculation of a required camber angle is involved. Equation (269) may be better for extrapolation and for comparison with Carter's rule.

As in the case for the zero-camber reference minimum-loss incidence angle, the zero-camber deviation angle can be represented as a function of blade thickness as

$$\delta_o^\circ = (K_\delta)_{sh}(K_\delta)_t(\delta_o^\circ)_{10} \qquad (271)$$

where $(\delta_o^\circ)_{10}$ represents the basic variation for the 10-percent-thick 65-series thickness distribution, $(K_\delta)_{sh}$ represents any correction necessary for a blade shape with a thickness distribution different from that of the 65-series blade, and $(K_\delta)_t$ represents any correction necessary for maximum blade thicknesses other than 10 percent. (For a 10-percent-thick 65-series blade, $(K_\delta)_t$ and $(K_\delta)_{sh}$ are equal to 1.) The problem, therefore, is reduced to finding the values of m, b, and δ_o° (through eq. (271)) as functions of the pertinent variables involved for the various blade shapes considered.

NACA 65-(A_{10})-series blades.—From an examination of the plots of equivalent deviation angle against equivalent camber angle at reference minimum-loss incidence angle obtained from the cascade data, values of zero-camber deviation angle can be determined by extrapolation. The deduced plots of zero-camber deviation angle $(\delta_o^\circ)_{10}$ and slope term m as functions of solidity and air-inlet angle are presented in figures 161 and 162 for these blades. The subscript 10 indicates that the δ_o° values are for 10-percent maximum-thickness ratio. Values of the intercept term δ_o° and the slope term m were obtained by fitting a straight line to each data plot of reference equivalent deviation angle against equivalent camber angle for a fixed solidity and air inlet angle. The straight lines were selected so that both a satisfactory representation of the variation of the data points and a consistent variation for the resulting δ_o° and m values were obtained. The extrapolation of the values of m to $\beta_1=0$ was guided by the data for the 65-($12A_{10}$)10 blade at solidities of 1 and 1.5 reported in the cascade guide-vane investigation of reference 213 (for an aspect ratio of 1, as in ref. 39).

For the deviation-angle rule as given by equation (269), deduced values of $m_{\sigma=1}$ and exponent b as functions of inlet-air angle are presented in figures 163 and 164. The deduced rule values (eq. (268) or (269)) and the observed data points are compared in figure 165 to indicate the effectiveness of the deduced representations. The flagged symbols in the high-camber range in the figure represent blade configurations for which boundary-layer separation is indicated (D greater than about 0.62). In view of the higher loss levels for this condition, an increase in the magnitude of the deviation angle is to be expected compared with the values extrapolated from the smaller cambers for which a lower loss level existed.

C-Series circular-arc blades.—In view of the absence of systematic cascade data for the C-series circular-arc blade, an accurate determination of the rule constants cannot be made for this blade shape. However, a preliminary relation can be deduced on the basis of limited data. It appears that, for the uncambered C.4 section (ref. 192), if a value of $(K_\delta)_{sh}$ equal to 1.1 (as for the determination of i_0) is used, a satisfactory comparison between predicted and observed δ_o° values is obtained.

The characteristic number $m_{\sigma=1}$ in the deviation-angle design rule of equation (269) for a given blade mean line corresponds to the value of $(\delta_0-\delta_o^\circ)/\varphi$ at a solidity of unity. Cascade data for a C.4 circular-arc profile obtained from tunnels with good boundary-layer control are presented in references 167 (pt. I) and 199 for a solidity of 1.0 for $\beta_1=30°$, 42.5°, 45°, and 60°. Values of $(\delta_0-\delta_o^\circ)/\varphi$ were computed for these blades according to the δ_o° variations of figure 161. A value of $m_{\sigma=1}$ for $\beta_1=0°$ was obtained from the per-

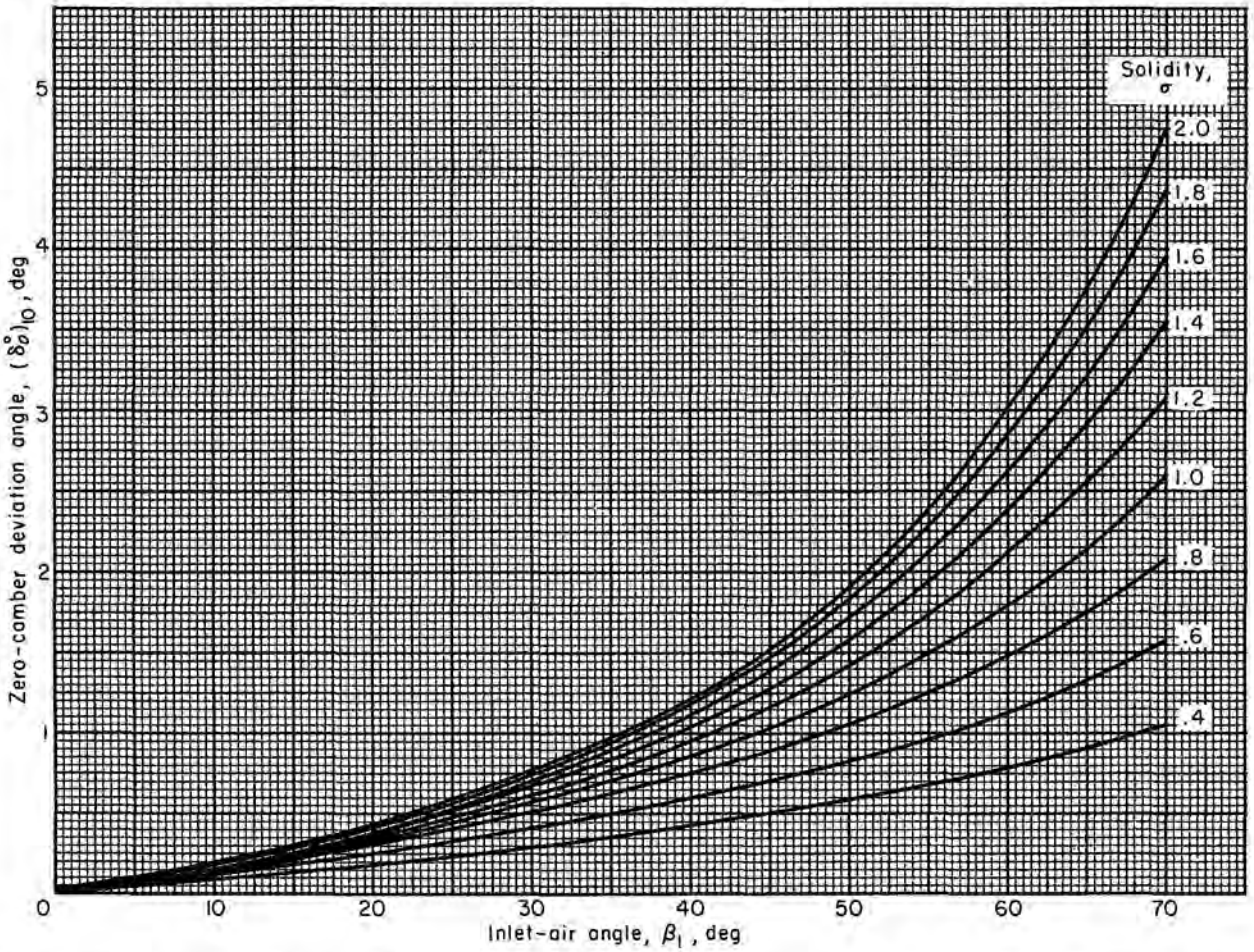

FIGURE 161.—Zero-camber deviation angle at reference minimum-loss incidence angle deduced from low-speed-cascade data for 10-percent-thick NACA 65-(A_{10})-series blades (ref. 39).

formance data of a free-stream circular-arc inlet guide vane presented in reference 214. These values of m are plotted in figure 166 against inlet-air angle, and the proposed variation of $m_{\sigma=1}$ for the circular-arc mean line is shown by the solid line.

In the absence of data covering a range of solidities, it is assumed that the solidity exponent b in the deviation-angle rule of equation (269) is independent of the profile shape and will therefore also be applicable for the circular-arc mean line. This assumption agrees with limited experimental data. The variation of ratio of deviation angle to camber angle obtained from constant-thickness circular-arc guide-vane sections of reference 215 ($\delta_0^\circ=0^\circ$ for guide vanes) over a wide range of solidities is shown in figure 167. A computed variation based on values of b and $m_{\sigma=1}$ obtained from figures 164 and 166, respectively, is shown in the figure by the solid line. A satisfactory agreement with these circular-arc data is thus demonstrated for the value of b obtained from the 65-series data. On the basis of these results, deduced curves of m against $\beta 1$ for a range of solidities (for use in conjunction with eq. (268)) were computed for the C-series circular-arc blade as indicated in figure 168.

Double-circular-arc blades.—Although limited data are available for the double-circular-arc blade (refs. 40 and 197), it was felt that these data could not be reliably utilized in the construction of a deviation-angle rule because of the questionable two-dimensionality of the respective test tunnels. However, since the C-series and the double-

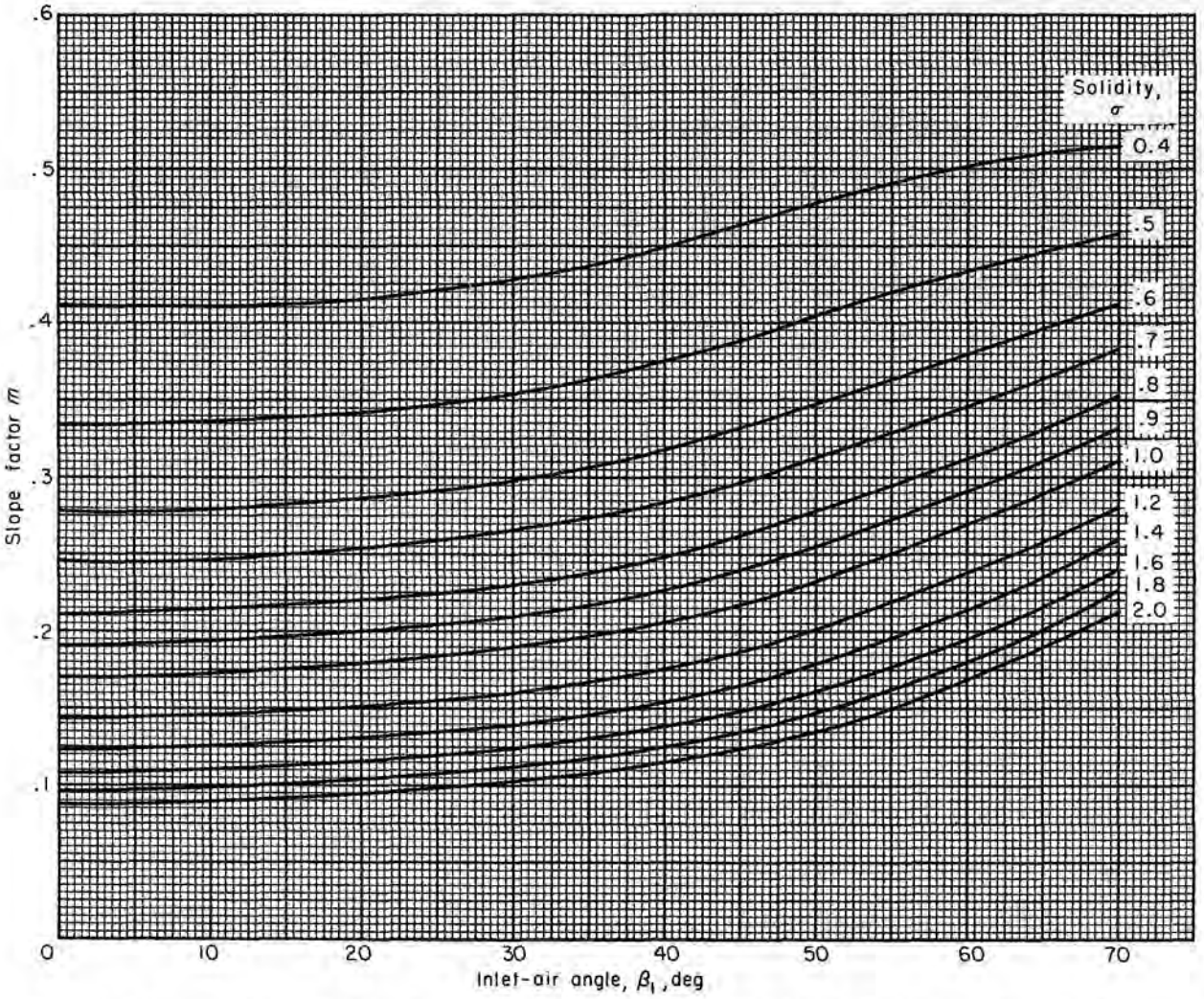

FIGURE 162.—Deduced variation of slope factor m in deviation-angle rule for NACA 65-(A_{10})-series blades as equivalent circular arc.

circular-arc blades differ only in thickness distribution, it is reasonable to expect that, as in the case of the reference-incidence-angle correlations, only the zero-camber deviation angles will be materially affected. Therefore, the slope-term value m deduced for the C-series circular-arc blade (fig. 168) might also be used for the double-circular-arc blade, but the δ_0° values may be different. An arbitrarily selected value of 0.7 for $(K_s)_{sh}$ in equation (271) (as for the reference-incidence-angle determination) is suggested for the double-circular-arc blade.

Comparison of rules.—In view of the widespread use of Carter's rule (eq. (270) with fig. 160) for predicting the deviation angle of circular-arc-mean-line blades, some results obtained from the use of Carter's rule were compared with the deduced rule of equation (269) with figures 161, 164, and 166. The principal difference between the two rules occurs in the blade orientation parameter used for the m variation and in the δ_0° and b variations. The value of the solidity exponent of ½ in equation (270) was originally obtained from limited data. Carter, in a later work (ref. 190), proposes a variable solidity exponent and indicates values close to 1 for accelerating cascades and close to ½ for decelerating cascades. The variation of b obtained from the NACA 65-(A_{10})-series blades

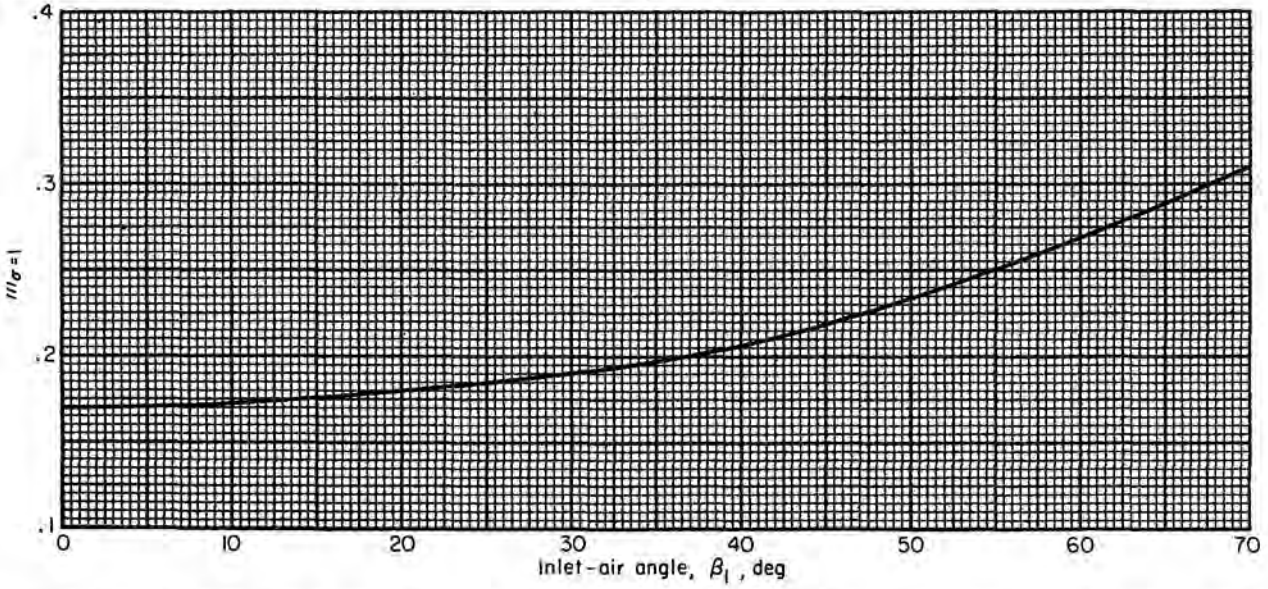

FIGURE 163.—Value of $m_{\sigma=1}$ in deviation-angle rule for 65–(A_{10})-series blades as equivalent circular arc (deduced from data of ref. 39).

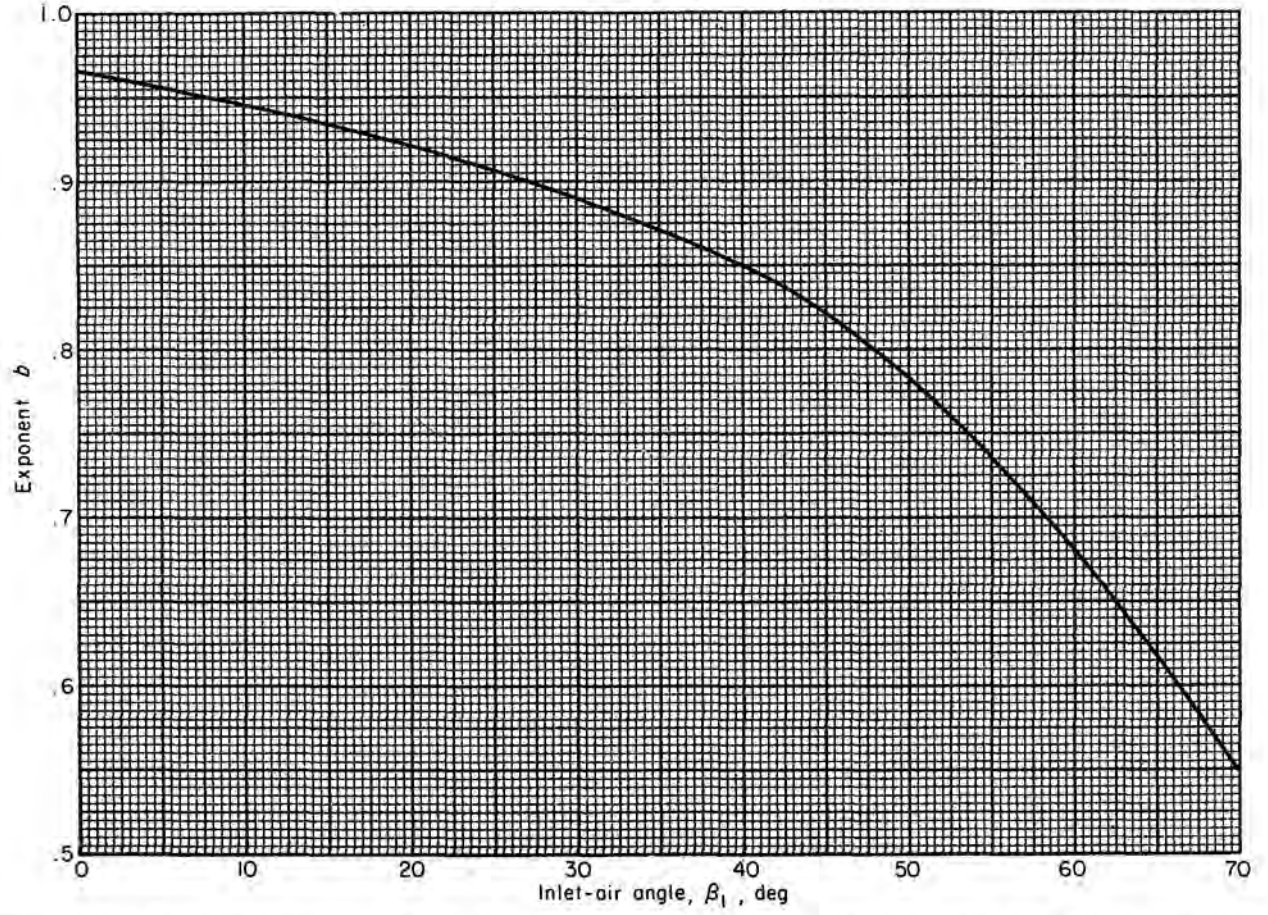

FIGURE 164.—Value of solidity exponent b in deviation-angle rule (eq. (269)) (deduced from data for 65–(A_{10})-series blades in ref. 39).

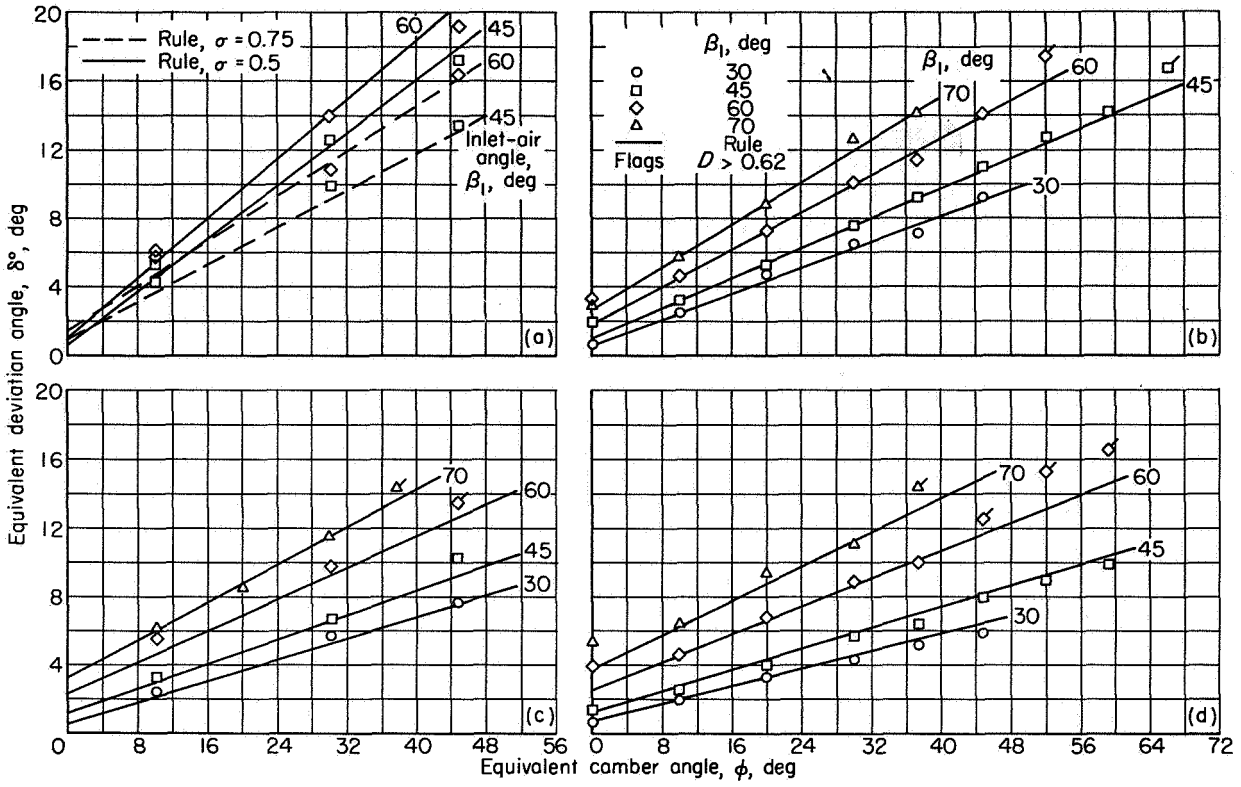

(a) Solidity, 0.5 and 0.75.
(b) Solidity, 1.0.
(c) Solidity, 1.25.
(d) Solidity, 1.5.

FIGURE 165.—Comparison between data values and deduced rule values of reference minimum-loss deviation angle for NACA 65-(A_{10})10-series blades as equivalent circular arc (data from ref. 39).

as equivalent circular arcs in figure 164 essentially confirms this trend. Actually, the deviation-angle rule in the form of equation (269) constitutes a modification of Carter's rule.

In addition to the basic differences between the rules in the magnitudes of the m, b, and δ_o° values, it is noted that Carter's rule was originally developed for the condition of nominal incidence angle, whereas the modified rule pertains to the reference minimum-loss incidence angle. However, since Carter's rule has frequently been used over a wide range of reference angle in its application, both rules were evaluated, for simplicity, for the reference minimum-loss incidence angle.

An illustrative comparison of predicted reference deviation angle as obtained from Carter's rule and the modified rule for a 10-percent-thick, thick-nosed circular-arc blade is shown by the calculated results in figure 169 for ranges of camber angle, solidity, and inlet-air angle. Deviation angles in figure 169 were restricted to cascade configurations producing values of diffusion factor less than 0.6. Blade-chord angle for Carter's rule was computed from the equation

$$\gamma^\circ = \beta_1 - i - \frac{\varphi}{2} \qquad (272)$$

Reference incidence angle was determined from equations (261) and (262) and figures 137 and 138.

The plots of figure 169 show that, in practically all cases, the deviation angles given by the modified rule are somewhat greater in magnitude than those predicted by Carter's rule for the 10-percent-thick blade. This is particularly true for the high inlet-air angles. Thus, greater camber angles are required for a given turning angle according to the modified rule. Differences are even less for the double-circular, arc blade, as indicated in figure 170, since the δ_o° values are smaller for these blades. However, it should be kept in mind that the magnitude of the factors in the modified rule are proposed values based on limited data. Further research is required to establish the modified rule on a firmer foundation.

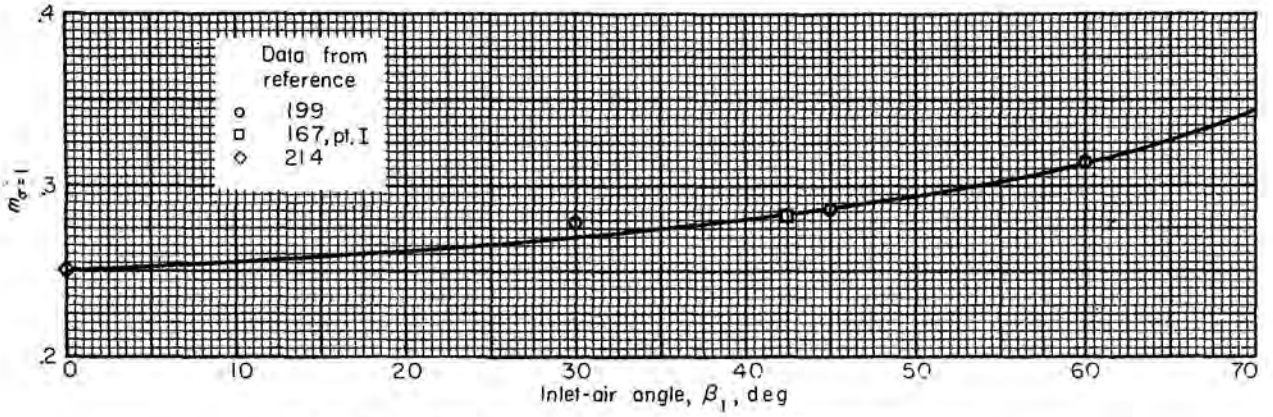

FIGURE 166.—Deduced values of $m_{\sigma=1}$ for circular-arc mean line.

Effect of blade maximum thickness.—Available data on the variation of reference deviation angle with blade maximum-thickness ratio obtained from cascade investigations of the 65-($12A_{10}$) blade of reference 202 are shown in figure 171. The solid symbols representing the values of deviation angle at zero thickness were determined by subtracting the values of $(\delta_o^\circ)_{10}$ obtained from figure 161 from the measured value of deviation angle at 10-percent maximum thickness obtained from the data in figure 171. A very reasonable variation with thickness ratio, as indicated by the faired curves, is thus obtained for all three configurations. The increasing slope of the deviation-angle variation with increasing thickness ratio is believed due to some extent to the accompanying increase in wake losses.

Preliminary values of a correction factor for maximum-thickness ratio $(K_\delta)_t$ deduced from the data of figure 171 are shown in figure 172. In the absence of further data, it is proposed that this correction curve is also applicable to other conventional blade shapes.

Effect of Reynolds number.—In view of the large rise in loss as blade-chord Reynolds number is reduced (fig. 152), a corresponding rise in deviation angle (or decrease in turning angle) is to be expected. Experimental confirmation of the marked effect of Reynolds number on blade deviation angle at fixed incidence angle is illustrated in figure 173 for several compressor blade shapes. The variation of deviation angle with Reynolds number over a range of incidence angle is demonstrated in figure 174. In all cases the variation of the deviation or turning angle closely parallels

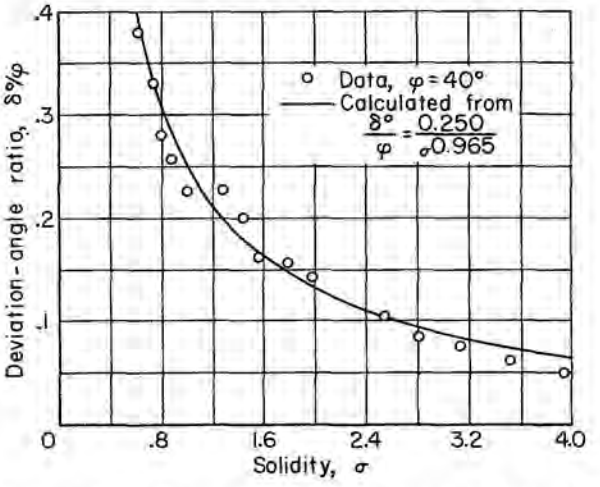

FIGURE 167.—Comparison of experimental deviation-angle ratio and rule values using solidity exponent given by figure 164. Data for circular-arc inlet guide vanes in annular cascade (ref. 215).

the variation of the loss. Therefore, factors involved in the deviation-angle variation are the same as those for the loss behavior. Correspondingly, no Reynolds number correction factors that will be applicable for all blade configurations have been established. The deduced deviation-angle rule developed herein is applicable at Reynolds numbers of about 2.5×10^5 and greater.

Effect of inlet Mach number.—Experimental variations of minimum-loss deviation angle with inlet Mach number are presented in figure 175 for two circular-arc blades. Further cascade data in terms of air-turning angle at fixed angle of attack are shown in figure 176 for two other compressor blade shapes. (Since the data in fig. 176 were

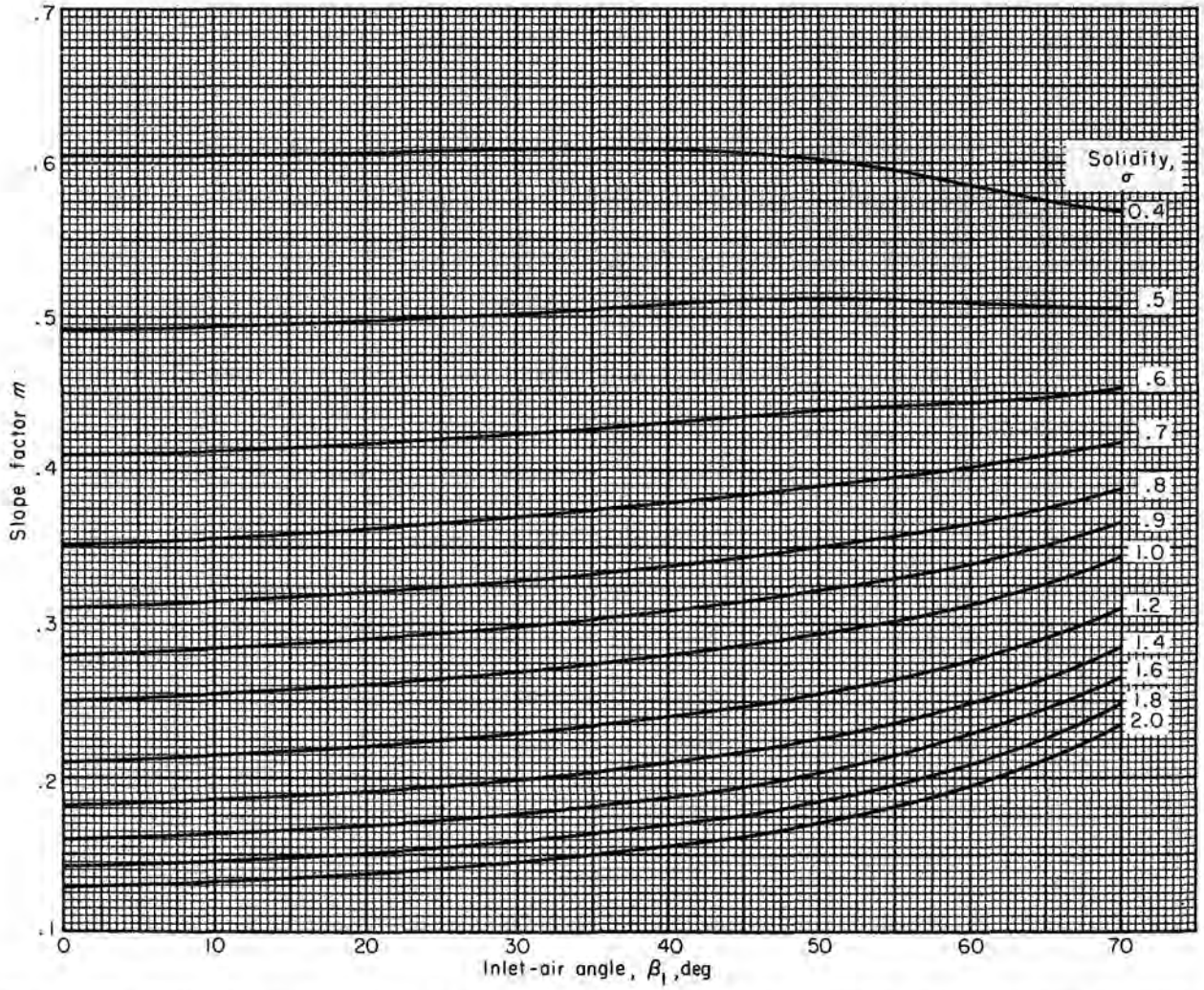

FIGURE 168.—Deduced variation of slope factor m in deviation-angle rule (eq. (268)) for circular-arc-mean-line blades.

obtained at constant angle of attack, the variation of turning angle is an inverse reflection of the variation of deviation angle.) The data of figures 175 and 176 indicate that deviation angle varies little with inlet Mach number up to the limiting value. As indicated in the Preliminary Analysis section, the resultant Mach number effect for a given blade configuration will depend on the relative magnitude of the various factors involved. Apparently, the net effect is small up to the limiting value of inlet Mach number. Large increases in deviation angle can be expected, however, when the loss rises rapidly at the limiting Mach number because of the adverse effects of the shock formation. (The rise in deviation angle in the data is always associated with the sharp rise in loss.)

Variation with incidence angle.—Thus far, of necessity, the analysis has been conducted for flow conditions at only one reference position on the general curve of loss against incidence angle. Ultimately, of course, it is desired to predict flow variations over the entire range of incidence angle. The variation of deviation angle with incidence angle for a fixed geometry in the two-dimensional cascade is primarily a function of the change in the guidance capacity of the cascade arising from the change in orientation of the approaching flow (a potential-flow effect) and of the variation in the wake loss. Since no information

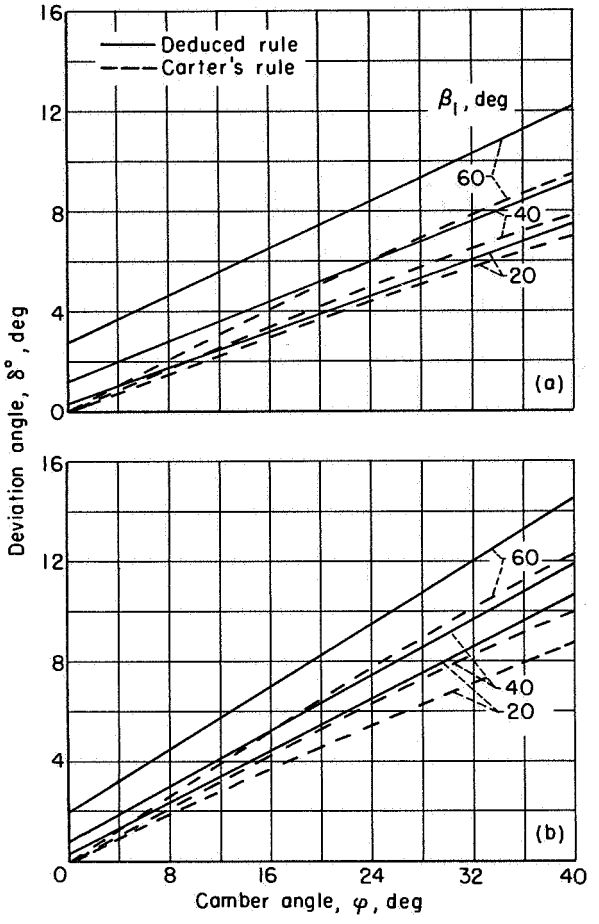

(a) Solidity, 1.5.
(b) Solidity, 1.0.

FIGURE 169.—Comparison of calculated reference deviation angles according to Carter's rule and deduced modified rule for 10-percent-thick, thick-nose circular-arc blades.

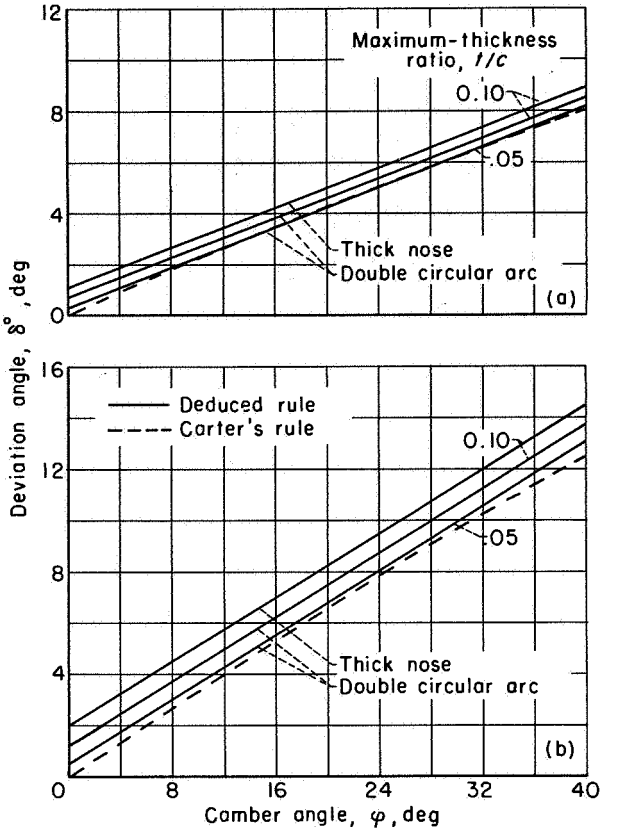

(a) Solidity, 1.5; inlet-air angle, 40°.
(b) Solidity, 1.0; inlet-air angle, 60°.

FIGURE 170.—Comparison of calculated reference deviation angles according to Carter's rule and deduced modified rule for circular-arc blades of different thickness.

is currently available on the effect of losses, attention is centered on deviation-angle variations in the region of low loss, where the trend of variation approaches that of the potential flow.

Examination of potential-flow theory (Weinig, ref. 80, e.g.) shows that a positive slope of deviation angle against incidence angle exists (i.e., deviation angle increases with incidence angle). Calculations based on the theory of Weinig reveal that the magnitude of the slope varies with solidity and blade-chord angle. The deviation-angle slope approaches zero for infinite solidity (deviation angle is essentially constant at high solidity) and increases as solidity is reduced. At

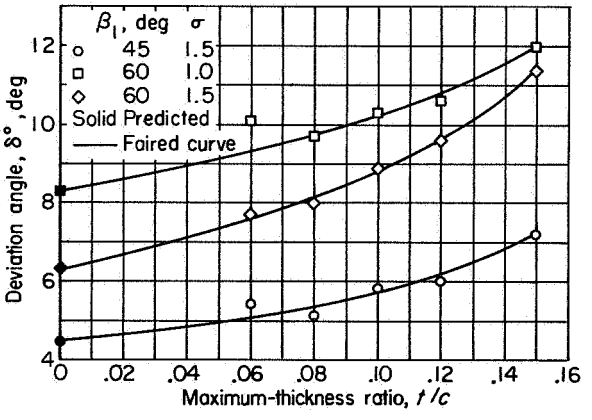

FIGURE 171.—Variation of deviation angle with blade maximum-thickness ratio for NACA 65-($12A_{10}$) blade in region of minimum loss (data from ref. 202).

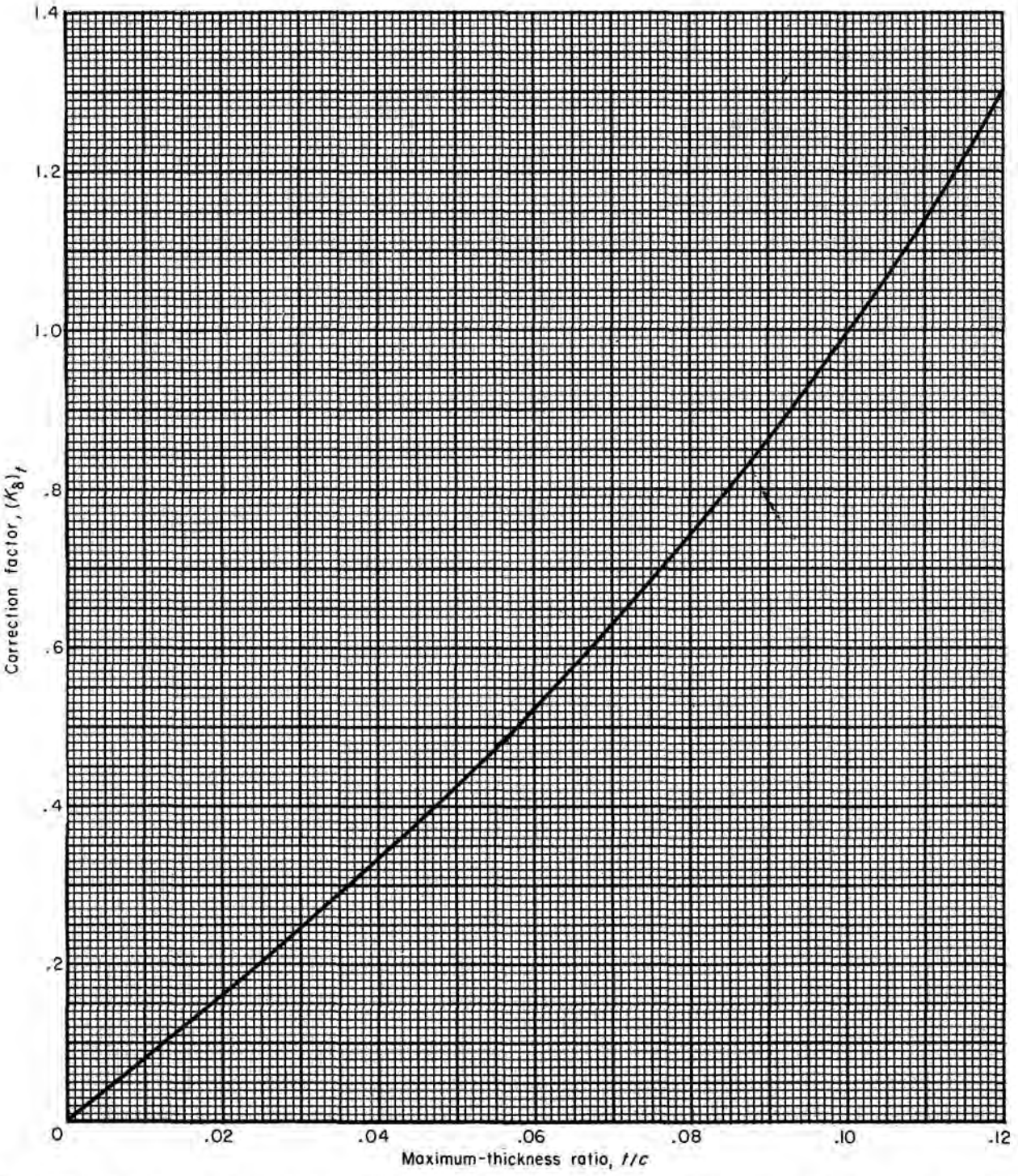

FIGURE 172.—Deduced maximum-thickness correction for zero-camber reference minimum-loss deviation angle (eq. (271)).

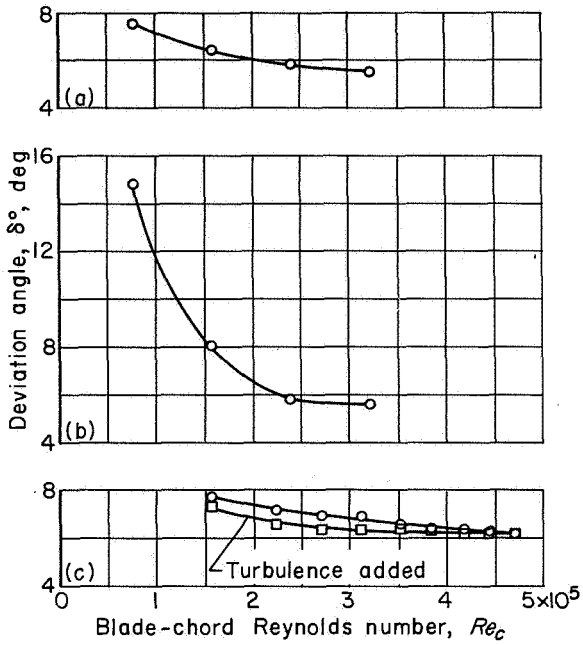

(a) 10C4/25C50 blade. Solidity, 1.33; blade-chord angle, 42.5° (ref. 40).
(b) 10.5 2A/25C50 blade. Solidity, 1.33; blade-chord angle, 42.5° (ref. 40).
(c) NACA 65–(12)10 blade. Solidity, 1.5; inlet-air angle, 45° (ref. 39).

FIGURE 173.—Illustrative variations of reference deviation angle with Reynolds number.

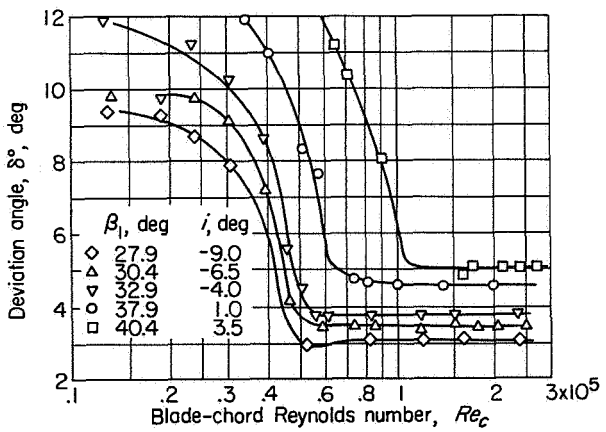

FIGURE 174.—Variation of deviation angle with Reynolds number for 10C4/40 P40 blade. Solidity, 1.33 (ref. 183).

constant solidity, the slope of deviation angle against incidence angle increases as the chord angle is increased. These trends indicate physically that the greater the initial guidance effect

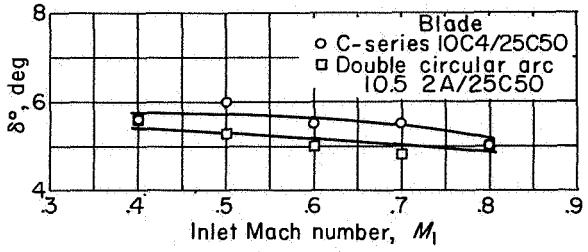

FIGURE 175.—Variation of reference deviation angle with inlet Mach number for circular-arc blades. Solidity, 1.333; blade-chord angle, 42.5° (ref. 40).

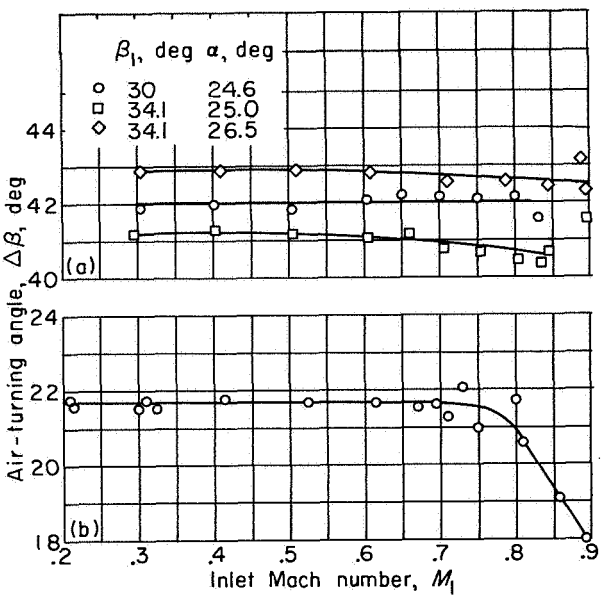

(a) T1($18A_8I_{4b}$)08 blade. Solidity, 1.5 (ref. 207).
(b) 65–($12A_{10}$)10 blade. Solidity, 1.0; inlet-air angle, 45°; angle of attack, 16.5° (ref. 122).

FIGURE 176.—Variation of air-turning angle with inlet Mach number in region of minimum loss.

(high solidity and low blade angle), the less sensitive the deviation angle is to changes in incidence angle.

For analysis purposes, since the region of low loss is generally small, the variation of deviation angle with incidence angle for a given cascade geometry in the region of minimum loss can be represented as

$$\delta^\circ = \delta^\circ_{ref} + (i - i_{ref}) \left(\frac{d\delta^\circ}{di}\right)_{ref} \qquad (273)$$

where $(d\delta^\circ/di)_{ref}$ represents the slope of the deviation-angle variation at the reference incidence

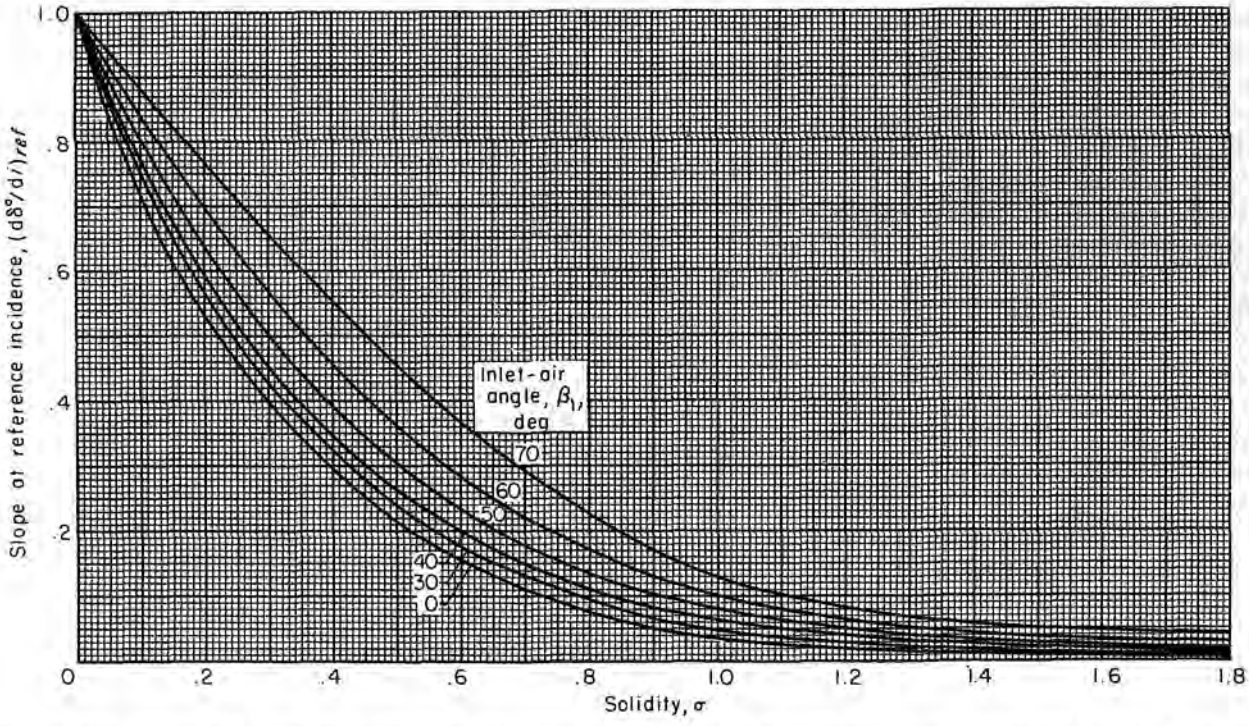

FIGURE 177.—Deviation-angle slope $d\delta°/di$ at reference incidence angle deduced from low-speed data for NACA 65-(A_{10})10 blades (ref. 39).

angle. An empirical determination of the magnitude of the slope of the variation of deviation angle with incidence angle was obtained from an analysis of the low-speed experimental data for the 65-(A_{10})10 blades of reference 39. From the plot of deviation angle against incidence angle for each configuration (as in fig. 127, e.g.), the slope of the curve at the minimum-loss incidence angle was evaluated graphically. The deduced variation of reference slope magnitude $d\delta°/di$ obtained from fairings of these values is presented in figure 177 as a function of solidity and inlet-air angle. Qualitative agreement with theory is strongly indicated by the data. Since the phenomenon is essentially a guidance or channel effect, it is anticipated that the slope values of figure 177 will also be applicable for other conventional blade shapes. Thus, it is possible to predict the deviation angle at incidence angles other than the reference location within the low-loss range of operation from the use of equation (273) and figure 177.

SUMMARY

The analysis of blade-section deviation angle shows that the variation of reference deviation angle with cascade geometry at low speed can be satisfactorily established in terms of an intercept value $\delta_0°$ and a slope value m as given by equation (268). The experimental data could also be expressed in terms of a rule similar in form to Carter's rule, as indicated by equation (269). Deduced values of $\delta_0°$ and m were obtained as a function of β_1 and σ from the data for the 10-percent-thick 65-(A_{10})-series blades of reference 39 as equivalent circular arc (figs. 161 and 162). Rules for predicting the reference deviation angle of the C-series and double-circular-arc blades were also deduced based on the correlations for the 65-(A_{10})-series blades and on limited data for the circular-arc blade (figs. 161 and 168).

The procedure involved in estimating the low-speed reference deviation angle of a blade section is as follows: From known values of β_1 and σ, $(\delta_0°)_{10}$ is selected from figure 161, and m is selected from figure 162 for the 65-(A_{10})-series blades or from figure 168 for circular-arc-mean-line blades. The value of $(K_\delta)_t$ for the blade maximum-thickness ratio is obtained from figure 172, and the approximate value of $(K_\delta)_{sh}$ is selected for the type of thickness distribution.

For the 65-series blades, $(K_\delta)_{sh}=1.0$, and it is proposed that $(K_\delta)_{sh}$ be taken as 1.1 for the C-series blades and as 0.7 for the double-circular-arc blade. The value of δ_o° is then computed from equation (271), and finally δ° is determined from the blade camber angle according to equation (268). As in the case of reference i_o values, the use of the proposed values of $(K_\delta)_{sh}$ is not critical for good accuracy in the final determination of δ°. Reference deviation angle can also be computed according to the rule in the form of equation (269) in conjunction with figures 163, 164, and 166.

The camber angle required to produce a given turning angle at the reference condition at low speed can readily be calculated by means of the preceding incidence-angle and deviation-angle correlations when the inlet-air angle and blade solidity are known. From equations (57), (261), and (268), the camber angle as a function of the turning, deviation, and incidence angle is

$$\varphi=\frac{\Delta\beta-(i_o-\delta_o^\circ)}{1-m+n} \tag{274}$$

or, in terms of the thickness corrections (eqs. (262) and (271)),

$$\varphi=\frac{\Delta\beta-[(K_t)_{sh}(K_t)_t(i_o)_{10}-(K_\delta)_{sh}(K_\delta)_t(\delta_o^\circ)_{10}]}{1-m+n} \tag{275}$$

For simplicity, since $(K_t)_{sh}=(K_\delta)_{sh}=K_{sh}$, equation (275) can be expressed in the form

$$\varphi=\frac{\Delta\beta-K_{sh}\overline{K}_t[(i_o)_{10}-(\delta_o^\circ)_{10}]}{1-m+n} \tag{276}$$

where $\overline{K}_t$ represents some correction factor for blade thickness, such that

$$\overline{K}_t[(i_o)_{10}-(\delta_o^\circ)_{10}]\cong(K_t)_t(i_o)_{10}-(K_\delta)_t(\delta_o^\circ)_{10} \tag{277}$$

Curves of the values of $(i_o)_{10}-(\delta_o^\circ)_{10}$ as a function of β_1 and σ are given in figure 178; curves of the values of $1-m+n$ as a function of β_1 and σ are given in figure 179(a) for the 65-(A_{10})-series mean line and in figure 179(b) for the circular-arc mean line; and values of $\overline{K}_t$ are plotted as a function of β_1 and t/c in figure 180. The use of the chart values of $\overline{K}_t$ in equation (276) gives results within about 0.1° of the exact values given by equation (275). Required camber angle can thus be determined readily by equation (276) in conjunction with figures 178 to 180.

CONCLUDING REMARKS

The foregoing analysis has presented a correlation of available two-dimensional experimental cascade data in terms of parameters significant in compressor design. The work essentially presents a summary of the state of experimental cascade research with regard to cascade performance at the reference incidence angle. Rules and procedures were evolved for the prediction of the magnitude of the reference total-pressure loss and the reference incidence and deviation angles in satisfactory agreement with existing cascade data. The rules may also be of help in reducing the necessary experimental effort in the accumulation of further cascade data.

However, the present analysis is incomplete. Many areas, such as the deviation-angle rule for the double-circular-arc blade, require further data to substantiate the correlations. Furthermore, additional information concerning the influence of high Mach number and off-design incidence angles of cascade performance is needed.

Finally, it is recognized that the performance of a given blade geometry in the compressor configuration will differ from the performance established in the two-dimensional cascade. These differences result from the effects of the various three-dimensional phenomena that occur in compressor blade rows. It is believed, however, that a firm foundation in two-dimensional-cascade flow constitutes an important step toward the complete understanding of the compressor flow. The extent to which cascade-flow performance can be successfully utilized in compressor design can only be established from further comparative evaluations. Such comparisons between observed compressor performance and predicted two-dimensional-cascade performance on the basis of the rules derived herein are presented in chapter VII.

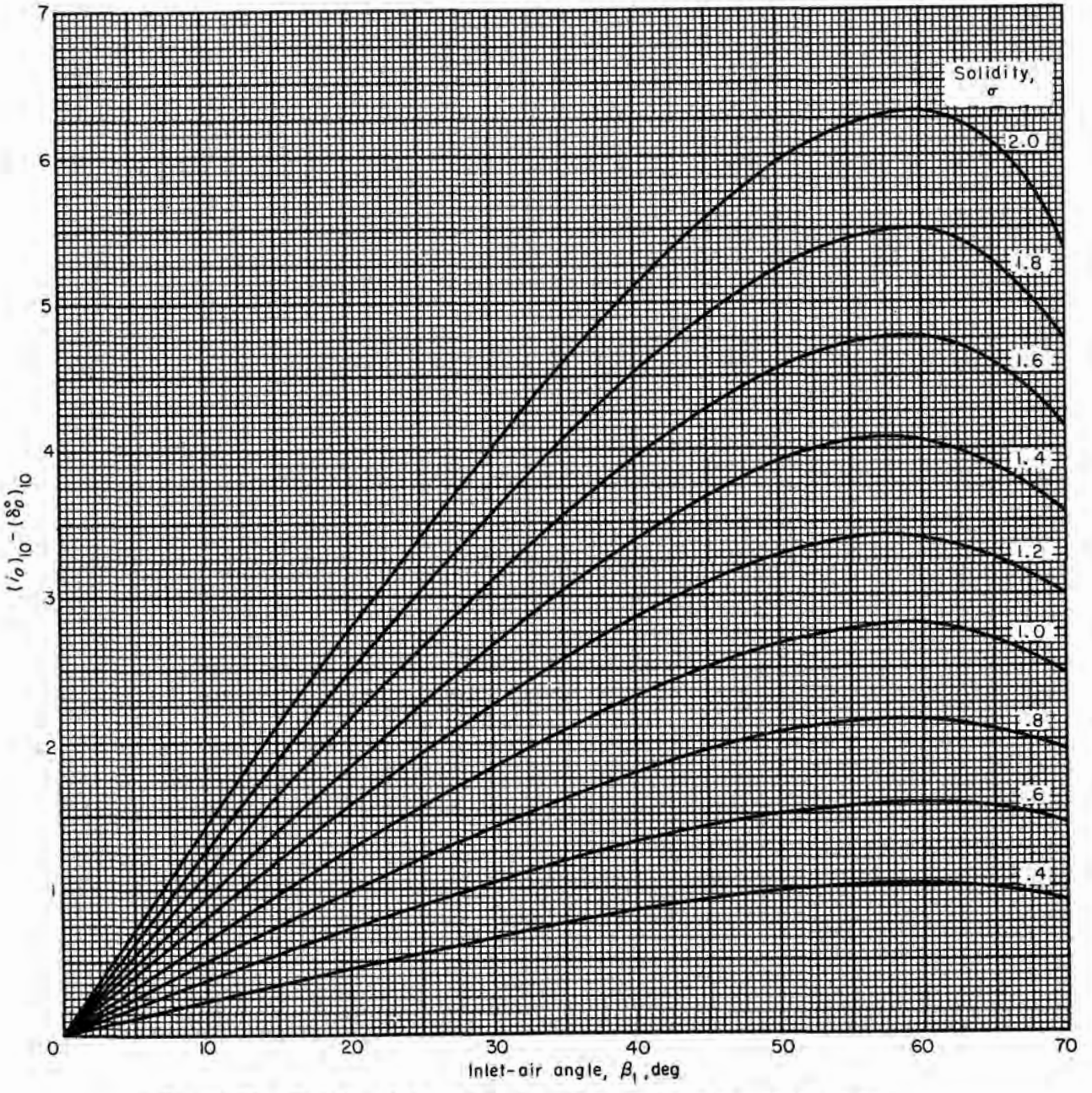

FIGURE 178.—Variation of $(i_o)_{10}-(\delta_o^*)_{10}$ with inlet-air angle and solidity (eq. (276)).

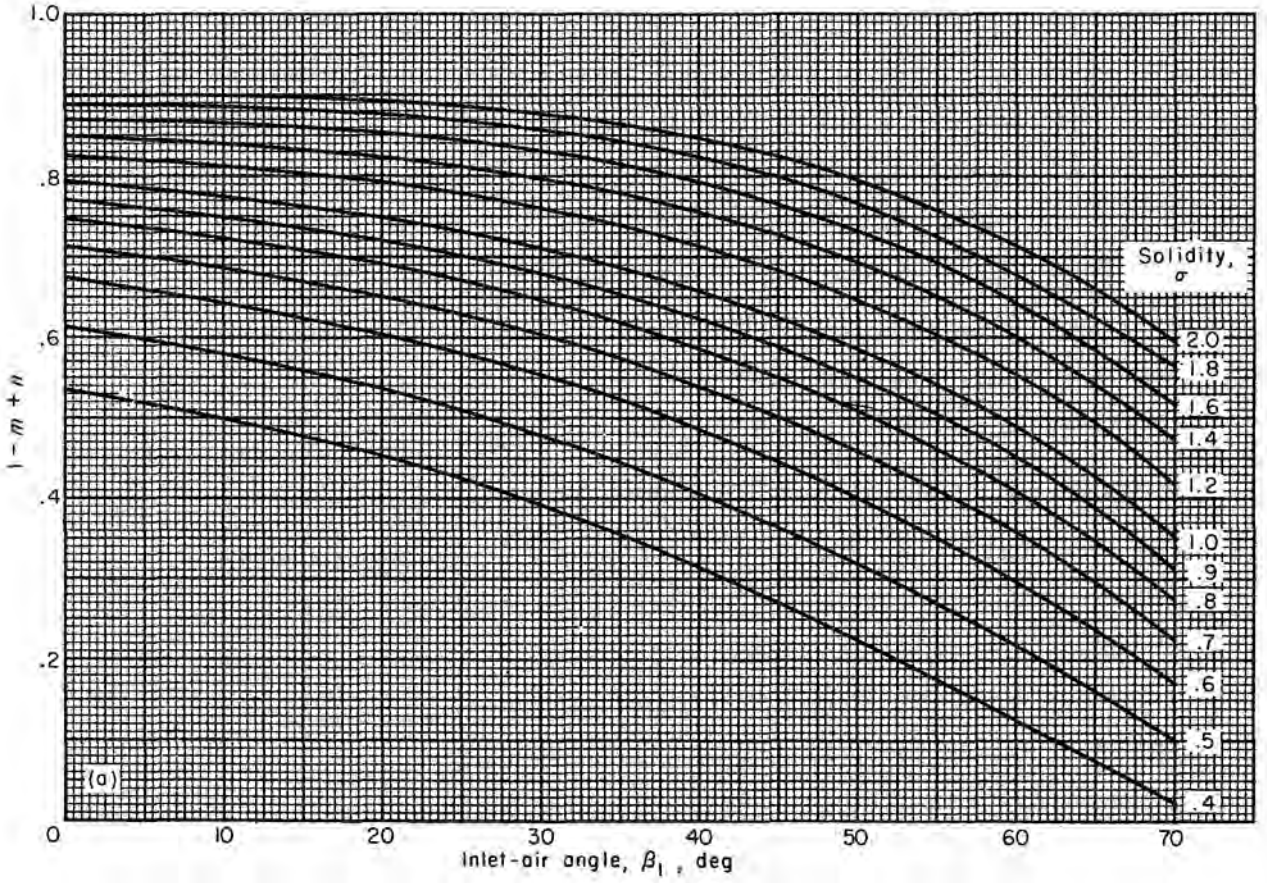

(a) NACA 65-(A_{10})-series blades as equivalent circular arc (eq. (276))

FIGURE 179.—Variation of $1-m+n$.

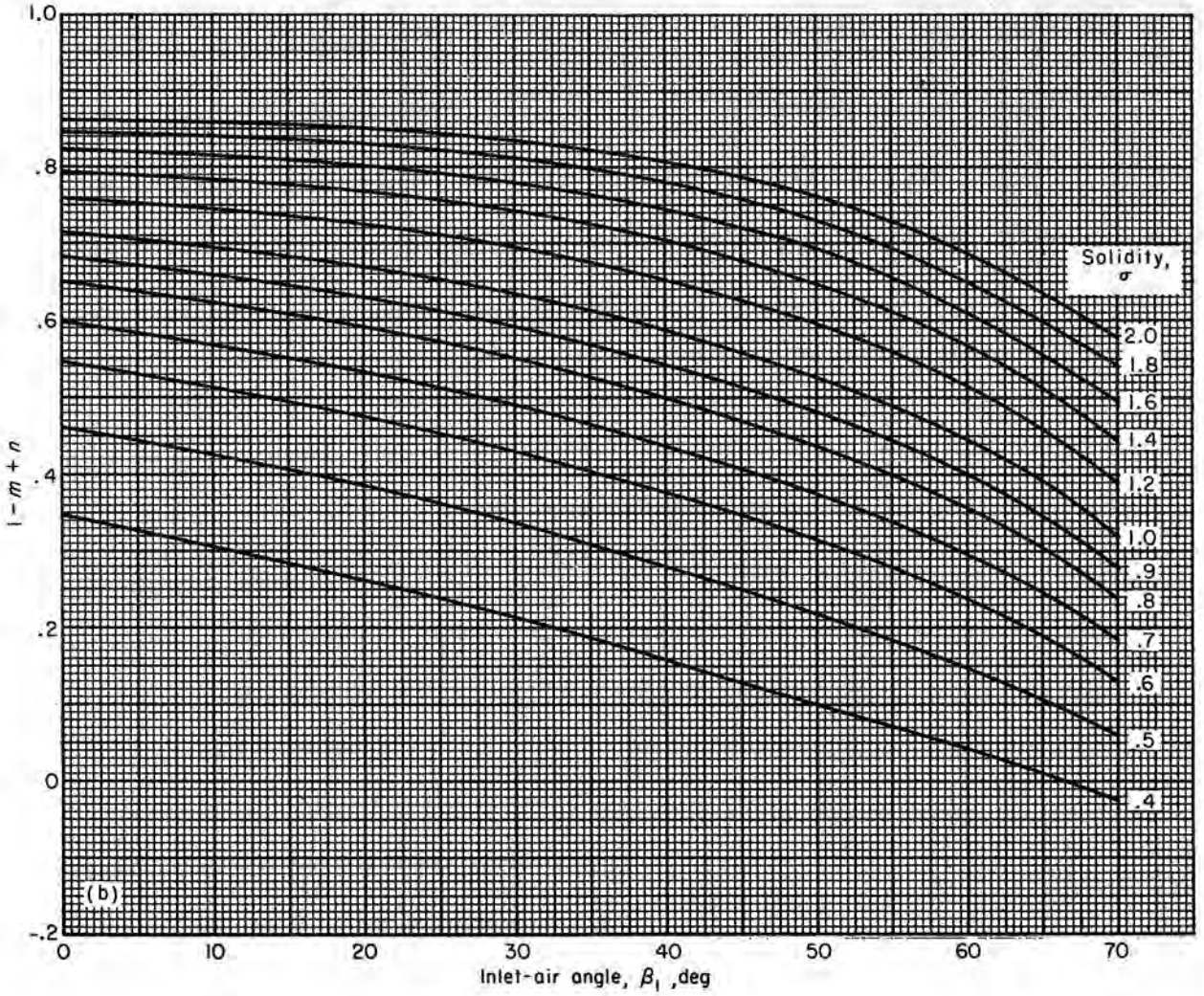

(b) Circular-arc-mean-line blades (eq. (276))

FIGURE 179.—Concluded. Variation of $1-m+n$.

691-564 O-65-16

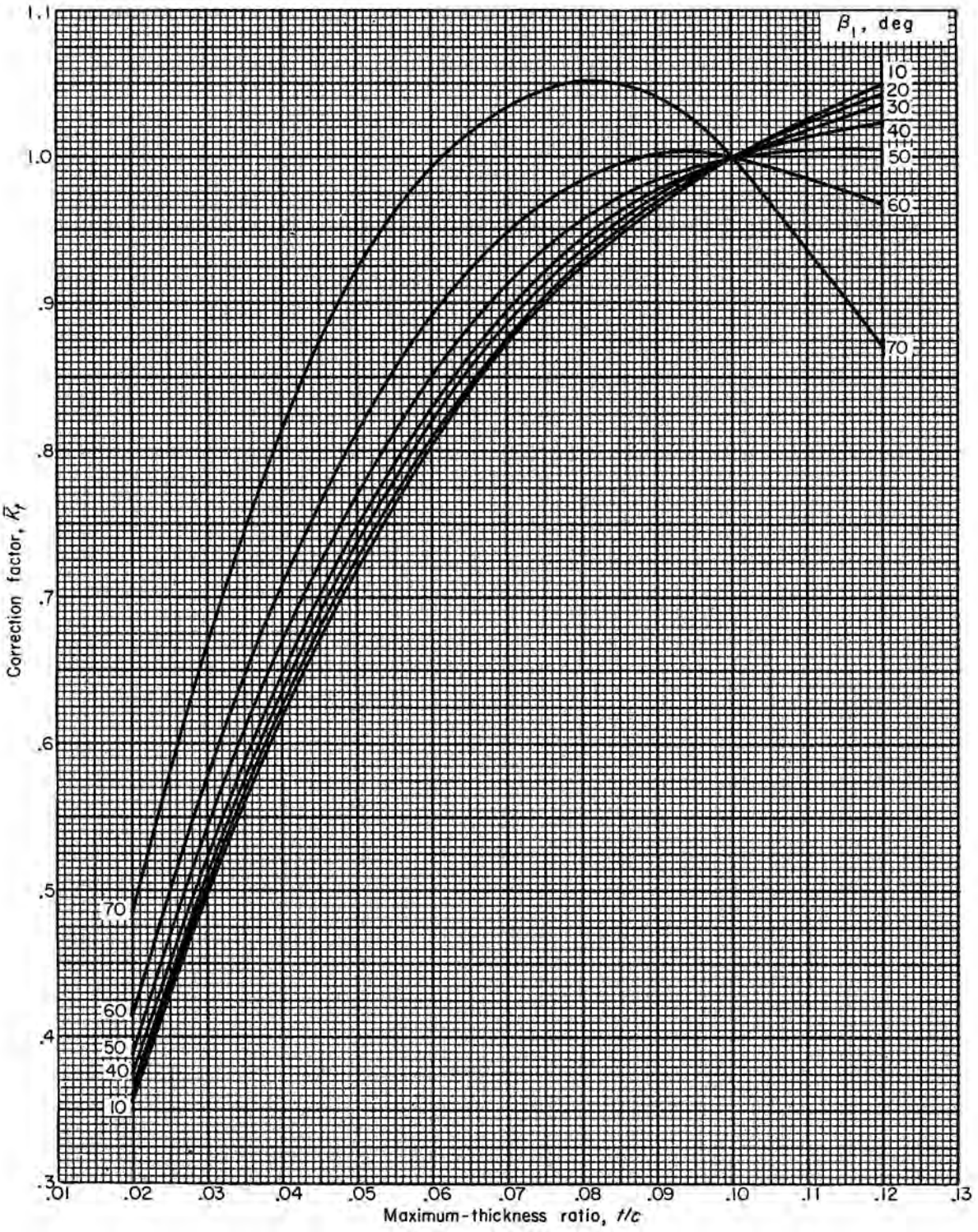

FIGURE 180.—Variation of thickness-correction factor $\bar{K}_t$ for camber calculation (eq. (276)).

CHAPTER VII

BLADE-ELEMENT FLOW IN ANNULAR CASCADES

By WILLIAM H. ROBBINS, ROBERT J. JACKSON, and SEYMOUR LIEBLEIN

A blade-element analysis is made of annular-cascade data obtained primarily from single-stage-compressor test installations. The parameters that describe blade-element flow (total-pressure loss, incidence angle, and deviation angle) are discussed with reference to the many variables affecting these parameters. The blade-element data are correlated over a fairly wide range of inlet Mach number and cascade geometry. Two blade shapes are considered in detail, the 65-(A_{10})-series profile and the double-circular-arc airfoil. Compressor data at three radial positions near the tip, mean, and hub are correlated at minimum-loss incidence angle. Curves of loss, incidence angle, and deviation angle are presented for rotor and stator blade elements. These correlation curves are presented in such a manner that they are directly related to the low-speed two-dimensional-cascade results. As far as possible, physical explanations of the flow phenomena are presented. In addition, a calculation procedure is given to illustrate how the correlation curves could be utilized in compressor design.

INTRODUCTION

Axial-flow-compressor research has generally been directed toward the solution of either compressor design or compressor analysis problems. In the design problem, the compressor-inlet and -outlet conditions are given, and the compressor geometry must be determined to satisfy these conditions. In contrast, for the analysis problem the inlet conditions and compressor are specified, and the outlet conditions are desired. (The analysis problem is sometimes referred to as the "direct compressor problem.")

There are two phases of the axial-flow-compressor design problem. In the first phase it is necessary to prescribe desirable velocity distributions at each radius of the compressor that will ultimately fulfill the design requirements. A discussion of the velocity-diagram phase of the compressor design procedure is given in chapter VIII. Secondly, proper blade sections are selected at each radial position and stacked in proper relation to each other to establish the design velocity diagrams at each radius. In order to satisfy the design requirements successfully, accurate blade-row design data are needed. Successful analysis of a compressor (the analysis problem) also depends upon accurate blade-row data, not only at the design point but also over a wide range of flow conditions (ch. X).

In general, compressor designers have relied primarily on three sources of blading information: (1) theoretical (potential-flow) solutions of the flow past airfoil cascades, (2) low-speed two-dimensional-cascade data, and (3) three-dimensional annular-cascade data. Potential-flow solutions have been used to a limited extent. In order to handle the complex mathematics involved in the theoretical solutions, it is necessary to make simplifying assumptions concerning the flow field. Among the most important of these is the assumption of a two-dimensional flow field with no losses. Unfortunately, in some cases these assumptions lead to invalid results unless experimental correction factors are applied to the computed results. These solutions are reviewed in chapter IV.

A considerable amount of blade design data has been obtained from low Mach number experimental two-dimensional cascades. A rather complete study of the cascade work that has been done to date is presented in chapter VI, which correlates cascade data at minimum-loss incidence angle for a wide range of inlet conditions and blade loadings. Low-speed two-dimensional-cascade data have been applied successfully in many compressor designs. However, with the design trends toward higher Mach numbers and higher blade loadings, these cascade results have not always been completely adequate for

describing the compressor flow conditions, particularly in regions of the compressor where three-dimensional-flow effects predominate.

Because of such effects, it becomes essential that blade-element data be obtained in a three-dimensional-compressor environment. These three-dimensional-cascade data (obtained primarily from single-stage compressors) may then be used to supplement and correct the theoretical solutions and the two-dimensional-cascade information. Some success has been obtained in correlating annular-cascade data with the theory and the two-dimensional-cascade results (refs. 32, 214, and 218 to 220); however, the range of variables covered in these investigations is not nearly complete.

The purpose of this chapter is to correlate and summarize the available compressor data on a blade-element basis for comparison with the two-dimensional-cascade data of chapter VI. An attempt is made to indicate the regions of a compressor where low-speed two-dimensional-cascade data can be applied to compressors and also to indicate the regions where cascade results must be modified for successful application to compressor design. Two blade sections are considered in detail, the NACA 65-(A_{10})-series blade and the double-circular-arc airfoil section. Particular emphasis is placed on obtaining incidence-angle, deviation-angle, and loss correlations at minimum loss for blade elements near the hub, mean, and tip radii of both rotor and stator blades. Empirical correction factors that can be applied to the two-dimensional-cascade design rules are given, and application of the design rules and correction factors to compressor design is illustrated.

SYMBOLS

The following symbols are used in this chapter:

a_a	speed of sound based on stagnation conditions, ft/sec
b	exponent in deviation-angle relation (eq. (280)), function of inlet-air angle
c	chord length, in.
D	diffusion factor
i	incidence angle, angle between inlet-air direction and tangent to blade mean camber line at leading edge, deg
K_i	correction factor in incidence-angle relation, function of blade maximum-thickness ratio and thickness distribution
K_δ	correction factor in deviation-angle relation, function of blade maximum-thickness ratio and thickness distribution
M	Mach number
m	factor in deviation-angle relation at $\sigma=1$ (eq. (280)), function of inlet-air angle
m_c	factor in deviation-angle relation (eq. (282)), function of blade-chord angle.
n	slope factor in incidence-angle relation (eq. 279)), function of inlet-air angle and solidity
P	total or stagnation pressure, lb/sq ft
p	static or stream pressure, lb/sq ft
r	radius
s	blade spacing, in.
T	total or stagnation temperature
t	blade maximum thickness, in.
V	air velocity, ft/sec
β	air angle, angle between air velocity and axial direction, deg
$\Delta\beta$	air-turning angle, $\beta_1-\beta_2$, deg
γ	ratio of specific heats
$\gamma°$	blade-chord angle, angle between blade chord and axial direction, deg
$\delta°$	deviation angle, angle between outlet-air direction and tangent to blade mean camber line at trailing edge, deg
η	efficiency
κ	blade angle, angle between tangent to blade mean camber line and axial direction, deg
σ	solidity, ratio of chord to spacing
φ	blade camber angle, difference between blade angles at leading and trailing edges, $\kappa_1-\kappa_2$, deg
ω	angular velocity of rotor, radians/sec
$\overline{\omega}$	total-pressure-loss coefficient

Subscripts:

ad	adiabatic
C	compressor
GV	inlet guide vanes
h	hub
id	ideal
m	mean
min	minimum
o	zero camber
R	rotor
S	stator
ST	stage
t	tip
z	axial direction
θ	tangential direction

1 station at inlet to blade row or stage
2 station at exit of blade row or stage
2-*D* low-speed two-dimensional cascade
10 blade maximum-thickness-to-chord ratio of 10 percent

Superscript:

′ relative to rotor

PRELIMINARY CONSIDERATIONS

BLADE-ELEMENT CONCEPT

In current design practice, the flow distribution at the outlet of compressor blade rows is determined from the flow characteristics of the individual blade sections or elements. The blade-element approach to compressor design is discussed in detail in chapter III and in reference 221. To review briefly, axial-flow-compressor blades are evolved from a process of radial stacking of individual airfoil shapes called blade elements. The blade elements are assumed to be along surfaces of revolution generated by rotating a streamline about the compressor axis; this stream surface of revolution may be approximated by an equivalent cone (fig. 181). Each element along the height of the blade is designed to direct the flow of air in a certain direction as required by the design velocity diagram of the blade row. The basic parameters defining the flow about a blade element are indicated in figure 182. Stated simply, blade-element flow is described by the variations of the loss in total pressure across the blade row and of the air-turning angle with the incidence angle (or angle of attack).

FACTORS AFFECTING BLADE-ELEMENT PERFORMANCE

The flow about a given blade element in a compressor configuration is different from that in a two-dimensional cascade because of three-dimensional effects in compressor blade rows. These three-dimensional effects influence the magnitude of the design incidence angle, the loss in total pressure, and the deviation angle.

Incidence angle.—In the low-speed two-dimensional cascade, the minimum-loss incidence angle depends on the blade geometry (camber, solidity, and blade thickness), the inlet-air angle, and inlet Mach number (ch. VI). In compressor operation, several additional factors can alter the minimum-loss incidence angle for a given element geometry—for example, differences in testing procedure. In compressor operation, incidence angle, inlet-air angle, and inlet Mach number vary simultaneously; in contrast, cascades are

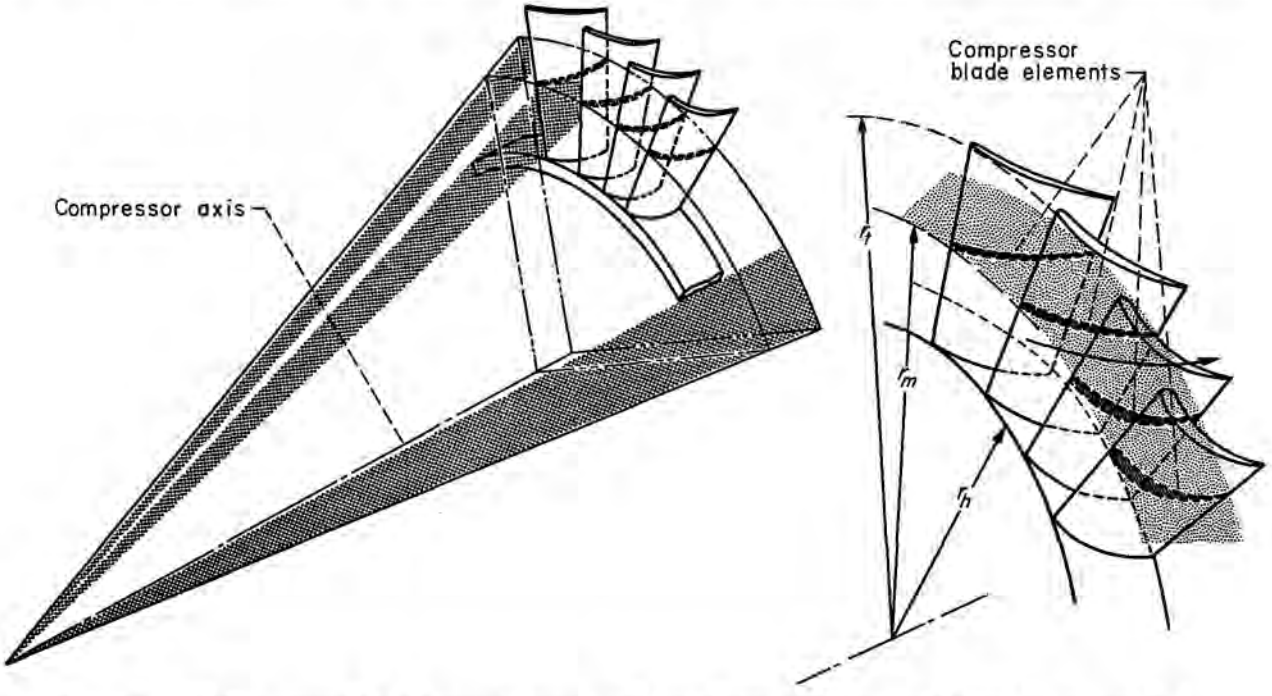

FIGURE 181.—Compressor blade elements shown along conical surface of revolution about compressor axis.

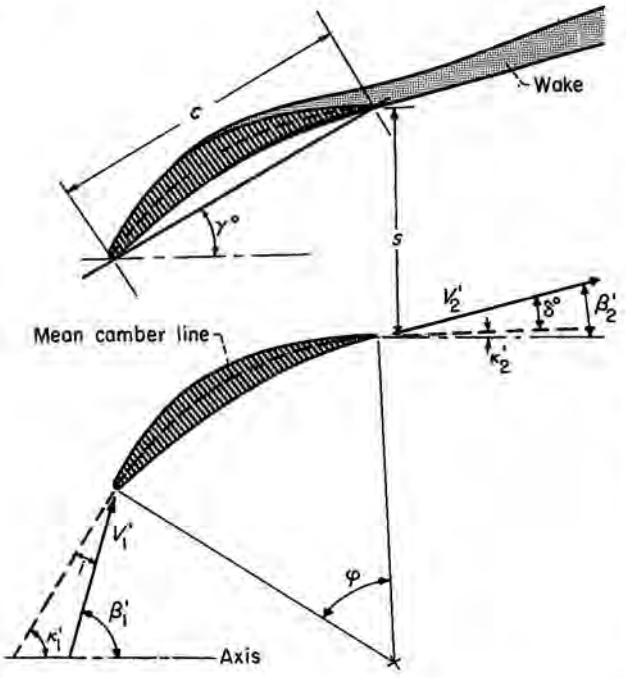

FIGURE 182.—Rotor blade-element properties.

often operated with fixed inlet-air angle and inlet Mach number. Some net difference may be obtained in the range characteristics and therefore in the location of the point of minimum loss between cascade operation at constant inlet-air angle and compressor test operation (with varying inlet-air angle).

In addition to these blade-element considerations, of course, there are sources of difference arising from compressor three-dimensional effects. For example, radial variations of minimum-loss incidence angle that are not consistent with the trends predicted from cascade blade-element considerations have been observed in compressor rotors (refs. 56 and 222). Apparently, radial position may also be a factor in determining compressor minimum-loss incidence angle.

Total-pressure loss.—In the two-dimensional cascade, the magnitude of the loss in total pressure across the blade element is determined from the growth of the blade surface boundary layers (profile loss). In the actual compressor, the loss in total pressure is determined not only by the profile loss, but also by the losses induced by the three-dimensional nature of the flow. These three-dimensional losses result from secondary motions and disturbances generated by the casing wall boundary layers, from blade tip clearance, from radial gradients of total energy, and from interactions of adjacent blade rows. The compressor loss picture is further complicated by the tendency of boundary-layer fluid on the compressor blade surfaces and in the blade wake to be displaced radially. As a consequence of this phenomenon, the loss measured downstream of a given blade element may not necessarily reflect the actual loss generated at that element, but something more or less, depending on the radial location of the element.

It is expected, therefore, that the factors influencing the magnitude of the blade-element loss in the compressor will include the factors affecting the profile loss (blade surface velocity distribution, inlet Mach number, blade-chord Reynolds number, free-stream turbulence, and blade surface finish) and the factors affecting the three-dimensional losses. Investigations of compressor blade-element losses based on surface velocity distribution, as expressed in terms of diffusion factors, are presented in references 9 and 35. The essentially secondary effects of blade surface finish and trailing-edge thickness on compressor loss are investigated in references 223 and 224. Results of tests of blade-element performance (ref. 225 and ch. V) and over-all performance (refs. 226 and 227) at varying Reynolds numbers indicate that there is no significant variation in loss for Reynolds numbers above approximately 2.5×10^5. (Since most of the compressor data used in this analysis are for Reynolds numbers greater than 2.5×10^5, no Reynolds number effects are believed to exist for the data.) Some variations of compressor loss with inlet Mach number have been established in references 52, 56, and 228. These results, however, are not complete indications of Mach number effects (shock losses), since the corresponding variations of blade diffusion with Mach number are not identified. An attempt to separate the variation of diffusion and shock losses with Mach number by means of an analysis based on the diffusion factor of reference 9 is presented in references 222 and 229.

Although some aspects of the compressor three-dimensional-flow phenomena are known (chs. XIV and XV), the specific factors or

parameter affecting compressor three-dimensional losses have not been established for analysis purposes. At present, the three-dimensional loss can be treated only on a gross basis as a difference between the total measured loss and the predicted profile loss.

Deviation angle.—In the two-dimensional cascade the minimum-loss deviation angle varies primarily with the blade geometry and the inlet-air angle. Experience with compressor operation indicates that blade-element minimum-loss deviation angle is also sensitive to three-dimensional effects. The two principal compressor effects are secondary flows and changes in axial velocity across the blade element. Secondary flows are treated in chapter XV and in reference 43. Corrections are established in reference 43 for the effect of secondary flows on the outlet angles of compressor inlet guide vanes. At present, however, rotor and stator secondary-flow effects can be treated only on a gross basis.

The effects of changes in axial velocity ratio on the turning angles of a fixed blade-element geometry are conclusively demonstrated in the rotor investigations of reference 218. There are several origins of varying axial velocity ratio across a compressor blade element: (1) contraction of the annulus area across the blade row, (2) compressibility, which varies axial velocity ratio for a fixed annulus area, and (3) differences in the radial gradient of axial velocity at blade-row inlet and outlet, which can arise from the effects of radial-pressure equilibrium (ch. VIII). Although several attempts have been made to establish corrections for the effect of change in axial velocity ratio on deviation angle (refs. 218 and 191), these proposed correction techniques have not been universally successful. The principal difficulty involved in the axial velocity corrections is the inability to determine the corresponding changes in blade circulation (i.e., tangential velocity). Values of axial velocity ratio were identified for the deviation-angle data presented, although no attempt was made to apply any corrections.

Some of the secondary factors influencing deviation angle, such as inlet Mach number and Reynolds number, are investigated in references 52, 56, and 218. These results indicate that the variations of deviation angle with Mach number and Reynolds number are small for the range of data considered in this survey.

CORRELATION APPROACH

In this chapter, annular-cascade data are compared with the two-dimensional-cascade correlations of minimum-loss incidence angle, total-pressure loss, and deviation angle of chapter VI. In this way, compressor investigations serve as both a verification and an extension of the two-dimensional-cascade data. Two-dimensional-cascade data correlations and rules, in conjunction with correction factors deduced from the three-dimensional data, can then be used for compressor design and analysis.

With this approach in mind, all available single-stage data were collected, computed, and plotted in a form considered convenient for correlation. The blade and performance parameters used in the analysis are similar to those used in the two-dimensional-cascade correlations of chapter VI. Camber angle, incidence angle, and deviation angle (fig. 182) are used to define the blade camber, air approach, and air leaving directions, respectively. These angles are based on tangents to blade mean camber line at the leading and trailing edges. As in chapter VI, the NACA 65-(A_{10})-series blades are considered in terms of the equivalent circular-arc camber line (figs. 125 and 126, ch. VI).

Loss in total pressure across the blade element is expressed in terms of the loss parameter $\overline{\omega}' \cos \beta_2'/2\sigma$, where the relative total-pressure-loss coefficient $\overline{\omega}'$ is defined as the mass-averaged defect in relative total pressure divided by the pressure equivalent of the inlet velocity head:

$$\overline{\omega}' = \frac{(P_2')_{id} - P_2'}{P_1' - p_1} \tag{58}$$

For stationary blade rows, or no change in streamline radius across the rotor, the numerator of equation (58) becomes the decrease in relative total pressure across the blade row from inlet to outlet. The relative total-pressure-loss coefficient was computed from stationary measurements of total pressure and total temperature and from the computed relative inlet Mach number according to reference 9. The total-pressure-loss parameter $\overline{\omega}' \cos \beta_2'/2\sigma$, as indicated in chapter VI, can be used as a significant parameter for correlating blade losses.

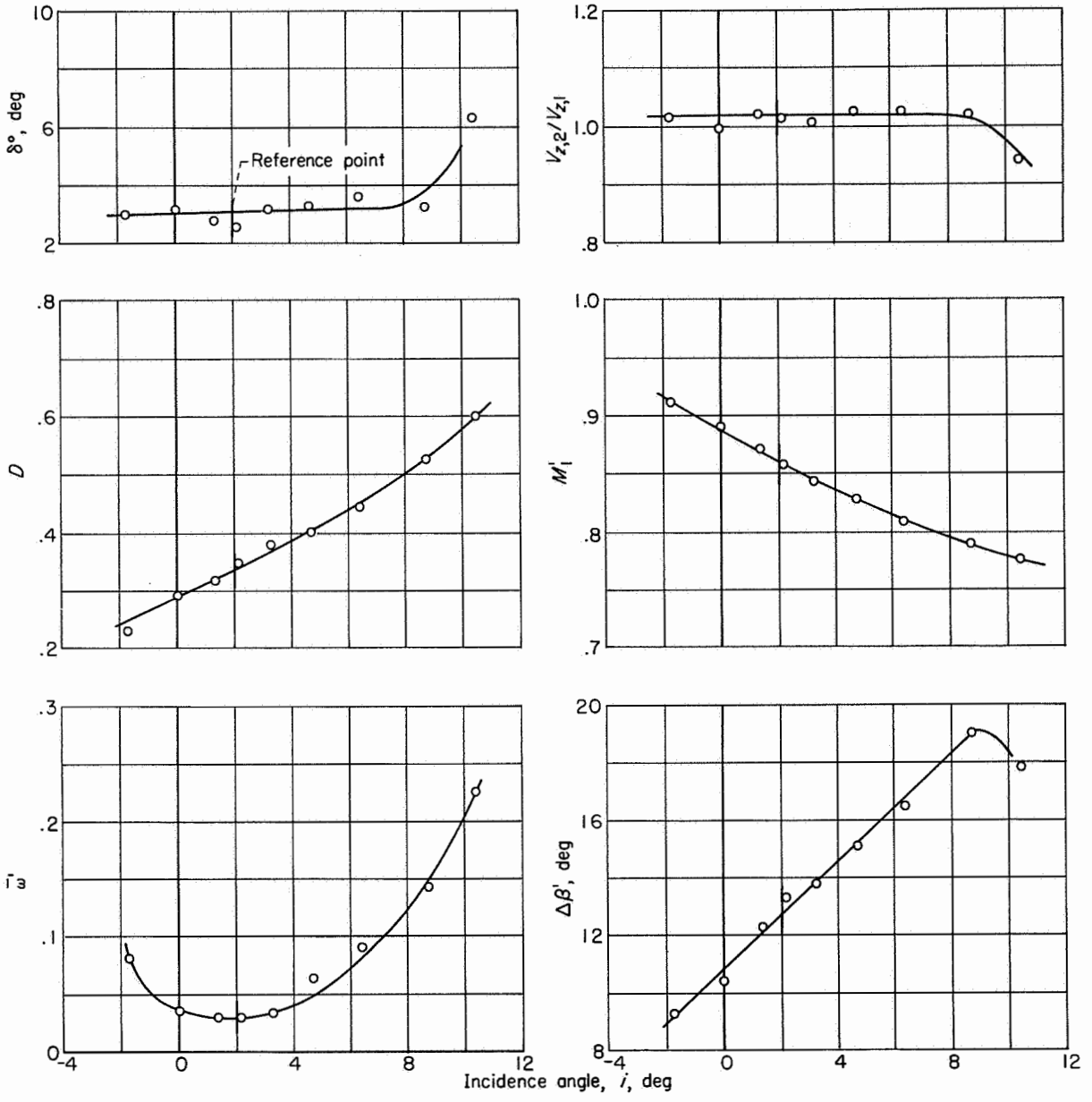

FIGURE 183.—Example of typical variation of blade-element performance parameters with incidence angle. Transonic rotor with double-circular-arc blade sections at tip speed of 800 feet per second; data for blade row 17 (table II) at tip position (ref. 55).

The diffusion factor, which is used as a blade-loading parameter, is defined in reference 9 for no change in radius as follows:

$$D=\left(1-\frac{V_2'}{V_1'}\right)+\frac{V_{\theta,1}'-V_{\theta,2}'}{2\sigma V_1'} \qquad (278)$$

A typical example of the plotted performance parameters for a rotor blade row is shown in figure 183. The data represent the variations of the flow at fixed rotational speed. Plots for stator blade rows show similar trends of variation. As in chapter VI, a reference point was established as the incidence angle for minimum loss (fig. 184(a)), and the blade-element flow was analyzed at this reference point. In cases where minimum-loss incidence was not clearly defined, the reference point was taken as the mean incidence of the

incidence-angle range for which values of $\bar{\omega}$ at the end points are twice the minimum value (fig. 184(b)). In some instances, near the compressor tip the loss-against-incidence-angle curve increased continuously from a minimum value of loss parameter at the open-throttle point. In presenting data for these cases several points near the minimum-loss value are plotted.

One of the primary objectives of this analysis is to determine differences in blade-element performance with compressor radial position. Therefore, three radial positions along the blade span (near the hub, mean radius, and tip) of each blade row are considered. The radial positions at the hub and tip are approximately 10 to 15 percent of the passage height away from the inner and outer walls, respectively, which are outside the wall boundary-layer region in all cases. The analysis is directed toward correlating the loss and deviation-angle data at reference incidence angle and determining the variation of reference incidence angle with blade geometry and Mach number at the three radial positions.

EXPERIMENTAL DATA SOURCES

There are three sources of three-dimensional-cascade blade-element data: stationary annular-cascade tunnel investigations, multistage-compressor investigations, and single-stage or single-blade-row compressor investigations. A relatively small amount of data has been accumulated from blade-row investigations conducted in stationary annular-cascade tunnels. Tunnels of this type have been used primarily for inlet-guide-vane investigations. Typical examples of annular-cascade tunnel investigations are reported in references 215 and 225. Numerous multistage-compressor investigations have been conducted both in this country and abroad. Unfortunately, the data obtained from these investigations are too limited to permit the construction of individual blade-row-element performance curves similar to those illustrated in figure 183.

The data used in this investigation were obtained primarily from investigations of single rotor rows or of single-stage compressors. A typical single-stage-compressor test installation is shown in figure 185. This particular compressor consists of a row of inlet guide vanes, a rotor blade row driven by a variable-speed motor, and a stator blade row. A discharge throttle is installed in the outlet system to vary the compressor back pressure. In this manner, the compressor mass-flow rate can be controlled. In an installation such as this, compressor performance over a range of speeds and mass flows can be obtained simply. In many cases, test rigs similar to figure 185 have been operated with only guide vanes and rotors or with rotors alone.

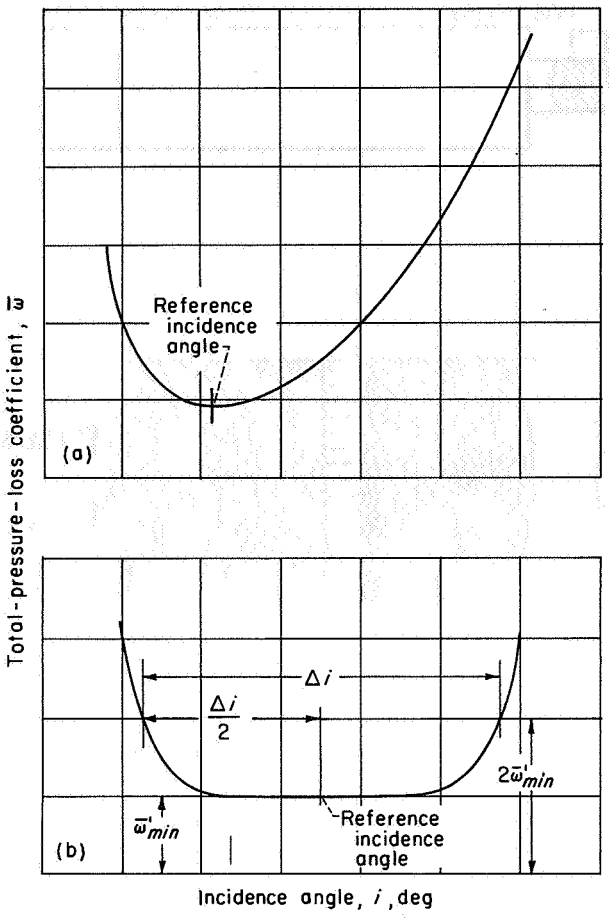

(a) Minimum loss.
(b) Mid-range.

FIGURE 184.—Definitions of reference incidence angle.

Many phases of compressor research have been conducted in single-stage-compressor test rigs; and, in reporting these phases, complete blade-element results are not usually presented. Therefore, it was necessary to collect available original data and rework them in terms of the parameters of the analysis. Since only NACA original data were available in blade-element form, the data analysis is based mainly on single-stage-compressor investigations conducted at the Lewis laboratory.

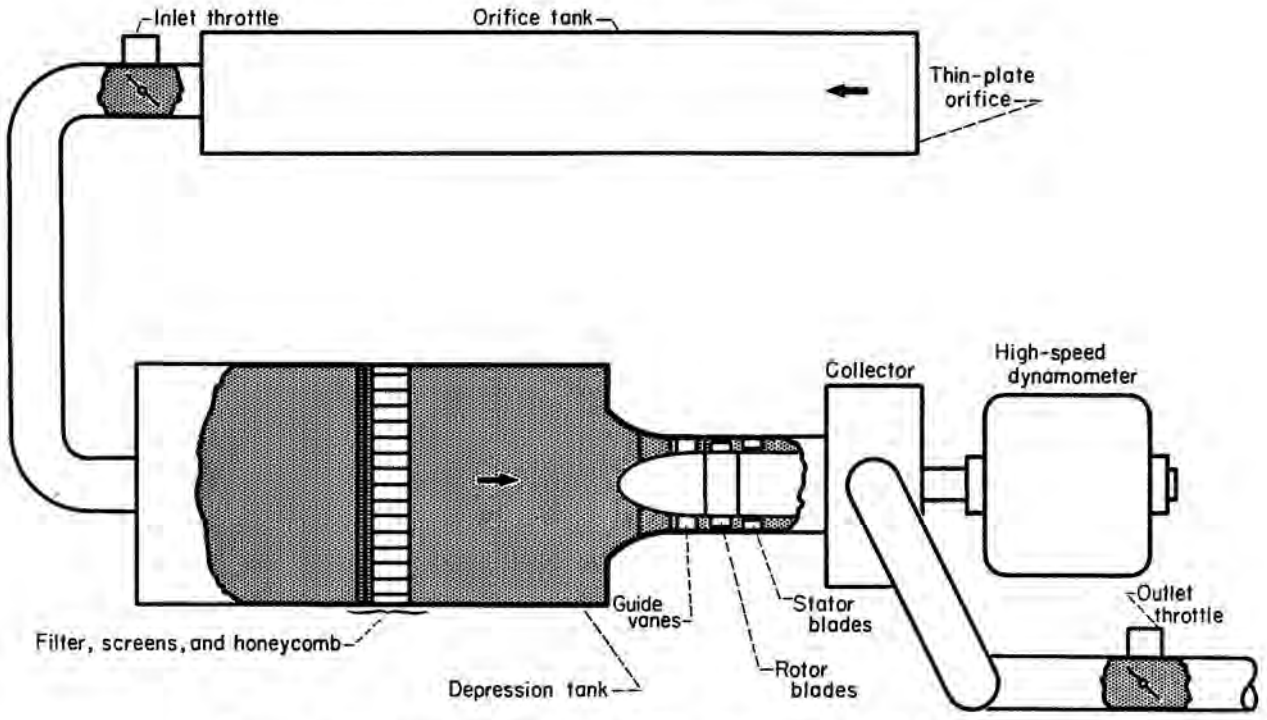

FIGURE 185.—Schematic diagram of single-stage-compressor test installation.

The measurements taken and the instrumentation used vary somewhat from compressor to compressor; in most cases, however, it is possible from the available data to reconstruct complete experimental velocity diagrams and to determine the blade-element performance. Radial survey measurements were made after each blade row. Normally, total pressure, static pressure, total temperature, and air direction were measured. The pressure- and temperature-measuring devices were calibrated for the effect of Mach number.

Most of the compressor investigations that were adaptable to this analysis were conducted on NACA -65(A_{10})-series airfoil shapes and double-circular-arc airfoils. Therefore, the analysis is concerned solely with these airfoils. The 65-(A_{10})-series airfoil has been used extensively in subsonic compressors; and the double-circular-arc airfoil, which is a relatively simple airfoil shape, has been used effectively in transonic compressors. Details of the characteristics of the various blade rows used in this analysis are summarized in table II, and details of the instrumentation, calculation procedure, and accuracy of measurement are given in the listed references.

INCIDENCE-ANGLE ANALYSIS

METHOD OF CORRELATION

In correlating blade-element reference-incidence-angle data, measured values of incidence angle are compared with values of reference incidence angle predicted for the geometry of the blade element according to the low-speed two-dimensional-cascade correlations of chapter VI. In chapter VI, the low-speed two-dimensional reference incidence angle is expressed in terms of the blade geometry as

$$i_{2-D}=K_t(i_o)_{10}+n\varphi \qquad (279)$$

where K_t is a function of blade thickness distribution and maximum-thickness ratio, $(i_o)_{10}$ is the zero-camber incidence angle for the 10-percent-thick airfoil section (function of air-inlet angle β_1' and solidity σ), and n is equal to $[(i-i_o)/\varphi]_{2-D}$ (also a function of β_1' and σ). Values of K_t, $(i_o)_{10}$, and n for the circular-arc and 65-(A_{10})-series blade are repeated in figures 186 to 188 for convenience.

The comparisons between measured blade-element reference incidence angle i_C and predicted two-dimensional incidence angle i_{2-D} are expressed

TABLE II.—DETAILS OF SINGLE-STAGE ROTORS AND STATORS

Blade row	Description	Outer diameter, in.	Hub-tip ratio	Rotor tip speed, ft/sec	Inlet Mach number, M_1	Camber angle, φ, deg		Chord, c, in.		Solidity, σ		Blade-chord angle, γ°, deg		Blade maximum thickness-chord ratio, t/c		Reference
						Hub	Tip	Hub	Tip	Hub	Tip	Hub	Tip	Hub	Tip	
65-Series blade section																
1	Rotor	14	0.5	552, 828, 994, 1104, 1214	0.30–0.75	19.9	15.3	1.31	1.31	1.010	0.590	30.8	56.4	10	10	230
2	Stator	14	.55	552, 1104	.26– .73	30.1	30.1	1.31	1.31	.996	.620	19.5	45.9	10	10	231
3	Rotor	30	.80	504, 672, 840	.36– .70	30.1	30.1	2.90	2.90	1.08	.906	28.8	45.9	10	10	44
4	Rotor	14	.50	1104, 1214	.60– .80	30.1	30.1	1.31	1.31	1.010	.590	21.1	56.0	10	10	231
5	Rotor	14	.50	557, 743	.39– .72	30.1	30.1	1.31	1.31	.962	.608	15.2	32.0	10	10	231
6	Stator	14	.52	371, 557, 743	.22– .66	30.1	30.1	1.31	1.31	.993	.631	16.2	32.2	10	10	231
7	Rotor	14	.50	546	.35– .56	40.0	23.9	1.31	1.31	.955	.600	21.0	58.0	10	10	230
8	Rotor	14	.50	552, 828, 1104	.30– .86	40.0	23.9	1.31	1.31	.955	.600	21.0	58.0	10	10	230
9	Rotor	14	.50	552, 828, 1104, 1214	.30– .76	40.0	23.9	1.31	1.31	.955	.600	21.0	58.0	10	10	230
10	Stator	14	.53	412, 617, 823	.25– .74	30.1	30.1	1.31	1.31	.870	.587	15.1	39.6	10	10	231
11	Rotor	14	.80	669, 753, 836	.52– .75	45.2	34.1	1.35	1.35	.823	.692	21.4	35.4	6	6	232
12	Rotor	14	.80	669, 753, 836	.49– .75	45.2	34.1	1.35	1.35	1.12	.943	21.4	35.4	6	6	232
13	Rotor	14	.80	669, 753, 836	.49– .75	45.2	34.1	1.35	1.35	1.69	1.35	21.4	35.4	6	6	232
14	Rotor	14	.80	600, 736, 874	.50– .92	30.3	19.4	1.46	1.82	1.20	1.20	42.5	48.8	10	8	224
Circular-arc blade section																
15	Rotor	14	0.4	600, 800, 1000, 1050	0.33–1.06	40.3	11.4	2.00	2.00	1.778	0.963	12.1	46.7	8	5	233
16	Rotor	18	.5	600, 700, 800, 900, 1000	.38–1.07	28.3	7	1.5	1.5	1.63	1.03	23.6	46.3	10	6	234
17	Rotor	14	.5	600, 800, 900, 1000	.37–1.17	29.4	13.7	2.09	2.32	1.28	1.04	23.0	44.1	8	5	55
18	Rotor	14	.5	800, 900	.55–1.12	29.4	13.7	2.09	2.32	.85	.66	23.0	44.1	8	5	55
19	Rotor	14	.5	800, 900, 1000, 1120	.50–1.22	23.1	4.3	1.50	1.50	1.40	.825	17.4	51.3	10	5	229
20	Rotor	14	.5	800, 900, 1000, 1120	.4 – .82	23.1	4.3	1.50	1.50	1.40	.825	17.4	51.3	10	5	229
21	Stator	17.36	.62	600, 800, 900	.41– .63	52.0	52.0	3.25	3.25	1.64	1.07	10.0	10.0	7	7	235
22	Stator	17.36	.60	800, 1000	.53– .66	20.6	20.0	2.66	3.23	1.45	1.08	34.0	28.0	8	6	222

in terms of the difference $(i_C - i_{2-D})$. Thus, a value of zero of the difference parameter corresponds to an equivalence of the two incidence angles. In view of the established tendency of the reference incidence angle to increase somewhat with inlet Mach number (ch. VI), it was thought desirable to plot the variation of the difference parameter $(i_C - i_{2-D})$ against relative inlet Mach number for the three radial positions at hub, mean, and tip.

NACA 65-(A_{10})-series blades.—The results of the comparison between compressor and two-dimensional-cascade reference incidence angles for the 65-(A_{10})-series blades are presented in figure 189 for hub-, mean-, and tip-radius regions. Both rotor and stator data are presented; the stator data being represented by the solid points. Different values of incidence angle for a given symbol represent different compressor tip speeds. As might be expected in a correlation of this type involving data from different test installations and instrumentations, the data are somewhat scattered, particularly in the hub and tip regions. It has not been possible in these instances to evaluate the significance or origin of the scatter. (In compressor investigations, instrumentation inaccuracy generally contributes heavily to the data scatter, especially at hub and tip.) Nevertheless, the results of the comparison are indicative of the trends involved, and it is possible to make some general observations.

For the rotor mean-radius region, where three-dimensional disturbances are most likely a minimum, the rotor minimum-loss incidence angles are, on the average, about 1° smaller than the corresponding cascade-predicted values. This difference may be a reflection of some of the compressor influences discussed previously. The data also indicate that no essential variation of reference incidence angle with relative inlet Mach number exists up to values of M_1' of about 0.8. The 65-(A_{10})-series blade, having a thick-nose profile, apparently exhibits the same approximate constancy of minimum-loss incidence angle with Mach number as indicated for the British thick-nose C-series profile in the cascade comparisons of chapter VI.

At the rotor tip, the compressor reference incidence angles are from 0° to 4° less than the predicted cascade values. As in the case of the rotor mean radius, no essential variation with inlet Mach number is observed in the range of

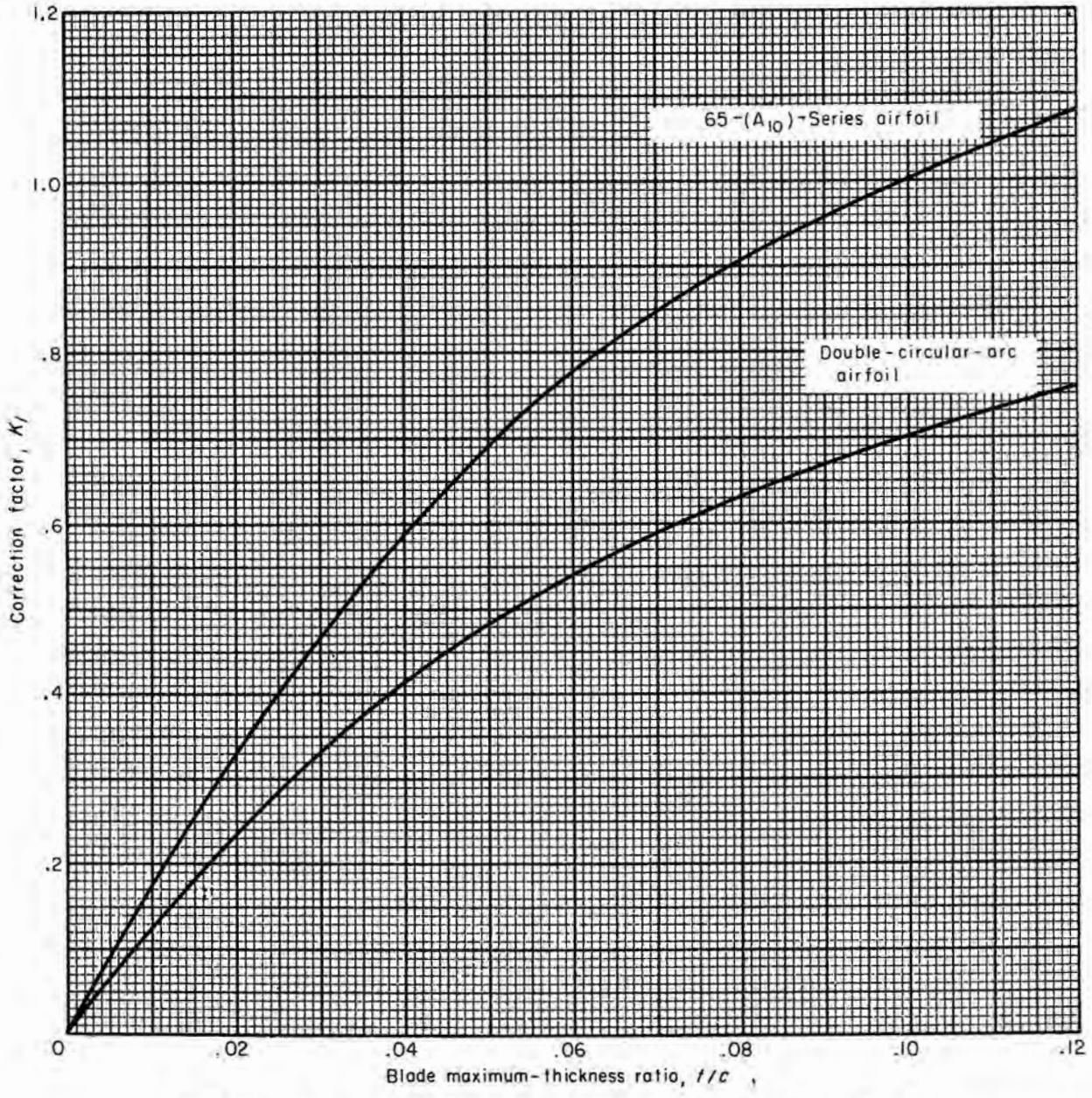

FIGURE 186.—Thickness correction for zero-camber reference incidence angle (ch. VI).

data covered. The lower values of rotor reference incidence angle were generally the result of a change in the form of the variations of loss against incidence angle in the rotor, as illustrated in figure 190. The change in form may be explained on the basis of a probable increase in rotor tip three-dimensional losses (centrifuging of blade boundary layer, tip-clearance disturbances, etc.) with increasing incidence angle.

At the rotor hub, the situation is somewhat confused by the wide range of data. A tendency of the compressor incidence angles to be somewhat larger than the corresponding cascade values, with an average difference of about 1° or 2°, is indicated.

For the stator mean-radius and hub regions, close agreement between compressor and cascade incidence angles is indicated for the range of Mach numbers covered (to about 0.7). Considerable scatter exists in the stator data at the

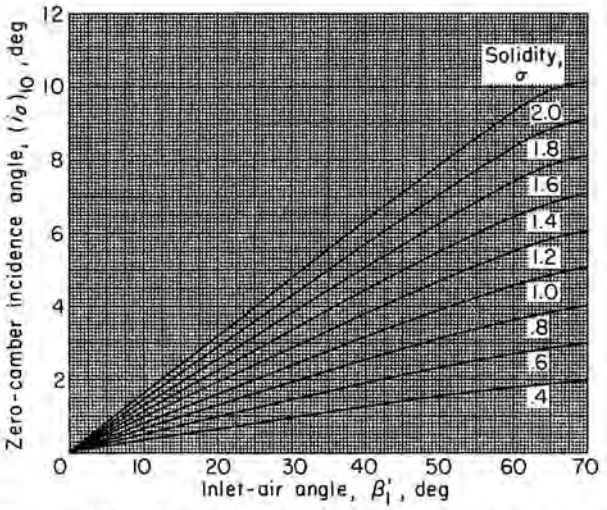

FIGURE 187.—Zero-camber reference incidence angle for NACA 65-(A_{10})-series and true circular-arc blades of 10-percent maximum-thickness ratio (see fig. 137, ch. VI, for larger print).

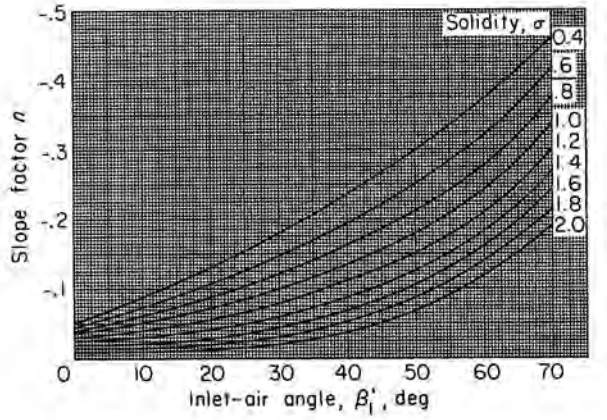

FIGURE 188.—Reference-incidence-angle slope factor for NACA 65-(A_{10})-series blades as equivalent circular arc and for true circular-arc blades (see fig. 138, ch. VI, for larger print).

compressor tip; therefore, no definite conclusions can be made concerning the variations of incidence angle.

Double-circular-arc blade.—The results of the double-circular-arc airfoil correlation are presented in figure 191, where compressor reference incidence angle minus low-speed-cascade-rule incidence angle (eq. (279)) is plotted against relative inlet Mach number for the hub, mean, and tip radial positions for both rotors and stators. The dashed curve represents the variation obtained with a 25°-camber double-circular-arc blade in high-speed two-dimensional cascade (ch. VI).

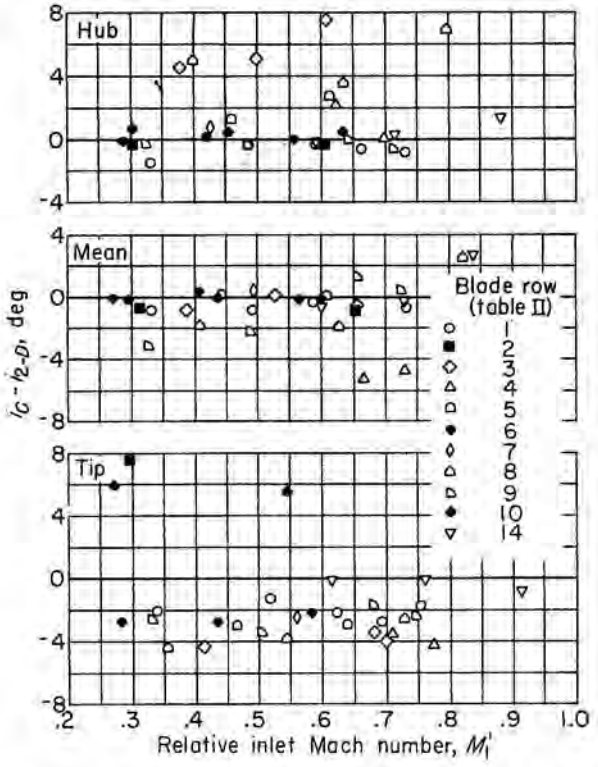

FIGURE 189.—Variation of compressor reference incidence angle minus two-dimensional-cascade-rule incidence angle with relative inlet Mach number for NACA 65-(A_{10})-series blade section.

It is immediately apparent that rotor reference incidence angle at all radial positions increases with increasing Mach number. The data indicate that the magnitude of the increase in reference incidence angle with Mach number is larger at the hub than at the tip. The hub data points in figure 191 were obtained from blade elements of relatively high camber. Both potential-flow and low-speed-cascade results indicate that this type of configuration is associated with a negative value of reference incidence angle. As inlet Mach number is increased, the increase in incidence angle in the positive direction must be fairly large in order to avoid high losses associated with blade-row choking. In contrast, at the compressor tip, since the blade cambers are generally lower (see table II), the low-speed incidence angle is higher and the required rate of change of incidence angle with increasing Mach number is not as large. Unfortunately, low Mach number data were not available to permit extrapolation of the rotor incidence-angle variations to zero Mach number (level of cascade correlation). However, it is

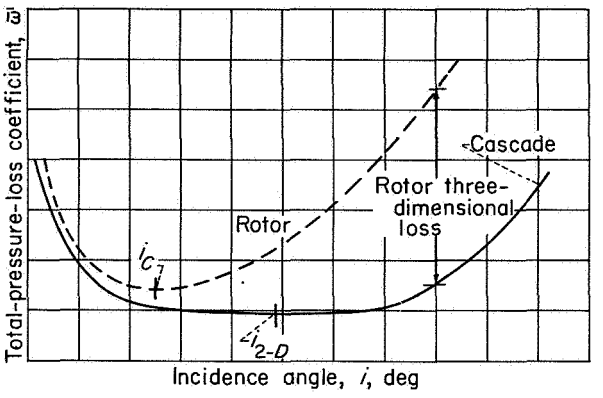

FIGURE 190.—Typical variation of loss with incidence angle for rotor blade element near tip and in two-dimensional cascade for same blade geometry and inlet Mach number.

believed that there will be very little change in the rotor incidence angle for values of Mach number below about 0.4 to 0.5. Extrapolated values of rotor reference incidence angle at zero Mach number appear to be of the order of 0.5° at the hub, 1.5° at the mean radius, and 2.5° at the tip below cascade-rule values.

The double-circular-arc blade element in the compressor rotor exhibits the same general incidence-angle characteristic with Mach number that was observed for sharp-nosed blade sections in the high-speed two-dimensional cascade (ch. VI). As indicated in chaper VI, the increase in reference incidence angle with Mach number is associated with the tendency of the range of the blade to be reduced only on the low-incidence side of the loss curve as the Mach number is increased.

The rotor data for the double-circular-arc section, like those for the 65-(A_{10})-series blades, are comparable with the cascade variations at the mean radius, somewhat higher at the hub at the higher Mach numbers, and noticeably lower at the tip. Apparently, the same type of three-dimensional phenomenon occurs at the tip for both blade shapes.

The available double-circular-arc stator data are too meager for any conclusions.

SUMMARY REMARKS

The variation of reference incidence angle for 65-(A_{10})-series and double-circular-arc blade sections has been presented. No Mach number effect on reference incidence angle was observed for the 65-(A_{10})-series blades for the range of Mach numbers considered. In contrast, the double-circular-arc blade sections exhibit a pronounced variation of reference incidence angle over the range of Mach number investigated. Significant differences between the two-dimensional-cascade data and the rotor data were observed at the compressor tip. In contrast, at the mean radius and hub, the differences in two-dimensional-cascade data and rotor data were relatively small, even though the flow field was three dimensional.

Additional data are required to determine the variation of stator reference incidence angle, particularly for the double-circular-arc airfoil sections. Also, no information has been presented concerning the allowable incidence-angle range for efficient (low-loss) operation and the variation of this range with inlet Mach number. Investigations of these phases of compressor research are very essential to fill gaps in the compressor design and analysis procedures.

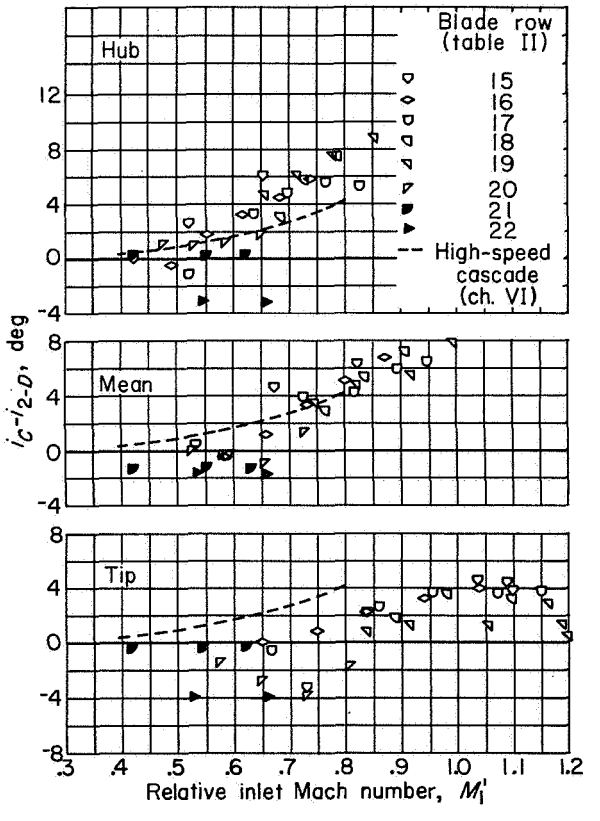

FIGURE 191.—Variation of compressor reference incidence angle minus two-dimensional-cascade-rule incidence angle with relative inlet Mach number for double-circular-arc blade section.

TOTAL-PRESSURE-LOSS ANALYSIS

CORRELATION OF DATA

For two-dimensional-cascade data obtained at low Mach numbers, the values of total-pressure-loss parameter $\bar{\omega} \cos \beta_2/2\sigma$ plotted against diffusion factor (eq. (278)) form essentially a single curve for all cascade configurations. The diffusion-factor correlation of loss parameter was applied to data obtained over a range of Mach numbers from single-stage axial-flow compressors of various geometries and design Mach numbers. Values of total-pressure-loss parameter calculated from single-stage-compressor data are plotted against diffusion factor for the hub, mean, and tip measuring stations in figure 192. Each symbol represents the value of diffusion factor and loss parameter at reference incidence angle at a given tip speed. Also plotted as a dashed curve is the corresponding correlation presented in chapter VI for the low-speed two-dimensional-cascade data. The data of figure 192, which were obtained from the rotor and stator configurations summarized in table II, represent both 65-(A_{10})-series and circular-arc blade sections. The plots of figure 192 essentially represent an elaboration of the loss-diffusion correlations of reference 9.

The most important impression obtained from the rotor data plots is the wide scatter and increasing loss trend with diffusion factor at the rotor tip, while no discernible trend of variation is obtained at the rotor hub and mean radii. For the rotor hub and mean radii, it can be assumed that the rotor blade-element loss parameter follows the cascade variation but at a higher average magnitude. Unfortunately, the range of diffusion factor that could be covered in the compressor tests was not sufficient to determine whether a marked rise in loss is obtained for values of diffusion factor greater than about 0.6 (as in the cascade).

It is apparent from the loss trend and data scatter at the rotor tip that a different loss phenomenon is occurring in the tip region. It is recognized that a part of the scatter is due to the general instrumentation inaccuracy in the highly turbulent tip regions. In view of the usually large radial gradients of loss existing in the blade tip region, small variations in positioning radial survey probes can cause noticeable differences in the computed results. Nevertheless, it is obvious that factors other than the blade-element diffusion are influencing the tip loss. The specific three-dimensional factors or origins involved in the loss rise at the tip are not currently known. The principal conclusion reached from the plot is that the likelihood of a rising loss trend on the rotor tip exists for values of diffusion factor greater than about 0.35.

The stator losses at all radial positions in figure 192 appear to be somewhat higher than those of the two-dimensional cascade, particularly at the higher values of diffusion factor.

SUMMARY REMARKS

Rotor and stator blade-element loss data were correlated by means of the diffusion factor. The losses for stator and rotor blade elements at hub and mean radii were somewhat higher than those for the two-dimensional cascade over the range of diffusion factor investigated. At the rotor tip, the losses were considerably higher at values of diffusion factor above approximately 0.35.

The foregoing blade-element loss analysis is clearly incomplete. The need for additional work is indicated for such purposes as evaluating the origin and magnitude of the tip-region losses. The loading limits for rotors at other than the tip region and for stators at all blade elements have not been determined, because, for the available data, the diffusion factors at reference incidence do not extend to sufficiently high values. Single-stage investigations are needed over the critical range of Reynolds number to determine the effect of Reynolds number on the blade-element loss. It is desirable to isolate the effects of velocity diffusion and shock waves on the loss at high Mach number operation. The loss correlations presented should also be extended so that the data are applicable over a range of incidence angle. This would be of extreme value in the compressor analysis problem.

DEVIATION-ANGLE ANALYSIS

In addition to design information concerning blade-element losses and incidence angle, it is desirable to have a rather complete picture of the air deviation-angle characteristics of axial-flow-compressor blade elements. Therefore, the two-dimensional-cascade correlation results are reviewed and supplemented with annular-cascade data in this section.

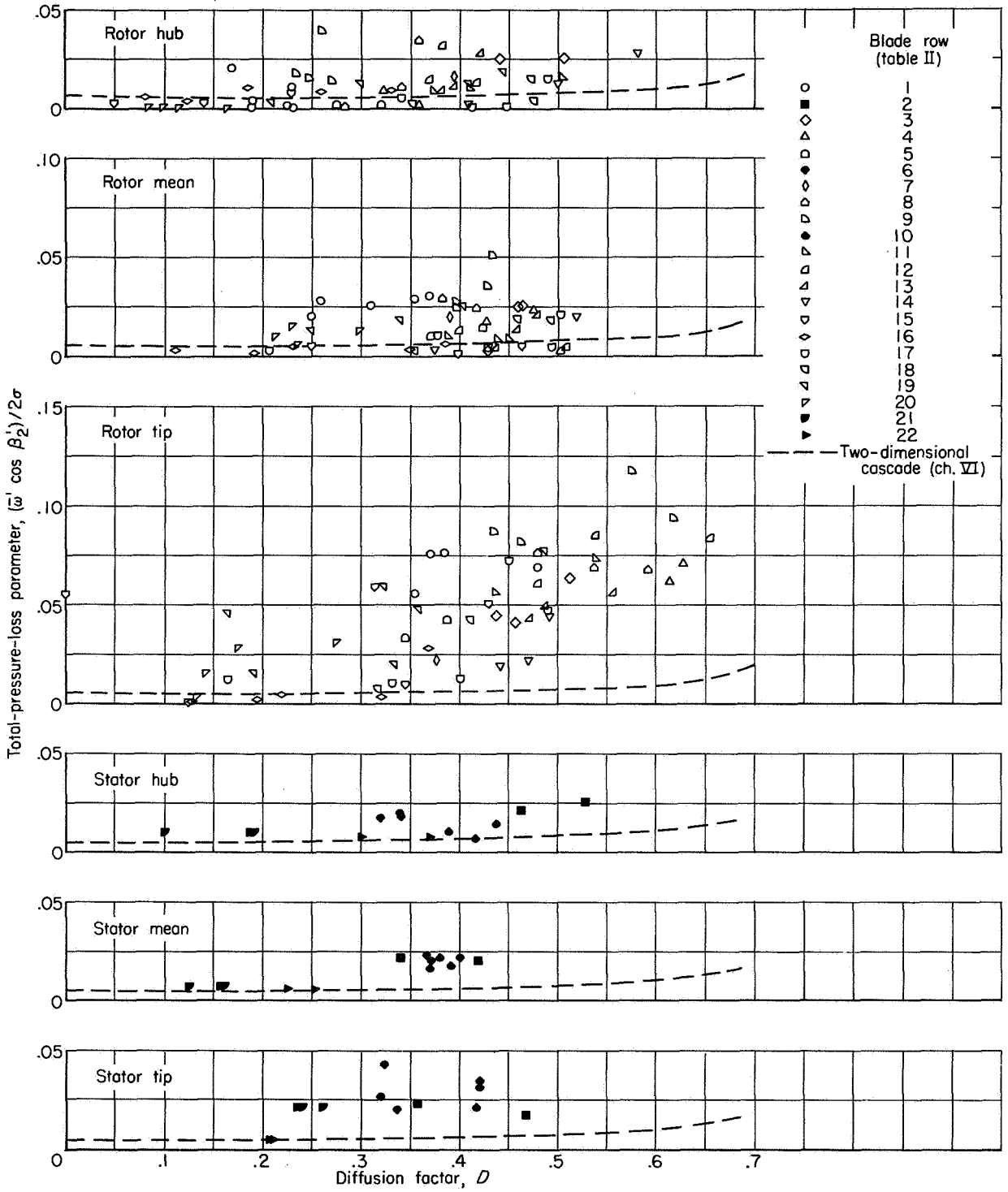

FIGURE 192.—Variation of total-pressure-loss parameter with diffusion factor at reference incidence angle for NACA 65-(A_{10})-series and double-circular-arc blade sections.

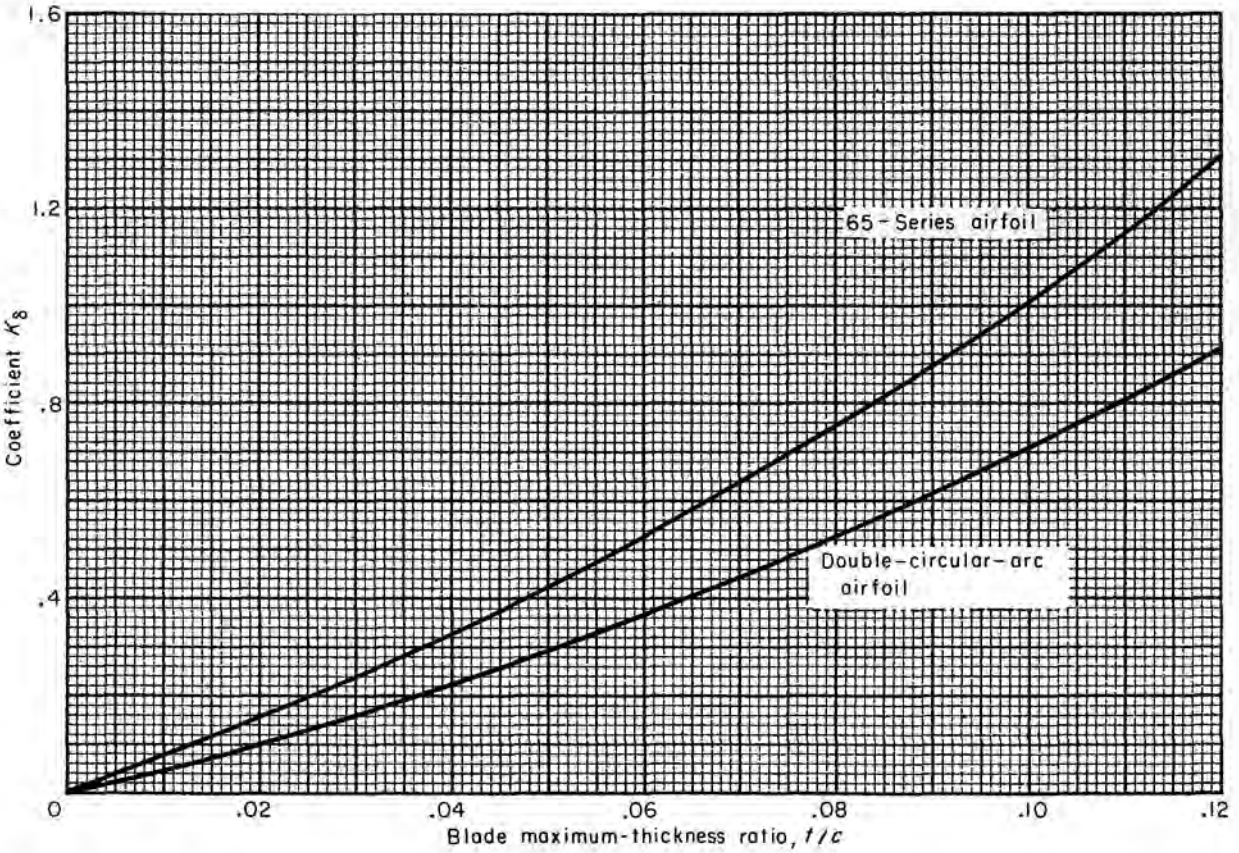

FIGURE 193.—Thickness correction for zero-camber deviation angle (ch. VI).

METHOD OF CORRELATION

As in the analysis of reference incidence angle, the correlation of blade-element deviation angle at reference incidence is presented in terms of a comparison between measured blade-element deviation angle and deviation angle predicted for the element according to the low-speed two-dimensional-cascade correlations of chapter VI. In chapter VI, the low-speed two-dimensional-cascade deviation angle at reference incidence angle is expressed in terms of blade geometry as

$$\delta^\circ_{2-D}=K_\delta(\delta^\circ_o)_{10}+\frac{m}{\sigma^b}\varphi \qquad (280)$$

where K_δ is a function of maximum-thickness-to-chord ratio and thickness distribution, $(\delta^\circ_o)_{10}$ is the zero-camber deviation angle for the 10-percent-thick airfoil section (function of β_1' and σ), m is a function of β_1' for the different basic camber distributions, and b is an exponent that is also a function of β_1'.

As was shown previously, the reference incidence angle of the compressor blade element may differ somewhat from the corresponding two-dimensional reference incidence angle. Since deviation angle will vary with changing reference incidence angle for a given blade geometry (depending on solidity), the two-dimensional deviation angles were corrected to the reference incidence angles of the compressor blade elements. The corrected deviation angle, as suggested in chapter VI, is given by

$$\delta^\circ_{2-D}=K_\delta(\delta^\circ_o)_{10}+\frac{m}{\sigma^b}\varphi+(i_C-i_{2-D})\left(\frac{d\delta^\circ}{di}\right)_{2-D} \qquad (281)$$

where $(d\delta^\circ/di)_{2-D}$ is the slope of the two-dimensional variation of deviation angle with incidence angle at reference incidence. Values of K_δ, $(\delta^\circ_o)_{10}$, m, b, and $(d\delta^\circ/di)_{2-D}$ for the circular-arc and 65-(A_{10})-series blade are repeated in figures 193 to 197 for convenience.

Deviation-angle comparisons for the double-circular-arc blade were also made on the basis of

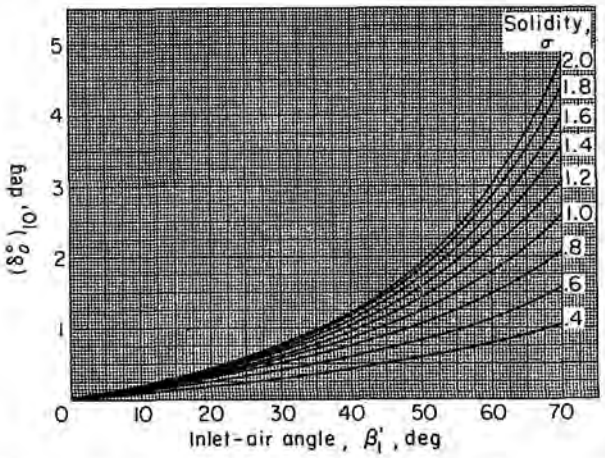

FIGURE 194.—Zero-camber deviation angle for NACA 65-(A_{10})-series and true circular-arc blades of 10-percent maximum-thickness ratio (see fig. 161, ch. VI, for larger print).

Carter's rule for cascade blades (ref. 88):

$$\delta^\circ_{2-D} = \frac{m_c}{\sigma^{0.5}} \varphi \qquad (282)$$

where m_c is a factor that is a function of blade-chord angle (fig. 198).

Carter's rule, which has been used extensively in the design of circular-arc blades, was used as the basis for the more elaborate rule of equation (280). In the calculations, Carter's rule was applied directly to the compressor reference incidence angles.

The comparisons between measured blade-element reference deviation angle δ°_C and predicted two-dimensional deviation angle δ°_{2-D} are expressed in terms of the difference parameter $(\delta^\circ_C - \delta^\circ_{2-D})$ against relative inlet Mach number for the three radial positions at hub, tip, and mean radius.

NACA 65-(A_{10})-series blades.—Curves of compressor deviation angle minus cascade-rule deviation angle (eq. (281)) for the 65-(A_{10})-series airfoil for both rotors and stators are plotted against relative inlet Mach number for the hub, mean, and tip radial positions in figure 199(a). All values of deviation angle correspond to those at compressor reference incidence angle. As in the case of the incidence-angle and loss correlations, there is considerable scatter of data, particularly in the hub and tip regions. Some of the scatter is believed due to the effects of three-dimensional flows and changes in axial velocity ratio across the element, but perhaps the most important factors are instrumentation differences and errors. It is generally recognized that it is difficult to measure compressor air angles with an accuracy better than about $\pm 1°$ to 1.5°. The correlations must therefore be evaluated on an average or trend basis.

The correlation of rotor data in the mean-radius region is fairly good; axial velocity ratio varied

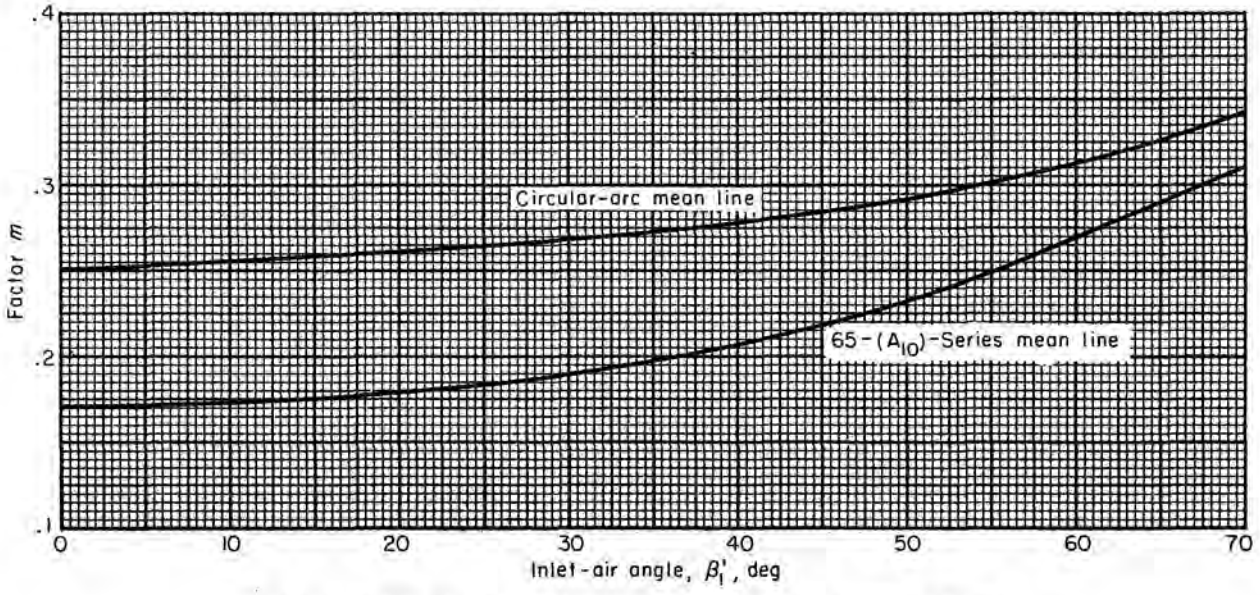

FIGURE 195.—Factor m in deviation-angle rule (see figs. 163 and 166).

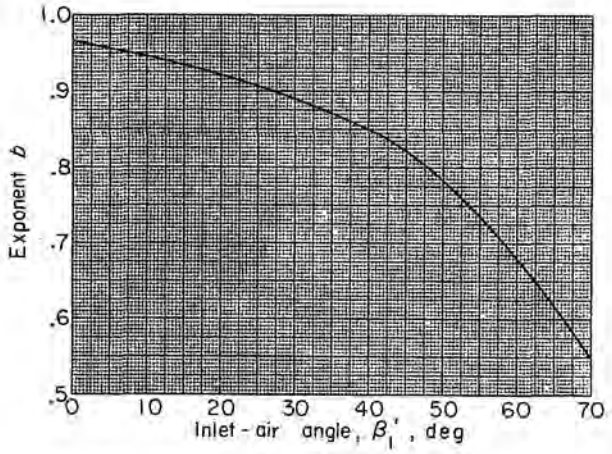

FIGURE 196.—Solidity exponent b in deviation-angle rule (see fig. 164, ch. VI, for larger print).

from about 0.9 to 1.10. On the average, the rotor mean-radius deviation angles are about 0.5° less than the cascade values. These results agree with previous experience (refs. 218 and 219), which indicated rotor turning angles approximately 1° greater (i.e., deviation angles 1° less) than the two-dimensional-cascade results. If data points for the rotor tip having axial velocity ratios less than 0.8 are neglected, the average deviation angle is about 0.5° less than the cascade value. Axial velocity ratio for the tip-region unflagged data varied between 0.8 and 1.05. For the hub, on the average, the blade-element deviation angles were about 1.0° greater than the corresponding two-dimensional values. Hub axial velocity ratios varied between 1.0 and 1.3. As in the two-dimensional cascade (ch. VI), no Mach number effect on deviation angle is indicated over the range of Mach number investigated for all three regions.

For the stator mean-radius ($V_{z,2}/V_{z,1}$=1.0 to 1.1) and hub-radius ($V_{z,2}/V_{z,1}$=0.85 to 1.05) regions, the average deviation angles are both about 1.0° lower than the corresponding two-dimensional values. At the stator tip, the average blade-element value is indicated to be about 4° less than the two-dimensional value. However, these data all have high axial velocity ratios (from 1.1 to 1.5). It is expected that, on the basis of constant axial velocity, the probable average blade-element deviation angles at the stator tip might be several degrees closer to the two-dimensional values. (Increasing axial velocity ratio at essentially constant circulation for the stator tends to decrease deviation angle.) As in the case of the rotor, no essential variation of deviation angle with Mach number is detected for the stator within the range of Mach numbers investigated.

Double-circular-arc blade.—Blade-element and two-dimensional-cascade deviation angles (eq. (281)) obtained for the double-circular-arc blade are compared in figure 199(b). The scatter of data is generally less than for the 65-(A_{10})-series blades, partly because of the generally more accurate measurements taken in these investigations (all are more recent than the data of fig. 199(a)).

On the average, at the lower Mach numbers the blade-element deviation angles were about 1.5° less than the two-dimensional values at the tip, 1.0° greater at the hub, and equal to the two-dimensional values at the mean region. Ranges of axial velocity ratio covered for the data were 0.85 to 1.05 at the tip, 0.95 to 1.5 at the hub, and 0.90 to 1.15 at the mean radius. A slightly increasing trend of variation with inlet Mach number may be indicated at the mean radius and possibly also at the hub.

The double-circular-arc stator data available (solid symbols) are too limited to permit any reliable conclusions to be drawn. It appears, however, that at the stator mean radius, the blade-element deviation angles may be about 0.5° less than the two-dimensional-cascade values. This is essentially the same trend observed for the 65-(A_{10})-series stators at mean radius in figure 199(a). Blade-element deviation angles appear to be greater at the tip and smaller at the hub

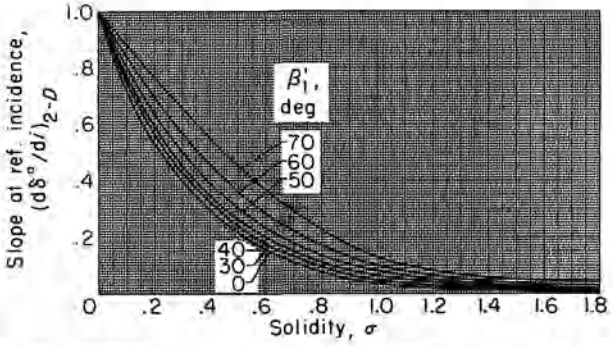

FIGURE 197.—Deviation-angle slope $(d\delta^\circ/di)_{2\text{-}D}$ at reference incidence angle (see fig. 177, ch. VI, for larger print).

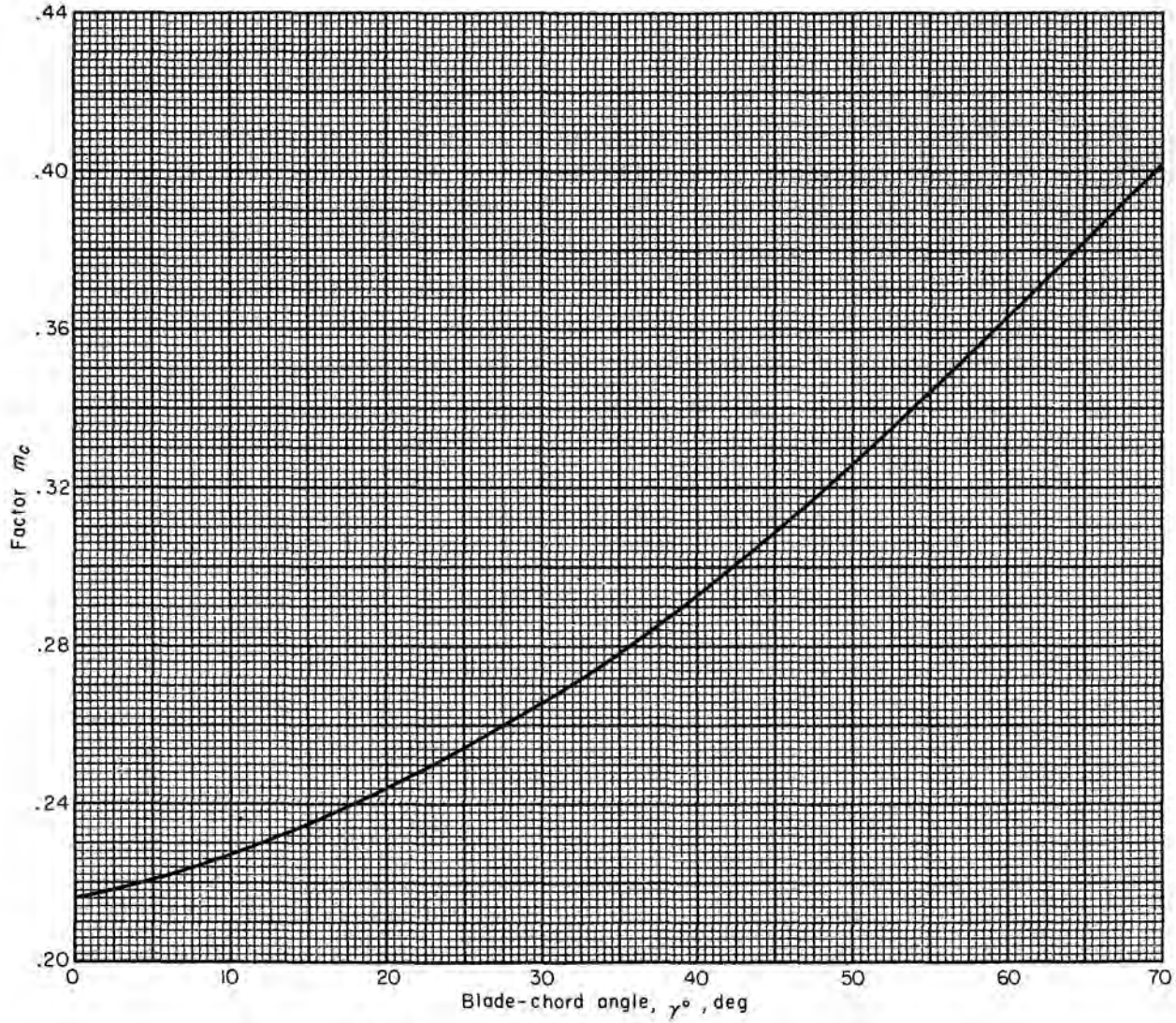

FIGURE 198.—Variation of m_c for circular-arc compressor cascades (ref. 88).

than the two-dimensional values. Ranges of axial velocity ratio were 1.0 to 1.25 at the tip, 0.95 to 1.27 at the mean radius, and 0.9 to 1.30 at the hub.

Blade-element deviation angles and two-dimensional values predicted by Carter's rule (eq. 282)) are compared in figure 200. Since Carter's rule results in values of two-dimensional deviation angle between 0.5° and 1.0° smaller than those obtained from the modified rule of equation (281) for the range of blade-element geometries included in the data, the agreement with the blade-element data remains quite good.

SUMMARY REMARKS

From the comparisons of measured and predicted reference deviation angles for the NACA 65-(A_{10})-series and double-circular-arc blades, it was found that the rules derived from two-dimensional-cascade data can satisfactorily predict the compressor reference blade-element deviation angle in the rotor and stator mean-radius regions for the blade configurations presented. Larger differences between rule and measured values were observed in the hub and tip regions. These differences can be attributed to the effects of three-dimensional flow, differences

in axial velocity ratio, and measurement inaccuracy. As in the cascade, essentially constant deviation angle with Mach number was indicated for the Mach number range covered. Additional stator blade-element data, particularly for the double-circular-arc blade, are required to establish the stator correlations more firmly.

APPLICATION TO DESIGN

DESIGN PROCEDURE

The foregoing correlations provide a means of establishing the reference incidence angle and estimating the corresponding deviation angle and total-pressure loss for rotor and stator blade elements of compressor designs similar to those covered in the analysis. This is accomplished by establishing deduced curves of compressor blade-element incidence-angle and deviation-angle corrections for the low-speed two-dimensional-cascade rules of chapter VI. Reference incidence and deviation angles for the compressor blade element are then given by

$$i_C = i_{2-D} + (i_C - i_{2-D}) \quad (283)$$

and

$$\delta_C^\circ = \delta_{2-D}^\circ + (\delta_C^\circ - \delta_{2-D}^\circ) \quad (284)$$

where i_{2-D} and δ_{2-D}° are given by equations (279) and by (281) or (282), respectively. Curves of incidence-angle and deviation-angle corrections deduced from the rotor blade-element data of figures 189, 191, 199, and 200 are shown as func-

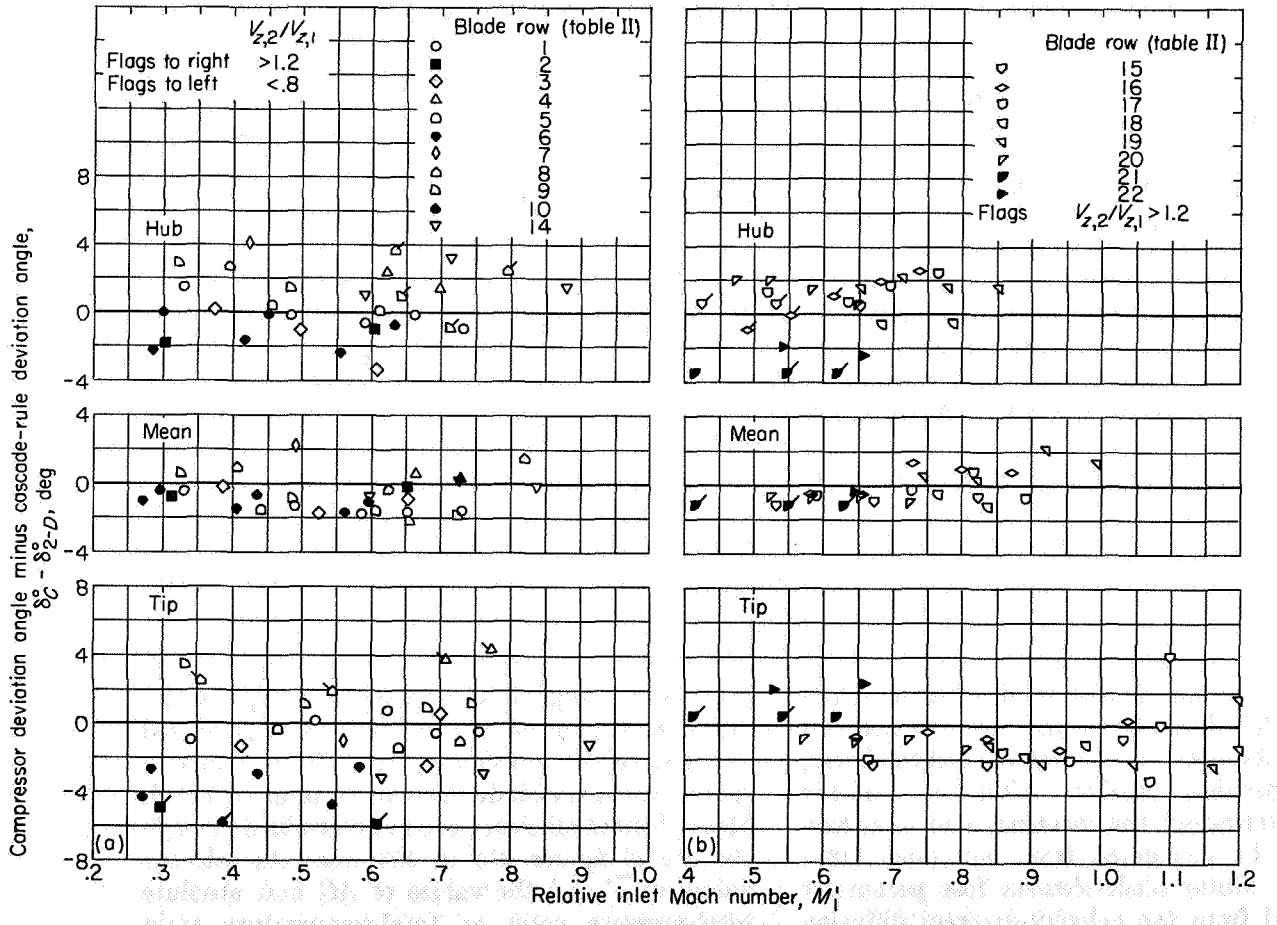

(a) 65-(A_{10})-series blade section. (b) Circular-arc blade section.

FIGURE 199.—Variation of compressor deviation angle minus two-dimensional-cascade deviation angle at compressor reference incidence angle with relative inlet Mach number.

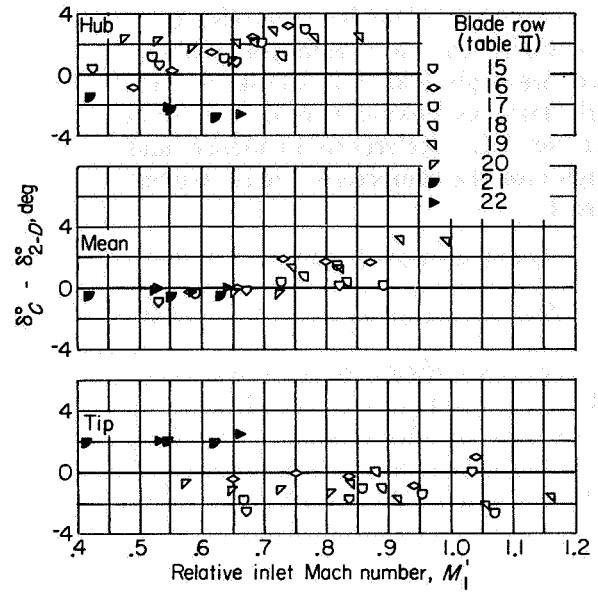

FIGURE 200.—Variation of compressor deviation angle minus deviation angle predicted by Carter's rule at reference incidence angle with relative inlet Mach number for double-circular-arc blade section.

tions of relative inlet Mach number for several radial positions along the blade height in figures 201 and 202. The curves in figures 201 and 202 are faired average values of the data spread and, strictly speaking, represent bands of values. In view of the very limited data available, compressor correction curves could not reliably be established for the stator deviation and incidence angles.

Establishing single deduced blade-element loss curves at reference incidence angle is a difficult task because of the scatter of the experimental data, especially in the rotor tip region. Nevertheless, for completeness, in order to illustrate the prediction procedures, curves of average total-pressure-loss parameter as a function of diffusion factor obtained from the data of figure 192 are shown in figure 203 for rotor and stator. The shaded part of the curve indicates the possible band of values obtainable at the rotor tip.

The procedure involved in determining blade-element camber angle and efficiency at reference incidence angle for a compressor design based on the blade-row velocity diagram and the foregoing correlation curves is now indicated. The desired blade-element turning angle $\Delta\beta'$ and relative inlet Mach number M_1' are obtained from the design velocity diagram. Camber and turning angles are related by the equation

$$\varphi=\beta_1'-\beta_2'+\delta^\circ-i \tag{285}$$

Compressor blade-element incidence angles (eqs. (279) and (283)) and deviation angles (eqs. (281) and (284)) are given by

$$i_C=K_i(i_o)_{10}+n\varphi+(i_C-i_{2-D}) \tag{286}$$

$$\delta_C^\circ=K_\delta(\delta_o^\circ)_{10}+\frac{m}{\sigma^b}\varphi+(i_C-i_{2-D})\left(\frac{d\delta^\circ}{di}\right)_{2-D}+(\delta_C^\circ-\delta_{2-D}^\circ) \tag{287}$$

Substituting equations (286) and (287) into equation (285) and rearranging terms yield

$$\varphi=\frac{\Delta\beta'+(\delta_C^\circ-\delta_{2-D}^\circ)-(i_C-i_{2-D})\left[1.0-\left(\frac{d\delta^\circ}{di}\right)_{2-D}\right]-K_i(i_o)_{10}+K_\delta(\delta_o^\circ)_{10}}{1-\frac{m}{\sigma^b}+n} \tag{288}$$

All terms on the right side of equation (288) can be determined from the velocity-diagram properties, the specified blade shape and thickness, and the specified solidity. After the camber angle is determined, the incidence and deviation angles can be calculated from equations (286) and (287). Rotor blade-element loss parameter is estimated from the velocity-diagram diffusion factor and the curves of figure 203. The total-pressure-loss coefficient $\bar{\omega}'$ is then readily obtained from the blade-element solidity and relative air outlet angle. Blade-element efficiencies for the rotor and complete stage can be computed by means of the techniques and equations presented in the appendix to this chapter. If the change in radius across the blade row can be assumed small, blade-element efficiency can be determined through the use of figures 204 to 206 from the selected values of $\bar{\omega}'$ and the values of M_1' and absolute total-pressure ratio or total-temperature ratio obtained from the velocity diagram.

The foregoing procedure can best be illustrated by a numerical example. Suppose the following specified rotor design values represent typical

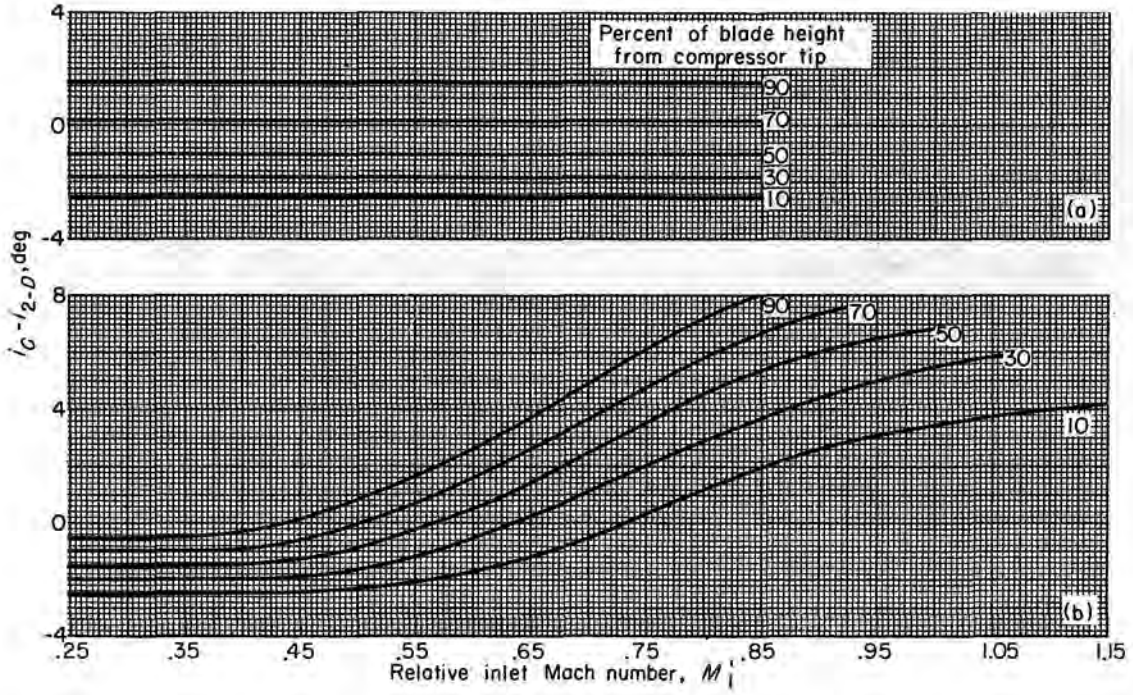

(a) NACA 65–(A_{10})-series blades.
(b) Double-circular-arc blades.

FIGURE 201.—Deduced variation of average rotor reference incidence angle minus low-speed two-dimensional-cascade-rule reference incidence angle with relative inlet Mach number.

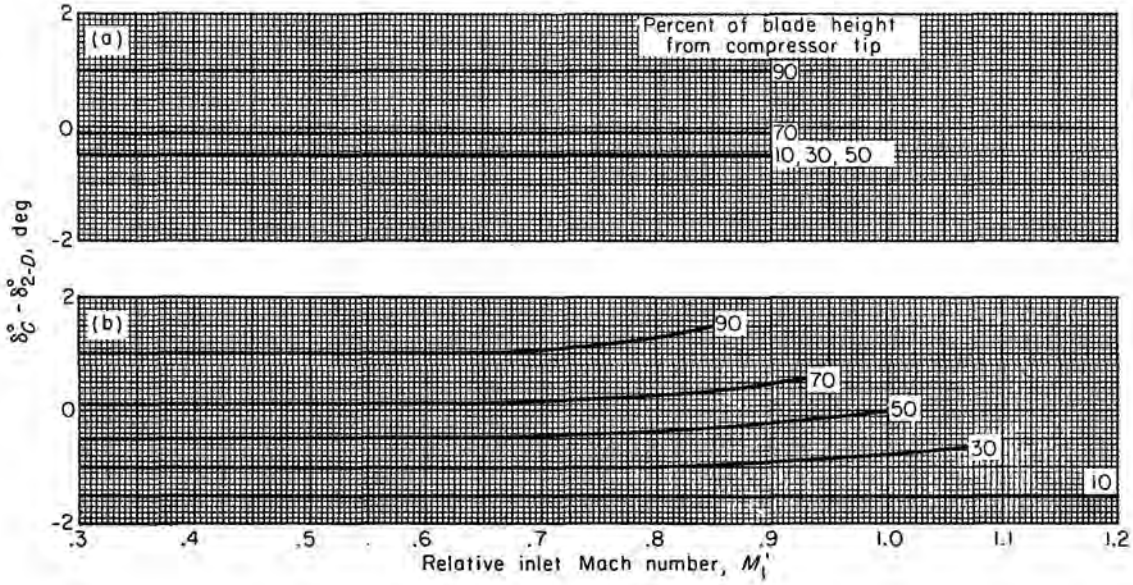

(a) NACA 65–(A_{10})-series blades.
(b) Double-circular-arc blades.

FIGURE 202.—Deduced variation of average rotor deviation angle minus low-speed two-dimensional-cascade-rule deviation angle at compressor reference incidence angle with relative inlet Mach number.

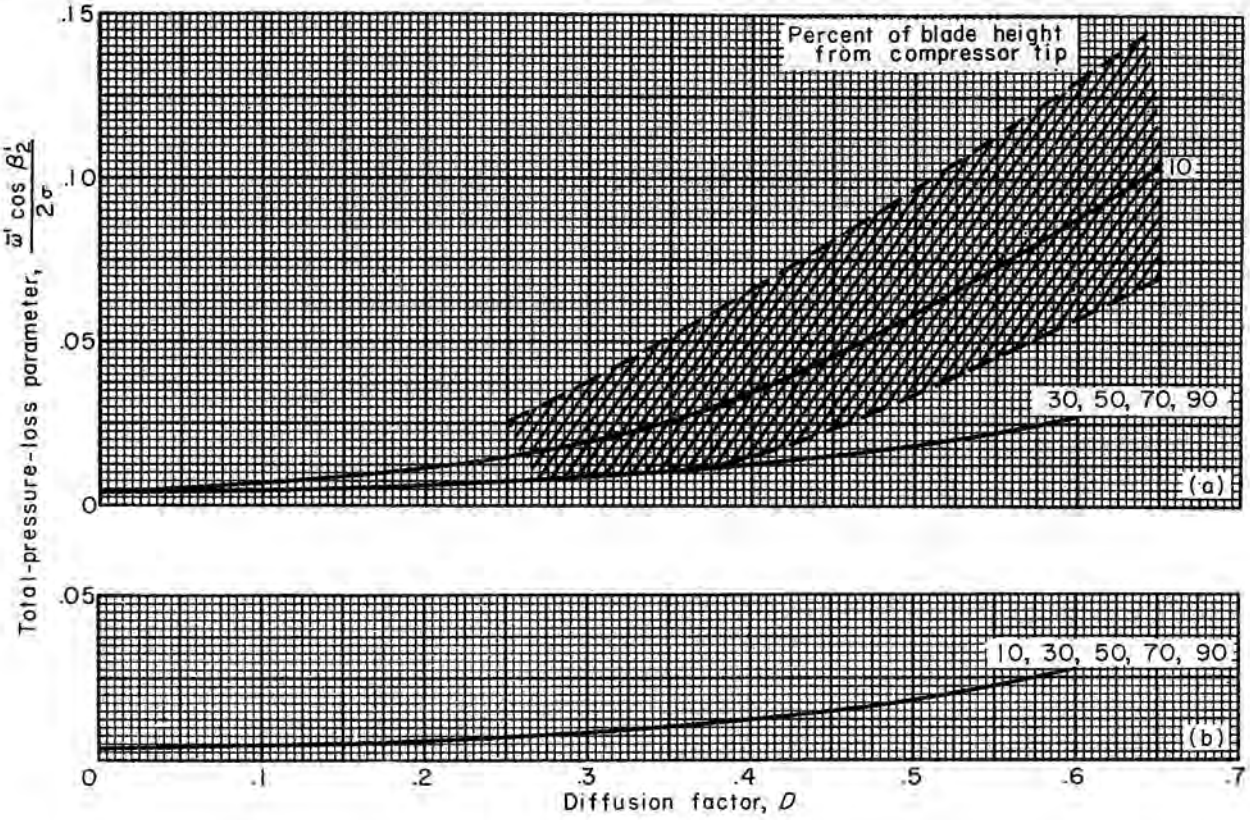

(a) Rotor.
(b) Stator.

FIGURE 203.—Deduced variation of total-pressure-loss parameter with diffusion factor at reference incidence angle for NACA 65-(A_{10})-series and double-circular-arc blades.

values at 10 percent of the passage height from the compressor tip:

$\beta_1'=56.9°$
$\Delta\beta'=10.9°$
$M_1'=1.1$
$D=0.35$
$\frac{T_2}{T_1}=1.091$
} obtained from velocity-diagram calculations (ch. VIII)

$\sigma=1.0$
$t/c=0.06$
} assumed values

The problem is to find the camber, incidence, and deviation angles and the total-pressure-loss coefficient for a double-circular-arc airfoil section that will establish the velocity-diagram values.

(1) From the value of M_1' and figures 201(b) and 202(b),

$$i_C-i_{2-D}=4.0° \qquad \delta_C°-\delta_{2-D}°=-1.5°$$

(2) From the values of β_1', σ, and t/c and figures 186 to 188 and 193 to 197,

$K_t=0.54$ $(i_o)_{10}=4.4°$ $n=-0.22$ $K_s=0.37$

$(\delta_o°)_{10}=1.6°$ $m=0.305$ $b=0.714$ $\left(\frac{d\delta°}{di}\right)_{2-D}=0.095$

(3) When the values of steps (1) and (2) are substituted in equation (288), the value of blade camber $\varphi=8.4°$.

(4) From equations (286) and (287), $i_C=4.5$ and $\delta_C°=2.0$.

(5) For calculation of the total-pressure-loss coefficient, the diffusion factor (0.35) and figure

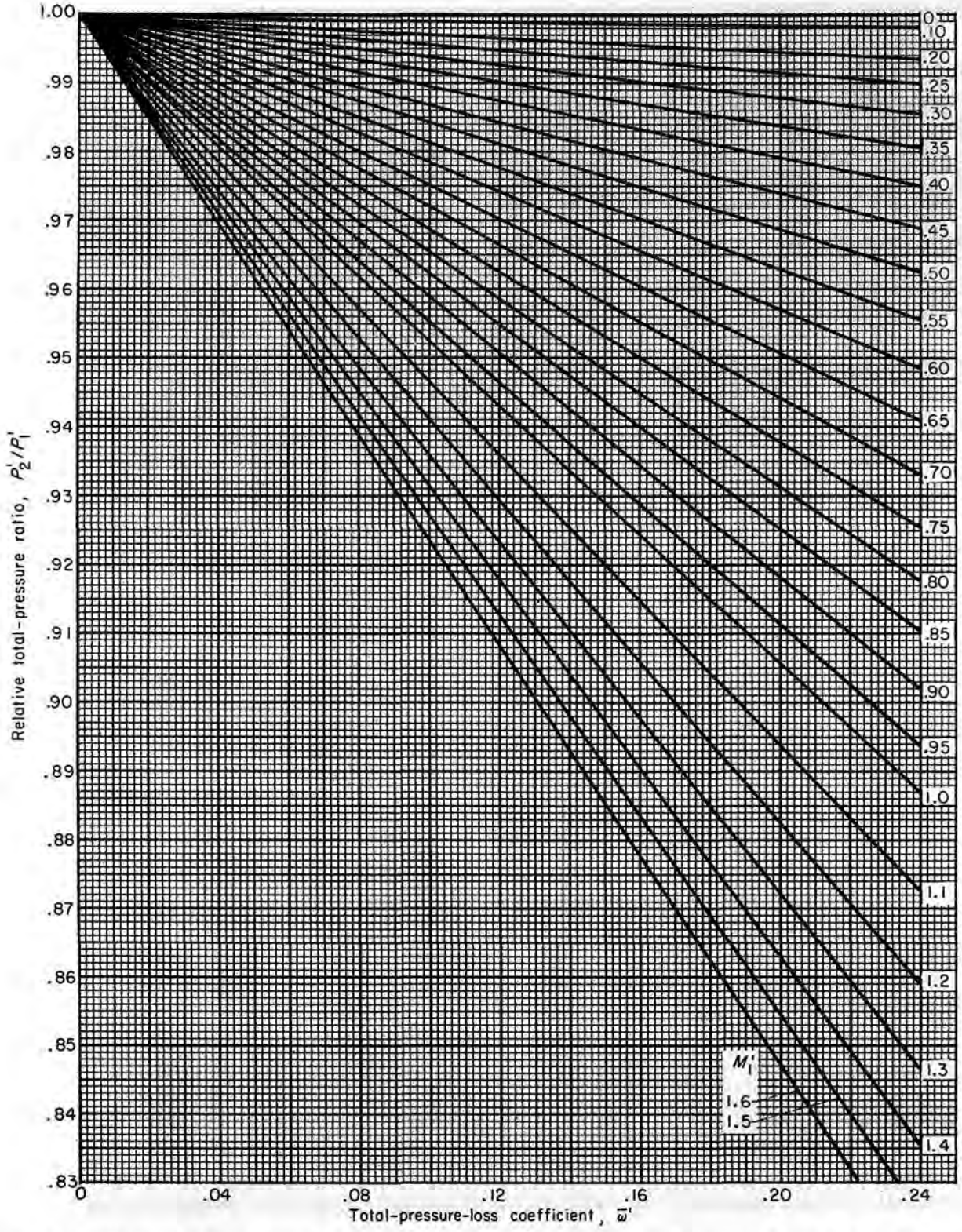

FIGURE 204.—Variation of rotor relative total-pressure ratio with total-pressure-loss coefficient and inlet Mach number.

$$\bar{\omega}'=\left(1-\frac{P_2'}{P_1'}\right)\Big/\left(1-\left\{1\Big/\left[1+\frac{\gamma-1}{2}(M_1')^2\right]^{\frac{\gamma}{\gamma-1}}\right\}\right).$$

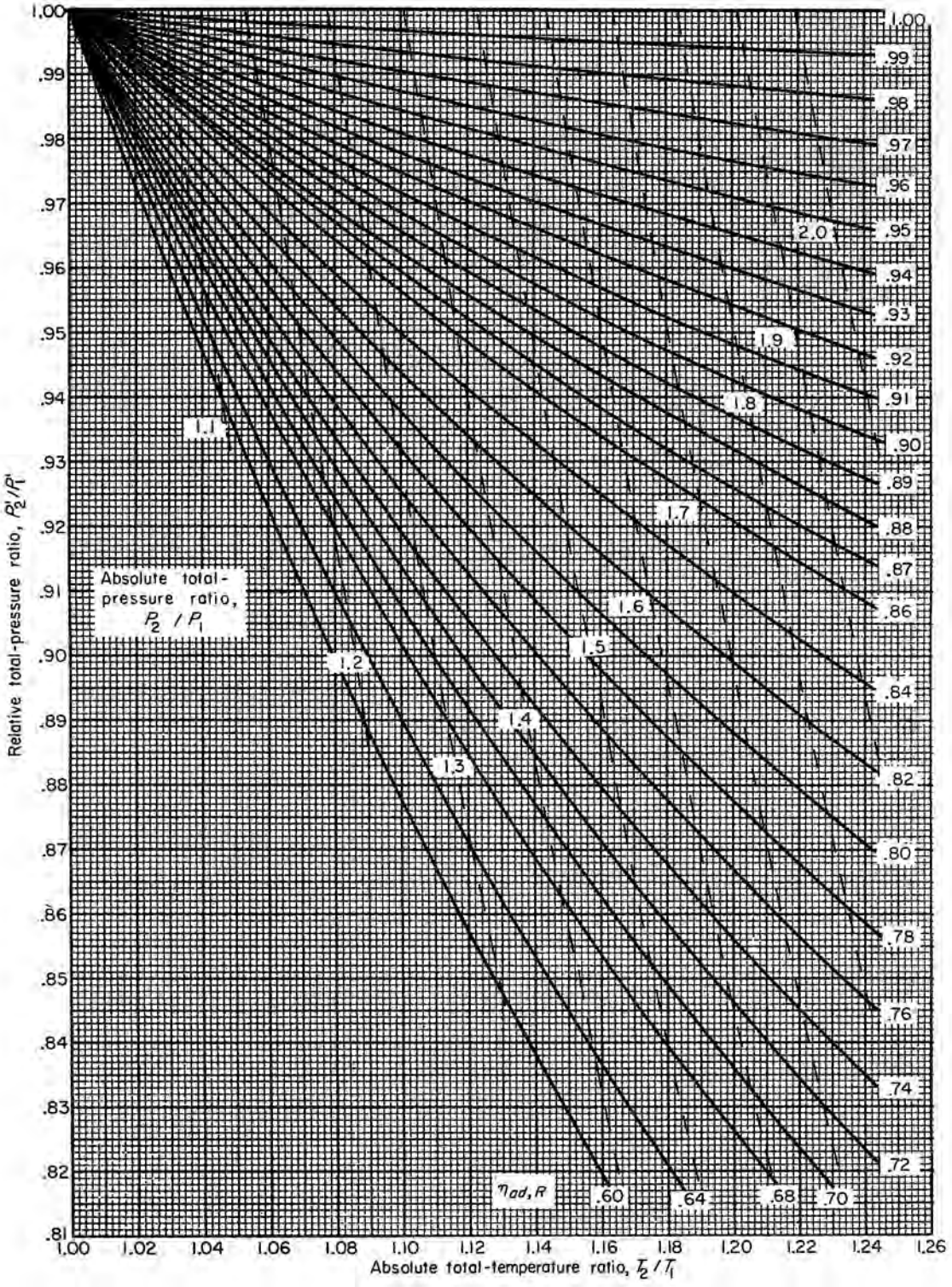

FIGURE 205.—Variation of relative total-pressure ratio with absolute total-temperature ratio and efficiency for rotor

$$\eta_{ad}=\left\{\left[\frac{P_2'}{P_1'}\left(\frac{T_2}{T_1}\right)\right]^{\frac{\gamma-1}{\gamma}}-1\right\}\Big/\left(\frac{T_2}{T_1}-1\right).$$

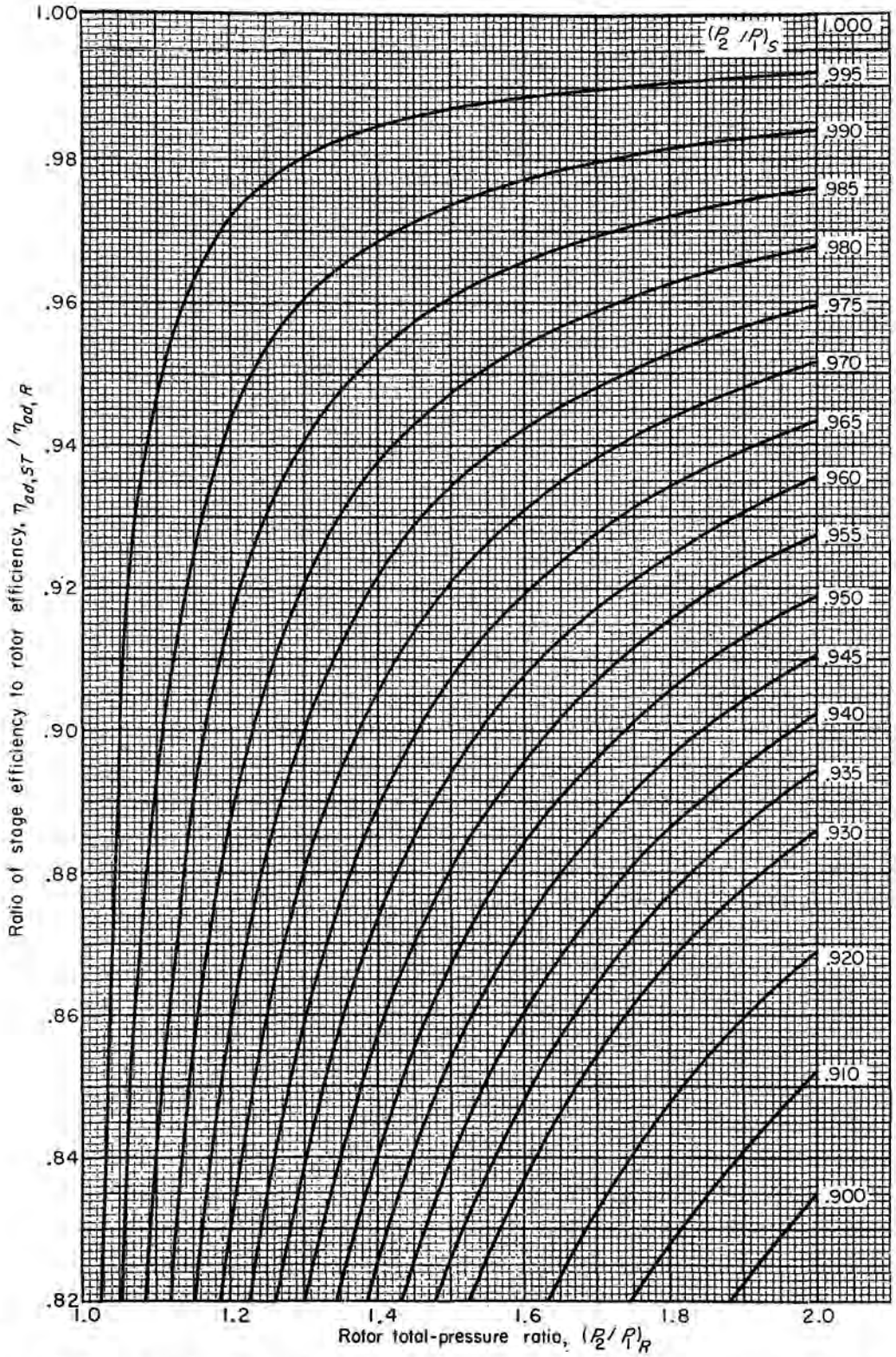

FIGURE 206.—Variation of ratio of stage to rotor efficiency with rotor absolute total-pressure ratio as function of stator recovery factor.

203(a) yield a value of 0.025 for the loss parameter $(\bar{\omega}' \cos \beta_2')/2\sigma$, and

$$\beta_2' = \beta_1' - \Delta\beta' = 56.9 - 10.9 = 46.0°$$

$$\cos \beta_2' = 0.6947$$

Therefore,

$$\bar{\omega}' = \left(\frac{\bar{\omega}' \cos \beta_2'}{2\sigma}\right) \frac{2\sigma}{\cos \beta_2'} = \frac{0.025 \times 2}{0.6947} = 0.072$$

(6) For a negligible change in radius across the blade element, the following values can be found from figures 204 and 205:

$$\frac{P_2'}{P_1'} = 0.962 \qquad \eta_{ad} = 0.87 \qquad \frac{P_2}{P_1} = 1.31$$

The preceding example has been carried out for a typical transonic rotor blade section. A similar procedure can be used for stator blade sections when adequate blade-element data become available.

SUMMARY REMARKS

The foregoing procedures and data apply only to the reference point (i.e., the point of minimum loss) on the general loss-against-incidence-angle variation for a given blade element. The reference minimum-loss incidence angle, which was established primarily for purposes of analysis, is not necessarily to be considered as a recommended design point for compressor application. The selection of the best incidence angle for a particular blade element in a multistage-compressor design is a function of many considerations, such as the location of the blade row, the design Mach number, and the type and application of the design. However, at transonic inlet Mach number levels, the point of minimum loss may very well constitute a desired design setting.

At any rate, the establishment of flow angles and blade geometry at the reference incidence angle can serve as an anchor point for the determination of conditions at other incidence-angle settings. For deviation-angle and loss variations over the complete range of incidence angles, reference can be made to available cascade data. Such low-speed cascade data exist for the NACA 65-(A_{10})-series blades (ref. 54).

It is recognized that many qualifications and limitations exist in the use of the foregoing design procedure and correlation data. For best results, the application of the deduced variations should be restricted to the range of blade geometries (camber, solidity, etc.) and flow conditions (inlet Mach number, Reynolds number, axial velocity ratio, etc.) considered in the analysis. In some cases for compressor designs with very low turning angle, the calculated camber angle may be negative. For these cases it is recommended that a zero-camber blade section be chosen and the incidence angle selected to satisfy the turning-angle requirements. The data used in the analysis were obtained for the most part from typical experimental inlet stages with essentially uniform inlet flow. Nevertheless, such data have been used successfully in the design of the latter stages of multistage compressors. It should also be remembered that the single curves appearing in the deduced variations represent essentially average or representative values of the experimental data spread. Also, in some cases, particularly for the stator, the available data are too limited to establish reliable correlations. Considerable work must yet be done to place the design curves on a firmer and wider basis. The design procedures established and trends of variation determined from the data, however, should prove useful in compressor blade-element design.

APPENDIX

EQUATIONS FOR BLADE-ELEMENT EFFICIENCY

By definition, for a complete stage consisting of inlet guide vanes, rotor, and stator, the adiabatic temperature-rise efficiency of the flow along a stream surface is given by

$$\eta_{ad,\,ST}=\frac{\left(\frac{P_2}{P_1}\right)_{ST}^{\frac{\gamma-1}{\gamma}}-1}{\left(\frac{T_2}{T_1}\right)_{ST}-1}=\frac{\left[\left(\frac{P_2}{P_1}\right)_{GV}\left(\frac{P_2}{P_1}\right)_{R}\left(\frac{P_2}{P_1}\right)_{S}\right]^{\frac{\gamma-1}{\gamma}}-1}{\left(\frac{T_2}{T_1}\right)_{R}-1} \tag{A1}$$

From the developments of reference 7 (eq. (B8) in the reference), the absolute total-pressure ratio across a blade row P_2/P_1 can be related to the relative total-pressure ratio across the blade row P_2'/P_1' according to the relation

$$\frac{P_2}{P_1}=\frac{\left(\frac{P_2'}{P_1'}\right)}{\left(\frac{P_2'}{P_1'}\right)_{id}}\left(\frac{T_2}{T_1}\right)^{\frac{\gamma}{\gamma-1}} \tag{A2}$$

where $(P_2'/P_1')_{id}$ is the ideal (no loss) relative total-pressure ratio. The relative total-pressure ratio is also referred to as the blade-row recovery factor. For stationary blade rows (i.e., inlet guide vanes and stators), $(P_2'/P_1')_{id}$ is equal to 1.0. For rotors, the ideal relative total-pressure ratio (eq. (B4) of ref. 9) is given by

$$\left(\frac{P_2'}{P_1'}\right)_{id}=\left\{1+\frac{\gamma-1}{2}M_T^2\left[1-\left(\frac{r_1}{r_2}\right)^2\right]\right\}^{\frac{\gamma}{\gamma-1}} \tag{A3}$$

in which M_T is equal to the ratio of the outlet element wheel speed to the inlet relative stagnation velocity of sound $(\omega r_2/a'_{a,1})$, and r_1/r_2 is the ratio of inlet to outlet radius of the streamline across the blade element. (For a flow at constant radius (cylindrical flow), $(P_2'/P_1')_{id}$ is equal to 1.0.) Thus, from equations (A1) and (A2),

$$\eta_{ad,\,ST}=\frac{\left[\left(\frac{P_2'}{P_1'}\right)_{GV}\frac{\left(\frac{P_2'}{P_1'}\right)_{R}}{\left(\frac{P_2'}{P_1'}\right)_{R,\,id}}\left(\frac{T_2}{T_1}\right)_{R}^{\frac{\gamma}{\gamma-1}}\left(\frac{P_2'}{P_1'}\right)_{S}\right]^{\frac{\gamma-1}{\gamma}}-1}{\left(\frac{T_2}{T_1}\right)_{R}-1} \tag{A4}$$

For the rotor alone, the blade-element efficiency is given by

$$\eta_{ad,\,R}=\frac{\left[\frac{\left(\frac{P_2'}{P_1'}\right)_{R}}{\left(\frac{P_2'}{P_1'}\right)_{R,\,id}}\left(\frac{T_2}{T_1}\right)^{\frac{\gamma}{\gamma-1}}\right]^{\frac{\gamma-1}{\gamma}}-1}{\left(\frac{T_2}{T_1}\right)_{R}-1} \tag{A5}$$

From equation (B3) of reference 9, the loss coefficient of the rotating blade row (based on inlet dynamic pressure) is given by

$$\bar{\omega}'=\left(\frac{P_2'}{P_1'}\right)_{id}\left\{\frac{1-\frac{\left(\frac{P_2'}{P_1'}\right)}{\left(\frac{P_2'}{P_1'}\right)_{id}}}{1-\left[\frac{1}{1+\frac{\gamma-1}{2}(M_1')^2}\right]^{\frac{\gamma}{\gamma-1}}}\right\} \tag{58}$$

For any blade element, then, from equation (58),

$$\frac{P_2'}{P_1'}=\left(\frac{P_2'}{P_1'}\right)_{id}-\bar{\omega}'\left\{1-\left[\frac{1}{1+\frac{\gamma-1}{2}(M_1')^2}\right]^{\frac{\gamma}{\gamma-1}}\right\} \tag{A6}$$

The relations presented in equations (A4), (A5), and (A6) indicate that four quantities are required for the determination of the blade-element efficiency across the rotor or stage: the rotor absolute total-temperature ratio, the relative total-pressure-loss coefficient (based on inlet dynamic pressure), the relative inlet Mach number, and the ideal relative total-pressure ratio. Thus, the blade-element efficiencies for a given stage velocity diagram can be calculated if the loss coefficients of the blade elements in the various blade rows can be estimated.

For simplicity in the efficiency-estimation procedure, effects of changes in radius across the blade row can be assumed small (i.e., $r_1=r_2$), so that the ideal relative pressure ratio is equal to

unity. Then, equations (A4), (A5), and (A6) become, respectively,

$$\eta_{ad,\,ST}=\frac{\left[\left(\frac{P_2'}{P_1'}\right)_{GV}\left(\frac{P_2'}{P_1'}\right)_R\left(\frac{T_2}{T_1}\right)_R^{\frac{\gamma}{\gamma-1}}\left(\frac{P_2'}{P_1'}\right)_S\right]^{\frac{\gamma-1}{\gamma}}-1}{\left(\frac{T_2}{T_1}\right)_R-1} \tag{A7}$$

$$\eta_{ad,\,R}=\frac{\left[\left(\frac{P_2'}{P_1'}\right)_R\left(\frac{T_2}{T_1}\right)_R^{\frac{\gamma}{\gamma-1}}\right]^{\frac{\gamma-1}{\gamma}}-1}{\left(\frac{T_2}{T_1}\right)_R-1} \tag{A8}$$

and

$$\frac{P_2'}{P_1'}=1-\bar{\omega}'\left\{1-\left[\frac{1}{1+\frac{\gamma-1}{2}(M_1')^2}\right]^{\frac{\gamma}{\gamma-1}}\right\} \tag{A9}$$

For purposes of rapid calculation and preliminary estimates, the efficiency relations are expressed in chart form in figures 204 to 206. The relation among relative recovery factor, blade-element loss coefficient, and inlet Mach number (eq. (A9)) is presented in figure 24. A chart for determining rotor blade-element efficiency from relative recovery factor and absolute total-temperature ratio (eq. (A8)) is given in figure 205. Lines of constant rotor absolute total-pressure ratio are also included in the figure. Figure 206 presents the ratio of stage efficiency to rotor efficiency for various stator or guide-vane recovery factors. The ratio of stage efficiency to rotor efficiency is obtained from equation (A1) in terms of rotor absolute total-pressure ratio as

$$\frac{\eta_{ad,\,ST}}{\eta_{ad,\,R}}=\frac{\left[\left(\frac{P_2}{P_1}\right)_R\left(\frac{P_2}{P_1}\right)_{GV}\left(\frac{P_2}{P_1}\right)_S\right]^{\frac{\gamma-1}{\gamma}}-1}{\left(\frac{P_2}{P_1}\right)_R^{\frac{\gamma-1}{\gamma}}-1} \tag{A10}$$

The charts are used as follows: For known or estimated values of rotor total-pressure-loss coefficient $\bar{\omega}'$ and relative inlet Mach number M_1' of the element, the corresponding value of relative recovery factor P_2'/P_1' is determined from figure 204. From the value of rotor-element absolute total-temperature ratio T_2/T_1 (obtained from calculations of the design velocity diagram) and the value of (P_2'/P_1') obtained from figure 204, the rotor-element efficiency is determined from figure 205. Rotor absolute total-pressure ratio can also be determined from the dashed lines in figure 205.

If inlet guide vanes and stators are present, the respective recovery factors of each blade row are first obtained from figure 204. The product of the two recovery factors is then calculated and used in conjunction with the rotor absolute total-pressure ratio in figure 206 to determine the ratio of stage efficiency to rotor efficiency. A simple multiplication then yields the magnitude of the stage efficiency along the element stream surface.

The charts can also be used to determine gross or mass-averaged efficiencies through the use of over-all loss terms. Furthermore, the charts can be used for the rapid determination of relative total-pressure-loss coefficient from known values of efficiency, pressure ratio, and inlet Mach number on an element or gross basis.

CHAPTER VIII

DESIGN VELOCITY DISTRIBUTION IN MERIDIONAL PLANE

By CHARLES C. GIAMATI, JR., and HAROLD B. FINGER

A discussion is presented of the general flow equations and methods to be used in determining the radial distributions of flow in the meridional (hub-to-tip) plane of an axial-flow compressor when the required performance is specified. The problem of determining the radial distributions of flow is simplified by considering conditions at axial stations between blade rows where nonviscous, axisymmetric flow equations are applied. The analysis presumes the availability of blade-element data on deviation angle and on stagnation-pressure loss for all design techniques. Methods for considering the effects of wall boundary layers on required annulus area and mass-averaged stage performance are presented. A sample stage design calculation is given.

INTRODUCTION

The design of a multistage axial-flow compressor consists in the successive design of several individual rotor and stator blade rows which are then compounded to form the multistage compressor. As pointed out in the general compressor design discussion of chapter III, the problem of blade-row design has been simplified by considering the flow in each of two planes, the hub-to-tip or meridional plane and the blade-to-blade or circumferential plane. The meridional-plane solution determines the radial distribution of flow conditions assuming that axial-symmetry conditions apply, and the circumferential-plane solution determines the air-turning characteristics through the blade element. A quasi-three-dimensional description of the actual flow is then obtained by juxtaposition of these two solutions.

The results of experimental blade-to-blade investigations are described in chapters VI and VII. These chapters present circumferentially averaged blade-element performance characteristics as determined from two- and three-dimensional cascades, respectively. The blade-element performance is presented in terms of incidence angle, deviation angle, and stagnation-pressure loss as functions of cascade geometry, inlet Mach number, and (for three-dimensional cascades) radial position in the blade row.

The present chapter discusses the general flow equations and presents methods to be used in determining the radial distributions of flow in the meridional plane. The problem of determining the radial distributions of flow is simplified by considering conditions only at axial stations between blade rows. In these regions, equations for nonviscous axisymmetric flow are applied to determine the design flow distributions when the required performance (weight flow and turning or energy addition) of the blade row is specified.

Since the calculation involves the determination of the velocities from the inner wall to the outer wall of the annular flow area, it is apparent that some consideration must be given to the boundary-layer accumulation on these walls. The most accurate and complete procedure requires a knowledge of the distribution of entropy from wall to wall as well as a knowledge of the rotor energy input across the entire annulus area including the boundary-layer region. Since complete data for this type of calculation are not currently available, simpler design techniques are required. Essentially, these simpler techniques involve computing the flow variables as if no wall boundary layer existed. Boundary-layer correction factors are then applied to determine the required geometric annulus area and mass-averaged stage performance (efficiency, temperature rise, and pressure ratio).

Since the determination of the flow conditions and annulus area configuration after each blade row in the compressor requires solution of the fundamental flow equations, the first part of this chapter is concerned with the development of the general flow equations. The assumptions and simplifications that are made to permit solution

of the equations are then discussed. The equations are applied to determine the design velocity distribution in the meridional plane after a blade row. The necessary boundary-layer correction factors are indicated. In addition, the selection of design variables is discussed. A numerical example is then carried out with the equations and methods presented.

SYMBOLS

The following symbols are used in this chapter:

A_F	frontal area, sq ft
a	speed of sound, ft/sec
$\mathcal{C}$	curvature of meridional streamline, ft.$^{-1}$
c_p	specific heat at constant pressure, Btu/(lb)(°R)
D	diffusion factor
$\mathcal{F}$	blade force acting on gas, lb/lb
g	acceleration due to gravity, 32.17 ft/sec^2
H	total or stagnation enthalpy, Btu/lb
J	mechanical equivalent of heat, 778.2 ft-lb/Btu
K_{bk}	weight-flow blockage factor
K_e	energy-addition-correction factor
K_P	pressure-correction factor
$K\eta$	efficiency-correction factor
M	Mach number
n	polytropic compression exponent
P	total or stagnation pressure, lb/sq ft
p	static or stream pressure, lb/sq ft
Q	external heat added to gas, Btu/(lb)(sec)
R	gas constant, 53.35 ft-lb/(lb)(°R)
r	radius, ft
r_c	radius of curvature of streamline in meridional plane, ft
S	entropy, Btu/(lb)(°R)
T	total or stagnation temperature, °R
t	static or stream temperature, °R
U	rotor speed, ft/sec
u	internal energy, Btu/lb
V	air velocity, ft/sec
w	weight flow, lb/sec
z	coordinate along axis, ft
β	air angle, angle between air velocity and axial direction, deg
γ	ratio of specific heats
δ	ratio of total pressure to NASA standard sea-level pressure of 2116 lb/sq ft
δ^*	boundary-layer displacement thickness, ft
ϵ	angle between tangent to streamline projected on meridional plane and axial direction, deg
η	efficiency
θ	ratio of total temperature to NASA standard sea-level temperature of 518.7° R
ν	kinematic viscosity, sq ft/sec
ρ	density, lb-sec^2/ft^4
σ	solidity, ratio of chord to spacing
τ	time
Φ	viscous dissipation of energy, Btu/(cu ft)(sec)
Ω	work-done factor
ω	angular velocity of rotor, radians/sec
$\bar{\omega}$	total-pressure-loss coefficient

Subscripts:

a	stagnation conditions
ad	adiabatic
av	average
d	design value neglecting wall boundary layer
h	hub
i	reference position, radial station where variables are known
id	ideal
m	meridional
$m.a.$	mass-averaged value
p	polytropic
R	rotor
r	radial direction
S	stator
ST	stage
t	tip
z	axial direction
$\alpha, \beta, \gamma, \delta, \epsilon$	radial design stations at 10, 30, 50, 70, and 90 percent of blade height from tip, respectively
θ	tangential direction
0	station ahead of guide vanes
1	station at rotor inlet
2	station at stator inlet
3	station at stator exit

Superscript:

′	relative to rotor

STATEMENT OF DESIGN PROBLEM

SPECIFICATION OF COMPRESSOR PERFORMANCE AND CONFIGURATION REQUIREMENTS

The design of the axial-flow compressor begins with the determination of the over-all performance specifications obtained from the over-all engine and airplane requirements. In general, the engine inlet-air conditions (pressure, temperature, and density), engine thrust, engine air-flow, turbine-inlet temperature, and compressor pressure ratio are fixed by cycle and flight-plan analyses such as are discussed in chapter II. The compressor-inlet hub-tip diameter ratio, the component tip diameters, the compressor rotational speed, the compressor-inlet axial velocity, and the compressor-discharge velocity are then determined considering the compressor efficiency, turbine stresses, compressor stresses, performance of the various components, engine weight, and engine space limitations in the airplane. The interrelation of some of these factors (compressor air-flow per unit frontal area, compressor pressure ratio, rotational speed, turbine size, and turbine stresses) is discussed in reference 17. It should be emphasized that a large number of compressor configurations are possible for given over-all performance requirements. The choice of a given configuration is based on a compromise among the various performance and geometric parameters. This compromise depends in turn on the intended use of the engine.

FLOW AND GEOMETRY CONDITIONS TO BE DETERMINED

The design procedure involves an iterative solution of the flow equations after each blade row. Thus, the flow conditions and hub and tip diameter after the first blade row must be calculated from the known inlet and the specified design conditions. The blade-element loadings and Mach numbers selected must be consistent with the attainment of low loss as indicated by the loss data presented in chapters VI and VII. The resulting flow must also be acceptable to the following blade row. After a satisfactory solution for these conditions has been found, the resulting flow distribution after the blade row becomes the inlet condition for the following row. The flow conditions and geometry of the second blade row are then determined. The same procedure is repeated all through the machine until the desired over-all pressure ratio and discharge velocity are obtained.

When the flow conditions have been calculated after a given blade row, the blade sections may be selected to give the desired air turning or the desired blade work. The incidence- and deviation-angle data correlated in chapter VII may be used to assist in this selection. Some consideration of off-design performance may be required in the selection of blading. In addition, the loss correlations that are presented in chapter VII enable the designer to reestimate the originally assumed blade-element losses for the particular blade configuration selected. These reestimated loss data are then used to recalculate the flow distribution after the blade row by the methods of the present chapter.

GENERAL EQUATIONS

The basic equations that apply to the general case of the flow of a real compressible fluid through a turbomachine can be formulated from the conservation laws of matter, momentum, and energy, along with the thermodynamic equation of state. As pointed out in reference 236, these general basic equations of the flow can be stated as follows:

The equation of state for a perfect gas:

$$p=\rho g R t \tag{34}$$

The energy equation:

$$\frac{Du}{D\tau}+p\frac{D\rho^{-1}}{D\tau}=Q+\frac{\Phi}{\rho} \tag{289}$$

The continuity equation:

$$\frac{\partial\rho}{\partial\tau}+\nabla\cdot(\rho\overline{V})=0 \tag{290}$$

The Navier-Stokes equation:

$$\frac{D(\overline{V})}{D\tau}=g\overline{\mathcal{F}}-\frac{1}{\rho}\nabla p+\nu\left[\nabla^2(\overline{V})+\frac{1}{3}\nabla(\nabla\cdot\overline{V})\right] \tag{291}$$

BASIC ASSUMPTIONS

The simplifying assumptions usually made in the treatment of the problem of flow through axial-flow compressors are as follows:

(1) The general flow equations are applied only to compute flow distributions between blade rows where blade forces are nonexistent.

(2) The flow is assumed to be steady and axially symmetric. The theoretical significance of this assumption is discussed in chapter XIV. However, when blade-element data including

691-564 O-65-18

some of the effects of unsteady asymmetric flow conditions are used in calculating the velocity distributions, the errors introduced by this assumption are expected to be small.

(3) The local shearing effects of viscosity (between blade rows) are neglected by dropping the viscosity terms in the flow equations. However, the accumulated effects of upstream viscous action in increasing entropy are considered by use of experimentally determined blade-element performance. Empirical corrections are also made when required for wall boundary-layer effects on required flow area and mass-averaged energy addition and efficiency.

(4) Heat transfer is neglected.

SIMPLIFIED FLOW EQUATIONS

As a result of the preceding assumptions and the use of the definition of entropy, the general flow equations may be combined and restated as follows:

$$Jg(H_2-H_1)=\omega[(rV_\theta)_2-(rV_\theta)_1]$$
$$=(UV_\theta)_2-(UV_\theta)_1=Jgc_p(T_2-T_1) \quad (292)$$

$$\nabla(\rho\overline{V})=0 \quad (293)$$

$$Jg\nabla H=Jgt\nabla S+\overline{V}\times(\nabla\times\overline{V}) \quad (294)$$

Equation (292) relates the change in stagnation enthalpy along a streamline at axial stations ahead of and behind a rotor blade row to the change in angular momentum and the angular velocity of the wheel. Of course, the stagnation enthalpy is constant along a streamline passing through a stator blade row if it is assumed that the heat transfer from streamline to streamline is negligible.

Equation (293) states the law of conservation of matter, which, for application to compressor design, may be expressed as

$$w_1=2\pi g\int_{r_{h,1}}^{r_{t,1}}\rho_1 V_{z,1}r_1\,dr_1=w_2 \quad (295)$$

This equation will be discussed in detail in a later section with reference to boundary-layer blockage corrections and with reference to application of the flow equations in the design procedure.

Equation (294) is referred to as the equilibrium equation for the fluid between the blade rows.

SOLUTIONS OF EQUILIBRIUM EQUATIONS

The equations presented in the preceding section may be solved in several ways within the assumptions stated. Most of these solutions differ only in the simplifications made in the equilibrium equation (eq. (294)).

Since the design methods presented here are concerned with finding the radial variation of flow at a specified axial station, the radial component of equation (294) is applicable. For the assumed axially symmetric flow between blade rows, this component equation is

$$Jgc_p\frac{\partial T}{\partial r}=Jgt\frac{\partial S}{\partial r}+V_\theta\frac{\partial V_\theta}{\partial r}+\frac{V_\theta^2}{r}+V_z\frac{\partial V_z}{\partial r}-V_z\frac{\partial V_r}{\partial z} \quad (296)$$

As in the method of reference 237, it has generally been assumed in design applications that the meridional velocity $V_m=\sqrt{V_z^2+V_r^2}$ is given by the axial velocity V_z and that $\partial V_r/\partial z=0$. Such a condition (generally referred to as the "simplified-radial-equilibrium" condition) has been successfully used in low-aspect-ratio and lightly loaded blade-row designs. However, a less restricted design solution may be necessary for high Mach number, highly loaded designs. Several analyses (refs. 34, 49, 236, 238, and 239) have been made to determine the factors influencing the meridional velocity distribution. The analysis of reference 236 considers the effect of the radial motion resulting from velocity-distribution changes through a blade row and evaluates the magnitude of this effect for several cases by assuming that the air flows through the compressor along sinusoidal streamlines. The analyses of references 238 and 239 for incompressible flow also consider the effects of radial motion due to velocity-distribution changes through the compressor. These analyses consider the effects of the velocity induced by the gradients in circulation or vorticity along the blade on the velocity distribution ahead of and behind the blade row. The procedure permits evaluation of the mutual interference effects of blade rows in the multistage compressor. These analyses neglect the radial motion due to the blade blockage resulting from blade thickness variations. Reference 34 presents a simplified analysis of the effect of the radial variation of blade thickness on inlet velocity and incidence-angle distributions. This analysis also

assumes axial symmetry but makes a correction in the flow continuity relation for blade thickness. In general, the higher the inlet Mach number, the greater the variation in the axial velocity from hub to tip.

All these investigations neglect the effects of gradients of entropy on radial distributions of velocity and therefore are not directly applicable in regions of high loss. Reference 49 applies experimental data to determine the relative magnitudes of the effects on velocity distributions of the entropy-gradient term for a wide variety of axial-flow-compressor blade rows. Although vast differences generally exist in the shapes of the velocity distributions in the inlet and the outlet stages of the multistage compressor, essentially the same techniques (assuming a knowledge of the entropy distribution across the annulus) can be used to calculate the velocities. Consideration of the entropy gradients was particularly necessary in the rear stages, where the accumulated effects of viscosity noticeably affected the velocity distribution. On the other hand, the complete radial acceleration term appeared to be significant for the highly loaded inlet stages investigated, where the wall curvatures were large.

The following discussion presents the various forms of the radial-equilibrium equation that may be used in the compressor design procedure.

SIMPLE-RADIAL-EQUILIBRIUM EQUATION NEGLECTING ENTROPY GRADIENTS

The simplest solution of the radial-equilibrium equation (eq. (296)), usually referred to as the "simple-radial-equilibrium solution," has been widely used in compressor design. It is arrived at by assuming (1) that the derivative of V_r with respect to z is zero, and (2) that the derivative of S with respect to r is zero. These assumptions are made, of course, only at the fixed value of z. The resulting equation is

$$Jgc_p\frac{\partial T}{\partial r}=V_\theta\frac{\partial V_\theta}{\partial r}+\frac{V_\theta^2}{r}+V_z\frac{\partial V_z}{\partial r} \qquad (297)$$

which is referred to herein as the "isentropic-simple-radial-equilibrium" or "isre" equation. In this case, "isentropic" refers simply to the condition of radially constant circumferentially averaged entropy within the space between blade rows outside the boundary layers. Thus, the entropy of the flow may still change through the blade row.

Equation (297) may be integrated between any two radial positions in the free-stream region of the annular flow area at an axial station between blade rows. For purposes of a design procedure, it is most convenient to integrate between some reference radius, at which the dependent variables are known or assumed, and the other radial positions. The resulting integrated form of the isre equation is

$$V_z^2-V_{z,t}^2=2gJc_p(T-T_t)-(V_\theta^2-V_{\theta,t}^2)-\int_{r_t}^{r}\frac{2V_\theta^2}{r}\,dr \qquad (298)$$

The radial variation of axial velocity or $V_z-V_{z,t}^2$ at the blade-row outlet is obtained by prescribing the distribution of either the stagnation temperature or the tangential velocity after the blade row. These two parameters (stagnation temperature and tangential velocity) are related by equation (292) for the known flow conditions at the inlet of the blade row. As will be shown later, the value of the reference axial velocity $V_{z,t}$ is assigned and the mass continuity condition is applied to determine the required annulus area. For those cases in which the annulus area is specified, the reference velocity is determined by application of the continuity relation.

A series of charts is presented in chapter IX to permit rapid solution of equation (298).

SIMPLE-RADIAL-EQUILIBRIUM EQUATION CONSIDERING RADIAL GRADIENTS OF ENTROPY

The major effect of upstream viscous action is manifested by an increase in the entropy of the flow. The major effects of viscosity on the axial velocity distribution are therefore accounted for in the radial-equilibrium equation through the use of the term involving the radial gradients of entropy. Thus, the equation presented here is obtained from equation (296) by assuming only that the derivative of the radial velocity V_r with respect to the axial distance z is zero. Equation (296) then becomes

$$Jgc_p\frac{\partial T}{\partial r}=Jgt\frac{\partial S}{\partial r}+V_\theta\frac{\partial V_\theta}{\partial r}+\frac{V_\theta^2}{r}+V_z\frac{\partial V_z}{\partial r} \qquad (299)$$

Equation (299), hereinafter referred to as the "nonisentropic-simple-radial-equilibrium" or "nisre" equation, may be integrated between two

radial positions at an axial station between blade rows to give

$$V_z^2-V_{z,t}^2=2gJc_p(T-T_t)-(V_\theta^2-V_{\theta,t}^2)$$

$$-2\int_{r_t}^{r}\frac{V_\theta^2}{r}\,dr-2JgR\int_{r_t}^{r}t\,\frac{\partial\left(\frac{S}{R}\right)}{\partial r}\,dr \quad (300)$$

The nisre equation can be solved in the same manner as the isre equation, except that the entropy term must be evaluated. By the definition of stagnation conditions, stagnation entropy is identically equal to static entropy at any given point. Therefore, the change in the entropy along a streamline from the inlet to the outlet of a blade row may be expressed as

$$J\left(\frac{S}{R}\right)_2-J\left(\frac{S}{R}\right)_1=\ln\left[\frac{\left(\frac{T_2}{T_1}\right)^{\frac{\gamma}{\gamma-1}}}{\frac{P_2}{P_1}}\right] \quad (301)$$

In the design procedure, the temperature ratio is assumed or is determined from a specified variation in tangential velocity by use of equation (292). The stagnation-pressure ratio may be related to the stagnation-temperature ratio in terms of either a polytropic blade-element efficiency η_p or a stagnation-pressure-loss coefficient $\bar{\omega}$.

When the polytropic efficiency or polytropic compression exponent is used, the stagnation-pressure ratio is given by

$$\frac{P_2}{P_1}=\left(\frac{T_2}{T_1}\right)^{\frac{\eta_p\gamma}{\gamma-1}}=\left(\frac{T_2}{T_1}\right)^{\frac{n}{n-1}} \quad (302)$$

The blade-element data of chapters VI and VII present the blade-element loss in terms of $\bar{\omega}$. When these data are used, it is more convenient to express the stagnation-pressure ratio across the blade element in terms of $\bar{\omega}'$, stagnation-temperature ratio, and inlet-air Mach number relative to the blade element. The expression for pressure ratio is restated from chapter VII as

$$\frac{P_2'}{P_1'}=\left(\frac{P_2'}{P_1'}\right)_{id}-\bar{\omega}'\left\{1-\left[1+\frac{\gamma-1}{2}(M_1')^2\right]^{\frac{-\gamma}{\gamma-1}}\right\} \quad (303)$$

where

$$\left(\frac{P_2'}{P_1'}\right)_{id}=\left[1+\frac{\gamma-1}{2}\,\frac{(\omega r_2)^2}{\gamma gRT_1'}\left(1-\frac{r_1^2}{r_2^2}\right)\right]^{\frac{\gamma}{\gamma-1}} \quad (59)$$

This equation holds for both rotor and stator when the appropriate indices are used.

The ideal relative pressure ratio $(P_2'/P_1')_{id}$ can be taken equal to 1.0 for those cases in which the variation in the streamline radius across the rotor is negligible, a condition obtained in high hub-tip ratio or lightly loaded blade rows.

For convenience in the design procedure, any upstream station at which the entropy is essentially constant radially—for example, the compressor-inlet station 0—is used as the reference station. Therefore, the radial variation of entropy is, from equation (301),

$$J\,\frac{\partial\left(\frac{S}{R}\right)_2}{\partial r_2}=\frac{\partial}{\partial r_2}\left\{\ln\left[\frac{\left(\frac{T_2}{T_0}\right)^{\frac{\gamma}{\gamma-1}}}{\frac{P_2}{P_0}}\right]\right\} \quad (304)$$

The static temperature appearing in the second integral of equation (300) can be expressed in terms of the velocity components and stagnation temperature as follows:

$$Jgc_pt=Jgc_pT-\frac{V_\theta^2}{2}-\frac{V_z^2}{2}-\frac{V_r^2}{2} \quad (305)$$

For the simplified-radial-equilibrium solutions, the radial velocity term is neglected in equation (305). In general, this V_r component can be neglected in the stages with high hub-tip ratio without introducing significant errors in static temperature. In the stages with low hub-tip ratio (where wall slopes may be large), however, V_r may have to be considered in this equation by estimating a streamline slope in the meridional plane and expressing V_r as a function of V_z and this slope.

RADIAL-EQUILIBRIUM EQUATION CONSIDERING RADIAL ACCELERATIONS

As pointed out in the previous discussions on the simple-radial-equilibrium equations, high hub-tip radius ratio and lightly loaded blade rows have been successfully designed by assuming that the meridional velocity V_m is equal to the axial velocity V_z and that the gradient of radial velocity V_r along the axial direction is zero. In this case, the radial gradient of static pressure is

$$\frac{dp}{dr}=\rho\,\frac{V_\theta^2}{r}$$

However, for high-aspect-ratio, highly loaded stages, the effects of streamline curvature become significant. In this case, the contribution of the radial acceleration of the meridional velocity to the pressure gradient in the radial direction must be considered. The radial gradient of static pressure for this general case of curved streamline flow may be stated as

$$\frac{dp}{dr}=\rho\left(\frac{V_\theta^2}{r}\pm\frac{V_m^2\cos\epsilon}{r_c}\right)$$

where ϵ is the angle of the streamline with respect to the axial direction, and r_c is the radius of curvature of the streamline.

An accurate determination of the radius of curvature of the streamline and the slope of the streamline (which determines the angle ϵ) requires a knowledge of the shape of the streamline through the blade row. The streamline configuration is a function of the annular-passage area variation, the camber and thickness distribution of the blades in the radial and axial directions, the blade forces existing within the blade row, and the flow angles at inlet and discharge of the blade row. Because the effects of radial acceleration have been small in conventional subsonic-compressor designs, very little information is available concerning the relative importance of each of these variables in determining the effects of radial accelerations in the highly loaded designs being studied. Therefore, the usefulness of several methods that have been proposed for evaluating these radial accelerations has not yet been established.

Several analyses, such as the work of references 58 and 62, have been applied to determine velocity distributions throughout the flow field in high-solidity mixed-flow compressors and axial-flow turbines. These procedures require estimation of a streamline-orthogonal flow system through the blade row. The distribution of velocity along the orthogonal is then determined from the known inlet conditions, a mean air-turning variation along each streamline, and a blade thickness variation along each streamline. Since this method requires estimation of the streamlines as well as a knowledge of the blade configuration, it is apparent that it becomes an iterative solution.

An approximate evaluation of the radial acceleration term is also made in reference 236 by assuming the streamline shape to be sinusoidal. A similar technique for evaluating the effect of radial accelerations is applied in reference 240. The analysis of reference 236 further assumes that the product of the radial velocity at a given axial station between blade rows and the axial gradient of axial velocity is negligible and that the slope of the streamlines at this axial station is zero. Therefore, for the assumptions of reference 236, the last term (the radial-flow term) of equation (296) may be expressed as

$$V_z\frac{\partial V_r}{\partial z}=CV_z^2$$

Results obtained with this procedure are shown in reference 241 to agree with results obtained from the general three-dimensional-flow solution described in reference 242 for a single-stage nontapered-passage compressor.

In addition to the preceding analyses, which attempt to consider the effects of the blades on the streamline configuration through the blade row, several analyses, such as the work of references 243 to 245, present methods of estimating the effects of radial velocity and curvature terms from simplified calculations of the flow only between blade rows. In these solutions, a set of smooth streamlines is estimated through the compressor stage on the basis of the velocities calculated between blade rows. It is apparent that these methods do not consider the effects of the blade thickness and camber distributions and the effects of the blade forces on the streamline curvature.

In view of the present meager knowledge of the effects of the various design parameters on the radial acceleration terms in the general flow equations, it seems reasonable to use the simpler methods of accounting for these effects as stop-gap design measures. In addition, it may be desirable at the present time to try to alleviate the conditions leading to large radial accelerations. In the case of highly loaded designs having high aspect ratios, one technique for reducing the effects of radial accelerations is to taper the tip of the compressor inward so that the hub curvature is reduced. Definitive experimental and analytical work is still required to evaluate the various techniques that have been suggested for computing velocity distributions including the effects of radial accelerations.

CONSIDERATION OF WALL BOUNDARY-LAYER EFFECTS

The equilibrium equations that must be solved in determining the meridional distribution of flow conditions between blade rows in the axial-flow machine were discussed in the preceding section. When the simple-radial-equilibrium equations are suitable, a procedure similar to the following is required to execute a blade-row design if the inlet conditions are given:

(1) The tip radius at the blade-row discharge is specified.

(2) The axial and tangential velocities at the tip radius after the blade row are assumed. These values must be consistent with the considerations for low losses and compatible with the requirements of the following blade row.

(3) The radial distribution of tangential velocity after the blade row is specified.

(4) The radial distribution of energy addition in the blade row is determined from the known inlet conditions and the specified distribution of tangential velocity by use of equation (292).

(5) The radial distribution of loss and therefore entropy is assumed based on blade-element data taken in a similar flow environment.

(6) The radial distribution of axial velocity is calculated.

(7) The radial distributions of all other flow properties are calculated.

(8) The continuity condition is used to calculate the hub radius from the known tip radius and mass flow and the calculated distributions of axial velocity and density.

When the radial acceleration terms associated with streamline curvature become significant, this procedure may be considered as an initial step in the design system. It then becomes necessary to recalculate the radial distributions of axial velocity and other flow properties (items (6) and (7)) and to determine a new hub radius (item (8)).

This technique is referred to as method I. The critical information in this solution is the radial distribution of loss or entropy from wall to wall. Figure 207 illustrates a form of the entropy distribution that might be encountered after a blade row in a compressor. The large rise in entropy at the end walls results from the losses in the wall boundary layers. Across the major portion of the flow passage, the entropy variation is illustrated as being relatively small. It must be emphasized that (as indicated in ref. 49) some cases have been encountered where the variation of entropy is large even in the main stream. In any case, the "nonisentropic" equations can be applied to determine the velocity distribution even into the boundary layers if means of predicting the entropy distribution are available. This procedure would be a direct process near the tip, since the tip radius is specified. Near the hub, however, the entropy and other flow properties could not be determined until after the hub radius is known. Therefore, iteration procedures must be used near the hub for this complete solution. The distribution of flow properties and the annulus area determined from these procedures then permit calculation of the mass-averaged energy addition, pressure ratio, and efficiency for the stage.

Of course, it is apparent that the determination of the entropy distribution from wall to wall for all the possible design velocity diagrams, blade-row geometries, and locations in the multistage compressor would require very extensive tests of many different compressors. Such detailed information requires the analysis of much more multistage-compressor data than are currently available. Substitute techniques for the determination of the annulus area after the blade row and the mass-

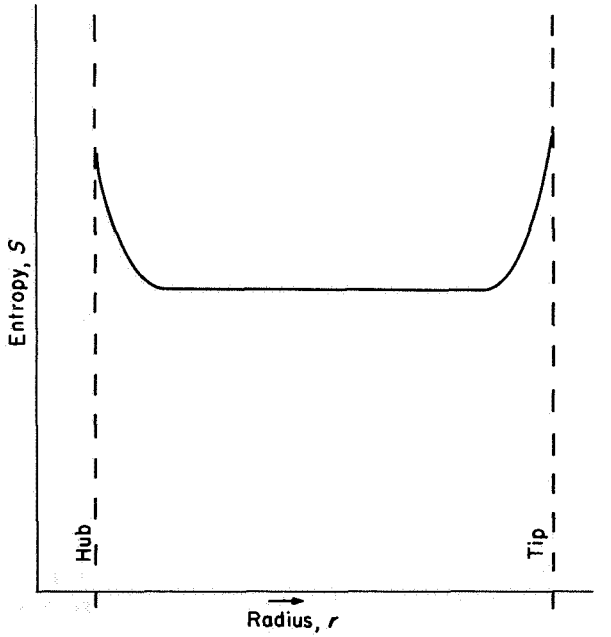

FIGURE 207.—Typical entropy distribution after compressor blade row.

averaged efficiency, energy addition, and pressure ratio have therefore been used.

One such technique (referred to herein as method II) involves dividing the flow passage into three parts, the tip boundary layer, the mainstream region, and the hub boundary layer. In the process of solution of the equations, the wall boundary-layer regions are actually treated as one region. The velocities across the annulus are computed by the previously itemized procedure assuming that no wall boundary layer exists. The entropy distribution used in the determination of the velocities is obtained from the blade-element loss data presented in chapter VII. If, as is illustrated in figure 207, the entropy gradient is small in the main stream, then the velocity distribution may be computed using the isre equation (eq. (297) or (298)). If the blade-element loss data indicate a large variation of entropy in the main stream, then the nisre equation (eq. (299) or (300)) must be used to determine the velocity distributions.

The effects of the wall boundary layers on the required annulus area and on the mass-averaged energy addition, pressure ratio, and efficiency are determined in method II from the velocity distributions calculated assuming appropriate "gross" correction factors and the absence of wall boundary layers. Although the evaluation of these gross correction factors will also require extensive compressor testing and analysis, it is anticipated that the general correlations with velocity-diagram parameters and environment may be more readily attainable than those for the detailed entropy distributions in the boundary layers. In addition, indications of the magnitudes of these gross correction factors may be obtained from comparisons of design and measured velocities in the mainstream region.

The general effects of wall boundary layers on rotor performance are indicated in figure 208. This figure is an example of a design that has been worked out for constant mass flow (fig. 208(a)) and energy addition (fig. 208(b)) along the radius without considering the effect of the end-wall boundary layers. The isre solution was used to determine the velocities across the annulus from the specified energy addition (fig. 208(b)), assuming that the stagnation-pressure loss was constant along the radius (fig. 208(c)) and that the effects of the wall boundary layers could be

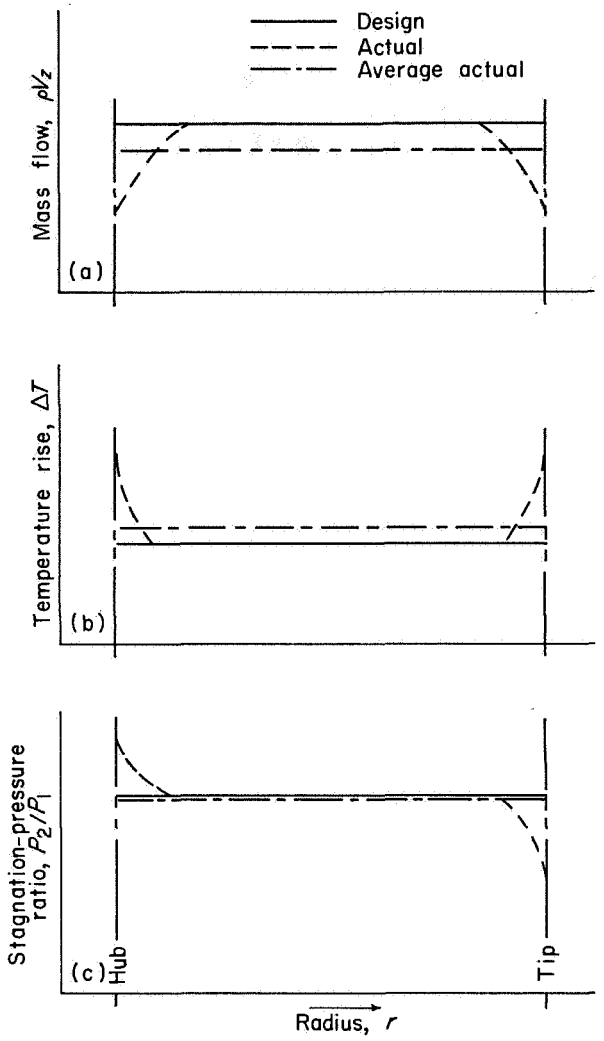

(a) Constant mass flow.
(b) Constant energy addition.
(c) Constant stagnation-pressure ratio.

FIGURE 208.—General effects of wall boundary layer.

neglected. For such a design, the conditions that might be measured in the flow annulus when the mainstream flow conditions are the same as the design conditions are indicated by the dashed curves. It is apparent that the integrated weight flow is less than the design weight flow, and the mass-averaged energy addition or temperature rise and the mass-averaged pressure ratio may differ from the design value. The average values of mass flow, temperature rise, and pressure ratio are indicated on the figure as the dot-dash lines. Therefore, three correction factors are required in method II to account for the presence of the wall

boundary layers. An annulus-area correction must be applied to account for the blockage effect of the wall boundary layer so as to ensure the attainment of the design weight flow; a temperature-rise factor must be applied to calculate the mass-averaged energy addition for the blade row at this design weight flow; and a pressure-ratio factor must be applied to permit calculation of the mass-averaged pressure ratio.

Another system of correction that has been used extensively involves specifying the annulus area and adjusting the axial velocity level across the mainstream region by the continuity equation to ensure the attainment of the design weight flow. This method of design and correction involves principally a rearrangement of the previously enumerated design steps. Other correction factors are still necessary to permit calculation of the mass-averaged energy addition and pressure ratio.

It must be emphasized that, in all the techniques described, the velocities across the mainstream region of the annulus area and the annulus area geometry are calculated with blade-element loss or efficiency data obtained from stages operating in environmental conditions similar to those of the stage being designed. Such blade-element data, principally for inlet stages, are presented in chapter VII.

For those cases where blade-element loss data are not available or where a general design review of a large number of multistage compressors is required, a blade-row and stage mass-averaged efficiency may be assumed to determine the total pressure at each blade element from the specified energy addition. It is assumed in this approach that the blade-element efficiency is equal to the blade-row mass-averaged efficiency. Although this is admittedly not an exact approach, it has been found to give reasonable design accuracy and serves as an extremely useful tool, especially as a first roughing-out step in the design procedure. This method is referred to in the present report as method III. It is described in detail and applied through the use of charts in chapter IX. The method usually assumes that the correction for determining mass-averaged energy addition is negligible. A correction is required for wall boundary-layer blockage in determining the annulus area.

The following discussion is concerned with the boundary-layer correction factors required in method II for the calculation of the annulus geometry and the mass-averaged temperature rise and pressure ratio. Although only very limited amounts of blade-element data and boundary-layer correction data are available, it is felt that this method offers the basis for an accurate design system.

CORRECTION FOR WEIGHT-FLOW BLOCKAGE FACTOR

The correction for weight-flow blockage factor is intended to ensure the attainment of the design weight flow with the design velocity distribution over the major portion of the annulus area. Because of the lack of extensive data on the boundary-layer characteristics in the compressor, an empirically obtained correction factor that is applied as a gross boundary-layer blockage factor has usually been applied. Although this empirical correction factor leaves much to be desired, it has been used successfully in design. This gross blockage factor is designated by K_{bk} and is defined by the following continuity equation:

$$w=\pi g\int_{r_h}^{r_t}\rho V_z\,\mathrm{d}(r^2)=K_{bk}\pi g\int_{r_h}^{r_t}[\rho V_z\,\mathrm{d}(r^2)]_d$$

$$=\pi g\int_{r_h+\delta_h^*}^{r_t-\delta_t^*}[\rho V_z\,\mathrm{d}(r^2)]_d \quad (306)$$

The subscript d refers to design values calculated across the annulus as if no wall boundary layer were present. In essence, this gross blockage factor involves the determination of the ideal (no boundary layer) velocity distribution required to pass a flow greater than the design flow. For a given value of tip radius, the hub radius is thus decreased as K_{bk} is decreased (or boundary-layer allowance is increased).

Very little useful data regarding the best values of blockage factor are currently available from multistage-compressor investigations. Reference 243 suggests values of 0.98 for inlet stages and 0.96 for all others. Some single-stage data indicate blockage factors of 0.96 after both rotor and stator. These blockage factors are not expected to be the same for compressors differing in size, axial velocity diffusion, chord length, and so forth.

CORRECTION FACTOR FOR STAGNATION-TEMPERATURE RISE

Besides occupying space and thereby affecting the weight flow, the wall boundary layer causes

the mass-averaged energy addition or stagnation-temperature rise to differ from the design value when the main stream velocities are equal to the design values. Application of the blockage-factor correction does not eliminate the need for the temperature-rise or energy-addition factor in computing the mass-averaged temperature rise for the stage from the design velocities. This temperature-rise or energy-addition factor K_e can be defined by the following equation:

$$\left(\frac{T_2}{T_1}\right)_{m.a.} - 1.0 = \frac{\int_{r_{h,2}}^{r_{t,2}} \left(\frac{T_2}{T_1} - 1\right) [\rho V_z \, d(r^2)]_2}{\int_{r_{h,2}}^{r_{t,2}} [\rho V_z \, d(r^2)]_2}$$

$$= \frac{K_e K_{bk} \int_{r_{h,2}}^{r_{t,2}} \left[\left(\frac{T_2}{T_1} - 1\right) \rho V_z \, d(r^2)\right]_{2,d}}{K_{bk} \int_{r_{h,2}}^{r_{t,2}} [\rho V_z \, d(r^2)]_{2,d}}$$

$$= K_e \frac{\int_{r_{h,2}}^{r_{t,2}} \left[\left(\frac{T_2}{T_1} - 1\right) \rho V_z \, d(r^2)\right]_{2,d}}{\int_{r_{h,2}}^{r_{t,2}} [\rho V_z \, d(r^2)]_{2,d}} \tag{307}$$

It should be emphasized that the temperature-correction factor is used only in calculating the mass-averaged energy addition once the design velocity distributions and the annulus area geometry have been determined in the design process. It does not influence the design velocity diagram or the hub radius.

In most cases, the temperature-rise correction factor is assumed equal to 1.0. However, analysis of limited data taken on the single-stage rotor of reference 57 indicates that a value of 1.03 for the temperature-rise correction factor may be more reasonable. More extensive and precise data are still required.

CORRECTION FACTOR FOR STAGNATION PRESSURE

In the design procedure, the value of the stagnation-pressure loss $\bar{\omega}$ at any blade element in the mainstream region can be estimated from the velocity diagram by using the correlation of diffusion factor with $\bar{\omega}$ presented in chapter VII. This method tends to give a higher mass-averaged value of stagnation pressure at a blade-row outlet and higher mass-averaged efficiency than are actually achieved, since consideration of the wall boundary layer is not completely included in the blade-element data. Hence, a correction for the wall boundary layer must be applied in determining the mass-averaged pressure ratio. This pressure-ratio correction factor K_P can be defined by the following equation:

$$\left(\frac{P_2}{P_1}\right)_{m.a.} = \left\{ \frac{K_P K_{bk} \int_{r_{h,2}}^{r_{t,2}} \left[\left(\frac{P_2}{P_1}\right)^{\frac{\gamma-1}{\gamma}} - 1\right] [\rho V_z \, d(r^2)]_{2,d}}{K_{bk} \int_{r_{h,2}}^{r_{t,2}} [\rho V_z \, d(r^2)]_{2,d}} + 1.0 \right\}^{\frac{\gamma}{\gamma-1}}$$

$$= \left\{ K_P \frac{\int_{r_{h,2}}^{r_{t,2}} \left[\left(\frac{P_2}{P_1}\right)^{\frac{\gamma-1}{\gamma}} - 1\right] [\rho V_z \, d(r^2)]_{2,d}}{\int_{r_{h,2}}^{r_{t,2}} [\rho V_z \, d(r^2)]_{2,d}} + 1.0 \right\}^{\frac{\gamma}{\gamma-1}} \tag{308}$$

Limited data on the rotor with 0.4 hub-tip diameter ratio described in reference 57 indicate that the value of K_P may be approximately 1.0 after a rotor. These data were taken from an inlet-stage rotor where wall boundary layers were small. Detailed data after stators are not yet available.

A knowledge of the mass-averaged temperature

rise and the mass-averaged pressure ratio permits calculation of the mass-averaged efficiency by the following equation:

$$\eta_{m.a.}=\frac{\left(\frac{P_2}{P_1}\right)_{m.a.}^{\frac{\gamma-1}{\gamma}}-1}{\left(\frac{T_2}{T_1}\right)_{m.a.}-1} \qquad (309)$$

It is apparent that an efficiency correction similar to the temperature-rise and pressure-ratio correction factors may also be applied to determine the mass-averaged efficiency of a stage if the average efficiency based on the mainstream velocities and blade-element losses is known. Thus, the average rotor efficiency is obtained by multiplying the efficiency calculated from the mainstream flow conditions by the efficiency-correction factor. As a result of the correction factors determined from the data of reference 57 for the temperature rise and the pressure ratio, the efficiency correction K_η for the rotor was found to be approximately equal to 0.97.

WORK-DONE-FACTOR SYSTEM

A boundary-layer correction procedure that has been widely used by British designers (refs. 2, 31 (pt. II), and 246) includes the "work-done" factor, which is used to estimate stage temperature rise from design values of axial velocity and air angles. In this case, the hub and tip radii of the blade row are prescribed. For a given weight flow through the blade row, the effect of the wall boundary layers is to increase the axial velocities above the design values across the mainstream portion of the annulus and to decrease the axial velocity near the end walls as shown in figure 209. Because of the high values of velocity over the major portion of the annulus, the mass-averaged energy addition at the design flow is lower than the design value (i.e., the low mass flow at the end walls does not weight the temperature rise in this region enough to compensate for the central-portion deficit in work), resulting in less "work done." Thus, the actual stage temperature rise is lower than that predicted on the basis of the design values of velocity and air angles. The work-done factor Ω is defined in reference 31 (pt. II) by the following relation:

$$c_p J g \Delta T=\Omega(U_2 V_{z,2}\tan\beta_2-U_1 V_{z,1}\tan\beta_1)_d$$

where the flow parameters are the ideal values

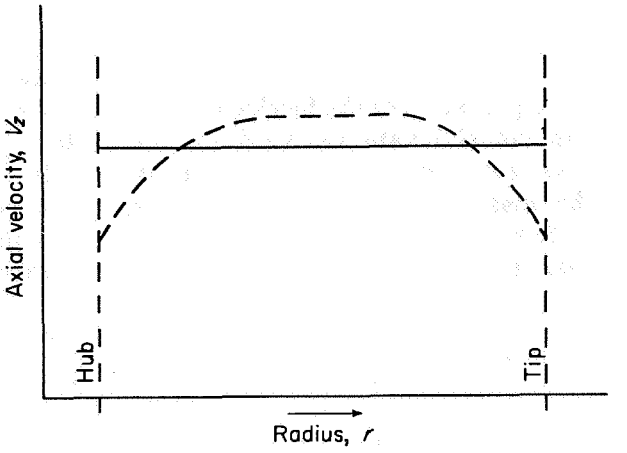

FIGURE 209.—Effect of wall boundary layer on axial velocity.

calculated assuming that wall boundary layers do not exist.

Although it was developed for designs with free-vortex velocity diagrams, the work-done factor has since been applied to other types of diagrams. It is necessary in this system to set the blades (on the basis of the design velocities) at an incidence angle higher than the optimum value. The higher velocities actually obtained across the main stream will then produce incidence angles close to the optimum values.

Thus, the design velocity and blade-angle distributions are set so as to ensure that application of the work-done factor will result in the desired energy addition. It is then usually assumed that the major part of the correction for boundary-layer blockage has been considered by application of the work-done factor.

SELECTION OF DESIGN VARIABLES

The design calculation of the multistage-compressor blade rows requires first the specification of certain aerodynamic and geometric characteristics. Among these are the inlet values of hub-tip radius ratio, weight flow, and wheel speed; the variation through the compressor of blade loading, axial velocity, and tip diameters; and an additional parameter specifying the radial distribution of work or velocity in each stage. Since the emphasis in aircraft compressors is for high mass flow per unit frontal area and high pressure ratio per stage, the discussion of the selection of design variables is slanted toward achieving these goals.

The selection of design variables and the entire design procédure involve an iterative process in which compromises are necessary at each step. The process can be shortened by using a quick approximate method for the initial parts of the design and, after a rough outline of the compressor is determined, using the more accurate methods to fix the details of the compressor blading. Thus, a trial hub and tip contour for the entire compressor can be obtained from the method that uses the isre equation along with an assumed efficiency for the blade rows. Most of the necessary compromises can be made in this step, so that the required performance is reasonably assured without exceeding specified limitations on divers flow variables.

VELOCITY DIAGRAMS

A general velocity diagram for a fixed radius is shown in figure 210. In the past, many compressors have been designed to achieve a specific type of velocity diagram at a given radius or given radii. A discussion of the commonly used velocity diagrams and their application in the design procedure is given in references 35 and 236. The free-vortex diagram has been widely used because of its simplicity and because of the accuracy with which flow distributions can be calculated for this type flow. Two-dimensional blade-element considerations (which are now known to be insufficient) showed that the symmetrical velocity diagram gave maximum blade-element-profile efficiency as well as high flow and stage pressure ratio for a subsonic Mach number limit. Therefore, this type of diagram also has been used extensively. As the various limitations of compressors became better known, more freedom was taken in the type of velocity diagram. With the advent of the transonic compressor and the removal of the subsonic Mach number limit, the free-vortex design returned to prominence for inlet stages. The absence of large gradients in outlet axial velocity with this type design facilitates the maintenance of recently established loading limits and the achievement of high pressure ratio.

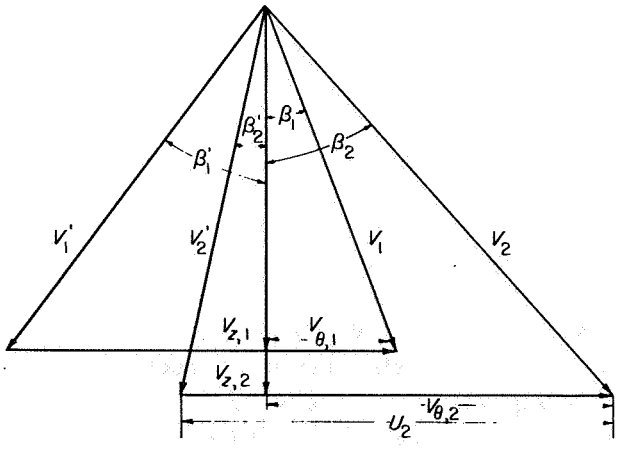

FIGURE 210.—General velocity diagram.

Experimental tests of axial-flow compressors show that satisfactory performance can be obtained for a wide range of velocity-diagram types if the blade-loading and Mach number limits are not exceeded. Therefore, present design philosophy emphasizes the limitations as determined by Mach number and diffusion factor rather than the specific velocity diagram used. In general, an iterative procedure of specifying radial distribution of work (ΔH or ΔT) and checking all radial sections for extremes in diffusion factor or Mach number is satisfactory. A specification of a velocity diagram may in some cases be desirable to systematize the procedure or to utilize past experience.

COMPRESSOR-INLET CONDITIONS

Inlet hub-tip radius ratio and axial velocity must be specified to satisfy the design weight-flow requirement, which is fixed by an engine analysis. Figure 211 presents curves of compressor weight flow per unit frontal area against axial Mach number for constant values of hub-tip radius ratio. It is apparent from this figure that weight flow per unit frontal area increases with decreasing hub-tip radius ratio and with increasing axial velocity (or Mach number). Reduction in hub-tip ratio below approximately 0.4 may be expected to result in aggravated aerodynamic as well as mechanical problems, thus giving diminishing returns. For instance, the blade-element-flow choking problem (M=1.0 at throat) at the compressor hub becomes more acute because of large fillets and blade thicknesses, while blade fastening may become difficult and blade stresses may become high.

Figure 211 also illustrates that the value of weight flow per unit frontal area depends on the value of inlet axial Mach number. However, design values of axial Mach number are fixed (for any desired blade speed and air prerotation) by

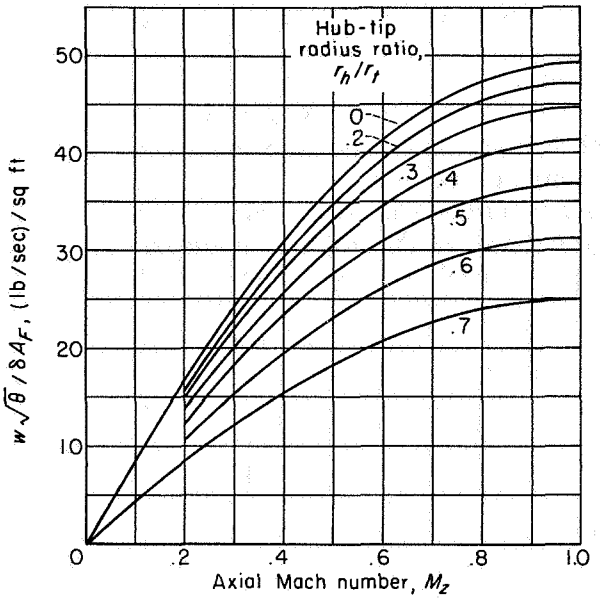

FIGURE 211.—Weight-flow—Mach number characteristics for various values of hub-tip radius ratio.

the limiting relative inlet Mach number of the blade sections used in the inlet row. Thus, the relative inlet Mach number becomes the important variable and will be considered here.

The limiting relative Mach number for conventional subsonic blade shapes and designs is usually set at 0.7 to 0.8; whereas good efficiencies have been obtained at Mach numbers up to 1.1 (ref. 41) and even higher for transonic blade shapes (thin blades with thin leading edges and solidity of the order of 1.0). These limits are determined from loss and efficiency considerations, which in turn may be affected by blade-row choking considerations, particularly at the compressor hub. An analysis of the choking problem is presented for two-dimensional cascades in reference 31 (pt. I). If a cascade analysis is applied to a compressor rotor and does not indicate choking, there will probably be a built-in safety factor because of the advantage of the energy rise through the rotor.

In the past, inlet corotation has been used to reduce the relative Mach number at the rotor inlet. Since compressors have been operated efficiently at high values of relative inlet Mach number, the role of inlet guide vanes has become decreasingly important in compressor design. However, the use of counterrotation inlet guide vanes to increase Mach number at a given wheel speed for the attainment of high stage pressure ratio should not be overlooked when blade speed is otherwise limited.

VARIATION OF DESIGN PARAMETERS THROUGH COMPRESSOR

Axial velocity.—In any compressor, values of axial velocity are fixed at two axial stations: at the compressor inlet by the weight flow and hub-tip ratio, and at the compressor exit by compressor-discharge diffuser and combustor-inlet requirements. With the trend toward higher compressor-inlet velocities, fixed combustor requirements will necessitate appreciable decreases in axial velocity through the unit. Care must also be taken that blade heights in the latter stages do not become so small that end-wall boundary layers and blade tip clearances occupy a large percentage of the passage and thus deteriorate performance. The exact scheduling of axial velocity through the compressor will depend largely on the individual blade-row requirements. Large axial velocity reductions across any blade element are to be avoided if high efficiency is desired.

Diffusion factor.—The diffusion factor, a blade-loading criterion discussed in reference 9, is given by

$$D=1-\frac{V_2'}{V_1'}+\frac{\Delta V_\theta'}{2\sigma V_1'} \tag{310}$$

The analysis of single-stage-compressor data in reference 9 indicates the following diffusion-factor limits for inlet stages: for the rotor tip, D less than 0.4; for the rotor hub, D less than 0.6; for the stator, D less than 0.6. The variation of limiting diffusion factor through the compressor is not yet known. Although this blade-loading parameter (eq. (310)) is a good stop-gap, a more complete and general loading criterion and a better correlation of loss with loading are still required.

Efficiency.—The stage or blade-row efficiency, rather than the blade-element loss, may be used as a design parameter in certain design procedures (e.g., method III). Experimental investigations of axial-flow compressors indicate that, where blade-loading limits are not exceeded, the stage efficiencies remain at a relatively constant high value. A slight decrease in efficiency in the rear stages of the compressor has usually been attributed to distortions of the radial distributions of velocity in these blade rows. Also, the ratio

of wetted area to flow area is greater in the latter stages than in the inlet stage, so that boundary-layer effects become more prominent. The design-speed peak adiabatic efficiency for an inlet stage operating as a single-stage unit is about 0.92. Of course, the assumed design efficiency will vary with the performance requirements of pressure ratio and weight flow and perhaps with axial position in the compressor.

Boundary-layer characteristics.—Unfortunately, there is very little information from which the boundary-layer growth through a compressor can be determined accurately beyond that mentioned in reference 243. Values of correction factors used to account for boundary-layer growth have been given and discussed in the section on weight-flow blockage. Data obtained from an 8-stage axial-flow compressor (ref. 247) indicate that the boundary-layer thickness (expressed as a percent of blade height) remained approximately constant through the last four stages near the design weight flow. Although the boundary layer in the compressor of reference 247 was thicker than might be generally expected, these results support the choice of a constant value of K_{bk} through the latter stages of an axial-flow compressor.

PHYSICAL ASPECTS

Physical considerations limit some compressor variables that affect the aerodynamics of the flow. The shape of the compressor outer casing is limited by restrictions on over-all size of the engine and accessories, and a constant-tip-radius configuration has been used in the past as a good compromise between aerodynamic and weight considerations. The required decrease in annular area from inlet to outlet is then obtained by gradually increasing the hub radius. Of course, other combinations of hub and tip shapes may be desirable for specific applications; for example, the section on radial-flow accelerations indicates that tapering the tip casing at the compressor inlet may be desirable to reduce hub-wall curvature effects, if these are otherwise detrimental.

The value of the solidity used in each blade row may be varied slightly to keep the blade loading (expressed for the present by the diffusion factor) within certain limits. Reasonable values of solidity for the transonic compressors appear to be in the order of 1.0 at the tip section. Extremely low solidities lead to poor guidance and high losses, while extremely high solidities lead to hub choking problems and high losses.

Although the tip clearance used in a compressor design is usually set by mechanical considerations, large effects of tip clearance on aerodynamic performance have been noted in various compressor investigations. Some effects of blade tip clearance are discussed in reference 5, which reports that the smallest clearance used in the series of tests gave the best rotor efficiency.

OFF-DESIGN PERFORMANCE

In regard to compressor weight, it is desirable to select a design for the minimum number of stages consistent with good aerodynamic efficiency to achieve a specified over-all pressure ratio. Since the compressor must also have good acceleration characteristics, good high flight Mach number performance, and a reasonable overspeed margin as well as satisfactory design-point operation, the off-design operating characteristics should be considered when the stagewise variation of blade loading is chosen. Possible means of determining the off-design operating characteristics are given in chapter X. At compressor speeds above and below design speed, the front and rear stages deviate considerably from design angle of incidence, operating over a range from choked flow to stall (ref. 248). Therefore, it is important to prescribe blading and velocity diagrams in the front and rear stages that will permit the attainment of a large stall-free range of operation.

Consideration of compressor-inlet flow distortions resulting from inlet-diffuser boundary layers, aircraft flight at angle of attack, and so forth, may also influence the stage design selection, especially in the inlet stages of the compressor.

APPLICATION OF EQUATIONS

DESIGN EQUATIONS

The equations to be used in a design are grouped in table III for ease of reference. They are either repeated or are directly derived from equations in the previous sections. Additional relations are obtained from the velocity diagram such as is shown in figure 210.

Equations (d1b) (the isre solution) and (d2b) (the nisre solution) for determining the axial velocity variation along the radius are obtained from equations (d1a) and (d2a) by evaluating the integrals by the trapezoidal rule. [In addi-

TABLE III.—DESIGN EQUATIONS

$$Jgc_p(T_2-T_1)=(UV_\theta)_2-(UV_\theta)_1 \tag{316}$$

$$V_z^2=V_{z,t}^2+2gJc_p(T-T_1)-(V_\theta^2-V_{\theta,t}^2)-\int_{r_t}^{r}\frac{2V_\theta^2}{r}\,dr \tag{d1a}$$

$$V_z^2=V_{z,t}^2+2gJc_p(T-T_t)-(V_\theta^2-V_{\theta,t}^2)-\left(\frac{V_\theta^2}{r}+\frac{V_{\theta,t}^2}{r}\right)(r-r_t) \tag{d1b}$$

$$V_z^2=V_{z,t}^2+2gJc_p(T-T_t)-(V_\theta^2-V_{\theta,t}^2)-\int_{r_t}^{r}\frac{2V_\theta^2}{r}\,dr-\int_{r_t}^{r}2gJRt\,\frac{\partial\left(\frac{S}{R}\right)}{\partial r}\,dr \tag{d2a}$$

$$V_z^2=\left\{\frac{1}{1-\frac{\gamma-1}{2\gamma}\ln\left[\frac{\left(\frac{T}{T_t}\right)^{\frac{\gamma}{\gamma-1}}}{\frac{P}{P_t}}\right]}\right\}\left\{V_{z,t}^2\left\{1+\frac{\gamma-1}{2\gamma}\ln\left[\frac{\left(\frac{T}{T_t}\right)^{\frac{\gamma}{\gamma-1}}}{\frac{P}{P_t}}\right]\right\}+2Jgc_p(T-T_t)-(V_\theta^2-V_{\theta,t}^2)-\left(\frac{V_\theta^2}{r}+\frac{V_{\theta,t}^2}{r_t}\right)(r-r_t)-\ln\left[\frac{\left(\frac{T}{T_t}\right)^{\frac{\gamma}{\gamma-1}}}{\frac{P}{P_t}}\right]\left[gR(T+T_t)-\frac{\gamma-1}{2\gamma}(V_\theta^2+V_{\theta,t}^2)\right]\right\} \tag{d2b}$$

$$\frac{P_2}{P_1}=\left(\frac{T_2}{T_1}\right)^{\frac{\eta_p\gamma}{\gamma-1}}=\left(\frac{T_2}{T_1}\right)^{\frac{n}{n-1}} \tag{302}$$

$$\frac{P_2}{P_1}=\left(\frac{T_2}{T_1}\right)^{\frac{\gamma}{\gamma-1}}\left[1-\frac{\bar{\omega}'}{\left(\frac{P_2'}{P_1'}\right)_{id}}\left\{1-\left[\frac{1}{1+\frac{\gamma-1}{2}(M_1')^2}\right]^{\frac{\gamma}{\gamma-1}}\right\}\right] \tag{d3a}$$

$$\frac{P_3}{P_2}=1-\bar{\omega}\left[1-\left(\frac{1}{1+\frac{\gamma-1}{2}M_2^2}\right)^{\frac{\gamma}{\gamma-1}}\right] \tag{d3b}$$

$$\left(\frac{P_2'}{P_1'}\right)_{id}=\left[1+\frac{\gamma-1}{2}\frac{(\omega r_2)^2}{\gamma gRT_1'}\left(1-\frac{r_1^2}{r_2^2}\right)\right]^{\frac{\gamma}{\gamma-1}} \tag{59}$$

$$g\rho=\frac{P}{RT}\left(1-\frac{V^2}{2gJc_pT}\right)^{\frac{1}{\gamma-1}} \tag{d4}$$

$$w=K_{bk}2\pi g\int_{r_h}^{r_t}(\rho V_z r\,dr)_d \tag{d5}$$

$$\eta_{ad}=\frac{\left(\frac{P_2}{P_1}\right)^{\frac{\gamma-1}{\gamma}}-1}{\frac{T_2}{T_1}-1} \tag{317}$$

$$D=1-\frac{V_2'}{V_1'}+\frac{\Delta V_\theta'}{2\sigma V_1'} \tag{310}$$

$$\frac{2\sigma}{\cos\beta_2'}+\tan\beta_2'=\frac{V_{z,1}}{V_{z,2}}\left[\frac{2\sigma(1-D)}{\cos\beta_1'}+\tan\beta_1'\right] \tag{d6}$$

$$V_z=V_{z,t}\,\frac{\cos\beta}{\cos\beta_1}\exp\left(-\int_{r_t}^{r}\frac{\sin^2\beta}{r}\,dr\right) \tag{d7}$$

$$J\left(\frac{S}{R}\right)_2-J\left(\frac{S}{R}\right)_1=\ln\left[\frac{\left(\frac{T_2}{T_1}\right)^{\frac{\gamma}{\gamma-1}}}{\frac{P_2}{P_1}}\right] \tag{301}$$

$$Jgc_pt=Jgc_pT-\frac{V^2}{2} \tag{d8}$$

tion, eqs. (304) and (305) or eqs. (301) and (d8) (with the radial velocity equal to zero) are applied to derive eq. (d2b) from eq. (d2a).] An accurate evaluation of the axial velocity distribution by use of equations (d1b) and (d2b) requires that the reference radius be shifted from point to point. That is, the integration is first carried out from the initial reference radius to an adjacent radial station. The computed values of velocity at this adjacent radial station are then used as the reference-point values to compute conditions at the following radial station. Thus, the effect of any variation of entropy, temperature, and tangential velocity on the axial velocity distribution may be accurately considered if enough radial stations are specified across the annulus area.

Equation (d7) is a form of (d1a) for the special case of inlet guide vanes where the stagnation temperature is constant. This equation is derived in reference 249. Equation (d6) is an alternate form of the diffusion-factor relation (eq. (310)). A graphical solution of equation (d6) is presented in chapter IX.

GENERAL DETERMINATION OF AXIAL VELOCITY DISTRIBUTION

The design of the multistage compressor requires the solution of the general flow equations after each blade row in the compressor. This section is concerned with the methods of determining the velocity distributions after the inlet guide vanes and rotor and stator blade rows.

For the case of no inlet guide vanes or for guide vanes that impose a vortex turning distribution, it may be assumed for the initial design trial that the axial velocity is constant along the radius at the inlet to the first rotor row. For compressors having inlet guide vanes imparting a nonvortex turning distribution to the flow, the axial velocities at the outlet of the guide vanes or at the inlet to the first rotor will vary with radius and must be computed. As indicated in the previous discussion, the effects of streamline curvature may be sufficiently large in certain cases to necessitate consideration of these effects in the calculation procedure. In the design procedure, corrections for these curvature effects may be applied after the preliminary velocity distributions and passage geometry have been specified.

After the flow conditions at the inlet to the rotor are determined, the steps previously enumerated in the section on CONSIDERATION OF WALL BOUNDARY-LAYER EFFECTS are used to determine the velocity distribution and annulus area geometry after the rotor. The design variables that must be specified for the first rotor are the tip radius at the rotor discharge, the tangential and axial velocity changes (based on blade-loading considerations) across the critical blade element (usually the tip) of the rotor, and the radial distributions of energy addition and blade-element loss. The specification of these quantities completely determines the flow parameters at the discharge of the blade row. Application of the blockage correction K_{bk} in the continuity equation then permits the determination of the hub radius of the annular flow passage after the rotor. A similar procedure is used to determine the flow conditions after the following stator.

It is then necessary to review completely the preliminary design in order to determine its critical and undesirable features with respect to both the compressor performance and the performance of the other engine components. For instance, it will be necessary to go through the design procedure again in order to correct for streamline-curvature effects, or to improve the shape of the hub contour, or to revise the loss assumptions made originally. A recalculation may also be required to change the loading or Mach number level because certain blade elements appear to be too critically loaded. The blade sections may then be determined from the two-dimensional and annular-cascade data of chapters VI and VII and the calculated design flow conditions.

Three methods discussed generally in the section on CONSIDERATION OF WALL BOUNDARY-LAYER EFFECTS for determining the flow conditions in the compressor are presented here to indicate the possible uses of the available equations and data. In discussing these methods, it is assumed that the compressor tip geometry and aerodynamic conditions are known (i.e., inlet and outlet tip radii, wheel speed, limiting-loading parameter, and axial velocity ratio) and that inlet values for pressure, temperature, weight flow, and velocity are known. It is assumed that the radial velocity terms may be neglected. The tangential velocity distribution is taken to be the prescribed outlet variable. The values selected are not to be considered as uniquely desirable values. They are chosen merely to illustrate the methods of solution of the design equations. It should be em-

phasized that, once the preliminary flow and geometry conditions are determined, it will be necessary to review the design procedure to ensure the attainment of satisfactory performance.

METHOD I

As pointed out previously, the solution of the flow equations by method I assumes a complete knowledge of the radial variations of energy addition or tangential velocity after the rotor as well as the radial variation of entropy even into the wall boundary layers. Because of the lack of sufficient data of this type, this method may not be generally usable at the present time.

The steps itemized in the following sections for application of method I follow as closely as possible the procedure enumerated in the previous section.

Inlet guide vanes.—

(1) Tip radius and hub-tip radius ratio at the discharge of the inlet guide vanes are specified.

(2) The desired weight flow is specified. This weight flow will be used in the continuity equation to determine the magnitude of axial velocity required.

(3) The radial distribution of tangential velocity is specified. (Some restrictions on this are given in ref. 43.)

(4) The outlet stagnation temperature is equal to the inlet stagnation temperature and is constant radially.

(5) The radial distribution of loss $\bar{\omega}$ is assumed from wall to wall on the basis of data obtained from similar blade sections. The radial distribution of outlet stagnation pressure is computed from equation (d3b).

(6) The radial variation of axial velocity is computed from equation (d2b).

(7) The density variation along the radius is computed from equation (d4).

(8) The magnitude of the axial velocity is determined by trial-and-error application of the continuity equation (eq. (d5)) with the blockage factor K_{bk} equal to 1.0. It should be emphasized that in this method the velocities are calculated into the wall boundary layer so that additional boundary-layer corrections are unnecessary.

Rotor.—

(1) The tip radius at the rotor discharge is specified.

(2) The axial velocity at the tip radius after the rotor is specified. The tip tangential velocity after the rotor is then calculated from equation (310) for a specified value of diffusion factor (consistent with low loss or high efficiency) and an assumed tip solidity.

(3) The radial distribution of tangential velocity after the rotor is specified.

(4) The radial distribution of stagnation temperature after the rotor is computed from equation (316).

(5) The radial distribution of loss from wall to wall is assumed from the diffusion-factor—loss correlation of figure 212 (which is the same as fig. 203, ch. VII) and from data taken in the wall boundary layers. The radial distribution of stagnation pressure after the rotor is calculated from equation (d3a).

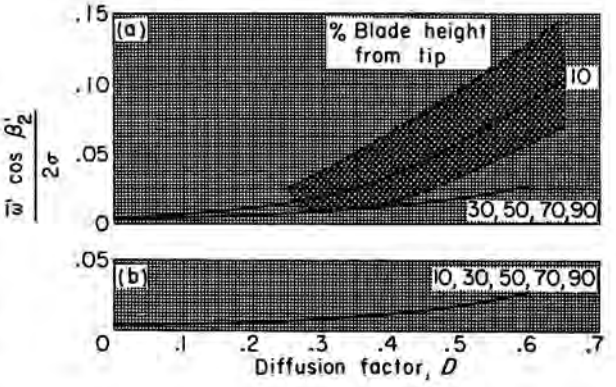

(a) Rotor.

(b) Stator.

FIGURE 212.—Design chart relating $\bar{\omega}'\cos\beta_2'/2\sigma$ to diffusion factor (see fig. 203, ch. VII, for larger print).

(6) The radial distribution of axial velocity is calculated from equation (d2b) using the specified tip axial velocity as the initial reference velocity $V_{z,t}$.

(7) The radial distribution of density is computed from equation (d4).

(8) The hub radius after the rotor is determined from equation (d5) with the blockage factor K_{bk} equal to 1.0. If this hub radius causes a shift in the streamline configuration from that used in the initial calculation, it may be necessary to repeat this procedure using the modified streamline locations.

Stator.—

(1) The tip radius at the discharge of the stator blade row is specified.

(2) The axial velocity and tangential velocity at the tip radius after the stator are specified considering the effect of these values on the losses and on the characteristics that are desirable for the following rotor row.

(3) The radial distribution of tangential velocity after the stator is specified.

(4) The radial variation of stagnation temperature is assumed to be the same after the stator as at the inlet to the stator.

(5) The radial distribution of loss from wall to wall is assumed from boundary-layer data of similar stators and from the diffusion-factor—loss correlation of chapter VII. The radial distribution of stagnation pressure is computed from equation (d3b).

(6) The radial distribution of axial velocity is computed from equation (d2b).

(7) The density variation along the radius is computed from equation (d4).

(8) The hub radius after the stator is determined from equation (d5) with the blockage factor K_{bk} equal to 1.0.

METHOD II

The essential difference between solution of the flow equations by methods II and I is that in method II the flow distributions are computed using available blade-element data as if no wall boundary layers were present. Appropriate correction factors for the effects of the wall boundary layers are then applied. Specifically, the principal differences are in the evaluation of the loss distribution along the radius (step (5) of method I) and in consideration of the wall boundary-layer blockage factor in the flow-continuity condition (step (8) of method I). The radial variation of loss for method II is determined from blade-element considerations alone and does not go into the wall boundary-layer effects. The blockage factor K_{bk} used in applying the continuity equation (d5) in method II is some value less than 1.0. As pointed out in reference 243, it may vary from 0.98 to 0.96 through the compressor.

The isre equation can also be used in this method for an initial approximation of the flow or for cases in which the radial gradients of entropy are negligible. In these cases, equation (d1a) or (d1b) is used in step (6) of method I. Equation (d7) may be used to compute the axial velocity distribution for blade rows having negligible radial gradients of stagnation temperature and pressure. In applying equation (d7), however, it is necessary to specify the flow-angle distribution after the blade row rather than the tangential velocity distribution.

METHOD III

The principal difference between the solution by method III and that by method II is in consideration of the blade-element loss. Rather than estimating a blade-element loss ω', an average rotor row efficiency is assigned in this method. It is then assumed that the rotor blade-element efficiency is equal to this average rotor efficiency. The stator losses may then be considered by specifying an average stage efficiency. The stagnation pressure after the rotor and stator blades may then be determined from the rotor and stage temperature ratios and the appropriate efficiencies. The isre equation ((d1a) or (d1b)) is then used in calculating the velocity distribution after the blade row. A method very similar to this one is presented in chapter IX, in which the solution is accomplished by the use of charts.

REMARKS

It must be emphasized that the previously outlined calculations are to be considered as preliminary calculations. After the annulus area geometry is determined, it will be necessary to review and probably recalculate the design to determine the final flow conditions through the compressor.

Naturally, other forms of these equations can lead to variations in the design procedure. It should be noted, however, that any variations must use self-consistent boundary-layer correction factors. Indiscriminate use of correction factors can lead to a design that is as poor as or worse than one in which boundary-layer corrections are completely neglected.

The radial velocity terms may be included in the methods presented if the streamline slope in the meridional plane is estimated. Thus, the radial velocity is related to the axial velocity. This necessitates retaining the radial velocity terms in equations (d4) and (d8).

Some secondary-flow effects may also be considered for certain specific cases in the design

691-564 O-65-19

system. For instance, reference 43 presents a method of considering the induced effects of the trailing vortex system on the inlet-guide-vane turning angle. Research on secondary-flow effects in annular cascades will no doubt eventually lead to corrections in the design system.

NUMERICAL EXAMPLE

As an illustration of the design procedure of method II, the design calculations for an inlet stage consisting of inlet rotor and stator are presented here. The given inlet conditions are as follows:

$P_1=2116$ lb/sq ft $\quad a_{a,1}=1116$ ft/sec

$T_1=518.7°$ R $\quad r_{1,t}=1.5$ ft

$V_{\theta,1}=0$ $\quad \frac{w\sqrt{\theta}}{\delta A_F}=35.0$ (lb/sec)/sq ft

The following design variables are selected:

Radial stations r_a, r_β, r_γ, r_δ, and r_ϵ at 10, 30, 50, 70, and 90 percent of passage depth.

$M_{z,1}=0.6 \quad V_{\theta,3}=0 \quad D_{R,\epsilon}\leqq 0.6$

$M'_{1,a}=1.1 \quad D_{R,a}=0.35 \quad D_S\leqq 0.6$

$K_{bk}=0.98$

K_P, K_e, and K_η are not used.

$\left(\frac{V_{z,2}}{V_{z,1}}\right)_a=1.0 \quad r_{2,t}=1.44$ ft, $r_{3,t}=1.44$ ft

$\left(\frac{V_{z,3}}{V_{z,2}}\right)_a=1.0 \quad \sigma_{R,a}=1.0, \ \sigma_{S,a}=0.7$

Values used for various constants are

$g=32.17$ ft/sec^2 $\quad c_p=0.243$ Btu/(lb)(°R)

$J=778.2$ ft-lb/Btu $\quad R=53.35$ ft-lb/(lb)(°R)

$\gamma=1.4$

The value of inlet hub-tip radius ratio is computed from the flow per unit frontal area, axial Mach number, and tip radius, as follows:

$$\frac{w\sqrt{\theta}}{\delta A_F}\frac{1}{K_{bk}}=\frac{35}{0.98}=35.7 \text{ (lb/sec)/sq ft}$$

From $M_{z,1}$, $w\sqrt{\theta}/\delta A_F$, and figure 211, $r_h/r_t=0.377$.

The actual weight flow is obtained from

$$A_{F,1}=\pi r_{1,t}^2=7.069 \text{ sq ft}$$

$$\frac{w\sqrt{\theta}}{\delta A_F}A_{F,1}=\frac{w\sqrt{\theta}}{\delta}=w=247 \text{ lb/sec}$$

The conditions at the rotor tip design station α (10 percent of passage depth) are computed next. From $M_{z,1}$ and reference 250,

$$\frac{a_1}{a_{a,1}}=0.9658$$

$$a_1=1078 \text{ ft/sec}$$

$$V_{z,1}=a_1M_{z,1}=(1078)(0.6)=647 \text{ ft/sec}$$

$$V'_{1,\alpha}=a_1M'_{1,\alpha}=(1078)(1.1)=1186 \text{ ft/sec}$$

$$U_{1,\alpha}=V_{\theta,1,\alpha}=[(V'_{1,\alpha})^2-V_{z,1,\alpha}^2]^{1/2}=994 \text{ ft/sec}$$

$$\beta'_{1,\alpha}=\tan^{-1}\left(\frac{U_1}{V_{z,1}}\right)_\alpha=56.9°$$

$$V_{z,2,\alpha}=(1.0)(V_{z,1,\alpha})=647 \text{ ft/sec}$$

The value of $\beta'_{2,\alpha}$ is computed from equation (d6) by application of the appropriate chart (fig. 217, ch. IX):

$$\beta'_{2,\alpha}=46.0°$$

$$V'_{\theta,2,\alpha}=V_{z,2,\alpha}\tan\beta'_{2,\alpha}=670 \text{ ft/sec}$$

$$V_{\theta,2,\alpha}=U_{2,\alpha}-V'_{\theta,2,\alpha}=297 \text{ ft/sec}$$

The iteration procedure for the computation of the radial variation of gas state is started by selecting the inlet radial stations. The computation lineups and results for the velocity calculations using the isre and nisre equations are shown in tables IV (a) and (b), respectively, where only the final results and final calculation lineups of the iteration procedure are presented.

In these designs the variation of outlet tangential velocity is prescribed as a function of r_2, so that an analytical integration of the isre equation is possible. Of course, graphical or numerical procedures may also be used. This velocity distribution is

$$V_{\theta,2}=V_{\theta,2,t}\left(2-\frac{r_2}{r_{2,t}}\right)$$

It should be emphasized that this distribution is chosen only to illustrate the design procedure for

TABLE IV.—CALCULATION PROCEDURES

(a) Using isre equations

Step	Parameter	Known design condition	Procedure	Radial position				
				α	β	γ	δ	ϵ
1	$r_1/r_{1,t}$	$r_{1,h}/r_{1,t}=0.377$	Choose 10, 30, 50, 70, 90 percent of passage depth	0.938	0.813	0.688	0.564	0.439
2	$U_1=V'_{\theta,1}$	$U_{1,t}=1060$	$U_{1,t}(r_1/r_{1,t})$	994	862	729	598	465
3	β'_1	$V_{m1}=647$	$\tan^{-1}(V'_{\theta,1}/V_{m1})$	56.9	53.1	48.4	42.8	35.7
4	V'_1		$\left[V^2_{z,1}+\left(V'_{\theta,1}\right)^2\right]^{1/2}$	1186	1078	975	881	797
5	M'_1	$a_1=1078$	V'_1/a_1	1.100	0.999	0.904	0.817	0.739
6	$r_2/r_{2,t}$	$r_{2,t}=1.44$	$r_{2,h}$ known from preliminary design (step 1)	0.950	0.832	0.720	0.608	0.496
7	$V_{\theta,2}$	$V_{\theta,2,t}=283$	$V_{\theta,2,t}[2-(r/r_t)_2]$	297	331	362	394	426
8	U_2	$U_{2,t}=1018$	$U_{2,t}(r/r_t)_2$	967	847	733	619	505
9	$T_2=T_3$	$T_1=518.7$	$T_1+[(U_2V_{\theta,2}-U_1V_{\theta,1})/gJc_p]$	566	565	562	559	554
10	$V_{m,2}$	$V_{m2,a}=647$	Eq. (311)	647	640	627	612	600
11	$V'_{\theta,2}$		$U_2-V_{\theta,2}$	670	516	371	225	79
12	β'_2		$\tan^{-1}(V'_{\theta,2}/V_{m,2})$	46.0	38.9	30.6	20.2	7.5
13	V'_2		$V_{m,2}/\cos\beta'_2$	932	822	728	652	605
14	$a_{w,2}$	$a_{w,1}=1116$	$a_{w,1}(T_2/T_1)^{1/2}$	1166	1165	1162	1158	1153
15	M_2		$V_2/a_{w,2}$ and ref. 250	0.635	0.644	0.649	0.655	0.666
16	M'_2		$M_2V'_2/V_2$	0.830	0.735	0.653	0.587	0.548
17	σ	$\sigma_a=1.0$	$\sigma_t(r_{1,t}+r_{2,t})/(r_1+r_2)$	1.00	1.15	1.34	1.61	2.02
18	D'		$1-(V'_2/V'_1)+(\Delta V'_\theta/2\sigma V'_1)$	0.351	0.377	0.390	0.391	0.360
19	$\bar{\omega}'$		D', $\cos\beta'_2/2\sigma$, and fig. 212	0.0734	0.0369	0.0405	0.0446	0.0489
20	$(p/P')_2$		M'_2 and ref. 250	0.636	0.699	0.751	0.792	0.816
21	P_2/P_1		$\left(\frac{T_2}{T_1}\right)^{\frac{\gamma}{\gamma-1}}\left[1-\bar{\omega}'\left(1-\frac{p_2}{P'_2}\right)\right]$	1.320	1.333	1.313	1.284	1.248
22	$g\rho_2$		$\frac{P_2}{RT_2}\left(1-\frac{V^2_{z,2}+V^2_{\theta,2}}{2Jgc_pT_2}\right)^{\frac{1}{\gamma-1}}$	0.0764	0.0769	0.0759	0.0744	0.0724
23	w	$K_{hb}=0.98$	$2\pi K_{hb}r_{2,t}\int_{(r_h/r_t)_2}^{1.0}(\rho V_{2'})_2\,d(r_2/r_{2,t})$			247		
24	$r_2/r_{2,t}$	$r_{2,t}=1.44$	$r_{2,h}$ known from preliminary design (step 1)	0.950	.838	0.730	0.622	0.514
25	$V_{m,2}=V_2$	$V_{m2,a}=V_{m2,a}$	$\left[V^2_{z,2,t}+2gJc_p(T_2-T_{2,t})\right]^{1/2}$	647	637	612	576	524
26	M_2	$a_{w,2}=a_{w,2}$	$V_2/a_{w,2}$ and ref. 250	0.573	0.564	0.527	0.498	0.455
27	σ	$\sigma_a=0.7$	$\sigma_t(r_{2,t}+r_{2,h})/(r_2+r_2)$	0.700	0.796	0.917	1.08	1.32
28	D		$1-(V_2/V_2)+(\Delta V_\theta/2\sigma V_2)$	0.389	0.405	0.427	0.458	0.507
29	$\bar{\omega}$		D, 2σ, and fig. 212	0.0182	0.0223	0.0275	0.0346	0.0501
30	$(p/P)_2$		M_2 and ref. 250	0.800	0.806	0.819	0.837	0.862
31	P_2/P_2		$1-\bar{\omega}\left(1-\frac{p_2}{P_2}\right)$	0.996	0.996	0.995	0.994	0.993
32	$g\rho_2$		$\frac{P_2}{RT_2}\left(1-\frac{V_2^2}{2gJc_pT_2}\right)^{\frac{1}{\gamma-1}}$	0.0788	0.0800	0.0800	0.0799	0.0799
33	w		$2\pi K_{hb}r_{2,t}\int_{(r_h/r_t)_2}^{1.0}(\rho V_{2'})_2\,d(r_2/r_{2,t})$			247		
34	P_2/P_1			1.32	1.33	1.31	1.28	1.24
35	$\eta_{ad,ST}$		$\left[\left(\frac{P_2}{P_1}\right)^{\frac{\gamma-1}{\gamma}}-1\right]\Big/\left(\frac{T_2}{T_1}-1\right)$	0.895	0.946	0.944	0.940	0.928
	$(T_2/T_1)_{av}$		Mass-average T_2/T_1			1.083		
	$(P_2/P_1)_{av}$		Mass-average P_2/P_1			1.29		
	$\eta_{ad,av}$		Mass-average $\eta_{ad,ST}$			0.932		

TABLE IV.—CALCULATION PROCEDURES—Concluded

(b) Using nisre equations

Step	Parameter	Known design condition	Procedure	Radial position				
				α	β	γ	δ	ϵ
36	$r_1/r_{1,t}$	$r_{1,h}/r_{1,t}$	(Step 1)	0.938	0.813	0.688	0.564	0.439
37	$U_1=V'_{\theta,1}$	$U_{1,t}=1060$	$U_{1,t}(r_1/r_{1,t})$	994	862	729	598	465
38	β'_1	$V_{a,1}=647$	$\tan^{-1}(V'_{\theta,1}/V_{a,1})$	56.9	53.1	48.4	42.8	35.7
39	V'_1		$[V^2_{a,1}+(V'_{\theta,1})^2]^{1/2}$	1186	1078	975	881	797
40	M'_1	$a_1=1078$	V'_1/a_1	1.100	0.999	0.904	0.817	0.739
41	$r_2/r_{2,t}$	$r_{2,t}=1.44$	$r_{2,h}$ known from preliminary design	0.950	0.838	0.730	0.622	0.514
42	$V_{\theta,2}$	$V_{\theta,2,t}=283$	$V_{\theta,2,t}\left[2-\left(\frac{r}{r_t}\right)_2\right]$	297	329	359	390	420
43	U_2	$U_{2,t}=1018$	$U_{2,t}(r_2/r_{2,t})$	967	853	743	633	523
44	$T_2=T_3$	$T_1=518.7$	$T_1+[(U_2V_{\theta,2}-U_1V_{\theta,1})/gJc_p]$	566	565	563	559	555
45	$\frac{S_{2,t}-S_2}{RJ^{-1}}$	P_2 known from previous trial	$\ln\left[\frac{\left(\frac{T_{2,t}}{T_2}\right)^{\frac{\gamma}{\gamma-1}}}{P_{2,t}/P_2}\right]$	--------	1.009	0.988	0.981	0.974
46	$V_{a,2}$	$V_{a,2,a}=647$	Eq. (312)	647	662	652	640	628
47	$V'_{\theta,2}$		$U_2-V_{\theta,2}$	670	524	384	243	103
48	β'_2		$\tan^{-1}(V'_{\theta,2}/V_{a,2})$	46.0	38.4	30.5	20.8	9.3
49	$a_{a,2}$	$a_{a,1}=1116$	$a_{a,1}(T_2/T_1)^{1/2}$	1166	1165	1162	1159	1154
50	M_2		$V_2/a_{a,2}$ and ref. 250	0.635	0.662	0.669	0.675	0.685
51	M'_2		$M_2V'_2/V_2$	0.830	0.756	0.680	0.617	0.577
52	σ	$\sigma_\alpha=1.0$	$\sigma_t(r_{1,t}+r_{2,t})/(r_1+r_2)$	1.0	1.14	1.33	1.59	1.98
53	D'		$1-(V'_2/V'_1)+(\Delta V'_\theta/2\sigma V'_1)$	0.351	0.353	0.356	0.350	0.316
54	$\bar{\omega}'$		D', $\cos\beta'_2/2\sigma$, and fig. 212	0.0734	0.0350	0.0371	0.0409	0.0422
55	$(p/P')_2$		M'_2 and ref. 250	0.636	0.685	0.734	0.774	0.798
56	P_2/P_1		$\left(\frac{T_2}{T_1}\right)^{\frac{\gamma}{\gamma-1}}\left[1-\bar{\omega}'\left(1-\frac{p_2}{P'_2}\right)\right]$	1.320	1.332	1.316	1.290	1.256
57	$g\rho_2$		$\frac{P_2}{RT_2}\left(1-\frac{V^2_{z,2}+V^2_{\theta,2}}{2gJc_pT_2}\right)^{\frac{1}{\gamma-1}}$	0.0764	0.0761	0.0750	0.0738	0.0719
58	w	$K_{bk}=0.98$	$2\pi K_{bk}r_{2,t}\int_{(r_h/r_t)_2}^{1.0}(\rho V_z r)_2\,d(r_2/r_{2,t})$			247		
59	$r_3/r_{3,t}$	$r_{3,t}=1.44$	$r_{3,h}$ known from preliminary design (step 1)	0.950	0.844	0.740	0.636	0.532
60	$\frac{S_{3,t}-S_3}{RJ^{-1}}$	P_3 known from previous trial	$\ln\left[\frac{\left(\frac{T_{3,t}}{T_3}\right)^{\frac{\gamma}{\gamma-1}}}{P_{3,t}/P_3}\right]$	--------	0.0152	0.0005	0.0000	−0.0004
61	$V_{a,3}=V_3$	$V_{a,3,a}=647$	Eq. (313)	647	658	638	606	559
62	M_3	$a_{a,2}=a_{a,3}$	$V_3/a_{a,3}$ and ref. 250	0.573	0.584	0.566	0.538	0.496
63	σ	$\sigma_\alpha=0.7$	$\sigma_t(r_{1,t}+r_{3,t})/(r_2+r_3)$	0.700	0.791	0.905	1.057	1.272
64	D		$1-(V_3/V_2)+(\Delta V_\theta/2\sigma V_2)$	0.390	0.391	0.410	0.438	0.480
65	$\bar{\omega}$		D, 2σ, and fig. 212	0.0182	0.0206	0.0253	0.0317	0.0445
66	$(p/P)_3$		M_3 and ref. 250	0.8005	0.794	0.804	0.822	0.845
67	P_3/P_2		$1-\bar{\omega}\left(1-\frac{p_3}{P_3}\right)$	0.9964	0.9958	0.9951	0.9941	0.9931
68	$g\rho_3$		$\frac{P_3}{RT_3}\left(1-\frac{V^2_3}{2gJc_pT_3}\right)^{\frac{1}{\gamma-1}}$	0.0788	0.0792	0.0791	0.0792	0.0791
69	w		$2\pi K_{bk}r_{2,t}\int_{r_{3,h}/r_{3,t}}^{1.0}\rho_3V_{z,3}r_3\,d(r_3/r_{3,t})$			247		
70	P_3/P_1		$\left[\left(\frac{P_3}{P_1}\right)^{\frac{\gamma-1}{\gamma}}-1\right]\Big/\left(\frac{T_3}{T_1}-1\right)$	1.315	1.327	1.309	1.282	1.247
71	$\eta_{ad,ST}$			0.895	0.947	0.946	0.940	0.932
	$(T_3/T_1)_{av}$		Mass-average T_3/T_1			1.090		
	$(P_3/P_1)_{av}$		Mass-average P_3/P_1			1.30		
	$\eta_{ad,av}$		Mass-average $\eta_{ad,ST}$			0.936		

the general case where radial temperature gradients are present and does not necessarily represent an optimum design condition. The isre equation (d1a) can then be directly integrated, with the following result:

$$V_{z,2}^2=V_{z,2,t}^2+2gJc_p(T_2-T_{2,t})-(V_{\theta,2}^2-V_{\theta,2,t}^2)$$
$$-8V_{\theta,2,t}^2\left[\ln\frac{r_2}{r_{2,t}}-\frac{1}{r_{2,t}}(r_2-r_{2,t})+\frac{1}{8}\left(\frac{1}{r_{2,t}^2}\right)(r_2^2-r_{2,t}^2)\right] \quad (311)$$

where the α station is used as the initial reference station. All the terms on the right side of equation (311) are known as functions of the trial values of r_2 (r_2 depends on the selection of $r_{2,t}$ and $r_{2,h}$, since in this procedure the radial stations were chosen at stated percentages of the passage depth). The final value of $r_{2,h}$ is obtained by the iteration procedure of steps 6 to 23 in table IV(a). The weight flow is computed numerically (e.g., by plotting $(2\pi K_{bk}\rho V_z r_t r)_2$ against $(r/r_t)_2$ and carrying out a graphical integration).

In order to compute weight flow, density and hence stagnation pressure must be calculated at the blade-row outlet. Stagnation pressure can be computed from stagnation temperature and the loss-velocity-diagram correlations presented in chapters VI and VII. The design chart (from data presented in ch. VII) used here to relate stagnation-pressure loss to velocity diagram is shown in figure 212. This chart is used in the design procedure shown in table IV, while an explanation of its significance is given in chapter VII. Here $(P_2'/P_1')_{id}$ is taken equal to 1.0, which is exact for a constant-radius blade element.

The stator design is simpler than that for the rotor in this case, since $V_{\theta,3}$ is chosen to be zero; however, the basic approach is the same. The isre equation becomes

$$V_{z,3}^2=V_{z,3,t}^2+2gJc_p(T_3-T_{3,t})$$

where again the α station is used as the initial reference station. The stator curve in figure 212 is used for all radial stations.

The rotor and stator design using the nisre equation is carried out with the same design conditions as prescribed for the design using the isre equation. Thus steps 36 to 44 of table IV(b) are the same as those from 1 to 9. The method of computing the outlet axial velocity is now changed, since data from a previous approximation are used in the solution. Here the final results of the isre solution are used to obtain the loss data for the initial nisre solution for outlet axial velocity. This is an intermediate step for which the data are not presented in the tables. The nisre equation for outlet axial velocity for the assumed conditions is

$$V_{z,2}^2\left[1+\frac{\gamma-1}{2\gamma}\frac{J}{R}(S_{2,1}-S_2)\right]$$
$$=V_{z,2,t}^2+2gJc_p(T_2-T_{2,t})-(V_{\theta,2}^2-V_{\theta,2,t}^2)$$
$$-8V_{\theta,2,t}^2\left[\ln\frac{r_2}{r_{2,t}}-\frac{r_2-r_{2,t}}{r_{2,t}}+\frac{1}{8r_{2,t}^2}(r_2^2-r_{2,t}^2)\right]$$
$$+\frac{J}{R}\left[gR(T_{2,t}+T_2)-\frac{\gamma-1}{2\gamma}(V_{\theta,2,t}^2+V_{\theta,2}^2+V_{z,2,t}^2)\right]$$
$$(S_{2,t}-S_2) \quad (312)$$

where

$$S_{2,t}-S_2=\frac{R}{J}\ln\frac{\left(\frac{T_{2,t}}{T_2}\right)^{\frac{\gamma}{\gamma-1}}}{\frac{P_{2,t}}{P_2}}$$

Equation (312) was obtained under the following restrictions: (1) that $V_r=0$, and (2) that entropy and static temperature vary linearly with radius in the interval of integration and thus the reference radius is shifted from point to point, starting at α near the tip. This solution illustrates a numerical solution of the equilibrium equation. The remainder of this calculation for the rotor is the same as that for the isre case.

The loss estimates for the stator are made initially from the isre solution for the stator, and the entropy variation is computed from these values. The stator velocity-diagram calculations then proceed as do the rotor nisre calculations, using the equation

$$V_{z,3}^2\left[1+\frac{\gamma-1}{2\gamma}\frac{J}{R}(S_{3,t}-S_3)\right]$$
$$=V_{z,3,t}^2+2gJc_p(T_3-T_{3,t})$$
$$+\frac{J}{R}\left[gR(T_{3,t}+T_3)-\frac{\gamma-1}{2\gamma}V_{z,2,t}\right]$$
$$(S_{3,t}-S_3) \quad (313)$$

CONCLUDING REMARKS

The general flow equations that must be solved in the determination of design velocity distributions and flow passage configuration in compressors have been presented. In general, it is felt that more data are required to establish accurately the boundary-layer effects and correction factors on weight flow or annulus area and average stage pressure ratio and efficiency. It is expected, however, that the boundary-layer correction system discussed in this chapter will lead to a satisfactory design approximation. The need for concentrated analytical and experimental work is indicated by the lack of satisfactorily evaluated calculation procedures for determination of velocity distributions where streamline-curvature effects are large. In the high-performance compressors being considered at the present time, accurate prediction of design-point performance may not be possible until these curvature effects can be considered in the design procedure. For the time being, these three-dimensional-flow problems may be alleviated by geometric modifications of the hub and casing profile. It should be reemphasized here that the compressor design procedure is a trial-and-error compromise procedure. It is generally necessary to go through the design calculations a number of times before all elements of the compressor may be considered to be satisfactorily designed with respect to aerodynamic and mechanical considerations.

CHAPTER IX

CHART PROCEDURES FOR DESIGN VELOCITY DISTRIBUTION

By Arthur A. Medeiros and Betty Jane Hood

A series of charts for the solution of the flow equations used in the design of axial-flow compressors is developed. The equations, which are presented in chart form, are radial equilibrium (in a simplified form), continuity of flow, energy addition, efficiency, vector relations, and diffusion factor.

Because the charts are based on general flow equations, they can be used in the design of any axial-flow compressor. An example of the use of the charts in the design of a stage consisting of a rotor and stator blade row is presented. Comparison of the pertinent design values obtained by the chart procedure with analytically calculated values indicates that good accuracy can be attained by careful use of the charts.

INTRODUCTION

The over-all design requirements of airflow and pressure ratio for the compressor component of a gas-turbine engine are generally determined on the basis of a cycle analysis for the particular application of the engine. For many present-day aircraft applications, an axial-flow compressor is selected because of its high efficiency and high flow per unit frontal area.

The general geometry of the compressor, such as the tip diameter, blade speed, inlet and discharge axial velocities, and inlet and discharge areas, is determined by consideration not only of the compressor but also of the combustor and turbine components of the engine. The selection of inlet axial velocity, compressor blade speed, and inlet hub and tip diameters involves a compromise among high weight flow per unit frontal area (low hub-tip diameter ratio and high axial velocity), high stage pressure ratio (high blade speed), and reasonable turbine blade stresses (low blade speed, low axial velocity, and high hub-tip diameter ratio). The magnitudes of the axial velocity and blade speed must also be compromised on the basis of the effects of the resultant Mach number on blade-section efficiency. Compressor blade stresses, other than vibratory stresses, play only a small part in this compromise. The factors affecting these considerations are discussed more completely in chapter II and in reference 17.

Other compromises must be made in the compressor design in addition to the inlet configuration. The compressor-discharge velocity must be adjusted on the basis of compressor diffuser and combustor-inlet requirements. Low compressor-discharge axial velocities are favorable with respect to combustor efficiency; however, high axial velocities are desirable through the compressor for attaining high stage pressure ratios and hence decreasing compressor weight. With the inlet and discharge axial velocities selected, it is then necessary to prescribe a stagewise variation in the axial velocities and blade-loading limits so that a reasonable hub shape is obtained.

Another variable that must be dealt with is the radial distribution of tangential velocities. Not a great deal of information is available on the over-all desirability of the various radial distributions of velocity diagrams, so that, for the most part, the choice is a matter of experience with some particular distribution.

It is obvious that, with this wide selection of combinations of axial and radial distributions of velocities and the compromises required because of the factors affecting aerodynamic performance, weight, and mechanical reliability of the various components, many compressor configurations are possible to meet the given over-all design requirements. Some preliminary design calculations are therefore necessary before a final compressor configuration is selected.

Each of these preliminary design calculations requires the solution of the fundamental flow equations after each blade row. The application of the fundamental flow equations to compressor

design is discussed in detail in chapter VIII. However, the complete design procedure presented in chapter VIII would be very time-consuming if used for the purpose of design evaluations. It is desirable to put the fundamental flow equations applicable to compressor design in simple and easily used chart form.

Another reason for simplifying the compressor design procedure for certain applications is the iterative nature of the complete design procedure. The iteration is a result of the mutual interrelation between the calculation of the radial distribution of velocities, the passage shape of the compressor, and the selection of blading to achieve the radial distributions of velocity. For example, the axial velocity distribution after any blade row is a function not only of the radial distribution of tangential velocities but also of the energy gradient and the gradient of losses. However, the tangential velocities (or energy) and losses are functions of the blading and the angular setting of the blading with respect to the flow. The general procedure is to prescribe the desired radial distribution of tangential velocity or energy and assume a loss at each radial station at which the axial velocity is to be calculated. The calculation of the axial velocity to satisfy the radial-equilibrium condition completes the vector diagram, and it is then possible to select blading on the basis of data such as that presented in chapters VI and VII. At this point, the losses for the selected blade section can be obtained from blade-element data and checked against the assumed losses. If the assumed and calculated losses are sufficiently different, the entire calculation must be repeated with new assumed values of losses.

Streamline curvature, particularly in stages with low hub-tip diameter ratios and high pressure ratios, will affect the radial distribution of axial velocity. Some of the factors that control the streamline curvature and methods of analytically correcting for the effect on axial velocity are discussed in chapter VIII and in references 34, 49, 236, 238, and 239. It is obvious that the hub and tip diameter variation through the compressor will greatly influence the streamline shape. Therefore, a preliminary design calculation is necessary to determine the approximate passage shape variation before streamline-curvature corrections to the axial velocity can be made. For this reason, also, it is advantageous to have the preliminary design procedure in easily used chart form.

This chapter develops and presents a chart procedure for the design of axial-flow compressors using any consistent set of assumed design values and velocity distributions. The radial-equilibrium equation (in simplified form), the continuity equation, the energy-addition and efficiency equations, vector relations, and the diffusion-factor equation (see ref. 9) are presented in graph form.

The method can be used for making preliminary design calculations to determine the compressor configuration to meet given over-all performance requirements with any given set of aerodynamic limitations such as Mach number and blade-loading levels. It can also be used as the first step in a complete design procedure to determine initial velocity diagrams and passage shape variations. An intelligent estimate of losses in the blading and streamline curvatures due to the walls can then be made, so that iterations in the complete design procedure can be minimized or eliminated. When the corrections to the design due to entropy gradients and streamline curvatures are expected to be small, the charts can be used for final design calculations, provided, of course, that they are used with care and judgment. An example of the use of the charts in the design of an axial-flow compressor stage is presented herein, and the results of the graphical procedure are compared for accuracy with analytically calculated values.

SYMBOLS

The following symbols are used in this chapter:

A	area, sq ft
a	speed of sound, ft/sec
a_a	speed of sound based on stagnation conditions, ft/sec
B	$C+V_z^2-V_{z,t}^2$, $(\text{ft/sec})^2$
C	$2gJc_p(T_t-T)$, $(\text{ft/sec})^2$
c_p	specific heat at constant pressure, 0.243 Btu/(lb)(°R)
D	diffusion factor
$\mathcal{F}$	blade force acting on gas, lb
g	acceleration due to gravity, 32.17 ft/sec^2
H	total or stagnation enthalpy, Btu/lb
J	mechanical equivalent of heat, 778.2 ft-lb/Btu
K_{bk}	weight-flow blockage factor
M	Mach number

P total or stagnation pressure, lb/sq ft
p static or stream pressure, lb/sq ft
R gas constant, 53.35 ft-lb/(lb)(°R)
r radius, ft
S entropy, Btu/(lb)(°R)
T total or stagnation temperature, °R
t static or stream temperature, °R
U rotor speed, ft/sec
V air velocity, ft/sec
w weight flow, lb/sec
z coordinate along axis, ft
β air angle, angle between air velocity and axial direction, deg
γ ratio of specific heats, 1.4
δ ratio of total pressure to NASA standard sea-level pressure of 2116 lb/sq ft
η_{ad} adiabatic efficiency
θ ratio of total temperature to NASA standard sea-level temperature of 518.7° R
ρ density, lb-sec^2/ft^4
σ solidity, ratio of chord to spacing
ω angular velocity of rotor, radians/sec
$\bar{\omega}$ total-pressure-loss coefficient

Subscripts:

an annulus
av average
b radial station midway between tip and mean
c radial station midway between mean and hub
F frontal
h hub
i reference position, radial station where variables are known
k continuity value, value corrected for boundary-layer blockage
l local value of flow per unit annulus area
m mean
R rotor
r radial direction
S stator
sl NASA standard sea-level conditions
t tip
z axial direction
θ tangential direction
1 station at inlet to rotor blade row at equispaced distances across annulus
2 station at exit of rotor blade row at equispaced distances from tip to assumed hub
2a station at exit of rotor blade row at equispaced distances across annulus
3a station at exit of stator blade row at equispaced distances across annulus

Superscript:

relative to rotor

DESIGN EQUATIONS

The flow equations applicable to compressor design are discussed in detail in chapters III and VIII. These equations, in the form usually used in compressor design, are as follows:

Radial equilibrium:

$$gJ\frac{\partial H}{\partial r}=\mathcal{F}_r+gJt\frac{\partial S}{\partial r}+\frac{V_\theta}{r}\frac{\partial(rV_\theta)}{\partial r}+V_z\frac{\partial V_z}{\partial r}-V_z\frac{\partial V_r}{\partial z} \quad (314)$$

Continuity:

$$w_k=2\pi K_{bk}\int_{r_h}^{r_t}\rho gVr\cos\beta\,dr \quad (315)$$

Energy addition:

$$gJc_p(T_2-T_1)=\omega(r_2V_{\theta,2}-r_1V_{\theta,1})=U_2V_{\theta,2}-U_1V_{\theta,1} \quad (316)$$

Adiabatic temperature-rise efficiency:

$$\eta_{ad}=\frac{\left(\frac{P_2}{P_1}\right)^{\frac{\gamma-1}{\gamma}}-1.0}{\frac{T_2}{T_1}-1.0} \quad (317)$$

Diffusion factor:

$$D=1-\frac{V_2'}{V_1'}+\frac{\Delta V_\theta'}{2\sigma V_1'} \quad (310)$$

State:

$$p=\rho gRt \quad (34)$$

Mach number:

$$M=\frac{V}{\sqrt{\gamma gRt}} \quad (318)$$

In addition to these are the trigonometric relations equating velocities and flow angles, and the adiabatic relations equating the static and stagnation values of pressure and temperature. The adiabatic relations, as function of Mach number, are presented in tabular form in reference 250.

Equations (34) and (318) can be handled conveniently by using readily computed stagnation conditions, instead of static conditions, and using the tables of reference 250; therefore, no charts are deemed necessary to determine state conditions and Mach numbers. Charts for the solution of equations (310) and (314) to (317) and the vector relations are presented herein.

FORMULATION OF CHARTS

RADIAL EQUILIBRIUM

In order to calculate the vector diagrams for an axial-flow turbomachine, it is necessary to satisfy the radial-equilibrium condition given as equation (314). For the purpose of preliminary design analyses and, in some instances, even for the final design procedure, it is possible to simplify the equation.

Since the equation is usually applied between blade rows, the blade force term $\mathcal{F}$ is zero. If the entropy gradient $\partial S/\partial r$ is assumed zero and the streamline curvature is assumed small so that the change in radial velocity in the axial direction $\partial V_r/\partial z$ can be neglected, equation (314) can be written

$$gJ\frac{\partial H}{\partial r}=\frac{V_\theta^2}{r}+\frac{V_\theta \partial V_\theta}{\partial r}+\frac{V_z \partial V_z}{\partial r} \qquad (319)$$

Equation (319) is the isentropic simplified-radial-equilibrium equation that is widely used in the design of axial-flow compressors and will be put in chart form.

Integration of equation (319) between any radius r and the radius at which all values are known r_t gives the following:

$$gJ(H_t-H)=\int_r^{r_t}\frac{V_\theta^2}{r}\partial r+\frac{V_{\theta,t}^2-V_\theta^2}{2}+\frac{V_{z,t}^2-V_z^2}{2} \qquad (320)$$

If the absolute tangential velocity V_θ is expressed analytically as a function of radius r, the integral in equation (320) can be evaluated analytically and the equation solved for any desired variable. However, it is sometimes impossible or undesirable to use a distribution of tangential velocity that makes equation (320) convenient to apply.

If it is assumed that V_θ^2/r is linear with respect to r over the interval r_t-r, equation (320) can be written

$$2gJc_p(T_t-T)+V_z^2-V_{z,t}^2=\left[\left(\frac{V_\theta^2}{r}\right)_t+\frac{V_\theta^2}{r}\right](r_t-r)+V_{\theta,t}^2-V_\theta^2 \qquad (321)$$

With a rearrangement of terms, equation (321) becomes

$$\frac{2gJc_p(T_t-T)+V_z^2-V_{z,t}^2}{V_{\theta,t}^2}=2\left(1-\frac{V_\theta^2}{V_{\theta,t}^2}\right)+\frac{r_t}{r}\left(\frac{V_\theta^2}{V_{\theta,t}^2}\right)-\frac{r}{r_t} \qquad (322)$$

Equation (322) is presented in graph form in figure 213. In the first quadrant, the tangential velocity ratio $V_\theta/V_{\theta,t}$ is plotted against the right side of equation (322) with the radius ratio r/r_t as a parameter. Then, with $V_{\theta,t}$ as a parameter in the second quadrant, the numerator of the left side of equation (322) appears as the abscissa. Therefore, if the tangential velocities are known at two radii, use of the first two quadrants of figure 213 will give a value for

$$2gJc_p(T_t-T)+V_z^2-V_{z,t}^2=B$$

If the radial interval is sufficiently close for the approximation of linearity between V_θ^2/r and r, the value of B will be that required to satisfy isentropic simplified radial equilibrium between radial stations r_t and r. For convenience, let

$$2gJc_p(T_t-T)=12{,}170(T_t-T)=C \qquad (323)$$

Then

$$V_z^2-V_{z,t}^2=B-C \qquad (324)$$

The third quadrant of figure 213 is a plot of $B-C$ against V_z with $V_{z,t}$ as the parameter. The abscissa of quadrants II and III, then, represents two values, depending on which quadrant is being used. When used with the second quadrant, its value is B; when used with the third quadrant, its value is $B-C$. If the temperature gradient is known, C can be calculated by the use of equation (323). This value is subtracted from the value of B, determined by use of the first two quadrants of figure 213, and the difference $(B-C)$ is used as the abscissa of the third quadrant together with the known value of axial velocity $V_{z,t}$ to determine the value of axial velocity V_z at radius r.

Although the use of figure 213 has been discussed on the basis of known tangential velocities and temperatures at all radii and solving for the axial velocities, it is obvious that the chart can also be used with other assumptions. For example, the axial velocities and temperatures can be assumed at all radii and the tangential velocity

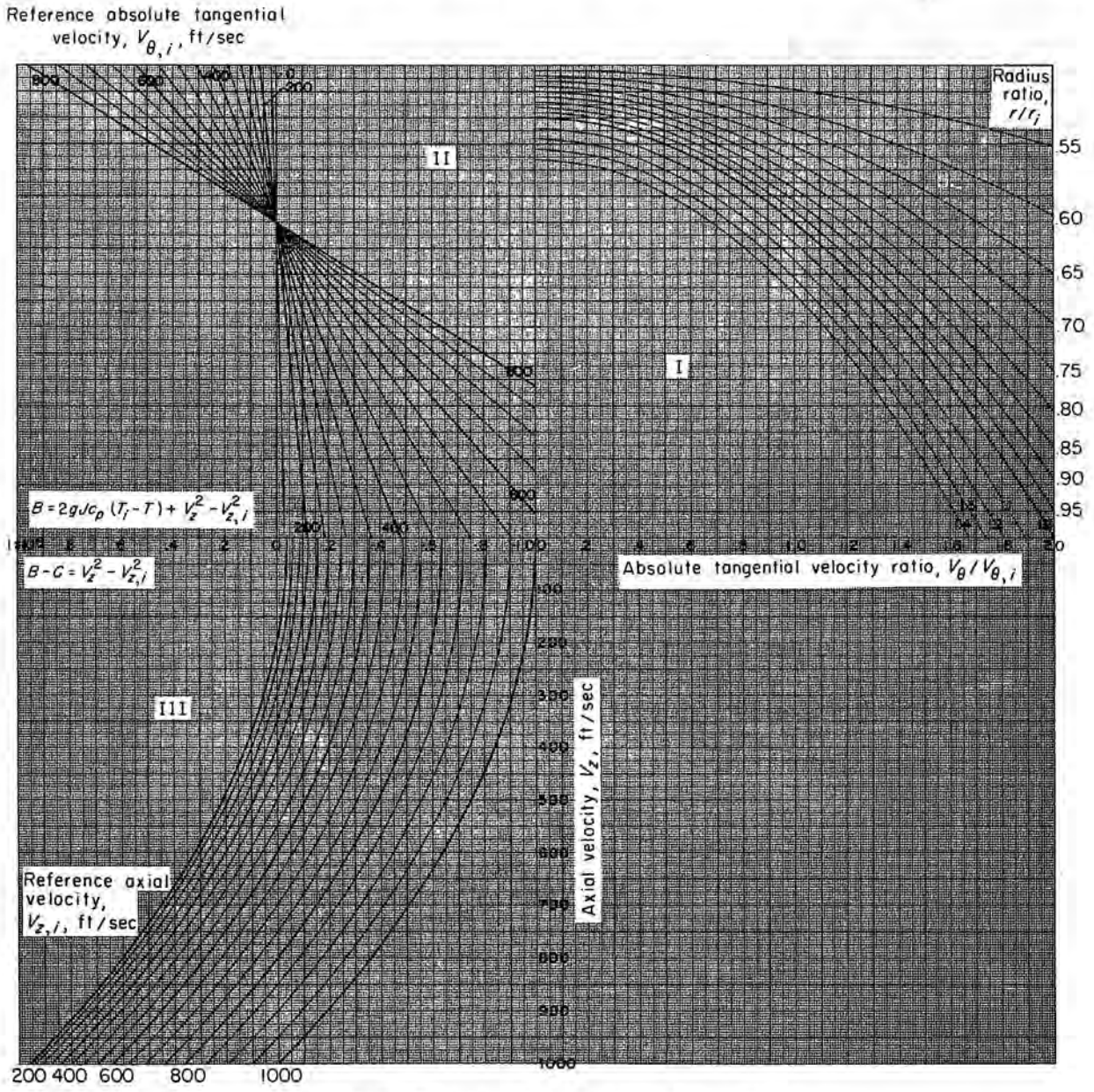

FIGURE 213.—Chart to satisfy simple radial equilibrium.

assumed at one radius. The tangential velocity required to satisfy radial equilibrium at all other radii can then be obtained from the chart. In other words, figure 213 may be used to determine any independent variable of equation (322).

The accuracy of the method of utilizing figure 213 is limited only by the assumption of linearity of V_θ^2/r with respect to radius. For wheel-type rotation, for example, V_θ^2/r is linear with radius; therefore, good accuracy can be expected regardless of the size of the interval $r_t - r$. However, with nonlinear radial variations of V_θ^2/r, the accuracy of the results obtained from figure 213 will depend on the interval used. For this reason, a small radial interval is recommended.

In order to illustrate the effect of the radial interval on the accuracy of the results of figure 213, axial velocities were read using 3 and 7 radial positions. An arbitrary, nonlinear radial distribution of V_θ^2/r was assumed. The distribution

of tangential velocity is a combination of constant, wheel, and vortex rotations. The assumptions and results are as follows:

$$V_\theta = 2400 - 900\frac{r}{r_t} - 900\frac{r_t}{r}$$

$$\frac{r_h}{r_t} = 0.5; \qquad V_{z,t} = 450; \qquad \frac{dT}{dr} = 0$$

$\frac{r}{r_t}$	V_θ	Calculated V_z	3-Point chart procedure		7-Point chart procedure	
			V_z	Percent error	V_z	Percent error
1.0	600	450	450	------	450	------
.9	590	538	------	------	536	0.4
.8	555	638	------	------	636	.3
.75	525	691	683	1.2	691	0
.7	484	744	------	------	743	.1
.6	360	846	------	------	844	.2
.5	150	921	910	1.2	921	0

As the table shows, even with the larger radial interval, the errors in axial velocity are only 1.2 percent; however, with the 7-radial-position procedure, the error is reduced to a maximum of 0.4 percent. It should be noted that the radial intervals used in the 7-position procedure are not all equispaced; an extra position was used at $r/r_t = 0.75$. The error in the region of this smallest interval was 0.1 percent. Thus, extremely good accuracy can be obtained by the use of the radial-equilibrium chart, even with nonlinear distributions of V_θ^2/r, if small radial intervals are used.

CONTINUITY

Another condition that must be satisfied, in addition to the radial-equilibrium condition, is continuity of flow:

$$w_k = 2\pi K_{bk}\int_{r_h}^{r_t} \rho g V r \cos\beta \, dr \qquad (315)$$

The use of the boundary-layer blockage factor K_{bk} in compressor design is discussed in chapter VIII. From the equations of state and Mach number and the adiabatic relations, the following equations can be obtained:

$$\rho g = \frac{P}{RT_t}\left(1+\frac{\gamma-1}{2}M^2\right)^{-\frac{1}{\gamma-1}} \qquad (325)$$

and

$$V = a_a\left(\frac{V}{a_a}\right) = \frac{M\sqrt{\gamma g RT}}{\sqrt{1-\frac{\gamma-1}{2}M^2}} \qquad (326)$$

Substituting equations (325) and (326) into the continuity equation (315) produces the following expression:

$$w_k = 2\pi K_{bk}\int_{r_h}^{r_t} \frac{\sqrt{\gamma g}PM\cos\beta}{\sqrt{RT}\left(1+\frac{\gamma-1}{2}M^2\right)^{\frac{\gamma+1}{2(\gamma-1)}}} r\,dr \qquad (327)$$

Writing equation (327) in terms of equivalent weight flow,

$$\left(\frac{w\sqrt{\theta}}{\delta}\right)_k = 2\pi K_{bk}\int_{r_h}^{r_t}\left[\frac{\gamma g P_{sl} M\cos\beta}{a_{sl}\left(1+\frac{\gamma-1}{2}M^2\right)^{\frac{\gamma+1}{2(\gamma-1)}}}\right] r\,dr \qquad (328)$$

The part of the integrand in brackets is the local value (value at radius r) of equivalent weight flow per unit annulus area:

$$\left(\frac{w\sqrt{\theta}}{\delta A_{an}}\right)_l = \frac{\gamma g P_{sl} M\cos\beta}{a_{sl}\left(1+\frac{\gamma-1}{2}M^2\right)^{\frac{\gamma+1}{2(\gamma-1)}}} \qquad (329)$$

The first quadrant of figure 214 is a plot of equation (329). The local value of equivalent flow per unit annulus area is plotted against absolute resultant Mach number for constant values of absolute flow angle. Local values of equivalent flow per unit annulus area can be determined from figure 214 for all radii at which the vector diagrams have been determined; then, the continuity value of equation (328) becomes

$$\left(\frac{w\sqrt{\theta}}{\delta}\right)_k = 2\pi K_{bk}\int_{r_h}^{r_t}\left(\frac{w\sqrt{\theta}}{\delta A_{an}}\right)_l r\,dr \qquad (330)$$

The integral can be evaluated by a graphical or mathematical procedure, and either the continuity value of equivalent flow, the tip radius, or the hub radius can be calculated, depending on which conditions are given.

If the radial gradient of $(w\sqrt{\theta}/\delta A_{an})_l$ is small, sufficient accuracy in evaluating the integral can be attained by using either an arithmetic average or the mean-radius value of local equivalent flow per unit annulus areas. This, of course, means that the hub and tip diameters must either be known or assumed. The continuity value of the

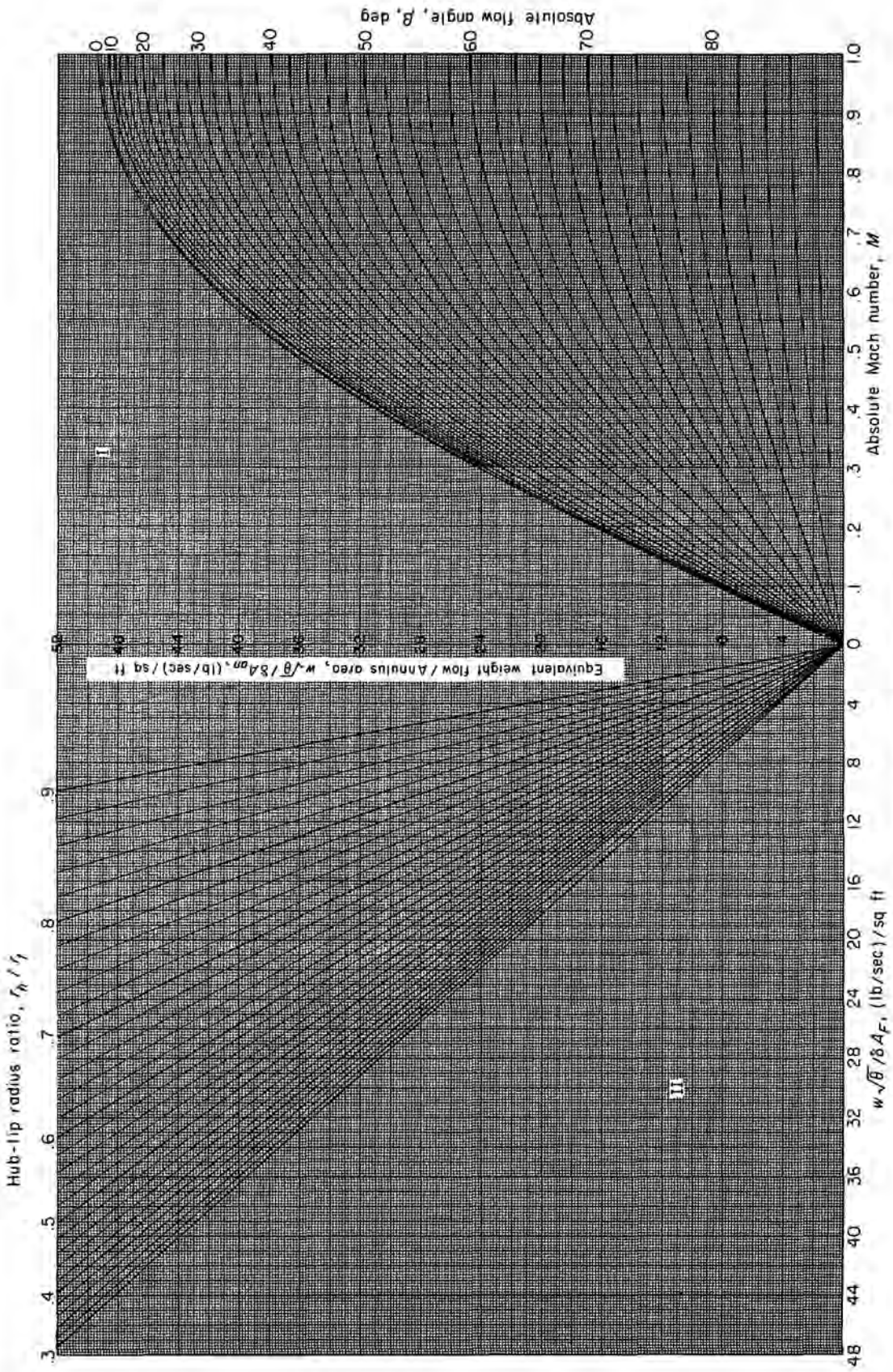

FIGURE 214.—Chart for satisfying continuity of flow.

flow per unit annulus area then becomes

$$\left(\frac{w\sqrt{\theta}}{\delta A_{an}}\right)_k = K_{bk}\left(\frac{w\sqrt{\theta}}{\delta A_{an}}\right)_{t,av} \tag{331}$$

The annulus area of the compressor in terms of the frontal area and hub-tip radius ratio is given by

$$A_{an} = A_F\left[1-\left(\frac{r_h}{r_t}\right)^2\right] \tag{332}$$

Combining equations (331) and (332) gives

$$\frac{w\sqrt{\theta}}{\delta A_F\left[1-\left(\frac{r_h}{r_t}\right)^2\right]} = K_{bk}\left(\frac{w\sqrt{\theta}}{\delta A_{an}}\right)_{t,av} = \left(\frac{w\sqrt{\theta}}{\delta A_{an}}\right)_k \tag{333}$$

Equation (333) is plotted in the second quadrant of figure 214, with $w\sqrt{\theta}/\delta A_{an}$ as the ordinate, $w\sqrt{\theta}/\delta A_F$ as the abscissa, and r_h/r_t as the parameter. After determining values of $(w\sqrt{\theta}/\delta A_{an})_t$ at all radii at which the vector diagrams have been calculated, $(w\sqrt{\theta}/\delta A_{an})_k$ is computed from equation (331). Then this value is used in the second quadrant to find the value of r_h/r_t for a given value of $w\sqrt{\theta}/\delta A_F$. If the specific weight flow $w\sqrt{\theta}/\delta A_F$ is specified at one axial station (1), the value at any other axial station (2) is obtained as follows:

$$\left(\frac{w\sqrt{\theta}}{\delta A_F}\right)_2 = \left(\frac{w\sqrt{\theta}}{\delta A_F}\right)_1 \frac{\sqrt{\left(\frac{T_2}{T_1}\right)_{av}}}{\left(\frac{P_2}{P_1}\right)_{av}\left(\frac{r_{t,2}}{r_{t,1}}\right)^2} \tag{334}$$

where $(T_2/T_1)_{av}$ and $(P_2/P_1)_{av}$ are arithmetically averaged values across the annulus.

If the value of hub-tip radius ratio determined by this procedure is greatly different from the value assumed for the purpose of averaging the local values of flow per unit annulus area in equation (331) and the temperature and pressure ratio in equation (334), it will be necessary to repeat the procedure with a new assumed radius ratio.

By proper use of figure 214 and equations (331) and (334), the continuity requirement, with any consistent set of assumptions, can be met. Use of the charts and equations is shown in a specific example later in this chapter.

ENERGY ADDITION AND EFFICIENCY

The energy addition across a rotor blade element is a function of both the change in tangential velocity and in blade speed across the blade row. The magnitude of the energy addition is given by Euler's equation as

$$gJc_p(T_2-T_1) = U_2V_{\theta,2} - U_1V_{\theta,1} \tag{316}$$

or

$$gJc_p(T_2-T_1) = U_1(V_{\theta,2}-V_{\theta,1}) + V_{\theta,2}(U_2-U_1) \tag{335}$$

Solving equation (335) for the temperature ratio T_2/T_1 across the blade element gives

$$\frac{T_2}{T_1} = 1.0 + \frac{U_1(V_{\theta,2}-V_{\theta,1}) + V_{\theta,2}(U_2-U_1)}{gJc_pT_1}$$

or, by using equivalent velocities,

$$\frac{T_2}{T_1} = 1.0 + \frac{\left(\frac{U_1}{\sqrt{\theta_1}}\right)\left(\frac{\Delta V_\theta}{\sqrt{\theta_1}}\right)}{gJc_pT_{s1}} + \frac{\left(\frac{V_{\theta,2}}{\sqrt{\theta_1}}\right)\left(\frac{\Delta U}{\sqrt{\theta_1}}\right)}{gJc_pT_{s1}} \tag{336}$$

where

$$\Delta V_\theta = V_{\theta,2} - V_{\theta,1}$$

and

$$\Delta U = U_2 - U_1 = \omega(r_2 - r_1)$$

The last term on the right side of equation (336) is the contribution to the temperature ratio of the change in radius across the blade element; therefore, if the design is carried out on cylindrical stream surfaces ($r_1 = r_2$), equation (336) can be used in the following form:

$$\frac{T_2}{T_1} = 1.0 + \frac{\left(\frac{U_1}{\sqrt{\theta_1}}\right)\left(\frac{\Delta V_\theta}{\sqrt{\theta_1}}\right)}{gJc_pT_{s1}} \tag{337}$$

Equation (337) is plotted in quadrant I of figure 215 with T_2/T_1 as a function of $\Delta V_\theta/\sqrt{\theta_1}$ for constant values of $U_1/\sqrt{\theta_1}$.

If there is a change in streamline radius across the blade element, figure 215 can still be used directly to determine the temperature ratio because of the change in tangential velocity. The contribution to the temperature ratio of the change in radius across the blade element can be obtained either by calculating the last term of equation (336) or by obtaining it from the chart, and adding this value to the temperature ratio previously obtained from the chart result based on $U_1/\sqrt{\theta_1}$ and $\Delta V_\theta/\sqrt{\theta_1}$. In order to use the chart for obtaining the last term of equation (336), the abscissa is considered as $\Delta U/\sqrt{\theta_1}$ and the parameter

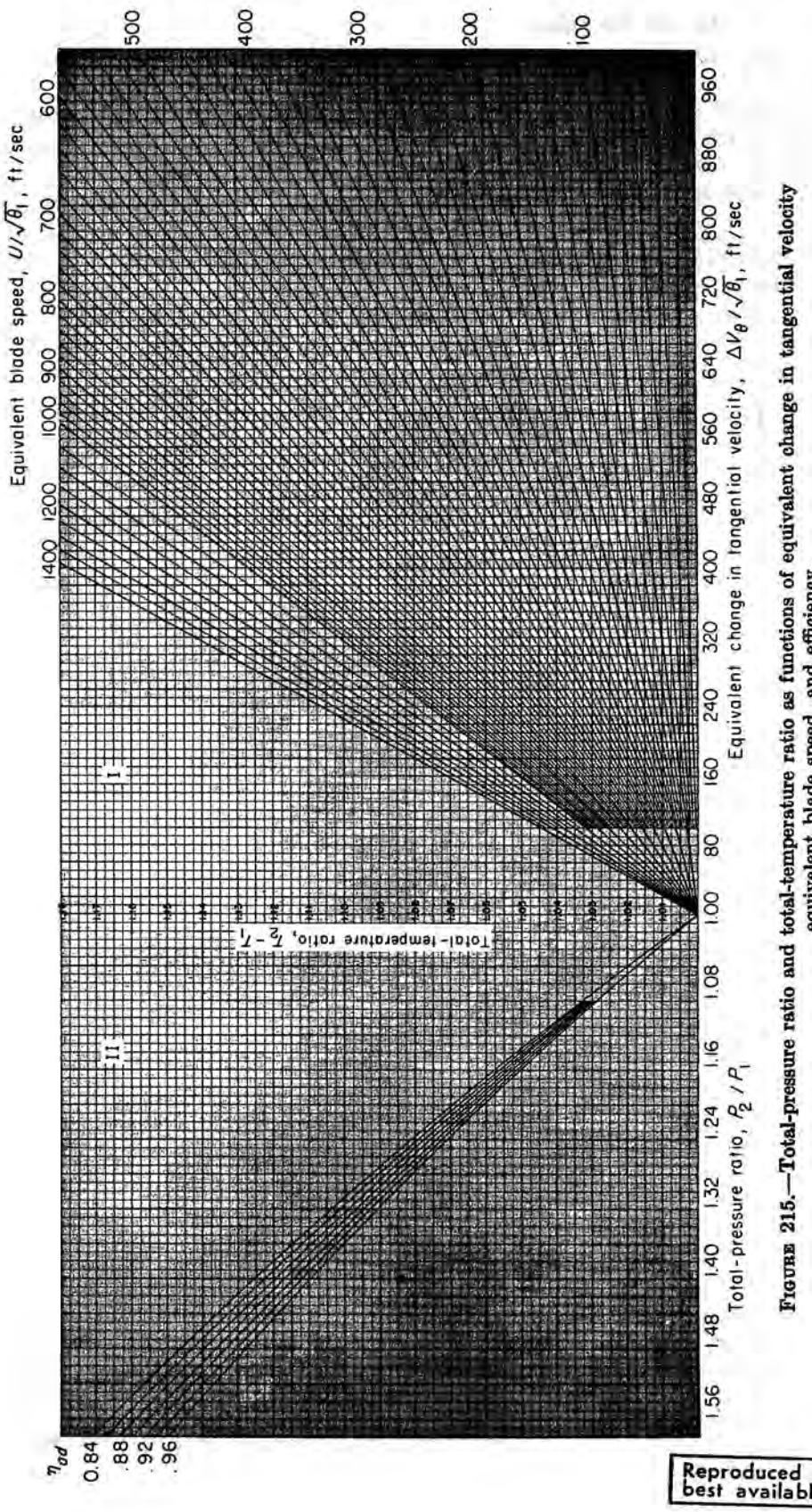

FIGURE 215.—Total-pressure ratio and total-temperature ratio as functions of equivalent change in tangential velocity equivalent blade speed, and efficiency.

as $V_{\theta;2}/\sqrt{\theta_1}$. The ordinate will then be the value of the last term of equation (336) plus 1; therefore, 1 should be subtracted from this value before it is added to the first two terms of equation (336).

The chart can also be used for any change in radius if either $V_{\theta,1}$ or $V_{\theta,2}$ is zero. If $V_{\theta,1}=0$, then $U=U_2$ and $\Delta V_\theta=V_{\theta,2}$; and, if $V_{\theta,2}=0$, then $U=U_1$ and $\Delta V_\theta=V_{\theta,1}$.

The second quadrant of figure 215 gives pressure ratio as a function of temperature ratio and adiabatic temperature-rise efficiency. The relation is as follows:

$$\frac{P_2}{P_1}=\left[\eta_{ad}\left(\frac{T_2}{T_1}-1.0\right)+1.0\right]^{\frac{\gamma}{\gamma-1}} \tag{338}$$

In compressor design it may be more desirable to specify a value of relative pressure-loss coefficient $\bar{\omega}$ instead of a blade-element efficiency. A discussion of the relative pressure-loss coefficient and its use in compressor design is presented in chapters VI and VII. If a relative pressure-loss coefficient is used, the adiabatic temperature-rise efficiency can be obtained from the following expression:

$$\eta_{ad}=\frac{\dfrac{T_2}{T_1}\left[1.0-\dfrac{\bar{\omega}_R'\left\{1.0-\left[\dfrac{1.0}{1.0+\frac{\gamma-1}{2}(M_1')^2}\right]^{\frac{\gamma}{\gamma-1}}\right\}}{\left\{1.0+\dfrac{\gamma-1}{2}\left(\dfrac{U_2}{a_{a,1}}\right)^2\left[1.0-\left(\dfrac{r_1}{r_2}\right)^2\right]\right\}^{\frac{\gamma}{\gamma-1}}}\right]^{\frac{\gamma-1}{\gamma}}-1.0}{\dfrac{T_2}{T_1}-1.0} \tag{339}$$

VECTOR RELATIONS

The constant use of the relations between velocities and angles in the compressor velocity diagram warrants a chart regardless of the simplicity of application. Construction of the chart can be illustrated by inspecting the following two relations:

$$V_z^2+V_\theta^2=V^2 \tag{340}$$

and

$$V_\theta=V_z\tan\beta \tag{341}$$

From equation (340) it can be seen that, if V_z and V_θ are used as rectilinear coordinates, constant values of V will be concentric circles with $V_\theta=V_z=0$ as a center. Using the same coordinates, a plot of equation (341) would produce a family of straight lines going through the origin ($V_\theta=V_z=0$). The angle between these lines and the V_z axis would be equal to the value of β.

Such a vector chart is shown in figure 216 with V_z as the abscissa and V_θ as the ordinate. Obviously, relative values of the velocities and flow angle can also be used in the chart. Further, the coordinates can represent Mach numbers if the decimal point is changed for the values appearing in both axes.

DIFFUSION FACTOR

A blade-element-loading criterion for axial-flow compressors is developed in reference 9. The application of this loading criterion to blade elements in cascades and in compressors is presented in chapters VI and VII. The loading criterion, or diffusion factor, in the form usually applied is given by the following expression:

$$D=1-\frac{V_2'}{V_1'}+\frac{\Delta V_\theta'}{2\sigma V'} \tag{342}$$

The diffusion factor can be used in two ways in compressor design: (1) With the vector diagrams known, the diffusion factor is computed and the energy losses across the blade element are estimated from data such as presented in chapters VI and VII; or (2) a limiting value of diffusion factor is prescribed and the conditions required to satisfy the assumed diffusion factor for given inlet or outlet conditions are calculated.

Although equation (342) is in satisfactory form for the first of these purposes, it is not directly applicable for the second purpose. In order to put equation (342) in a form that can be used to determine conditions for a prescribed diffusion

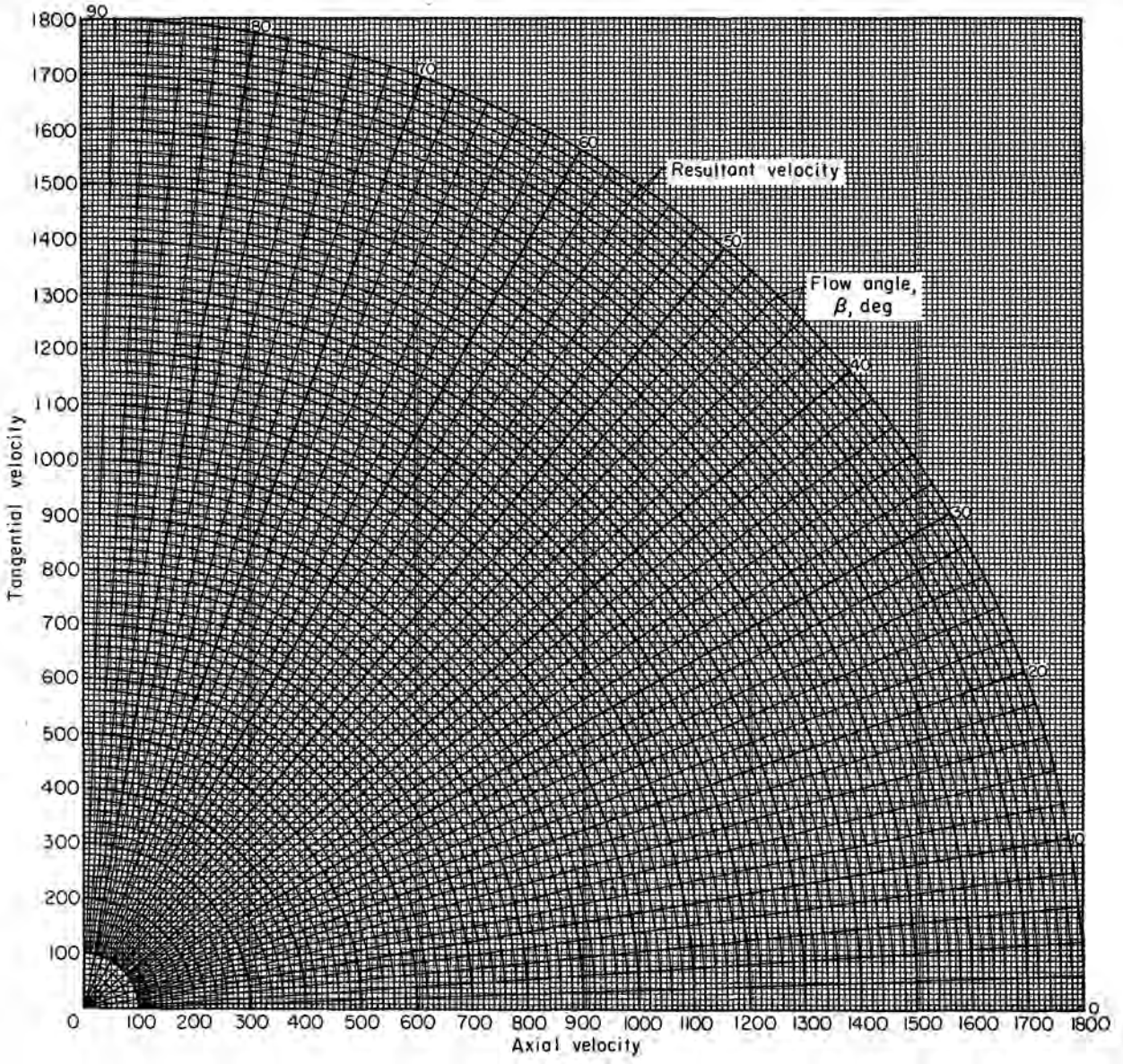

FIGURE 216.—Chart for vector relations.

factor, it can be written in terms of flow angles and axial velocities:

$$1-D=\left(\frac{V_{z,2}}{V_{z,1}}\right)\left(\frac{\cos\beta_1}{\cos\beta_2}\right)-\left(\frac{V_{z,1}\tan\beta_1-V_{z,2}\tan\beta_2}{2\sigma V_{z,1}}\right)\cos\beta_1$$

In the application of this equation, flow angles are always taken relative to the blade row under consideration.

A rearrangement of terms produces the following expression:

$$\left[\frac{\sigma(1-D)}{\cos\beta_1}+\frac{\tan\beta_1}{2}\right]=\frac{V_{z,2}}{V_{z,1}}\left[\frac{\sigma}{\cos\beta_2}+\frac{\tan\beta_2}{2}\right] \quad (343)$$

Equation (343) is readily adaptable to chart form. The terms in brackets on both sides of the equation are identical with β_1 substituted for β_2 and $\sigma(1-D)$ substituted for σ; therefore, a single family of curves can be used to represent each function

691-564 O-65-20

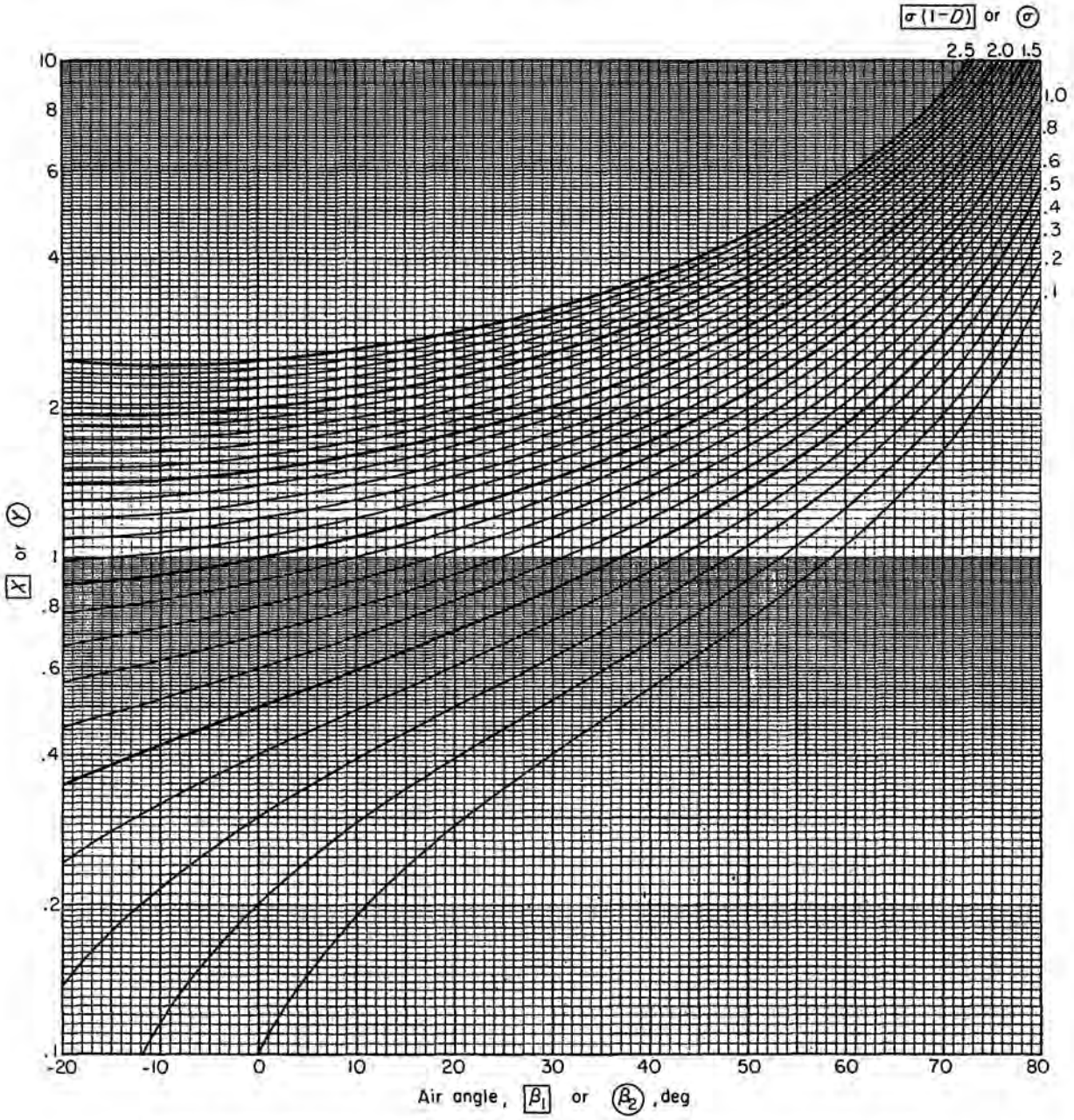

FIGURE 217.—Chart for solution of diffusion-factor equation (see eqs. (343) to (345)).

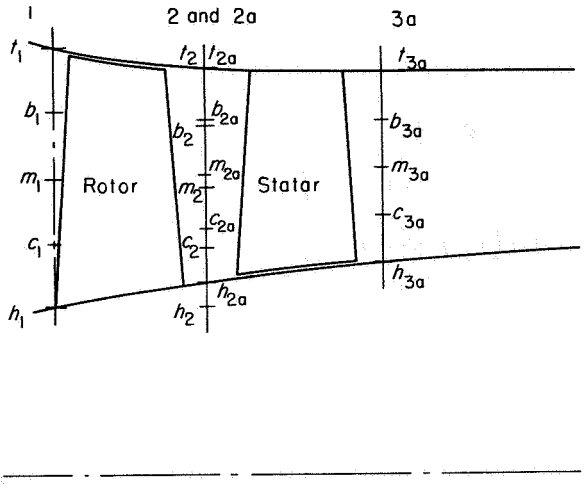

FIGURE 218.—Crosss section of typical stage showing axial and radial stations.

inside the brackets. The ratio of the two functions will be equal to the axial velocity ratio across the blade row. In order to simplify the expression, let

$$X=\frac{\sigma(1-D)}{\cos\beta_1}+\frac{\tan\beta_1}{2} \tag{344}$$

and

$$Y=\frac{\sigma}{\cos\beta_2}+\frac{\tan\beta_2}{2} \tag{345}$$

Then,

$$\frac{V_{z,2}}{V_{z,1}}=\frac{X}{Y} \tag{346}$$

Figure 217 is a plot of X as a function of β_1 for constant values of $\sigma(1-D)$. The same family of curves represents Y as a function of β_2 for constant values of σ. Figure 217 and equation (346) can be used for the solution of equation (343) for any desired parameter. The use of figure 217 to compute diffusion factor with the velocity diagrams known and to compute the discharge flow angle for given diffusion factor, inlet conditions, and axial velocity ratio, is shown in the following example.

EXAMPLE

The procedure in using the charts is best illustrated by an example of the design of an axial-flow-compressor stage. The stage design assumptions were made so that they would provide a stringent case for the charts and also to illustrate as many uses of the charts as possible. The axial and radial station designations and a typical vector diagram are shown in figures 218 and 219, respectively. The design assumptions and calculation procedure are as follows.

Compute the vector diagrams, pressure ratio, temperature ratio, Mach number, and diffusion factor at five equispaced radial positions and the passage shape for an axial-flow-compressor stage consisting of rotor and stator blade row to meet the following specifications:

Assumed design parameters: [a]

Parameter	Design value	Parameter	Design value
$(w\sqrt{\theta}/\delta A_F)_1$	35.0 (lb/sec)/sq ft	dT/dr	12° R/ft
$M_{z,1}$	0.6	$D_{R,t}$	0.35
$M'_{t,1}$	1.2	$D_{R,h}$	$\leq$0.6
$r_{t,1}$	1.50 ft	$D_{S,h}$	$\leq$0.6
$r_{t,2}=r_{t,2a}$	1.42 ft	$\sigma_{R,t}$	1.0
$r_{t,3a}$	1.41 ft	$\sigma_{S,t}$	0.7
$(V_{z,2}/V_{z,1})_t$	1.1	K_{sh}	0.98
$(V_{z,3a}/V_{z,1a})_t$	1.0	$\bar{\omega}_S$	0.02
$V_{\theta,1}=V_{\theta,3a}$	0	$T_1=T_{s1}$	518.7° R
$\eta_{ad,R}$	0.92	$P_1=P_{s1}$	2116 lb/sq ft

[a] Blade chords constant from hub to tip.

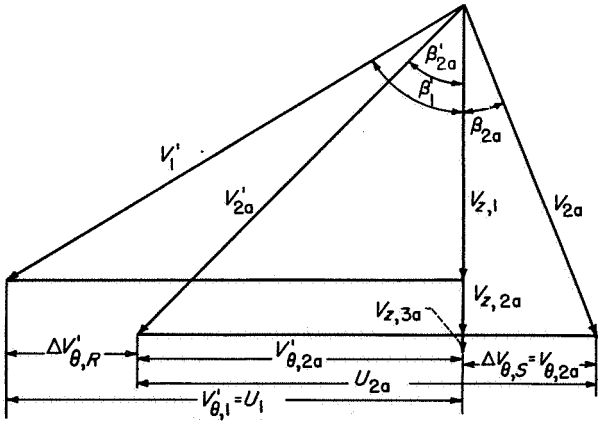

FIGURE 219.—Vector diagram for typical stage; $\beta_1=\beta_{3a}=0$.

Calculated design parameters:

Parameter	Procedure	Value	Parameter	Procedure	Value
$A_{F,1}$	$\pi r_{t,1}^2=\pi(1.5)^2$	7.069 sq ft	Y	$X/\left(\frac{V_{z,2}}{V_{z,1}}\right)_t=\frac{2.16}{1.1}$	1.96
$\left(\frac{w\sqrt{\theta}}{\delta}\right)_1$	$\left(\frac{w\sqrt{\theta}}{\delta A_F}\right)_1 A_{F,1}=(35)\ (7.069)$	247 lb/sec	$\beta'_{t,2}$	$Y=1.96$, $\sigma_{R,t}=1.0$, and fig. 217	46.3°
$\left(\frac{w\sqrt{\theta}}{\delta A_{an}}\right)_{t,1}$	$M_{z,1}=0.6$, $\beta_1=0$, and fig. 214	41.6 (lb/sec)/sq ft	$V_{z,t,2}$	$V_{z,1}\left(\frac{V_{z,2}}{V_{z,1}}\right)_t=(647)\ (1.1)$	712 ft/sec
$\left(\frac{w\sqrt{\theta}}{\delta A_{an}}\right)_{h,1}$	$K_{bk}\left(\frac{w\sqrt{\theta}}{\delta A_{an}}\right)_{t,1}=(0.98)\ (41.6)$	40.8 (lb/sec)/sq ft	$V'_{\theta,t,2}$ $V'_{t,2}$	$V'_{z,t,2}=712$, $\beta'_{t,2}=46.3$, and fig. 216	744 ft/sec 1028 ft/sec
$\left(\frac{r_h}{r_t}\right)_1$	$\left(\frac{w\sqrt{\theta}}{\delta A_{an}}\right)_{h,1}=40.8$, $\left(\frac{w\sqrt{\theta}}{\delta A_F}\right)_1=35.0$, and fig. 214	0.378	$U_{t,2}$	$U_{t,1}\left(\frac{r_2}{r_1}\right)_t=(1120)\left(\frac{1.42}{1.50}\right)$	1060 ft/sec
			$V_{\theta,t,2}=\Delta V_{\theta,t}=\Delta V'_{\theta,2}$	$U_{t,2}-V'_{\theta,t,2}=1060-744$	316 ft/sec
$r_{h,1}$	$r_{t,1}\left(\frac{r_h}{r_t}\right)_1=(1.5)\ (0.378)$	0.567 ft	$\left(\frac{T_2}{T_1}\right)_t$	$\frac{U_{t,2}}{\sqrt{\theta_1}}=1060$, $\frac{\Delta V_{\theta,t}}{\sqrt{\theta_1}}=316$, $\sqrt{\theta_1}=1.0$, and fig. 215	1.1061
$(a/a_a)_1$	$M_{z,1}=0.6$ and ref. 250	0.9658			
a_1	$a_{a,1}\left(\frac{a}{a_a}\right)_1=(1116)\ (0.9658)$	1078 ft/sec	$\left(\frac{P_2}{P_1}\right)_t$	$\left(\frac{T_2}{T_1}\right)_t=1.1061$, $\eta_{ad,R}=0.92$, and fig. 215	1.386
$V_{z,1}$	$a_1 M_{z,1}=(1078)\ (0.6)$	647 ft/sec			
$V'_{t,1}$	$a_1 M'_{t,1}=(1078)\ (1.2)$	1294 ft/sec			
$V'_{\theta,t,1}=U_{t,1}$ $\beta'_{t,1}$	$V_{z,1}=647$, $V'_{t,1}=1294$, and fig. 216	1120 ft/sec 60°	ΔT_t	$T_{t,2}-T_{t,1}=T_1\left[\left(\frac{T_2}{T_1}\right)_t-1.0\right]$ $=518.7(1.1061-1.0)$	55.03° R
$\sigma_{R,t}(1-D_{R,t})$	1.0 (1.00−0.35)	0.65			
X	$\sigma_{R,t}(1-D_{R,t})=0.65$, $\beta'_{t,1}=60$, and fig. 217	2.16			

Vector-diagram calculation:

Step	Parameter	Known design condition	Procedure	Radial position				
				Tip	b	Mean	c	Hub
1	r_1	$r_{t,1}=1.50$ $r_{h,1}=0.567$		1.500	1.267	1.034	0.800	0.567
2	$U_1=V'_{\theta,1}$	$U_{t,1}=1120$ $r_{t,1}=1.50$	$\left(\frac{rU_t}{r_t}\right)_1$	1120	946	772	597	423
3	V'_1	$V_{z,1}=647$	$V_{z,1}$, U_1, and fig. 216	1294	1144	1006	879	772
4	β'_1			60.0	55.6	50.0	42.7	33.1
5	M'_1	$a_1=1078$	$\left(\frac{V'}{a}\right)_1$	1.200	1.061	0.933	0.815	0.716
6	r_2	$r_{t,2}=1.42$ $r_{h,2}=r_{h,1}=0.567$		1.420	1.207	0.994	0.780	0.567
7	ΔT	$\Delta T_t=55.03$ $\left(\frac{dT}{dr}\right)=12$	$\Delta T_t-\left(\frac{dT}{dr}\right)(r_{t,2}-r_2)$	55.03	52.47	49.92	47.35	44.79
8	$\frac{T_2}{T_1}$	$T_1=518.7$	$\frac{\Delta T}{T_1}+1.0$	1.1061	1.1012	1.0962	1.0913	1.0864
9	U_2	$U_{t,2}=1060$ $r_{t,2}=1.42$	$\left(\frac{rU_t}{r_t}\right)_2$	1060	901	742	582	423
10	$\frac{\Delta V_\theta}{\sqrt{\theta_1}}=V_{\theta,2}$	$\theta_1=1.0$	$\frac{U_2}{\sqrt{\theta_1}}$, $\frac{T_2}{T_1}$, and fig. 215	316	355	409	496	645
11	$\frac{P_2}{P_1}$	$\eta_{ad,R}=0.92$	$\frac{T_2}{T_1}$, $\eta_{ad,R}$, and fig. 215	1.386	1.366	1.346	1.326	1.308
12	$\left(\frac{r}{r_t}\right)_2$		Example at mean $\left(\frac{r}{r_t}\right)_2=\left(\frac{r_m}{r_b}\right)_2$	------	0.85	0.82	0.78	0.73
13	$\left(\frac{V_\theta}{V_{\theta,t}}\right)_2$		Example at hub $\left(\frac{V_\theta}{V_{\theta,t}}\right)_2=\left(\frac{V_{\theta,h}}{V_{\theta,t}}\right)_2$	------	1.123	1.152	1.213	1.300
14	B_2		$\left(\frac{V_\theta}{V_{\theta,t}}\right)_2$, $\left(\frac{r}{r_t}\right)_2$, $V_{\theta,2,t}$, and fig. 213	------	0.012×10^6	0.021×10^6	0.025×10^6	0.050×10^6
15	C_2		$12{,}170(\Delta T_t-\Delta T)$	------	0.031×10^6	0.031×10^6	0.031×10^6	0.031×10^6
16	$(V_z^2-V_{z,t}^2)_2$		$(B-C)_2$	------	-0.019×10^6	-0.010×10^6	-0.006×10^6	0.019×10^6

Step	Parameter	Known design condition	Procedure	Radial position				
				Tip	b	Mean	c	Hub
17	$V_{m,2}$	$V_{s,t,2}=712$	$(V_s^2-V_{s,t}^2)_2$, $V_{s,2,t}$, and fig. 213	712	696	688	683	698
18	$V'_{\theta,2}$		$(U-V_\theta)_2$	744	546	333	86	−222
19	V'_2		$V_{s,2}$, $V'_{\theta,2}$, and fig. 216	1028	883	763	689	732
20	β'_2			46.3	38.2	25.8	7.0	−17.6
21	V_2		$V_{s,2}$, $V_{\theta,2}$, and fig. 216	778	780	800	843	949
22	β_2			23.8	27.0	30.6	36.0	42.7
23	$\left(\frac{V}{a_a}\right)_2$	$a_{a,1}=1116$	$\frac{V_2}{a_{a,1}\sqrt{\frac{T_2}{T_1}}}$	0.6629	0.6661	0.6847	0.7231	0.8159
24	M_2		$\left(\frac{V}{a_a}\right)_2$ and ref. 250	0.694	0.698	0.719	0.764	0.876
25	$\left(\frac{w\sqrt{\theta}}{\delta A_{an}}\right)$		M_2, β_2, and fig. 214	41.2	40.2	39.3	37.8	35.8
26	$\left(\frac{w\sqrt{\theta}}{\delta A_{an}}\right)$	$K_{bk}=0.98$	$K_{bk}\left(\frac{w\sqrt{\theta}}{\delta A_{an}}\right)_{1,2}$	40.4	39.4	38.5	37.0	35.1
27	$\left(\frac{w\sqrt{\theta}}{\delta A_F}\right)_2$	$\left(\frac{w\sqrt{\theta}}{\delta A_F}\right)_1=35$ $r_{t,1}=1.50$ $r_{t,2}=1.42$	$\frac{\left(\frac{w\sqrt{\theta}}{\delta A_F}\right)_1\sqrt{\frac{T_2}{T_1}}}{\left(\frac{P_2}{P_1}\right)\left(\frac{r_{t,2}}{r_{t,1}}\right)^2}$	29.6	30.0	30.4	30.8	31.1
28	$\left(\frac{r_h}{r_t}\right)_2$		$\left(\frac{w\sqrt{\theta}}{\delta A_{an}}\right)_{k,2,av}$, $\left(\frac{w\sqrt{\theta}}{\delta A_F}\right)_{2,av}$, and fig. 214	0.450				
29	r_{2a}	$r_{t,2a}=r_{t,2}=1.42$						
30	$\left(\frac{w\sqrt{\theta}}{\delta A_{an}}\right)_{k,2a}$		From plot of $\left(\frac{w\sqrt{\theta}}{\delta A_{an}}\right)_{k,2}$ (step 26) against r_2 (step 6) read at r_{2a} (step 29)	1,420 40.4	1,225 39.7	1,030 38.7	0.834 37.5	0.639 35.8
31	$\left(\frac{w\sqrt{\theta}}{\delta A_F}\right)_{2a}$		From plot of $\left(\frac{w\sqrt{\theta}}{\delta A_F}\right)_2$ (step 27) against r_2 read at r_{2a}	29.6	30.0	30.3	30.7	31.0
32	$\left(\frac{r_h}{r_t}\right)_{2a}$		$\left(\frac{w\sqrt{\theta}}{\delta A_{an}}\right)_{k,2a,av}$, $\left(\frac{w\sqrt{\theta}}{\delta A_F}\right)_{2a,av}$, and fig. 214	0.460				
33	r_{2a}	$r_{t,2a}=1.42$		1.420	1.228	1.037	0.845	0.653
			Using value of r_{2a} from step 33 repeat steps 30 to 33 until consecutive values of $\left(\frac{r_h}{r_t}\right)_{2a}$ in step 32 agree					
34	$\frac{T_{2a}}{T_1}=\frac{T_{2a}}{T_1}$		From plots of $\frac{T_2}{T_1}$, $\frac{P_2}{P_1}$, $V_{\theta,2}$, $V_{s,2}$, β'_2 and M_2 against r_2 read at r_{2a}	1.1061	1.1017	1.0973	1.0929	1.0885
35	$\frac{P_{2a}}{P_1}$		(final)	1.386	1.368	1.350	1.332	1.315
36	$V_{\theta,2a}$			316	350	397	463	579
37	$V_{s,2a}$			712	697	689	684	689
38	β'_{2a}			46.3	39.2	28.5	13.1	−6.7
39	M_{2a}			0.694	0.697	0.712	0.744	0.822
40	V_{2a}		$V_{s,2a}$, $V_{\theta,2a}$, and fig. 216	778	780	794	824	900
41	β_{2a}			23.8	26.6	30.0	34.0	40.0
42	$\sigma_{R,av}$	$\sigma_{R,t}=1.0$ $r_{t,1}=1.50$ $r_{t,2a}=1.42$	$\sigma_{R,t}\left(\frac{r_{t,1}+r_{t,2a}}{r_1+r_{2a}}\right)$	1.00	1.17	1.41	1.78	2.39
43	Y		$\sigma_{R,av}$, β'_{2a}, and fig. 217	1.96	1.91	1.89	1.94	2.34
44	X	$V_{s,1}=647$	$Y\left(\frac{V_{s,2a}}{V_{s,1}}\right)$	2.16	2.06	2.01	2.05	2.49
45	$\sigma_{R,av}(1-D_R)$		X, β'_1, and fig. 217	0.65	0.76	0.91	1.17	1.80
46	D_R		$1.0-\left[\frac{\sigma_{R,av}(1-D_R)}{\sigma_{R,av}}\right]$	0.35	0.35	0.35	0.34	0.25
47	C_{2a}	$T_1=518.7$	$12{,}170\,T_1\left[\left(\frac{T_{2a}}{T_1}\right)_i-\left(\frac{T_{2a}}{T_1}\right)\right]$	------	0.028×10^6	0.028×10^6	0.028×10^6	0.028×10^6

Step	Parameter	Known design condition	Procedure	Radial position				
				Tip	b	Mean	c	Hub
48	$(V_z^2-V_{z,\,c}^2)_{2a}$	$V_{\theta,\,2a}=0$ $\therefore B_{2a}=0$	$(B-C)_{2a}$	------	-0.028×10^6	-0.028×10^6	-0.028×10^6	-0.028×10^6
49	$V_{z,\,2a}=V_{2a}$	$\left(\frac{V_{z,\,2a}}{V_{z,\,2a}}\right)_t=1.0$	$(V_z^2-V_{z,\,c}^2)_{2a}$, $V_{z,\,2a,\,t}$, and fig. 213	712	691	670	650	629
50	$\left(\frac{V}{a_a}\right)_{2a}$	$a_{a,\,1}=1116$	$\frac{V_{2a}}{a_{a,\,1}\sqrt{\frac{T_{2a}}{T_1}}}$	0.6067	0.5899	0.5732	0.5572	0.5402
51	M_{2a}		$\left(\frac{V}{a_a}\right)_{2a}$ and ref. 250	0.630	0.612	0.593	0.575	0.557
52	$\left(\frac{p}{P}\right)_{2a}$		M_{2a} and ref. 250	0.7248	0.7229	0.7132	0.6925	0.6417
53	$\frac{P_{2a}}{P_1}$	$\bar{\omega}_S=0.02$	$\frac{P_{2a}}{P_1}\left[1.0-\bar{\omega}_S\left(1.0-\frac{p_{2a}}{P_{2a}}\right)\right]$	1.378	1.360	1.342	1.324	1.306
54	$\left(\frac{w\sqrt{\theta}}{\delta A_{an}}\right)_{1,\,2a}$	$\beta_{2a}=0$	M_{2a}, β_{2a}, and fig. 214	42.8	42.0	41.3	40.5	39.7
55	$\left(\frac{w\sqrt{\theta}}{\delta A_{an}}\right)_{k,\,2a}$	$K_{k2}=0.98$	$K\left(\frac{w\sqrt{\theta}}{\delta A_{an}}\right)_{1,\,2a}$	41.9	41.2	40.5	39.7	38.9
56	$\left(\frac{w\sqrt{\theta}}{\delta A_F}\right)_{2a}$	$\left(\frac{w\sqrt{\theta}}{\delta A_F}\right)_1=35$ $r_{t,1}=1.50$ $r_{t,2a}=1.41$	$\frac{\left(\frac{w\sqrt{\theta}}{\delta A_F}\right)_1\left(\sqrt{\frac{T_{2a}}{T_1}}\right)}{\left(\frac{P_{2a}}{P_1}\right)\left(\frac{r_{t,\,2a}}{r_{t,\,1}}\right)^2}$	30.2	30.6	30.9	31.3	31.6
57	$\left(\frac{r_h}{r_t}\right)_{2a}$		$\left(\frac{w\sqrt{\theta}}{\delta A_{an}}\right)_{h,\,2a,\,ae}$, $\left(\frac{w\sqrt{\theta}}{\delta A_F}\right)_{2a,\,ae}$, and fig. 214	0.484				
58	r_{2a}	$r_{t,\,2a}=1.41$		1.410	1.228	1.046	0.864	0.682
59	$\sigma_{S,\,ae}$	$\sigma_{S,\,t}=0.7$ $r_{t,\,2a}=1.42$ $r_{t,\,2a}=1.41$	$\sigma_{S,\,t}\left(\frac{r_{t,\,2a}+r_{t,\,2a}}{r_{2a}+r_{2a}}\right)$	0.70	0.81	0.95	1.16	1.48
60	Y	$\beta_{2a}=0$	$\sigma_{S,\,ae}$, β_{2a}, and fig. 217	0.70	0.81	0.95	1.16	1.48
61	X		$Y\left(\frac{V_{z,\,2a}}{V_{z,\,2a}}\right)$	0.70	0.80	0.92	1.10	1.35
62	$\sigma_{S,\,ae(1-DS)}$		X, β_{2a}, and fig. 217	0.44	0.49	0.54	0.63	0.72
63	DS		$1.0-\left[\frac{\sigma_{S,\,ae(1-DS)}}{\sigma_{S,\,ae}}\right]$	0.37	0.40	0.43	0.46	0.51
64	η_{ad}		$\frac{P_{2a}}{P_1}$, $\frac{T_{2a}}{T_1}$, and fig. 215	0.904	0.902	0.900	0.899	0.896

COMPARISON OF CHART AND CALCULATED VALUES

The more important parameters obtained by use of the chart procedures are summarized in the following table. The analytically calculated values of the parameters are also given for comparison and an indication of accuracy:

Parameter	Chart procedure					Analytical calculation				
	Radial position					Radial position				
	Tip	*b*	Mean	*c*	Hub	Tip	*b*	Mean	*c*	Hub
M_1^i	1.200	1.061	0.933	0.815	0.716	1.200	1.064	0.934	0.817	0.717
β_1^i	60.0	55.6	50.0	42.7	33.1	60.0	55.7	50.0	42.7	33.2
β_1^1	46.3	39.2	28.5	13.1	−6.7	46.3	39.8	29.1	15.4	−5.1
β_{2a}^{1a}	23.8	26.6	30.0	34.0	40.0	24.0	26.6	29.9	34.1	39.7
$V_{z,2a}$	712	697	689	684	689	712	697	686	679	678
M_{2a}	.694	.697	.712	.744	.822	.695	.697	.710	.740	.804
D_R	.35	.35	.35	.34	.25	.35	.35	.35	.33	.25
$V_{z,2a}$	712	691	670	650	629	712	692	671	648	625
M_{2a}	.630	.612	.593	.575	.557	.630	.612	.594	.574	.553
D_S	.37	.40	.43	.46	.51	.38	.39	.42	.45	.51
T_{2a}/T_1	1.1061	1.1017	1.0973	1.0929	1.0885	1.1066	1.1021	1.0976	1.0928	1.0882
P_{2a}/P_1	1.378	1.360	1.342	1.324	1.306	1.380	1.360	1.342	1.324	1.305
$(r_h/r_t)_1$	0.378					0.377				
$(r_h/r_t)_{1a}$	0.460					0.471				
$(r_h/r_t)_{2a}$	0.484					0.495				

Comparison of the values in the table indicates that good accuracy can be obtained with the charts. The largest differences in axial velocities and resultant Mach numbers were about 2 percent, occurring at the hub of the rotor-discharge station. At all other stations the differences were less than 0.7 percent. The flow angles agreed within 0.6° at all stations except the hub and c positions at the rotor discharge, where the chart values of the relative flow angles varied 1.6° and 2.3°, respectively, from the analytically calculated values. The passage areas obtained by the chart procedure were within 1.4 percent of the analytically calculated areas.

CHAPTER X

PREDICTION OF OFF-DESIGN PERFORMANCE OF MULTISTAGE COMPRESSORS

By WILLIAM H. ROBBINS and JAMES F. DUGAN, JR.

Three techniques are presented for estimating compressor off-design performance. The first method, which is based on blade-element theory, is useful for obtaining only a small part of the compressor map over which all blade elements in the compressor operate unstalled. The second method, which involves individual stage performance curves and a stage-by-stage calculation, is useful for estimating the performance of a compressor for which reliable stage performance curves are available. The third method, which is based on over-all performance data of existing compressors, may be used to estimate the complete performance map of a new compressor if the compressor design conditions are specified.

INTRODUCTION

The availability of good analytical techniques for predicting performance maps of designed compressors reduces costly and time-consuming testing and development and in addition aids in selecting the best compressor for a given application. Specific information that is required to achieve these goals is the relation between the stall-limit line and the operating line and the variation of efficiency and pressure ratio along the operating line. Therefore, one of the goals of compressor research is to obtain reliable performance prediction methods. This problem, which can be considered as an analysis of off-design compressor performance, is one of the most difficult tasks facing the compressor designer.

Off-design performance is defined as the performance of the compressor at flow conditions and speeds other than those for which the compressor was specifically designed. The off-design analysis differs from the design case in that the compressor geometry is given and the object is to find the compressor-outlet conditions for a range of speeds and weight flows. It is sometimes referred to as the "direct compressor problem," whereas the original design is called the "inverse" or "design problem." The design problem is discussed in detail in chapter VIII.

Prediction of off-design performance is considered in this chapter. A typical compressor performance map is shown in figure 220 with the design point and the stall-limit or surge line indicated. The regions of the performance map that are discussed herein are those to the right of the stall-limit line along lines of constant speed; in other words, the complete compressor map. Three techniques for predicting off-design performance are presented.

In the first method, compressor performance is obtained by first radially integrating compressor blade-element data to obtain blade-row performance. The performance of successive blade rows is determined by utilizing the computed outlet conditions of one blade row as the inlet conditions to the following blade row until complete compressor performance is obtained. This type of solution for compressor off-design performance, of course, requires a rather complete knowledge of compressor blade-element flow, radial integration techniques, boundary-layer growth, blade-row interactions, and the radial mixing process. Some of this information is currently available; although it is limited in many cases, the amount is steadily increasing. For example, the axial-flow-compressor blade-element theory and correlation results are given in chapters VI and VII for cascades and single-stage compressors. By utilizing this type of data, the performance of a compressor blade element can be determined. Furthermore, the results of chapter VIII provide a means for radial stacking of blade elements to estimate blade-row performance and axial stacking of blade rows to determine design-point performance, provided adequate blade-element performance data are available.

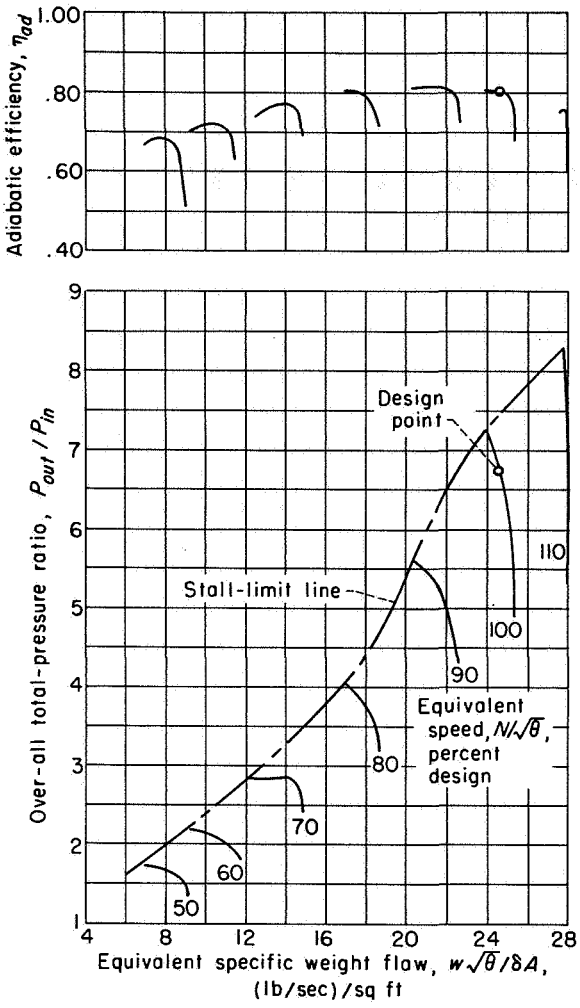

FIGURE 220.—Typical axial-flow-compressor over-all performance map.

This information can be applied to the off-design problem and is discussed in detail herein.

The second method is somewhat more simplified than the first, in that the average performance of each stage is obtained and the stages are axially stacked to acquire the compressor map. Therefore, neither blade-element data nor radial integration is necessary to obtain a performance map by this method. The success or failure of the technique depends upon the accuracy of the individual stage performance curves used for the computation of over-all performance. This method is used in the analyses of multistage-compressor performance in references 248 and 251 to 255 and in chapter XIII.

The final method of predicting multistage-compressor performance that is discussed in this chapter is based on data obtained from over-all performance maps of previously designed compressors. It is considerably more simplified than the first two methods, because there are no integration procedures or stage-stacking techniques involved in the computation of performance maps. This method was first proposed in reference 256 and was subsequently used in the analysis of two-spool compressor performance in reference 26. In the present chapter, data from several multistage compressors are correlated, so that it is possible to obtain a complete performance map from known compressor design conditions by means of a few simple and short numerical calculations.

Essentially, the purpose of this chapter is to review the methods currently available for predicting multistage-compressor performance. Although the techniques apply primarily to fixed-geometry compressors, they may be adapted to study operation with variable geometry and bleed. The advantages, disadvantages, limitations, and applicability of each method are discussed.

SYMBOLS

The following symbols are used in this chapter:

A	area, sq ft
a	speed of sound, ft/sec
c_p	specific heat at constant pressure, Btu/(lb)(°R)
g	acceleration due to gravity, 32.17 ft/sec^2
H	total or stagnation enthalpy, Btu/lb
J	mechanical equivalent of heat, 778.2 ft-lb/Btu
K_{bk}	weight-flow blockage factor
M	Mach number
N	rotational speed, rpm
P	total or stagnation pressure, lb/sq ft
R	gas constant, 53.35 ft-lb/(lb)(°R)
r	radius, ft
S	entropy, Btu/(lb)(°R)
T	total or stagnation temperature, °R
t	static or stream temperature, °R
U	rotor speed, ft/sec
V	air velocity, ft/sec
w	weight flow, lb/sec
Y	$\left(\frac{P_3}{P_1}\right)^{\frac{\gamma-1}{\gamma}}-1$
z	coordinate along axis, ft

β	air angle, angle between air velocity and axial direction, deg
γ	ratio of specific heats
δ	ratio of total pressure to NASA standard sea-level pressure of 2116 lb/sq ft
δ^*	boundary-layer displacement thickness
η	efficiency
θ	ratio of total temperature to NASA standard sea-level temperature of 518.7° R
ρ	density, lb-sec^2/ft^4
φ	flow coefficient
ψ	pressure coefficient

Subscripts:

a	stagnation conditions
ac	actual conditions
ad	adiabatic
an	annulus
b	backbone
d	design
h	hub
i	reference position, radial station where variables are known
id	ideal
in	compressor inlet
m	mean
out	compressor outlet
r	radial direction
ref	reference
s	stall limit
sl	NASA standard sea-level conditions
t	tip
z	axial direction
θ	tangential direction

0, 1, 2, 3 station numbers (fig. 221)

Superscript:

$'$	denotes conditions relative to rotor blade row

METHODS OF PREDICTING OFF-DESIGN PERFORMANCE

BLADE-ELEMENT METHOD

Blade-element theory is used extensively in the compressor design technique (ch. VIII). Compressor blades are evolved by a radial stacking of a series of blade sections or blade elements to form the complete blade. The theory proposes, therefore, that the blade-row characteristics can be determined if the performance of each blade element is known and that over-all compressor performance can then be obtained by an integration of the performance of each blade row. In this section, blade-element theory is applied to solve the off-design problem.

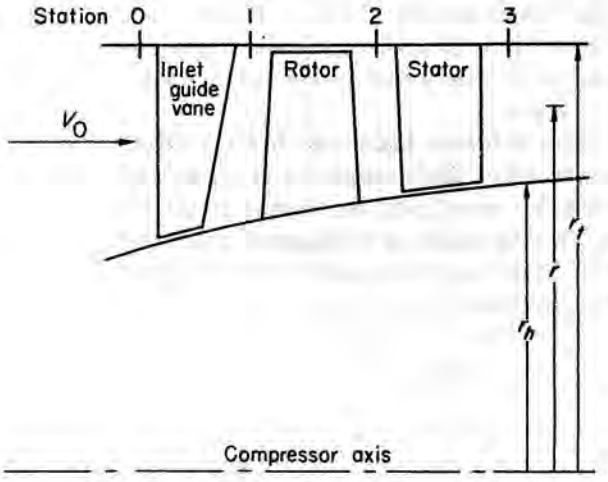

FIGURE 221.—Schematic diagram of compressor stage.

Basically, the solution for the off-design compressor performance proceeds as follows: From specified inlet conditions and blade geometry, the outlet conditions are computed from a knowledge of the flow about blade elements and with the conditions that continuity and radial equilibrium must be satisfied. Allowances must be made for boundary-layer growth, blade-row interaction effects, and radial mixing of blade wakes. The approach is admittedly an idealized one at present, since much of the information (blade-element losses at off-design operating conditions, boundary-layer growth, interactions, and radial mixing of blade wakes) required to carry out this calculation is not currently available. The general method is presented, because it has the greatest potentiality for providing a picture of the internal-flow mechanism through a compressor at off-design operating conditions. A method for computing the performance of a complete compressor stage (inlet guide vanes, rotors, and stators) is outlined; recourse is made to the equations and techniques for radial stacking of blade elements presented in chapter VIII. The performance of successive stages can be determined by utilizing the computed outlet conditions of one stage as the inlet conditions to the following stage.

Performance of inlet guide vanes.—Guide vanes are utilized to establish a specified prerotation

at the design condition (ch. VIII). For the off-design problem, it is necessary to determine the effect of changes in weight flow and speed on guide-vane performance.

Experimental evidence indicates that the effect of variations of inlet Mach number and secondary flows (caused by variations in weight flow) on guide-vane turning angle is very small over the range of inlet Mach numbers usually encountered in axial-flow-compressor guide vanes (0.3 to 0.5). Also, changes in rotor speed have very little effect on turning angle. Therefore, for the purpose of this analysis it can be assumed that, for fixed-geometry guide vanes, the guide-vane-outlet angle remains constant (the design value) for all values of speed and weight flow if the subsequent rotor is operating unstalled.

With the guide-vane-outlet angle fixed, the outlet velocity distribution may be computed. The radial variation of axial and tangential velocity leaving an annular row of blades for steady axially symmetric flow, neglecting terms involving viscosity, is expressed in chapter VIII as follows:

$$Jg\frac{\partial H}{\partial r}=Jgt\frac{\partial S}{\partial r}+V_\theta\frac{\partial V_\theta}{\partial r}+V_z\frac{\partial V_z}{\partial r}+\frac{V_\theta^2}{r}-V_z\frac{\partial V_r}{\partial z} \tag{347}$$

For flow across inlet guide vanes, the total enthalpy is constant and entropy variations along the radial height can be considered negligible in most cases, making $\partial H/\partial r=0$ and $t\frac{\partial S}{\partial r}=0$. In addition, experimental data for guide vanes with small wall taper and relatively low-aspect-ratio blading indicate that the effect of radial accelerations and the radial velocity component can be neglected with little error. Therefore, when equation (347) is integrated with respect to r, the following equation results:

$$\left(\frac{V_z}{V_{z,t}}\right)_1=\left(\frac{\cos\beta}{\cos\beta_t}\right)_1 exp\left(-\int_{r_t}^{r}\frac{\sin^2\beta_1}{r}\,dr\right) \tag{348}$$

Equation (348) can be utilized to express the axial velocity in terms of outlet angle and radial position for zero radial gradients of enthalpy and entropy and no radial velocity component. (Subscripts 0, 1, 2, and 3 denote axial stations and are indicated in fig. 221 on a schematic diagram of a compressor stage. A typical velocity diagram is shown in fig. 222.) In order to solve for values of axial velocity at all radial positions, a value of reference axial velocity must be assumed.

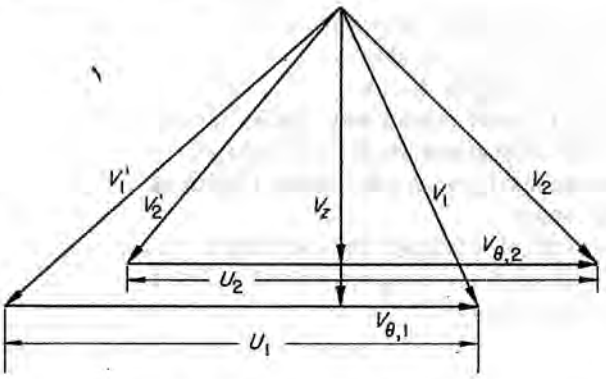

FIGURE 222.—Typical velocity diagram.

The assumption of the reference axial velocity can be checked by means of the continuity equation, since the condition that the inlet weight flow equals the outlet weight flow must be satisfied. The continuity equation can be expressed as follows:

$$w_0=w_1=K_{bk}2\pi\rho_{a,0}g\int_{r_h}^{r_t}\frac{\rho_1}{\rho_{a,0}}V_{z,1}r\,dr$$

$$=2\pi\rho_{a,0}g\int_{r_h+\delta^*}^{r_t-\delta^*}\frac{\rho_1}{\rho_{a,0}}V_{z,1}r\,dr \tag{349}$$

where

$$\frac{\rho_1}{\rho_{a,0}}=\left[1-\frac{\gamma-1}{2}\left(\frac{V_1}{a_{a,0}}\right)^2\right]^{\frac{1}{\gamma-1}}$$

for inlet guide vanes.

From equations (348) and (349) an iteration solution is necessary to solve for the correct axial velocity to satisfy weight flow. The area blockage caused by boundary-layer growth is taken into account by the limits of integration of equation (349), so that values of $(r_h+\delta^*)$ and $(r_t-\delta^*)$ correspond to the effective passage area rather than to the geometric area, or by the use of the blockage factor K_{bk} described in chapter VIII. Experimental results indicate that the ratio of effective area to actual passage area is approximately 0.98 at station 1. Equations (347) to (349) do not consider guide-vane losses. Since little data are available for estimating guide-vane losses, it is difficult to obtain a complete loss picture. However, if at all possible, it is desirable that a reasonable estimate of the

losses be made. In some cases a guide-vane over-all efficiency is assumed. Some information that may be helpful in estimating losses is presented in reference 213.

Rotor and stator analysis.—With the guide-vane-outlet (rotor-inlet) conditions fixed, the rotor-outlet calculations can proceed. The procedure for determining the performance of the rotor is more complicated than that for the guide vanes, and the following information must be provided:

(1) Blade camber (2) Blade angle (3) Solidity	Determined from blade geometry
(4) Relative inlet-air angle (5) Relative inlet Mach number (6) Rotor speed	Determined from inlet conditions

With this information available, blade-element results similar to those in chapters VI and VII are required to determine the turning angle and therefore the variation of rotor-outlet air angle.

In order to obtain an approximate velocity distribution at the rotor exit, zero losses are assumed between stations 1 and 2 and simple radial equilibrium with no radial entropy gradient is assumed at station 2. The simple-radial-equilibrium equation can be expressed as follows:

$$V_{z,2}^2-V_{z,2,t}^2=[(U-V_z\tan\beta')_{2,t}^2-(U-V_z\tan\beta')_2^2]+2Jgc_p(T_2-T_{2,t})+2\int_r^{r_t}\frac{(U-V_z\tan\beta')_2^2}{r}\,dr \quad (350)$$

where

$$Jgc_pT_2=Jgc_pT_1-U_1V_{\theta,1}+U_2(U-V_z\tan\beta')_2$$

As in the case of the inlet guide vanes, the variation of outlet axial velocity V_z can be determined by assuming a reference value of outlet axial velocity $V_{z,t}$. The assumption of $V_{z,t}$ can be verified by means of the continuity equation (eq. (349)), where

$$\frac{\rho_2}{\rho_{a,1}}=\left(\frac{Jgc_pT_1+U_2V_{\theta,2}-U_1V_{\theta,1}-\frac{V_2^2}{2}}{Jgc_pT_1}\right)^{\frac{1}{\gamma-1}} \quad (351)$$

for the rotor blade row with no losses. The simultaneous solutions of equations (349) and (350) for the rotor require a double iteration for axial velocity. Solutions of equations of this type are readily adaptable to high-speed electronic computing equipment.

The solution of equations (349) and (350) provides only a first approximation to the rotor-outlet velocity distribution, because no allowance for losses is included in the calculation. One way of refining this calculation to account for losses is by the use of the equilibrium equation with the entropy-gradient term included. The equilibrium equation with entropy gradient is given in chapter VIII and can be expressed as follows:

$$V_{z,2}^2-V_{z,2,t}^2=[(U-V_z\tan\beta')_{2,t}^2-(U-V_z\tan\beta')_2^2]+2Jgc_p(T_2-T_{2,t})+2\int_r^{r_t}\frac{(U-V_z\tan\beta')_2^2}{r}\,dr+2JgR\int_r^{r_t}t\,\frac{\partial\left(\frac{S}{R}\right)}{\partial r}\,dr \quad (352)$$

A detailed discussion of the solution of equations (352) and (349) for the design case is presented in chapter VIII. A solution of these equations to satisfy the off-design problem is similar and requires detailed knowledge of boundary-layer growth and blade-element losses over the complete range of operating conditions. Although complete loss information is not readily available at the present time, the relations between the diffusion factor and blade-element losses (chs. VI and VII) might be used for operating points in the vicinity of the design point. If a solution of these equations is obtained, mass-averaged values of rotor over-all pressure ratio and efficiency can be calculated.

The blade-element calculations for the stator blade performance are similar to those for the rotor. Values of outlet axial velocity can be determined by an iteration solution of equation (352) where the subscript 1 becomes 2, the subscript 2 becomes 3, and the term $(U-V_z\tan\beta')$ becomes $(V_z\tan\beta)$. Continuing this iteration process blade row by blade row through the compressor will ultimately provide the compressor-outlet conditions.

Remarks on blade-element method.—Unfortunately, at present the complete blade-element-flow picture is unknown. In the region near the compressor design point, adequate blade-element data are available for entrance stages. However,

the variations of loss and turning angle have not been established as compressor stall is approached. In addition, boundary-layer theory does not as yet provide a means of calculating the boundary-layer growth through a multistage compressor, and there are no unsteady-flow results, blade-row interaction effects, nor data concerning radial mixing of blade wakes that can be applied directly to compressor design.

The preceding analysis reveals the gaps in our knowledge (particularly off-design blade-element data) that must be bridged by future research programs. In view of the length of the preceding calculation, it probably is not justified at present unless a good estimate can be made of the blade-element flow at off-design operating conditions. As stated previously, the method is presented because it has the greatest potentiality for providing a complete picture of the internal-flow mechanism through a compressor at off-design operating conditions. Of course, one obvious way of simplifying the calculation would be to carry it out at only one radius of the compressor. This procedure would not be exact; however, a qualitative picture could be obtained of the compressor operating characteristics.

STAGE-STACKING METHOD

Over-all compressor performance for a range of speeds and weight flows may be estimated by a stage-stacking method. The performance of each stage of the multistage compressor is obtained and presented so that its performance is a function only of its inlet equivalent weight flow and wheel speed. For assigned values of compressor weight flow and speed, the first-stage performance yields the inlet equivalent flow and wheel speed to the second stage. A stage-by-stage calculation through the compressor gives the individual stage pressure and temperature ratios, so that over-all compressor pressure ratio and efficiency can be calculated for the assigned values of compressor weight flow and wheel speed.

Stage performance.—Single-stage performance tests are conveniently made at constant speed, so that performance is very often presented as plots of pressure ratio and adiabatic efficiency against equivalent weight flow for constant values of equivalent speed. Such plots, however, are not convenient to use in applying the stage-stacking method, and stage performance for this use is presented as plots of efficiency and pressure coefficient against a flow coefficient. These dimensionless quantities are defined by the following equations:

$$\eta_{ad}=\frac{\Delta H_{id}}{\Delta H_{ac}} \tag{353}$$

$$\psi=\frac{\frac{\Delta H_{id}}{\theta}}{\left(\frac{U_m}{\sqrt{\theta}}\right)^2}=\frac{Jgc_pT_{s1}Y}{\left(\frac{U_m}{\sqrt{\theta}}\right)^2} \tag{354}$$

$$\varphi=\left(\frac{V_z}{U}\right)_m \tag{355}$$

Representative single-stage performance curves are shown in figure 223. These curves may vary in the multistage environment (ch. XIII); however, for undistorted inlet flow, stage performance generalizes quite well for a considerable range of Reynolds and Mach numbers. The stage characteristics at different speeds may be presented as a single line (fig. 223) for relative stage-inlet Mach numbers up to approximately 0.75. An exception is made for stage operation at low angles of attack. Even for relatively low values of relative stage-inlet Mach number, the flow coefficient denoting a choked condition changes with wheel speed, so that a family of curves is required in the high-flow-coefficient range. Stage performance for relative stage-inlet Mach numbers higher than about 0.75 may be presented as a family of curves for the different wheel speeds. Stage performance is influenced by flow distortion at its inlet, but very little quantitative information is available.

Sources of stage performance.—The stage performance curves needed for the stage-stacking method may be obtained from single-stage and multistage testing or from theoretical calculations. The chief shortcoming of the single-stage test data available to date is the lack of information concerning radial maldistribution of flow and unsteady flow. Such information is needed to estimate over-all compressor performance by the stage-stacking method; for example, at low wheel speeds, the inlet stage of a multistage compressor operates stalled so that the inlet flow to the second stage often is far from uniform.

Stage performance obtained from interstage data on multistage compressors (see refs. 253, 257, and 258) includes specific amounts of radial maldistribution of flow; for example, the stalled

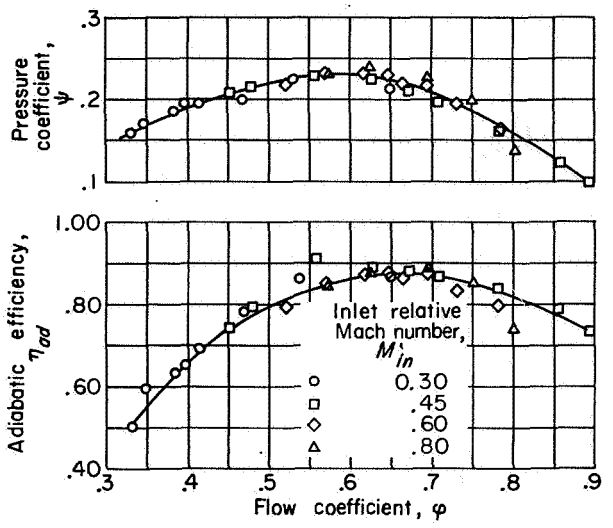

FIGURE 223.—Typical stage characteristic curves.

portions of the second-stage curves are obtained for inlet flow affected by stall in the first stage.

The difficulty in estimating stage performance from theoretical calculations is concerned with the fact that the flow in a compressor is three-dimensional, while the basic data normally used are based on two-dimensional flow. Employing blade-element theory to obtain stage performance involves all the difficulties discussed in the section entitled Blade-Element Method. As before, the calculation breaks down when a blade element stalls. A theoretical method of estimating stage performance along the mean line is presented in reference 256. Conditions at the mean diameter are taken as representative for the stage. For stages having hub-tip radius ratios lower than 0.6, reference 256 indicates that some form of integration of the individual blade-element characteristics (possibly by means of the blade-element method) along the blade height should be attempted. An example of stage performance calculated from mean diameter conditions is presented in appendix I of reference 256.

Stacking procedure.—In order to estimate the performance of a multistage axial-flow compressor with a stacking procedure, the following must be known:

(1) Stage performance curves of each stage
(2) Annulus area at inlet to each stage
(3) Mean radius at inlet to each stage
(4) Design value of absolute flow angle at inlet to each stage

The over-all compressor performance can be calculated for assigned values of compressor-inlet equivalent weight flow $w\sqrt{\theta_1}/\delta_1$ and rotative speed $U_{m,1}/\sqrt{\theta_1}$. The value of flow coefficient into the first stage is found from

$$\varphi_1=\frac{\dfrac{V_{z,1}}{\sqrt{\theta_1}}}{\dfrac{U_{m,1}}{\sqrt{\theta_1}}} \tag{356}$$

where the value of $V_{z,1}/\sqrt{\theta_1}$ is read from curves representing the following equation:

$$\frac{w\sqrt{\theta}}{\delta A_{an}}=\frac{V_z}{\sqrt{\theta}}\left[1-\left(\frac{V_z}{\sqrt{\theta}}\right)^2\frac{1}{2Jgc_pT_{s1}\cos^2\beta}\right]^{\frac{1}{\gamma-1}}g\rho_{s1} \tag{357}$$

The area term A_{an} in equation (357) is commonly taken as the geometrical annulus area. However, experience has shown that more realistic values of axial velocity are obtained from equation (357) if effective annulus area is used. In order to determine effective annulus area, the boundary-layer growth through the compressor must be known (ch. VIII). Again, information concerning the growth and behavior of the boundary layer in an axial-flow compressor is required for the off-design case.

The first-stage performance curves yield values of ψ_1 and η_1 that permit calculation of the first-stage pressure ratio and temperature ratio from the following equations:

$$\frac{P_3}{P_1}=\left[1+\frac{\psi_1\left(\dfrac{U_{m,1}}{\sqrt{\theta_1}}\right)^2}{Jgc_pT_{s1}}\right]^{\frac{\gamma}{\gamma-1}} \tag{358}$$

$$\frac{T_3}{T_1}=\left[1+\frac{\psi_1\left(\dfrac{U_{m,1}}{\sqrt{\theta_1}}\right)^2}{\eta_1 Jgc_pT_{s1}}\right] \tag{359}$$

The values of equivalent flow and speed at the inlet to the second stage are calculated from

$$\frac{w\sqrt{\theta_3}}{\delta_3}=\frac{w\sqrt{\theta_1}}{\delta_1}\frac{\sqrt{\dfrac{T_3}{T_1}}}{\dfrac{P_3}{P_1}} \tag{360}$$

$$\frac{U_{m,3}}{\sqrt{\theta_3}}=\frac{U_{m,1}}{\sqrt{\theta_1}}\frac{r_{m,3}}{r_{m,1}}\frac{1}{\sqrt{\dfrac{T_3}{T_1}}} \tag{361}$$

The values of equivalent weight flow and equivalent wheel speed at the second-stage inlet determine the value of the flow coefficient φ_2, so that the second-stage pressure and temperature ratios may be calculated from the values of ψ_2 and η_2. The stage-by-stage calculation is continued throughout the compressor, and over-all pressure ratio and efficiency are calculated from the compressor-inlet and -outlet pressures and temperatures. Thus, for any wheel speed, the over-all compressor pressure ratio and efficiency can be calculated for each assigned value of compressor weight flow.

In calculating a compressor performance map, some means must be employed for estimating the surge line, which influences starting, acceleration, and control problems. One scheme is to draw the surge line through the peak-pressure-ratio points of the over-all performance map. If the stage performance curves exhibit discontinuities, surge at any compressor speed may be taken to correspond to flow conditions for which a discontinuity is encountered in the performance curve of any stage.

Remarks on stage-stacking method.—The stage-stacking method may be used as a research tool to investigate compressor off-design problems or to estimate the performance of an untested compressor. In reference 3, the stage-stacking method was employed to indicate qualitatively the operation of each stage in a high-pressure-ratio multistage compressor over a full range of operating flows and speeds, the effect of stage performance on off-design performance, the effect of designing for different stage-matching points, and the effect on over-all performance of loading exit stages and unloading inlet stages by resetting stator blade angles. The part-speed operation for high-pressure-ratio multistage axial-flow compressors is analyzed in chapter XIII with regard to the surge-line dip and the multiple performance curves that exist in the intermediate-speed range. In both these references, stage performance curves were assumed.

The difficulty in estimating the performance of an actual compressor lies in obtaining reliable stage performance curves. Use of stage curves obtained from a given multistage compressor results in good performance estimation of a compressor having similar stages and only a slightly different over-all design pressure ratio. This is illustrated in reference 254, where the performance of a modified compressor is predicted from the stage curves of the original version of the compressor. The results of this performance-map prediction by the stage-stacking method are illustrated in figure 224. Calculated and measured values agreed particularly well at the higher compressor speeds.

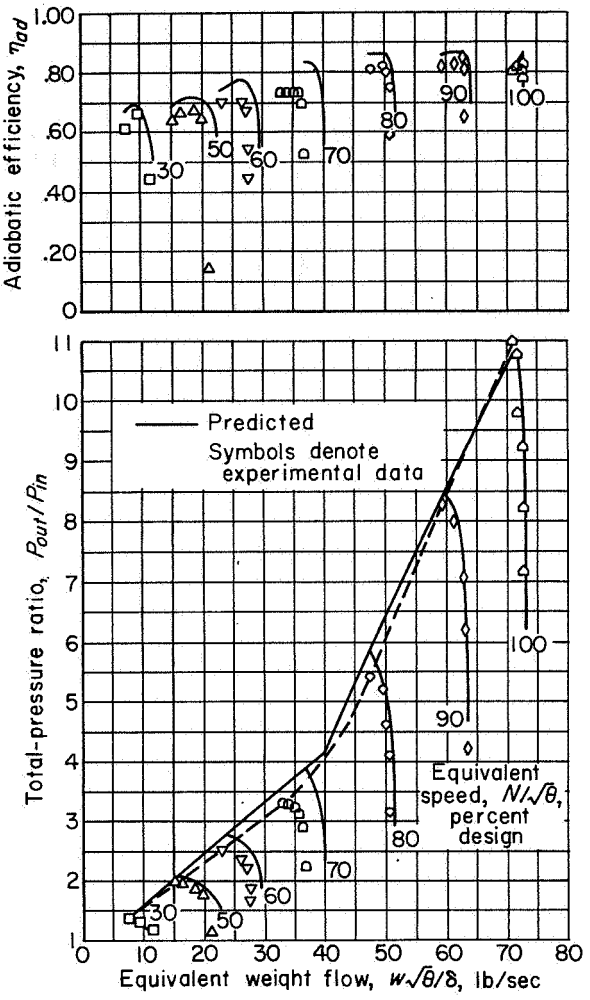

FIGURE 224.—Comparison of predicted and experimental over-all performance for modified eight-stage compressor.

This method is also useful for determining the effects of interstage bleed and variable geometry on compressor performance. In the interstage-bleed calculation, the flow coefficient φ can be adjusted for the amount of air bled from the compressor. The effect of variable geometry can be accounted for in the calculation procedure if the variation of the stage curves is known as the compressor geometry is varied.

SIMPLIFIED METHOD

A drawback common to the blade-element and stage-stacking methods of estimating over-all compressor performance is the length of time required for the calculations. A simplified method requiring much less calculating time is discussed herein. This method provides a means of obtaining the performance map of a new compressor from the results of previously designed compressors. Correlation curves are provided to facilitate the calculation.

Background information.—In reference 256 a method for predicting multistage-compressor performance is outlined. It was used to estimate the performance map of a newly designed compressor having blading similar to an existing compressor but slightly different design values of weight flow, pressure ratio, wheel speed, and number of stages. The application of this method to new compressor designs is, of course, restricted to cases where a compressor map of a similar existing compressor is available.

In this report, an attempt is made to extend the method presented in reference 256 to a more general case. Therefore, experimental data on eight multistage compressors were collected, correlated, and plotted in curve form, so that multistage-compressor performance maps of new compressors could be obtained easily from a knowledge of the design conditions alone. The method presented herein is similar to that used in reference 26 to obtain multistage performance maps. There are three phases of the calculation procedure. First, points of maximum efficiency at each speed are calculated. The line of maximum efficiency is called the backbone of the compressor map, and values along this line are termed backbone values. Second, the stall-limit line is determined, and values along the stall-limit line are referred to as stall-limit values or stall-limit points. Finally, points along lines of constant speed are calculated from the stall limit to maximum flow. The integration of these phases results in a complete compressor performance map.

Calculation of compressor backbone.—Experimental over-all performance maps (similar to fig. 220) of eight compressors (listed in table V) were obtained. For the condition of maximum adiabatic efficiency at each speed, values of pressure ratio, weight flow, and efficiency were tabulated. From these backbone values, the reference-point values of speed, pressure ratio, weight flow, and adiabatic efficiency were found. The reference point of a compressor map, which is not necessarily the design point, is defined as the point of maximum polytropic efficiency of the compressor backbone.

The effect of reference-point pressure ratio on backbone characteristics is shown in figure 225, where each backbone value is plotted as a percentage of its reference-point value. In figure 225(a), values of backbone pressure ratio are plotted against reference pressure ratio with equivalent rotor speed as a parameter. Similar plots of backbone weight flow and adiabatic efficiency are shown in figures 225 (b) and (c), respectively.

The backbone of a new compressor may be calculated from figure 225 and known reference-point values of pressure ratio, weight flow, adiabatic efficiency, and rotor speed. For the reference pressure ratio, the backbone values of pressure ratio, weight flow, and efficiency at various speeds are read from figure 225. Absolute backbone values are obtained by multiplying the values

TABLE V.—EXPERIMENTAL COMPRESSOR DATA

Compressor	Inlet guide vanes	Reference pressure ratio	Stages	Outer diameter, in.	Inlet hub-tip ratio	Reference
1. Subsonic	Yes	2.08	6	15.75	0.575	--------
2. Subsonic	Yes	3.00	10	19	0.5	--------
3. Subsonic	Yes	3.48	12	Variable	0.6	--------
4. Transonic	No	4.02	5	20	0.50	51
5. Subsonic	Yes	5.53	10	20	0.55	47
6. Transonic	No	7.35	8	20	0.48	53
7. Subsonic	Yes	9.20	16	33.5	0.55	253
8. Transonic	No	10.26	8	Variable	0.46	255

691-564 O-65-21

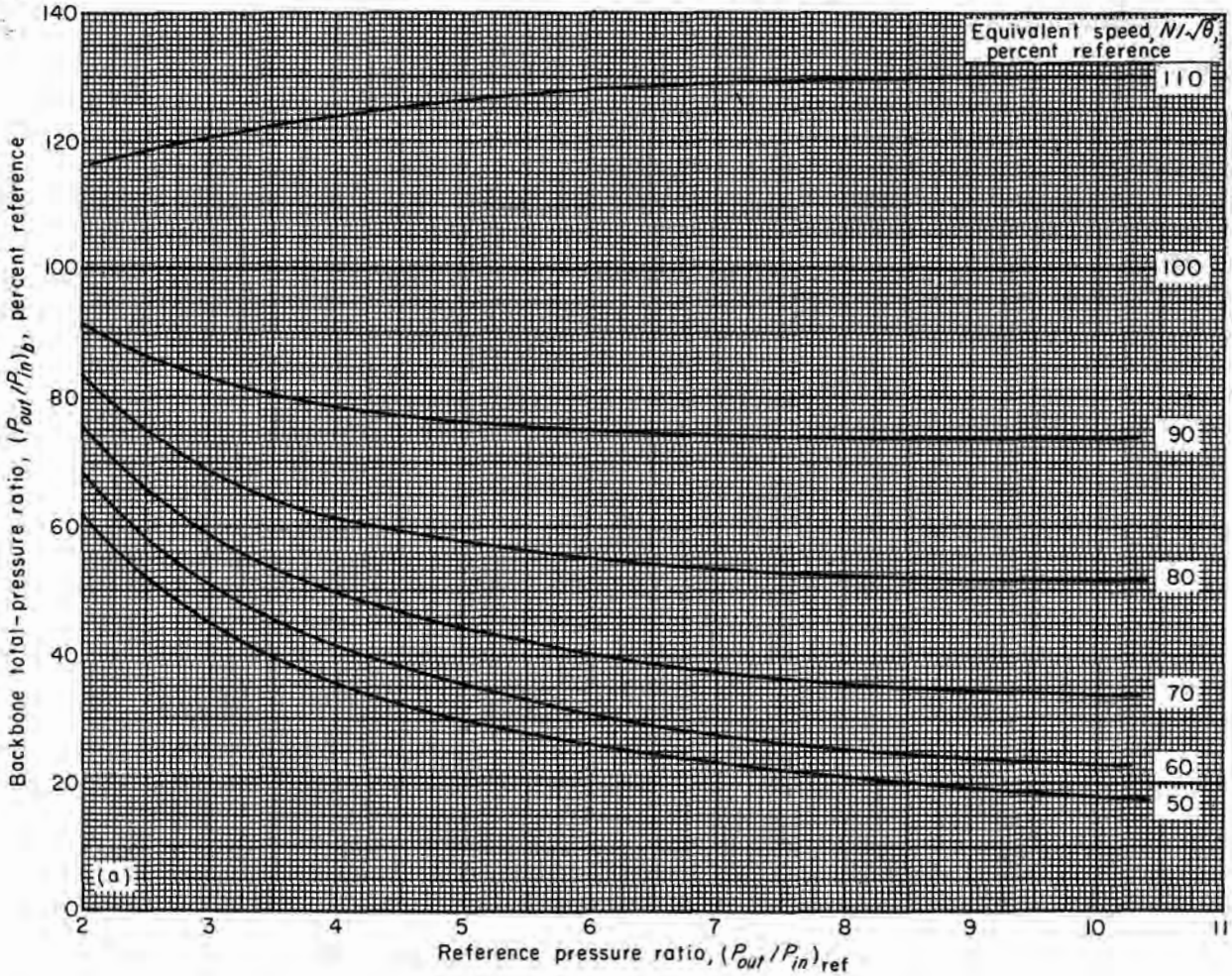

(a) Pressure ratio.

FIGURE 225.—Effect of reference pressure ratio on stall-limit line.

read from figure 225 by appropriate reference-point values.

Calculation of stall-limit line.—The effect of reference pressure ratio on stall-limit or surge-line characteristics is shown in figure 226, in which stall-limit pressure ratio is plotted against reference pressure ratio with stall-limit weight flow as a parameter. The values of stall-limit weight flow and pressure ratio are plotted as percent of the reference values. The stall-limit line of a new compressor may be calculated by multiplying the stall-limit values of pressure ratio and weight flow read from figure 226 for the known reference pressure ratio by their respective reference values. Stall-limit lines estimated in this manner are single-valued; whereas, the stall-limit lines of some actual compressors are multivalued (ch. XIII).

Constant-speed characteristics.—The constant-speed characteristics of an existing compressor may be obtained from its performance map. For several points along each speed line, values of temperature rise $(T_{out}-T_{in})/\theta_1$, adiabatic efficiency η_{ad}, and flow parameter $(w_{in}\sqrt{\theta_{in}}/\delta_{in})(\sqrt{T_{out}/T_{in}}/\sqrt{P_{out}/P_{in}})$ are calculated and divided by their respective backbone values to yield relative temperature rise, efficiency, and flow parameter. Values from the entire compressor map tend to give a single curve of relative temperature rise against relative flow parameter and a single curve of relative efficiency against relative flow parameter. These two curves define the constant-speed characteristics of a compressor. Plots of this type are illustrated in figure 227. The data points represent seven different compressor speeds,

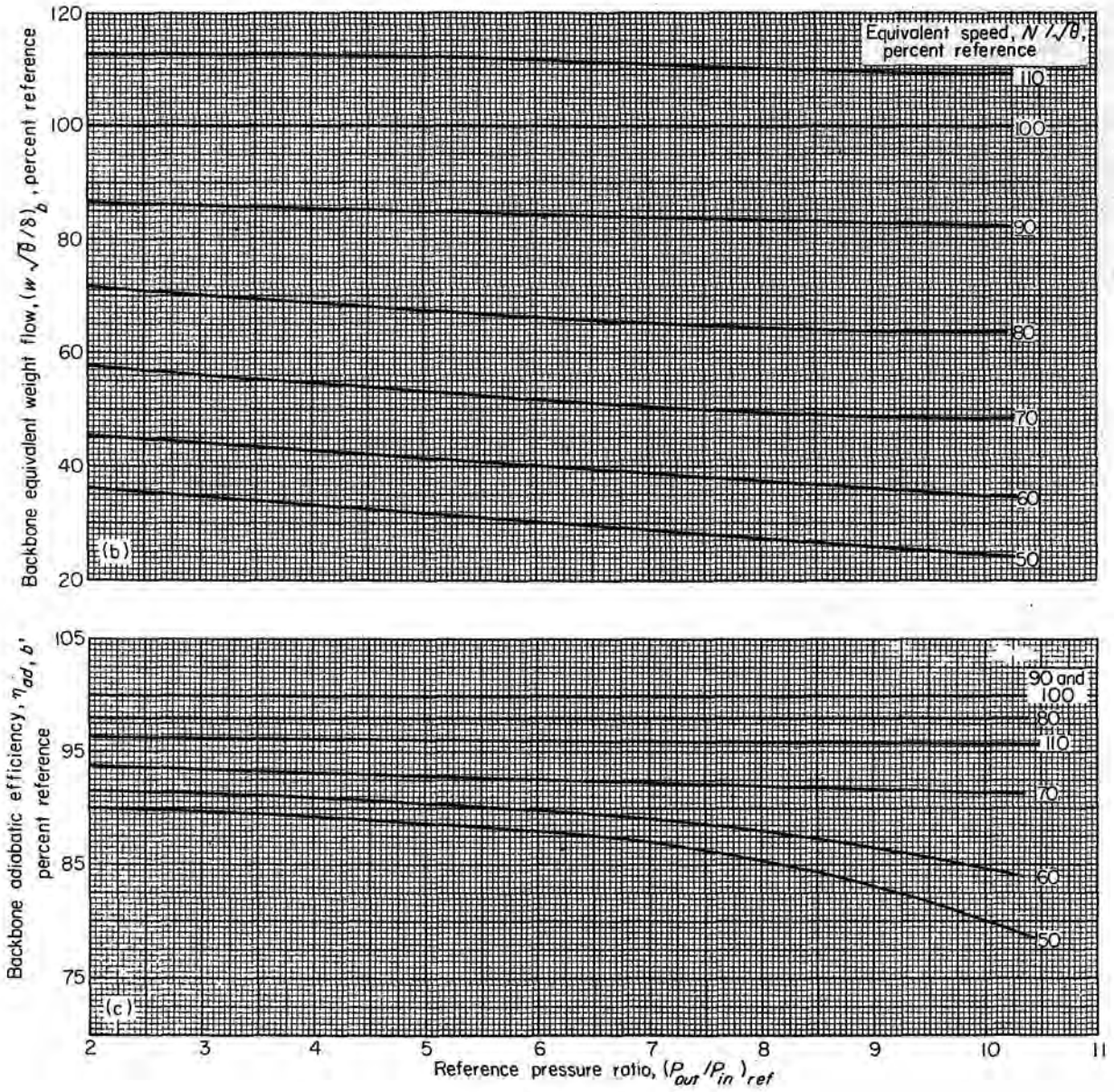

(b) Weight flow.
(c) Efficiency.

FIGURE 225.—Concluded. Effect of reference pressure ratio on backbone characteristics.

and in general the correlation of data at all speeds is relatively good.

In figure 228 faired curves are plotted representing the constant-speed characteristics of four compressors designed according to the basic principles outlined in chapter VIII. When specific data are lacking on the constant-speed characteristics of a newly designed compressor, an average of the curves of figure 228 could probably be used successfully for the compressor constant-speed characteristics, if the design system is similar to that presented in chapter VIII.

The lines of constant speed for a desired compressor performance map may be calculated from a given set of constant-speed characteristic curves and the calculated backbone values. For each speed, relative values of flow parameter are assigned and relative values of temperature rise

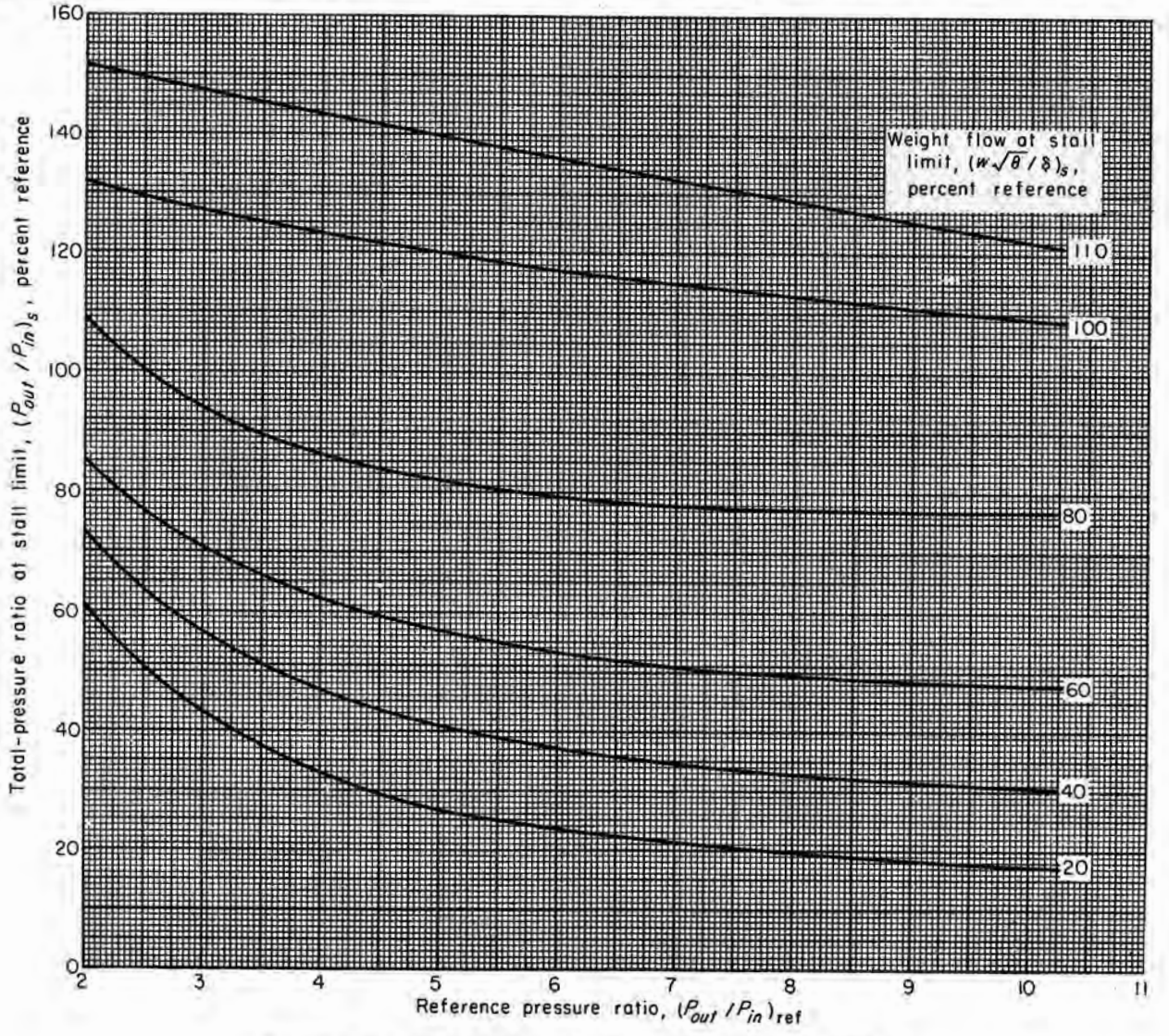

FIGURE 226.—Effect of reference pressure ratio on stall-limit line.

and efficiency are read from the constant-speed curves. Absolute values are calculated from these relative values and the appropriate backbone values. In the use of these curves, one end is limited by the stall-limit line and the other end by the maximum-weight-flow value. Compressor pressure ratio is calculated from the values of temperature rise and efficiency, and compressor weight flow is calculated from values of temperature ratio, pressure ratio, and flow parameter.

Comments on reference point.—As stated previously, the reference point is defined as the point of maximum polytropic efficiency of the compressor map. Experimental data indicate that the reference point is usually found at values of compressor speed somewhat below the actual design speed. Unfortunately, attempts to obtain an exact relation between the actual compressor design point and the reference point were unsuccessful. In the case of the four NACA compressors that utilized the design principles of chapter VIII, the reference speed varied from 90 to 100 percent of the actual design speed. This fact may be helpful in establishing the relation of these two points.

The following procedure may be used to compute reference conditions from design conditions

for a particular ratio of design speed to reference speed $(N/\sqrt{\theta})_d/(N/\sqrt{\theta})_{ref}$:

(1) A trial value of reference pressure ratio $(P_{out}/P_{in})_{ref}$ is selected.

(2) A value of backbone total-pressure ratio $\frac{(P_{out}/P_{in})_b}{(P_{out}/P_{in})_{ref}}100$ is read from figure 225(a) for the values of $(P_{out}/P_{in})_{ref}$ and $\frac{(N/\sqrt{\theta})_d}{(N/\sqrt{\theta})_{ref}}100$.

(3) A value of $(P_{out}/P_{in})_{ref}$ is calculated from

$$\left(\frac{P_{out}}{P_{in}}\right)_{ref}=\frac{\left(\frac{P_{out}}{P_{in}}\right)_d}{\frac{\left(\frac{P_{out}}{P_{in}}\right)_b}{\left(\frac{P_{out}}{P_{in}}\right)_{ref}}} \tag{362}$$

If this calculated value does not equal the trial value from step (1), steps (1) to (3) are repeated until the two values do agree.

(4) A value of $\frac{(w\sqrt{\theta}/\delta)_b}{(w\sqrt{\theta}/\delta)_{ref}}100$ is read from figure 225(b) for the values of $\left(\frac{P_{out}}{P_{in}}\right)_{ref}$ and $\frac{(N/\sqrt{\theta})_d}{(N/\sqrt{\theta})_{ref}}100$.

(5) The value of $(w\sqrt{\theta}/\delta)_{ref}$ is calculated from

$$\left(\frac{w\sqrt{\theta}}{\delta}\right)_{ref}=\frac{\left(\frac{w\sqrt{\theta}}{\delta}\right)_d}{\frac{\left(\frac{w\sqrt{\theta}}{\delta}\right)_b}{\left(\frac{w\sqrt{\theta}}{\delta}\right)_{ref}}} \tag{363}$$

(6) A value of $\frac{\eta_{ad,b}}{\eta_{ad,ref}}100$ is read from figure 225(c) for the values of $\left(\frac{P_{out}}{P_{in}}\right)_{ref}$ and $\frac{(N/\sqrt{\theta})_d}{(N/\sqrt{\theta})_{ref}}100$.

(7) The value of $\eta_{ad,ref}$ is calculated from

$$\eta_{ad,ref}=\frac{\eta_{ad,d}}{\frac{\eta_{ad,b}}{\eta_{ad,ref}}} \tag{364}$$

Remarks on simplified method.—How closely the performance map calculated by the simplified method will conform with the actual performance map depends on each phase of the calculation. The agreement depends on (1) how well the available compressor performance maps generalize to backbone, stall-limit, and constant-speed curves, (2) how closely design conditions are realized in the new compressor, and (3) how accurately reference-point conditions are calculated from design conditions. The performance maps of the limited number of compressors designed along the lines suggested in this volume have had some affinity in shape. As previously noted, however, double-valued stall lines cannot be anticipated by this method.

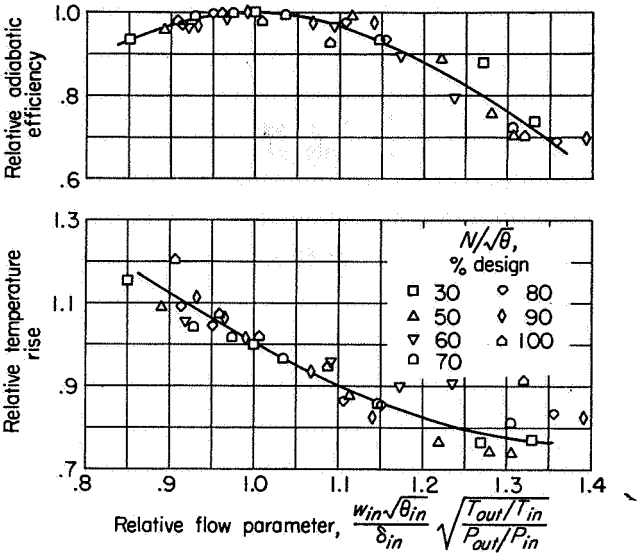

FIGURE 227.—Generalized performance parameters at several speeds for typical axial-flow compressor.

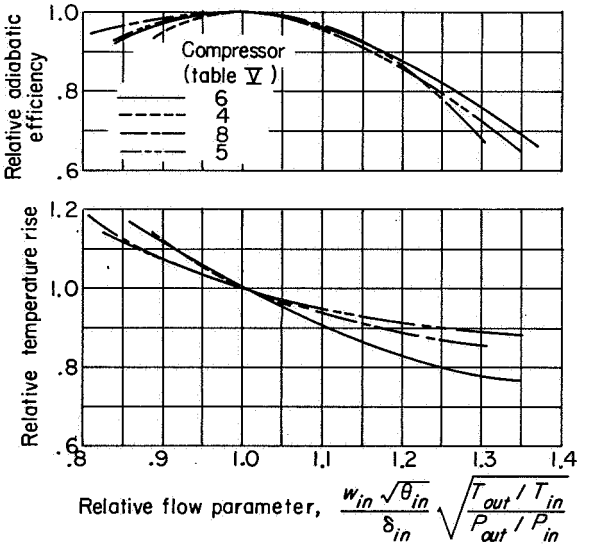

FIGURE 228.—Generalized performance curves of four multistage compressors.

CONCLUDING REMARKS

Three techniques have been presented for estimating compressor off-design performance. The first method, which is based on blade-element theory, is useful for obtaining only a small part of the compressor map over which all blade elements in the compressor remain unstalled. This technique is restricted at present because of the limited amount of available information concerning off-design blade-element data, boundary-layer growth, blade-row interaction effects, and radial mixing of blade wakes. This method has the greatest potential for providing a complete picture of the internal-flow mechanism through a compressor.

The second method, which involves individual stage performance curves and a stage-by-stage calculation, is useful for estimating the performance of a compressor for which reliable stage performance curves are available. In addition, this method has been used effectively as a research tool to determine the effects of interstage bleed and variable geometry on compressor performance.

The third method, which is based on over-all performance data of existing compressors, may be used to estimate the complete performance map of a new compressor if the compressor design conditions are specified. At present, it is as effective as the other methods and has the advantages of simplicity and short calculating time.

CHAPTER XI

COMPRESSOR STALL AND BLADE VIBRATION

By Robert W. Graham and Eleanor Costilow Guentert

The extent of the useful operating range of the multistage axial-flow compressor is greatly influenced by its stalling characteristics. Over the entire range of possible compressor speeds there is a minimum flow point for each speed where the compressor will either surge or stall, depending upon the geometry of the compressor receiver. If surge does not occur, the efficiency will be so poor in the stalled condition that the compressor will limit the useful operation of a turbojet engine. These surge or stall points define the familiar surge or stall-limit line. In addition to this stall line, stall of the front and rear stages occurs at part-speed and overspeed operation, respectively. Serious blade vibrations may occur for either of these conditions as a result of stall.

Compressor stall may be manifested as rotating stall, individual stall of each blade, or stall flutter. From experimental evidence, the first of these seems the most prevalent.

Several theories of rotating stall in single-stage compressors appear in the literature, none of which can be used to predict propagation rates with any appreciable degree of reliability. However, these theories are useful in evaluating the significance of parameters pertinent to the stall-propagation mechanism and thus in planning experimental research programs. The prediction of rotating-stall data for multistage compressors is even more complicated, because of interaction effects among the stages.

AUTHOR

INTRODUCTION

Historically, it is interesting that one of the earliest references to rotating stall appeared in 1945 in a British report on the performance of a centrifugal compressor (ref. 259). In 1950 an NACA publication (ref. 260) reported the occurrence of an asymmetric flow pattern in an impulse axial-flow compressor. In both of these early investigations, flow patterns were detected by means of wool tufts. This asymmetric flow phenomenon was labeled as a propagating stall in reference 261 (1951), which presented the stalling characteristics of an axial-flow compressor. The rotating-stall patterns found in that investigation were detected with high-frequency-response hot-wire anemometers. During the past three years, much research effort has been devoted to the study of rotating stall in both single- and multistage compressors.

OFF-DESIGN OPERATION

With the use of aerodynamic theory, the design-point performance of a multistage compressor can be predicted with reasonable accuracy. However, as is pointed out in chapter X, current design techniques cannot be used to predict compressor operation that deviates markedly from design. Since the compressor of a turbojet engine must operate at part design speed during acceleration of the engine and also at high flight Mach numbers, analytical methods for accurately predicting part-speed operation are desired by compressor designers. In addition, designers are concerned with blade vibrations that occur during operation in stall.

The internal aerodynamics of the compressor must be throughly understood at off-design conditions before design techniques applicable to this region of operation can be developed. During compressor off-design operation, degeneration of the performance of a stage is accompanied by a serious flow separation in the blade passages. This unfavorable operating condition is termed stall. Two significant areas of off-design performance are labeled in figure 229, which is a representative multistage-compressor map: (1) inlet-stage stall, and (2) the stall-limit or surge line. These conditions result from stall of some of the compressor blade elements. The occurrence of separated flow at each of these regions can be explained without an elaborate analysis.

Inlet-stage stall.—At low speeds, insufficient pressure rise in the stages causes the density level

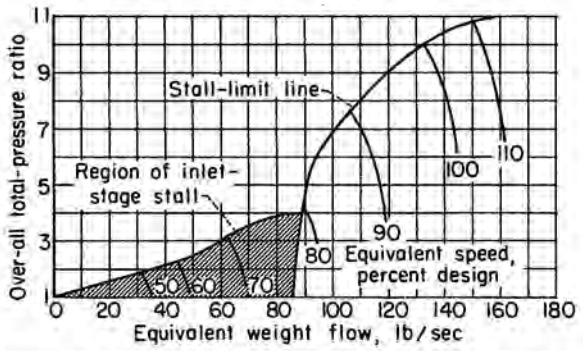

FIGURE 229.—Over-all performance of a multistage compressor.

of the fluid to be too low in the rear stages. The resulting high relative velocities and incidence angles cause choking in the rear stages. This choking limits the flow through the front stages and causes excessively high angles of attack or stall.

Stall-limit or surge line.—The stall-limit line represents the locus of minimum-flow points just before the performance of the compressor deteriorates abruptly. This deterioration in performance, which is attributed to the operation of one or more of the stages in severe stall, is sometimes called "complete compressor stall." In chapter XIII, the stages instigating the stall limit are analyzed and the significance of the shape of the stall-limit line and its relative position on the compressor map is discussed. The stall-limit is often referred to as the surge line, since surge may occur, depending on the geometry of the compressor receiver. An analysis of surge in the multistage compressor is presented in chapter XII.

In addition to the part-speed stalling conditions discussed earlier, the possibility of rear-stage stall at near-design and overspeed operation of the compressor must be admitted. Experimental evidence for overspeed stall is lacking, but such a stalling condition seems possible. At these conditions, continuity requirements in the rear stages cause some of the blade elements to operate at stalled angles of attack. Chapter XIII concludes that stall of the rear stages determines the stall-limit line at high part-speed and overspeed operation.

STALL PHENOMENA

Experimental data and analyses give credibility to the existence of at least three distinct phenomena during stall operation, the first two being aerodynamic phenomena and the last an aeroelastic phenomenon:

(1) Rotating or propagating stall, which consists of large stall zones covering several blade passages and propagating at some fraction of rotor speed in the absolute direction of rotor rotation. These stall zones can produce resonant blade vibrations. The number of stall zones and the propagation rate vary considerably. Compressor investigation has shown rotating stall to be the most prevalent type of stall phenomenon.

(2) Individual blade stall, which is characterized by the development of large separated-flow regions or zones of low flow in the wake of each blade.

(3) Stall flutter, which is a self-excited blade oscillation that must be distinguished from the more familiar classical flutter. The latter, which is a self-sustained oscillation caused by the coupling of the inertia, damping, elastic, and aerodynamic forces on a wing section, takes place at low angles of attack (unstalled flow) when a certain critical velocity that is a function of the wing design is reached. In contrast, stall flutter takes place at high angles of attack and is associated with individual blade stall.

The present report summarizes the pertinent experimental and theoretical work that has been done on these three stall phenomena. The assumptions and analytical techniques are emphasized in presenting the theories. Wherever possible, theoretical results are compared with experimental data. The discussion includes experimental data on blade vibration incurred during rotating stall.

SYMBOLS

The following symbols are used in this chapter:

N	rotational speed, rpm
U	rotor speed, ft/sec
V	air velocity, ft/sec
β	air angle, angle between air velocity and axial direction, deg
θ	ratio of total temperature to NACA standard sea-level temperature of 518.7° R
ρ	density, lb-sec^2/ft^4
$\Delta\rho V/\overline{\rho V}$	amplitude of ρV fluctuation divided by average ρV based on average anemometer current

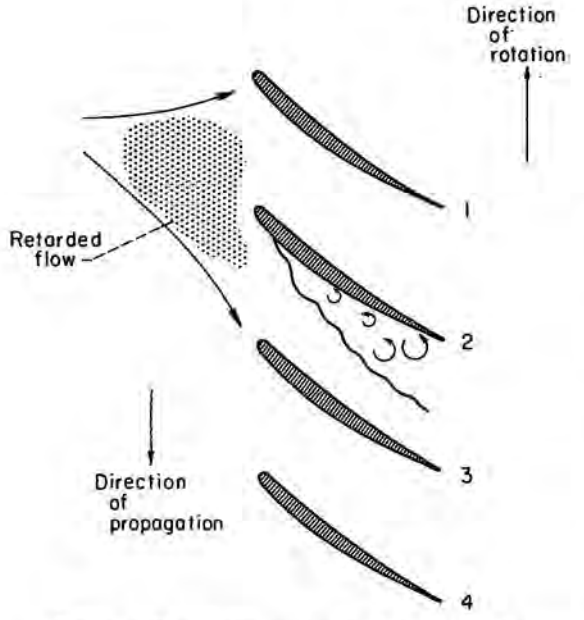

FIGURE 230.—Propagating stall in a cascade.

Subscripts:

t	tip
z	axial direction
1	station at exit of guide vanes
2	station at rotor exit
3	station at stator exit

Superscript:

relative to rotor

ROTATING STALL

MECHANISM OF STALL PROPAGATION

Rotating stall has been depicted as the propagation of large stall zones relative to the blade row. The propagation mechanism can be described by considering the blade row to be a cascade of blades similar to that shown in figure 230. Assuming that some flow perturbation has caused blade 2 to reach a stalled condition before the other blades in the cascade, then this stalled blade does not produce sufficient pressure rise to maintain the flow around it. Consequently, effective flow blockage or a zone of reduced flow develops. This retarded flow (shaded in fig. 230) diverts the flow around it so that the angle of attack increases on blade 3 and decreases on blade 1. The stall propagates downward relative to the blade row; the diverted flow stalls the blades below the retarded-flow zone and unstalls the blades above it. The retarded-flow or stall zone moves from the pressure side to the suction side of each blade (the opposite direction of rotor rotation). The stall zone may cover several blade passages. From compressor tests, the relative speed of propagation has been observed to be less than absolute rotor speed. Consequently, as observed from an absolute frame of reference, the stall zones appear to be moving in the direction of rotor rotation.

EXPERIMENTAL DETECTION OF ROTATING STALL

The hot-wire anemometer has generally been used at the NACA Lewis laboratory to detect and measure the flow fluctuation of stall. However, since a pressure change accompanies these flow fluctuations, a high-frequency-response electronic pressure pickup is also a suitable detection device. The hot-wire-anemometer probe and two types of hot-wire-anemometer amplifying systems, the constant-current and the constant-temperature, are discussed in references 262 to 264. A method of determining from hot-wire-anemometer data the number of stall zones in a given pattern and the magnitude of the flow fluctuation in the stall zones with respect to some mean flow value is given in reference 265.

The testing procedure generally followed in determining the rotating-stall characteristics of a compressor is to operate the compressor at a constant speed and gradually decrease the weight flow while observing the resulting changes in the hot-wire-anemometer output. The hot-wire-anemometer signal, usually observed on an oscilloscope, follows a definite evolutionary process as the weight flow is decreased. As an illustration, this process is described in conjunction with the performance characteristic of a single-stage axial-flow compressor (fig. 231).

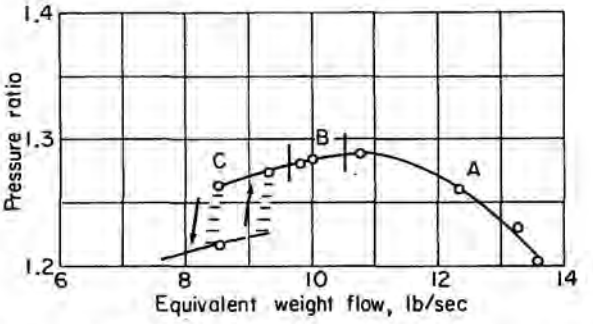

FIGURE 231.—Performance of compressor as operation point varies from unstalled to stalled.

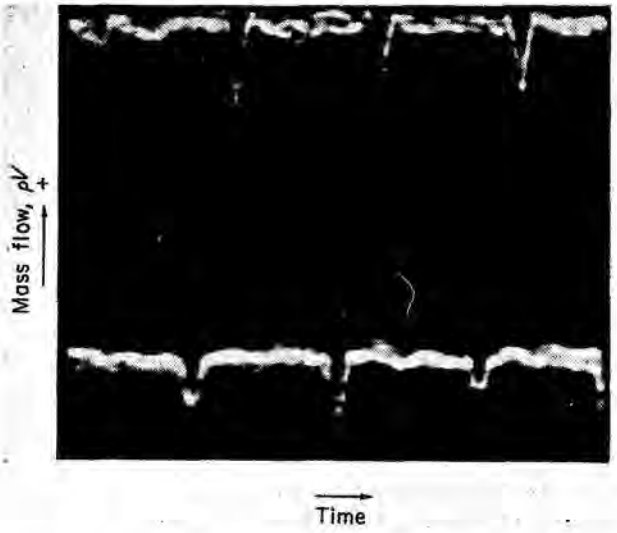

FIGURE 232.—Oscillograms of blade wakes.

When the test is begun, at high weight flows near the best operating point of the compressor, the hot-wire signal viewed on the oscilloscope indicates sharply defined blade wakes in region A. Typical oscillograms showing these blade wakes are given in figure 232. As the weight flow is reduced below the peak-pressure-ratio weight flow denoted by region B of figure 231, the blade wakes become wider and less well defined, indicating flow separation and the possibility of stall somewhere along the blade. A momentary or unstable stall zone covering several blade passages is occasionally observed on the oscilloscope. The sporadic stall zone is often the herald of a periodic rotating-stall pattern that develops at lower weight flows. Periodic rotating-stall zones are observed as the weight flow is further reduced to region C of figure 231. A typical rotating-stall pattern for this area is shown by the oscillogram of figure 233. Further throttling of the compressor weight flow may promote changes in the rotating-stall patterns with respect to the number and size of the stall zones. If the weight flow is gradually increased, generally the same rotating-stall patterns will appear; however, the stall pattern will be instigated at higher weight flow, as shown in figure 231. This behavior of stall instigation is called hysteresis.

Characteristics of experimentally observed stall patterns.—Single-stage compressors: Rotating-stall characteristics have been investigated in a considerable number of single-stage experimental compressors with symmetrical, solid-body, or free-vortex velocity diagrams and a variety of blade shapes. The rotating-stall data obtained embrace a wide range of stall-propagation rates and number of zones in each stall pattern. The number of zones varies from 1 to 12, and the absolute propagation rate varies from approximately 10 to 85 percent of rotor speed. Generally, more than one stall pattern occurs; that is, the number of zones and the geometric configuration of the stall-zone region change as the flow is varied in a given compressor. Figure 234 is a typical single-stage-compressor performance map with the stall patterns observed and the weight-flow range of each pattern indicated on the figure. Generally, as in the example used in the figure, the propagation rate remained essentially constant over the entire stall region, notwithstanding changes in the number of stall zones. Some exceptions to the consistency of the stall-propagation rate have been observed when appreciable changes in the radial extent of the stall zone take place.

Multistage compressors: Multistage compressors exhibit stall characteristics similar to those of the single-stage units. The stall zones appear to extend axially through the compressor, that is, with little or no spiraling. As the weight flow was throttled at a constant speed, the number of stall zones in the annulus varied from 1 to 7 among the several compressors investigated. Rotating stall in multistage compressors may exist from choked flow to surge at low speeds. The rotational speed of the stall zones ranged from 43 to 57 percent of

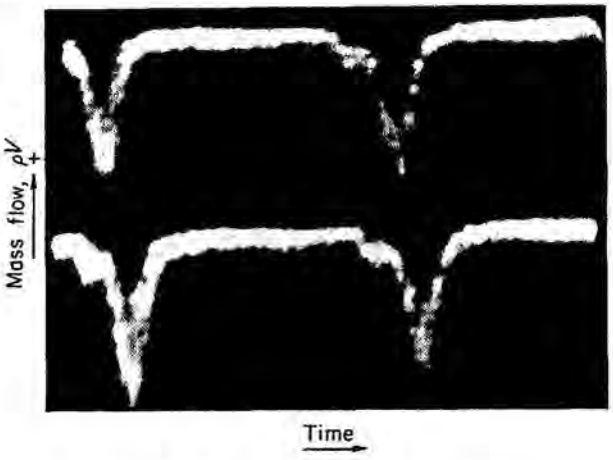

FIGURE 233.—Typical rotating-stall oscillogram.

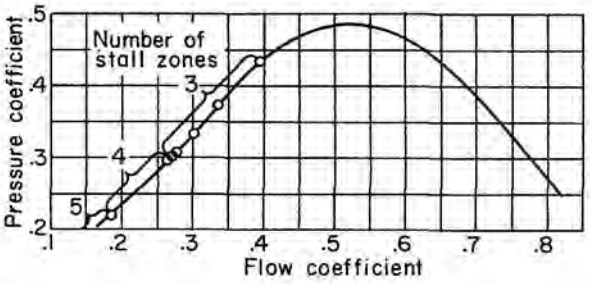

FIGURE 234.—Performance of single-stage compressor showing conditions at which rotating stall occurs.

the rotor speed, and the stall propagated in the direction of the rotor rotation (absolute frame of reference) for all compressors investigated.

Rotating-stall characteristics are superimposed on a typical multistage-compressor performance map in figure 235. For this compressor, stall existed throughout the compressor in the intermediate-speed range. The number of stall zones increased with a decrease in the weight flow at a given speed.

Single-stage and multistage stall data summary.—Tables VI (a) and (b) give a general summary of the stall data from single-stage and multistage compressors, respectively. More information regarding stall has been taken for single-stage units than for multistage compressors.

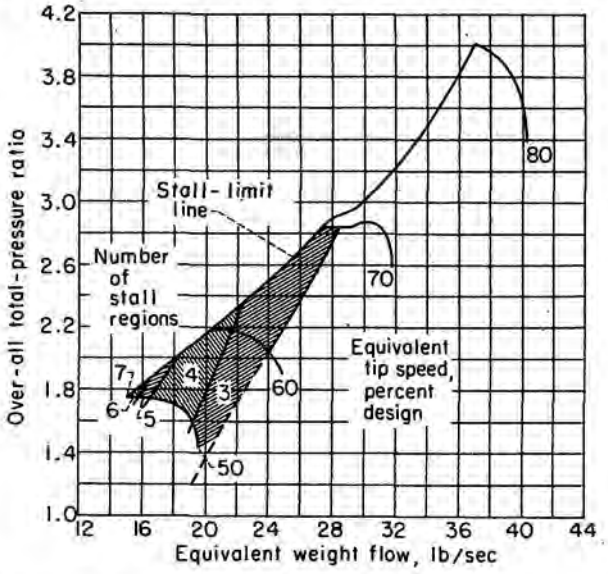

FIGURE 235.—Performance of multistage compressor showing conditions at which rotating stall occurs.

Single-stage-compressor design data are given in table VII.

CLASSIFICATION OF STALL

Rotating stall may be classified as progressive or abrupt, according to the performance characteristic of the compressor. In addition, the stall pattern is described as partial or total span and

TABLE VI.—SUMMARY OF ROTATING-STALL DATA

(a) Single-stage compressors

Type of velocity diagram	Compressor number	Hub-tip radius ratio	Number of stall zones	Propagation rate, Stall speed, abs/rotor speed	Weight-flow fluctuation during stall, $\Delta\rho V/\overline{\rho V}$	Radial extent of stall zone	Type of stall	Reference
Symmetrical	1	0.50	3 4 5	0.420 .475 .523	1.39 2.14 1.66	Partial ↓	Progressive ↓	265
	2	0.90	1	0.305	1.2	Total	Abrupt	
	3	0.80	8 1	0.87 .36	0.76 1.30	Partial Total	Progressive Abrupt	
	4	0.76	7 8 5 3 4 3 2	0.25 .25 .25 .23 .48 .48 .49	2.14 1.10 1.10 2.02 1.47 2.02 1.71	Partial ↓ Total ↓	Progressive ↓	278
	5	0.72	6, 8	0.245	0.71 to 1.33	Total	Progressive	271
Free vortex	6	0.60	1 2 1	0.48 .36 .10	0.60 .60 .68	Partial Partial Total	Progressive Progressive Abrupt	268
Solid body	7	0.60	1 1	0.45 .12	0.60 .65	Partial Total	Progressive Abrupt	
Vortex transonic	8	0.50	3 2	0.816 .634	---------- ----------	Partial Total	Progressive Progressive	55
	9	0.50	1	0.565	----------	Total	Abrupt	------
	10	0.40	2	----------	----------	Partial	Progressive	233

TABLE VI.—Concluded. SUMMARY OF ROTATING-STALL DATA

(b) Multistage compressors

Compressor number	Number of stall zones	Propagation rate, Stall speed, abs/rotor speed	Radial extent of stall zone	Periodicity	Type of stall	Reference
1	3 4 5 6 7	0.57	Partial	Steady	Progressive	Unpublished data
2	4 5 6	0.55	Partial	Intermittent	Progressive	19
3	1	0.48	Partial	Steady	Progressive	Unpublished data
4	1 2 3 4	0.57	Partial	Steady	Progressive	
5	1 2 3 4 5	0.57	Partial	Intermittent	Progressive	20
6	1	0.47	Total	Steady	Abrupt	Unpublished data
7	1	0.43	Total	Steady	Abrupt	267
8	1	0.53	Total	Steady	Abrupt	20

TABLE VII.—SINGLE-STAGE-COMPRESSOR DESIGN DATA

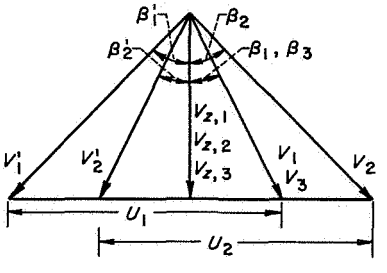

Compressors 2, 4, 5, and 10

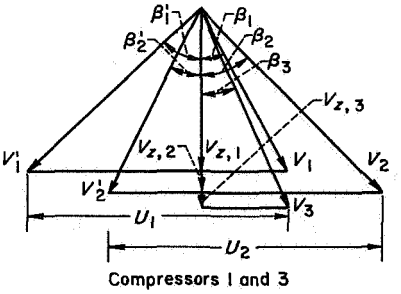

Compressors 1 and 3

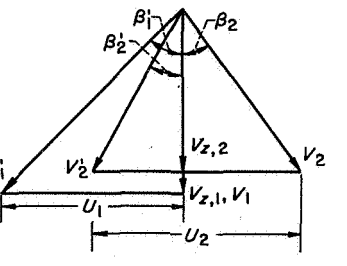

Compressor 8

Compressor (table VI(a))	Hub-tip ratio	O.D., in.	I.D., in.	Design tip speed, ft/sec	V_1/U_t	V_1'/U_t	V_2/U_t	V_2'/U_t	V_3/U_t	$\frac{V_{z,1}}{U_t}$	$\frac{V_{z,2}}{U_t}$	$\frac{V_{z,3}}{U_t}$	U_1/U_t	U_2/U_t	β_1, deg	β_1', deg	β_2, deg	β_2', deg	β_3, deg
1	0.50	14	7	777.5	0.706	0.846	0.856	0.740	0.745	0.669	0.694	0.716	0.749	0.763	18.9	37.9	36.0	20.48	15.9
2	.90	14	12.6	------	.725	.9475	.9475	.725	.725	.670	.670	.670	.950	.950	22.68	45	45	22.68	22.68
3	.80	14	11.2	826	.635	.915	.941	.670	.701	.600	.637	.670	.898	.898	18.95	49.12	47.38	17.92	17.1
4	.76	14	10.62	790	.9471	.9585	.9585	.9471	.9471	.7328	.7328	.7328	.8807	.8807	20.30	39.70	39.70	20.30	20.30
5	.72	14	10.09	790	.9273	.9363	.9363	.9273	.9273	.7213	.7213	.9213	.8594	.8594	20.49	39.25	39.25	20.49	20.49
6	.60	----	-----	------	-----	-----	-----	-----	-----	-----	-----	-----	-----	-----	-----	-----	-----	-----	-----
7	.60	----	-----	------	-----	-----	-----	-----	-----	-----	-----	-----	-----	-----	-----	-----	-----	-----	-----
8	.50	14	7	1000	.60	.92	.65	.67	-----	.60	.558	-----	.698	.698	0	49.30	30.67	33.40	-----
9	.50	18	9	1000	-----	-----	-----	-----	-----	-----	-----	-----	-----	-----	-----	-----	-----	-----	-----
10	.40	14	5.6	1000	.647	.953	.762	.743	-----	.647	.647	-----	.7597	.7597	0	47.3	31.9	28.9	-----

steady or intermittent, according to the geometry of the stall zone and the periodicity.

Progressive or abrupt stall.—Classifying rotating stall by the type of stage performance characteristic associated with it is probably the most important way to denote stall types. A smooth, continuous stage performance characteristic in the stall region similar to that shown in figure 234 indicates the gradual increase in blocked annulus area due to stall. Appropriately, this type is

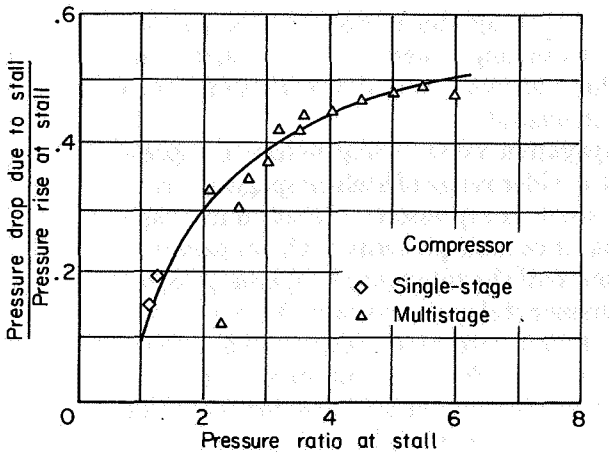

FIGURE 236.—Correlation of pressure drop at stall with compressor pressure ratio at stall.

called "progressive" stall. In contrast, a discontinuous stage performance characteristic like that shown in figure 231 has also been observed during stall. Generally, for this type of performance curve a single stall zone covering as much as half the annulus area and extending over the entire blade span has been observed. Because of the discontinuity in the pressure curve, this type of stall is called "abrupt."

The term "complete compressor stall" is applied to multistage compressors to describe a discontinuous performance curve similar to that for abrupt stall of single-stage compressors. The complete-compressor-stall points on the performance may define the stall-limit line.

The magnitude of the pressure drop at the discontinuous point of the performance characteristic is shown in figure 236 for abrupt stall of blade elements. Here the pressure drop due to stall divided by the pressure rise immediately before encountering stall is plotted against the compressor pressure ratio measured just before compressor stall. Both single-stage and multistage data are included; that is, both abrupt and complete-compressor stall data are plotted. Evidently, abrupt stall of some blade elements and complete compressor stall are similar. From this figure it is apparent that the pressure drop accompanying complete compressor stall is severe and will result in appreciable penalties in compressor efficiency.

Partial- or total-span stall.—The radial extent of the stall zone along a blade is another convenient characteristic for classifying rotating stall. In addition to extending circumferentially over several blade passages, the stall zone also covers part or all of the blade span. Thus, the term partial-span stall is used to denote stall covering part of the blade span, and total-span refers to stall covering the whole blade length. Figure 237 shows the type of oscillogram obtained during a radial traverse with a hot-wire-anemometer probe. The large-amplitude pulsations from hub to tip (fig. 237(a)) are typical for total-span stall. Figure 237(b) shows a partial-span stall concentrated at the tip, as shown by the disappearance of the stall "blip" from the anemometer trace at the hub.

Steady or intermittent stall.—It has been observed that compressors may also have an intermittent type of stall pattern for a given operating point. In this case one stall pattern exists for an instant, then changes to a new stall pattern. Intermittent changing among three different stall patterns has been observed in one multistage compressor.

GENERAL OBSERVATIONS ON ROTATING-STALL PHENOMENA

The following general observations concerning rotating-stall phenomena are made from examination of the existing data. The remarks apply to both single-stage and multistage compressors. Exceptions to the generalizations are also discussed.

Hysteresis effect.—When a compressor is being run at a constant aerodynamic speed and a rotating-stall pattern is encountered during a throttling of the weight flow, usually that same stall pattern will be observed for subsequent repeated tests. In fact, for single-stage tests over a range of speeds the stall pattern will be repeated for all speeds if the compressor is operated at the same flow coefficient in each case. However, it is interesting that once a stall pattern has been established during a throttling process, if the flow is allowed to increase, the pattern will persist above the value of the throttled weight flow (or flow coefficient for single-stage compressors) to a higher weight flow before disappearing. A graphical superposition of this apparent reluctance of the stall pattern to change on a compressor performance curve resembles the well-known hysteresis loop of other physical phenomena. Consequently, it has been labeled "hysteresis," although no time-dependency is involved. The resemblance is most

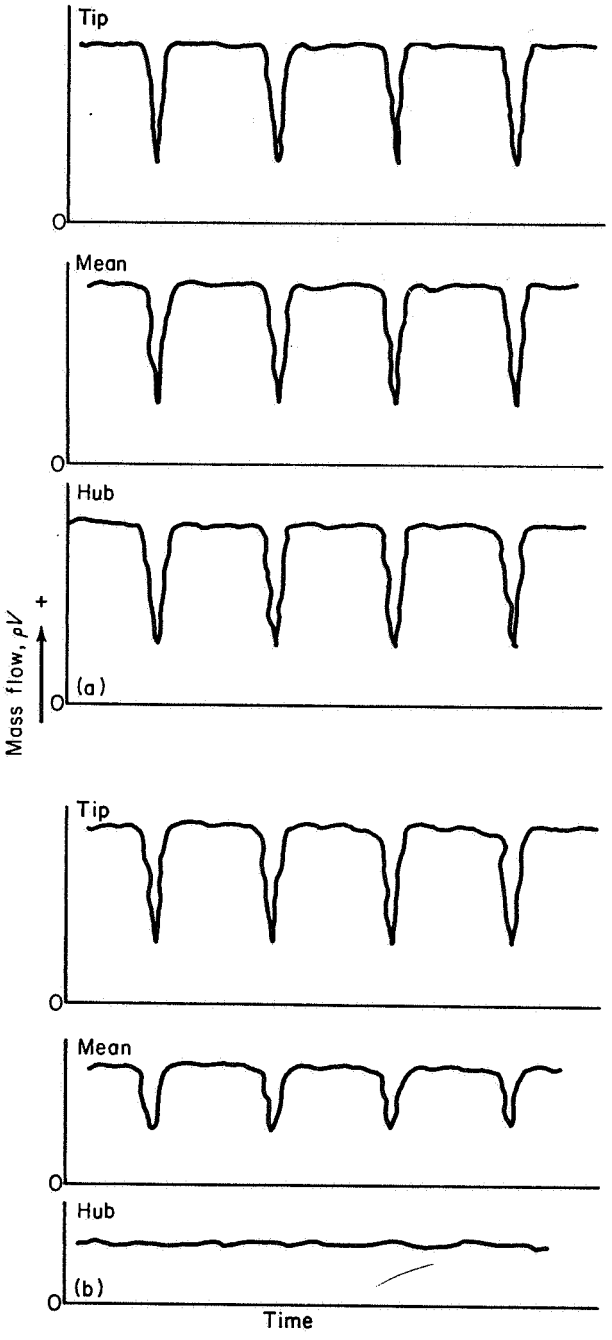

(a) Total-span stall.
(b) Partial-span stall.

FIGURE 237.—Sketches of typical oscilloscope traces of total- and partial-span rotating stall.

striking for abrupt stall, because a distinct loop is formed.

This so-called hysteresis effect is also present when a change in the stall pattern occurs. The weight flow marking the inception of a pattern during the throttling process is lower than that marking the disappearance of the pattern when the flow is increased.

Stall-propagation rates.—Single-stage compressors exhibit a wider range of stall-propagation rate than multistage compressors. Most multistage compressors have stall patterns with propagation rates of about half the rotor speed; whereas, single-stage-compressor stall patterns range from approximately 10 to 85 percent of rotor speed. Both multi-stage and single-stage compressors usually exhibit one stall-propagation rate for all stall patterns, if the geometry of the stall pattern does not change. Exceptions to this generality have been mentioned in the discussion of single-stage stall data. No exceptions have been observed for multistage compressors.

Flow and pressure fluctuations.—Table VI(a) includes a column in which the flow fluctuation accompanying rotating stall in a single-stage compressor is listed in terms of the parameter $\Delta\rho V/\overline{\rho V}$. The magnitude of $\Delta\rho V/\overline{\rho V}$ varies from 0.6 to 2.14. No apparent correlation of the magnitude of the parameter with the size or number of stall zones can be obtained from the existing data on single-stage compressors.

The magnitude of $\Delta\rho V/\overline{\rho V}$ for blade wakes measured during design flow conditions may range from approximately 0.1 to 0.2. By comparison, the stall disturbance is rather severe.

The magnitude of the parameter $\Delta\rho V/\overline{\rho V}$ in the inlet stage of a 10-stage research compressor was found to be similar to that observed in single-stage compressors. The stall data reported in reference 266 were obtained at 50, 60, and 70 percent of design speed. This operating region is the inlet-stage stall region indicated in figure 229. By locating hotwire anemometers at various axial stages, the magnitude of the flow fluctuation throughout the entire compressor was measured. The data of figure 238 (ref. 266) show that the intensity of the flow-fluctuation level diminished appreciably after the fourth or fifth stage of the compressor.

The pressure fluctuations peculiar to the abrupt stall that occurs along the stall-limit or surge line of multistage compressors are significant, because the attendant efficiency drop limits the useful engine operating range. In discussing figure 236, it was pointed out that an abrupt (40- or 50-percent)

drop in pressure rise may occur when the compressor operating point reaches the stall-limit line. In reference 267 the drop in the discharge pressure and the pressure fluctuation accompanying abrupt stall were measured during stalled operation. At 82-percent design speed, when the compressor reached the stall-limit line, the mean level of the discharge pressure dropped 50 percent and the discharge pressure fluctuated 25 percent above and below the mean pressure level of the stalled operation.

Usually, the rotating-stall pattern observed when the stall-limit line is reached is a single-zone total-span stall. Because of the discontinuity in the performance curve, the stall is classified as abrupt.

Multistaging effect.—Experimental evidence has shown that data on propagation rate or number of stall zones in single-stage compressors do not apply to the rotating-stall characteristics of multistage units composed of these stages. In reference 268, the single-stage stall data for three identical stages composing a multistage compressor are compared with the multistage stall data. In order to explain the difference in the stall of stages tested individually and as a part of a multistage compressor, multistaging or interaction effects must be considered.

In multistage compressors, each stage operates in an aerodynamic environment determined to some extent by all the compressor stages. This environment comprises two multistaging or interaction effects:

(1) The radial gradients in axial velocity emanating from a stage at off-design operation, which may be sufficiently severe to cause a stall angle of attack over a part of the blade span of some downstream blade row

(2) The influence of low-flow or stall zones emanating from other stages of the compressor

The result of the radial gradient in axial velocity might well be the development of a rotating-stall pattern considerably different from anything expected from single-stage stall data alone. In a series of tests conducted at the NACA Lewis laboratory on a production turbojet engine, it was observed that the stall characteristics of the compressor could be changed by altering the velocity profile entering the first blade row. Wire screens

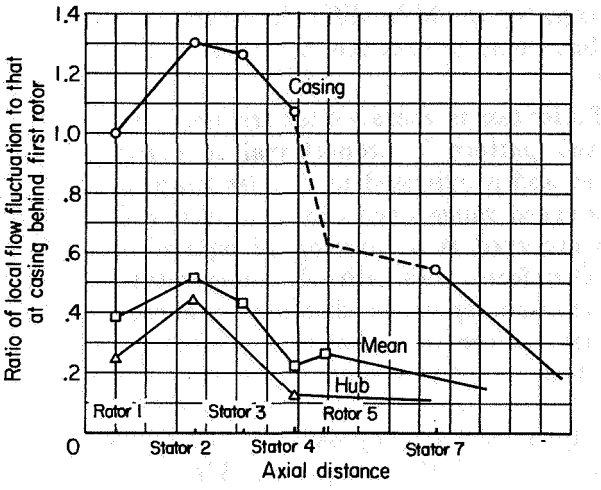

FIGURE 238.—Variation of flow fluctuation with axial distance in compressor at three radii at 50-percent design speed (ref. 266).

were used to block part of the flow into the compressor inlet. When the screens were arranged to produce circumferential variation in the flow, no appreciable changes in the stalling characteristics were evident. However, when radial gradients in the flow were achieved by partial blockage of the whole annulus of the inlet passage, the stalling characteristic of the compressor was altered significantly.

It was previously pointed out that, when rotating stall occurs in multistage compressors, the stall zones extend throughout the entire axial length of the compressor, as shown in figure 238. This means that each stage in the compressor will experience periodically recurring low-flow zones. If a stage or stages operate sufficiently near the stall point, the presence of the low-flow zones may cause stall angles of attack to occur when the blades pass through the stall zones.

Variation in stall patterns.—One of the objectives in presenting table VI is to emphasize the great variety of stall patterns that have been observed. At present, there appears to be no way of cataloging the stall with respect to any type of compressor design. Among several commercial engines of one type, each of which was installed in the same test facility, the stall patterns were different, although the propagation rate remained essentially the same. Apparently, in this case the stall pattern was sensitive to such small changes in compressor geometry as would result from production tolerances. Such minute differ-

ences in geometry would be difficult to include in a theory that would predict the stall pattern from design data.

Effect of inlet temperature.—Stall frequency for a given stall pattern is proportional to actual engine speed and is independent of inlet temperature. The speed range over which a given stall pattern is observed is a function of equivalent speed and therefore varies with inlet temperature. If the mechanical speed is changed to accommodate inlet temperature changes, so that the corrected speed $N/\sqrt{\theta}$ is constant, the stall frequency will vary with the mechanical speed. Consequently, it will be impossible to tune the natural frequency of the compressor blades to avoid a resonance with the fundamental stall disturbance or its harmonics over a range of compressor-inlet temperatures.

BLADE VIBRATION INCURRED DURING ROTATING STALL

Since rotating stall consists of one or more low-flow zones that rotate in the compressor annulus, usually at constant speed, the blade rows experience periodic aerodynamic forces as the low- and high-flow zones go by the blades. In reference 269 the fluctuating forces due to rotating stall were measured on the guide vanes and stators of a single-stage compressor. The blade-force fluctuations during rotating stall were comparable to the steady-state blade force measured during unstalled operation. This periodic force can therefore be a source of resonant blade vibration, where the frequency of the stall relative to the blades excites the blades. From current evidence, the compressor designer must always be concerned with the possibility of blade failure due to resonance between the blade frequency and the stall frequency.

Single-stage compressors.—When the high stresses accompanying rotating stall are investigated, it is necessary first to determine the magnitude of the blade stresses when accompanied by rotating stall. An investigation of the effect of rotating stall on the blading of a single-stage compressor with a hub-tip radius ratio of 0.5 is reported in reference 270. The experimental results show that stall zones can excite blade vibration with resultant bending stresses sufficiently severe to cause blade failure. Fatigue cracks were observed in the aluminum stator blades. The blades were in resonance with the first two harmonics, as shown in figure 239, which is a plot of the ratio of the stall frequency to the natural bending frequency of the blade against rotor speed. Resonant vibrations occur at compressor speeds corresponding to the intersection of the stall-frequency line with horizontal lines representing resonance with the fundamental stall frequency and the first two harmonics.

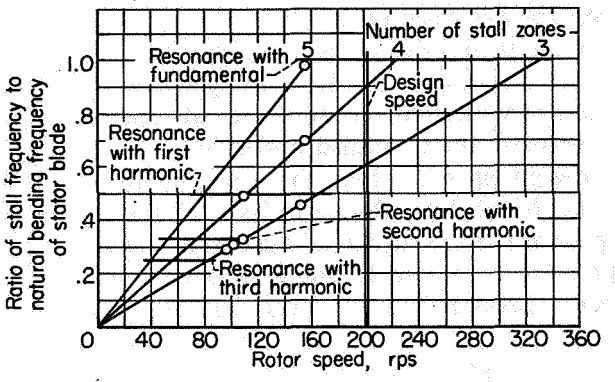

FIGURE 239.—Variation of stall frequency with rotor speed for three stall patterns in a single-stage compressor.

Other fatigue failures of experimental single-stage compressors have been attributed to rotating stall. Stall data were not obtained for all the compressors that failed, but each compressor had been operated in the stalled region. Most of these compressors were stages of 0.5 hub-tip ratio. A fatigue failure with much shorter blades, where the hub-tip ratio was 0.72, was attributed to resonance between the relative fundamental stall frequency and the natural bending frequency of the blades (see ref. 271).

Multistage compressors.—Although several multistage-compressor failures at the NACA might be attributable to rotating stall, only one was sufficiently instrumented with strain gages and hot-wire anemometers to trace the failure directly to rotating stall. This investigation is reported in reference 19, in which a resonant-vibration condition was found in the first-stage rotor at approximately 62- and 70-percent design speed, as shown in figure 240. The strain-age data indicated vibratory stresses of approximately $\pm 13{,}500$ and $\pm 34{,}800$ pounds per square inch, respectively, at these operating points, which were sufficient to cause fatigue failure of the aluminum blades. Typical high-stress vibration bursts caused by rotating stall as recorded from the strain gages are shown in figure 241 for 62-percent design speed.

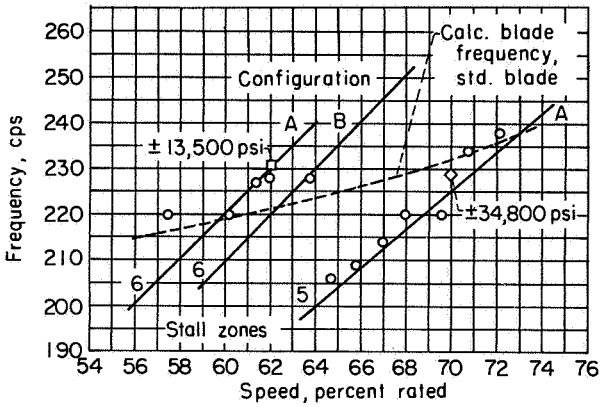

FIGURE 240.—Correlation of relative stall frequency with rotor blade-vibration frequency for a multistage compressor (ref. 19).

Methods of alleviating blade vibration.—To the axial-flow-compressor designer, the most serious result of rotating stall is blade failure. The theory of rotating stall developed thus far does not provide a method for predicting stall frequency for new designs and thus "tuning" blades out of dangerous blade-vibration frequencies. Furthermore, as mentioned in the discussion of the effect of inlet temperature on the stall frequency, it appears impossible to tune the blades for all the troublesome stall frequencies over the range of inlet temperature encountered in flight.

Since it appears impossible to tune blades to avoid critical stall frequencies, other possible means of circumventing the blade-vibration problem must be considered. These include (1) increasing the damping of the blades, (2) preventing the operation of any compressor blade row in a stalled attitude, and (3) disrupting the periodicity of the stall patterns so that a resonant condition between the blade frequency and the stall frequency cannot exist.

Increasing blade damping: The vibration-damping properties of a blade may be changed markedly by changing the blade material. Some materials exhibit greater damping properties than others; for example, stainless steel has better damping properties than aluminum. Blades fabbricated from plastics are currently being investigated for their damping qualities. Obviously, the damping properties of a blade may also be improved by changing the mechanical design of the blade. Such modifications as altering the thickness-chord ratio, the aspect ratio, or the fillet radius may substantially increase the stiffness of blades. In addition, the method of blade attachment or blade support is a design variable that can alter the damping.

Preventing stalled attitude: As was mentioned in the INTRODUCTION, part-speed operation of multistage compressors causes the exit stages to choke, which limits the flow in the inlet stages and causes them to stall. Any bleed-off system that unchokes the rear stages will alleviate the stalling condition in the inlet stages and consequently will increase the stall-free range of the compressor.

Another possible method of increasing the stall-free range of a compressor is the use of adjustable guide vanes and stators. By this method, the angle of attack on the inlet rotors is diminished so that stall of the early stages is delayed. By increasing the angle of attack in the latter stages, the situation there is improved. This device is currently being used in one commercial multistage compressor as a means of improving the part-speed operation.

Disrupting periodicity of stall: As a means of controlling the stalling characteristics of multistage compressors, adjustable inlet ramps or baffles have been used. Reference 20 reports the successful application of ramps at the hub that appreciably reduced the range of inlet-stage stall. The effect of the ramps or baffles is to reduce the inlet flow area. In engines tested with the baffles, rotating-stall patterns were no longer periodic, and the danger of blade failure due to resonant vibration was eliminated.

THEORIES OF ROTATING STALL

Several theoretical analyses have been proposed to predict the propagation rate of rotating stall. In order to identify the theories for discussion, each is referred to by the name of the first author. The notation is that used in the original references.

Emmons theory.—In the presentation of the Emmons theory in reference 272, the authors did not produce a result involving the prediction of stall-propagation rates. The purpose of the analysis was to establish the necessary conditions for the amplification of small disturbances of asymmetric flow corresponding to those observed in stall propagation.

The physical model analyzed was a cascade in which total-pressure losses were considered by

691-564 O-65-22

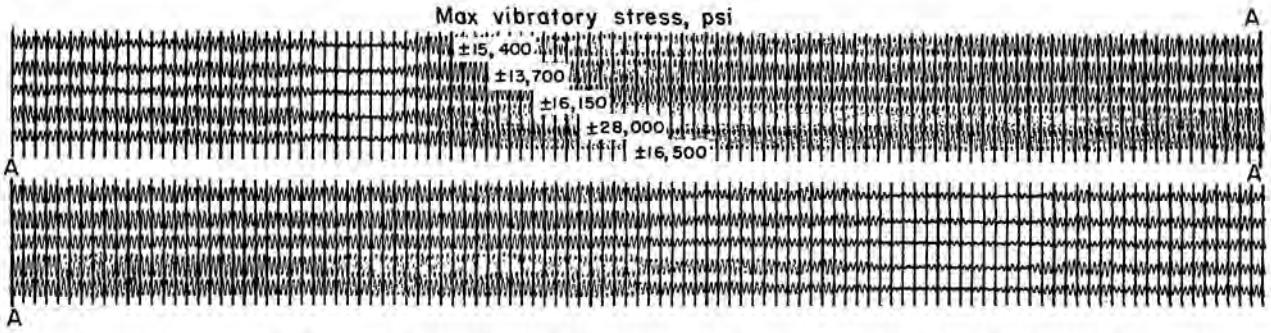

FIGURE 241.—Oscillogram of vibration burst caused by six-zone stall pattern. Engine speed, 62-percent design; blade-vibration frequency, 219 cps (ref. 19).

introducing a parameter α, which consisted of the ratio of an isentropic flow area required to carry the inlet flow to the actual exit flow area. A linear dependence between this parameter and the tangent of the inlet flow angle of the cascade was assumed, and the static pressure behind the blade row was considered constant. (NACA data (ref. 273) show that the static pressure behind the blade row varies appreciably.) Under certain circumstances, with the assumption of an initial small asymmetric disturbance at the cascade entrance, the analysis showed emphatically that the asymmetric flow will develop into a large disturbance.

As a result of the small-perturbation analysis, the authors of the Emmons theory concluded that the velocity of propagation is proportional to the wavelength. The Emmons theory suggests that an analysis involving finite disturbances will yield an answer to the size of the stall zones.

Stenning theory.—The Stenning theory (ref. 274) extends the work of Emmons by more precisely defining the time-delay mechanisms on which the velocity or propagation of rotating stall depends. The principal time delays considered are the inertia of the fluid between the airfoils and the response of the boundary layer.

Theory: The author bases his analysis on the same model setup used by Emmons, where it was assumed that the effective outlet area of a channel representing the blade passage is reduced as a result of stall and that the static pressure remains constant behind the cascade. By considering small perturbations in velocity from the steady flow, a solution is obtained from momentum considerations within the cascade for the velocity of stall propagation in terms of inlet and exit angle, chord to wavelength ratio, and effective-area to inlet-area ratio.

Results and conclusions: According to Stenning, the equation for stall-propagation rate is

$$\frac{U_m}{c_x}=\frac{\cot \beta_1}{\alpha^2 \cos \beta_2\left(\frac{Ln\pi}{b}+\cos \beta_2\right)} \tag{365}$$

where

U_m	stall-zone velocity relative to blade row
c_x	axial velocity
β_1	relative inlet-air angle
α	ratio of effective exit area to inlet area
β_2	relative outlet-air angle
L	blade chord
n	integers giving harmonics
b	one-half wavelength of disturbance

A carpet plot of equation (365) is shown in figure 242. The inlet-air angle β_1 and the outlet-air angle β_2 are treated as variables in the plot, and the ratio L/b is considered as a parameter. The ordinate of the graph is the stall-propagation parameter (ratio of relative stall speed U to rotor speed at mean blade height ωR) multiplied by the square of the area-ratio parameter α. Data from table VI(a) are presented for comparison with the values predicted by theory. It should be pointed out that the configuration of the compressors did not closely correspond to Stenning's model. Because it is impossible to obtain reliable measurements of flow angles during stall, the inlet angle was calculated from the weight-flow data, and outlet angle could only be estimated. In addition, the ratio α is not a measurable quantity and could only be estimated as some value less than unity. (Stenning considers it to be

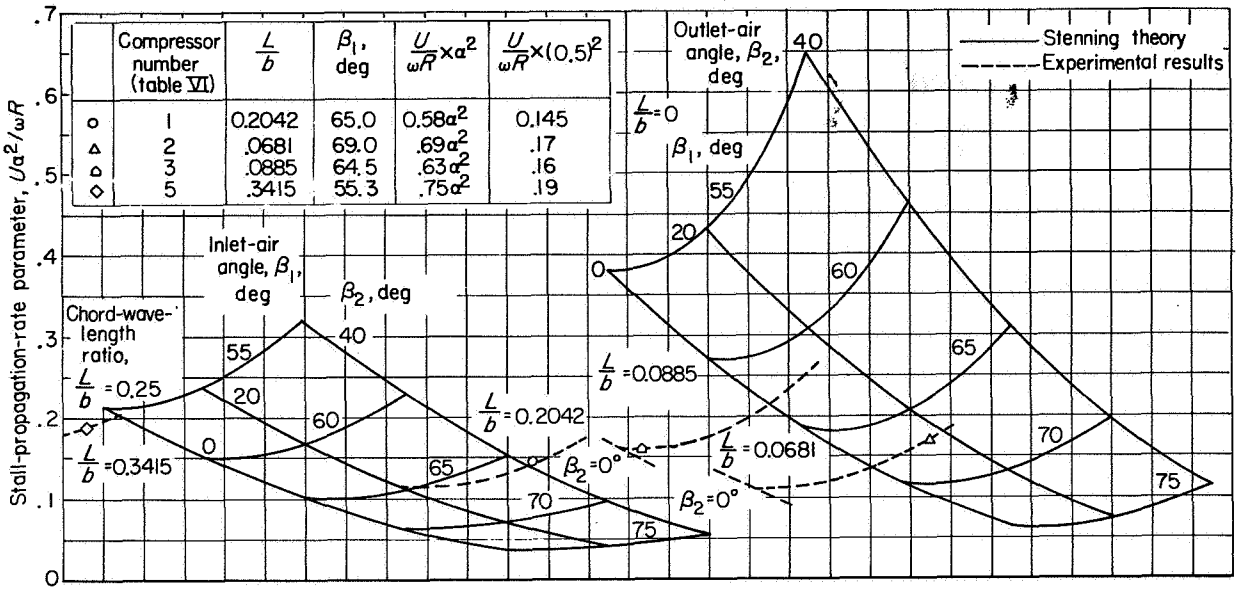

FIGURE 242.—Carpet plot of Stenning's results (eq. (365)); $0° < \beta_2 < 40°$.

0.75.) Thus, only the inlet-air angle, the propagation-rate parameter, and the value of L/b could be considered to be "data" in the comparison. The carpet surfaces were drawn to extend over a wide range of possible exit and inlet flow angles. Assuming α to be 0.5, most experimental data of table VI(a) are within the values predicted by the Stenning theory. These points are plotted on the interpolated L/b carpet plots indicated by the dashed lines. If α is taken as 0.75 as Stenning suggests, the data do not agree well with the theoretical values. These points do not appear in figure 242. It is not clear whether the inconsistency of the predicted values as compared with the data should be attributed to the limitations of the theory or to inappropriate application of the theory to compressors not similar to the model used by Stenning.

The theoretical results show that the velocity of stall propagation relative to the rotor increases with the size of the stall zone. A comparison with the test results of Emmons also shows this to be true; however, stall data taken from the compressors of table VI(a) indicate this may not always be the case. The inclusion of a boundary-layer time delay in the analysis had the effect of decreasing the velocity of propagation of the stall zone and indicated that rotating stall is possible for a range of inlet angles.

Sears airfoil theory.—Sears has published two papers on the subject of stall propagation. The first paper (ref. 275) demonstrates that asymmetric flow can exist in a cascade. It also presents a picture of the model used by Sears for the second paper.

Theory: To represent a blade row in a compressor, an annulus of infinitely many blades of small chord was chosen. This configuration amounts to an actuator disk or vortex sheet simulating the blade row, as shown in figure 243. The flow pattern was considered steady with respect to a rotating coordinate system (rotating slower than rotor speed), so that the circulation distribution in the disk could be assumed to be a function of the

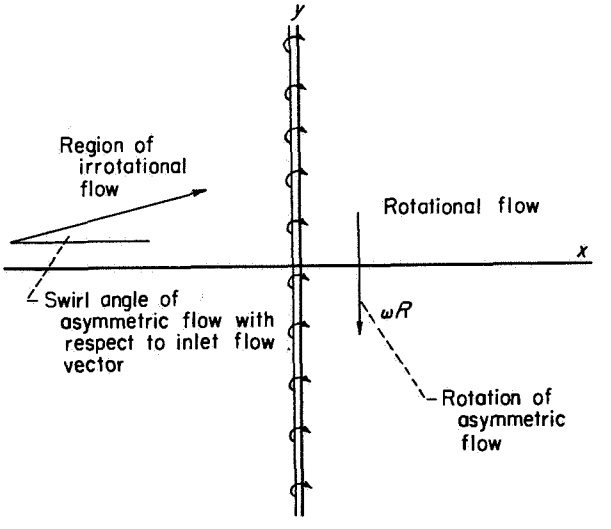

FIGURE 243.—Actuator disk employed by Sears.

y-coordinate of figure 243. An incompressible flow field was assumed, and small-perturbation theory was applied in the analysis. Since the blades of this rotor move relative to a fixed circulation distribution, they experience unsteady flow. Unsteady-flow theory states that airfoils will shed wakes at their trailing edges. The complete model, then, consists of a vortex sheet representing the rotor, an irrotational flow field representing the flow entering the rotor, and a rotational flow representing the wake leaving the rotor disk.

The model proposed by Sears differs from that used by Emmons in the following respects: Sears used an actuator disk where Emmons used a cascade of finite length; and, while Emmons assumed constant static pressure at the exit of the cascade, Sears considered the vorticity following the blade row to be uniformly distributed and did not impose any restrictions on the pressure field.

The principal object of Sears in reference 275 was to develop the relation between the induced velocities at the rotor disk and the circulation distribution. Briefly, the manner of solving the problem was to divide the flow field into two parts, an irrotational part and a rotational part, and then to devise relations between the x and y velocity components in each type of flow (see fig. 243). The next step was to develop expressions for the circulation in terms of the velocity distribution. The induced inflow velocities at the actuator disk could then be calculated when the circulation distribution was known. To complete the solution, airfoil theory was used to relate the circulation function to the incidence angle of the blade row. This type of solution is called the "airfoil theory" to distinguish it from another analysis in which Sears substituted a so-called "channel theory."

Results and conclusions: Assuming a sinusoidal variation in the circulation distribution, Sears found that no solution could be obtained for a lift function that was linear with incidence angle, whether the airfoil is stalled or unstalled. However, when a phase angle was introduced between the lift and angle of attack so that the lift lagged the angle of attack, a solution was found, which means that a permanent asymmetric flow pattern exists. The phase-angle concept used by Sears was based on the work presented in reference 276.

Emmons and Stenning studied the stability of an asymmetric pattern imposed on the flow field; Sears did not employ a stability study to show that an asymmetric flow could initiate itself under the conditions mentioned in the preceding paragraph.

Sears channel theory.—Theory: The second paper by Sears (ref. 277) presents an extension of the first theory. The analysis involving the airfoil relations is repeated, but the final results are presented in a somewhat different manner. The phase angle Δ is related to the asymmetric-flow propagation rate and the properties of the cascade by the following formula:

$$\tan \Delta = b + \left(\frac{2k+b}{k^2}\right)(1+b^2) \qquad (366)$$

where

b $\quad \frac{1}{\Phi}\left(\frac{h}{N} - \Phi \tan \beta\right)$

k $\quad \left(1-\frac{h}{N}\right)\Big/\Phi$

Φ flow coefficient

h/N ratio of stall-propagation rate to rotor speed, absolute frame of reference

β absolute inlet-air angle

The analysis also presents an equation that relates the slope of the lift curve m to the variables appearing in equation (366):

$$\frac{-m\sigma}{4} = \frac{1+b^2}{k^2}\sqrt{1+(b+k)^2}\cos \Delta \qquad (367)$$

where σ is the solidity. The curves of the predicted asymmetric flow patterns for the airfoil theory (fig. 244(a)) result from the simultaneous solution of equations (366) and (367). It should be noted that the parameter k used by Sears is the ratio of the stall-propagation speed to the axial velocity.

In this theory, an analysis involving channel relations is substituted for the airfoil analysis. The so-called channel theory is based on empirical relations derived from cascade tests. The two principal relations of the channel theory state that the relative outlet-air angle is a function of the inlet angle and that the pressure rise across the blade row is independent of the inlet-air angle. The principal distinction between the airfoil theory and the channel theory is an inclusion of the total-pressure loss in the latter. Since stall implies large losses, it would seem at the outset that the

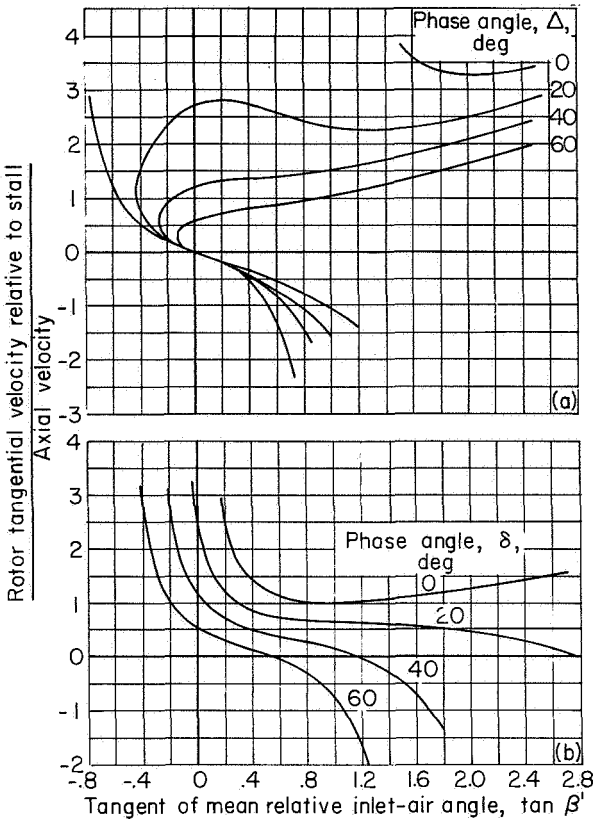

(a) Airfoil theory.
(b) Channel theory.

FIGURE 244.—Predicted asymmetric flow patterns obtained from Sears theory of rotating stall.

channel theory would conform more nearly to the physics of the actual flow. The procedure of the analysis involving channel theory is similar to that of the airfoil theory previously outlined. Also, a phase angle δ comparable to the phase angle Δ of airfoil theory is introduced.

Results and conclusions: Solutions for asymmetric flows satisfying the conditions of the problem were found for both types of analysis. The results of both airfoil and channel analyses are presented in reference 277 in graphical form and are reproduced here in figure 244. The ordinate and abscissa are labeled with Sears' notation and in terms of the vector-diagram terminology. The ordinate is the rotor tangential velocity relative to the tangential velocity of the stall propagation divided by the axial velocity, and the abscissa is simply the tangent of the mean relative inlet-air angle β'. The ordinate may also be expressed as the tangent of the swirl angle of the asymmetric flow pattern relative to the rotor.

For the airfoil analysis, solutions were found for a considerable range of phase angles including zero. In reference 275 Sears assumed a small swirl angle and did not obtain a solution for zero phase angle; but in reference 277 the swirl angle considered was larger, and a solution resulted for zero phase angle. However, the zero-phase-angle solutions do seem out of the range of the compressor data and consequently are of little interest.

The channel-analysis solution shown in figure 244(b) indicates that asymmetric flow patterns are possible for a wider range of conditions than was evident from the airfoil analysis. For flow conditions comparable to actual compressor data, asymmetric flow solutions are possible with zero phase lag. The equation for the phase angle δ used in the channel analysis is

$$\tan \delta=\frac{1+b^2-k^2}{b(b+k)^2+2k+b} \tag{368}$$

where k and b are the same parameters used in the airfoil analysis. In the channel-theory analysis, the slope of the pressure-rise curve plays a role analogous to that of the slope of the lift curve in the airfoil theory. The expression for the slope m of the pressure-rise curve is

$$\frac{m}{\sqrt{1+b^2}}=1+(b+k)^2 \tag{369}$$

The curves of the asymmetric flow patterns for the channel theory shown in figure 244(b) result from simultaneous solution of equations (368) and (369).

Experimental comparison: In reference 278, experimental rotating-stall data from several single-stage compressors are compared with the results of Sears' theory. Both the airfoil and channel analyses were tried; however, it was found that, in using the channel analysis, the phase angle δ was consistently negative. To the authors of reference 278, a negative phase angle seemed inconsistent with physical interpretation, and for this reason the comparison was limited to the airfoil analysis, where the computed phase angle Δ was positive for all the data used.

The points in figure 245 represent experimental data superimposed on the theoretically derived curves. The data points for each stall-propaga-

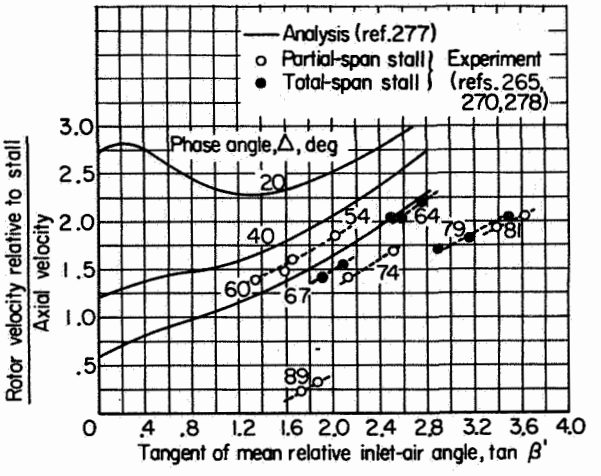

FIGURE 245.—Correlation of stall data with analytically derived phase angle (Sears theory).

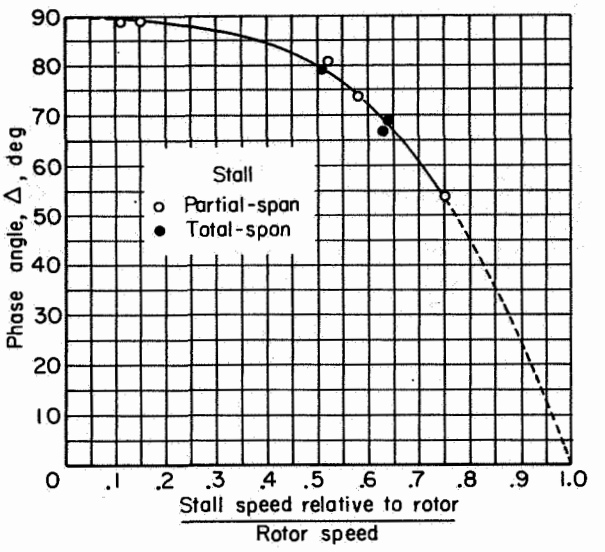

FIGURE 246.—Relation between stall rotational speed relative to rotor and phase angle (ref. 278).

tion rate lie along curves of approximately constant phase angle. Furthermore, if the phase angle is plotted as a function of the stall-propagation rate, a correlation exists, as shown by figure 246. The stall-propagation rate diminishes as the phase angle increases, which seems to be in accord with the generally accepted mechanism of stall propagation. Also apparently involved in the process of stall propagation is a time constant that governs the propagation rate. The greater the time constant, the slower the propagation rate. The correlation of phase angle and stall-propagation rate of figure 246 does not permit the prediction of stall-propagation rates, since the phase angle cannot be determined from design data.

Marble theory.—A recent analysis of rotating stall is presented by Marble in reference 279. In this theory, an expression for the stall-propagation rate and the peripheral extent of the stall zone is developed.

Theory: The model employed in the analysis is similar to that used by Sears in his channel theory, in that the blade row is simulated by means of an actuator disk across which pressure and fluid velocity change discontinuously. Using an actuator disk to represent the blade row without the introduction of a phase angle prohibits Marble from introducing inertia effects within the blade row. The Stenning analysis demonstrated the significance of inertia in the blade passage and its effect on stall-propagation velocity. Experimental characteristics of a cascade were utilized to prescribe the change in pressure and velocity across the actuator disk. The pressure-rise curve across the disk (based on experimental evidence) was assumed to be a linear function of the air inlet angle for unstalled flow, but for stalled flow the pressure rise was assumed to drop discontinuously to zero. In choosing this discontinuous lift curve, Marble more fully described the performance of the channel in comparison with the Sears linearized lift curve. Consequently, Marble was able to obtain solutions for the peripheral extent of the stall zone as well as the stall-propagation rate.

The expression for stall-propagation rate differs from that of Sears, in that a phase angle was not included in Marble's equation. By considering the pressure-rise parameter to be a function of the air inlet angle and to behave as described, the increased losses attending stall were included in the analysis. Marble simulated the asymmetric flow in his model by considering a stall zone of variable circumferential width to exist in the actuator disk. It was assumed that small-perturbation theory could be applied to describe the influence of rotating stall on the velocity and pressure. The coordinate system used in the analysis was selected to rotate at stall frequency so that the steady-flow equations would apply.

In order to describe the flow field upstream and downstream of the actuator disk, it was assumed that the pressure and angle perturbations vanished far upstream and were at most a constant value

far downstream. When these upstream and downstream conditions were known, as well as the pressure rise and flow angle for both the stalled and unstalled region of the actuator disk, the problem was to find a stall zone of suitable size and propagation rate to satisfy these flow conditions. First of all, Marble solved the problem for a "simple cascade," one in which deviation angle remained constant for all values of incidence angle. A very simple expression for stall-propagation rate and circumferential extent of the stall zone was obtained.

The equation for stall-propagation speed is

$$\frac{\omega R}{u}=\csc 2\beta_1 \tag{370}$$

where

ωR stall-propagation speed
u axial velocity
β_1 relative inlet-air angle

The peripheral extent of the stall zone α is given by the following expression:

$$\alpha=\frac{1}{2}-4(\beta_1^*-\beta_1)\csc 2\beta_1\left(\frac{\frac{1}{2}\rho u^2}{\Delta p^*}\right) \tag{371}$$

where

β_1^* relative inlet-air angle at stall
ρ density
Δp^* static-pressure rise at stall

After solving the problem for the simple cascade, a solution was completed with "general cascade characteristics." For the general characteristics the pressure rise across the cascade and the deviation angle are considered functions of the incidence angle. This is a more realistic representation of an actual cascade. Expressions were developed for the stall-propagation rate and the circumferential extent of the stall zone that were more complicated than for the simple case. The expression for the stall-propagation rate based on general cascade characteristics is

$$\frac{\omega R}{u}=\left(1+a\frac{\cos^2\beta_1}{\cos^2\beta_2}\right)\csc 2\beta_1 \tag{372}$$

where a is the ratio of outlet-angle perturbation to inlet-angle perturbation, and β_2 is the relative outlet-air angle.

The peripheral extent of the stall zone α for the more general cascade model is given by

$$\alpha=\frac{1}{2}-4(\beta_1^*-\beta_1)\frac{\frac{1}{2}\rho u^2}{\Delta p^*}\left[\left(1+a\frac{\cos^2\beta_1}{\cos^2\beta_2}\right)\csc 2\beta_1+\frac{b}{8}\right] \tag{373}$$

where b is a constant in the expression for pressure rise across the cascade.

Marble concluded that the ratio a is generally a small positive quantity, and that variations in the deviation angle prescribed by the "general cascade characteristics" would not alter the stall-propagation rate predicted from the simple-cascade equation. Consequently, variations in the deviation angle do not influence the stall-propagation rate. This conclusion agrees with most experimental evidence. As has been pointed out in the general discussion of rotating-stall characteristics, stall-propagation rate remains constant over a wide range of weight-flow conditions in the stall region.

Experimental comparison: Because of the lack of unclassified experimental rotating-stall data, Marble was able to use the data from only one compressor to compare the experimental stall-propagation rates with predictions from his theory. Stall data from several NACA single-stage compressors were compared with propagation rates predicted by Marble. Included in the comparison were data on total-span rotating-stall patterns in order to resemble more closely the geometry of the stall zone used in Marble's model. Equation (370), which is the solution for the simple cascade, was used to calculate the propagation rates. The equation was modified so that the guide-vane turning and the stall-propagation-rate parameter of table VI could be used.

The ordinate of figure 247 is the absolute stall-propagation-rate parameter, and the abscissa is the inlet-airflow angle computed at the mid-radius station. Good agreement was obtained between Marble's predicted propagation rate and the data from compressor 4 of table VI(a), but the comparison with the other data on the curve was poor.

As is shown in figure 247, Marble's theory predicts that, for proper inlet angle and counter-rotating guide-vane turning, the stall zones should rotate in the opposite direction (absolute coordi-

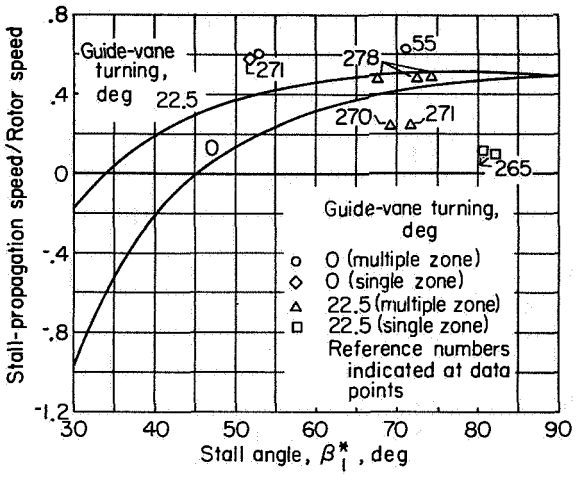

FIGURE 247.—Comparison of single-stage stall data with Marble's theory.

nate system) to rotor rotation. Experimental evidence has shown that this does not occur. The sense of the stall-zone rotation is the same for counterrotating guide-vane turning as for conventional guide vanes.

Remarks on stall theories.—In order to compare the results of the Stenning, Sears, and Marble theories, the phase angle introduced by Sears in the channel theory is considered to be zero. For this condition the results show that the Sears and Marble theories are identical in their expression of propagation rate. A comparable result from Stenning's analysis indicates that his predicted propagation rate is twice that of the other two investigators.

Experimental evidence shows that the radial extent of the stall zones varies considerably, but none of the existing theories include radial effects. All the theories apply to a single blade row. There is considerable doubt whether the theories can be applied to a single stage including guide vanes, rotor, and stators, or whether the theories can be further extended to the more complicated case of the multistage compressor.

INDIVIDUAL BLADE STALL

A type of stall in which all the blades around the compressor annulus stall simultaneously, without the occurrence of a stall-propagation mechanism, has been observed. The circumstances under which individual blade stall is established rather than rotating stall are unknown at present. It appears that the stalling of a blade row generally manifests itself in some type of propagating stall and that individual blade stall is an exception.

STALL FLUTTER

DISTINCTION BETWEEN STALL AND CLASSICAL FLUTTER

Before flutter is discussed, the distinction between classical flutter and stall flutter should be made clear. Classical flutter is a coupled torsional-flexural vibration that occurs when the free-stream velocity over a wing or airfoil section reaches a certain critical velocity. For wings of low frequency, this critical velocity can be calculated. According to reference 280, classical flutter cannot occur with compressor or turbine blades, because the critical velocity required would be unreasonably high. Stall flutter, on the other hand, is a phenomenon that has been explained on the basis of the behavior of the lift characteristic at stall.

MECHANISM OF STALL FLUTTER

At stall the lift may decrease sharply as shown in figure 248, where a typical lift characteristic is plotted as a function of angle of attack. According to reference 280, the aerodynamic damping of a blade is a function of the partial derivative of lift with respect to angle of attack. When this derivative becomes negative, stall flutter is likely to take place. That is, a reduction in the aerodynamic damping allows the airstream to feed energy into the blades and produce a self-excited oscillation.

Another explanation for stall flutter is presented in reference 281, in which the airfoil vibration is considered to result from a system of Kármán vortices in the airfoil wake. Whenever the frequency of these vortices coincides with a natural frequency of the airfoil, flutter will occur.

The concept of an aerodynamic hysteresis was developed by Studer to show that energy could be absorbed from the airstream to promote blade vibration (ref. 276). It was hypothesized in this explanation of stall flutter that separation at the stall point was delayed until the oscillating blade reached its position of maximum angle of attack, and then the nonseparated flow was not established until the blade reached its minimum angle of attack. The maximum and minimum angles of attack were considered to be above and below the stalling angle of attack, respectively, giving rise to the hysteresis effect.

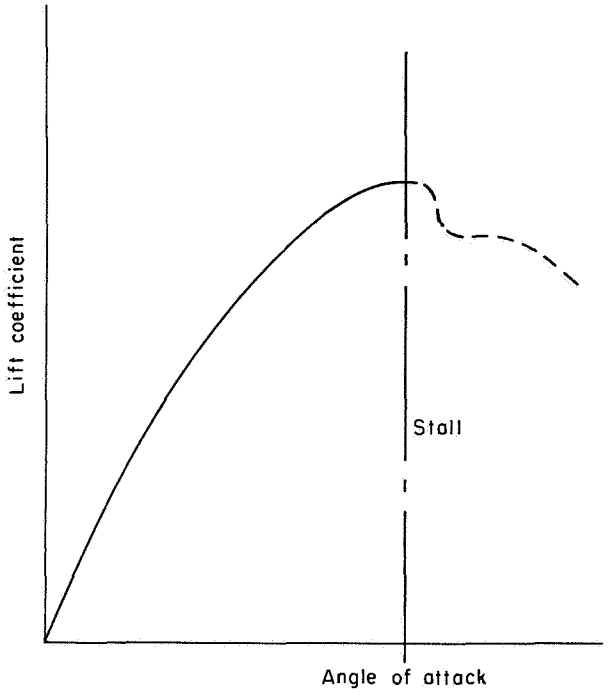

FIGURE 248.—Life characteristic of an airfoil.

Brief literature survey.—The general theory of flutter, even for an isolated airfoil in a potential flow, is not a very elementary mathematical problem. The problem becomes much more complicated when flutter in a cascade of airfoils is considered, because the effects of the geometry of the cascade must be included in the theory in order to account for the interference effects between the blades. Much of the early work on flutter theory was devoted to airfoils with but one degree of freedom, a torsional oscillation or vibration.

However, in the type of cascade that more accurately represents conditions in a turbine or compressor, according to reference 282, the stall-flutter oscillations may have at least two degrees of freedom, torsional oscillation and flexural bending. This latter type of flutter is treated in reference 283. The experimental observations of such a cascade showed that either torsional or flexural vibrations were obtained, depending upon the velocity of the airstream; and the frequencies of each mode were practically identical. The two modes of vibration were not coupled as in the case of the classical flutter for wings. The flutter or bending self-excited vibrations were explained as the result of variations in the angle of incidence, which in turn caused the lift force to vary. However, the lift force always lags the elastic force by a phase angle. The forces acting on a blade are shown in figure 249. Whenever the component of the force parallel to the damping force exceeds the damping force, a self-excited vibration of the blade takes place.

The authors of reference 283 observed that self-induced vibrations occurred whenever the free-stream velocity entering the cascade reached a critical value. They found that the critical velocity could be determined from a dimensionless velocity coefficient that was shown to be a function of the geometry of the cascade (stagger angle and angle of incidence) and the angle between the direction of the blade displacement and the blade chord.

In a more recent paper (ref. 284), only one degree of freedom, a flexural oscillation, is admitted as a possible mode of stall-flutter vibration in a two-dimensional cascade representing compressor blades. A different interpretation of the mechanism of flexural vibration is also presented in this paper. After rather extensive experimental observations, it was concluded that no appreciable changes in lift were observed for varying positions of the cascade in a separated-flow field; consequently, no self-excited flexural vibrations could

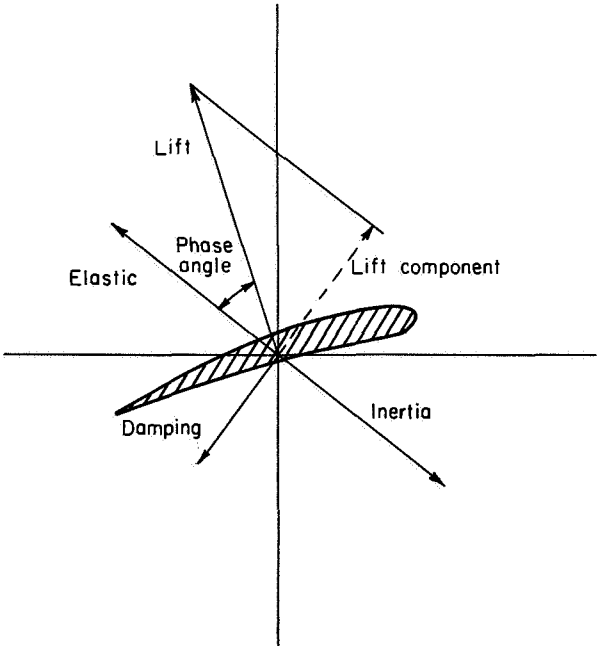

FIGURE 249.—Diagram of forces on blade.

be established by this mechanism as proposed in reference 283. However, it was observed that, when an airfoil is translated in separated flow, the lift force will feed energy into the blade and thus sustain a self-excited motion.

Other more mathematically complicated treatments of flutter in cascades have been considered in papers such as reference 285. Phase differences in the mode of the vibration between the blades in the cascade are considered mathematically in this paper.

Extension of flutter theory to compressor blades brings up a most complicated problem, because not only cascading effects but also centrifugal effects must be considered. The cascading or interference effects on flutter are not well understood for the compressor.

Experimental evidence.—Although stall flutter has been considered to be a cause of compressor blade failure, there is insufficient experimental evidence to support this view. According to reference 282, conditions where flutter exists do not correspond to operation at high angles of incidence and low speed, the mode of operation that has caused compressor blades to fail. The measurements required of rotating rigs in order to investigate the possibility of stall flutter are almost impossible to make with current research techniques.

CONCLUSIONS

AERODYNAMIC ASPECT

The stalled operation of a compressor may be described as the degeneration of compressor performance accompanied by serious flow separation in the flow passages. Three distinctively different phenomena may occur during stalled operation: (1) rotating stall, (2) individual blade stall, or (3) stall flutter. The first two are aerodynamic effects and the third is an aeroelastic effect. Rotating stall has been found to be the most prevalent type of stall phenomenon. A large amount of data is available which demonstrates that poor performance of compressors may be directly attributable to the occurrence of rotating stall.

In this chapter, rotating-stall patterns are cataloged according to their effect on the performance characteristic of single-stage compressors. A progressive rotating stall is associated with a smooth continuous performance characteristic; and an abrupt rotating-stall pattern, with a discontinuous performance characteristic that is coincident with an abrupt drop in compressor pressure. Similar types of stall are observed in multistage compressors; however, the discontinuous performance characteristic for a multistage unit is defined here as complete compressor stall. The pressure rise across a multistage compressor may drop as much as 50 percent after complete compressor stall is initiated. This stalling condition is particularly important, because it determines the limit of useful operation of the compressor (the surge limit or stall limit shown in fig. 229).

With a single blade row as a model, several theories have been developed showing the existence of asymmetric flow and in some cases predicting the rotative speed and the size of the pattern. The results of the theories are in poor agreement with experimental data.

VIBRATION ASPECT

Although rotating stall seems to be the most significant cause of blade vibration in compressors, it must be recognized from cascade data that stall flutter may be a possible cause of blade vibration. No experimental evidence is presently available to show that stall flutter has been the cause of compressor blade excitation. If the rotating-stall frequency coincides with the natural bending frequency of the blade or a harmonic thereof, a resonant condition will result that may cause blade failure. Other possible causes of blade vibration include (1) resonance of the rotor blade frequency with the frequency of wakes from stators or supporting struts, and (2) mechanical failures resulting from a resonance between the natural bending frequency of the blade and transmitted vibrations emanating from the gearing or shafts. These effects are considered unimportant compared with the problem of rotating stall.

CHAPTER XII

COMPRESSOR SURGE

By MERLE C. HUPPERT

Experimental data indicate that there are two principal types of surge in compressors: (1) surge due to an abrupt stall, and (2) surge due to progressive stall. Surge due to abrupt stall is generally violent and audible, whereas that occurring with progressive stall is generally mild and inaudible. The violent surge obtained in jet engines during engine acceleration is identified as surge due to abrupt stall.

INTRODUCTION

The effect of unsteady flows on compressor performance and life expectancy has become of considerable interest and importance in the application of axial-flow compressors to jet engines. Perhaps the most significant flow fluctuations are those associated with stall of blade elements within the compressor. In the past, any audible flow fluctuation or rumbling noise emanating from a compressor was loosely defined as surge. Comparatively recent investigations show that certain flow fluctuations are not due to surge in a strict sense, but are due to a phenomenon called propagating or rotating stall. Rotating stall, which is discussed in detail in chapter XI, consists of zones of low flow that revolve about the compressor axis.

The term surge, as used herein, defines flow fluctuations distinctly different from those due to rotating stall. Surge involves fluctuations in the net flow through the compressor; whereas rotating stall consists of low-flow zones revolving about the compressor axis, but with a constant net or average flow through the compressor.

This chapter presents a discussion of surge in axial-flow compressors. Pressure- and flow-fluctuation data obtained from surging compressors are presented and discussed. Data obtained from both compressor test facilities and jet engines are included. Some theoretical aspects of surge are discussed, and a distinction is made between surge due to abrupt stall and surge due to progressive stall. The surging compressor is compared with other types of oscillators.

SYMBOLS

The following symbols are used in this chapter:

f_{stall}	frequency of flow fluctuations due to rotating stall, cps
f_{surge}	frequency of flow fluctuations due to surge, cps
P	total or stagnation pressure, lb/sq ft
ΔP_C	compressor total-pressure rise at stall point, lb/sq ft
ΔP_{stall}	decrease in compressor-discharge total pressure due to abrupt stall, lb/sq ft
ΔP_{surge}	amplitude of total-pressure fluctuation due to surge, lb/sq ft
V	air velocity, ft/sec
w	weight flow, lb/sec
$w\sqrt{\theta}/\delta$	equivalent weight flow, lb/sec
α	angular spacing of hot-wire-anemometer probes, deg
δ	ratio of total pressure to NASA standard sea-level pressure of 2116 lb/sq ft
θ	ratio of total temperature to NASA standard sea-level temperature of 518.7° R
λ	number of stall zones in stall pattern
ρ	density, lb/cu ft
$\Delta\rho V/\overline{\rho V}$	amplitude of ρV fluctuation divided by average ρV based on average anemometer current (see ch. XI)

Subscripts:

1	station at compressor inlet
2	compressor-discharge station

STEADY-STATE COMPRESSOR CHARACTERISTIC

Before the phenomenon of surge is considered, "steady-state" or "surge-free" compressor operation should be discussed. Steady-state operation (sometimes called static operation) is operation under conditions in which the net flow through the compressor and the torque required to drive the compressor are constant for any given operating

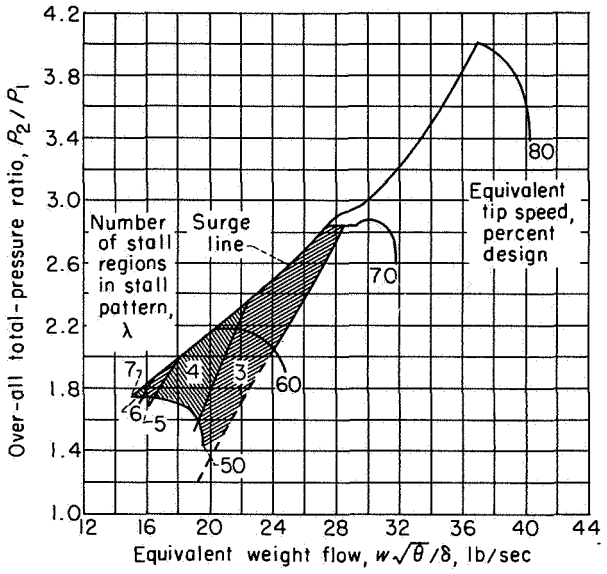

FIGURE 250.—Over-all compressor performance map showing conditions at which rotating stall occurred in 10-stage subsonic axial-flow research compressor (ref. 266).

point. From this definition, operation with rotating stall is considered a steady-state condition. (Rotating stall is discussed in detail in ch. XI.) Figure 250 shows the range of flow for each of several compressor speeds over which steady-state operation occurred in a 10-stage axial-flow research compressor. The shaded areas indicate the flow range where rotating stall existed. At 50 percent of design speed, rotating stall occurred over the entire range of flow from the surge point to the maximum flow obtainable. The number of zones in the stall pattern, however, varies from 3 at the highest flow attainable to 7 at the surge point. At higher values of rotational speed, rotating stall existed over only a part or none of the flow range between maximum flow and the surge line. The surging obtained was due to abrupt stall of the compressor, as will be discussed later.

Stall may, in most cases, be classified as either progressive or abrupt (ch. XI). Progressive stall results in a gradual reduction in stage pressure ratio and efficiency as the flow is decreased and generally results in the formation of a rotating-stall pattern consisting of more than one stall zone. The shaded area of figure 250 represents the condition of progressive stall in the inlet stages. Abrupt stall in single- or multistage compressors results in an abrupt or apparently discontinuous drop in compressor pressure rise and efficiency and a "hysteresis" loop between stall and stall recovery. A single-zone stall pattern is associated with abrupt stall.

In the intermediate-speed range, the steady-state performance at a given compressor speed is not always unique. As discussed in chapter XIII, several steady-state performance characteristics may be obtained at a single compressor speed.

EXPERIMENTAL INVESTIGATIONS OF SURGE

On the basis of experimental evidence, two types of surge may be distinguished as follows: (1) surge associated with discontinuous compressor characteristics due to abrupt stall, and (2) surge associated with apparently continuous compressor characteristics where blade-row stall is progressive rather than abrupt.

SURGE DUE TO ABRUPT STALL

In order to describe the flow fluctuations due to surge associated with abrupt stall, the results of recent investigations in which fast-response pressure and flow instrumentation were used will be reviewed.

10-Stage subsonic axial-flow research compressor.—The investigation reported in reference 266 was conducted with a 10-stage subsonic axial-flow research compressor. The test facility incorporated a large inlet tank and a large receiver at the compressor discharge. The overall compressor performance map showing the speed and flow range where rotating stall occurred is presented in figure 250. At all rotational speeds investigated, the useful operating flow range was terminated at low flows by a violent surge.

The flow fluctuations associated with surge at 50 percent of design speed were investigated in some detail; the variation in compressor-inlet and -discharge total pressure and the variation in flow rate measured behind the first rotor due to surge are shown in figure 251. The amplitude of the compressor-discharge total-pressure variation (fig. 251(a)) was 75 percent of the compressor pressure rise at the surge point. The variation in compressor-inlet stagnation pressure was somewhat smaller. The compressor-discharge pressure recovered to the value at the surge point at the end of each surge pulse. The hot-wire-anemometer signal (flow fluctuations, fig. 251) indicates

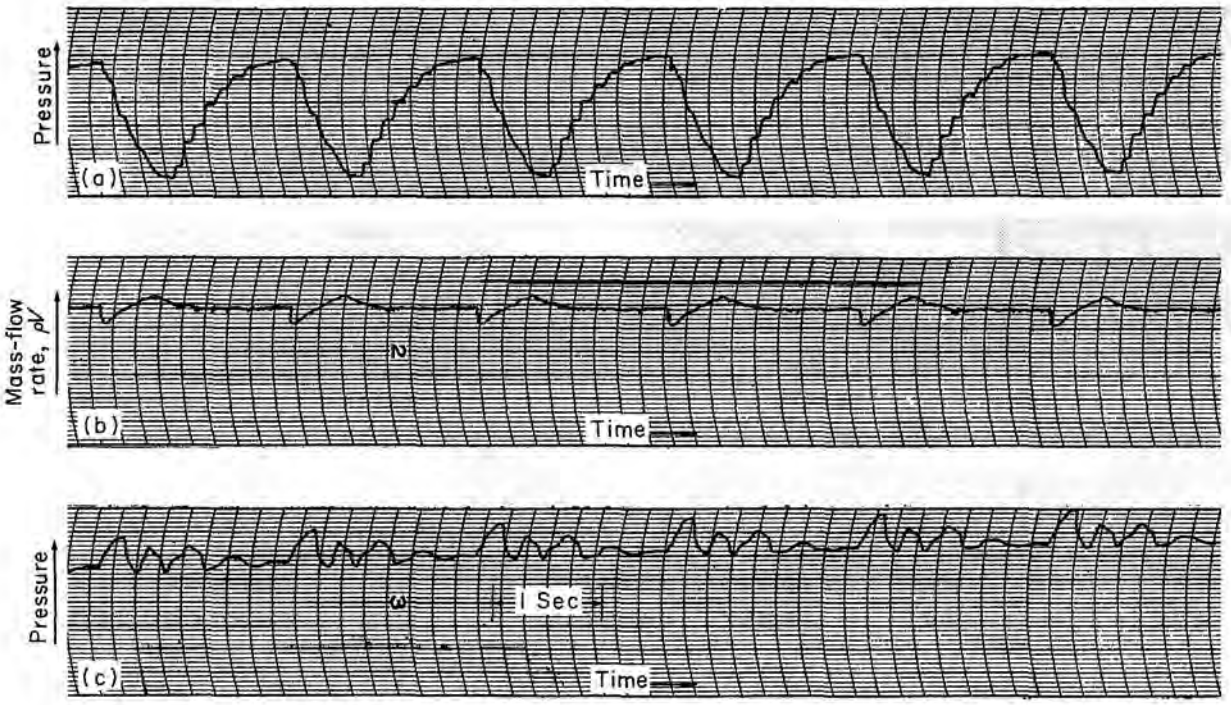

(a) Compressor-discharge total pressure $(\Delta P_{surge})_2/\Delta P_C = 0.75$.
(b) Hot-wire anemometer behind first rotor near tip.
(c) Compressor-inlet total pressure $(\Delta P_{surge})_1/P_1 = 0.1$.

FIGURE 251.—Variation of compressor-inlet and -discharge total pressures and mass-flow rate during surge of 10-stage axial-flow compressor at 50 percent of design speed. Surge frequency, 0.57 cps (ref. 266).

that the initial drop in compressor-discharge pressure was coincident with a sharp drop in flow. As the compressor-discharge pressure continued to decrease, however, the flow increased and exceeded its value at the beginning of the surge pulse.

The flow is maximum when the compressor-discharge pressure is minimum. The recording oscilliograph used to obtain the oscillogram reproduced in figure 251 was not capable of recording frequencies greater than about 90 cps. Consequently, these oscillograms indicate only the low-frequency components of the variation in flow and pressure during surging operations.

The flow fluctuations that occurred during a surge pulse are shown in much greater detail in figure 252. The oscillograms shown (film strips) were obtained from hot-wire-anemometer signals recorded from a dual-beam direct-coupled cathode-ray oscilloscope (signal filtered to pass frequencies from 0 to 10,000 cps). Signals from anemometer probes installed behind the third, seventh, and tenth stators are shown along with the signal from an anemometer probe installed behind the first rotor. A rotating-stall pattern with a single stall zone is shown at all four axial stations at the beginning of the surge pulse. As pointed out in chapter XI, single-zone rotating stall is typical of abrupt stall. As the flow was reduced following the formation of the single-zone stall pattern, the stall zone evidently spread to cover the complete annulus of the compressor. Stall-zone spreading to cover the complete annulus during surge, as noted in this investigation, is not typical. Surge data obtained from several jet engines and from other compressors operating in compressor test facilities indicate that the single-zone rotating-stall pattern usually exists up to the time of stall recovery. Stall recovery resulted in a marked increase in flow followed by a comparatively gradual reduction. As the flow was reduced following stall recovery, the first stall pattern indicated on the oscillogram was the one consisting of three stall zones. Although not shown in figure 252, the stall patterns with four, five, and six stall zones appeared in succession as the flow was further reduced. Just

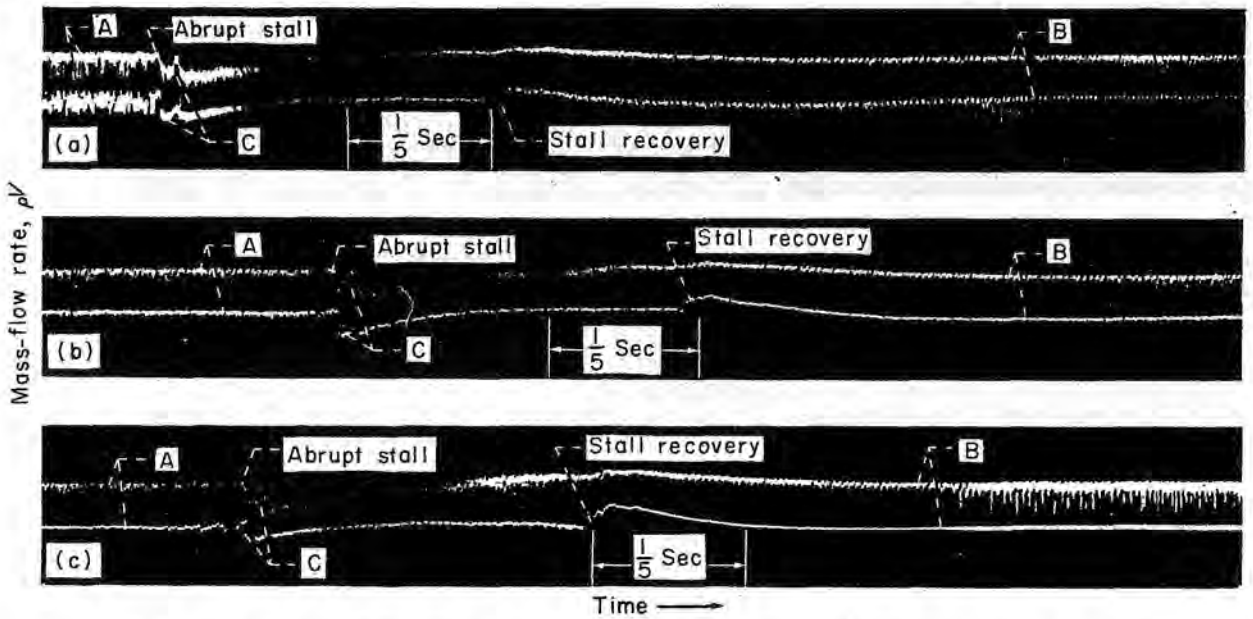

(a) Upper trace behind first rotor; lower trace behind third stator. Angle between probes, 64.6°.
(b) Upper trace behind first rotor; lower trace behind seventh stator. Angle between probes, 104.1°.
(c) Upper trace behind first rotor; lower trace behind tenth stator. Angle between probes, 104.9°.

FIGURE 252.—Oscillogram of surge at various axial stations in 10-stage axial-flow compressor at 50 percent of design speed. Anemometer probes near casing; surge frequency, 0.57 cps (ref. 266). (A indicates λ of 7, f_{stall} of 340 cps; B indicates λ of 3, f_{stall} of 140 cps; C indicates λ of 1, f_{stall} of 30 cps.)

before abrupt stall (end of one surge pulse and beginning of next), the stall pattern with seven stall zones was indicated (fig. 252). The stall patterns obtained after stall recovery (weight flow decreasing) were the same as those obtained during steady-state operation (fig. 250). Abrupt stall without surge was not obtained during this investigation.

16-Stage subsonic axial-flow compressor.—The test facility used for the investigation of the 16-stage subsonic axial-flow compressor was similar to that used for the 10-stage compressor. A large inlet tank was used at the compressor inlet. The construction of the receiver at the compressor discharge permitted the installation of flow-control devices (throttles) at two stations. The throttle close to the compressor permitted operation with a small receiver volume, and the throttle somewhat downstream of the compressor permitted operation with a much larger effective receiver volume. The large receiver volume was approximately 9 times that of the small receiver volume.

A violent audible surge was obtained at all compressor speeds from 30-percent design to design speed when the large receiver volume was used. Figure 253 is an oscillogram showing the variation in total pressure at the compressor inlet and discharge during surging operation with the large receiver volume at 50 percent of design speed. The surge frequency was about 1 cps. The compressor-discharge pressure reduction during the surge was about 40 percent of the compressor pressure rise at the surge point. The inlet pressure increased about 8 percent during a surge pulse. Rotating stall is indicated on the oscillograms during the time interval in which the compressor-discharge pressure is decreasing. The rotating stall is, however, shown much better by the hot-wire-anemometer trace in figure 254. The oscillogram shown in figure 254 was also obtained during surging operation at 50 percent of design speed. The surge frequency, however, was 1.6 cps at the time the oscillogram was obtained. The rotating-stall pattern contained one stall zone and was rotating about the compressor axis in the direction of rotor rotation (absolute frame of reference) at about 45 percent of compressor speed.

The pressure and flow fluctuations due to surge obtained with the 16-stage axial-flow compressor are quite similar to those obtained with the 10-

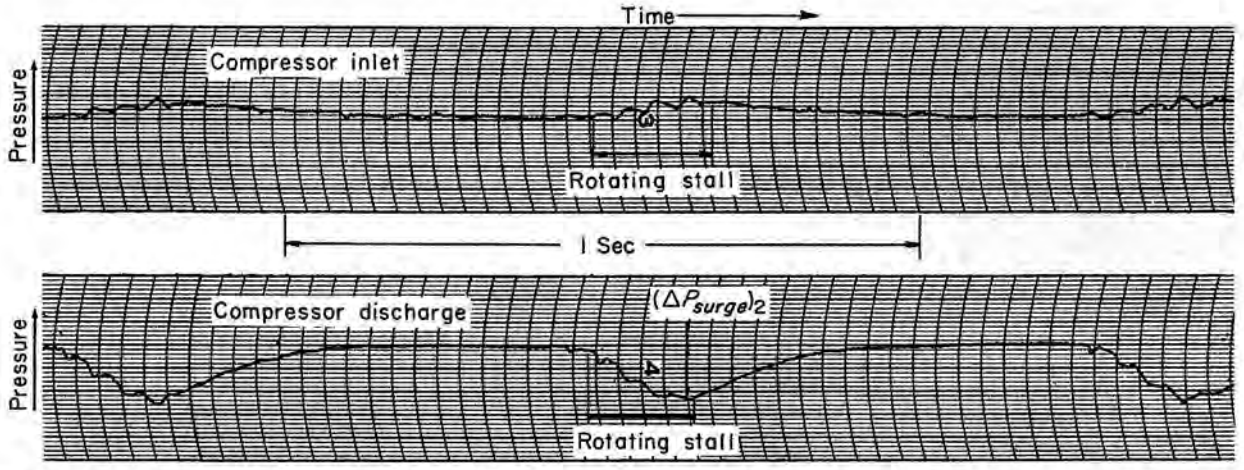

FIGURE 253.—Variation of compressor-inlet and -discharge total pressures during surge of 16-stage axial-flow compressor at 50 percent of design speed. Large receiver volume; $(\Delta P_{surge})_2/\Delta P_C$, 0.41; $(\Delta P_{surge})_1/P_1$, 0.085 (ref. 265).

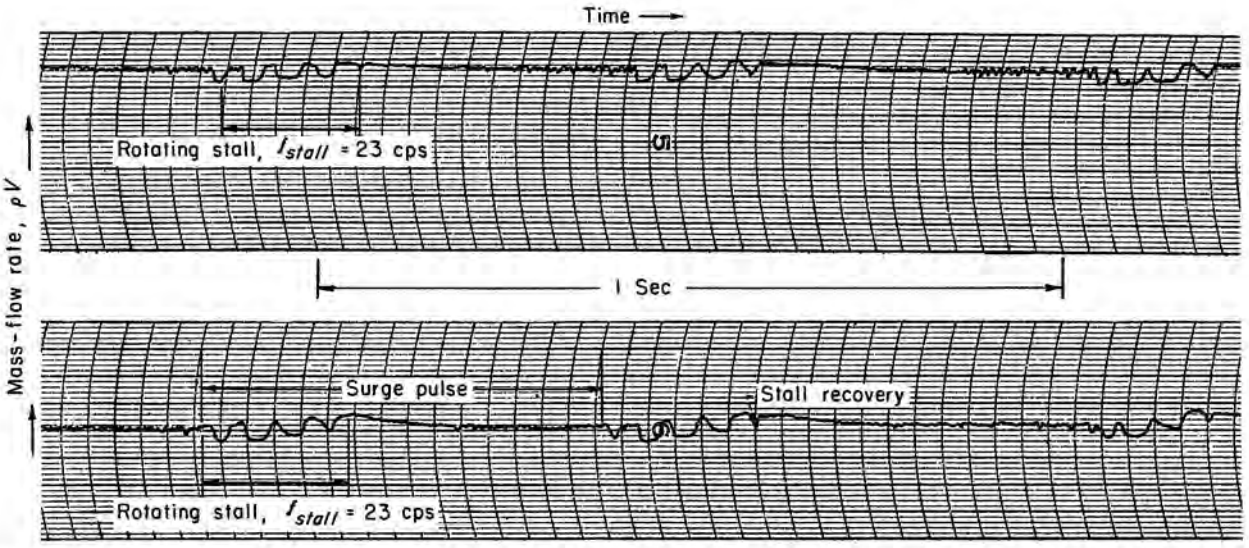

FIGURE 254.—Hot-wire-anemometer output during surge of 16-stage axial-flow compressor at 50 percent of design speed. Anemometer in seventh-stage stator; large receiver volume; probe spacing, 105°; surge amplitude, $\Delta\rho V/\overline{\rho V}$, ±0.3; rotating-stall amplitude, $\Delta\rho V/\overline{\rho V}$, 1.2 (ref. 265).

stage compressor. The surge pulse was initiated by the formation of a single-zone rotating-stall pattern; but, unlike that of the 10-stage compressor, the stall pattern persisted until stall recovery was effected. Actually, the persistence of the single-zone rotating-stall pattern, until stall recovery occurs, is fairly typical of compressors surging in jet engines.

When the compressor was operated with the small receiver volume, audible surge was not obtained at 50 percent of design speed. Instead, abrupt stall was obtained as shown by the oscillogram in figure 255. The rotating-stall pattern obtained is the same as that indicated during the surging operation when the large receiver volume was used. The decrease in compressor-discharge pressure due to abrupt stall was approximately the same as the amplitude of the compressor-discharge pressure oscillation due to surge (fig. 253). The compressor-inlet and -discharge pressures increased gradually following stall because of the flow reduction through the inlet throttle. The compressor pressure ratio following abrupt stall was essentially constant. Audible surge was

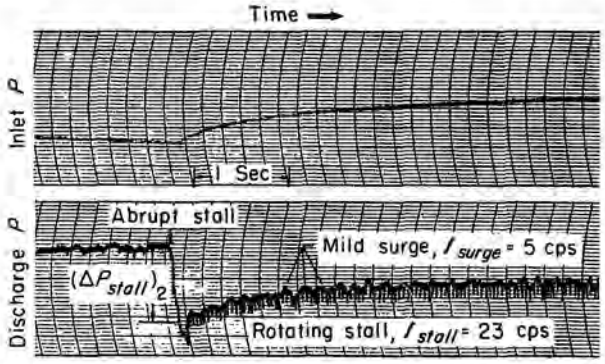

FIGURE 255.—Abrupt stall of 16-stage axial-flow compressor at 52 percent of design speed. Small receiver volume; $(\Delta P_{stall})_2/\Delta P_C$, 0.41; compressor pressure ratio at stall point, 1.7.

not obtained when the small receiver volume was used, presumably because stall recovery did not occur during the flow transient caused by abrupt stall. The reduced receiver volume resulted in a more rapid adjustment in receiver pressure following stall and consequently smaller oscillations in net flow. It is of interest to note that, although audible surge due to cyclic stall and stall recovery was not obtained when the small receiver volume was used, stalled operation was not completely stable. A mild inaudible surge with a frequency of approximately 5 cps was indicated (fig. 255). The amplitude of these mild surge oscillations appeared to vary in a somewhat random fashion.

Operation at 30 percent of design speed with the large receiver volume resulted in intermittent abrupt stall and surge, as shown in figure 256. The oscillogram was obtained with a fixed setting of both the inlet and discharge throttles. While the compressor remained stalled, a single-zone rotating stall with a frequency of about 14 cps was indicated. The stall zone was rotating at approximately 45 percent of compressor speed. Also, during stalled operation a mild inaudible surge was indicated on the oscillogram. The mild surge frequency, about 2 cps, was somewhat less than that obtained with stalled operation at 50 percent of design speed (fig. 255), where the mild-surge frequency was about 5 cps.

According to reference 272, the frequency of surge should be proportional to the reciprocal of the square root of the receiver volume. The large receiver volume was approximately 9 times that of the small receiver volume. Then, according to reference 272, the surge frequency with the small receiver volume would be approximately 3 times that with the large receiver volume. This is in agreement with mild-surge data. The surge data obtained for the 16-stage axial-flow compressor demonstrate that surge may or may not result from abrupt stall, depending on the volume of the receiver into which the compressor is discharging. In addition, the data demonstrate that, with a given receiver volume, surge due to abrupt stall is more likely to occur at high than at low compressor speeds. In many cases, abrupt stall is obtained without surge as defined herein (e.g., refs. 260 and 286). But, for high-pressure-ratio compressors, surge due to abrupt stall is common in compressor test facilities and in jet engines.

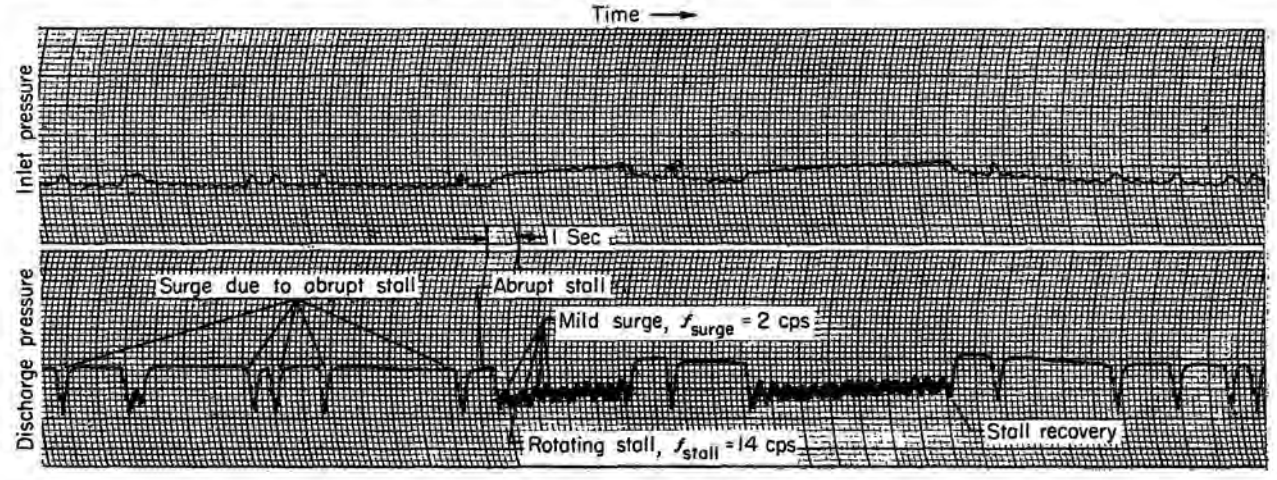

FIGURE 256.—Intermittent abrupt stall and surge of 16-stage axial-flow compressor at 30 percent of design speed. Large receiver volume; $(\Delta P_{stall})_2/\Delta P_C$, 0.30; compressor pressure ratio at stall point, 1.25.

Surge in jet engines.—Surge in the compressor component of a jet engine is much the same as surge obtained with the 16-stage axial-flow compressor operating in a test facility. The principal difference is that the surge frequency in a jet engine is generally somewhat greater (5 to 15 cps) than that for the same compressor operating in a test facility. The surge frequency in a jet engine is increased mainly because the volume of jet-engine combustors is somewhat smaller than that of the receivers used in compressor test facilities.

An experimental investigation of stall and surge in a jet engine is reported in reference 267. Surge was obtained by subjecting the engine to a step increase in fuel flow. For the particular jet engine used in the investigation, surge occurred as a result of abrupt stall at compressor rotational speeds where the pressure drop due to stall was greater than 16 percent of the pressure rise at the stall point. The pressure ratio at which stall occurred is referred to as the critical pressure in reference 267. Figure 257, taken from reference 267, shows the pressure-ratio oscillations due to surge obtained by step increases in fuel flow at compressor speeds of 72.8 and 78 percent of design speed. Also shown are the pressure ratio at the stall point, the pressure ratio after stall, and the steady-state or equilibrium operating line. The sequence of events following the increase in fuel flow was as follows: The compressor-discharge pressure increased until the stall point was reached. Several cycles of surge occurred, and then surging ceased and the compressor remained stalled. The engine speed increased even though surging occurred. When the compressor quit surging and was operating stalled, the rate of speed increase (acceleration) was markedly reduced.

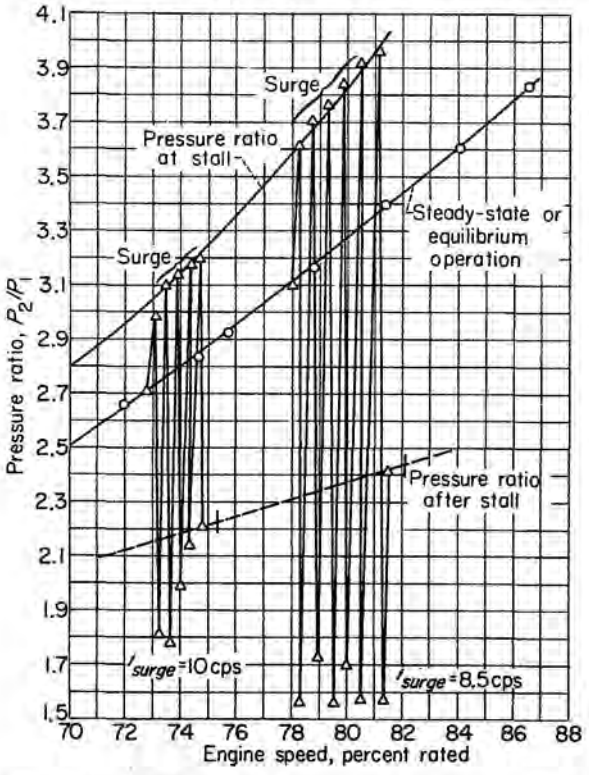

FIGURE 257.—Behavior of compressor total-pressure ratio in surge encountered during engine acceleration from initial speeds of 72.8 and 78 percent of rated speed (ref. 267).

During surge investigations in jet engines it has been noted that surge does not, in all cases, begin immediately after the stall point is reached. In some cases, surging does not begin until after the compressor has operated in a stalled condition (abrupt stall) for a short time and the engine speed has increased somewhat.

SURGE DUE TO PROGRESSIVE STALL

Surge due to progressive stall involves flow fluctuations in the flow range of the compressor map where there are no apparent abrupt changes in pressure ratio due to stall. Progressive stall may occur at flows greater or less than that at which abrupt stall occurs. Surge associated with progressive stall is generally quite mild compared with surge caused by abrupt stall. Mild surge obtained during stalled operation of the 16-stage axial-flow compressor is shown in figures 255 and 256. The amplitude of the compressor-discharge total-pressure fluctuations that occurred during mild surge is from 15 to 20 percent of that for surge due to abrupt stall.

Mild inaudible surge is sometimes observed in single-stage compressors operating near the peak of the characteristic curve. In these cases, a partial-span rotating-stall pattern is generally associated with the surge. The amplitude of the flow fluctuation due to rotating stall varies as the net flow rate varies. An example of this type of surge obtained with a single-stage compressor is shown in figure 258 (taken from ref. 263). The stall pattern obtained contained eight stall zones, and the flow-fluctuation frequency due to the stall pattern was 1420 cps. The surge frequency was from 10 to 15 cps. The amplitude of the flow fluctuations of rotating stall is greatest when the

691-564 O-65-23

net flow is minimum and smallest when the net flow rate is maximum. The amplitude of the net flow variation due to surge shown in figure 258 was estimated to be 10 percent of the average flow rate. The amplitude of the surge fluctuations, however, increased and decreased in a somewhat random fashion similar to the mild surge shown in figures 255 and 256.

Although a rotating-stall pattern is generally present during all or part of the surge cycle, mild inaudible surge without rotating stall has been observed in single-stage compressors. Presumably, individual blade stall had occurred without rotating stall. (See ch. XI for discussion of individual blade stall.) Other examples of mild surge are reported in references 55 and 272.

THEORETICAL INVESTIGATIONS OF SURGE

Theories of surge have been concerned primarily with the question of the stability of the flow through the compressor and the system in which it is operating. The complexity of the flow system associated with the compressor considered in the theories has varied considerably. The analysis in reference 287 involves a relatively simple system consisting of an inlet throttle for controlling the flow and an inlet duct or tank followed by the compressor. Reference 272 considers a somewhat more complete system consisting of an inlet duct and an inlet tank followed by the compressor, which discharges into a discharge tank or receiver connected to an exit duct. The analysis presented in reference 288 is somewhat more complex than those presented in references 272 or 287, in that the inertia and capacitance effects of each stage of a multistage compressor are considered.

The analysis of the stability of an operating point of the compressor in equilibrium with a flow system involves setting up linear differential equations in an approximate way to describe the dynamics of the system. The stability of the system may be determined without actually solving the differential equations by use of the method of Routh (see ref. 289 or 290, e.g.).

In general, the conclusions drawn as a result of all surge analyses are essentially the same: The system becomes unstable at compressor operating points where the slope of the compressor characteristic is zero or slighly positive. When the system is unstable, the system damping is negative, so that any small distrubances will grow in amplitude. A point of critical stability has no damping. As the flow varies, however, the system damping also varies. That is, the system damping depends on the slope of the compressor characteristic at the instantaneous operating point during the flow fluctuation. As a consequence, the linear theory used to determine the stability no longer applies after the amplitude of the flow fluctuations becomes finite. Surge occurs as a result of the instability if the nonlinearities of the system are such as cause oscillations to grow in amplitude until some limiting stable value of steady-state oscillations occurs. The resulting cycle of oscillations is called the "limit cycle" (e.g., ref. 290). So far as is known, there are no

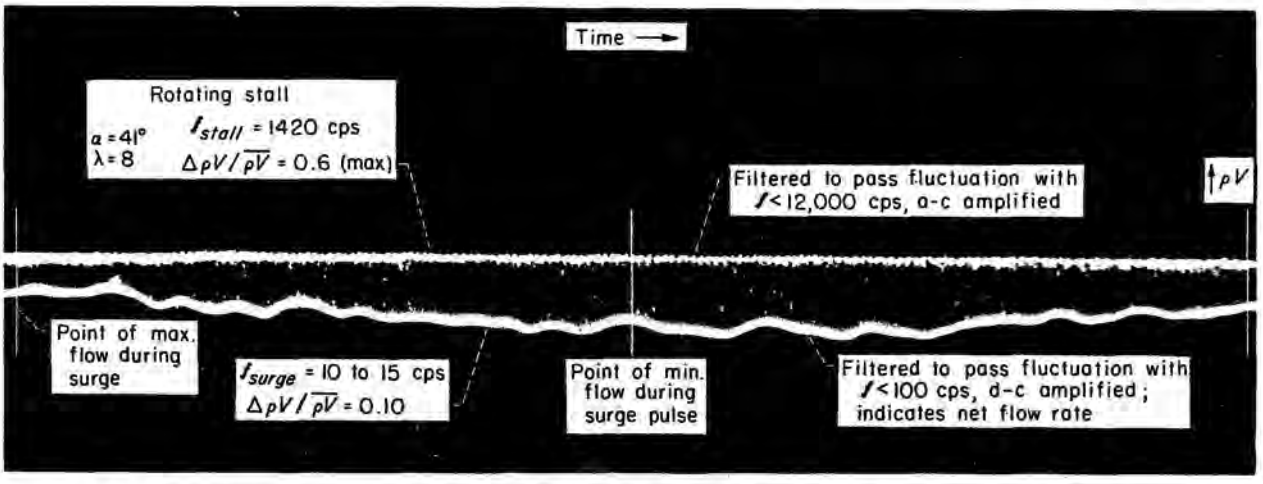

FIGURE 258.—Hot-wire-anemometer oscillogram of flow fluctuations during mild inaudible surge of single-stage compressor with hub-tip ratio of 0.8 at 70 percent of design speed (ref. 265).

published analyses of surge that consider the nonlinear aspects of the problem. It seems evident, however, that the flow oscillations that result from an instability will depend to a great extent on the shape of the compressor characteristic. That is, the variation in the slope of the compressor characteristic with flow, at flows greater and less than that at an unstable operating point, probably constitutes the principal nonlinearity of the system.

In chapter XI compressor characteristics are classified as either continuous or discontinuous, depending on whether stall occurred in a gradual or progressive manner or abruptly. It seems appropriate to classify surge in a similar way. That is, surge may occur because of the discontinuous decrease in pressure ratio due to abrupt stall, or because of an instability resulting from a gradual reduction in compressor pressure ratio due to progressive stall.

SURGE DUE TO ABRUPT STALL

Surge due to abrupt stall may be described in a qualitative manner with the aid of figure 259. The compressor static or steady-state characteristic is represented by the solid line. The throttle characteristic is represented by the dashed line that crosses the compressor characteristic curve at points A and B. Point C is the stall recovery point. The compressor is operating at point A (the stall point). Point B is a possible stable operating point. Point A is unstable, because a small reduction in flow will cause the compressor to stall and immediately become incapable of producing a discharge pressure equal to that in the receiver. If the receiver volume were infinite, the direction of flow through the compressor would reverse after stall, and steady backflow would occur with operation at point D. If the receiver volume were very small, its pressure would adjust very quickly after stall to that which the compressor is capable of producing, and operation would instantaneously come to equilibrium at point B.

In any compressor installation the receiver volume would be neither large enough to permit steady operation at point D nor small enough to cause equilibrium to be established instantaneously at point B. In the practical case, then, the pressure and flow fluctuations may follow paths depicted in figure 259 as surge or abrupt stall. For the case of abrupt stall, the receiver pressure and flow may follow the path indicated. After

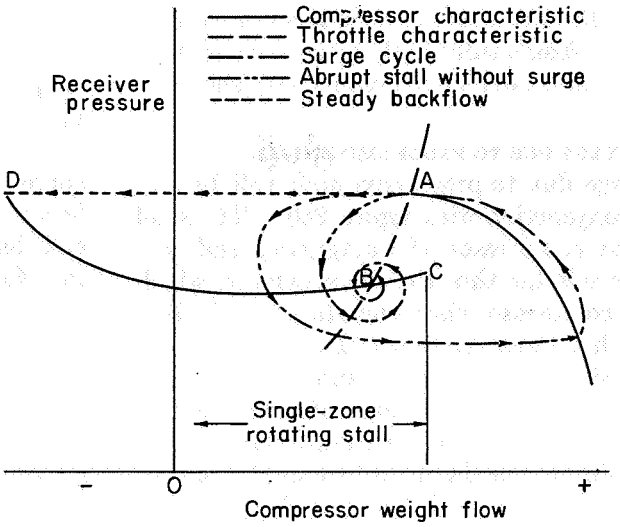

FIGURE 259.—Flow and pressure oscillations due to abrupt stall.

a few damped oscillations in pressure and flow (indicated by the spiral path), the system comes to equilibrium at point B. If, however, the flow oscillations are sufficiently large to exceed the value required for stall recovery (point C), equilibrium will not be established at point B. Instead, stall recovery will occur and result in an increase in flow followed by a gradual increase in receiver pressure and decrease in flow. Following stall recovery, the system tends toward equilibrium at point A. Stall will occur again, and the cycle (called the limit cycle) will be repeated as indicated in figure 259. Surging will cease if the throttle is opened (throttle curve moved to the right in fig. 259) sufficiently to prevent stall from occurring during the flow transient following stall recovery. Similarly, surging will cease if the throttle is closed (throttle curve moved to the left in fig. 259) sufficiently that stall recovery does not occur during the flow transient following stall. If equilibrium is established on the stalled branch of the compressor characteristic and the throttle is then opened so that the throttle characteristic passes through the stall recovery point C, the situation is quite similar to that with operation at the stall point. A small disturbance in the flow may cause stall recovery, and a surge cycle may be established similar to that which occurs with the throttle characteristic passing through the stall point. Equilibrium operation after stall is not always completely stable. Mild surge may occur after abrupt stall has occurred (figs. 255 and

256). The flow fluctuations of mild surge may, in some cases, become sufficiently large to cause stall recovery, as indicated by the oscillogram shown in figure 256.

SURGE DUE TO PROGRESSIVE STALL

Mild surge due to progressive stall will be discussed in conjunction with figure 260. The solid curve is the compressor characteristic, and the dashed curve is the throttle characteristic, which crosses the compressor characteristic at the highest flow at which the system is critically stable. That is, small oscillations about the intersection point are undamped. Since the slope of the compressor characteristic becomes larger positively at flows less than point A, the damping becomes larger negatively if the flow is reduced a finite amount. If the flow increases to a value greater than that at point A, the slope of the compressor characteristic becomes negative and the system damping becomes positive. As a consequence of the variation system damping with compressor flow, any small disturbance will grow in amplitude, as indicated by the spiral path from point A, until the effective or average damping of the cycle vanishes (see ref. 290). The resulting cycle of oscillation is the limit cycle. Rotating stall may exist during all or part of the surge cycle (fig. 258). Presumably, surge could occur at any compressor operating point where the system damping is negative, since the flow is unstable there.

As pointed out in the section on experimental investigations, most data obtained with surge associated with progressive stall indicate a mild inaudible surge. Although the relation between the shape of the compressor characteristic and the amplitude of the flow fluctuations of surge has not been established, it seems quite likely that surge with progressive stall may, in some cases, become quite violent. In fact, if the damping is sufficiently negative, the situation is not unlike that for abrupt stall.

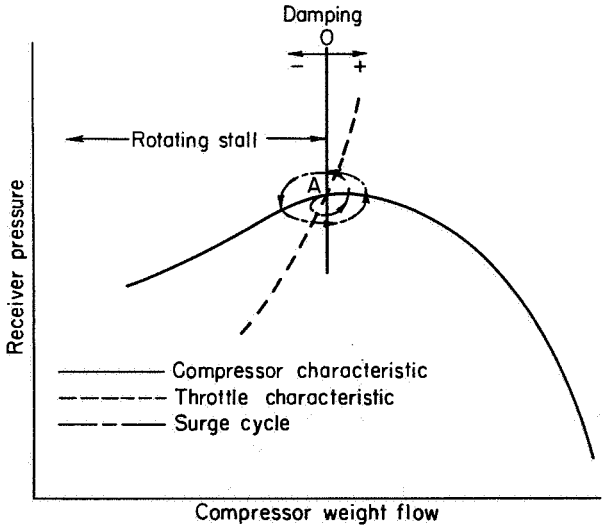

FIGURE 260.—Flow and pressure fluctuations due to surge associated with progressive stall.

COMPARISON OF COMPRESSOR SURGE WITH OTHER OSCILLATORY PHENOMENA

Although surge in compressors is very undesirable, there are many technologically useful devices that utilize oscillatory phenomena. Since much of the theory of nonlinear effects has been developed through the study of oscillators, it seems appropriate to apply some of concepts and terminology used in oscillator theory to explain compressor surge.

According to reference 290, there are two principal kinds of oscillators, feedback and relaxation oscillators. All oscillators depend for their operation on some nonlinear action, and feedback and relaxation oscillators are distinguished by the type of nonlinearity utilized to control the amplitude of the oscillations. Relaxation oscillators operate by virtue of some discontinuous or quasi-discontinuous effect. Certain trigger circuits used with relaxation oscillators are discussed in reference 291. The effects of the discontinuous steady-state compressor characteristic are evidently analogous to those of the trigger circuits used with relaxation oscillators. Consequently, it seems justifiable to refer to surge associated with abrupt stall as a relaxation oscillation. Similarly, it seems justifiable to refer to surge associated with progressive stall as feedback-type oscillations. Progressive stall results in a progressive nonlinearity. The theoretical treatment of compressor surge could undoubtedly be enhanced by use of the theory of nonlinear systems.

SUMMARY OF RESULTS

A survey of available data obtained from surging compressors indicates that there are two principal types of surge: (1) surge due to abrupt stall, which is generally a violent audible surge, and (2) surge due to progressive stall, which is generally a mild inaudible surge detectable by use of fast-response instrumentation. The violent surge obtained in jet engines during engine acceleration is identified as surge due to abrupt stall.

CHAPTER XIII

COMPRESSOR OPERATION WITH ONE OR MORE BLADE ROWS STALLED

By WILLIAM A. BENSER

An analysis of the part-speed operating problems of high-pressure-ratio multistage axial-flow compressors is made by means of a simplified stage-stacking study. The principal problems considered are poor low-speed efficiency, multiple-valued performance characteristics at intermediate speeds, and poor intermediate-speed compressor surge or stall-limit characteristics. The analysis indicates that all these problems can be attributed to discontinuities in the performance characteristics of the front stages. Such discontinuities can be due to the type of stage stall or to a deterioration of stage performance resulting from stall of adjacent stages.

The effects of compromises of stage matching to favor part-speed operation are also considered. This phase of the study indicates that such compromises would severely reduce the complete-compressor-stall margin. Furthermore, the low-speed stage stall problem is transferred from the inlet stages to the middle stages, which are more susceptible to abrupt-stall characteristics.

The analysis indicates that inlet stages having continuous performance characteristics at their stall points are desirable with respect to part-speed compressor performance. However, these characteristics must be obtained when the stages are operating in the flow environment of the multistage compressor. Alleviation of part-speed operational problems may also be obtained by improvement in either stage flow range or stage-loading margin.

The results of this analysis are only qualitative. The trends obtained, however, are in agreement with those obtained from experimental studies of high-pressure-ratio multistage axial-flow compressors, and the results are valuable in developing an understanding of the off-design problem. In addition to these stage-matching studies, a general discussion of variable-geometry features such as air bleed and adjustable blades is included.

INTRODUCTION

High-pressure-ratio multistage axial-flow compressors frequently exhibit extremely low efficiencies and severe blade-vibration problems at intermediate and low rotational speeds. In addition, such compressors may exhibit a sharp dip or kink in the surge or stall-limit line at intermediate rotational speeds, so that the attainable pressure ratios in this speed range are severely limited. Multiple performance characteristics have also been observed in this intermediate-speed range. Operation such as engine acceleration and high Mach number flight requires that the compressor component of the engine operate satisfactorily in the low- and intermediate-speed ranges. In order to alleviate these part-speed compressor problems, an understanding of the flow mechanism that causes poor part-speed performance is required. Such variable-geometry features as adjustable guide vanes or compressor air bleed may solve some part-speed operating problems, but satisfactory application of such features also depends on a knowledge of the flow mechanism.

As indicated by the stage-matching analysis of reference 248, the fundamental difficulty of low-speed operation results from stalling of the front stages of the compressor. As compressor speed is decreased, the density ratio across the compressor decreases rapidly; and at low values of density ratio the small flow area of the rear stages seriously limits the flow through the compressor. Thus, the inlet stages are forced to operate at flows well below their stall limits. These trends have been verified experimentally. For example, reference 253 indicated first-stage stall for speeds below 80 percent of design speed, and reference 257 indicated first-stage stall for speeds below 70 percent of design speed. It should be noted that

this mismatching of the front and rear stages of the compressor at low speeds will, in general, be more severe for high-pressure-ratio than for low-pressure-ratio compressors. A further indication as to the source of the part-speed problem can be obtained from chapter XI, which shows that rotating stall is the prevalent type of stage stall and that rotating stall originating in the first stage of a multistage compressor results in flow fluctuations that extend completely through the compressor. The flow fluctuations of rotating stall are also a serious source of compressor blade vibrations (ch. XI).

As pointed out in chapter XII, serious compressor surge is a result of a discontinuity in the compressor performance characteristics. This discontinuity of performance may result from the abrupt type of stage stall discussed in chapter XI or from a deterioration of the performance of several stages as a result of the flow fluctuations imposed by the instigation of rotating stall in the inlet stage. The dip or kink in the surge-limit line of a 16-stage research compressor (ref. 253) was attributed to these interaction effects or to deterioration of performance of several stages as a result of stall of the inlet stage.

The existence of multiple-valued performance characteristics is shown in reference 292, which presents data showing three separate and distinct performance curves for a three-stage axial-flow compressor operating at a constant value of rotational speed. Tests of a high-pressure-ratio multi-stage compressor (ref. 293) show the existence of six separate performance characteristic curves for a rotational speed of approximately 75 percent of the design value. Hot-wire-anemometer data taken during this investigation indicate a correlation between compressor performance and the number of stall zones in the rotating-stall pattern.

It is evident that the problems of poor part-speed efficiency, compressor blade vibration, intermediate-speed surge or stall limit, and multiple-valued performance characteristics of high-pressure-ratio multi-stage axial-flow compressors are all related to rotating stall and the attendant interactions or deteriorations of stage performance due to unsteady flow. The experimental approach does not yield a complete understanding of the general part-speed performance problem, because the inherent performance of each stage is not easily obtained, particularly in the range of speeds and flows where rotating stall exists in the compressor. Furthermore, the range of stage operation that can be studied experimentally is limited because of compressor surge. Therefore, to obtain a qualitative evaluation of the effects of stage stalling characteristics and of stage interactions on the general part-speed compressor performance problem, a simplified stage-stacking study was made. The basic hypothetical compressor considered was a 12-stage unit with an overall pressure ratio of 7.75. The stage performance characteristics used in the computation of multistage performance were assumed to be similar to those obtained from single-stage compressors. Interaction effects were evaluated by arbitrary modification of the assumed stage performance curves. The first three cases considered herein (repeated from refs. 294 and 295) concern various severities of interaction effects. The last two cases considered evaluate the effect of compromises of stage matching to favor part-speed performance as suggested in reference 248. When possible, the results of these studies are compared with experimental data.

Because of the assumptions made in regard to stage performance characteristics and stage interaction effects and because of the simplified stacking technique used, the computed values of compressor performance must be considered only as qualitative values. The general trends, however, are valuable in obtaining an understanding of the part-speed efficiency problem, the intermediate-speed surge or stall problem, and the multiple-valued performance characteristic problem of high-pressure-ratio axial-flow compressors. An indication of desirable types of stage performance characteristics is obtained; and, in addition, this analysis indicates some of the factors that must be evaluated if accurate performance predictions are to be obtained for the range of compressor operation where one or more of the elements are stalled. This analysis, however, does not consider the adverse effects of inlet flow distortion on the compressor stall limit.

GENERAL CONSIDERATIONS

SINGLE-STAGE STALL CHARACTERISTICS

As discussed in chapter XI, stage stall may be divided into two types: (1) progressive stall, characterized by a gradual but continuous decrease in

stage performance as the flow coefficient is decreased below the stalling value, and (2) abrupt stall, characterized by a sudden or abrupt drop in stage performance at the stalling value of flow coefficient. Either type of stage stall normally results in the formation of one or more low-flow or stalled zones that rotate about the compressor axis and are thus defined as rotating stall. Progressive stall is normally associated with rotating-stall zones that start at one end of the blade and grow radially and circumferentially as the flow coefficient is decreased. The stall pattern for this type of stall may consist of from one to twelve stall zones, and the number of stall zones generally increases as flow coefficient is decreased. Abrupt stall is normally associated with a simultaneous stall of all radial elements of the blade, and the stall pattern generally consists of a single stall zone.

Progressive stall is prevalent in low hub-tip ratio or inlet stages, whereas abrupt stall is prevalent in high hub-tip ratio or exit stages. Typical middle stages of a multistage compressor or intermediate hub-tip ratio stages may exhibit a progressive stall followed by an abrupt stall as flow is further reduced. Both progressive and abrupt stalls exhibit a hysteresis effect, in that the flow coefficient at which stall recovery is achieved is higher than that at which stall was first encountered as the flow was decreased. This hysteresis effect is also discussed in chapter XI.

STAGE INTERACTIONS

The performance and stalling characteristics may be appreciably different when a stage is operated as a single stage and when it is operated as a stage of a multistage compressor. These differences of performance, which may be designated as interaction effects, result from the radial and circumferential variations of stage-inlet conditions that may exist in the multistage compressor. As pointed out in chapter XI, interaction effects may be attributed to two main sources: (1) radial maldistribution of flow due to off-design performance of adjacent stages, and (2) circumferential maldistribution of flow or unsteady flow due to rotating stall originating in adjacent stages.

Radial maldistribution of flow.—Radial maldistribution may be defined as large variations from the design radial distribution of flow. For any stage other than the first stage of a multistage compressor, these radial maldistributions of flow result from off-design performance of preceding stages. For example, as the flow coefficient of the first stage is decreased, the energy addition at the tip of this stage usually increases more rapidly than that at the root. Requirements of radial equilibrium of static pressure at the exit of the first-stage stator may therefore lead to a ratio of axial velocity at the blade tip to that at the blade root that is larger than the design value. This radial variation from design flow may be aggravated through the first few stages of the compressor and may alter the relative rate of approach to stall for the tip and root sections of subsequent stages. Thus, a stage that exhibits a partial-span progressive stall when tested as a single stage may exhibit an abrupt total-span stall when operated as a stage of a multistage compressor. Furthermore, radial maldistribution of flow can result in appreciable variations in average stage-work input for a given value of flow coefficient as well as in variations in the stalling value of flow coefficient for any stage.

Unsteady flow.—When rotating stall exists in a multistage compressor, the resulting flow fluctuations extend through all stages (ch. XI). These flow fluctuations of rotating stall impose a time-unsteady circumferential velocity variation on all stages, and the instantaneous loading of the blades is certainly altered from that for steady flow at the same mean value of flow coefficient. Thus, when rotating stall is instigated by an inlet stage, the performance of all subsequent stages may be altered because of the resulting variations in circumferential flow distribution.

Imposition of flow fluctuations of rotating stall on any stage that is operating near its stall point may result in stall of that stage. Thus, the flow fluctuations may be increased in magnitude, as was the case for the 10-stage compressor discussed in chapter XI. In addition to premature incurrence of stall in a given stage due to stall of an adjacent stage, the resulting stall pattern and performance of the given stage may be appreciably different from those predicted by single-stage tests. Stages operating at flow coefficients appreciably above the value for stall or near their choke limit, however, tend to decrease the amplitude of

flow fluctuations resulting from rotating stall originating in preceding stages. Consequently, the effects of flow fluctuations on the performance of such stages may be small.

COMPLETE COMPRESSOR STALL AND SURGE

Abrupt stall of one or more stages and progressive stall of the inlet stage, which result in deterioration of the performance of several subsequent stages, will both result in discontinuities in over-all performance of a multistage compressor. For the purposes of this analysis, discontinuity points in the over-all compressor performance characteristic at a given speed are designated as complete compressor stall to differentiate between stall of the over-all compressor and stall of the individual stages. As discussed in chapter XII, discontinuities in over-all compressor performance may result in compressor surge. The occurrence of surge will, of course, depend on the external system characteristics as well as the compressor characteristics. If surge does not occur, stable performance at a lower level of pressure ratio and efficiency will be obtained. During component tests of a multistage compressor, these discontinuities in performance are not often observed, because compressor surge is encountered. Complete compressor stall and surge, however, represent the same limit of compressor operation.

STAGE STACKING

As pointed out in chapter X, the off-design performance of a multistage axial-flow compressor may be approximated by a simplified stage-stacking technique if the generalized stage performance characteristics are known. The main purpose of the analysis reported herein is to study qualitatively the effects of various stage stall characteristics and stage interactions on the part-speed operating characteristics of multistage axial-flow compressors. In order to simplify the computations, effects of radial maldistribution of flow and effects of Mach number on stage flow range and efficiency are ignored. The detailed stacking procedure used for these computations is given in appendix B of reference 294 and is similar to that outlined in chapter X.

For this analysis the stage curves are assumed in terms of adiabatic efficiency and pressure coefficient as functions of flow coefficient. The adiabatic efficiency is the ratio of useful or isentropic work input to actual work input; the pressure coefficient is a function of useful work input divided by the square of the mean-radius wheel speed; and the flow coefficient is the ratio of the average inlet axial velocity to the wheel speed at the mean radius. Study of the performance of numerous stages indicates that stage performance for a range of speeds can be generalized to a single curve on the basis of these parameters. The effectiveness of this manner of generalization of data is illustrated in figure 261, which is a plot of the performance of the first, fifth, and tenth stages of the compressor reported in reference 257. Some random variations exist because of the difficulty of obtaining accurate stage performance data in the multistage compressor. The stage data, however, can be well approximated by a single curve for all speeds except for the maximum-flow points in the tenth or last stage of the compressor. In this case the effect of stage-inlet Mach number on the negative-incidence stalling angle tends to decrease the choking value of flow coefficient as compressor speed is increased. Similar Mach number effects may exist in the inlet stage. At any given speed, however, the inlet stage covers only a small part of its total range. Therefore, the Mach number effect is not noted on such a plot of experimental data. The fifth stage does not cover an appreciable flow range and thus does not exhibit a noticeable Mach number effect. Since the inclusion of Mach number effects would not appreciably alter the trend obtained from the stage-stacking analysis, these effects are not considered in the computation of compressor performance.

Interaction effects were small for the compressor of reference 257, as indicated by the measured stage performance characteristics. For the compressor of reference 253, however, appreciable interaction effects were noted. For the computations reported herein, interaction effects due to unsteady flow resulting from stall in the inlet stage were estimated by altering the individual stage performance curves of several succeeding stages for those conditions where stall existed in the inlet stage. Estimated hysteresis effects in the unstalling characteristics are also incorporated in the stage curves.

For cases I to III, three combinations of stage stall, interaction effects, and unstalling hysteresis are considered. In cases IV and V, stage matching

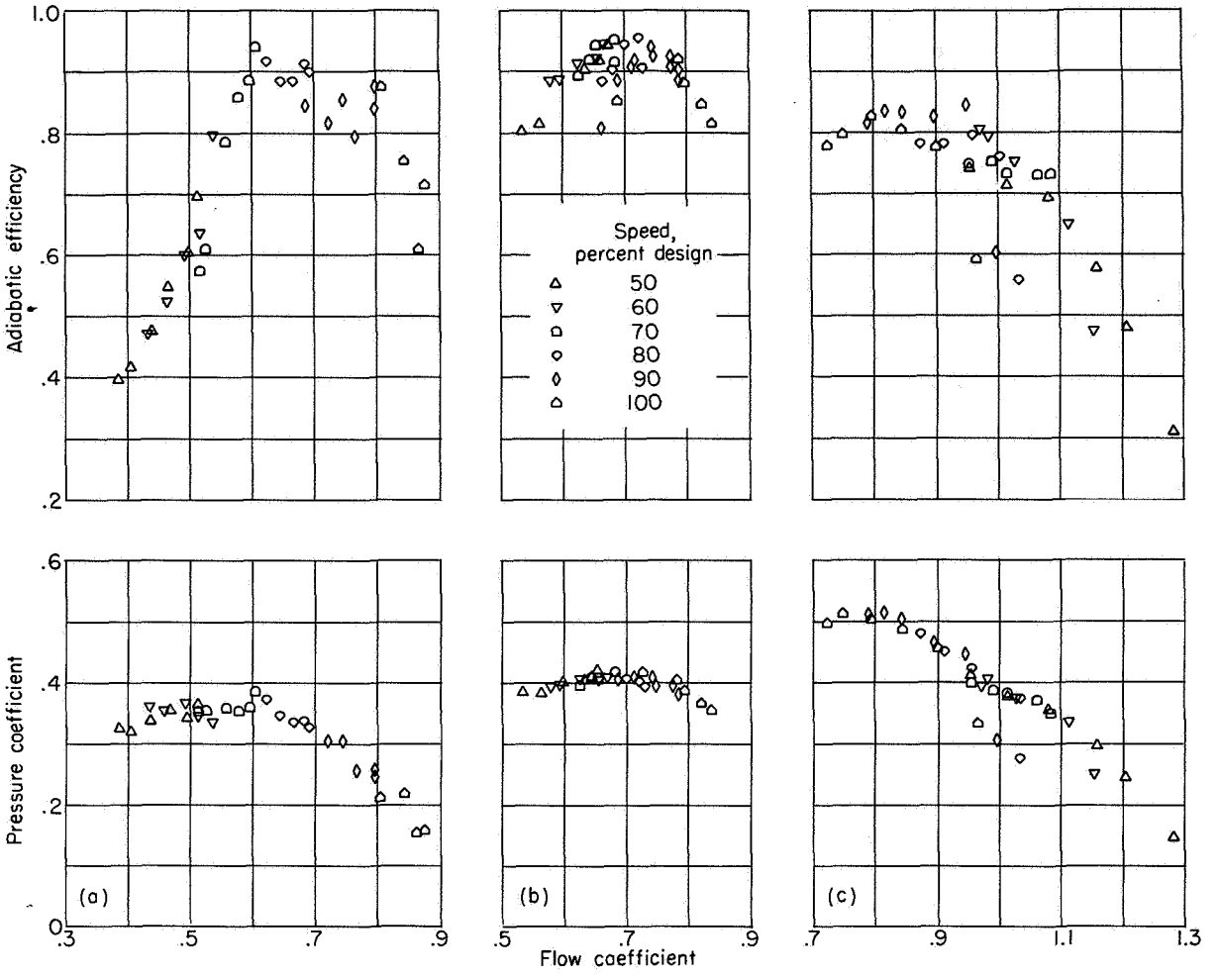

(a) Stage 1. (b) Stage 5. (c) Stage 10.

FIGURE 261.—Generalized stage performance for stages 1, 5, and 10 of reference 258.

is compromised to favor part-speed operation. No effects of interaction or unstalling hysteresis are evaluated for cases IV and V.

HYPOTHETICAL COMPRESSOR, CASES I, II, AND III

The basic hypothetical compressor was identical for the first three cases considered and was the same as that presented in references 294 and 295. The compressor had 12 stages of constant tip diameter. All stages had identical performance in terms of pressure coefficient and efficiency against flow coefficient, except for the stalling characteristics. Pertinent reference-point details of the compressor are as follows:

Over-all total-pressure ratio	7.75
Inlet specific weight flow, equivalent flow per sq ft annulus area	33.5
Inlet corrected tip speed, ft/sec	950
Absolute inlet-air angle at pitch radius of each stage, deg	22½
Flow coefficient for each stage	0.69
Pressure coefficient for each stage	0.3

Individual stage hub-tip radius ratios, area ratios, mean-radius ratios and reference-point pressure ratios are listed in table VIII(a).

The assumptions of stall type, interactions, and hysteresis effects for cases I to III are as follows:

Case	Type of stall			Interactions	Hysteresis effects
	Stages 1 to 4	Stages 5 to 8	Stages 9 to 12		
I	Progressive	Progressive and abrupt	Abrupt	None	None
II	Progressive	Progressive and abrupt	Abrupt	Stages 1 to 4	Stage 1
III	Progressive	Progressive and abrupt	Abrupt	Stages 1 to 8	Stage 1

The individual stage curves assumed for each configuration are discussed in the section DISCUSSION OF COMPUTED PERFORMANCE.

HYPOTHETICAL COMPRESSOR, CASES IV AND V

Reference 248 suggests that improvements in part-speed performance of multistage compressors might be obtained by matching the stages so that at design speed the inlet stages operate at the high end and the rear stages at the low end of their flow-coefficient ranges. Case IV was therefore considered in order to evaluate the potential of such stage-matching compromises. Thus, the match-point flow coefficients for case IV were arbitrarily varied from 0.76 in the first stage to 0.63 in the twelfth stage, as compared with a constant value of 0.69 for cases I to III. The stage characteristics used were identical to those for case I. Since the results of case IV indicated that this stage-matching compromise greatly reduced the complete-compressor-stall or surge margin at design speed, case V was considered, in which a thirteenth stage was added. The performance characteristics for this added stage were assumed identical to those for stages 9 to 12, and the match-point flow coefficient was taken as 0.626. As in previous cases, the compressor was assumed to have a constant tip diameter.

Pertinent reference-point values for cases IV and V are as follows:

	Case IV	Case V
Number of stages	12	13
Over-all total-pressure ratio	7.73	9.10
Inlet specific weight flow, equivalent flow per sq ft of annulus area	35.96	35.96
Inlet corrected tip speed, ft/sec	950	950
Absolute inlet-air angle at pitch radius of each stage, deg	22½	22½

Individual stage parameters for these two cases are listed in table VIII(b).

TABLE VIII.—REFERENCE-POINT VALUES

(a) Cases I, II, and III

Stage	Area ratio [a]	Mean-radius ratio [b]	Hub-tip radius ratio	Stage pressure ratio
1	0.8431	1.071	0.5000	1.179
2	.8510	1.046	.6063	1.196
3	.8547	1.033	.6795	1.203
4	.8580	1.025	.7348	1.204
5	.8630	1.019	.7779	1.202
6	.8695	1.015	.8120	1.198
7	.8720	1.012	.8389	1.192
8	.8780	1.010	.8613	1.186
9	.8835	1.008	.8794	1.179
10	.8875	1.007	.8943	1.172
11	.8920	1.0055	.9068	1.166
12	.8960	1.0045	.9173	1.159

(b) Cases IV and V

Stage	Area ratio [a]	Mean-radius ratio [b]	Hub-tip radius ratio	Stage pressure ratio	Flow coefficient	Pressure coefficient
1	0.9009	1.046	0.5000	1.136	0.760	0.231
2	.8929	1.038	.5696	1.157	.741	.252
3	.8889	1.031	.6299	1.173	.723	.270
4	.8857	1.026	.6810	1.186	.705	.287
5	.8818	1.022	.7246	1.197	.686	.304
6	.8803	1.018	.7623	1.205	.668	.320
7	.8806	1.018	.7944	1.210	.650	.335
8	.8651	1.014	.8261	1.205	.650	.335
9	.8787	1.010	.8516	1.198	.650	.335
10	.8850	1.008	.8709	1.193	.643	.340
11	.8857	1.007	.8867	1.189	.636	.346
12	.8889	1.006	.9003	1.183	.630	.350
13	.8897	1.006	.9100	1.177	.626	.353

[a] Ratio of exit to inlet area for stage.
[b] Ratio of exit to inlet mean radius for stage.

RANGE OF CALCULATIONS

For each case considered, calculations were made for a range of speeds of 50 to 110 percent of the reference value. The maximum flow considered at each speed was the estimated exit-vane choke flow. For these examples, choke flow was assumed to exist at a value of specific weight flow at the exit of the last stage of 41.4 pounds per second per square foot of annulus area. This value of specific flow is based on flow conditions at the exit of the last stage. The minimum flow considered at each speed was that at which a discontinuity in the performance curve of any stage was encountered. As indicated in chapter XII, discontinuities in multistage-compressor performance at a given speed may lead to either compressor surge or complete compressor stall. In the computation of intermediate-speed performance for cases II and III, operation with the inlet stage stalled and unstalled was considered.

DISCUSSION OF COMPUTED PERFORMANCE

CASE I

The assumed stage performance curves for case I are presented in figure 262. The first four stages were assumed to have only a progressive stall, and the pressure coefficient and efficiency were taken as continuous functions of the flow coefficient, as shown in figure 262(a). Stages 5 to 8 were assumed to have an initial progressive stall and an abrupt stall at lower values of flow coefficient (fig. 262(b)). Stages 9 to 12 were assumed to have only an abrupt stall (fig. 262(c)). As noted in figures 262 (b) and (c), a discontinuity of stage performance characteristics was considered to result from abrupt stall. The stage characteristics for stage pressure ratios below 1.00, which were the same for all stages, are given in figure 263.

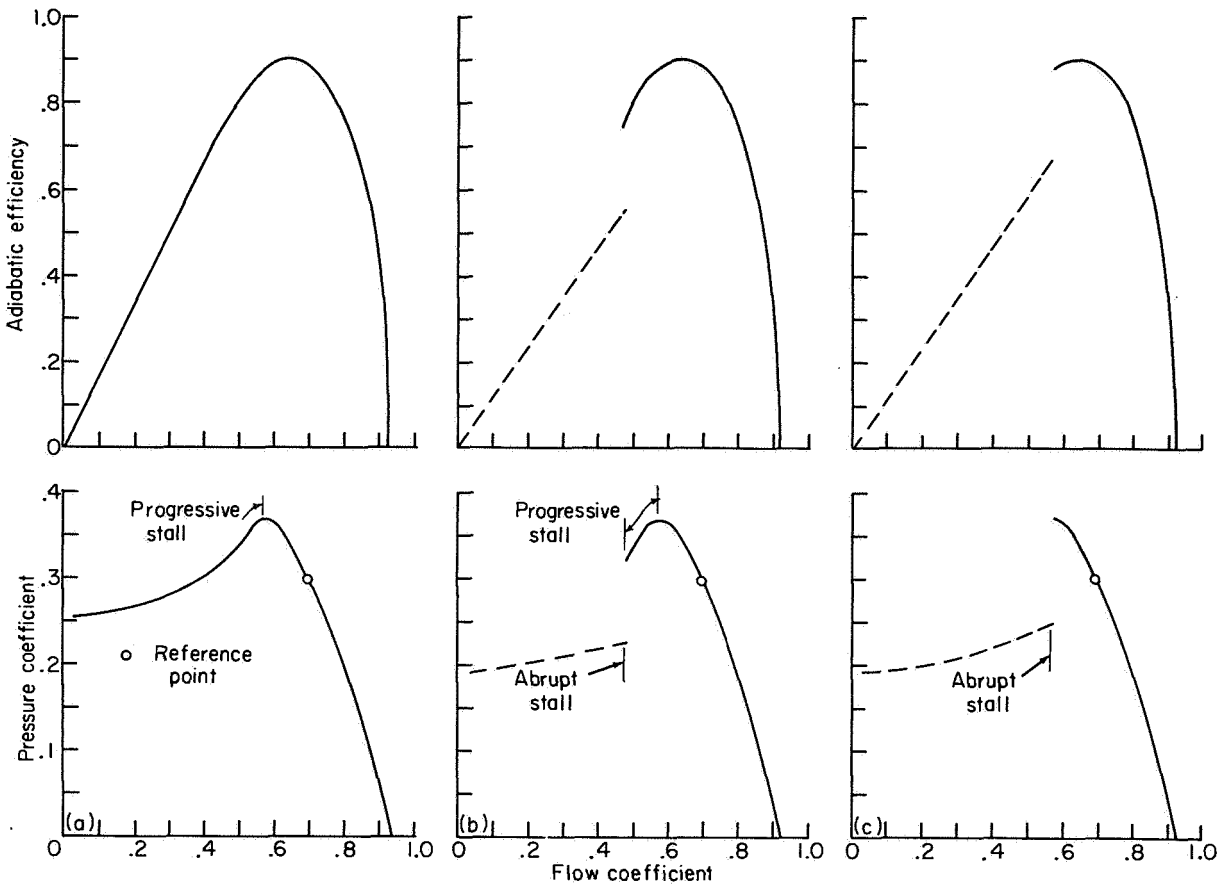

(a) Stages 1 to 4. (b) Stages 5 to 8. (c) Stages 9 to 12.

FIGURE 262.—Assumed stage performance characteristics for case I.

As noted in appendix B of reference 294, a modified computational procedure was used when stages operated at turbining pressure ratios. Interaction effects were considered negligible throughout the compressor.

Computed over-all performance.—The computed over-all performance map for case I is given in figure 264 as a plot of over-all total-pressure ratio against specific weight flow. The over-all total-pressure ratio, which is the ratio of total pressure at the exit of last stage to that at the compressor inlet, would not include an exit-vane or diffuser loss. The specific weight flow is the equivalent weight flow per square foot of annulus area at the compressor inlet. Also shown in figure 264 are contours of constant efficiency, the estimated choking-flow condition for the exit vanes, and the estimated complete-compressor-stall limit.

The computed maximum efficiencies for this case varied from slightly over 0.70 at 50 percent of reference speed to approximately 0.87 at 100-percent speed. The values of computed efficiency at the lowest speeds considered indicate that stage mismatching at low speeds will not completely explain the extremely low efficiencies obtained experimentally for some high-pressure-ratio multistage axial-flow compressors.

The exit-vane choke limit was the maximum flow considered at each speed. Further decreases in over-all pressure ratio would not alter the stage matching but would merely increase the losses downstream of the point of choking.

The complete-compressor-stall limit at each speed was the flow at which a discontinuity of performance occurred because of abrupt stall of some stage. Occurrence of abrupt stall in a stage results in very large flow fluctuations that could